

nature

QUANTUM MOTION

Precise measurement of trapped nanosphere enables cooling to ground state

Coronavirus
Genetic association studies reveal links to COVID risk

Climate imbalance
Deforestation turns part of Amazonia from carbon sink to source

Internal exam
Probing microbial metabolism in the microbiome of the gut

Nature.2021.07.17

[Sat, 17 Jul 2021]

- [This Week](#)
- [News in Focus](#)
- [Opinion](#)
- [Work](#)
- [Research](#)

| [Next section](#) | [Main menu](#) |

Donation

| [Next section](#) | [Main menu](#) |

This Week

- **[Cities must protect people from extreme heat](#)** [14 July 2021]
Editorial • The North American heatwave highlights the need for urban planners to target extreme heat when designing climate-adaptation strategies.
- **[Does the fight against hunger need its own IPCC?](#)** [13 July 2021]
Editorial • Any plan to create an intergovernmental science panel on food science and policy must protect its independence.
- **[I critiqued my past papers on social media — here's what I learnt](#)** [12 July 2021]
World View • The systems of science must reward honesty about mistakes to speed progress.
- **[Genomics charts a deadly bacterium's leap from pigs to humans](#)** [07 July 2021]
Research Highlight • Samples collected over several decades help scientists to trace the path taken by *Streptococcus suis*.
- **[Beetles make 'Teflon' to grease their knees](#)** [07 July 2021]
Research Highlight • The protein-based substance found in the leg joints of beetles and at least one other insect is a superb lubricant.
- **[Newfound 'fairy lantern' could soon be snuffed out forever](#)** [07 July 2021]
Research Highlight • Wild boars have destroyed three of the four known specimens of a bizarre plant in the forests of Malaysia.
- **[A swarm of black holes could explain Galactic fluffiness](#)** [12 July 2021]
Research Highlight • Diffuse Milky Way formation might have been depleted by star-hurling black holes.
- **[A graphene cloak keeps artworks' colours ageless](#)** [07 July 2021]
Research Highlight • A layer of carbon atoms preserves a painting's vibrant hues — and can be applied and removed without damage.

- **Telecoms satellites' new purpose: spying on Earth's magnetic field** [08 July 2021]

Research Highlight • Clues to the forces generated by the planet's core emerge from observations intended for satellite navigation.

- **Meth-addicted trout swim for a hit** [06 July 2021]

Research Highlight • Fish that have been exposed to the highly addictive stimulant for several weeks show signs of withdrawal if deprived of the drug.

- EDITORIAL
- 14 July 2021

Cities must protect people from extreme heat

The North American heatwave highlights the need for urban planners to target extreme heat when designing climate-adaptation strategies.





•

[Download PDF](#)



Boys cooling themselves on a hot day in Ahmedabad, India, where a heatwave action plan is helping to save lives. Credit: Amit Dave/Reuters/Alamy

Last month's heatwave shattered temperature records across the western United States and Canada. On 29 June, the Canadian village of Lytton hit nearly 50 °C — an astonishing increase of almost 5 °C on the previous national high. A day later, fire burnt most of Lytton to the ground, killing two people. Elsewhere, the cities of Vancouver, Portland and Seattle saw hundreds of people die during the same three-day heatwave.

As global temperatures rise, [the risks from extreme heat](#) — defined as periods when a region's temperatures are abnormally high compared with the average — are also rising. Heat has always posed a threat to urban living, with heat-absorbing surfaces such as asphalt sending the mercury soaring. But climate change means that heatwaves now happen more frequently and are more intense than in the past. This is one of the most underappreciated hazards of climate change. Researchers say that the Pacific

Northwest heatwave, for instance, would have been “virtually impossible” in the absence of human-induced global warming (see go.nature.com/3xatcgw).

And although heat can kill anywhere, the risk is greater in cities. One study presented at a conference last December estimates that people’s exposure to extreme heat in more than 13,000 cities more than doubled between 1983 and 2016. Another study published last year estimated that air temperatures in two cities — Jacobabad in southern Pakistan and Ras Al-Khaimah in the United Arab Emirates — have already passed the human body’s limits of survivability on their hottest and most humid days ([C. Raymond et al. Sci. Adv. 6, eaaw1838; 2020](https://doi.org/10.1126/sciadv.6.eaaw1838)).

Climate researchers have long warned that global warming makes heatwaves such as that seen in North America this year much more likely. This means that urban planners must work harder to incorporate extreme heat into climate-adaptation strategies.

Some city authorities have been preparing for such a scenario. Take Ahmedabad in western India. After a devastating heatwave in 2010, the city developed an action plan with three elements: raising awareness about how people can protect themselves from extreme heat; creating an early warning system for when meteorologists forecast a heatwave; and training medical staff to better recognize and treat people suffering from extreme heat. One estimate suggests that the programme has saved 1,190 lives a year, and a similar approach has been rolled out for more than a dozen other cities across India.

Another idea known as ‘cool roofs’, which are painted white or covered with energy-reflecting materials that absorb less heat, can reduce temperatures inside buildings by 2–5 °C when compared with conventional roofing.

But such climate solutions need to be implemented effectively and efficiently on a city-wide scale for them to have any significant impact. And for that to happen, governments need to require the construction industry to incorporate heat mitigation into their building projects through green building-certification programmes. The provision of subsidies for green buildings is also an option. In Barcelona, Spain, for example, the authorities are subsidizing 75% of the costs of 10 new green-roof projects in the city.

At the same time, cities must target heat-mitigation efforts at those most affected by the heat. That includes people in lower-income neighbourhoods, which have, historically, often been deprived of parks, tree-lined streets and other green spaces that are a common component of wealthier areas. Scientists have also found shocking correlations between race and heat exposure in cities in the United States. Studies show that historical urban policies have left communities of colour at higher risk of heat-related illness or death than people in predominantly white neighbourhoods.

Cool corridors

One pioneer in this concept of ‘heat equity’ is Paris, where officials are building a city-wide network of ‘cooling islands’ — which include spaces such as parks and pools — linked by cool walkways. Meanwhile, Medellín in Colombia has targeted low-income areas of the city for tree planting; more than 10,000 trees have been planted along 36 ‘green corridors’, resulting in a 2 °C reduction in surface temperatures. Government officials must continue to track the results of such experiments and make use of the best available evidence to green their cities.

This week, the mayors of 31 cities in the C40 global network of cities working to fight climate change have committed to ensuring that, by 2030, 70% of city residents can get to a green or blue public space with no more than a 15-minute walk or bicycle ride. Annual accountability check-ins must ensure that true progress is made on this ambitious goal.

In all cases, city and regional governments must better organize their heat-fighting efforts. It’s not feasible to react to heat after the fact — by the time hospitals are overcrowded with people affected by heat stroke, electrical grids have crashed under the weight of demand for air conditioning, and coroners are counting the bodies, it’s too late. Every death from heat is preventable if a person can access shade, water or other means of cooling.

As we face a future with longer, hotter and more frequent heatwaves, cities must escalate their planning for extreme heat. It needs to be on a par with preparations for other disasters such as earthquakes, floods and hurricanes. That applies not only to tropical cities but also to those in temperate climes.

Who, after all, would have flagged heat as a major risk factor for Vancouver, at a latitude of more than 49 degrees north? Yet, after June's deadly heatwave, the city's officials are now working to incorporate extreme heat into their emergency plans. It is the only way forwards.

Nature **595**, 331-332 (2021)

doi: <https://doi.org/10.1038/d41586-021-01903-1>

Related Articles



- [**Racism is magnifying the deadly impact of rising city heat**](#)



- [**Climate change made North America's deadly heatwave 150 times more likely**](#)



- [**Climate change made Australia's devastating fire season 30% more likely**](#)



- [**Climate change made European heatwave up to 3°C hotter**](#)

Subjects

- [**Climate change**](#)

- [Climate sciences](#)
- [Policy](#)

nature careers

[Jobs](#) >

- [Postdoctoral Training Fellow](#)

Francis Crick Institute

London, United Kingdom

- [Senior Business Manager](#)

Francis Crick Institute

London, United Kingdom

- [Postdoctoral Research Fellow in Pharmacogenomics Pain Management](#)

The University of British Columbia (UBC)

Vancouver, Canada

- [Postdoctoral Research Fellow in Pain Management and C. elegans](#)

The University of British Columbia (UBC)

Vancouver, Canada

[Download PDF](#)

Related Articles

-  Racism is magnifying the deadly impact of rising city heat
-  Climate change made North America's deadly heatwave 150 times more likely
-  Climate change made Australia's devastating fire season 30% more likely
-  Climate change made European heatwave up to 3°C hotter

Subjects

- Climate change
- Climate sciences
- Policy

This article was downloaded by **calibre** from <https://www.nature.com/articles/d41586-021-01903-1>

- EDITORIAL
- 13 July 2021

Does the fight against hunger need its own IPCC?

Any plan to create an intergovernmental science panel on food science and policy must protect its independence.





•

[Download PDF](#)



Any process to strengthen science in food-systems policy must protect the knowledge of vulnerable groups, especially Indigenous farmers (pictured, rice farming in Bangladesh). Credit: Rehman Asad/Barcroft Media/Getty

Later this year, politicians and policymakers are due to meet to make crucial decisions on protecting biodiversity, mitigating climate change and ending hunger — all part of the United Nations Sustainable Development Goals. Delegates at two of these meetings — on biodiversity and climate — benefit from the advice of organizations in which thousands of scientists periodically review research in the field. There is no analogous system of scientific advice informing policymaking in food and agriculture. But that might be about to change.

September sees the UN Food Systems Summit. ‘Food systems’ incorporates the processes and the people involved in catching and growing, processing, transporting and eating food. Delegates will discuss how to strengthen scientific advice, possibly by creating an intergovernmental panel of scientists, who would review relevant research, for example on improving diet and nutrition, or on how to raise standards of living for small farmers — enabling policymakers to make evidence-based decisions.

It's an idea inspired by the Intergovernmental Panel on Climate Change (IPCC), whose reports inform conferences of world leaders — such as the UN climate convention, which will meet in Glasgow, UK, in November. IPCC reports led to the 2015 Paris agreement to keep average global temperature rise to within 2 °C of pre-industrial levels, and to the 1997 Kyoto Protocol on reducing emissions.



[Imagine a world without hunger, then make it happen with systems thinking](#)

There are hundreds of food systems researchers advising various organs of the UN, including the Food and Agriculture Organization and the Committee on World Food Security, both in Rome. But the Sustainable Development Goals overall have no political body of world leaders similar to the UN climate convention, and most of the individual goals — including ending hunger — lack an intergovernmental scientific panel with the budget and profile of the IPCC or the Intergovernmental Science-Policy Platform on Biodiversity and Ecosystem Services (IPBES).

The UN has appointed a scientific group to channel research input into the Food Systems Summit. Last week, the group held two days of talks, where many researchers voiced frustration at their inability to break through to decision makers. They say that boosting the profile of the science-to-policy process is more urgent now than ever. More than 800 million people go

hungry every day. Even before the coronavirus pandemic, the Sustainable Development Goal to end hunger by 2030 was out of reach.

The idea of creating an intergovernmental panel of scientists in food systems isn't new. And as talks to develop it get under way, at least two things need to happen. First, it will be important to review existing and previous efforts to organize scientific advice related to food systems. Second, those charged with developing any new science-to-policy process must study and learn from the IPCC and IPBES: how they are structured and governed; how they are starting to work together; how they navigate topics that, like food systems, are both deeply political, and must take into account the voices of industry, non-governmental organizations, farmers, Indigenous people and others. And, crucially, how they are reaching out to under-represented groups, incorporating their knowledge, and protecting their interests. Between them, the IPCC, IPBES, experts advising the Committee on Food Security, and UN environment conventions have a reservoir of experience.

Integrity and independence

One overarching lesson from both the IPCC and IPBES is the need to maintain integrity in the research-review process. This is not easy. It requires a high degree of trust between the participants, and the governments that fund the panels must protect the independence of the processes.



Ending Hunger: Science must stop neglecting smallholder farmers

For much of the 1990s, lobby groups representing governments and businesses with fossil-fuel interests tried hard to interfere with the IPCC's work. They came closest in the mid-1990s, when researchers concluded that humans are warming the planet. The stakes were high because this finding effectively signalled the beginning of the end of the fossil-fuel age. Instead of accepting it and leading the necessary energy transformation, some governments and corporations challenged the findings and criticized the scientists involved, both during the review process and after the IPCC's second assessment report was issued in 1995. Fortunately, the IPCC's leaders stood firm and the conclusions were not changed; it was only because of the body's design that they were able to do so.

The world of the Sustainable Development Goals has many of the same stakeholders as climate change. And an intergovernmental scientific body for today must value the knowledge and perspectives of small family farmers, artisanal fishers and large numbers of Indigenous people — whose knowledge and needs have long been neglected by science and in policy.

Hunger — along with biodiversity loss and climate change — is an existential threat facing much of humanity. Scientists advocating stronger science–policy links need to do their due diligence. Whether the outcome is a new intergovernmental science-to-policy process, or more powers for existing ones, a stronger partnership between scientists, key stakeholders and politicians is now needed more than ever.

Nature **595**, 332 (2021)

doi: <https://doi.org/10.1038/d41586-021-01904-0>

Related Articles

-  • [Ending Hunger: Science must stop neglecting smallholder farmers](#)



- [Imagine a world without hunger, then make it happen with systems thinking](#)
- [The problem with growing corporate concentration and power in the global food system](#)
- [Transforming food systems is within reach](#)
- [We all stand together](#)

Subjects

- [Agriculture](#)
- [Government](#)
- [Policy](#)
- [Sustainability](#)

nature careers

[Jobs](#) >

- [Postdoctoral Training Fellow](#)

Francis Crick Institute

London, United Kingdom

- [Senior Business Manager](#)

Francis Crick Institute

London, United Kingdom

- [Postdoctoral Research Fellow in Pharmacogenomics Pain Management](#)

The University of British Columbia (UBC)

Vancouver, Canada

- [Postdoctoral Research Fellow in Pain Management and C. elegans](#)

The University of British Columbia (UBC)

Vancouver, Canada

[Download PDF](#)

Related Articles



- [Ending Hunger: Science must stop neglecting smallholder farmers](#)



- [Imagine a world without hunger, then make it happen with systems thinking](#)
- [The problem with growing corporate concentration and power in the global food system](#)
- [Transforming food systems is within reach](#)
- [We all stand together](#)

Subjects

- [Agriculture](#)
 - [Government](#)
 - [Policy](#)
 - [Sustainability](#)
-

This article was downloaded by **calibre** from <https://www.nature.com/articles/d41586-021-01904-0>

| [Section menu](#) | [Main menu](#) |

- WORLD VIEW
- 12 July 2021

I critiqued my past papers on social media — here's what I learnt



The systems of science must reward honesty about mistakes to speed progress.

- [Nicholas P. Holmes](#) 0

1. [Nicholas P. Holmes](#)

1. Nicholas P. Holmes studies hand movements and perception at the University of Nottingham, UK, and hosts 'The Error Bar' podcast.

[View author publications](#)

You can also search for this author in [PubMed](#) [Google Scholar](#)





•

[Download PDF](#)

Every year in June, I discover that the most self-critical scientists are final-year undergraduates. In the results section of their dissertations, they mercilessly apply the rules that we teach them. Their discussions are largely of limitations, catalogues of failure. Their conclusions can be brutal.

Somewhere between graduating and beginning our careers, we researchers seem to lose this flair for self-criticism. We become more invested in publications, grants and jobs. These incentives drive us on. But they also

narrow our vision. As investment in our work deepens, we become blind to its faults.

The incentives of academic life seem to require that we abandon self-criticism. Papers are typically written after the results are known, as if everything worked as expected. Manuscripts are often submitted without acknowledgement of limitations; perhaps to be added later, if reviewers request. Guidelines for funding applications offer little opportunity to talk about error, uncertainty or failure. Candidates applying for academic jobs rarely discuss experiments that didn't replicate, rejected papers or unsuccessful grant applications. It is as though any admission of fallibility will be treated harshly by reviewers.



Beware performative reproducibility

A scientific record that includes only successes is incomplete. Failure, error, reflection and self-correction are too rarely published. If we are not honest about our mistakes, scientific progress will be slowed.

On Good Friday this year, traditionally a time of self-reflection in the Christian calendar, I began critiquing my own scientific record — writing down something critical about each of my publications. Much of my career, my writing and now my podcast, 'The Error Bar', has been spent criticizing others' work.

In 57 tweets (see go.nature.com/2vhm7sb), I recalled the worst things about each of my publications. What I did wrong, what I wouldn't repeat, what would work better. "The effect size we studied was too small to be worth any further study," I wrote of one. "Too many behavioural tasks," I noted of another.

I didn't know it at the time, but I was following the example of psychologists engaged in the Loss-of-Confidence Project, who seek to encourage scientific self-correction ([J. M. Rohrer et al. Perspect. Psychol. Sci. https://doi.org/gh6f6r; 2021](https://doi.org/gh6f6r)).



What my retraction taught me

Like them, I found this reflection enlightening — it highlighted my mistakes and removed a weight of self-doubt. I now worry less that I've missed something big, or got something very wrong.

Most illuminating were other scientists' reactions. Some told me it was "brave" or "crazy". I understand why, but that reaction is troubling. Self-criticism in science is desirable, so a system that discourages authors from doing it needs fixing. How should we begin?

To start, be your own harshest critic. On social media or PubPeer, be explicit about the weaknesses of your work. When reviewing or editing

others, remember your own failings, the constraints on your work and the incentives that drove you. If you discover serious errors, be willing to correct or retract. This could be a positive process of study, development and communication rather than hiding, moving on or doubling-down. One excellent example is from Sam Schwarzkopf's laboratory at University College London, which retracted a brain-imaging paper after discovering, studying and publicizing their analytical errors ([B. de Haas *Nature* 589, 331; 2021](#)).

In addition, the systems of publication, funding and employment need to nurture and reward such honesty. Open Science lends itself to self-criticism and self-correction. When you pre-register a study, you specify what you're going to do and how. When you publish, you either confirm that you did it or explain why you didn't. This mode of publishing encourages honesty and transparency. On publication, making data freely available improves transparency; acknowledging errors improves the public's perception of trustworthiness in science. The [*Journal of Trial and Error*](#), which launched last year, encourages authors to reflect on errors and discuss them when they inevitably come to light. But science shouldn't need separate journals for reporting failures — it must be part of normal practice.

People applying for research funds could be required to include criticism of their own work, and to deal explicitly with alternative hypotheses. Those who are lucky enough to receive funding should then report on the project's errors and failures, not just on its outputs and successes. Hunting out our own weaknesses will make us better scientists.

In 2019, my institution, the University of Nottingham in the United Kingdom, signed the San Francisco Declaration on Research Assessment. This committed us to stop using journal impact factors and similar metrics to assess individuals. This changed our hiring, evaluation and promotion criteria. To build on these improvements, we could ask candidates to engage in self-criticism, to say what they would now do differently. We could request a 'negative CV' — a list of failed applications and rejected papers.

By rediscovering our inner undergraduate, reflecting on our errors and opening up our science to scrutiny, we can free ourselves from the fear that our failings might be uncovered.

Nature **595**, 333 (2021)

doi: <https://doi.org/10.1038/d41586-021-01879-y>

Competing Interests

The author declares no competing interests.

Related Articles



- [Beware performative reproducibility](#)



- [How quality control could save your science](#)



- [What my retraction taught me](#)



- [Institutions can retool to make research more rigorous](#)



- [Reform retractions to make them more transparent](#)



- [Pandemic researchers — recruit your own best critics](#)

Subjects

- [Research management](#)
- [Lab life](#)

nature careers

[Jobs](#) >

- [Postdoctoral Training Fellow](#)

Francis Crick Institute

London, United Kingdom

- [Senior Business Manager](#)

Francis Crick Institute

London, United Kingdom

- [Postdoctoral Research Fellow in Pharmacogenomics Pain Management](#)

The University of British Columbia (UBC)

Vancouver, Canada

- [Postdoctoral Research Fellow in Pain Management and C. elegans](#)

The University of British Columbia (UBC)

Vancouver, Canada

[Download PDF](#)

Related Articles



- [Beware performative reproducibility](#)



- [How quality control could save your science](#)



- [What my retraction taught me](#)



- [Institutions can retool to make research more rigorous](#)



- [Reform retractions to make them more transparent](#)



- [**Pandemic researchers — recruit your own best critics**](#)

Subjects

- [Research management](#)
- [Lab life](#)

This article was downloaded by **calibre** from <https://www.nature.com/articles/d41586-021-01879-y>.

| [Section menu](#) | [Main menu](#) |



Pork is sprinkled with disinfectant in Beijing in 2005, when a pig-borne disease made scores of people in China ill. Credit: China Photos/Getty

Microbiology

07 July 2021

Genomics charts a deadly bacterium's leap from pigs to humans

Samples collected over several decades help scientists to trace the path taken by *Streptococcus suis*.





•

A genomic analysis has narrowed down where and when a deadly bacterium jumped from pigs to humans: in Europe in the 1960s or 1970s.

The bacterium *Streptococcus suis* has long been known as a pig pathogen. But, since 1998, it has caused three large outbreaks in people in China, and a sharp increase in human infections globally, making it a serious public-health concern.

To trace the evolution of *S. suis*, Jinquan Li at Huazhong Agricultural University in Wuhan, China, Ye Feng at Zhejiang University in Hangzhou, China, and their colleagues analysed 1,634 *S. suis* genomes collected from pigs and humans across 14 countries over 36 years. The genomes fell into

three distinct groups, one of which was found mostly in humans. This group included strains that caused severe disease in zebrafish, which the authors used as a model of human disease.

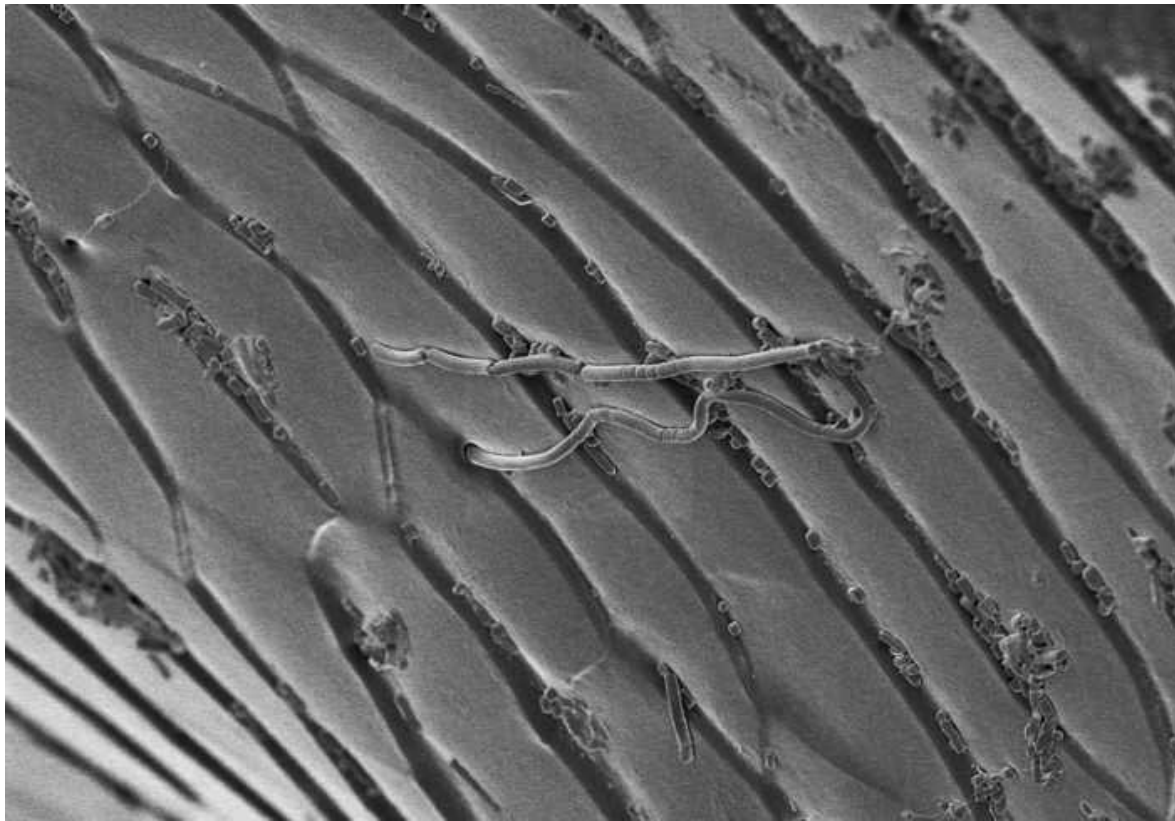
Some of those strains had been collected from pigs that showed no signs of illness, suggesting that asymptomatic animals might have acted as carriers, spreading the bacterium to people. The researchers traced the human group's origins to Europe during the 1960s and 1970s, when the continent was exporting pigs worldwide.

[EMBO Mol. Med. \(2021\)](#)

- [Microbiology](#)

This article was downloaded by **calibre** from <https://www.nature.com/articles/d41586-021-01845-8>

| [Section menu](#) | [Main menu](#) |



A lubricant seeps from pores on the leg of a darkling beetle. Credit: K. Nadein *et al./Proc. R. Soc. B* ([CC BY 4.0](#))

Biomaterials

07 July 2021

Beetles make ‘Teflon’ to grease their knees

The protein-based substance found in the leg joints of beetles and at least one other insect is a superb lubricant.





•

The leg joints of beetles are lubricated with a versatile substance that is as hard-wearing as Teflon.

Until now, scientists have had little understanding of how insects' joints reduce friction and are protected from wear and tear. Vertebrates have enclosed joints that are bathed in a liquid lubricant, which minimizes friction and helps to protect the surfaces of bones where they meet. But insects have an external skeleton, and their joints are open to the air.

Konstantin Nadein at the Christian-Albrechts University of Kiel in Germany and his colleagues used a scanning electron microscope to image the 'knee' joint of the darkling beetle (*Zophobas morio*). They found that the joint's

surfaces are covered in pores through which a protein-based substance oozes. Chemical analysis found that this is made up of proteins and fatty acids.

When the authors compared this grease to other lubricants experimentally, they found that the substance reduced friction to a similar degree as the chemical coating Teflon. They also found pores and lubricant in the joints of several other species of beetle and a wood roach.

[Proc. R. Soc. B \(2021\)](#)

- [Biomaterials](#)

This article was downloaded by **calibre** from <https://www.nature.com/articles/d41586-021-01853-8>

| [Section menu](#) | [Main menu](#) |



An umbrella-shaped structure of unknown function crowns a recently described species of fairy lantern. Credit: Siti Munirah Mat Yunoh *et al./PhytoKeys* ([CC BY 4.0](#))

Conservation biology

07 July 2021

Newfound ‘fairy lantern’ could soon be snuffed out forever

Wild boars have destroyed three of the four known specimens of a bizarre plant in the forests of Malaysia.





•

Researchers have discovered a new species of ‘fairy lantern’, leafless plants that look like tiny glowing lights. Sadly, however, the organism might already be on the verge of extinction.

Plants in the genus *Thismia*, colloquially called ‘fairy lanterns’, draw nutrients from underground fungi and grow in parts of Asia, Australasia and the Americas. Siti Munirah Mat Yunoh at the Forest Research Institute Malaysia in Kepong and her colleagues described a new species of *Thismia* that was first found in 2019 in a Malaysian rain forest. The scientists named the plant *Thismia sitimeriamiae* after the mother of the local explorer who

discovered it, in honour of her support for her son's nature-conservation efforts.

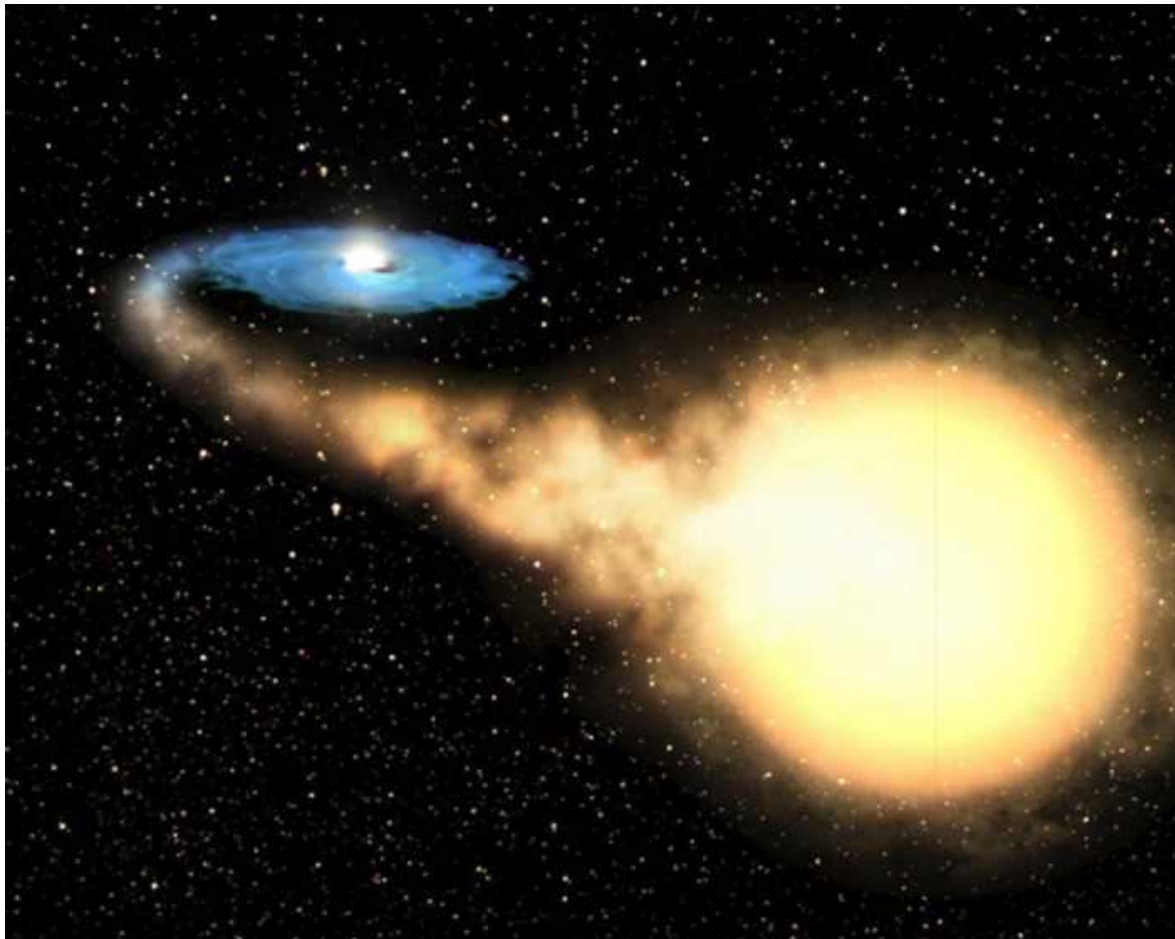
Thismia sitimeriamiae is only about two centimetres tall, and sports an orange flower shaped like a funnel with an umbrella-like structure on top. The plant seems to be so rare that it should be considered critically endangered: just four individuals of *T. sitimeriamiae* have ever been seen, and wild boars have destroyed all but one of these, the authors say.

[PhytoKeys \(2021\)](#)

- [Conservation biology](#)

This article was downloaded by **calibre** from <https://www.nature.com/articles/d41586-021-01858-3>

| [Section menu](#) | [Main menu](#) |



Although black holes (left, surrounded by a disc of hot gas; artist's impression) often consume matter from stars, their gravity can also fling stars outwards. Credit: ESA, NASA and Felix Mirabel

Astronomy and astrophysics

12 July 2021

A swarm of black holes could explain Galactic fluffiness

Diffuse Milky Way formation might have been depleted by star-hurling black holes.





•

An ancient star cluster's long 'tails' of stars seem to be the handiwork of an unseen clutch of black holes: their gravitational tugs fling stars outwards, and Galactic forces then pull the stars farther out.

Astronomers classify the group of stars called Palomar 5 as a globular cluster, a roughly spherical collection of old stars. Located some 20,000 parsecs from Earth, Palomar 5 is among the 'fluffiest' — or least dense — of the Milky Way's globular clusters. But Mark Gieles at the University of Barcelona in Spain and his colleagues say the evidence suggests that the cluster was once much denser.

The researchers modelled how a variety of star clusters with Palomar 5's orbit would evolve over a period of 11.5 billion years. The starting points that evolved into the best matches for Palomar 5 and its stellar tails were clusters in which black holes formed and stuck around, their gravity helping to push stars out to create the fluffy cluster we see today.

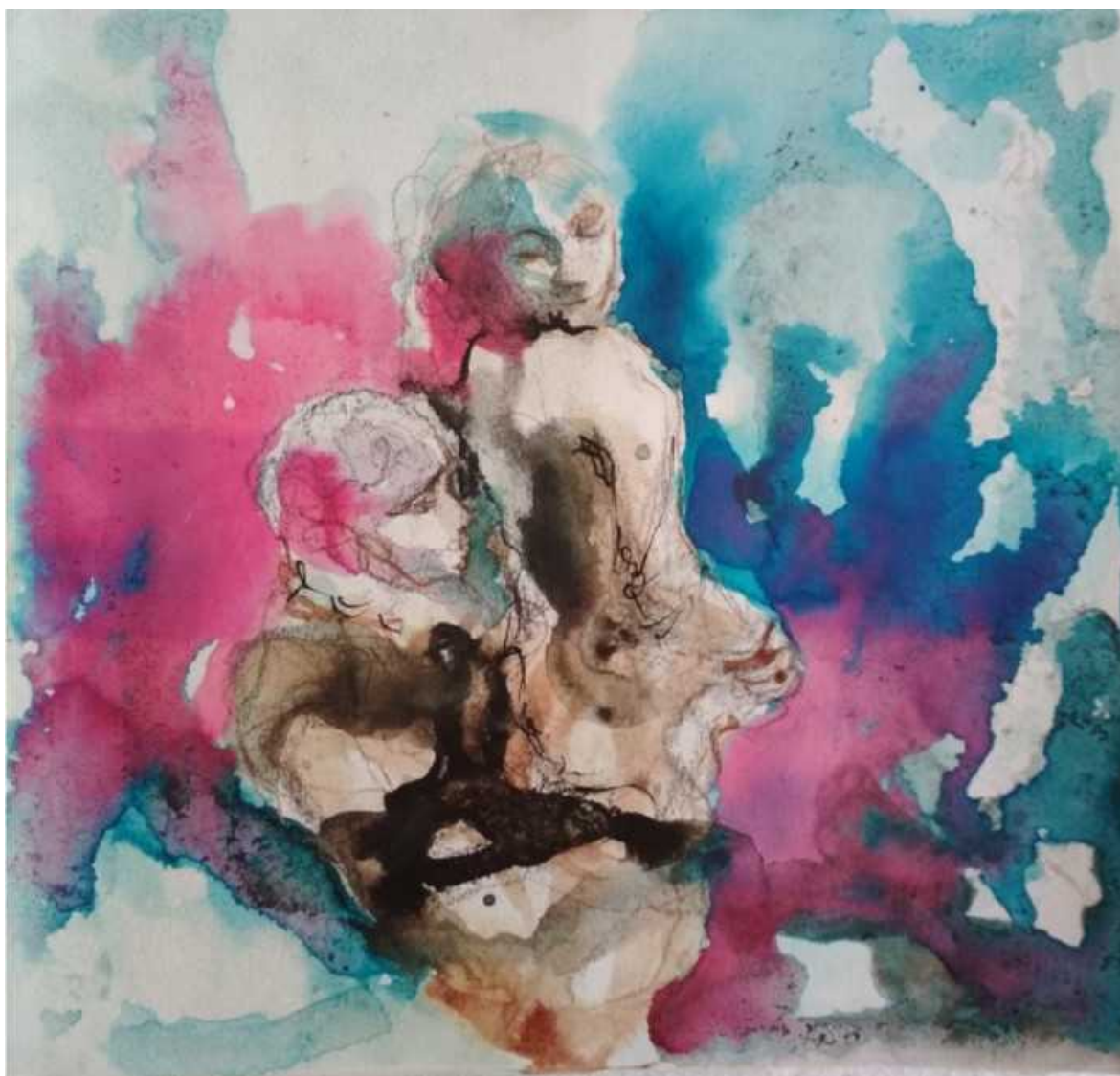
One billion years from now, the team's work suggests, Palomar 5 will have jettisoned all of its stars; only black holes will remain.

[Nature Astron. \(2021\)](#)

- [Astronomy and astrophysics](#)

This article was downloaded by **calibre** from <https://www.nature.com/articles/d41586-021-01859-2>

| [Section menu](#) | [Main menu](#) |



After 130 hours of artificial ageing by visible light, the painting *Triton and Nereid* has lost some of the purple tint to the figures' right, but a graphene film kept the bright pink at upper left undimmed. Credit: M. Kotsidi *et al.*/Nature Nanotechnol.

Materials science

07 July 2021

A graphene cloak keeps artworks' colours ageless

A layer of carbon atoms preserves a painting's vibrant hues — and can be applied and removed without damage.





•

The colours on half of the painting *Triton and Nereid* faded as it languished in a bright, warm and humid chamber. Those on the other half, however, held fast, protected by an invisible ‘veil’ of graphene.

The ‘wonder material’ graphene can block ultraviolet light, oxygen and moisture — the biggest nemeses of museum conservators. To shield paintings with graphene, Costas Galiotis at the Foundation for Research and Technology — Hellas, in Greece, and his colleagues custom-built a machine to apply the one-atom-thick material to a painting without damaging either.

The machine’s two rollers can gently press thin layers together and unroll one layer from another. The researchers rolled an adhesive film on top of a

graphene sheet, then rolled the graphene onto a painting while unrolling the adhesive.

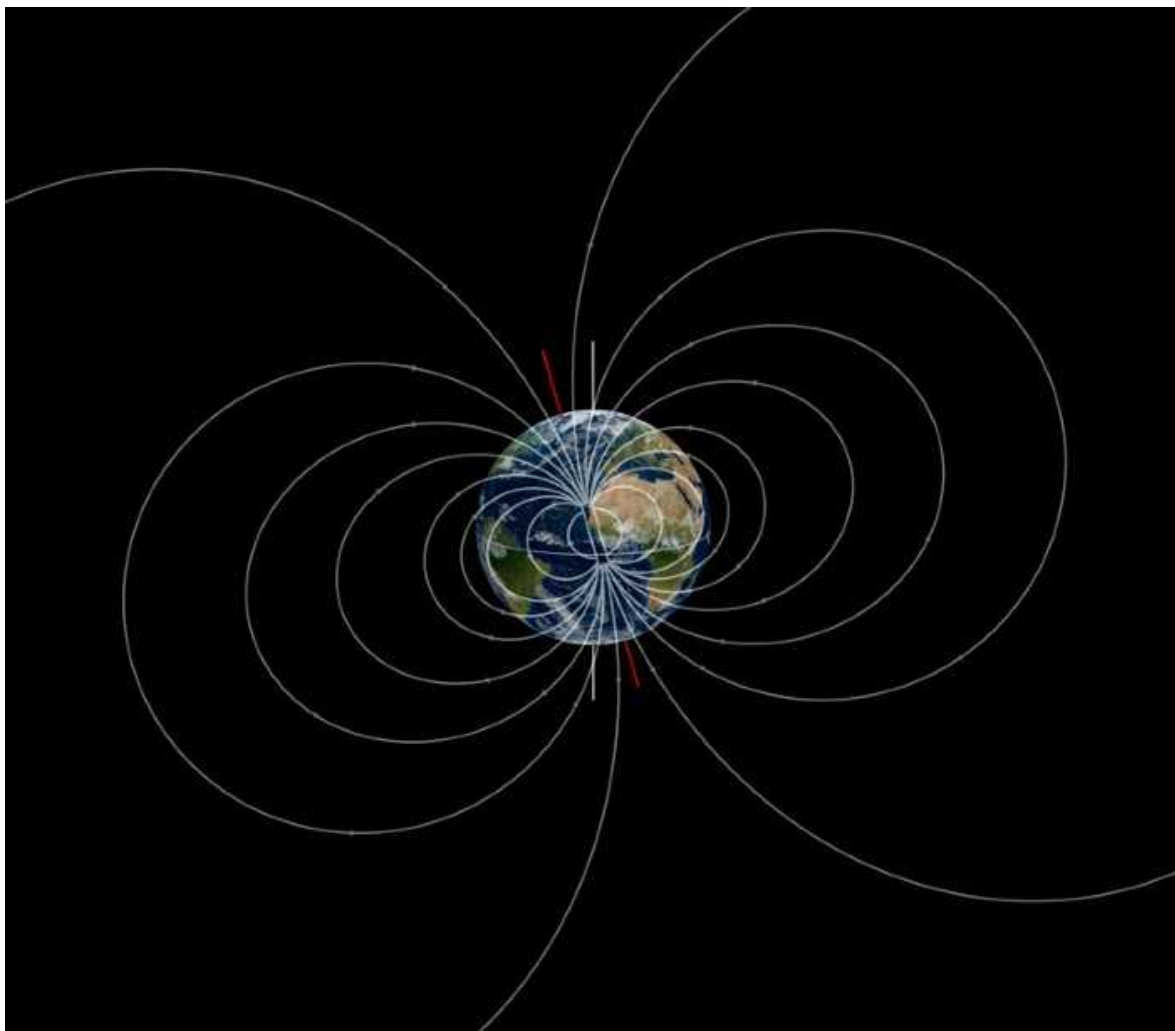
The team subjected *Triton and Nereid* to conditions simulating more than 200 years of museum display. In that time, the graphene veil did not crack or delaminate. It also was flexible enough to bend with the painting, so it could protect paintings on display or on the move. If desired, the veil can be erased.

[Nature Nano. \(2021\)](#)

- [Materials science](#)

This article was downloaded by **calibre** from <https://www.nature.com/articles/d41586-021-01854-7>

| [Section menu](#) | [Main menu](#) |



Earth's magnetic field (depicted as white lines in this artist's impression) can be studied with observations from a constellation of commercial satellites.

Credit: Mikkel Juul Jensen/Science Photo Library

Geophysics

08 July 2021

Telecoms satellites' new purpose: spying on Earth's magnetic field

Clues to the forces generated by the planet's core emerge from observations intended for satellite navigation.





•

Satellites that were never meant to map Earth's magnetic field turn out to be good at the job.

The company Iridium Communications, based in McLean, Virginia, has operated a constellation of 66 satellites in low Earth orbit since 1997. Each carries a device to detect the planet's magnetic field so that the satellite can orient itself properly.

Brian Anderson at the Johns Hopkins University Applied Physics Laboratory in Laurel, Maryland, and his colleagues analysed magnetic data collected by Iridium satellites between 2010 and 2015. The measurements are low-resolution compared with those from spacecraft dedicated to

studying Earth's magnetic field, but because of the number of Iridium satellites and the orbits in which they travel, they can map the entire field in a single day.

Global maps made with the Iridium data could reveal new details about changes in Earth's magnetic field, which is generated by molten iron sloshing in the planet's outer core. That could help researchers to develop better systems for navigating using the magnetic field.

[Geochem. Geophys. Geosyst. \(2021\)](#)

- [Geophysics](#)

This article was downloaded by **calibre** from <https://www.nature.com/articles/d41586-021-01860-9>

| [Section menu](#) | [Main menu](#) |



Brown trout can get hooked on methamphetamine, a highly addictive drug found in waterways around the world. Credit: Getty

Ecology

06 July 2021

Meth-addicted trout swim for a hit

Fish that have been exposed to the highly addictive stimulant for several weeks show signs of withdrawal if deprived of the drug.





•

Human drug use can spill over into streams and rivers, because the chemicals pass through wastewater systems that weren't designed to extract them. To study the effects of a common illicit drug on wildlife, Pavel Horký at the Czech University of Life Sciences Prague and his colleagues looked to brown trout, *Salmo trutta*.

For 8 weeks, the researchers held 60 trout in a tank spiked with methamphetamine at a concentration of 1 microgram per litre, and 60 control trout in a meth-free tank. The fish were then placed in a tank containing two separate streams of water — one with methamphetamine and one without — between which they could swim freely. Trout that had spent

2 months swimming in meth-spiked water were found on the meth side in 50.5% of observations, compared with only 41.5% for control trout. The authors interpret this preference as a sign of addiction.

Fish from the drugged tank were also markedly less mobile for the first 96 hours after their last exposure to meth, suggesting that they were experiencing withdrawal. The researchers warn that fish that become addicted to drugs could congregate around wastewater discharges, with unknown ecological effects.

J. Exp. Biol. (2021)

- Ecology

This article was downloaded by **calibre** from <https://www.nature.com/articles/d41586-021-01846-7>

| [Section menu](#) | [Main menu](#) |

News in Focus

- **[Mars auroras, deadly heatwave and new ERC president](#)** [14 July 2021]
News Round-Up • The latest science news, in brief.
- **[Mounting evidence suggests Sputnik COVID vaccine is safe and effective](#)** [06 July 2021]
News • Russia's vaccine is in use in nearly 70 nations, but its adoption has been slowed by controversies and questions over rare side effects, and it has yet to garner World Health Organization approval.
- **[The COVID pandemic's lingering impact on clinical trials](#)** [28 June 2021]
News • Medical researchers are beginning to shift their focus away from COVID-19 — but the pandemic could continue to affect studies focused on other diseases.
- **[COVID vaccines to reach poorest countries in 2023 — despite recent pledges](#)** [05 July 2021]
News • Amid a COVID surge in Africa, vaccine promises from richer nations are not enough to bring an early end to the pandemic, experts say.
- **[Will COVID become a disease of the young?](#)** [08 July 2021]
News • A growing share of infections among unvaccinated youths in countries with high vaccination rates is putting the spotlight on the role of young people in the pandemic.
- **[Mix-and-match COVID vaccines: the case is growing, but questions remain](#)** [01 July 2021]
News • A slew of studies suggests that mixing vaccines provokes potent immune responses, but scientists still want answers on real-world efficacy and rare side effects.
- **[The quest to find genes that drive severe COVID](#)** [08 July 2021]
News Feature • Genome studies have discovered some genetic risk factors for disease — and could point to treatments.
- **[Racism is magnifying the deadly impact of rising city heat](#)** [14 July 2021]
News Feature • Scientists are mapping correlations between race, poverty and heat in cities, and suggesting solutions to reduce the dangers.

| [Next section](#) | [Main menu](#) | [Previous section](#) |

- NEWS ROUND-UP
- 14 July 2021

Mars auroras, deadly heatwave and new ERC president

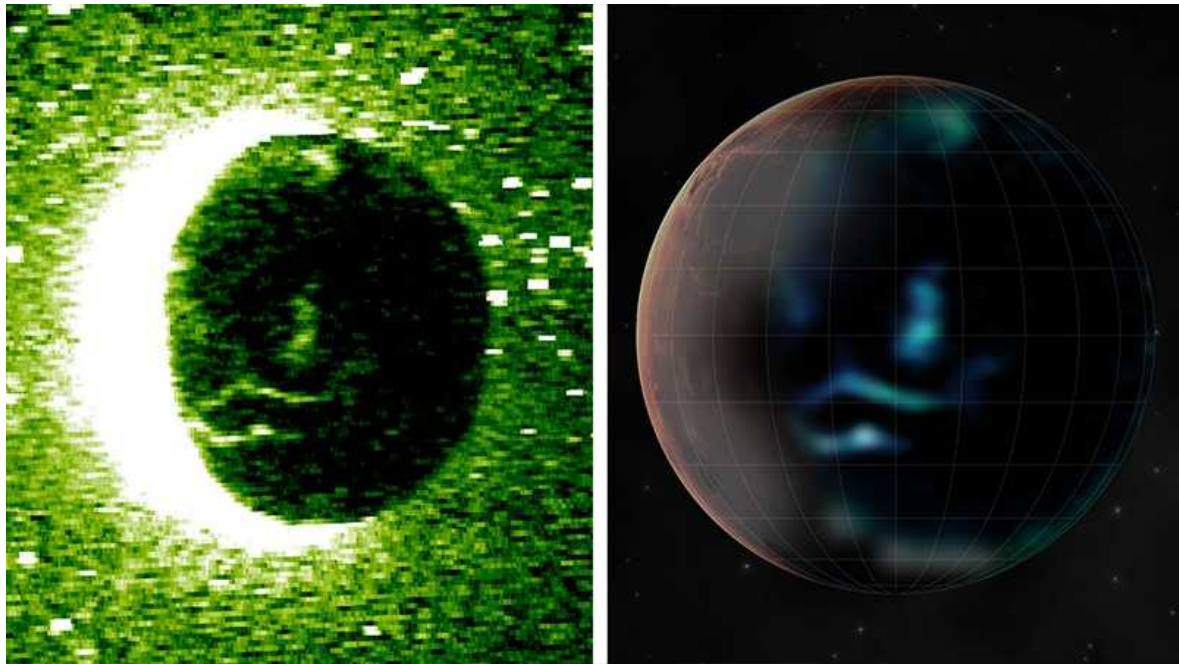
The latest science news, in brief.





•

[Download PDF](#)



Images taken by Hope's onboard spectrometer (left-hand panel) and an artist's impression (right) show discrete auroras on Mars's night side. Credit: Emirates Mars Mission

Mars's glowing auroras snapped by Hope spacecraft

The United Arab Emirates' Hope spacecraft has taken the [most detailed pictures yet](#) of the 'discrete auroras' of Mars. The ultraviolet emissions — seen on the planet's night side by the orbiter's onboard spectrometer — arise when the solar wind runs into magnetic fields that emanate from Mars's crust. Charged particles then collide with oxygen in the upper atmosphere, causing it to glow.

Hope, formally known as the Emirates Mars Mission (EMM), arrived at Mars in February. Its primary science goals focus on the planet's atmosphere, not on its magnetism, so the aurora images came as a bonus. "Seeing it has been just a gift," says Hessa Al Matroushi, the EMM's science lead at the Mohammed Bin Rashid Space Centre in Dubai. She adds that her team plans to publish a study based on the observations.

Mars researchers had previously detected ‘diffuse’ auroras during solar storms, as well as ‘proton’ auroras emanating from high altitudes when solar-wind protons rip electrons off atoms to form hydrogen ([J. Deighan et al. *Nature Astron.* 2, 802–807; 2018](#)). The discrete auroras seem to follow the patterns of Mars’s crustal magnetism, which suggests that the planet once had a global magnetic field similar to Earth’s.

Deadly heatwave ‘unlikely’ without climate change

The devastating heatwave that struck parts of Canada and the United States late last month would have been extremely unlikely without global warming, [researchers have concluded](#).

The heatwave lasted from 25 June to 1 July, and affected areas that rarely experience extreme heat. More than 500 excess deaths and 180 wildfires were recorded in the western Canadian province of British Columbia.



Wildfire burns near the Canadian village of Lytton. Credit: James MacDonald/Bloomberg via Getty

A group of 27 scientists with the World Weather Attribution project compared the observed heat with maximum daily temperatures predicted by

climate models, including simulations of temperatures in an atmosphere unaltered by the effect of rising greenhouse-gas concentrations. They concluded that the global average temperature increase of 1.2 °C since pre-industrial times [made the extreme heatwave at least 150 times more likely to happen.](#)

“This heatwave would have been virtually impossible without the influence of human-caused climate change,” says Sjoukje Philip, a climate scientist at the Royal Netherlands Meteorological Institute (KNMI) in De Bilt and a co-author of the analysis. “It was probably still a rare event, but if global warming might exceed two degrees, it might occur every five to ten years in the future.”

Biologist to lead Europe’s premier research funder

German developmental geneticist Maria Leptin will become [the next president of the European Research Council](#) (ERC), Europe’s major funding agency for basic research.



Maria Leptin will become president of the European Research Council in October.Credit: Michael Wodak/MedizinFotoKöln 2021

The European Commission announced the decision on 30 June, and Leptin will take the reins in October.

Her appointment follows the brief and controversial tenure of Mauro Ferrari, who resigned in April last year after just three months.

Leptin is currently director of EMBO, Europe's life-sciences organization, which is based at the European Molecular Biology Laboratory (EMBL) in Heidelberg, Germany. She runs research groups at EMBL and the University of Cologne in Germany.

Leptin says that one of her main priorities as president will be to persuade the commission to increase funding in its next financing round, and to launch grass-roots outreach campaigns to convey the value of basic, knowledge-seeking research.

She intends to wind down her labs at EMBL and Cologne. “My job will be ERC president and nothing else,” she says. “But I will miss doing research very much — that’s the one painful thing.”

Nature **595**, 337 (2021)

doi: <https://doi.org/10.1038/d41586-021-01880-5>

Subjects

- [Planetary science](#)
- [Climate change](#)
- [Funding](#)

nature careers

[Jobs](#) >

- **Postdoctoral Training Fellow**

Francis Crick Institute
London, United Kingdom

- **Senior Business Manager**

Francis Crick Institute
London, United Kingdom

- **Postdoctoral Research Fellow in Pharmacogenomics Pain Management**

The University of British Columbia (UBC)

Vancouver, Canada

- **Postdoctoral Research Fellow in Pain Management and C. elegans**

The University of British Columbia (UBC)

Vancouver, Canada

[Download PDF](#)

Subjects

- Planetary science
- Climate change
- Funding

| [Section menu](#) | [Main menu](#) |

- NEWS
- 06 July 2021
- Correction [07 July 2021](#)
- Correction [08 July 2021](#)

Mounting evidence suggests Sputnik COVID vaccine is safe and effective

Russia's vaccine is in use in nearly 70 nations, but its adoption has been slowed by controversies and questions over rare side effects, and it has yet to garner World Health Organization approval.

- [Bianca Nogrady](#)
 1. Bianca Nogrady
[View author publications](#)

You can also search for this author in [PubMed](#) [Google Scholar](#)





•

[Download PDF](#)



Vials of the Sputnik V COVID-19 vaccine pass along a production line at a manufacturing facility near St Petersburg, Russia. Credit: Olga Maltseva/AFP/Getty

Russia's COVID-19 vaccine, Sputnik, has been the subject of fascination and controversy since the Russian government authorized its use last year, before early-stage trial results were even published. Evidence from Russia and many other countries now suggests it is safe and effective — but questions remain about the quality of surveillance for possible rare side effects.

Sputnik V — also known as Gam-COVID-Vac — was the first COVID-19 vaccine to be registered for use in any nation, and it has since been approved in 67 countries, including Brazil, Hungary, India and the Philippines. But the vaccine — and its one-dose sibling Sputnik Light — has yet to receive approval for emergency use from the European Medicines Agency (EMA) or the World Health Organization (WHO). Approval by the WHO is crucial for widespread distribution through the COVID-19 Vaccines Global Access (COVAX) initiative, which is providing doses for lower-income nations.

Developed by scientists at the Gamaleya National Research Center of Epidemiology and Microbiology in Moscow, the vaccine was authorized for use by the Russian Ministry of Health on 11 August 2020, more than a month before phase I and II trial results were published, and before the phase III trial had even begun.

The scientific community greeted Russian President Vladimir Putin's announcement of the vaccine's registration with outrage. "If the government's going to approve a vaccine before they even know the results of the trial, that does not build confidence," said epidemiologist Michael Toole at the Burnet Institute in Melbourne, Australia.

Access to full data

Some of that concern was allayed when the phase III trial results¹, published in February by the vaccine's developers, suggested that it is 91.6% effective at preventing symptomatic COVID-19 infection and 100% effective at preventing severe infection. However, some scientists [criticized the authors](#) for failing to provide access to the full raw data from the early-stage trials, and also voiced concerns about changes in the vaccine's administration protocol and inconsistencies in the data.



[Researchers highlight 'questionable' data in Russian coronavirus vaccine trial results](#)

The authors responded by saying that they had provided the regulatory authorities with all the data necessary for obtaining approval, and that the data included with the paper² were enough for readers to confirm the reported vaccine efficacy. They also addressed the protocol queries, and said numerical inconsistencies were “simple typing errors that were formally corrected”.

Despite the absence of approval from the EMA or the WHO, several countries, including South Korea, Argentina and India, are already manufacturing Sputnik V. And India plans to pump out at least 850 million doses, to help speed up the vaccination of its embattled population. Many other countries, such as Hungary and Iran, are importing Sputnik V, and it has become a key plank of their vaccination campaigns.

But it hasn’t all been plain sailing. Brazil’s health regulator rejected an application to import Sputnik V in April over concerns at a lack of data on safety, quality and effectiveness. That decision was reversed in June, but the vaccine has been approved only for healthy adults.



An elderly man receives a dose of the Sputnik V vaccine in Caracas, Venezuela.Credit: Federico Parra/AFP/Getty

Two viral vectors are better than one?

Sputnik V is an adenovirus vaccine, which means that it uses an engineered adenovirus — a family of viruses that generally cause only mild illness — as a delivery mechanism for inserting the genetic code for the SARS-CoV-2 spike protein into human cells.

It is similar to the Oxford–AstraZeneca and Johnson & Johnson vaccines. But instead of using one engineered adenovirus, as those two vaccines do, Sputnik V uses different adenoviruses, called rAd26 and rAd5, for the first and second doses, respectively.

Dmitry Kulish, a biotechnology researcher at the Skolkovo Institute of Science and Technology in Moscow, who is not involved in the development of Sputnik V, says the scientific reasoning would have been to increase efficacy. The two adenoviruses have slightly different methods of introducing their genetic material into a host cell, he says, which would theoretically improve the success rate of getting the viral genetic material where it needs to go.

The two preliminary studies from the vaccine developers, published in September 2020², involved 76 healthy adults who received the two doses with different viral vectors three weeks apart. All participants produced antibodies to the SARS-CoV-2 spike protein, and adverse events reported were mainly mild pain at the injection site, fever, headache, fatigue and muscle aches — adverse events typical of other SARS-CoV-2 vaccines.



Can Cuba beat COVID with its homegrown vaccines?

In the randomized phase III trial, published in interim form in February, 14,964 adults received the two-dose vaccine and 4,902 received two doses of placebo. Only 16 subjects in the vaccine group developed symptomatic COVID-19, compared with 62 in the placebo group, representing a vaccine efficacy of 91.6%. Furthermore, there were no cases of moderate to severe disease in the vaccine group, but 20 in the placebo group.

Unpublished data on 3.8 million Russians vaccinated with two doses also point to an efficacy of 97.6%, according to an April [press release](#) from the Gamaleya Institute. Figures released by the United Arab Emirates Ministry of Health, on some 81,000 individuals who had received two doses of the vaccine, suggested 97.8% efficacy in preventing symptomatic COVID-19 and 100% efficacy in preventing severe disease.

Russia's phase III study also found that even one dose was 73.6% effective at preventing moderate to severe disease. This led the Russian health authorities to approve the one-dose Sputnik Light — which uses the rAd26 vector — in May, on the basis of [data from the country's own vaccination programme](#), which suggested that it was 79.4% effective at preventing symptomatic disease.

Since then, an as-yet unpublished study from the Buenos Aires health ministry in Argentina, involving 40,387 vaccinated and 146,194

unvaccinated people aged 60–79, found that a single dose of Sputnik Light reduced symptomatic infections by 78.6%, hospitalizations by 87.6% and deaths by 84.7%.

Side-effect questions

Sputnik's side effects are also becoming clearer; studies so far suggest that they are similar to those of the other adenovirus vaccines, with the notable exception of rare blood-clotting conditions. Unlike for both the Oxford–AstraZeneca and Johnson & Johnson vaccines, there have been no reports of these disorders from Russian health authorities or from the other nations using Sputnik V.

A preprint³ from the Italian Hospital of Buenos Aires in Argentina reported no cases of clotting disorders or adverse events of special interest among 683 health-care workers vaccinated with Sputnik V. And an analysis of 2.8 million doses of Sputnik V administered in Argentina reported no deaths associated with vaccination, and mostly mild adverse events. Furthermore, a study posted as a preprint in May, from the republic of San Marino, found no serious adverse events in 2,558 adults who received one dose of Sputnik V and 1,288 who received two doses⁴.

Virologist Alyson Kelvin at Dalhousie University in Halifax, Canada, says there is a theory that the clotting disorder is associated with viral-vector vaccines, but adds, “I don’t think we have exact causation of what component of those vaccines are causing it”, or whether Sputnik might also be affected. She notes that although the phase III study of Sputnik V enrolled only 21,977 people, and thus was too small to pick up rare adverse events, the vaccine is now in widespread use globally, which means that reports should appear “if a safety signal comes up”.



Palestinian health workers unload boxes of the Sputnik V vaccine from a truck in the Gaza Strip.Credit: Said Khatib/AFP/Getty

It is not clear whether Russia is in a position to detect such rare events. Those associated with the Oxford–AstraZeneca vaccine first came to light through adverse-event monitoring in Austria, which prompted the EMA to review the vaccine’s safety.

But Russia’s adverse-event monitoring might be less effective, Kulish argues, partly because of a cultural resistance to seeking medical care. “Most Russian people will call [the] doctor only when they cannot breathe any more,” he quips. Furthermore, doctors in remote regions of Russia might not connect a stroke caused by blood clots, for example, to a recent vaccination, he says.

Argentina has not reported any clotting events, despite receiving more than four million doses of the vaccine, Kulish notes. Serbia, which has also been using Sputnik V widely, has so far reported no cases of the blood-clotting condition reported with other adenovirus vaccines.

WHO and EMA wait to authorize Sputnik

Scientists say that concerns over side-effect monitoring could be why the WHO and EMA are yet to issue emergency-use authorization. The WHO has requested more data from the Gamaleya Institute, and inspections by the agency of Russia's vaccine-manufacturing and clinical-trial facilities are ongoing. So far, nine sites have been inspected, and the WHO has flagged concerns over one manufacturing site. Similarly, the EMA lists the vaccine's authorization as being under "rolling review".

Sputnik's developers have accused the European Union of being biased, citing a comment from EU internal-market commissioner Thierry Breton in March that the EU has "absolutely no need of Sputnik V".



[China's COVID vaccines are going global — but questions remain](#)

Kulish suggests there is also a "pro-Pfizer" stance within the EMA that is hampering Sputnik's quest for authorization — a reference to the Pfizer–BioNTech vaccine co-developed by Pfizer in New York City and BioNTech in Mainz, Germany. A spokesperson for the EMA responded to that suggestion by pointing out that "the same standards" apply to all COVID-19 vaccine applicants, "no matter where in the world they are located".

Toole says he suspects the EMA's main concern is that "they're not that comfortable" with Russia's adverse-event surveillance.

There are also concerns about Sputnik in Russia, which has high rates of COVID-vaccine hesitancy. A survey in March suggested that 62% of Russians did not plan to get vaccinated, and Russia is now introducing mandatory vaccinations for some government and other workers to boost vaccination rates. As of 28 June, only around 15% of Russia's population of more than 140 million had received one dose of a vaccine.

Several other studies are currently under way in countries that have approved Sputnik, including in Argentina, Venezuela, Russia and Turkey, which should help to build a more accurate picture of the vaccine's safety and efficacy.

Nature **595**, 339-340 (2021)

doi: <https://doi.org/10.1038/d41586-021-01813-2>

Updates & Corrections

- **Correction 07 July 2021:** An earlier version of this story stated incorrectly that an analysis of 2.8 million doses that reported no deaths took place in Brazil. In fact, it was in Argentina. The text has been updated.
- **Correction 08 July 2021:** An earlier version of this story used the figure for the number of adults randomized to the two doses of placebo in the phase III trial, instead of the figure for the number of adults who actually received two doses of placebo in that trial. That figure has been updated.

References

1. 1.

Logunov, D. Y. *et al. Lancet* **397**, 671–681 (2021).

[PubMed](#) [Article](#) [Google Scholar](#)

2. 2.

Logunov, D. Y. *et al.* *Lancet* **396**, 887–897 (2020).

[PubMed](#) [Article](#) [Google Scholar](#)

3. 3.

Pagotto, V. *et al.* Preprint at medRxiv
<https://doi.org/10.1101/2021.02.03.21251071> (2021).

4. 4.

Montalti, M. *et al.* Preprint at medRxiv
<https://doi.org/10.1101/2021.05.03.21256509> (2021).

[Download references](#)

Related Articles



- [**Can Cuba beat COVID with its homegrown vaccines?**](#)



- [**Six months of COVID vaccines: what 1.7 billion doses have taught scientists**](#)



- [**China's COVID vaccines are going global — but questions remain**](#)



- [Researchers highlight ‘questionable’ data in Russian coronavirus vaccine trial results](#)

Subjects

- [Epidemiology](#)
- [Vaccines](#)
- [SARS-CoV-2](#)

nature careers

[Jobs](#) >

- [Postdoctoral Training Fellow](#)

Francis Crick Institute

London, United Kingdom

- [Senior Business Manager](#)

Francis Crick Institute

London, United Kingdom

- [Postdoctoral Research Fellow in Pharmacogenomics Pain Management](#)

The University of British Columbia (UBC)

Vancouver, Canada

- [Postdoctoral Research Fellow in Pain Management and C. elegans](#)

The University of British Columbia (UBC)

Vancouver, Canada

[Download PDF](#)

Related Articles



- [Can Cuba beat COVID with its homegrown vaccines?](#)



- [Six months of COVID vaccines: what 1.7 billion doses have taught scientists](#)



- [China's COVID vaccines are going global — but questions remain](#)



- [Researchers highlight ‘questionable’ data in Russian coronavirus vaccine trial results](#)

Subjects

- [Epidemiology](#)
- [Vaccines](#)
- [SARS-CoV-2](#)

This article was downloaded by **calibre** from <https://www.nature.com/articles/d41586-021-01813-2>

| [Section menu](#) | [Main menu](#) |

- NEWS
- 28 June 2021

The COVID pandemic's lingering impact on clinical trials

Medical researchers are beginning to shift their focus away from COVID-19 — but the pandemic could continue to affect studies focused on other diseases.

- [Heidi Ledford](#)
 1. Heidi Ledford
[View author publications](#)

You can also search for this author in [PubMed](#) [Google Scholar](#)





•

[Download PDF](#)



In some hospitals, makeshift intensive-care units were set up to deal with an influx of people with COVID-19. Credit: Mario Tama/Getty

“It’s like time stopped,” says Emilia Bagiella, a clinical trial statistician at the Icahn School of Medicine at Mount Sinai in New York City.

When Bagiella left work one day in early March 2020, she hadn’t fully grasped how long it would be until she came back. “See you in a couple of weeks, when this is over,” she told her co-workers. But even though the reality of the pandemic had not fully hit her, a thought crossed her mind: “What’s going to happen to all of these clinical trials?”

For the next year, says Bagiella, it felt as if the clock had stopped ticking for some clinical trials, even as researchers, patients and funders fought to keep studies on track. Now that vaccines have sent the crisis phase of the pandemic into remission in some countries, researchers such as Bagiella are returning to their workplaces, finding out what impact the delays of the past year have had, and wondering what lasting lessons will be drawn from the pandemic.

“COVID-19 taught us that there’s a lot more flexibility in the clinical trials system than we realized,” says Meg Mooney, associate director of the Cancer Therapy Evaluation Program at the US National Cancer Institute (NCI) in Bethesda, Maryland. “But when you lose time, you lose time. It’s going to delay results.”

Enrolment paused

For many regions in the United States, the biggest blows to clinical research came between March and May 2020. Trial enrolments plummeted at many medical centres as prospective participants shied away from risky trips to hospital, and research staff were either furloughed or co-opted to aid hospitals’ COVID-19 treatment efforts. Some trials were deemed too dangerous to continue. Bagiella recalls the decision to pause a heart-transplant trial: transplants, and the treatments for suppressing the immune system that often come with them, were especially risky during a pandemic. She adds that “operating rooms around the country became intensive care units”, so trials involving elective heart surgery were disrupted.



[Coronavirus shuts down trials of drugs for multiple other diseases](#)

Researchers worked hard to keep trials that were deemed as “life-saving” open, Bagiella says, particularly cancer-treatment studies. Even so, enrolment in clinical trials run by the SWOG Cancer Research Network, a large clinical-trials programme funded by the NCI, dropped by about half

between March and May 2020. Small, early clinical trials — which often focus on establishing the safety of a new medicine — were more likely to pause enrolment than larger trials designed to demonstrate how well a therapy works against disease, Mooney found when analyzing data from two large NCI study networks.

The pandemic also took a bite out of new study launches: one study, which examined more than 62,000 trials that started before and during the pandemic, found that the number of studies initiated in the United States from February to May last year was only 57% of what would have been expected had the pandemic not occurred.¹ The impact outside the United States was smaller, with 77% of the expected number of new studies launching.

Flexible arrangements

Funders and the US Food and Drug Administration responded with a series of guidelines on how clinical trials could be altered to allow them to continue during the public-health emergency. Investigators were allowed to deliver some experimental medicines to participants' homes, rather than asking them to come to a medical centre to pick them up. Participants could use online platforms to consent to taking part in a clinical trial, rather than doing so in person. Investigators lengthened the time between doctors' visits for some study participants and performed more of those visits remotely, using phone or video calls or online questionnaires. And participants were sometimes allowed to visit their local doctor for basic procedures and assessments, rather than travelling to a central study site.

Charles Blanke, an oncologist at Oregon Health and Science University in Portland, credits those policies with getting SWOG's enrolment back up to near-normal levels, and keeping it there even during the country's biggest COVID-19 surge in early 2021. "We truly believe this made a gigantic difference," says Blanke. "And we and our patients are desperate to keep it in place."

But that added flexibility could have come at a cost. Longer intervals between assessments might mean less data for each participant. And some

studies will have to make do without medical images that they were unable to collect during coronavirus surges.

If regulators and funders are to consider making this flexibility permanent, researchers will probably need to show that the quality of clinical studies has not fallen as a result. “It’s going to be something that’s quite difficult to quantify,” says Daniel Tan, an oncologist at the National Cancer Centre Singapore, who notes that the waves of lockdowns and reopenings at varying times in different countries could complicate the analysis of international trials.



Some clinical studies had to be paused, or handled differently, during the height of the pandemic.Credit: Saul Loeb/AFP via Getty

Studies to assess the impact of the pandemic on the quality of trial data are now underway. Joseph Unger, a health-services researcher and biostatistician at the Fred Hutchinson Cancer Research Center in Seattle, Washington, has been collecting questionnaires from clinical trial participants for years, to assess whether patient-reported outcomes vary if they are reported over the phone rather than in person. He hopes to use that information to gauge the

effect of the remote assessments that have frequently been used during the pandemic.

Unger says that SWOG is also looking at metrics for treatment trials, and at whether the data quality has dropped off during the pandemic. “If not, then I do think that you’re going to see a lot of these adaptations become permanent,” he says.

Lasting changes

Some research centres say that the urgency of the pandemic forced them to accelerate their procedures in ways that will carry over to future trials, regardless of whether changes to official guidelines stay in place. Katherine Tuttle, a nephrologist and executive director for research at Providence Health Care in Spokane, Washington, points out that her centre can now get clinical trials running in a matter of days, rather than having to wait six weeks or more, as was typical before the pandemic. “A lot of things that we knew we were doing before, that should change, finally changed because we were in a state of emergency,” she says. “We’re not going back to doing it the old way.”

But some negative impacts could also linger. Blanke points to a survey showing that about 20% of cancer survivors are less likely to enrol in a clinical trial than they were before the pandemic². “I do worry that there’s a core of patients who will not go on a clinical trial for the next five years,” he says.



Evidence-based medicine: how COVID can drive positive change

The cutbacks in elective surgeries and other hospital services have also had a lasting effect on the tumour banks that store cancer samples for use in additional research, says Bruce Johnson, an oncologist at the Dana-Farber Cancer Institute in Boston, Massachusetts. Johnson specializes in treating lung cancer, and many clinical trials for the disease attempt to match treatments with the DNA mutations present in participants' tumours. "They cancelled elective biopsies," says Johnson. "And so many of our trials are based on them."

Although elective biopsies have restarted, cancer researchers have complained that depleted supplies of patient samples have curtailed basic research. Johnson, who is an investigator on a project to characterize the individual cells in tumours, says that the project is struggling to get the samples it needs. "It's a challenge to meet our goals," he says.

Over the past few months, Bagiella's team has been coming back to the office, and trials that had been pushed aside to free up resources for COVID-19 are blossoming again. The heart transplant trial that had been put on hold is enrolling participants, and research staff that were dedicated to COVID-19 studies are turning back to non-COVID conditions.

The pandemic crisis has eased so much that Mount Sinai is struggling to find enough people infected with SARS-CoV-2 to enrol in — and complete — its ongoing COVID-19 trials. “And thank God for it,” says Bagiella. She is eager to see the COVID-19 trials close, freeing up more resources for studies of other conditions. “It’s been a long, long time,” she says. “It’s good to see some of these trials coming back to life.”

Nature **595**, 341-342 (2021)

doi: <https://doi.org/10.1038/d41586-021-01569-9>

References

1. 1.

Unger, J. M. & Xiao, H. *Trials* **22**, 260 (2021).

[PubMed](#) [Article](#) [Google Scholar](#)

2. 2.

Fleury, M. E., Farner, A. M. & Unger, J. M. *JAMA Oncol.* **7**, 131–132 (2021).

[Article](#) [Google Scholar](#)

[Download references](#)

Related Articles

-  [**How COVID broke the evidence pipeline**](#)



- [Evidence-based medicine: how COVID can drive positive change](#)



- [It's time to invite more people to join clinical trials](#)



- [Coronavirus shuts down trials of drugs for multiple other diseases](#)

Subjects

- [Health care](#)
- [SARS-CoV-2](#)
- [Medical research](#)

nature careers

[Jobs](#) >

- [Postdoctoral Training Fellow](#)

Francis Crick Institute

London, United Kingdom

- [Senior Business Manager](#)

Francis Crick Institute

London, United Kingdom

- [**Postdoctoral Research Fellow in Pharmacogenomics Pain Management**](#)

The University of British Columbia (UBC)

Vancouver, Canada

- [**Postdoctoral Research Fellow in Pain Management and C. elegans**](#)

The University of British Columbia (UBC)

Vancouver, Canada

[Download PDF](#)

Related Articles



- [**How COVID broke the evidence pipeline**](#)



- [**Evidence-based medicine: how COVID can drive positive change**](#)



- [**It's time to invite more people to join clinical trials**](#)



- [Coronavirus shuts down trials of drugs for multiple other diseases](#)

Subjects

- [Health care](#)
- [SARS-CoV-2](#)
- [Medical research](#)

This article was downloaded by **calibre** from <https://www.nature.com/articles/d41586-021-01569-9>

| [Section menu](#) | [Main menu](#) |

- NEWS
- 05 July 2021
- Clarification [09 July 2021](#)

COVID vaccines to reach poorest countries in 2023 — despite recent pledges

Amid a COVID surge in Africa, vaccine promises from richer nations are not enough to bring an early end to the pandemic, experts say.

- [T. V. Padma](#) ⁰

1. T. V. Padma

1. T. V. Padma is a science journalist based in New Delhi, India.

[View author publications](#)

You can also search for this author in [PubMed](#) [Google Scholar](#)





•

[Download PDF](#)



COVID-19 testing in Johannesburg. South African President Cyril Ramaphosa has reintroduced restrictions following a surge of the Delta variant. Credit: Emmanuel Croset/AFP/Getty

Most people in the poorest countries will need to wait another two years before they are vaccinated against COVID-19, researchers have told *Nature*.

Around 11 billion doses are needed to fully vaccinate 70% of the world's population against COVID-19. As of 4 July, 3.2 billion doses had been administered. At the current vaccination rate, this will increase to around six billion doses by the end of the year, [researchers from the International Monetary Fund](#), based in Washington DC, project.

But so far, more than 80% of the doses have gone to people in high-income and upper-middle-income countries. Only 1% of people in low-income countries have been given at least one dose, according to the website [Our World in Data](#).

Last month, the leaders of the G7 group of wealthy nations pledged extra doses for low- and middle-income countries (LMICs) by the end of 2022, at

a summit in Cornwall, UK. The centrepiece was a promise from US President Joe Biden to donate 500 million doses of the vaccine made by pharmaceutical company Pfizer of New York City and biotechnology company BioNTech in Mainz, Germany. This is in addition to 87.5 million previously pledged. The United Kingdom pledged 100 million, and France, Germany and Japan have pledged around 30 million each.

China has donated around 30 million vaccine doses to at least 59 countries, according to [data published on 2 July](#) by researchers from the Duke Global Health Innovation Center in Durham, North Carolina.

Andrea Taylor, a health policy researcher and the centre's assistant director, says these pledges are unlikely to get more vaccines to the world's poorest people more quickly. In March, [her group projected that the world would be vaccinated in 2023](#); Taylor says that date still stands.

The extra pledges will be offset by restrictions on exports. The European Union and the United States both prohibit exports of some vaccines and vaccine ingredients. The EU is insisting companies fulfil their pledges to deliver vaccines to the EU before exporting elsewhere. In February, India, where around six in ten of the world's vaccine doses are made, ordered the country's manufacturers to stop exporting COVID-19 vaccines — including to the COVAX initiative, which was established by groups including the World Health Organization (WHO) to distribute vaccines to LMICs. This was a major setback, Taylor says.

COVAX has pledged to vaccinate one-fifth of the population of each LMIC by delivering two billion doses by the end of this year. It has purchased 2.4 billion doses — [up from 1.1 billion in March](#), according to data from the Duke Global Health Innovation Center. But as of 2 July, COVAX had shipped 95 million doses, up from 65 million in May.

Meanwhile, COVID-19 cases are now surging across Africa. The World Health Organization's Africa office, based in Brazzaville, Republic of Congo, says the number of COVID-19 infections rose by 39% from 13 to 20 June, and by 25% in the week ending 27 June. At least 20 countries, including Zambia, Uganda, South Africa and the Democratic Republic of the Congo, are experiencing a third wave of infections, according to the Africa

Centres for Disease Control and Prevention (Africa CDC), based in Addis Ababa, Ethiopia. Health facilities are becoming overwhelmed.

Behind schedule

Pharmaceutical company AstraZeneca, based in Cambridge, UK, is one of COVAX's main sources of vaccine doses. In June 2020, the company signed a deal with the Serum Institute of India (SII) in Pune, one of the world's largest vaccine makers, to manufacture one billion doses of the vaccine that the company developed with the University of Oxford, UK, and send them to LMICs. Of these, 400 million doses were to be provided before the end of 2020.

But infections began to resurge in India's second wave in March. The government in February directed the SII to divert all vaccine supplies to meet domestic demand. This has hit COVAX particularly hard.

By the end of March this year, COVAX had received just 28 million doses of the AstraZeneca–Oxford vaccine. It was due to receive another 90 million by the end of April; these are now on hold.

Overall, between February and May, African countries received only 18.2 million of the 66 million doses they had expected through COVAX. Out of nearly 1.3 billion people in Africa, just 2% have received one dose of a COVID-19 vaccine. And a little over 1% — 26 million people — are fully vaccinated, according to the WHO's Africa office.

An SII spokesperson told *Nature* that the company expects to resume global exports by the end of 2021. A COVAX spokesperson says that in spite of the delays, the organization is confident that it can meet its goal of supplying two billion doses by the end of the year.

The African Union is, meanwhile, exploring other options. With financial help from the World Bank, it has secured 400 million doses of the single-shot vaccine developed by pharmaceutical company Johnson & Johnson, based in New Brunswick, New Jersey.

“Let me put it bluntly, we are not winning in Africa this battle against the virus so it does not really matter to me whether the vaccines are from COVAX or anywhere. All we need is rapid access to vaccines,” said Africa CDC director John Nkengasong at a briefing at the end of last month.

Individual African countries are also negotiating deals with vaccine companies to fill the hole left by the SII. But these countries are often at the back of the queue, Taylor says, because they lack the purchasing power of richer countries.

Vaccines needed now

With India’s manufacturers out of the picture for now, the United States is emerging as the world’s leading supplier of vaccine doses to LMICs, Taylor explains, and has begun to distribute some of its surplus supplies.

However, according to WHO chief scientist Soumya Swaminathan, this could be too late. “The inequitable distribution of vaccines has allowed the virus to continue spreading,” she says. Unvaccinated populations are already at risk, especially from new coronavirus variants, such as Delta (also known as B.1.617.2). “We need countries with substantial supply to donate 250 million doses for September,” Swaminathan says.

The WHO is calling on its member states to support a huge effort to vaccinate at least 10% of people in every country by September, along with a “drive to December” to vaccinate at least 30% by the end of the year. This will happen only if countries immediately share doses with COVAX and if manufacturers prioritize COVAX orders, Swaminathan says.

The timing is extremely important, adds Taylor. “Doses shared now will be so much more impactful than doses in six months. We need wealthy countries to send doses immediately.”

Nature **595**, 342-343 (2021)

doi: <https://doi.org/10.1038/d41586-021-01762-w>

Updates & Corrections

- **Clarification 09 July 2021:** An earlier version of this story said that China had shipped 30 million vaccines. In fact, that's the number China had donated; it has exported many more to fulfil orders.

nature careers

Jobs >

- **Postdoctoral Training Fellow**

Francis Crick Institute

London, United Kingdom

- **Senior Business Manager**

Francis Crick Institute

London, United Kingdom

- **Postdoctoral Research Fellow in Pharmacogenomics Pain Management**

The University of British Columbia (UBC)

Vancouver, Canada

- **Postdoctoral Research Fellow in Pain Management and *C. elegans***

The University of British Columbia (UBC)

Vancouver, Canada

Download PDF

| [Section menu](#) | [Main menu](#) |

- NEWS
- 08 July 2021

Will COVID become a disease of the young?

A growing share of infections among unvaccinated youths in countries with high vaccination rates is putting the spotlight on the role of young people in the pandemic.

- [Smriti Mallapaty](#)
 1. Smriti Mallapaty
[View author publications](#)

You can also search for this author in [PubMed](#) [Google Scholar](#)





•

[Download PDF](#)



A dose of vaccine is administered to a boy in Holon, near Tel Aviv, after Israel begins to vaccinate 12 to 15-year-olds.Credit: Jack Guez/AFP via Getty

On 21 June, Israel’s Ministry of Health recommended that all individuals aged 12–15 be vaccinated against COVID-19 — making the nation one of the few that have so far approved vaccinations for younger adolescents. The decision came in response to a trend that many countries with high rates of vaccination are experiencing: an ever-increasing proportion of new infections are in younger age groups (see ‘Trending younger’).

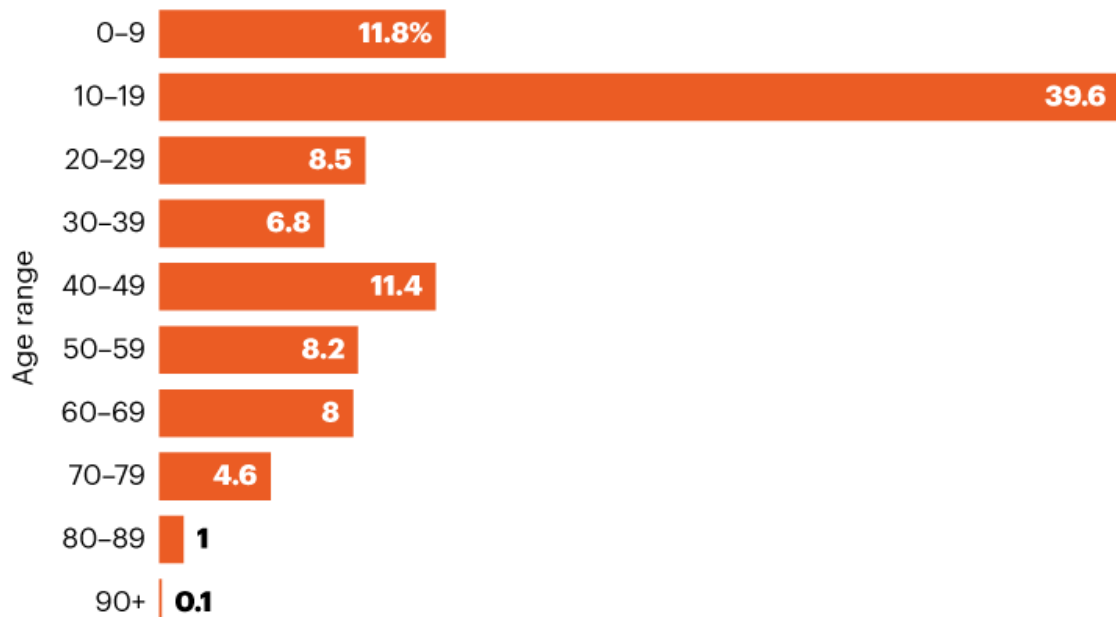
Israel’s swift vaccination campaign — which has now reached more than 85% of the adult population — saw case numbers drop to around a dozen a day in early June. But later that month, cases began to rise to more than 100 a day, many of in people under 16, leading the government to open up vaccinations to all teenagers.

The younger profile of cases is not surprising, says Ran Balicer, an epidemiologist at Israel’s largest health-care provider, Clalit Health Services, in Tel Aviv. But it highlights the possibility that subsequent waves of community spread could be driven by younger age groups, especially in the presence of new, more transmissible variants.

TRENDING YOUNGER

With the majority of adults in Israel now vaccinated, just over half of the country's new COVID-19 cases in the month up to 5 July were in people aged 19 and under.

Proportion of recent COVID-19 cases in Israel by age group



©nature

Source: Israel Ministry of Health

Growing trend globally

It's a trend that's not restricted to Israel. In the United States and the United Kingdom, COVID-19 has "become a disease of the unvaccinated, who are predominantly young", says Joshua Goldstein, a demographer at the University of California, Berkeley.

This shift is occurring in many countries that vaccinated older people first, and are now reaching high levels of vaccination in the adult population. It follows an earlier drop in age resulting from public-health measures to prevent the spread of COVID-19 among older people who are most at risk of severe disease, such as those in nursing homes, say researchers.

And the shift has brought fresh impetus to studies of transmission and disease in younger age groups. To make better policy decisions, “it’s becoming more and more important to understand the burden of disease among children and adolescents”, says Karin Magnusson, an epidemiologist at the Norwegian Institute of Public Health in Oslo.

Magnusson has looked at the impact of COVID-19 in children on Norway’s health-care system. In a 5 June preprint¹, she reported that although they didn’t need specialist care, children often needed to see their doctor repeatedly for up to six months after contracting the virus.

Balicer is studying viral spread in multigenerational households in Israel. Beyond decisions about [vaccinating children](#), the changing patterns of COVID-19 infection have also fuelled discussions about extending health measures such as mask wearing to adolescents and kids in Israel, he says.

Proportional not absolute increase

“As the burden of cases shifts towards younger people, arguments for vaccinating adolescents will become slightly more compelling,” agrees Nick Bundle, an epidemiologist at the European Centre for Disease Prevention and Control in Stockholm. However, the overall [risk of severe disease](#) in children remains low, and in many countries that have observed the proportion of cases rising in younger age groups, the total number of cases has fallen, he points out.

And countries also need to consider the global context, say researchers. “Are we really better off giving the vaccine to kids in rich countries than to older people [in less wealthy countries] where it might have a much bigger impact on people’s lives?” says Jennie Lavine, who studies infectious-disease dynamics at Emory University in Atlanta, Georgia. “It seems hard for me to imagine a really good argument for that.”

Although the downward shift in the average age of infections in countries with high COVID-19 vaccination rates is an interesting phenomenon, it might be short-lived, say some researchers. A few scenarios could shift the balance back, says Henrik Salje, an infectious-disease epidemiologist at the

University of Cambridge, UK. Many countries could start to vaccinate younger people — as Israel and the United States are already doing — or new variants and waning immunity among older age groups could make them freshly susceptible, he says.

COVID-19 could still become a disease of the young, says Bundle. “But how big a problem that is, is not a simple thing to respond to.”

Nature **595**, 343-344 (2021)

doi: <https://doi.org/10.1038/d41586-021-01862-7>

References

1. 1.

Magnusson, K. *et al.* Preprint at medRxiv
<https://doi.org/10.1101/2021.06.02.21258211> (2021).

[Download references](#)

Related Articles



- [Does vaccinating adults stop kids from spreading COVID too?](#)



- [How kids' immune systems can evade COVID](#)



- [COVID vaccines and kids: five questions as trials begin](#)

Subjects

- [Public health](#)
- [SARS-CoV-2](#)
- [Epidemiology](#)

nature careers

[Jobs](#) >

- [Postdoctoral Training Fellow](#)

Francis Crick Institute

London, United Kingdom

- [Senior Business Manager](#)

Francis Crick Institute

London, United Kingdom

- [Postdoctoral Research Fellow in Pharmacogenomics Pain Management](#)

The University of British Columbia (UBC)

Vancouver, Canada

- [Postdoctoral Research Fellow in Pain Management and C. elegans](#)

The University of British Columbia (UBC)

Vancouver, Canada

[Download PDF](#)

Related Articles

-  [Does vaccinating adults stop kids from spreading COVID too?](#)
-  [How kids' immune systems can evade COVID](#)
-  [COVID vaccines and kids: five questions as trials begin](#)

Subjects

- [Public health](#)
- [SARS-CoV-2](#)
- [Epidemiology](#)

This article was downloaded by **calibre** from <https://www.nature.com/articles/d41586-021-01862-7>

- NEWS
- 01 July 2021

Mix-and-match COVID vaccines: the case is growing, but questions remain

A slew of studies suggests that mixing vaccines provokes potent immune responses, but scientists still want answers on real-world efficacy and rare side effects.

- [Dyani Lewis](#) 0

1. Dyani Lewis

1. Dyani Lewis is a freelance science journalist in Melbourne, Australia.

[View author publications](#)

You can also search for this author in [PubMed](#) [Google Scholar](#)





•

[Download PDF](#)



A mixture of two COVID-19 vaccines could provide a similar immune response to two doses of a single vaccine. Credit: Canadian Press/Shutterstock

Mixing COVID-19 vaccines is emerging as a good way to get people the protection they need when faced with safety concerns and unpredictable supplies. Most vaccines against SARS-CoV-2 must be given in two doses, but multiple studies now back up the idea that mixing the Oxford–AstraZeneca jab and the Pfizer–BioNTech vaccine triggers an immune response similar to — or even stronger than — two doses of either vaccine.

Results [announced on Monday¹](#) by a UK group suggest that the combination sometimes outperforms two shots of the same vaccine, and a similar picture is emerging from German studies^{2,3}.



Mix-and-match COVID vaccines trigger potent immune response

People can now “feel a bit more comfortable” with the idea of mix-and-match, says immunologist Leif Erik Sander at Charité University Hospital in Berlin.

The results are also giving researchers confidence that combining other COVID-19 vaccines, that haven’t yet been tested together, might also work. But at least 16 vaccines have been approved for use in one or more countries, and mix-and-match studies so far have been small, so more extensive trials and long-term monitoring for side effects are sorely needed.

Immune system boost

Mix-and-match studies were prompted, in large part, by concerns over the safety of the vaccine developed by the University of Oxford and pharmaceutical company AstraZeneca in Cambridge, both in the United Kingdom. The jab has been associated with rare instances of a blood-clotting condition known as thrombosis with thrombocytopenia — and in March, some European countries decided to halt its use in some groups of people. This left many people partially vaccinated, unless they switched to a different brand for their second dose.

In May, researchers at the Carlos III Health Institute in Madrid announced results⁴ from the [CombiVacS trial](#). The study found a strong immune

response in people who were dosed with the vaccine developed by pharmaceutical company Pfizer, based in New York City, and biotechnology firm BioNTech in Mainz, Germany, 8–12 weeks after receiving a dose of the Oxford–AstraZeneca vaccine.

There was no head-to-head comparison with people who received two doses of the same vaccine, but the authors found that in laboratory tests, those who received the combination produced 37 times more SARS-CoV-2 neutralizing antibodies and 4 times more SARS-CoV-2-specific immune cells, called T cells, than did people who had just one dose of the Oxford–AstraZeneca jab.

By the end of June, more results had emerged showing a similar effect.

Sander and his colleagues looked at 340 health-care workers who had received either two doses of the Pfizer–BioNTech vaccine, or an initial shot of the Oxford–AstraZeneca vaccine followed by a dose of Pfizer–BioNTech. Both regimens triggered an immune response that included neutralizing antibodies and T cells².

A third study, by researchers at Saarland University in Homburg, Germany, found³ that the mixed regimen was better at eliciting an immune response than were two Oxford–AstraZeneca shots. It was also as good as or better than two shots of Pfizer–BioNTech.



[Six months of COVID vaccines: what 1.7 billion doses have taught scientists](#)

And on 25 June, the team behind the UK trial — known as the Com-COV study — posted a preprint online¹ showing that a good immune response resulted irrespective of the order in which the two vaccines were given.

However, the trials so far have been too small to test how effective combinations of vaccines are at preventing people from developing COVID-19. “As long as you don’t have any long-term or any follow-up studies with efficacy calculations, it’s hard to say” the level or duration of protection, says Martina Sester, an immunologist who led the Saarland study.

Another limitation of the work so far is that there’s no easy way to compare different combinations between studies. Large-scale efficacy studies are becoming more difficult, says Sester. That’s because, as infection rates decrease, the number of people in a study must increase to detect any difference in rates of infection and disease. Trials pitting mix-and-match vaccine sequences against a placebo control would also be unethical, she adds.

That’s one reason why efforts are under way to determine a ‘[correlate of protection](#)’ — a defined level of immune response that confers protection against infection and disease. “This is extremely urgent,” says Sander.

A nuanced picture

But a nuanced picture is emerging of the magnitude and types of immune response that mixing vaccines produces. And these differences could be exploited to provide the best protection.

The Oxford–AstraZeneca vaccine uses a harmless virus called an adenovirus to carry genetic material from SARS-CoV-2 into cells. Vaccines using this technology have a good track record of inducing strong T-cell responses, says Sander, whereas vaccines using messenger RNA, such as Pfizer’s, have proved “exceptionally good” at inducing high levels of antibodies.



Combining vaccines could help ease supply problems in remote locations, such as rural areas of India. Credit: Dibyangshu Sarkar/AFP/Getty

Sester says that high levels of antibodies after the second shot are an indicator that the combination approach works. “Neutralizing antibodies are probably a good surrogate for predicting efficacy,” she says, because they help to prevent viral infection. But T cells, especially ‘killer’ T cells that carry a protein called CD8, protect against severe disease by killing cells that have already been infected.



What scientists do and don't know about the Oxford–AstraZeneca COVID vaccine

In the Com-COV study, the highest antibody response was in people receiving the standard two shots of Pfizer–BioNTech, but the response was almost as high in the combination of Oxford–AstraZeneca followed by Pfizer–BioNTech. This combination also had the best T-cell response — more than twice as high as that from the two Pfizer–BioNTech doses.

Mixing an mRNA vaccine and an adenovirus-based one could therefore provide “the best of two worlds”, Sander explains.

Sester and her colleagues found subtle differences in T-cell populations depending on the vaccines given. She says that understanding these nuances could lead to individualized strategies. Combinations that provoke good T-cell responses might be better for people who have had organ transplants and are taking medication to suppress their immune systems, for instance, because their bodies will struggle to produce antibodies. “There are many ways of exploiting this knowledge in a strategic way,” she says.

Safety concerns remain

No mix-and-match trials have yet reported severe side effects. In the Com-COV study, mixing vaccines elicited more side effects than did administering two doses of the same vaccine, according to preliminary data released in May⁵. But this wasn't the case in the Charité and Saarland studies or CombiVacS, where side effects were no worse than for two shots of the same vaccine.

That's probably due to the interval between doses, says Sester. Com-COV participants discussed in the latest paper received their second shot four weeks after the initial dose, whereas participants in the German studies had at least nine weeks between shots. Some Com-COV participants did receive doses at a longer interval; their data are anticipated in July.



[WHO approval of Chinese CoronaVac COVID vaccine will be crucial to curbing pandemic](#)

Some safety concerns remain, says Sander. "You're combining two different vaccines, both of which might have their own profile of adverse events and effects," he says, which could amplify any problems.

The studies so far have enrolled only a few hundred people. This means that they are too small to pick up rare events such as the clotting conditions, which according to current estimates occur in around one in 50,000 people after the first Oxford–AstraZeneca vaccine dose and in less than one in 1.7 million after the second. The condition has also been associated with an

adenovirus vaccine produced by pharmaceutical company Johnson & Johnson in New Brunswick, New Jersey.

In small studies, “you do not pick up your one-in-1,000 side effect, let alone your one-in-50,000 side effect”, said Matthew Snape, an Oxford vaccine researcher who is leading the Com-COV study, at a press conference on 28 June.



Seven COVID-19 vaccines have been approved in the Philippines, where a trial will test China’s CoronaVac in combination with the others. Credit: Ted Aljibe/AFP/Getty

The new norm?

The lingering possibility of rare side effects is one reason some researchers recommend that people stick to the standard two shots of a single vaccine for now. “To my mind, you are better defaulting to the ones where we know that they work and there’s a known quantity when it comes to their safety,” says Snape.

But as new variants of SARS-CoV-2 emerge, the results of mix-and-match trials could provide policymakers with the data they need to switch to more protective combinations. “It’s good to have that data in readiness,” says Fiona Russell, a vaccine researcher at the Murdoch Children’s Research Institute in Melbourne, Australia.

Mix-and-match vaccines could also be used to prevent roll-outs stalling because of supply issues. “If there’s a global shortage of one particular vaccine, then rather than stopping the vaccination programme, it can continue,” says Russell.



[Variant-proof vaccines — invest now for the next pandemic](#)

“If it’s an option of either getting a mixed schedule or no second dose, then certainly go for the mixed schedule,” says Snape.

The Com-COV study has already begun testing other vaccines in people who have received an initial Oxford–AstraZeneca or Pfizer–BioNTech shot. One combination includes the yet-to-be-approved protein-based vaccine developed by the pharmaceutical company Novavax in Gaithersburg, Maryland. Another uses the mRNA vaccine from Moderna in Cambridge, Massachusetts, which has been approved for use in several countries.

In the Philippines, a study combining the inactivated-virus vaccine CoronaVac, developed by the company Sinovac in Beijing, with the six other vaccines approved in the country will run until November 2022. And a study by AstraZeneca and the Gamaleya Research Institute in Moscow will test combinations of the Oxford–AstraZeneca jab and Gamaleya’s adenovirus-based Sputnik V shot.

Nature **595**, 344-345 (2021)

doi: <https://doi.org/10.1038/d41586-021-01805-2>

References

1. 1.

Liu, X. *et al.* Preprint at SSRN <https://doi.org/10.2139/ssrn.3874014> (2021).

2. 2.

Hillus, D. *et al.* Preprint at medRxiv
<https://doi.org/10.1101/2021.05.19.21257334> (2021).

3. 3.

Schmidt, T. *et al.* Preprint at medRxiv
<https://doi.org/10.1101/2021.06.13.21258859> (2021).

4. 4.

Borobia, A. M. *et al.* Preprint at SSRN
<https://doi.org/10.2139/ssrn.3854768> (2021).

5. 5.

Shaw, R. H. *et al.* *Lancet* **397**, 2043–2046 (2021).

[PubMed](#) [Article](#) [Google Scholar](#)

[Download references](#)

Related Articles



- [Mix-and-match COVID vaccines trigger potent immune response](#)



- [Six months of COVID vaccines: what 1.7 billion doses have taught scientists](#)



- [Coronapod: Is mixing COVID vaccines a good idea?](#)

Subjects

- [Vaccines](#)
- [SARS-CoV-2](#)
- [Immunology](#)

nature careers

[Jobs >](#)

- [Postdoctoral Training Fellow](#)

Francis Crick Institute

London, United Kingdom

- [**Senior Business Manager**](#)

Francis Crick Institute
London, United Kingdom

- [**Postdoctoral Research Fellow in Pharmacogenomics Pain Management**](#)

The University of British Columbia (UBC)
Vancouver, Canada

- [**Postdoctoral Research Fellow in Pain Management and C. elegans**](#)

The University of British Columbia (UBC)
Vancouver, Canada

[Download PDF](#)

Related Articles



- [**Mix-and-match COVID vaccines trigger potent immune response**](#)



- [**Six months of COVID vaccines: what 1.7 billion doses have taught scientists**](#)



- [Coronapod: Is mixing COVID vaccines a good idea?](#)

Subjects

- [Vaccines](#)
- [SARS-CoV-2](#)
- [Immunology](#)

This article was downloaded by **calibre** from <https://www.nature.com/articles/d41586-021-01805-2>

| [Section menu](#) | [Main menu](#) |

- NEWS FEATURE
- 08 July 2021

The quest to find genes that drive severe COVID

Genome studies have discovered some genetic risk factors for disease — and could point to treatments.

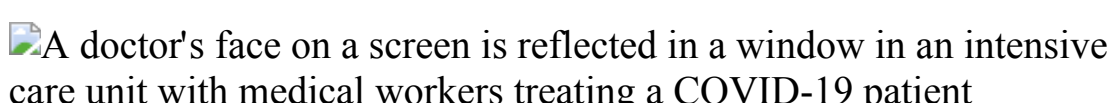
- [Ewen Callaway](#)
 1. Ewen Callaway
[View author publications](#)

You can also search for this author in [PubMed](#) [Google Scholar](#)





•



People with COVID-19 being treated in an intensive care unit in El Centro, California. Credit: Melina Mara/The Washington Post/Getty

[Download PDF](#)

Since last March, research teams around the world have scoured the genomes of more than 100,000 people with COVID-19, hoping to find genetic clues to who will be hit hardest by an infection with the virus SARS-CoV-2. What's emerged from this effort is a dozen or so genetic

variants that have a strong statistical association with a person's chances of developing COVID-19 and becoming gravely ill with the disease, the teams report in a summary analysis published on 8 July in *Nature*¹.

"There were actually quite a few very common genetic variants that were really important in COVID-19," says Guillaume Butler-Laporte, an infectious-disease physician and genetic epidemiologist at McGill University in Montreal, Canada. "I don't think we expected to find them so clearly."

The loosely aligned teams involved in the analysis include both academic laboratories and private firms such as the US companies 23andMe and AncestryDNA, and have been releasing their work steadily over the past year. Known collectively as the COVID-19 Host Genetics Initiative (HGI), they first posted their summary — an amalgamation of 46 separate studies covering, at the time of analysis, almost 50,000 people with COVID-19 — on the medRxiv preprint server in March.

The genetic associations they found increase risk by a relatively small amount, although some of the rises are comparable to those for risk factors such as obesity, diabetes and other underlying health conditions (see 'Genetic variants that change COVID-19 risk').

Genetic variants that change COVID-19 risk

The Host Genetics Initiative has found more than a dozen areas of the genome that are statistically associated with susceptibilities to SARS-CoV-2 infection or severe illness.

| Clinical effect | Effect on risk (% increase)* | Possible genetic link | Chromosome |
|--------------------|------------------------------|-----------------------|------------|
| Susceptibility 4–8 | Unclear | | 19 |

| Clinical effect | Effect on risk (%) increase)* | Possible genetic link | Chromosome |
|------------------------|--------------------------------------|---|-------------------|
| Susceptibility 5–8 | | Unclear | 3 |
| Susceptibility 9–12 | | <i>ABO</i> (determines blood group) | 9 |
| Susceptibility 13–18 | | <i>SLC6A20</i> (interacts with ACE2 receptor, which mediates SARS-CoV-2 entry) | 3 |
| Severity 9–18 | | Unclear | 17 |
| Severity 13–20 | | <i>IFNAR1/2</i> (part of cell receptor for interferon, proteins that bolster immune response) | 21 |
| Severity 14–26 | | <i>OAS</i> family (enzymes that digest viral RNA) | 12 |
| Severity 17–36 | | <i>FOXP4</i> (involved in lung diseases) | 6 |
| Severity 20–32 | | <i>DPP9</i> (enzyme involved in lung disease) | 19 |

| Clinical effect | Effect on risk (% increase)* | Possible genetic link | Chromosome |
|-----------------|------------------------------|--|------------|
| Severity | 24–52 | Unclear | 8 |
| Severity | 28–64 | Unclear | 17 |
| Severity | 29–59 | <i>TYK2</i> (enzyme involved in interferon signalling) | 19 |
| Severity | 56–74 | Unclear | 3 |

*In the HGI summary, risk estimates are for people with one copy of the risk-increasing allele for the variant and were determined in groups that had varying criteria for inclusion, so might not be directly comparable. Other studies give different estimates.

But the findings can shed light on biological mechanisms of the disease, and suggest which drugs to test, says Kenneth Baillie, an intensive-care physician and a geneticist at the University of Edinburgh, UK. In other research, scientists have also picked out rare genetic mutations — in contrast to the relatively common variants listed in the latest HGI study — that might also explain the root causes of severe disease.

Not everyone is convinced that the genetic work gives immediate insight. “We’re starting to get a pretty good genetic map,” says Julian Knight, a human geneticist at the University of Oxford, UK. “To move that on to where we’ve got good drug targets or an understanding of disease variability, that’s going to be a big step.” This, he says, is a typical issue for research that tries to link common variations in genomes with people’s risk of complex diseases.

And Kári Stefánsson, chief executive of deCODE Genetics in Reykjavik and a member of the HGI, doesn't feel that the work to find genetic 'hits' has been especially fruitful — at least so far. Still, Stefánsson says, "I think it's extremely important to follow as many of these as possible. You may be able to find a mechanism of major importance."

Although geneticists don't yet have all the answers, they've moved extremely rapidly to unpick associations with COVID-19, says Brent Richards, a geneticist and endocrinologist at McGill University who is part of the HGI. "The human-genetics community hasn't slept much this year," he says.

Genetic hits for COVID-19

The HGI worked less like a consortium focused on a single unifying project, and more as a clearing house for collaborations, support and advice. Teams were free to publish their own studies, while contributing to pooled studies that combined individual efforts. "It was just a matter of creating a place that people would feel comfortable together, and work together," says Andrea Ganna, a statistical geneticist who co-founded the HGI with geneticist Mark Daly; both are at the University of Helsinki and the Broad Institute in Cambridge, Massachusetts.

Ganna is a specialist in genome-wide association studies (GWAS) — the bread and butter of genetic epidemiology. These examine hundreds of thousands of relatively common single-letter DNA differences across the genome in large numbers of people, to see whether any are enriched in people with a particular disease or trait. It was inevitable that people would apply GWAS to COVID-19, Ganna says.



The race for antiviral drugs to beat COVID — and the next pandemic

One genomic variant identified by Baillie's team and confirmed in other HGI efforts is near a family of antiviral genes called *OAS* (oligoadenylate synthase). The genes activate enzymes that chew up viral RNA, and HGI studies^{1,2} show that a variant that leads to lower circulating levels of the OAS1 enzyme in the lungs increases risk of infection, hospitalization and critical illness. Most coronaviruses counteract this protection using proteins called PDEs, or phosphodiesterases, but SARS-CoV-2 doesn't make PDEs. "So this might provide an Achilles heel," explains Richards, who is aware of pharmaceutical companies that are pursuing the target, but declines to reveal details. On the basis of the genetic association, drugs known as phosphodiesterase 12 inhibitors are predicted to boost natural antiviral defences, Baillie says.

Another variant spotted by Baillie's team and confirmed in other COVID-19 GWAS is near a gene that encodes a portion of a cellular receptor for molecules called interferons¹, which are well known for boosting people's immune responses to viruses. Because of this antiviral role, one kind of interferon molecule had already been tested in trials, before the genetic association came to light. It was one of the [first drugs included in the World Health Organization-sponsored 'Solidarity' trial](#) of COVID-19 treatments, but didn't help patients. It's possible that the genetic prediction was wrong,

Baillie says, but it could be that interferon needs to be administered earlier in infection, or in a different manner to the subcutaneous or intravenous injections that Solidarity trial participants received.

Baillie also says that other genetic associations are now being used to prioritize treatments. One example is in the widely praised UK-based RECOVERY trial, which most famously showed the benefit of a common steroid for people with severe COVID-19³. The trial is using genetic data to help select drugs to test — including a rheumatoid arthritis drug called baricitinib and a treatment for psoriasis and multiple sclerosis called dimethyl fumarate, says Baillie, who is part of the effort.

Baricitinib inhibits the protein encoded by a gene, *TYK2*, that was associated with life-threatening COVID-19². The relationship between *TYK2* activity and risk of severe COVID-19 isn't clear-cut from the genetic studies, "but it did provide a big extra source of support for the idea", says Baillie. Dimethyl fumarate was included largely for its known role in quelling an inflammatory process involved in severe COVID-19, but genetic links provided added support for testing it in RECOVERY, says Baillie.

GWAS, however, also have a reputation for delivering head-scratching results. That has happened with COVID-19, too: the strongest association between any gene variant and severe COVID-19 lies in a poorly studied region of chromosome 3¹. "We still don't quite know, as a scientific community, why it's so important," says Butler-Laporte. The chromosome 3 region includes several genes involved in immune signalling, lung biology and other plausible mechanisms. But it's not clear which of these genes explains the association with COVID-19.

People who carry this gene variant are around twice as likely as others to be hospitalized with COVID-19. A study⁴ led by Richards, Ganna and Tomoko Nakanishi, a geneticist and respiratory physician at McGill, found that the variant raises the odds of people aged 60 or under becoming critically ill or dying from COVID-19 as much as and perhaps even more than risk factors including diabetes, obesity and chronic obstructive pulmonary disease.

Risk scores

As a result of such associations, some researchers are exploring whether the genetic links turned up in GWAS could be used to predict an individual's risk of a life-threatening SARS-CoV-2 infection. Risk scores, which amalgamate associations discovered in GWAS, have been used to measure an individual's risk of conditions such as type 2 diabetes, various cancers and cardiovascular disease.

But it's not clear whether this approach could work for COVID-19 — or is even needed, given the availability of vaccines. In June, a firm in Fitzroy, Australia, called Genetic Technologies launched a US\$175 test to predict people's risk of developing severe COVID-19. But it also relies on age, sex and health, all factors that significantly improve the predictive power of the GWAS associations⁵.



[How COVID broke the evidence pipeline](#)

Chief scientific officer Richard Allman says that the firm's test, which was developed and validated using data from the UK Biobank database, might be most useful for middle-aged people. Most will have a relatively small risk of severe COVID-19, but the test could identify those rare individuals with vastly increased (or dramatically reduced) chances of developing a

life-threatening infection. The firm's test is currently available only in the United States, through a company called Infinity BiologiX in Piscataway, New Jersey, and with consultation from a health professional. Still, Genetic Technologies is in talks with companies interested in offering the test to employees, says Allman, who says he does not have sales figures.

Nakanishi, Richards and Ganna say that it's not clear whether the test has been validated enough to be reliable, but that that doesn't mean such tests couldn't be useful as another motivation for higher-risk people to get vaccinated. "It might get a few people over the edge who are worried [about vaccination]," adds Genetic Technologies biostatistician Gillian Dite.

Genetic studies of COVID-19 — like those of most other diseases — have overwhelmingly been based on people with European ancestry. That's a problem, says Knight, because of the global burden of COVID-19 and elevated rates of disease in minority ethnic groups in countries such as the United States and United Kingdom. "We really need to make the investment in genetics in those populations."

Diversifying genetic studies can not only improve understanding of risk variants identified in European populations, but also identify new ones in other groups. A GWAS that included more than 2,000 people hospitalized with COVID-19 in Japan⁶ identified many of the variants flagged by studies of European populations, as well as an immune gene, called *DOCK2*, with a role in interferon production that hadn't come up in other studies. The *DOCK2* variant that increased COVID-19 risk was relatively common in East Asians, but very rare in people of European, South Asian and African ancestry. "This tells us the importance of increasing diversity in host genetics of COVID-19," says study leader Yukinori Okada, a statistical geneticist at Osaka University in Japan.

Rare mutations

Some researchers feel that the GWAS approach, which has found common variants that raise an individual's risk only by a small amount, is less fruitful than spotting much rarer mutations that might explain why some otherwise healthy people are in intensive care with COVID-19.

That's the view of Jean-Laurent Casanova, a geneticist at the Rockefeller University in New York City. He co-leads a consortium called the COVID Human Genetic Effort, which in September 2020 reported⁷ spotting mutations in people with severe COVID-19 that disable genes involved in a potent antiviral response, called type 1 interferon immunity. (One of the genes in which they found mutations, *IFNAR2*, which codes for a subunit of an interferon receptor, has also been flagged by multiple GWAS.) The mutations identified by Casanova's team were rare, but in a follow-up study⁸, the researchers found that 10% of people with life-threatening COVID-19 produced antibodies that inactivate type 1 interferons — mimicking the effects of the gene mutations. Casanova says his team looked for them only after they identified the genetic mutations, underscoring the power of his approach to point to new lines of research. "Essentially what we've cracked is a mechanism of critical COVID-19 pneumonia," he says.



Rogue antibodies could be driving severe COVID-19

Rare mutations with profound consequences are “a great torch to use” to uncover disease mechanisms, says Akiko Iwasaki, an immunologist at Yale University in New Haven, Connecticut, whose team is [studying the role of ‘autoantibodies’](#), which attack the body’s own immune defences, in severe COVID-19. The effects of common variants identified in GWAS might be subtler, she adds, but the unbiased way in which they are identified means

that the hits can give credence to insights from other disciplines, such as immunology. “It’s explaining some of the things we’re seeing,” she says. “I love that aspect of it.”

Richards is part of a team that is trying to replicate Casanova’s genetic finding, without success so far. He and his colleagues found that mutations in 13 type-1 interferon genes were no more common in nearly 2,000 people with COVID-19 than in controls not known to have been infected⁹, echoing the conclusions of an analysis led by researchers at the biotechnology firm Regeneron in Tarrytown, New York, who looked at protein-coding genes in more than half a million UK Biobank participants¹⁰. This doesn’t mean that the type 1 interferon pathways are not important, Richards says, and he agrees that the autoantibody connection looks promising.

Alessandra Renieri, a geneticist at the University of Siena, Italy, and an early member of the HGI, says that GWAS findings need to be integrated with links to rare variants and other forms of genetic diversity if researchers are to fully understand COVID-19 susceptibility, and to come up with treatments. She is part of a team that has applied for permission from Italian regulators to test therapies based on genetic findings.

For instance, the team wants to test an adjuvant (which awakens the immune system) in people with rare mutations that disable a virus-detecting gene called *TLR7*, which might be connected to severe COVID-19¹¹. It also wants to test whether the hormone testosterone might be able to prevent life-threatening COVID-19 in men with a common variation in a gene that encodes a receptor for the hormone, after finding a link between severe COVID-19 and gene variants associated with reduced levels of testosterone circulating in the blood¹².

The success of such trials should not be the only metric by which to judge the fruits of genetic studies into COVID-19, say researchers. Other biologists are drawing on the genetic studies to help make sense of their own experiments on the virus. And puzzling associations such as the chromosome 3 link could reveal important insights that help in treating COVID-19 — and whatever disease is caused by the next new coronavirus.

Each new genetic finding is like a piece of a puzzle, Renieri says. “Several pieces are coming together. I’m sure that the picture will be much more clear in the very near future.”

Nature **595**, 346-348 (2021)

doi: <https://doi.org/10.1038/d41586-021-01827-w>

References

1. 1.

COVID-19 Host Genetics Initiative. *Nature*
<https://doi.org/10.1038/s41586-021-03767-x> (2021).

[Article](#) [Google Scholar](#)

2. 2.

Pairo-Castineira, E. *et al.* *Nature* **591**, 92–98 (2021).

[PubMed](#) [Article](#) [Google Scholar](#)

3. 3.

The RECOVERY Collaborative Group *N. Engl. J. Med.* **384**, 693–704 (2021).

[PubMed](#) [Article](#) [Google Scholar](#)

4. 4.

Nakanishi, T. *et al.* Preprint at medRxiv
<https://doi.org/10.1101/2021.03.07.21252875> (2021).

5. 5.

Dite, G. S., Murphy, N. M. & Allman, R. Preprint at medRxiv
<https://doi.org/10.1101/2021.03.09.21253237> (2021).

6. 6.

Namkoong, H. *et al.* Preprint at medRxiv
<https://doi.org/10.1101/2021.05.17.21256513> (2021).

7. 7.

Zhang, Q. *et al.* *Science* **370**, eabd4570 (2020).

[PubMed](#) [Article](#) [Google Scholar](#)

8. 8.

Bastard, P. *et al.* *Science* **370**, eabd4585 (2020).

[PubMed](#) [Article](#) [Google Scholar](#)

9. 9.

Povysil, G. *et al.* Preprint at medRxiv
<https://doi.org/10.1101/2020.12.18.20248226> (2020).

10. 10.

Kosmicki, J. A. *et al.* Preprint at medRxiv
<https://doi.org/10.1101/2020.10.28.20221804> (2021).

11. 11.

Fallerini, C. *et al.* *eLife* **10**, e67569 (2021).

[PubMed](#) [Article](#) [Google Scholar](#)

12. 12.

Baldassarri, M. *et al.* *EBioMedicine* **65**, 103246 (2021).

[PubMed Article](#) [Google Scholar](#)

[Download references](#)

Related Articles



- [Rogue antibodies could be driving severe COVID-19](#)



- [How COVID broke the evidence pipeline](#)



- [The race for antiviral drugs to beat COVID — and the next pandemic](#)

Subjects

- [SARS-CoV-2](#)
- [Genetics](#)

nature careers

[Jobs](#) >

- [Postdoctoral Training Fellow](#)

Francis Crick Institute

London, United Kingdom

- [**Senior Business Manager**](#)

Francis Crick Institute
London, United Kingdom

- [**Postdoctoral Research Fellow in Pharmacogenomics Pain Management**](#)

The University of British Columbia (UBC)
Vancouver, Canada

- [**Postdoctoral Research Fellow in Pain Management and C. elegans**](#)

The University of British Columbia (UBC)
Vancouver, Canada

[Download PDF](#)

Related Articles

-  [**Rogue antibodies could be driving severe COVID-19**](#)
-  [**How COVID broke the evidence pipeline**](#)



- **The race for antiviral drugs to beat COVID — and the next pandemic**

Subjects

- SARS-CoV-2
- Genetics

This article was downloaded by **calibre** from <https://www.nature.com/articles/d41586-021-01827-w>

| [Section menu](#) | [Main menu](#) |

- NEWS FEATURE
- 14 July 2021

Racism is magnifying the deadly impact of rising city heat

Scientists are mapping correlations between race, poverty and heat in cities, and suggesting solutions to reduce the dangers.

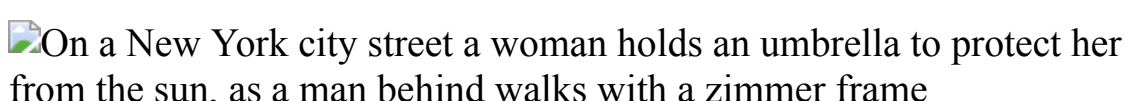
- [Alexandra Witze](#)
 1. Alexandra Witze
[View author publications](#)

You can also search for this author in [PubMed](#) [Google Scholar](#)





•



New York City residents endured near-record high temperatures in late June during a heatwave that caused power outages. Credit: Mark Kauzlarich/Bloomberg/Getty

[Download PDF](#)

Luis Rodriguez holed up in his kids' bedroom last month as a brutal heatwave baked his Los Angeles neighbourhood and the rest of the southwestern United States. The space was their only room with an air-

conditioning unit, and the safest place in the house when temperatures outside soared above 40 °C.

All day, Rodriguez tapped on his computer, working remotely as a volunteer manager for TreePeople, a non-profit environmental organization in Beverly Hills, California, that plants and cares for trees across Los Angeles. His two young sons crammed into the bedroom with him to avoid the dangerous heat. Only as evening fell would they emerge, after temperatures in the house had climbed so high that it was cooler outside. The boys played in the shade of the fig tree Rodriguez planted in front of his house — as much for its large, shade-producing leaves as for its delicate fruit.

From Los Angeles to Lagos, extreme heat is a growing problem. As temperatures soar and heatwaves become more common because of global warming, people living in cities are particularly at risk. Asphalt, concrete and other surfaces that absorb and emit heat make many urban environments much hotter than suburban or rural areas.



How cities can beat the heat

To help reduce the risk of heat stroke and other heat-related illnesses, urban planners, meteorologists, climate experts and other scientists are working to identify the most vulnerable neighbourhoods. Underlying such efforts is a growing awareness of how extreme heat takes a disproportionate toll on

people of colour and those in lower-income communities. Racist urban policies, particularly in the United States, have left communities of colour at higher risk of heat-related illness or death than their white neighbours.

In the past few years, a growing body of research has revealed the environmental injustices that have left some residents baking in vast expanses of asphalt while other urban neighbourhoods benefit from green parks, spacious lawns and sprawling trees. “It’s really shocking,” says Angel Hsu, a climate scientist at the University of North Carolina in Chapel Hill. “We have to ask ourselves why — to try to figure out why these patterns are so consistent and so pervasive.”

Similar inequalities threaten urban residents in many other countries, but some of the best-documented examples are in the United States, where researchers are increasingly exploring the links between discriminatory policies and heat risks. Many cities are now working to incorporate heat equity into their urban planning, such as by planting trees and painting roofs white in neighbourhoods that have typically received fewer resources. But such climate-adaptation plans have a long way to go to counter decades of deliberate neglect of the most vulnerable residents.

Fatal conditions

Worldwide, more than 166,000 people died in heatwaves between 1998 and 2017, according to the World Health Organization. That makes heat among the deadliest of all weather-related disasters, including cold spells, floods, lightning and hurricanes. Yet its impact is routinely underestimated, because death certificates commonly list a cause of death, such as heart failure, without noting that the person had been exposed to high temperatures.

In a study¹ of deaths and emergency hospital admissions in Houston, Texas, between 2004 and 2013, scientists found that people older than 65 were probably dying as a result of hot days at higher rates than had been officially recorded. “Extreme heat is one of the underappreciated natural hazards,” says Olga Wilhelmi, a geographer at the National Center for Atmospheric Research in Boulder, Colorado, and an author of the study.



How hot will Earth get by 2100?

Extreme heat can trigger fatal heat exhaustion or heat stroke, which occur when a person's body cannot cool itself enough. Heat stress can also kill by exacerbating underlying conditions, such as cardiovascular or respiratory disease. Most vulnerable are children, older people and those with chronic health conditions or who work outdoors. But even healthy younger adults can die if the heat is bad enough. Many people die during stretches of hot weather, especially when temperatures don't drop much at night^{2,3}.

Some of the most lethal heatwaves have occurred in temperate cities that were suddenly exposed to extreme heat. At least 14,000 people died in a heatwave that blasted France in 2003, and more than 700 perished in Chicago, Illinois, in 1995. The full toll of a record-breaking heatwave in the northwestern United States and southwestern Canada last month is not yet clear, but hundreds of people are thought to have died from the heat.



Residents of Portland, Oregon, seek relief in a cooling centre on 28 June, the third straight day of record high temperatures for the city.Credit: Kathryn Elsesser/AFP/Getty

Although heatwaves affect people in rural areas, cities often bear the brunt of the impact. That's because of the urban heat-island effect, in which the materials that make up streets and buildings cause the air to heat up more than in leafier areas. On average, central urban areas are several degrees celsius warmer during the day than the surrounding countryside — but they can be much hotter than that.

In many cities around the world, the most vulnerable residents face the greatest risk. In Qatar, many migrant workers in the construction industry die from cardiovascular failure brought on by heat stroke⁴; a study of more than 1,300 workers from Nepal who died between 2009 and 2017 found that heat-protection measures could have saved the lives of up to 200 of them had effective programmes been in place⁴. In Bangkok, a survey⁵ of 505 residents conducted during the hot season in 2016 found that people on low

incomes were more likely to report experiencing heat stress than were those on high incomes.

Climate models project that the problem will only get worse. Not only are average summer temperatures rising, but heatwaves are becoming more frequent and more intense, and are lasting longer. An international research team reported in May that approximately 37% of heat-related deaths across 43 countries can be linked to human-induced climate change⁶.

Inequality in hotspots

For Hsu, the challenge became clear when she was working in Singapore, where parts of the urban core can be up to 7 °C hotter than nearby regions. She now runs a data-analytics group that works on climate-change solutions — and has taken a hard look at the racism that helps to determine who in the United States is most exposed to extreme heat, and why.

Hsu likes to point out that her hometown of Greenville, South Carolina, is not green for everyone. The parts of town that experience the most heat stress are populated mostly by Black people, Hsu has found. In one of the broadest studies yet to look at differential heat exposure in the United States, she and her colleagues combined satellite measurements of urban heat with census data that included detailed demographic information about who was living in which parts of 175 cities⁷.



Heatwaves blamed on global warming

Hsu says she expected to find disproportionate exposure, but was shocked by the sheer magnitude of the difference. In 97% of the cities, communities of colour were exposed to temperatures a full degree celsius higher, on average, than communities composed mostly of non-Hispanic white people. “We see systemic, pervasive and widespread evidence of environmental racism with respect to urban heat island exposure,” she says. “I didn’t think it was going to be basically universal.”

Exposure to heat also correlated with income; people living below the poverty line, irrespective of race or ethnicity, were exposed to higher temperatures than were those above the poverty line.

Yet race remains the factor that shapes so much of US urban heat exposure. And the history traces back more than a century and a half. After the United States abolished slavery in 1865, housing policies across the nation were designed to systemically exclude people of colour, particularly Black people, from living in certain neighbourhoods.



Cities must protect people from extreme heat

One major driver for today's differential heat exposure was a federal loan-approval programme created by Congress in 1933, which was meant to help people to pay their mortgages during the Great Depression. The corporation overseeing the loans drew up detailed neighbourhood maps in 239 US cities, ranking them from A (perceived as the safest place for banks to invest) to D (perceived as the riskiest). Neighbourhoods with a high percentage of minority racial or ethnic groups or immigrants were almost inevitably graded as D — often with racist annotations from the corporation representative — and marked as red on city maps.

This 'redlining' practice led to deliberate decisions that affect nearly all aspects of many US cities, including access to schools, parks and other community facilities. And over the past several years, the environmental non-profit organization Groundwork USA, a network of local groups across the country, has worked with various research teams to compare those redlining maps against modern environmental risks such as extreme heat and flooding (see 'Inequality and extreme heat'). "You can see how little investment has been done in the areas that were redlined," says Jasmin Barco, a community organizer at Groundwork Denver in Colorado. "It's just crazy."

On average, temperatures in redlined areas in 108 US urban areas are 2.6 °C warmer than in non-redlined areas, according to an influential 2020 paper⁸ in the journal *Climate*. That's a result of the impervious surfaces and lack of tree canopy, but is probably also linked to racist urban-planning policies, such as decisions to build large highways and industrial buildings (with their heat-absorbing concrete) in communities of colour. “This is a clear case of systemic planning processes that had marginalized communities for generations,” says Vivek Shandas, an urban ecologist at Portland State University in Oregon and a co-author of the paper.

Temperature patrols

Shandas remembers when he first got his driver’s licence and would eagerly cruise around his home town to see as much as possible. He was struck by how temperature displays outside banks differed across the city. That didn’t mean the banks had malfunctioning thermometers, Shandas says; each bank displayed the temperature in its particular environment, whether that was a hot reflective parking lot or a cool, shaded street.

Later, when he began working in climate science, Shandas recruited people to travel around various cities with temperature sensors mounted to their cars or bikes. He was surprised by how detailed and revealing the measurements from different blocks were. “We had a hunch there would be a difference,” he says. “But we didn’t know it would translate so explicitly and so systematically to air temperatures.”



How environmental racism is fuelling the coronavirus pandemic

These crowdsourced temperature-mapping projects have expanded over the past few years. This summer, the US National Oceanic and Atmospheric Administration is running an urban heat-island mapping campaign — which Shandas advises on — in cities in 11 states.

On extremely hot days, volunteers will drive and bike across the cities, starting in the early morning. By building up a temperature and humidity profile across the city and throughout the day, the researchers will gather data to help them understand which neighbourhoods get the hottest. They can then combine those data with satellite measurements to predict which blocks are likely to be the most vulnerable as hot air masses move in above a city.

Ultimately, Shandas dreams of building an urban map of air temperatures across the entire United States. With such precise predictions, he says, officials can better plan where to deploy their resources to fight extreme conditions.

Cool ideas

Around the world, city officials have many ways to try to beat the heat. One approach is to keep public spaces such as parks or air conditioned community centres open for extended hours during heatwaves — providing a respite for people sweltering in their apartments. And lives can be saved by spreading awareness about impending extreme heat, such as by texting people an advance warning of a heatwave or displaying temperature readings on electronic billboards around a city.

Officials in Ahmedabad, India, adopted a pioneering heat action plan after a heatwave in 2010 killed more than 1,300 people. The strategy involves rolling out public warnings and other resources when the temperature is forecast to exceed 41 °C. In the years after the heat action plan was implemented, it saved an average of 1,190 lives annually⁹.



Climate change made Europe's mega-heatwave five times more likely

A number of cities target their mitigation efforts at their most vulnerable communities. “There’s an increasing interest in making sure that the most marginalized, vulnerable and excluded populations are the focus of a lot of these efforts,” says Kurt Shickman, executive director of the Global Cool Cities Alliance in Washington DC. For instance, a study¹⁰ done in Durban, South Africa, late last year used projections of future climate change to calculate which areas will be most exposed to heat stress in the future, but

also wrapped in data on socioeconomic factors to identify which at-risk neighbourhoods should be targeted for adaptation projects.

In France, Paris has an ‘oasis’ programme aimed at turning public school yards into cool spaces, particularly in the city’s more racially and ethnically diverse suburbs. And in the United States, many cities provide financial assistance to residents to help defray energy bills in the summer, when the costs of air-conditioning can be so high that people cannot afford to turn the units on.

Small initiatives can often punch above their weight in terms of their impact. Because social isolation increases the risk of someone dying in a heatwave, New York City encourages a buddy system in which residents check in with friends and family on hot days. This summer in Phoenix — the hottest major city in the United States — researchers at Arizona State University are trialling an in-home temperature sensor that would text a friend or family member if the indoor temperature got too hot.

Other changes can be as simple as putting in a pedestrian crossing so that people can easily reach the shady side of a street. Such relatively straightforward steps can help to relieve heat stress in many people, says David Hondula, a climate scientist at Arizona State. “I’m really encouraged by where we could be headed in the next five to ten years,” he says.



Droughts, heatwaves and floods: How to tell when climate change is to blame

In Los Angeles, researchers have calculated that two basic interventions — planting trees and painting roofs white — could have prevented at least one-quarter of the deaths attributed to recent heatwaves¹¹. As in other cities, those deaths occurred disproportionately in communities of colour, says Edith de Guzman, director of the Los Angeles Urban Cooling Collaborative. But the answer isn't as simple as just plopping trees into underserved areas of the city. Trees need to be carefully selected not only for their resilience to heat but also for how much shade the species will provide, she says.

Los Angeles has yet to meet an ambitious million-tree goal announced by the city's mayor in 2006. But Rodriguez is doing his part from his home in the notoriously hot San Fernando Valley. His neighbourhood is mostly 1950s-era single-family homes that were built to house veterans after the Second World War; it is now much more racially and ethnically diverse.

Many of the sweetgum trees originally planted along his street have toppled or died. Rodriguez has planted not only his favourite fig tree, but also guava, pomegranate and plum trees. The four stand close together in front of his house and will one day generate a larger shade canopy.

It's part of his plan to keep his family cool in the hotter future.

Nature **595**, 349-351 (2021)

doi: <https://doi.org/10.1038/d41586-021-01881-4>

References

1. 1.

O'Lenick, C. R. *et al. Environ. Health Perspect.* **128**, 127007 (2020).

[PubMed](#) [Article](#) [Google Scholar](#)

2. 2.

Murage, P., Hajat, S. & Kovats, R. S. *Environ. Epidemiol.* **1**, e005 (2017).

[PubMed](#) [Article](#) [Google Scholar](#)

3. 3.

Royé, D. *et al.* *Epidemiology* **32**, 487–498 (2021).

[PubMed](#) [Article](#) [Google Scholar](#)

4. 4.

Pradhan, B. *et al.* *Cardiology* **143**, 37–48 (2019).

[PubMed](#) [Article](#) [Google Scholar](#)

5. 5.

Arifwidodo, S. D. & Chandrasiri, O. *Environ. Res.* **185**, 109398 (2020).

[PubMed](#) [Article](#) [Google Scholar](#)

6. 6.

Vicedo-Cabrera, A. M. *et al.* *Nature Clim. Change* **11**, 492–500 (2021).

[Article](#) [Google Scholar](#)

7. 7.

Hsu, A., Sheriff, G., Chakraborty, T. & Manya, D. *Nature Commun.* **12**, 2721 (2021).

[PubMed](#) [Article](#) [Google Scholar](#)

8. 8.

Hoffman, J. W., Shandas, V. & Pendleton, N. *Climate* **8**, 12 (2020).

[Article](#) [Google Scholar](#)

9. 9.

Hess, J. J. *et al.* *J. Environ. Public Health* **2018**, 7973519 (2018).

[PubMed](#) [Article](#) [Google Scholar](#)

10. 10.

Jagarnath, M., Thambiran, T. & Gebreslasie, M. *Clim. Change* **163**, 807–829 (2020).

[Article](#) [Google Scholar](#)

11. 11.

de Guzman, E. *et al.* *Rx for Hot Cities: Climate Resilience through Urban Greening and Cooling in Los Angeles* (Los Angeles Urban Cooling Collaborative, 2020).

[Google Scholar](#)

[Download references](#)

Related Articles



- [Cities must protect people from extreme heat](#)



- [Climate change made Europe's mega-heatwave five times more likely](#)



- [How environmental racism is fuelling the coronavirus pandemic](#)



- [Droughts, heatwaves and floods: How to tell when climate change is to blame](#)



- [How hot will Earth get by 2100?](#)



- [How cities can beat the heat](#)



- [Heatwaves blamed on global warming](#)

Subjects

- [Climate change](#)
- [Society](#)
- [Climate sciences](#)

nature careers

[Jobs](#) >

- [Postdoctoral Training Fellow](#)

Francis Crick Institute
London, United Kingdom

- [**Senior Business Manager**](#)

Francis Crick Institute
London, United Kingdom

- [**Postdoctoral Research Fellow in Pharmacogenomics Pain Management**](#)

The University of British Columbia (UBC)
Vancouver, Canada

- [**Postdoctoral Research Fellow in Pain Management and C. elegans**](#)

The University of British Columbia (UBC)
Vancouver, Canada

[Download PDF](#)

Related Articles

-  [**Cities must protect people from extreme heat**](#)
-  [**Climate change made Europe's mega-heatwave five times more likely**](#)



- [How environmental racism is fuelling the coronavirus pandemic](#)



- [Droughts, heatwaves and floods: How to tell when climate change is to blame](#)



- [How hot will Earth get by 2100?](#)



- [How cities can beat the heat](#)



- [Heatwaves blamed on global warming](#)

Subjects

- [Climate change](#)
- [Society](#)
- [Climate sciences](#)

This article was downloaded by **calibre** from <https://www.nature.com/articles/d41586-021-01881-4>

Opinion

- **[Mental health: set up long-term cohort studies](#)** [13 July 2021]
Correspondence •
- **[Italy: scientists petition against biodynamic farming law](#)** [13 July 2021]
Correspondence •
- **[To build resilience, study complex systems](#)** [13 July 2021]
Correspondence •
- **[Scale up rapid research autopsies for tissue immunology](#)** [13 July 2021]
Correspondence •
- **[Africa: renewables infrastructure avoids stranded assets](#)** [13 July 2021]
Correspondence •
- **[Pollution from hydrogen fuel could widen inequality](#)** [13 July 2021]
Correspondence •
- **[Italy: Forest harvesting is the opposite of green growth](#)** [13 July 2021]
Correspondence •

- CORRESPONDENCE
- 13 July 2021

Mental health: set up long-term cohort studies

- [Ralf Buckley](#)⁰ &
- [Paula Brough](#)¹

1. [Ralf Buckley](#)

1. Griffith University, Gold Coast, Australia.

[View author publications](#)

You can also search for this author in [PubMed](#) [Google Scholar](#)

2. Paula Brough

1. Griffith University, Gold Coast, Australia.

[View author publications](#)

You can also search for this author in [PubMed](#) [Google Scholar](#)





•

[Download PDF](#)

The world missed an opportunity to test the effects of nature deprivation on mental health during COVID-19 lockdowns, because pre-lockdown control data were unavailable. To restore mental health at population scale in the face of future social disruptions (see [Nature 593, 331–333; 2021](#)), reliable evidence is needed from large-scale, long-term, repeated, representative population samples (called ‘panels’ or ‘cohorts’). These must include social-science parameters such as access to nature and activities, as well as addressing health and household economics.

Australia, China, Italy, Japan, the United States and the United Kingdom are testing access to nature as an affordable mental-health therapy (see, for example, [R. Buckley and D. Westaway *Ann. Tour. Res.* **85**, 103041; 2020](#) and [go.nature.com/3wkqjxt](#)), but these assessments are not randomized controlled trials. We have compiled social-media data from 17 nations, showing that family health, continuing livelihood, and access to nature have been the main factors influencing mental health during the COVID-19 pandemic — but these data are not rigorous enough to guide national health-care policies. Because mental ill-health now affects up to 40% of people living in developed countries (see, for example, [go.nature.com/2umgdmЬ](#)), using reliable panels for research would yield high returns on investment.

Nature **595**, 352 (2021)

doi: <https://doi.org/10.1038/d41586-021-01924-w>

Competing Interests

The authors declare no competing interests.

Subjects

- [Human behaviour](#)
- [Psychology](#)
- [Research management](#)

nature careers

[Jobs](#) >

- [**Postdoctoral Training Fellow**](#)

Francis Crick Institute

London, United Kingdom

- [Senior Business Manager](#)

Francis Crick Institute
London, United Kingdom

- [Postdoctoral Research Fellow in Pharmacogenomics Pain Management](#)

The University of British Columbia (UBC)
Vancouver, Canada

- [Postdoctoral Research Fellow in Pain Management and C. elegans](#)

The University of British Columbia (UBC)
Vancouver, Canada

[Download PDF](#)

Subjects

- [Human behaviour](#)
- [Psychology](#)
- [Research management](#)

This article was downloaded by **calibre** from <https://www.nature.com/articles/d41586-021-01924-w>

- CORRESPONDENCE
- 13 July 2021

Italy: scientists petition against biodynamic farming law

- [Giorgio Parisi](#)⁰,
- [Maria Pia Abbracchio](#)¹,
- [Gennaro Ciliberto](#)²,
- [Massimo Tagliavini](#)³,
- [Karin Metzlaff](#)⁴ &
- [Alan Schulman](#)⁵

1. Giorgio Parisi

1. Accademia Nazionale dei Lincei, Rome, Italy.

[View author publications](#)

You can also search for this author in [PubMed](#) [Google Scholar](#)

2. Maria Pia Abbracchio

1. The 2003 Group for Scientific Research, Milan, Italy.

[View author publications](#)

You can also search for this author in [PubMed](#) [Google Scholar](#)

3. [Gennaro Ciliberto](#)

1. Italian Federation of Life Sciences, Rome, Italy.

[View author publications](#)

You can also search for this author in [PubMed](#) [Google Scholar](#)

4. Massimo Tagliavini

1. Italian Association of the Agricultural Science Societies, Bolzano, Italy.

[View author publications](#)

You can also search for this author in [PubMed](#) [Google Scholar](#)

5. Karin Metzlaff

1. European Plant Science Organization, Brussels, Belgium.

[View author publications](#)

You can also search for this author in [PubMed](#) [Google Scholar](#)

6. Alan Schulman

1. European Plant Science Organization, Helsinki, Finland.

[View author publications](#)

You can also search for this author in [PubMed](#) [Google Scholar](#)





•

[Download PDF](#)

A new Italian law could see research money and public educational resources being funnelled towards ‘biodynamic’ farming — a practice that invokes cosmic forces to improve soil quality. We are among those representatives of the European agricultural- and general-research community who organized a petition against this alarming development (see go.nature.com/3dganms).

The draft law DDL988 would put biodynamic farming on the same legal footing as organic farming — the latter based on solid scientific evidence

(see for example [A. Muller et al. *Nature Commun.* **8**, 1290; 2017](#)). In our view, government economic policy should not be shaped by esoteric astrological principles. Italy should have learnt, following the scandal that arose over unproven stem-cell treatments ([Nature **539**, 340; 2016](#)), that explicit government approval of pseudoscience is ill-advised.

Nature **595**, 352 (2021)

doi: <https://doi.org/10.1038/d41586-021-01886-z>

Competing Interests

The authors declare no competing interests.

Subjects

- [Agriculture](#)
- [Government](#)
- [Law](#)

nature careers

[Jobs](#) >

- [Postdoctoral Training Fellow](#)

Francis Crick Institute

London, United Kingdom

- [Senior Business Manager](#)

Francis Crick Institute

London, United Kingdom

- [**Postdoctoral Research Fellow in Pharmacogenomics Pain Management**](#)

The University of British Columbia (UBC)

Vancouver, Canada

- [**Postdoctoral Research Fellow in Pain Management and C. elegans**](#)

The University of British Columbia (UBC)

Vancouver, Canada

[Download PDF](#)

Subjects

- [Agriculture](#)
- [Government](#)
- [Law](#)

This article was downloaded by **calibre** from <https://www.nature.com/articles/d41586-021-01886-z>

| [Section menu](#) | [Main menu](#) |

- CORRESPONDENCE
- 13 July 2021

To build resilience, study complex systems

- [Len Fisher](#) 0
 - 1. [Len Fisher](#)
 - 1. University of Bristol, UK.

[View author publications](#)

You can also search for this author in [PubMed](#) [Google Scholar](#)





•

[Download PDF](#)

Research has armed us against the COVID-19 pandemic with genomic surveillance, vaccines, social distancing and face masks. But differences in countries' death and vaccination rates indicate that society needs more than technological solutions. To prevent future pandemics, reduce inequality, stabilize democracy and guide the transition to net-zero carbon emissions, researchers need insight into the effects of increasing social, economic and ecological interconnectedness.

Our socio-economic-ecological world is a complex adaptive network, in which behaviours emerge that cannot be understood by looking at the interacting components in isolation. Such a networked system can undergo sudden, often unpredictable, change, for example in the climate or the global economy, as I have written about in several books (see, for example, *Crashes, Crises, and Calamities*; Basic Books, 2011).

Understanding how the world might become resilient to such collapses requires ‘complexity thinking’. Scientists must collaborate with a wide sphere of fellow thinkers — from economists to social scientists, political scientists and historians. One upside in this dark time is that such interdisciplinary work can be fun. It provides new outlets to rekindle the curiosity and delight of discovery that drew most of us to research in the first place. Try it.

Nature **595**, 352 (2021)

doi: <https://doi.org/10.1038/d41586-021-01925-9>

Competing Interests

The author declares no competing interests.

Subjects

- [Diseases](#)
- [Society](#)

nature careers

[Jobs](#) >

- [Postdoctoral Training Fellow](#)

Francis Crick Institute

London, United Kingdom

- **Senior Business Manager**

Francis Crick Institute

London, United Kingdom

- **Postdoctoral Research Fellow in Pharmacogenomics Pain Management**

The University of British Columbia (UBC)

Vancouver, Canada

- **Postdoctoral Research Fellow in Pain Management and C. elegans**

The University of British Columbia (UBC)

Vancouver, Canada

[Download PDF](#)

Subjects

- [Diseases](#)
- [Society](#)

This article was downloaded by **calibre** from <https://www.nature.com/articles/d41586-021-01925-9>

- CORRESPONDENCE
- 13 July 2021

Scale up rapid research autopsies for tissue immunology

- [Stephen A. Rawlings](#) ORCID: <http://orcid.org/0000-0003-3637-1447>⁰,
- [Antoine Chaillon](#) ORCID: <http://orcid.org/0000-0001-9490-3857>¹,
- [Davey Smith](#) ORCID: <http://orcid.org/0000-0003-3603-1733>² &
- [Sara Gianella](#) ORCID: <http://orcid.org/0000-0002-9927-0849>³

1. Stephen A. Rawlings

1. University of California, San Diego, California, USA.

[View author publications](#)

You can also search for this author in [PubMed](#) [Google Scholar](#)

2. Antoine Chaillon

1. University of California, San Diego, California, USA.

[View author publications](#)

You can also search for this author in [PubMed](#) [Google Scholar](#)

3. Davey Smith

1. University of California, San Diego, California, USA.

[View author publications](#)

You can also search for this author in [PubMed](#) [Google Scholar](#)

4. [Sara Gianella](#)

1. University of California, San Diego, California, USA.

[View author publications](#)

You can also search for this author in [PubMed](#) [Google Scholar](#)

•



•

[Download PDF](#)

We have developed rapid research autopsies to explore the immune system in tissues (see [D. L. Farber *Nature* 593, 506–509; 2021](#)). This model is well suited to investigating COVID-19 — caused by the SARS-CoV-2 virus invading multiple tissues — as well as other diseases.

To study where HIV, for example, hides in the body, we conducted autopsies on people with HIV who had consented to whole-body donation. Autopsies took place within 6 hours of death to allow optimal preservation

of more than 60 tissue types for flash-freezing, RNA stabilization, histology and single-cell suspension.

Support for the research from the community and participants' next of kin is essential. Speed is ensured by pre-labelling of sample containers and systematic deployment of supplies and reagents, and by close collaboration with the health-care facilities where participants expire. We have performed 15 such autopsies over the past 3.5 years, and have enrolled 12 people for future autopsy.

To realize the value of participants' donations, we have distributed important biological specimens to a dozen collaborators. We would be happy to share our experiences with researchers and institutions interested in implementing such programmes.

Nature **595**, 352 (2021)

doi: <https://doi.org/10.1038/d41586-021-01887-y>

Competing Interests

The authors declare no competing interests.

Subjects

- [Immunology](#)
- [Ethics](#)

nature careers

[Jobs](#) >

- [Postdoctoral Training Fellow](#)

Francis Crick Institute

London, United Kingdom

- [Senior Business Manager](#)

Francis Crick Institute
London, United Kingdom

- [Postdoctoral Research Fellow in Pharmacogenomics Pain Management](#)

The University of British Columbia (UBC)
Vancouver, Canada

- [Postdoctoral Research Fellow in Pain Management and *C. elegans*](#)

The University of British Columbia (UBC)
Vancouver, Canada

[Download PDF](#)

Subjects

- [Immunology](#)
- [Ethics](#)

This article was downloaded by **calibre** from <https://www.nature.com/articles/d41586-021-01887-y>.

- CORRESPONDENCE
- 13 July 2021

Africa: renewables infrastructure avoids stranded assets

- [Zhanyun Wang](#) ORCID: <http://orcid.org/0000-0001-9914-7659>⁰ &
- [Miriam Diamond](#) ORCID: <http://orcid.org/0000-0001-6296-6431>¹

1. [Zhanyun Wang](#)

1. Swiss Federal Institute of Technology (ETH), Zürich, Switzerland.

[View author publications](#)

You can also search for this author in [PubMed](#) [Google Scholar](#)

2. Miriam Diamond

1. University of Toronto, Toronto, Canada.

[View author publications](#)

You can also search for this author in [PubMed](#) [Google Scholar](#)





•

[Download PDF](#)



A student examines solar panels at Strathmore University in Nairobi. Credit: Thomas Imo/Photothek/Getty

We applaud Vijaya Ramachandran's call for a stable energy supply on the African continent ([*Nature* 592, 489; 2021](#)), but disagree that this might be best achieved by wealthy countries continuing to invest in fossil-fuel projects in Africa. These would bring insurmountable costs to Africa in the long term.

As fossil-fuel infrastructure builds up, its facilities become deeply rooted in society. This creates carbon lock-in, a resistance to shifting over to low-carbon living — even when cost-effective renewable alternatives exist, and the social and environmental costs to consumers are rising. Exporting old fossil-fuel technologies and infrastructure to energy-poor African countries risks trapping them in an outdated techno-institutional complex for decades to come, and would stifle the innovation that is essential for alleviating poverty.

Advanced economies recognize that investment in renewables will maintain the energy supply as well as the competitive technological advantage that

underpins prosperity. Development projects therefore need to focus on these new technologies, by investing in both the physical and the institutional infrastructure that can foster a stable and innovative low-carbon future.

Nature **595**, 353 (2021)

doi: <https://doi.org/10.1038/d41586-021-01927-7>

Competing Interests

The authors declare no competing interests.

Subjects

- [Energy](#)
- [Renewable energy](#)
- [Developing world](#)

nature careers

[Jobs](#) >

- [Postdoctoral Training Fellow](#)

Francis Crick Institute

London, United Kingdom

- [Senior Business Manager](#)

Francis Crick Institute

London, United Kingdom

- [Postdoctoral Research Fellow in Pharmacogenomics Pain Management](#)

The University of British Columbia (UBC)

Vancouver, Canada

- **Postdoctoral Research Fellow in Pain Management and C. elegans**

The University of British Columbia (UBC)

Vancouver, Canada

[Download PDF](#)

Subjects

- [Energy](#)
- [Renewable energy](#)
- [Developing world](#)

This article was downloaded by **calibre** from <https://www.nature.com/articles/d41586-021-01927-7>

| [Section menu](#) | [Main menu](#) |

- CORRESPONDENCE
- 13 July 2021

Pollution from hydrogen fuel could widen inequality

- [Alastair Lewis](#) 0
 - 1. [Alastair Lewis](#)
 - 1. National Centre for Atmospheric Science, University of York, Heslington, UK.

[View author publications](#)

You can also search for this author in [PubMed](#) [Google Scholar](#)





•

[Download PDF](#)

Hydrogen holds promise as a clean, low-carbon fuel (see, for example, go.nature.com/3arm2nq). But under current plans — including those in the United Kingdom’s sixth carbon budget (see go.nature.com/3hjkgyv) — the gas would be mostly burnt in engines and boilers rather than being used in fuel cells. The burning of hydrogen generates toxic nitrogen oxides (NO_x) as well as steam ([Y. B. Zel’dovich *Acta Physicochimica URSS* **11**, 577–628; 1946](#)). This pollution could disproportionately impact the urban poor.

Reducing nitrogen-oxide emissions from hydrogen boilers and engines is possible. But there is often a trade-off with fuel efficiency or with cost, because of the need for exhaust-gas after-treatment equipment (A. C. Lewis *Environ. Sci: Atmos.* <https://doi.org/gmjm>; 2021). By the 2040s, hydrogen combustion for domestic heating could be the last major source of NO_x in cities, as ever more road vehicles switch to electric power.

Nitrogen-oxide emissions from hydrogen boilers will be concentrated in areas of high-density housing, often associated with low-income households. A widening of inequality in exposure to NO₂ could be an unwelcome side effect of this net-zero policy without new regulation and innovation in after-treatment technologies.

Nature **595**, 353 (2021)

doi: <https://doi.org/10.1038/d41586-021-01926-8>

Competing Interests

The author declares no competing interests.

Subjects

- [Engineering](#)
- [Society](#)
- [Environmental sciences](#)
- [Chemistry](#)

nature careers

[Jobs](#) >

- [Postdoctoral Training Fellow](#)

Francis Crick Institute

London, United Kingdom

- **Senior Business Manager**

Francis Crick Institute

London, United Kingdom

- **Postdoctoral Research Fellow in Pharmacogenomics Pain Management**

The University of British Columbia (UBC)

Vancouver, Canada

- **Postdoctoral Research Fellow in Pain Management and C. elegans**

The University of British Columbia (UBC)

Vancouver, Canada

[Download PDF](#)

Subjects

- Engineering
- Society
- Environmental sciences
- Chemistry

This article was downloaded by **calibre** from <https://www.nature.com/articles/d41586-021-01926-8>

- CORRESPONDENCE
- 13 July 2021

Italy: Forest harvesting is the opposite of green growth

- [Roberto Cazzolla Gatti](#)⁰,
- [Gianluca Piovesan](#)¹ &
- [Alessandro Chiarucci](#)²

1. Roberto Cazzolla Gatti

1. Tomsk State University, Russia.

[View author publications](#)

You can also search for this author in [PubMed](#) [Google Scholar](#)

2. Gianluca Piovesan

1. University of Tuscany, Viterbo, Italy.

[View author publications](#)

You can also search for this author in [PubMed](#) [Google Scholar](#)

3. [Alessandro Chiarucci](#)

1. University of Bologna, Italy.

[View author publications](#)

You can also search for this author in [PubMed](#) [Google Scholar](#)





•

[Download PDF](#)

We question plans to step up the harvesting of forest biomass, as set out in Italy's [Fourth Report on the State of Natural Capital](#). Rather than supporting a transition to a green economy, this could translate into more logging and perturbation of forest ecosystems.

The loss of trees in Italy's forests in recent years (go.nature.com/3yzvdp9) is only partly explained by disturbances such as Storm Vaia in 2018, and salvage logging thereafter. The dominant driver is the production of wood fuel ([D. Pettenella et al. Forest@ 18, 1–4; 2021](#)), mainly from coppice. This

probably removes about 50% of estimated annual growth (see go.nature.com/3xr1mzc).

The new biomass policy could threaten the functionality of forest ecosystems unless it includes measurable targets and a reliable monitoring system for tracking the impacts of removing wood. In a geographically complex country, rich in biodiversity, this could undermine progress towards the European Union's 2030 biodiversity strategy.

For Italy's forests to contribute to the economy, provide ecosystem services, halt biodiversity loss and mitigate climate change, the country needs ecological planning, data monitoring, forest protection, restoration and rewilding.

Nature **595**, 353 (2021)

doi: <https://doi.org/10.1038/d41586-021-01923-x>

Competing Interests

The authors declare no competing interests.

Subjects

- [Conservation biology](#)
- [Sustainability](#)
- [Climate change](#)

nature careers

Jobs >

- [Postdoctoral Training Fellow](#)

Francis Crick Institute

London, United Kingdom

- [Senior Business Manager](#)

Francis Crick Institute
London, United Kingdom

- [Postdoctoral Research Fellow in Pharmacogenomics Pain Management](#)

The University of British Columbia (UBC)
Vancouver, Canada

- [Postdoctoral Research Fellow in Pain Management and C. elegans](#)

The University of British Columbia (UBC)
Vancouver, Canada

[Download PDF](#)

Subjects

- [Conservation biology](#)
- [Sustainability](#)
- [Climate change](#)

This article was downloaded by **calibre** from <https://www.nature.com/articles/d41586-021-01923-x>

Work

- **Being fluent in a second language can boost your research** [30 June 2021]
Career Column • Scientists who speak different languages can bring science to a whole new audience — and use it to their advantage, says Jamie Sugrue.
- **Impact factor abandoned by Dutch university in hiring and promotion decisions** [25 June 2021]
Career News • Faculty and staff members at Utrecht University will be evaluated by their commitment to open science.
- **Tracking Chernobyl's effects on wildlife** [12 July 2021]
Where I Work • Evolutionary ecologist Germán Orizaola Pereda analyses how species have been affected, 35 years after the world's worst nuclear accident.

- CAREER COLUMN
- 30 June 2021

Being fluent in a second language can boost your research

Scientists who speak different languages can bring science to a whole new audience — and use it to their advantage, says Jamie Sugrue.

- [Jamie Sugrue](#) ⁰
 1. Jamie Sugrue
1. Jamie Sugrue is a PhD student in viral immunology at Trinity College Dublin, the University of Dublin, Ireland.

[View author publications](#)

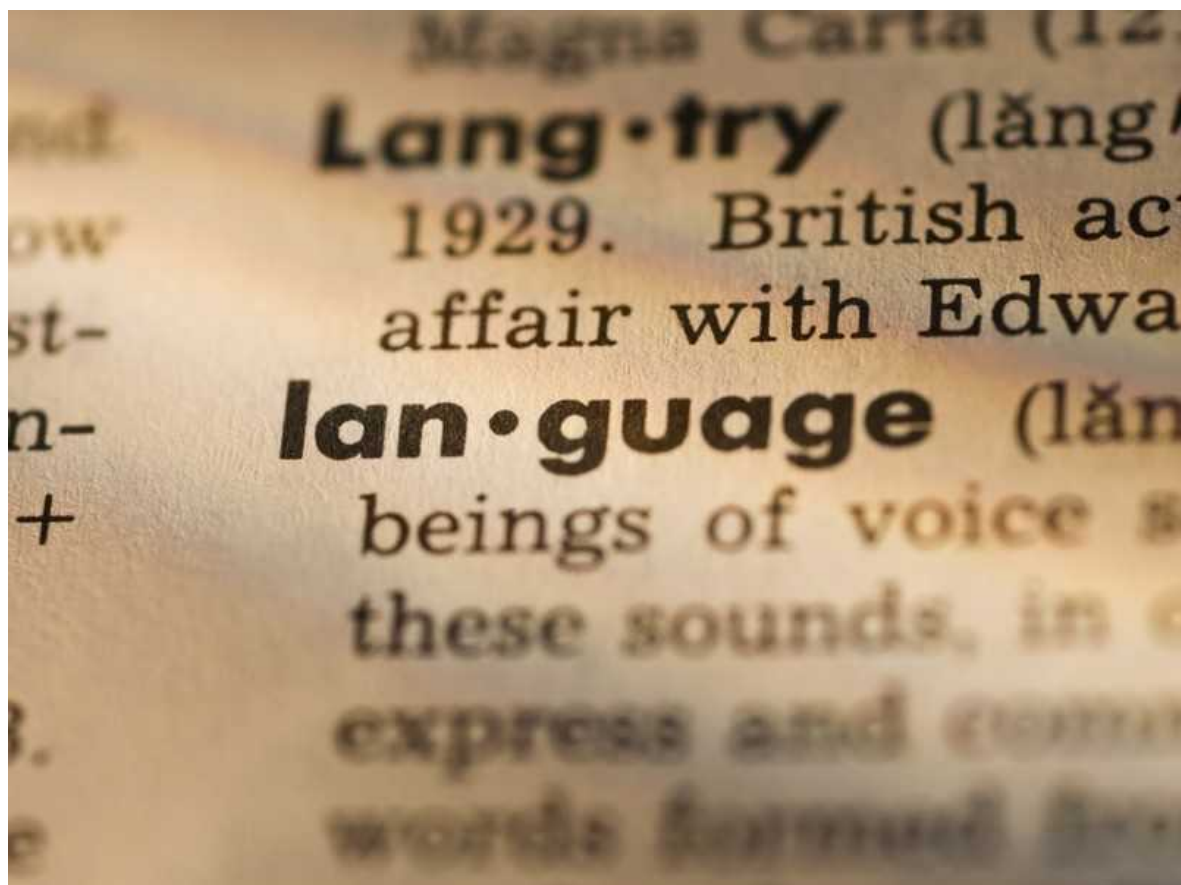
You can also search for this author in [PubMed](#) [Google Scholar](#)





•

[Download PDF](#)



Speaking and writing in multiple languages can help scientists to reach more people with their research.Credit: Getty

In Ireland, where I am studying for a PhD in immunology at Trinity College Dublin, we have two official languages. Irish is the first and national language, English the second. Internationally, this fact isn't widely appreciated, but before the nineteenth century, Irish was the predominant language of Ireland. The reasons for its decline are contentious and complex, but include its repression under English rule, along with the famine of 1845–50, which decimated Ireland's population.

Today, Irish is still the first language in broad areas of counties in the south and west of Ireland, including Dingle in County Kerry and Connemara in County Galway, and is the second language in many urban areas. According to Irish census data from 2016, some 70,000 people speak the Irish language daily, and a further 110,000 speak it at least weekly. It is the only minority language recognized as one of the official working languages of the European Union.

I grew up speaking Irish in a small pocket of Ireland, in Ballinskelligs, County Kerry, where the language is still relatively common. Much to my surprise, I have found a practical use for it during my PhD programme.

In December last year, as Ireland started to reopen following its second wave of the SARS-CoV-2 pandemic, I was contacted by producers at the national Irish-language radio station (*Raidió na Gaeltachta*), which has a weekly listenership of more than 100,000. They wanted to know whether I would be interested in joining a current-affairs panel discussion in January, and highlighted the difficulty of finding people with a strong background in immunology who spoke Irish fluently.



Collection: Science communication

I have since been a guest on the show several times. Because [English is the primary language of science](#), I had never considered Irish to be directly useful in my chosen career. It wasn't until I was asked to do the radio programme that I realized how important it is to have someone who can speak Irish and communicate effectively about the pandemic. I began to see a mutual benefit in having a platform for talking about the science that I love, while getting the chance to convey important information to people who might not otherwise have access to it in English.

In another surprise, I was asked to join a new initiative by Ireland's Department of Health to communicate with younger people about the pandemic. I think the science-communication work I had begun to do in Irish played a big part in my being chosen for this role.

Irish impact

Not only has Irish been useful for engagement in a broader sense, but it has also directly helped me with my PhD programme. I study Irish women who were exposed to the hepatitis C virus through contaminated blood products between 1977 and 1979. We were interested in recruiting these women in an attempt to understand natural resistance to infection. We ran a public media campaign to find 1,200 women who had been exposed to the virus during that period, out of a total population of almost 2.5 million women in Ireland.

I appeared on radio shows to talk in Irish about the study; my team and I also used television and national newspapers to ask women to participate if they felt they met the criteria. Because we were targeting a small group of people, every media appearance helped to boost recruitment. The Irish language is an important part of Irish society, so it made sense for us to use it in our communication strategy. Ultimately, we recruited almost 300 women — a number with which we were satisfied, given the average age (70 and older) of our target demographic and its specificity. Some learnt about our project as a result of my efforts to reach out to them in Irish.

English is the working language of laboratories across the world; it is used in presentations at international conferences and in published papers. In some respects, this is a positive step for science. Mobility of researchers, communication and dissemination are the three pillars on which science is built, and a common language across borders strengthens these core values.

However, to move beyond science and communicate with the public, researchers must be able to speak the language of our audience in a literal sense — which is not always English. There's an expression in Irish: '*Tír gan teanga, thír gan anam*', which means, 'A country without a language is a country without a soul'. Like a country, science needs to reflect the linguistic diversity of the general population. Having people at all levels of academia who speak multiple languages, including Irish and other minority languages,

is important in bringing science to the masses and can benefit our scientific endeavours.

Nature **595**, 461 (2021)

doi: <https://doi.org/10.1038/d41586-021-01797-z>

This is an article from the Nature Careers Community, a place for Nature readers to share their professional experiences and advice. [Guest posts are encouraged.](#)

Competing Interests

J.S. has received funds for media appearances from Radio na Gaeltachta. J.S. has also received financial support from the Irish Department of Health as part of the Science Communication Collective.

Related Articles

- [English is the language of science – but precision is tough as a non-native speaker](#)
- [Watch your language](#)

-  [Six tips for adapting to a new language and culture](#)

Subjects

- [Careers](#)
- [Lab life](#)
- [Policy](#)

Jobs >

- [Postdoctoral Training Fellow](#)

Francis Crick Institute

London, United Kingdom

- [Senior Business Manager](#)

Francis Crick Institute

London, United Kingdom

- [Postdoctoral Research Fellow in Pharmacogenomics Pain Management](#)

The University of British Columbia (UBC)

Vancouver, Canada

- [Postdoctoral Research Fellow in Pain Management and C. elegans](#)

The University of British Columbia (UBC)

Vancouver, Canada

[Download PDF](#)

Related Articles

- [English is the language of science – but precision is tough as a non-native speaker](#)
- [Watch your language](#)



- [Six tips for adapting to a new language and culture](#)

Subjects

- [Careers](#)
- [Lab life](#)
- [Policy](#)

This article was downloaded by **calibre** from <https://www.nature.com/articles/d41586-021-01797-z>

| [Section menu](#) | [Main menu](#) |

- CAREER NEWS
- 25 June 2021

Impact factor abandoned by Dutch university in hiring and promotion decisions

Faculty and staff members at Utrecht University will be evaluated by their commitment to open science.

- [Chris Woolston](#) ⁰

1. Chris Woolston

1. Chris Woolston is a freelance writer in Billings, Montana.

[View author publications](#)

You can also search for this author in [PubMed](#) [Google Scholar](#)





•

[Download PDF](#)



Credit: Getty

A Dutch university says it is formally abandoning the impact factor — a standard measure of scientific success — in all hiring and promotion decisions. By early 2022, every department at Utrecht University in the Netherlands will judge its scholars by other standards, including their commitment to teamwork and their efforts to promote open science, says Paul Boselie, a governance researcher and the project leader for the university's new [Recognition and Rewards scheme](#). "Impact factors don't really reflect the quality of an individual researcher or academic," he says. "We have a strong belief that something has to change, and abandoning the impact factor is one of those changes."



Nature special: Young scientists

A scientist's impact factor is a score that takes into account the number of publications and the citation rate of the journals where those papers are published. In this system, articles in highly cited journals such as *Science*, *Nature* or *Cell* count for more than articles in journals whose content is cited less frequently. Boselie says that impact factors — as well as a related measure called the h-index — contribute to a ‘product-ification’ of science that values sheer output over good research. “It has become a very sick model that goes beyond what is really relevant for science and putting science forward,” he says.

The new scheme is part of Utrecht’s [Open Science programme](#), a multi-track effort to make research more transparent and cooperative. Open-science fellows embedded within each department will assess progress towards open-access publishing, public engagement and data sharing.

The decision to revamp hiring and promotion was partly inspired by the Declaration on Research Assessment (DORA), a document created in 2012 at the annual meeting of the American Society for Cell Biology. [The declaration](#) aims to “improve the ways in which researchers and the outputs of scholarly research are evaluated” and specifically calls for doing away with impact factors as a way to judge the merit of academics. So far, it has been signed by nearly 20,000 individuals and institutions. Utrecht University

signed the document in 2019. At the time, Anton Pijpers, the president of the university's executive board, said that signing DORA wasn't a "symbolic step" but "a 'pledge' for which UU can be held accountable".



How a hiring quota failed

Among academic researchers, dissatisfaction with use and misuse of the impact factor in evaluations and tenure, promotion and hiring decisions has grown in recent years. A 2018 report called the impact factor "an inadequate measure for assessing the impact of scientists" and concluded that failure to modify the current assessment system is likely to lead to "continued bandwagon behaviour that has not always resulted in positive societal behaviour"¹. Despite this, a 2019 study found that 40% of research-intensive universities in the United States and Canada specifically mention impact factors or closely related terms in documents related to tenure, review and promotion². Only a few of those references strike a note of caution, and most suggest that a high impact score would be necessary for career advancement.

Every university in the Netherlands, Utrecht included, has signed on to '[Room for Everyone's Talent](#)', a [2019 position paper](#) led by the VSNU, the employee association for Dutch universities. That paper calls for a system of recognition and rewards that "enables the diversification and vitalization of career paths".

On a practical level, evaluating researchers on qualities beyond easy-to-measure metrics can be messy and complicated. “It’s going to be quite challenging to apply,” Boselie says. He explains that each department will have to develop its own systems and strategies to identify researchers and academics who are making the most meaningful contributions to their fields. The process might involve interviews with other researchers in a given field, he says. “There are alternative ways to evaluate individuals on their quality.”



Tenure denial, and how early-career researchers can survive it

Still, doing away with standard metrics could be a risky move for the university and its faculty and staff members. As long as other universities continue to rely on impact factors and other productivity metrics for hiring and promotion, researchers who come up through the Utrecht system might be at a competitive disadvantage if they eventually try to find a job at a different institution, Boselie acknowledges. “There are feelings of insecurity among young academics,” he says. “We feel that it’s a risk that we are willing to take because we believe [the evaluation system] will change in the end.”

Utrecht will not be standing alone in its efforts to change the way researchers are evaluated, says Lynn Kamerlin, a computational biochemist at Uppsala University in Sweden. “As open science becomes more and more important in policy and decision-making surrounding research funding and

strategies, I think it will almost be a necessity for institutions to follow suit,” says Kamerlin, who is a member of a European Union group that published [a 2019 report on ways to evaluate researchers’ contributions to open science](#). “It’s always frightening to go first, so having institutions that break ground ahead of you is helpful.”

Nature **595**, 462 (2021)

doi: <https://doi.org/10.1038/d41586-021-01759-5>

References

1. 1.

Moher, D. *et al.* *PLoS Biol.* **16**, e2004089 (2018).

[PubMed](#) [Article](#) [Google Scholar](#)

2. 2.

McKiernan, E. C. *et al.* *eLife* **8**, e47338 (2019).

[PubMed](#) [Article](#) [Google Scholar](#)

[Download references](#)

Related Articles

- [Nature journals announce first open-access agreement](#)



- [How a hiring quota failed](#)

-  [Tenure denial, and how early-career researchers can survive it](#)
-  [Nature special: Young scientists](#)

Subjects

- [Careers](#)
- [Policy](#)
- [Institutions](#)

nature careers

[Jobs](#) >

- [Postdoctoral Training Fellow](#)

Francis Crick Institute

London, United Kingdom

- [Senior Business Manager](#)

Francis Crick Institute

London, United Kingdom

- [Postdoctoral Research Fellow in Pharmacogenomics Pain Management](#)

The University of British Columbia (UBC)

Vancouver, Canada

- [**Postdoctoral Research Fellow in Pain Management and C. elegans**](#)

The University of British Columbia (UBC)

Vancouver, Canada

[Download PDF](#)

Related Articles

- [**Nature journals announce first open-access agreement**](#)



[**How a hiring quota failed**](#)



• [**Tenure denial, and how early-career researchers can survive it**](#)



[**Nature special: Young scientists**](#)

Subjects

- [Careers](#)
- [Policy](#)
- [Institutions](#)

This article was downloaded by **calibre** from <https://www.nature.com/articles/d41586-021-01759-5>

| [Section menu](#) | [Main menu](#) |

- WHERE I WORK
- 12 July 2021

Tracking Chernobyl's effects on wildlife

Evolutionary ecologist Germán Orizaola Pereda analyses how species have been affected, 35 years after the world's worst nuclear accident.

- [Virginia Gewin](#) ⁰

1. Virginia Gewin

1. Virginia Gewin is a freelance writer in Portland, Oregon.

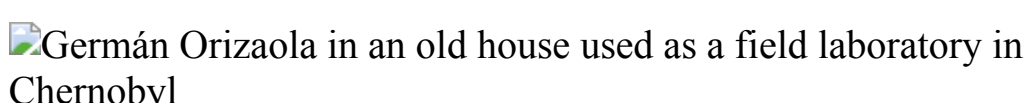
[View author publications](#)

You can also search for this author in [PubMed](#) [Google Scholar](#)





•



Germán Orizaola Pereda is an evolutionary ecologist at the University of Oviedo in Mieres, Spain. Credit: Germán Orizaola

[Download PDF](#)

Thirty-five years after the explosion and meltdown at the Chernobyl Nuclear Power Plant in Ukraine, I study how amphibians in the region have changed, physically and genetically. In 2016, I joined an international research team to do this; since then, I have obtained various grants to

continue the work. Chernobyl is a phenomenal place to study rapid evolution. I typically spend two to three weeks in the forests during the frogs' spring breeding season.

When I work in the 'exclusion zone', the 4,700 square kilometres around the reactor, I stay in a hostel in Chernobyl (20 kilometres from the reactor site), where we have a field laboratory inside an abandoned building. The radiation in the exclusion zone is roughly 1,000 times lower than at the time of the accident, and there are now two hostels, a bar, a couple of restaurants and a cash machine. In this image, I'm running a blood analysis on one of the tree frogs we have collected. The contamination maps on the wall behind me show that some hotspots of radiation persist.

Around 8 p.m., we listen for male tree frogs calling in the field. Wearing chest waders and head lamps, we enter the ponds to gather frogs until 1 or 2 a.m.. Frogs in the exclusion zone are darker than those outside it, thanks to higher levels of melanin, which might be an adaptation that protects them from ionizing radiation. We analyse how much radiation their bodies contain, and tend to find damage to some, often to the liver.

Once expected to become a wasteland, the Chernobyl area is now a nature reserve. New species have arrived, including European bison (*Bison bonasus*) and the wild Przewalski's horse (*Equus ferus przewalskii*). We're beginning to monitor these horses, originally from the Asian steppes: the effects on their health could be a proxy for what happens when humans return. The first 31 horses were released here in 1998, 12 years after the disaster, and it is one of the few places where they continue to live freely.

Nature **595**, 464 (2021)

doi: <https://doi.org/10.1038/d41586-021-01883-2>

Related Articles



- [**The zoologist tracking an island's rebirth**](#)



- [Extreme research](#)



- [Collection: Fieldwork](#)

Subjects

- [Careers](#)
- [Ecology](#)
- [Evolution](#)

nature careers

[Jobs](#) >

- [Postdoctoral Training Fellow](#)

Francis Crick Institute

London, United Kingdom

- [Senior Business Manager](#)

Francis Crick Institute

London, United Kingdom

- [Postdoctoral Research Fellow in Pharmacogenomics Pain Management](#)

The University of British Columbia (UBC)

Vancouver, Canada

- [**Postdoctoral Research Fellow in Pain Management and *C. elegans***](#)

The University of British Columbia (UBC)

Vancouver, Canada

[Download PDF](#)

Related Articles



- [**The zoologist tracking an island's rebirth**](#)



- [**Extreme research**](#)



- [**Collection: Fieldwork**](#)

Subjects

- [Careers](#)
- [Ecology](#)
- [Evolution](#)

This article was downloaded by **calibre** from <https://www.nature.com/articles/d41586-021-01883-2>

Research

- **[Southeast Amazonia is no longer a carbon sink](#)** [14 July 2021]
News & Views • Atmospheric measurements show that deforestation and rapid local warming have reduced or eliminated the capacity of the eastern Amazonian forest to absorb carbon dioxide — with worrying implications for future global warming.
- **[Deciphering metabolism, one microbe at a time](#)** [14 July 2021]
News & Views • Small molecules produced and modified by gut microorganisms can influence human physiology. An atlas of metabolic outputs of diverse gut microbes offers new ways to decipher the microbial mechanisms behind their production.
- **[Measurement-based system provides quantum control of nanoparticles](#)** [14 July 2021]
News & Views • Precise measurements of the position of a levitating nanosphere have been used to control forces that damp the nanosphere's motion — potentially opening the way to quantum control of larger objects.
- **[A long-term perspective on immunity to COVID](#)** [14 June 2021]
News & Views • Determining the duration of protective immunity to infection by SARS-CoV-2 is crucial for understanding and predicting the course of the COVID-19 pandemic. Clinical studies now indicate that immunity will be long-lasting.
- **[Designing the next generation of proton-exchange membrane fuel cells](#)** [14 July 2021]
Perspective • This Perspective reviews the recent technical developments in the components of the fuel cell stack in proton-exchange membrane fuel cell vehicles and outlines the road towards large-scale commercialization of such vehicles.
- **[The \$^{13}\text{CO}\$ -rich atmosphere of a young accreting super-Jupiter](#)** [14 July 2021]
Article • Observations of ^{13}CO in the atmosphere of a young, accreting super-Jupiter indicate a ^{13}C -rich atmosphere, which is attributed to the accretion of carbon from ices enriched in ^{13}C through fractionation.
- **[Real-time optimal quantum control of mechanical motion at room temperature](#)** [14 July 2021]

Article • Optimal quantum control of an optically trapped nanoparticle in its ground state is demonstrated at room temperature, using Kalman filtering to track its quantum trajectory in real time.

- **Quantum control of a nanoparticle optically levitated in cryogenic free space** [14 July 2021]

Article • Quantum control of an optically levitated nanoparticle with a mass of just one femtogram is demonstrated in a cryogenic environment by feedback-cooling the motion of the particle to the quantum ground state.

- **Exponential suppression of bit or phase errors with cyclic error correction** [14 July 2021]

Article • Repetition codes running many cycles of quantum error correction achieve exponential suppression of errors with increasing numbers of qubits.

- **Amazonia as a carbon source linked to deforestation and climate change** [14 July 2021]

Article • Aircraft observations of atmospheric carbon dioxide and monoxide concentrations in Brazil show higher carbon emissions in eastern Amazonia than in the western part, which are linked to increased ecosystem stress and fire occurrence.

- **A lithium-isotope perspective on the evolution of carbon and silicon cycles** [14 July 2021]

Article • Analysis of shallow-water marine carbonate samples from 101 stratigraphic units allows construction of a record of lithium isotopes from the past 3 billion years, tracking the evolution of the global carbon and silicon cycles.

- **Pleistocene sediment DNA reveals hominin and faunal turnovers at Denisova Cave** [23 June 2021]

Article • Ancient mitochondrial DNA from sediments reveals the sequence of Denisovan, Neanderthal and faunal occupation of Denisova Cave, and evidence for the appearance of modern humans at least 45,000 years ago.

- **Mechanism of disease and therapeutic rescue of Dok7 congenital myasthenia** [23 June 2021]

Article • In a mouse model of congenital myasthenia caused by mutations in the Dok7 gene, agonist antibodies against MUSK restore synaptic function and survival.

- **Microbiota regulate social behaviour via stress response neurons in the brain** [30 June 2021]

Article • The gut microbiota in mice can modulate social behaviour by influencing activity in stress-related brain areas.

- **A metabolomics pipeline for the mechanistic interrogation of the gut microbiome** [14 July 2021]

Article • A microbiome-focused metabolomics pipeline and interactive metabolomics profile explorer are a powerful tool for the characterization of gut-resident microorganisms and the interactions between microorganisms and their host.

- **SARS-CoV-2 infection induces long-lived bone marrow plasma cells in humans** [24 May 2021]

Article • SARS-CoV-2 infection induces long-lived bone marrow plasma cells that correlate with anti-SARS-CoV-2 spike protein antibody titres in individuals who have recovered from COVID-19.

- **Naturally enhanced neutralizing breadth against SARS-CoV-2 one year after infection** [14 June 2021]

Article • Antibodies against SARS-CoV-2 continue to evolve 6 to 12 months after infection in patients who have recovered from COVID-19, increasing in potency and breadth with time.

- **ctDNA guiding adjuvant immunotherapy in urothelial carcinoma** [16 June 2021]

Article • The authors report on prospective exploratory analyses of circulating tumour DNA in an urothelial carcinoma immunotherapy clinical trial.

- **A transcriptional switch governs fibroblast activation in heart disease** [23 June 2021]

Article • BET proteins regulate a reversible transcriptional switch that governs fibroblast activation in heart disease through the transcription factor MEOX1.

- **Shape of promoter antisense RNAs regulates ligand-induced transcription activation** [30 June 2021]

Article • The authors describe a role for the non-coding antisense transcripts produced at promoters in regulating ligand-induced activation of gene transcription.

- **G-protein activation by a metabotropic glutamate receptor** [30 June 2021]

Article • Cryo-electron microscopy structures show that metabotropic glutamate receptor 2 forms a dimer to which only one G protein is coupled, revealing the basis for asymmetric signal transduction.

- **Asymmetric activation of the calcium-sensing receptor homodimer** [30 June 2021]

Article • Cryo-EM structures of human calcium-sensing receptor reveal intrinsic asymmetry in the receptor homodimer upon activation that is stabilized by calcimimetic drugs adopting distinct poses in the two protomers, priming one protomer for G-protein coupling.

| [Next section](#) | [Main menu](#) | [Previous section](#) |

- NEWS AND VIEWS
- 14 July 2021

Southeast Amazonia is no longer a carbon sink

Atmospheric measurements show that deforestation and rapid local warming have reduced or eliminated the capacity of the eastern Amazonian forest to absorb carbon dioxide — with worrying implications for future global warming.

- [Scott Denning](#) 9

1. [Scott Denning](#)

1. Scott Denning is in the Department of Atmospheric Science, Colorado State University, Fort Collins, Colorado 80523, USA.

[View author publications](#)

You can also search for this author in [PubMed](#) [Google Scholar](#)



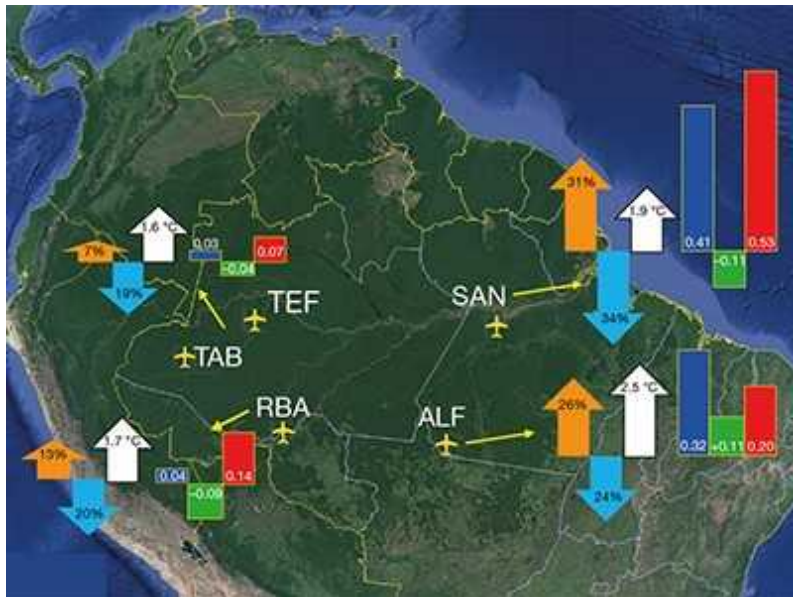


•

[Download PDF](#)

Since at least the inception of modern records of atmospheric carbon dioxide levels in the 1950s, there has been a small global excess (about 2%) in the amount of CO₂ taken up by land plants for photosynthesis, compared with the amount emitted as a result of the decomposition of organic material. This land carbon sink has absorbed around 25% of all fossil-fuel emissions since 1960 (ref. 1)¹, offsetting some global warming. Tropical forests have been a major component of the land carbon sink, and the largest intact tropical forest is in Amazonia. [Writing in Nature](#), Gatti *et al.*² report extensive direct sampling of the atmosphere over this region. Their data reveal that western

Amazonia is still a relatively weak carbon sink, but suggest that deforestation and warming over eastern Amazonia have degraded — or even reversed — regional uptake of carbon by the forest.



[Read the paper: Amazonia as a carbon source linked to deforestation and climate change](#)

The sink arises from a combination of the increased vegetation growth that occurs in response to rising levels of CO₂ and other nutrients, changes in land management and ecosystem responses to climate change³. Tropical forests are Earth's most productive ecosystems, but they are not recovering from past human disturbance as their counterparts at mid-latitudes have done, nor are they benefiting from the markedly longer growing seasons associated with climate change, as are boreal and arctic ecosystems.

Carbon has accumulated in the biomass of Amazonian forests for decades⁴, but studies in the past few years suggest that Amazonian carbon sinks are threatened by deforestation and forest degradation⁵, progressive drying of the climate, and fires⁶. However, it is difficult to make direct measurements that reflect the local carbon balance of many Amazonian ecosystems, because access to those regions is limited. And it is hard to extrapolate available local data^{7,8} across the whole region, because Amazonian ecosystems vary enormously.

Satellite measurements of atmospheric levels of CO₂ and carbon monoxide (a tracer of combustion), and of solar-induced fluorescence from vegetation (a proxy for photosynthesis), show that the year-to-year carbon balance in Amazonia is quite sensitive to drought and fire⁹. However, persistent cloud cover in this region complicates the acquisition of such measurements, and the collection of these data began only about a decade ago. Direct measurements of the atmosphere could constrain estimates of regional carbon balance, but are sparse for Amazonia.

Enter Gatti and colleagues, who have directly measured the atmosphere in four regions across Amazonia for nine years (2010–18; Fig. 1). The authors used aircraft to collect air samples from near the surface up to an altitude of 4.5 kilometres at each region, then analysed the samples to produce a vertical profile of the concentrations of a suite of gases, including CO₂ and CO. The authors produced 590 vertical profiles during their study, with a typical sampling period of about twice a month at each region.

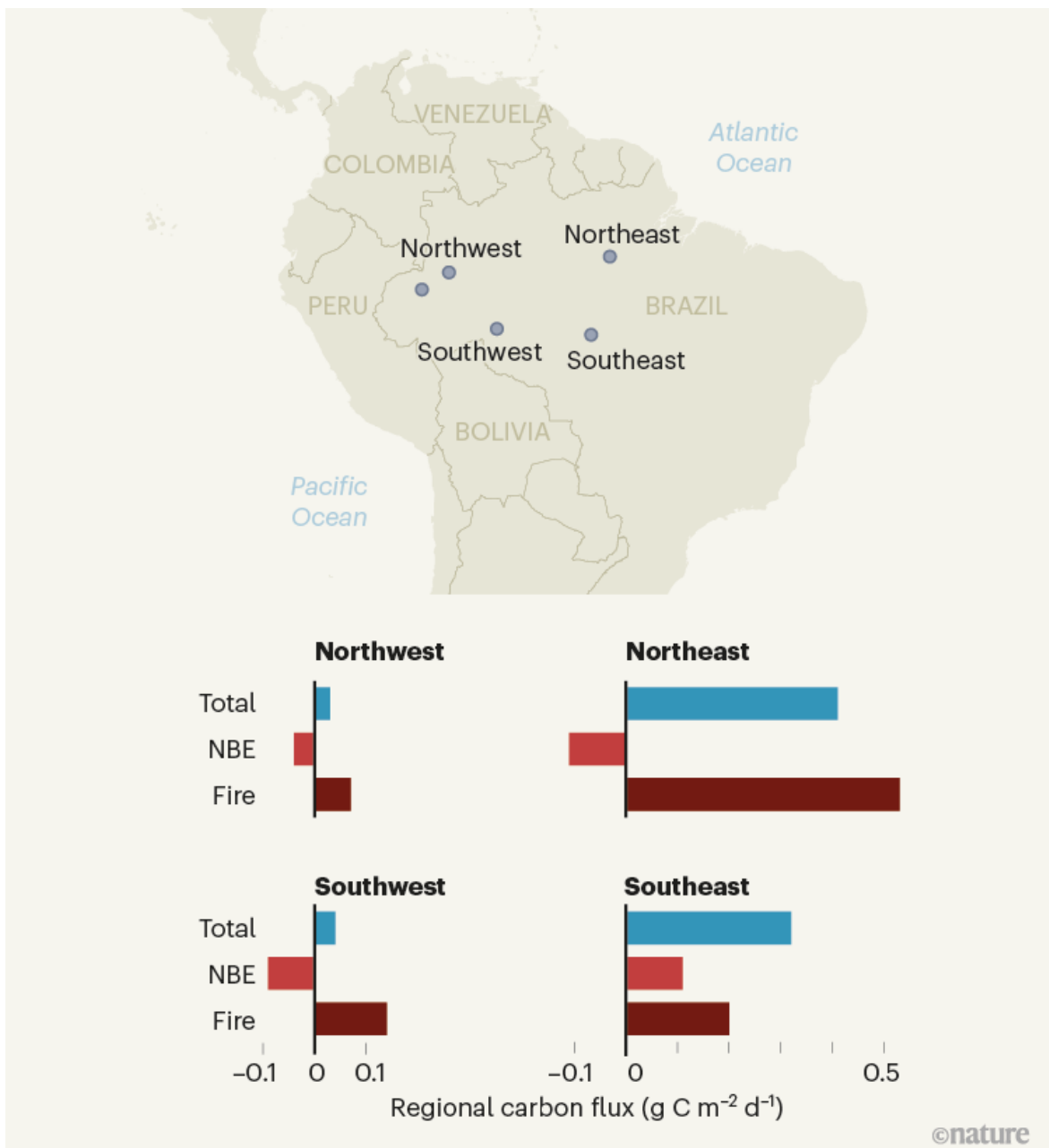


Figure 1 | Carbon fluxes in different Amazonian regions. From 2010 to 2018, Gatti *et al.*² measured vertical profiles of atmospheric concentrations of carbon dioxide and carbon monoxide above four regions in Amazonia (the two locations shown in northwestern Amazonia were counted as one region), and thereby calculated regional carbon fluxes upwind of each site, measured in grams of carbon per square metre per day. In the bar charts, net biome exchange (NBE) represents the average annual balance of CO_2 absorbed by forests for photosynthesis compared with the amount of CO_2

produced by the decay of organic matter (negative NBE values indicate that the forest acts as a carbon sink); ‘fire’ represents the average carbon emissions produced by fires; and ‘total’ represents the sum of NBE and fire emissions. The NBE values indicate that most regions of Amazonia are weak carbon sinks, but southeastern Amazonia is actually a carbon source.

Gatti *et al.* also used data from several sites on remote islands and coastal headlands around the South Atlantic Ocean to establish background concentrations of gases. This allowed them to compute spatial gradients of CO₂ and CO concentrations between the background sites and each of the profiled regions in Amazonia. The authors analysed their data by season and by year, and determined how the spatial patterns of CO₂ and CO concentrations varied according to the region over which sampled air had passed before collection. Finally, they used the seasonal CO₂ concentration gradients to estimate regional carbon flux associated with forest growth and decay, and estimated carbon emissions produced by fires from the CO gradients.

Northwestern Amazonia is almost always very wet, and shows little seasonal variation in growth and decay. Gatti and colleagues’ atmospheric profiling indicates that this region was close to carbon balance during the period of the study — about as much carbon was taken up by plants for growth as was emitted from decay processes.

However, the moisture and fertility of Amazonian forests changes substantially farther south and east. Dry seasons (periods with rainfall of less than 100 millimetres per month) get progressively longer, eventually lasting for 5 months or more as the forest grades into savannah¹⁰. Gatti and colleagues find that the drier forests in the northeastern and southeastern regions studied were close to carbon balance during the wet season, but that carbon release from decomposition and fire tended to exceed carbon uptake by photosynthesis during the dry season. The observed regional and seasonal patterns of carbon uptake in the northwest transitioning to carbon release in the drier east were consistent with the year-to-year variability of the data — which revealed that greater carbon releases, associated with decomposition and fire, occurred during hotter and drier years.

Gatti and co-workers show that the transition of eastern Amazon forests from carbon sink to carbon source during the dry season is associated with strong regional warming trends. Eastern Amazon sites have warmed by as much as about 0.6°C per decade during the dry season over the past 40 years. This is more than three times the rate of global warming and about the same rate as for the Arctic. Wet-season and western Amazonian forests have warmed, too, but at a much slower rate. Warming rates in the dry season for eastern Amazonia might have been amplified by deforestation and forest degradation. Gatti *et al.* conclude that increases in fires, and in physiological stress, mortality and decomposition of trees in this area, are associated with increasing carbon loss from regional ecosystems.



African forest maps reveal areas vulnerable to the effects of climate change

The authors have documented the accelerating transition of forests from carbon sinks to sources using direct measurements of large-scale gradients of atmospheric gas concentrations. The overall pattern of deforestation, warmer and drier dry seasons, drought stress, fire and carbon release in eastern Amazonia seriously threatens the Amazon carbon sink. Indeed, the results cast doubt on the ability of tropical forests to sequester large amounts of fossil-fuel-derived CO₂ in the future.

For decades, ecologists have been surprised that the fraction of fossil-fuel emissions absorbed by land ecosystems has remained fairly constant¹¹, even

though these emissions have increased. Forests at high latitudes have continued to accumulate carbon because their growing seasons have lengthened as a result of climate change. Mid-latitude forests have done so because they have been recovering from past clearance, and because they have benefited from the increased availability of nutrients (produced as a result of human activities, or mobilized in soils by climate warming).

By contrast, increased carbon sequestration by tropical forests must be driven largely by an increase in photosynthesis associated with rising CO₂ levels — but regional atmospheric profiling¹² suggests that this carbon sink is threatened by forest degradation and warming. Another complication is that fossil-fuel emissions must be quickly reduced to meet international climate targets, but it is not clear how the CO₂-driven carbon sinks of tropical forests will respond to a rapidly warming world in which CO₂ levels are no longer rising¹³. The future of carbon accumulation in tropical forests has therefore long been uncertain. Gatti and colleagues' atmospheric profiles show that the uncertain future is happening now.

Nature **595**, 354–355 (2021)

doi: <https://doi.org/10.1038/d41586-021-01871-6>

References

1. 1.

Friedlingstein, P. *et al.* *Earth Syst. Sci. Data* **12**, 3269–3340 (2020).

[Article](#) [Google Scholar](#)

2. 2.

Gatti, L. V. *et al.* *Nature* **595**, 388–393 (2021).

[Article](#) [Google Scholar](#)

3. 3.

Fung, I. *Annu. Rev. Earth Planet. Sci.* **48**, 1–20 (2020).

[Article](#) [Google Scholar](#)

4. 4.

Pan, Y. *et al. Science* **333**, 988–993 (2011).

[PubMed](#) [Article](#) [Google Scholar](#)

5. 5.

Song, X.-P. *et al. Nature* **560**, 639–643 (2018).

[PubMed](#) [Article](#) [Google Scholar](#)

6. 6.

Aragão, L. E. O. C. *et al. Nature Commun.* **9**, 536 (2018).

[PubMed](#) [Article](#) [Google Scholar](#)

7. 7.

Hayek, M. N. *et al. Biogeosciences* **15**, 4833–4848 (2018).

[Article](#) [Google Scholar](#)

8. 8.

Malhi, Y. *et al. Biol. Conserv.* **253**, 108889 (2021).

[Article](#) [Google Scholar](#)

9. 9.

Liu, J. *et al. Science* **358**, eaam5690 (2017).

[PubMed](#) [Article](#) [Google Scholar](#)

10. 10.

Marengo, J. A., Liebmann, B., Kousky, V. E., Filizola, N. P. & Wainer, I. C. *J. Clim.* **14**, 833–852 (2001).

[Article](#) [Google Scholar](#)

11. 11.

Ballantyne, A. P., Alden, C. B., Miller, J. B., Tans, P. P. & White, J. W. C. *Nature* **488**, 70–72 (2012).

[PubMed](#) [Article](#) [Google Scholar](#)

12. 12.

Hubau, W. *et al.* *Nature* **579**, 80–87 (2020).

[PubMed](#) [Article](#) [Google Scholar](#)

13. 13.

Kaushik, A. *et al.* *Eos* **101**, <https://doi.org/10.1029/2020EO140276> (2020).

[Download references](#)

Competing Interests

The author declares no competing interests.

Related Articles

- [Read the paper: Amazonia as a carbon source linked to deforestation and climate change](#)

-  [African forest maps reveal areas vulnerable to the effects of climate change](#)
-  [Tropical carbon sinks are saturating at different times on different continents](#)
- [See all News & Views](#)

Subjects

- [Biogeochemistry](#)
- [Climate sciences](#)
- [Environmental sciences](#)

nature careers

Jobs >

- [Postdoctoral Training Fellow](#)

Francis Crick Institute

London, United Kingdom

- [Senior Business Manager](#)

Francis Crick Institute

London, United Kingdom

- [Postdoctoral Research Fellow in Pharmacogenomics Pain Management](#)

The University of British Columbia (UBC)

Vancouver, Canada

- [Postdoctoral Research Fellow in Pain Management and C. elegans](#)

The University of British Columbia (UBC)

Vancouver, Canada

[Download PDF](#)

Related Articles



- [Read the paper: Amazonia as a carbon source linked to deforestation and climate change](#)



- [African forest maps reveal areas vulnerable to the effects of climate change](#)



- [Tropical carbon sinks are saturating at different times on different continents](#)

- [See all News & Views](#)

Subjects

- [Biogeochemistry](#)
 - [Climate sciences](#)
 - [Environmental sciences](#)
-

This article was downloaded by **calibre** from <https://www.nature.com/articles/d41586-021-01871-6>

| [Section menu](#) | [Main menu](#) |

- NEWS AND VIEWS
- 14 July 2021

Deciphering metabolism, one microbe at a time

Small molecules produced and modified by gut microorganisms can influence human physiology. An atlas of metabolic outputs of diverse gut microbes offers new ways to decipher the microbial mechanisms behind their production.

- [William F. Kindschuh ORCID: http://orcid.org/0000-0002-7433-7808⁰](#) &
- [Tal Korem ORCID: http://orcid.org/0000-0002-0609-0858¹](#)

1. William F. Kindschuh

1. William F. Kindschuh is at the Program for Mathematical Genomics and the Department of Systems Biology, Columbia University, New York, New York 10032, USA.

[View author publications](#)

You can also search for this author in [PubMed](#) [Google Scholar](#)

2. [Tal Korem](#)

1. Tal Korem is at the Program for Mathematical Genomics and the Department of Systems Biology, Columbia University, New York, New York 10032, USA.

[View author publications](#)

You can also search for this author in [PubMed](#) [Google Scholar](#)





•

[Download PDF](#)

The microorganisms in our gut can have far-reaching effects — on our liver¹, arteries² and potentially even on our behaviour³. One way these microbes exert their effects is through the generation or consumption of small molecules, termed metabolites. Measuring metabolite levels, an approach called metabolomics, has led to ever-increasing recognition of their importance. And yet only rarely do we understand the underlying mechanisms driving these levels: namely, which microbes, enzymes and interactions are involved in the production and uptake of a specific metabolite. This task is further hindered by the complexity of microbial

communities such as the gut microbiome, studies of which have to take into account the large number of microbes, the interactions between them, their diverse metabolic capabilities and several hard-to-measure non-microbial factors, such as host diet⁴. [Writing in Nature](#), Han *et al.*⁵ present a comprehensive approach to addressing this major challenge, by carrying out metabolic and genetic analyses of a broad set of microbes commonly found in the human gut.

The authors' approach (Fig. 1) has been facilitated by notable technical advances. Using liquid chromatography–mass spectrometry (LC–MS), a technique that quantifies metabolites on the basis of their polarity, mass and charge, Han and colleagues compiled a reference database of 833 metabolites that are relevant to microbial metabolism. They confirmed that these metabolites are detectable in biological samples, and that their measurement is consistent in several types of sample, such as faeces or blood, and quantifiable over a wide range of concentrations. The authors also developed an analysis pipeline that enables compound identification and statistical analysis. With this infrastructure in place, Han *et al.* measured metabolite levels in thousands of samples from *in vitro* cultures of 178 microbial strains grown separately in multiple media types, and from various tissues taken from mice whose intestines were colonized by the same strains, either alone or in communities of five or six species.

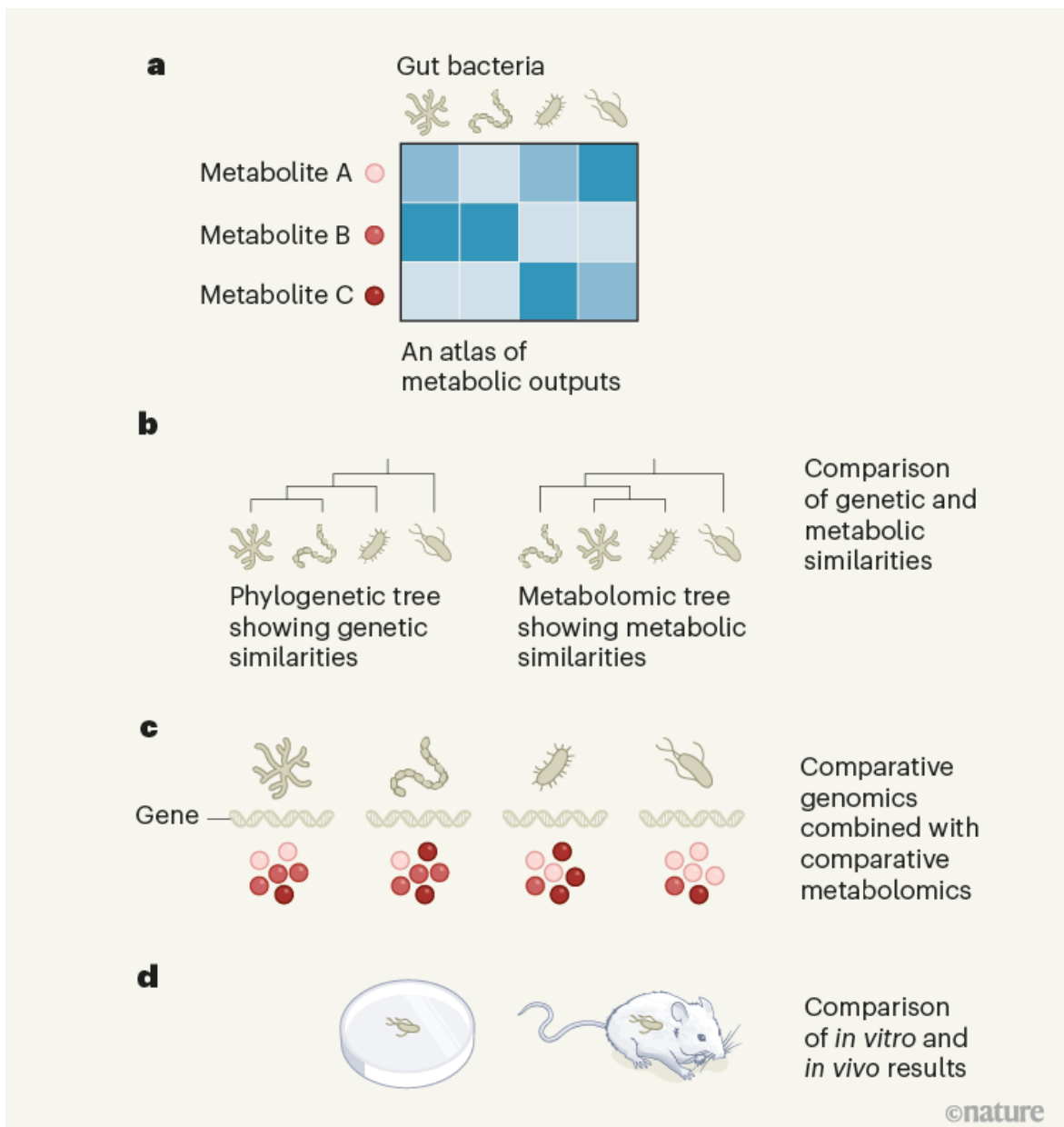
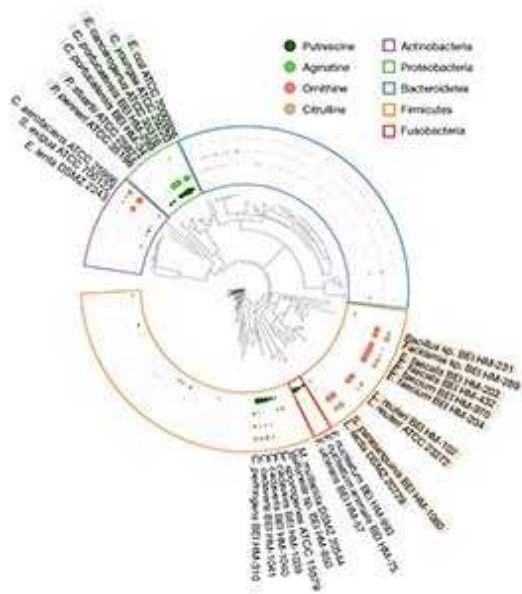


Figure 1 | An approach to studying microbial metabolism. **a**, Han *et al.*⁵ generated a reference library of 833 small molecules (metabolites) relevant to gut-microbial metabolism, and used it to assess the metabolic output generated by 178 bacterial strains commonly found in the human gut. The authors thereby generated an atlas of metabolic outputs, as shown in this hypothetical example. Darker blue on the heat map indicates higher levels of production. **b**, The authors present a range of approaches for studying microbial metabolism using these data. They investigated the correspondence between the evolutionary relationships of different microbes

(their phylogeny) and their metabolic output. Phylogeny and metabolism generally correspond; however, the authors found some exceptions and divergences. **c**, Han and colleagues further show that a parallel comparison between microbial genomes and their metabolic outputs could suggest genes responsible for unexplained metabolic capacities. **d**, The authors also investigated the correspondence between *in vitro* and *in vivo* microbial metabolism, identifying many metabolites produced in both contexts.

Having compiled an atlas of single-microbe *in vitro* metabolic outputs, Han and colleagues set out to address a long-standing question: to what degree is the evolutionary relationship between two microbes (their phylogeny) related to their metabolic capacity? The authors show that, although the two generally correspond, this correspondence is not perfect. For example, Han *et al.* report that *Clostridium sporogenes* and *Clostridium cadaveris*, two closely related species, have strikingly different metabolic profiles. By contrast, *Atopobium parvulum* and *Catenibacterium mitsuokai*, two phylogenetically distant species, have similar metabolic profiles.



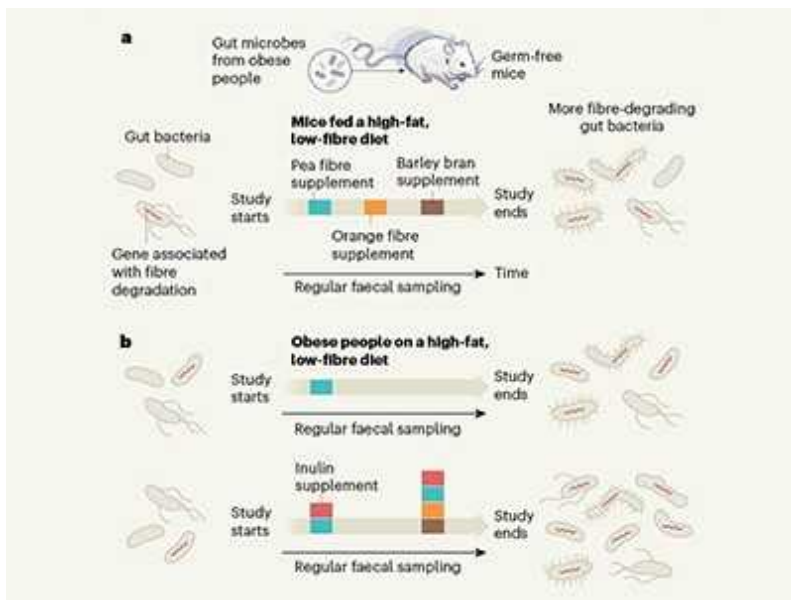
[Read the paper: A metabolomics pipeline for the mechanistic interrogation of the gut microbiome](#)

Furthermore, although the authors could identify some strong species-specific associations with the production of particular metabolites, such as production of the molecule tyramine by *Enterococcus faecalis*, metabolomic

profiles were insufficient to independently distinguish between members of different species. A machine-learning algorithm trained to identify a species on the basis of its metabolomic profile was correct only about 30% of the time, and even members of different genera or families were not well separated by the algorithm (in such analyses, it achieved an accuracy of approximately 70%). These results raise a note of caution regarding typical microbiome analyses, which often rely on microbial-abundance estimates at the genus and species levels, and thus might miss crucial metabolic aspects of the microbial community.

Although the correspondence between phylogeny and metabolism is imperfect, the authors present an analytical approach using the association between specific genes and metabolic outputs to obtain insights into microbial metabolism. Han and colleagues paired their metabolomic analyses with analyses of bacterial genomes to uncover the genes responsible for unexplained metabolic capacities. The authors identify a previously unknown mechanism by which microbes of the phylum Bacteroidetes utilize the amino acids glutamine and asparagine. Nevertheless, the *spe* genes responsible for producing the molecules putrescine and agmatine in several species are not present in three species of *Fusobacterium* that the authors found to produce these molecules — a result that demonstrates the limitations of this analytical method.

Han and colleagues conclude by turning to the most challenging aspect of their approach: assessing the correspondence between *in vitro* and *in vivo* metabolic output. Strains with a prominent metabolic capacity, such as *Citrobacter portucalensis*, which produces agmatine from the amino acid arginine, maintained some of this capacity both in culture and in mice. In some cases, this led to effects reaching beyond the gut (systemic effects). For example, agmatine levels were increased in the urine of mice if the animals were colonized by *C. portucalensis*.



Designer fibre meals sway human gut microbes

However, such a high level of correspondence between *in vitro* and *in vivo* data was not observed for the overall metabolic output, as tested by the authors for two strains. For these strains, there was only a moderate correlation between the *in vitro* metabolic profile of the strain and the profile measured from the intestines or faeces of a mouse colonized by it. Furthermore, no correlation was found between the *in vitro* profiles of these strains and the blood or urine profiles of mice colonized by them. This was the case despite the simplified ‘mono-colonization’ scenario, in which each mouse harboured only a single microbial strain, without other members of the bacterial community and the complex effects that arise from the interactions between them⁶.

These results highlight a major challenge left in the wake of this impressive endeavour, which is to use this extensive atlas of metabolic measurements, taken in simplified settings, to provide accurate models of complex community metabolism. This could be done experimentally — for example, by extending the work performed by Han *et al.* to assess combinatorial co-cultures — or by harnessing various computational and mathematical methods^{7,8}. Future work could further validate the utility of this data set for studying the human gut microbiome; extend the data set to strains that are found in, and have probably adapted to, a specific host⁹; and expand the data

set to microbes and metabolites that are relevant to other human-associated microbial communities, such as the vaginal and skin microbiomes.

Han and colleagues provide useful resources for the research community, including an extensive metabolomics data set consisting of thousands of samples, web resources with which to explore it and analytical approaches for studying microbial metabolism. Moreover, this work provides a truly open-source technical resource, with protocols, analysis pipelines and an extensive metabolite reference library, which the authors demonstrate to be applicable, with minimal calibration, to different machines. This resource could be used by others as they pursue similar experimental set-ups, thereby promoting the democratization of metabolomics. Altogether, this work lays a foundation for future work seeking to decipher microbial metabolism — an important step towards new therapeutics that target the microbiome.

Nature **595**, 355–357 (2021)

doi: <https://doi.org/10.1038/d41586-021-01774-6>

References

1. 1.

Yoshimoto, S. *et al.* *Nature* **499**, 97–101 (2013).

[PubMed](#) [Article](#) [Google Scholar](#)

2. 2.

Koeth, R. A. *et al.* *Nature Med.* **19**, 576–585 (2013).

[PubMed](#) [Article](#) [Google Scholar](#)

3. 3.

Lynch, J. B. & Hsiao, E. Y. *Science* **365**, 1405–1409 (2019).

[PubMed](#) [Article](#) [Google Scholar](#)

4. 4.

Bar, N. *et al.* *Nature* **588**, 135–140 (2020).

[PubMed](#) [Article](#) [Google Scholar](#)

5. 5.

Han, S. *et al.* *Nature* <https://doi.org/10.1038/s41586-021-03707-9> (2021).

[Article](#) [Google Scholar](#)

6. 6.

Coyte, K. Z., Schluter, J. & Foster, K. R. *Science* **350**, 663–666 (2015).

[PubMed](#) [Article](#) [Google Scholar](#)

7. 7.

Venturelli, O. S. *et al.* *Mol. Syst. Biol.* **14**, e8157 (2018).

[PubMed](#) [Article](#) [Google Scholar](#)

8. 8.

Chiu, H.-C., Levy, R. & Borenstein, E. *PLoS Comput. Biol.* **10**, e1003695 (2014).

[PubMed](#) [Article](#) [Google Scholar](#)

9. 9.

Zhao, S. *et al.* *Cell Host Microbe* **25**, 656–667 (2019).

[PubMed](#) [Article](#) [Google Scholar](#)

[Download references](#)

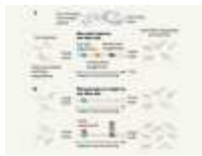
Competing Interests

The authors declare no competing interests.

Related Articles



- [Read the paper: A metabolomics pipeline for the mechanistic interrogation of the gut microbiome](#)



- [Designer fibre meals sway human gut microbes](#)



- [Bacterial species singled out from a diverse crowd](#)
- [See all News & Views](#)

Subjects

- [Microbiome](#)
- [Metabolism](#)
- [Microbiology](#)

nature careers

[Jobs](#) >

- [Postdoctoral Training Fellow](#)

Francis Crick Institute
London, United Kingdom

- [**Senior Business Manager**](#)

Francis Crick Institute
London, United Kingdom

- [**Postdoctoral Research Fellow in Pharmacogenomics Pain Management**](#)

The University of British Columbia (UBC)
Vancouver, Canada

- [**Postdoctoral Research Fellow in Pain Management and C. elegans**](#)

The University of British Columbia (UBC)
Vancouver, Canada

[Download PDF](#)

Related Articles

-  [**Read the paper: A metabolomics pipeline for the mechanistic interrogation of the gut microbiome**](#)



- [Designer fibre meals sway human gut microbes](#)



- [Bacterial species singled out from a diverse crowd](#)
- [See all News & Views](#)

Subjects

- [Microbiome](#)
- [Metabolism](#)
- [Microbiology](#)

This article was downloaded by **calibre** from <https://www.nature.com/articles/d41586-021-01774-6>

| [Section menu](#) | [Main menu](#) |

- NEWS AND VIEWS
- 14 July 2021

Measurement-based system provides quantum control of nanoparticles

Precise measurements of the position of a levitating nanosphere have been used to control forces that damp the nanosphere's motion — potentially opening the way to quantum control of larger objects.

- [Tania S. Monteiro](#) 0

1. [Tania S. Monteiro](#)

1. Tania S. Monteiro is in the Department of Physics and Astronomy, University College London, London WC1E 6BT, UK.

[View author publications](#)

You can also search for this author in [PubMed](#) [Google Scholar](#)





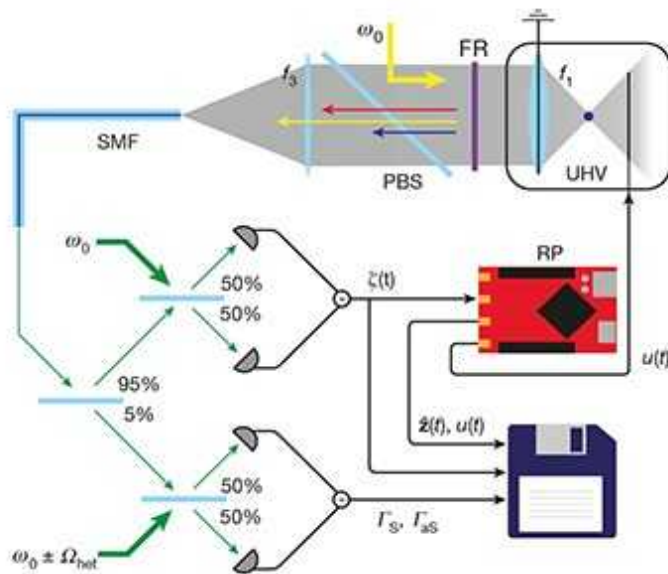
•

[Download PDF](#)

The Heisenberg uncertainty principle states that certain incompatible pairs of properties of a particle cannot be determined simultaneously with unlimited precision. It is often taught using a thought experiment for the case involving position and momentum: if the position of an atom is measured with light, the back-action of the scattered photons on the atom invariably disturbs the atom's momentum. The back-action can be reduced by using less-energetic or fewer photons, but this also reduces the precision of the measurement. More specifically, the Heisenberg uncertainty principle stipulates that the product of the uncertainties in measurements of position

and momentum must be greater than or equal to half of Planck's constant, \hbar . But this constant is so tiny (1.05×10^{-34} joule seconds) that the trade-offs between the back-action and imprecision can be observed only in carefully controlled experiments, typically using objects at the size scale of atoms.

Now, [Magrini et al.¹](#) and [Tebbenjohanns et al.²](#) report independent studies in which they were able to track the position not of a single atom, but of a nanosphere containing billions of atoms, with a precision close to the Heisenberg limit (the minimum possible product of the uncertainties of the measured quantities). This enabled them to use a technique called measurement-based quantum control to cool the nanosphere from highly excited thermal states down to average energies that are close to the lowest energy state of the particle (the quantum ground state).

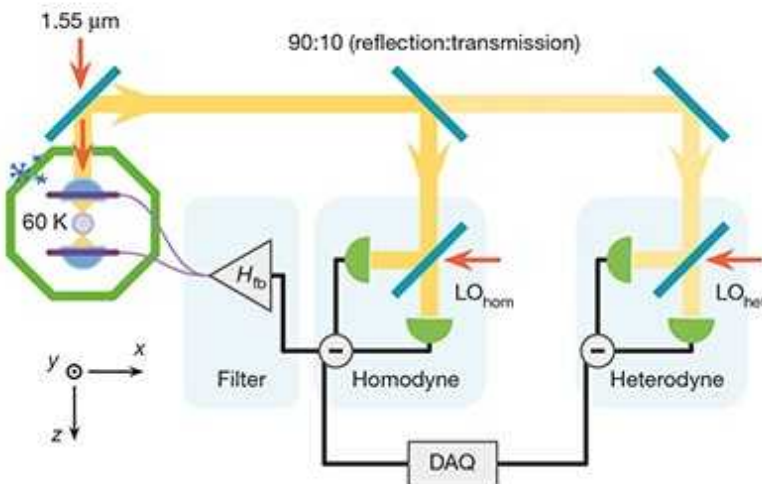


[Read the paper: Real-time optimal quantum control of mechanical motion at room temperature](#)

The results of the two studies are a breakthrough in optomechanics, the research field that aims to bring small mechanical oscillators into quantum regimes through their interaction with light. In the subfield of levitated quantum optomechanics, the oscillator is a silica particle about the size of a virus (100–200 nanometres in diameter), and is trapped and controlled by light. This minimizes both unwanted heating of the particle and decoherence — the loss of the particle's quantum behaviour through interactions with the

environment. Decoherence typically occurs much faster in experiments with oscillators that are directly tethered to their environment than in levitated systems.

After a decade of effort by several groups worldwide³, light-induced cooling of a levitated nanoparticle to the quantum ground state was finally reported⁴ in 2020. But that experiment relied on the quantum mode of light bouncing between two highly reflective mirrors, a set-up known as an optical cavity. This approach comes with limitations: only particles with certain ranges of oscillation frequency can be cooled in each set-up. Moreover, it is challenging to control the operation of an optical cavity sufficiently well to hold a particle stably, and then to cool it.



[Read the paper: Quantum control of a nanoparticle optically levitated in cryogenic free space](#)

Magrini *et al.* and Tebbenjohanns *et al.* used a completely different approach, dispensing with the optical cavity, and thus evading the associated problems. Their technique might therefore offer a more robust and straightforward way to prepare quantum states of mesoscopic objects (those between about 100 nanometres and one micrometre in size).

The authors' approach (Fig. 1) is an extension of a method termed feedback cooling, in which continuous measurement of an oscillator's position

enables a force (the feedback) to be applied that counters and damps the oscillator's motion. Although feedback cooling has been extensively investigated, for some years there was considerable scepticism as to whether this approach alone, without cavity cooling, could reach the milestone of cooling a levitated particle to an average energy that corresponds to less than a single quantum of energy above the fundamental zero-point motion (the residual motion that an oscillator retains in the quantum ground state). The current studies demonstrate that this milestone can indeed be reached using this method.

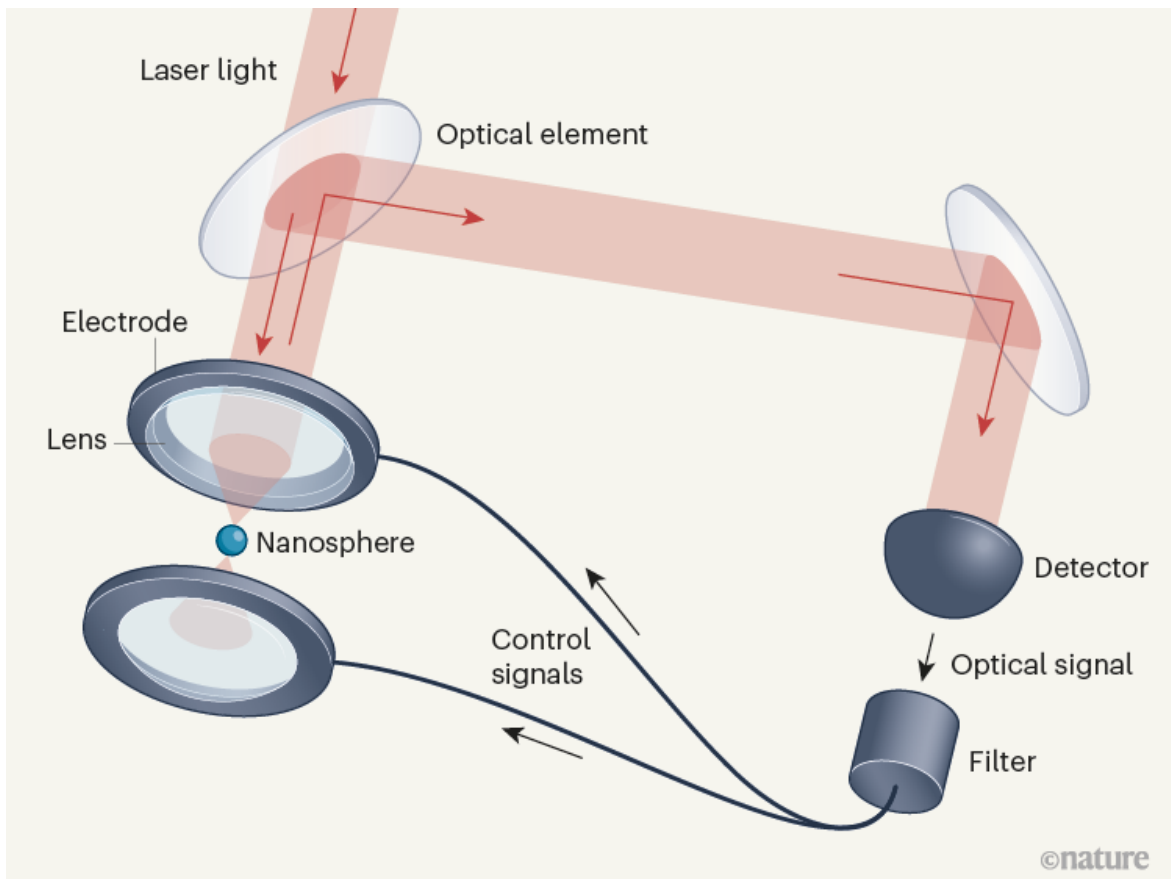


Figure 1 | A measurement-based approach for cooling nanoparticles.

Magrini *et al.*¹ and Tebbenjohanns *et al.*² have used a system called measurement-based quantum control to damp the motion of a spherical nanoparticle. The nanosphere is captured by a tightly focused beam of laser light known as an optical trap. Light scattered from the particle is reflected by a system of optical elements to a detector, producing an optical signal that is processed by a filter to determine the nanosphere's position. This

position measurement is then used to generate a signal that controls the electric field generated by a pair of electrodes around the nanosphere — thereby damping (cooling) the nanosphere's oscillatory motion.

Several advances have paved the way to this achievement. A feedback technique known as cold damping, which applies a force that is proportional to the velocity of the particle, was in the past few years^{5,6} shown to yield highly efficient cooling. Importantly, the nanospheres are naturally charged, which means that the feedback force can be applied using an electric field⁷, rather than light — thus avoiding extra photon back-action being exerted on the nanospheres. The experimental set-ups in the two new studies also operate at ultrahigh-vacuum levels (about 10^{-12} of normal air pressure), largely eliminating heating and decoherence associated with collisions of the nanosphere with surrounding gas molecules. And both studies benefited from improvements in the efficiency with which scattered photons are collected to measure the position of the nanosphere⁸.

Furthermore, the two experiments used a technique for measuring the energy of a particle⁹ that not only is calibration-independent, but also involves a characteristic of particles that are approaching the quantum regime: the spectra of the light scattered by such particles have two peaks, one of which corresponds to the particle absorbing a quantum of energy and the other to the loss of one quantum. The precise ratio of the areas of the peaks corresponds to the ratio of n to $n + 1$, where n is the number of energy quanta of the nanosphere (n is 0 in the quantum ground state, for example). A version of this technique, often called sideband asymmetry, is used in optical-cavity optomechanics⁴, but its applicability to experiments that use scattered light for measurements was not recognized until 2019 (ref. 9)⁹.

There are also differences between the two experiments. Magrini *et al.* cooled their particle from room temperature, which corresponds to a state in which n is in the tens of millions, down to a measured average energy of $n = 0.56$ — which means that, although the particle is not exactly in the quantum ground state, it has more than a 50% probability of being in that state, and a sharply falling probability of being in successively higher quantum states (with $n > 1$). To achieve this cooling, they used a statistical algorithm called a Kalman filter¹⁰ to optimize the feedback forces applied in real time to the

nanosphere in response to a continuous measurement. A Kalman filter is especially well suited for controlling quantum systems that have states typical of mechanical oscillators¹¹.

By contrast, Tebbenjohanns *et al.* used a straightforward control system that relies on the harmonic (pendulum-like) nature of the nanosphere's motion to predict the velocity of the nanosphere from its measured position, and hence to drive the feedback force. They also immersed the trapped nanosphere in a cryostat that reduced the initial temperature from about 300 to 60 kelvin. This cryogenic cooling will fulfil a crucial function in future experiments: it will ensure that the internal temperature of the nanosphere is low, thus reducing the emission of thermal radiation from the nanosphere. Such radiation is a major source of decoherence, and can potentially be produced from the relatively hot interior of a nanosphere even when the centre-of-mass motion of the object is in the quantum ground state. Tebbenjohanns and colleagues cooled nanospheres to an average energy corresponding to $n = 0.65$.

Measurement-based control techniques similar to those used in the two present studies were reported¹² last month to strongly damp the oscillations of a tethered 10-kilogram mirror in the 4-kilometre-long optical cavity of the Laser Interferometer Gravitational-Wave Observatory (LIGO). This achievement increased the formidable precision of the LIGO experiment, which can measure mirror displacements equivalent to a small fraction of an atomic nucleus. The mirror was cooled to an average energy corresponding to an n value of a little over 10. The big goal now is to demonstrate that cold oscillators — whether levitated or tethered — exhibit quantum behaviour in cavity-free experiments.

The new generation of table-top, optically levitated experiments^{12,4} are relatively simple, cheaper than LIGO and open up research possibilities not available using tethered oscillators. The optical forces holding the nanoparticles are fully controllable, allowing the trapped objects to be guided in space or fully released. Because they are highly decoupled from sources of decoherence, the nanoparticles might retain their quantum coherence for long enough to exhibit the effects of quantum-wave interference. They might also exhibit a quantum effect called entanglement, possibly in experiments with multiple nanospheres. Finally, they could be

used as ultrasensitive force detectors for practical applications such as accelerometry, or for testing fundamental physics such as quantum gravity.

Nature **595**, 357–358 (2021)

doi: <https://doi.org/10.1038/d41586-021-01872-5>

References

1. 1.

Magrini, L. *et al.* *Nature* **595**, 373–377 (2021).

[Article](#) [Google Scholar](#)

2. 2.

Tebbenjohanns, F., Mattana, M. L., Rossi, M., Frimmer, M. & Novotny, L. *Nature* **595**, 378–382 (2021).

[Article](#) [Google Scholar](#)

3. 3.

Millen, J., Monteiro, T. S., Pettit, R. & Vamivakas, A. N. *Rep. Prog. Phys.* **83**, 026401 (2020).

[PubMed](#) [Article](#) [Google Scholar](#)

4. 4.

Delić, U. *et al.* *Science* **367**, 892–895 (2020).

[PubMed](#) [Article](#) [Google Scholar](#)

5. 5.

Millen, J., Fonseca, P. Z. G., Mavrogordatos, T., Monteiro, T. S. & Barker, P. F. *Phys. Rev. Lett.* **114**, 123602 (2015).

[PubMed](#) [Article](#) [Google Scholar](#)

6. 6.

Rossi, M., Mason, D., Chen, J., Tsaturyan, Y. & Schliesser, A. *Nature* **563**, 53–58 (2018).

[PubMed](#) [Article](#) [Google Scholar](#)

7. 7.

Tebbenjohanns, F., Frimmer, M., Militaru, A., Jain, V. & Novotny, L. *Phys. Rev. Lett.* **122**, 223601 (2019).

[PubMed](#) [Article](#) [Google Scholar](#)

8. 8.

Jain, V. *et al.* *Phys. Rev. Lett.* **116**, 243601 (2016).

[PubMed](#) [Article](#) [Google Scholar](#)

9. 9.

Tebbenjohanns, F., Frimmer, M., Jain, V., Windey, D. & Novotny, L. *Phys. Rev. Lett.* **124**, 013603 (2020).

[PubMed](#) [Article](#) [Google Scholar](#)

10. 10.

Setter, A., Toroš, M., Ralph, J. F. & Ulbricht, H. *Phys. Rev. A* **97**, 033822 (2018).

[Article](#) [Google Scholar](#)

11. 11.

Belavkin, V. P. *Radiotech. Electron.* **25**, 1445–1453 (1980).

[Google Scholar](#)

12. 12.

Whittle, C. *et al.* *Science* **372**, 1333–1336 (2021).

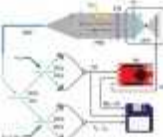
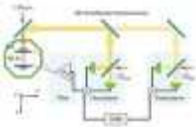
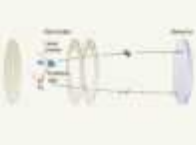
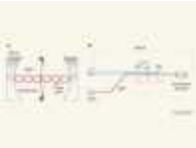
[PubMed](#) [Article](#) [Google Scholar](#)

[Download references](#)

Competing Interests

The author declares no competing interests.

Related Articles

-  [Read the paper: Real-time optimal quantum control of mechanical motion at room temperature](#)
-  [Read the paper: Quantum control of a nanoparticle optically levitated in cryogenic free space](#)
-  [Ultracold chemical reactions reveal the quantum mechanisms of produce formation](#)
-  [Mechanical quantum systems controlled](#)

- [See all News & Views](#)

Subjects

- [Quantum physics](#)
- [Optics and photonics](#)
- [Physics](#)

nature careers

[Jobs](#) >

- [Postdoctoral Training Fellow](#)

Francis Crick Institute

London, United Kingdom

- [Senior Business Manager](#)

Francis Crick Institute

London, United Kingdom

- [Postdoctoral Research Fellow in Pharmacogenomics Pain Management](#)

The University of British Columbia (UBC)

Vancouver, Canada

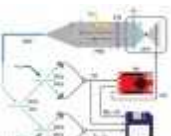
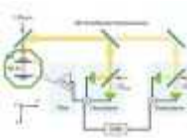
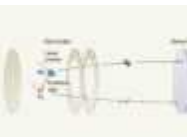
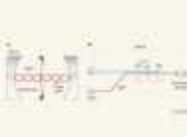
- [Postdoctoral Research Fellow in Pain Management and C. elegans](#)

The University of British Columbia (UBC)

Vancouver, Canada

[Download PDF](#)

Related Articles

-  [**Read the paper: Real-time optimal quantum control of mechanical motion at room temperature**](#)
-  [**Read the paper: Quantum control of a nanoparticle optically levitated in cryogenic free space**](#)
-  [**Ultracold chemical reactions reveal the quantum mechanisms of produce formation**](#)
-  [**Mechanical quantum systems controlled**](#)
- [**See all News & Views**](#)

Subjects

- [**Quantum physics**](#)
- [**Optics and photonics**](#)
- [**Physics**](#)

| [Section menu](#) | [Main menu](#) |

- NEWS AND VIEWS
- 14 June 2021

A long-term perspective on immunity to COVID

Determining the duration of protective immunity to infection by SARS-CoV-2 is crucial for understanding and predicting the course of the COVID-19 pandemic. Clinical studies now indicate that immunity will be long-lasting.

- [Andreas Radbruch](#) ⁰ &
- [Hyun-Dong Chang](#) ¹

1. [Andreas Radbruch](#)

1. Andreas Radbruch is at the German Rheumatism Research Centre Berlin (DRFZ), a Leibniz Institute, Berlin 10117, Germany.

[View author publications](#)

You can also search for this author in [PubMed](#) [Google Scholar](#)

2. [Hyun-Dong Chang](#)

1. Hyun-Dong Chang is at the German Rheumatism Research Centre Berlin (DRFZ), a Leibniz Institute, Berlin 10117, Germany.

[View author publications](#)

You can also search for this author in [PubMed](#) [Google Scholar](#)

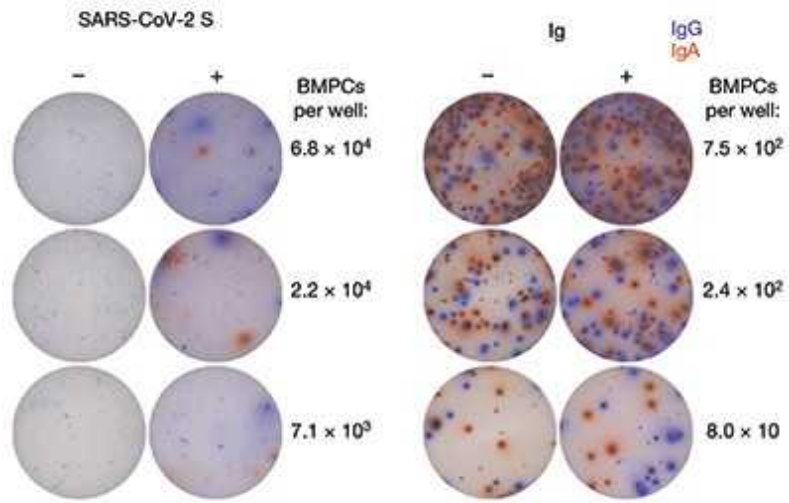




•

[Download PDF](#)

Generating immunity against the SARS-CoV-2 coronavirus is of the utmost importance for bringing the COVID-19 pandemic under control, protecting vulnerable individuals from severe disease and limiting viral spread. Our immune systems protect against SARS-CoV-2 either through a sophisticated reaction to infection or in response to vaccination. A key question is, how long does this immunity last? Writing in *Nature*, [Turner et al.](#)¹ and [Wang et al.](#)² characterize human immune responses to SARS-CoV-2 infection over the course of a year.

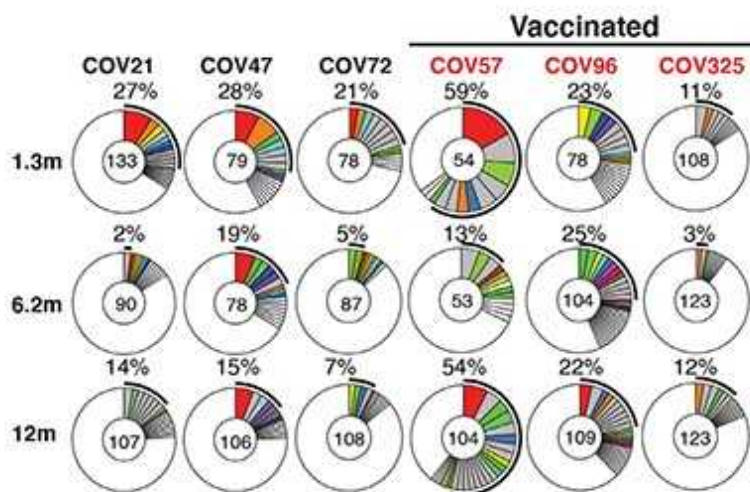


[Read the paper: SARS-CoV-2 infection induces long-lived bone marrow plasma cells in humans](#)

There is ongoing discussion about which aspects of the immune response to SARS-CoV-2 provide hallmarks of immunity (in other words, correlates of immunological protection). However, there is probably a consensus that the two main pillars of an antiviral response are immune cells called cytotoxic T cells, which can selectively eliminate infected cells, and neutralizing antibodies, a type of antibody that prevents a virus from infecting cells, and that is secreted by immune cells called plasma cells. A third pillar of an effective immune response would be the generation of T helper cells, which are specific for the virus and coordinate the immune reaction. Crucially, these latter cells are required for generating immunological memory — in particular, for orchestrating the emergence of long-lived plasma cells³, which continue to secrete antiviral antibodies even when the virus has gone.

Immunological memory is not a long-lasting version of the immediate immune reaction to a particular virus; rather, it is a distinct aspect of the immune system. In the memory phase of an immune response, B and T cells that are specific for a virus are maintained in a state of dormancy, but are poised to spring into action if they encounter the virus again or a vaccine that represents it. These memory B and T cells arise from cells activated in the initial immune reaction. The cells undergo changes to their chromosomal DNA, termed epigenetic modifications, that enable them to react rapidly to

subsequent signs of infection and drive responses geared to eliminating the disease-causing agent⁴. B cells have a dual role in immunity: they produce antibodies that can recognize viral proteins, and they can present parts of these proteins to specific T cells or develop into plasma cells that secrete antibodies in large quantities. About 25 years ago⁵, it became evident that plasma cells can become memory cells themselves, and can secrete antibodies for long-lasting protection. Memory plasma cells can be maintained for decades, if not a lifetime, in the bone marrow⁶.



[Read the paper: Naturally enhanced neutralizing breadth against SARS-CoV-2 one year after infection](#)

The presence in the bone marrow of long-lived, antibody-secreting memory plasma cells is probably the best available predictor of long-lasting immunity. For SARS-CoV-2, most studies so far have analysed the acute phase of the immune response, which spans a few months after infection, and have monitored T cells, B cells and secreted antibodies⁷. It has remained unclear whether the response generates long-lived memory plasma cells that secrete antibodies against SARS-CoV-2.

Turner and colleagues took up the challenge of [identifying antibody-secreting memory plasma cells](#) in the bone marrow of people who have recovered from COVID-19 (called convalescent individuals). Memory plasma cells are rare, and those specific for a particular disease-causing

agent will obviously be extremely scarce. Nevertheless, Turner and colleagues detected memory plasma cells that secreted antibodies specific for the spike protein encoded by SARS-CoV-2 in 15 of 19 individuals, approximately 7 months after infection. Notably, when the authors obtained samples 4 months later (11 months after SARS-CoV-2 infection), the number of such plasma cells had remained stable in all but one of the individuals analysed. Those plasma cells did not proliferate, which classifies them as bona fide memory plasma cells. Their numbers equalled those of memory plasma cells found in the individuals after vaccination against tetanus or diphtheria, and which provide long-term immunity to those diseases.

When Turner *et al.* tracked the concentrations of antibodies against SARS-CoV-2 in the individuals' blood serum for up to one year, they observed a biphasic pattern (Fig. 1). In the acute immune response around the time of initial infection, antibody concentrations were high. They subsequently declined, as expected, because most of the plasma cells of an acute immune response are short-lived. After a few months, the antibody concentrations levelled off and remained more or less constant at roughly 10–20% of the maximum concentration observed. This is consistent with the expectation that 10–20% of the plasma cells in an acute immune reaction become memory plasma cells⁵, and is a clear indication of a shift from antibody production by short-lived plasma cells to antibody production by memory plasma cells. This is not unexpected, given that immune memory to many viruses and vaccines is stable over decades, if not for a lifetime⁸.

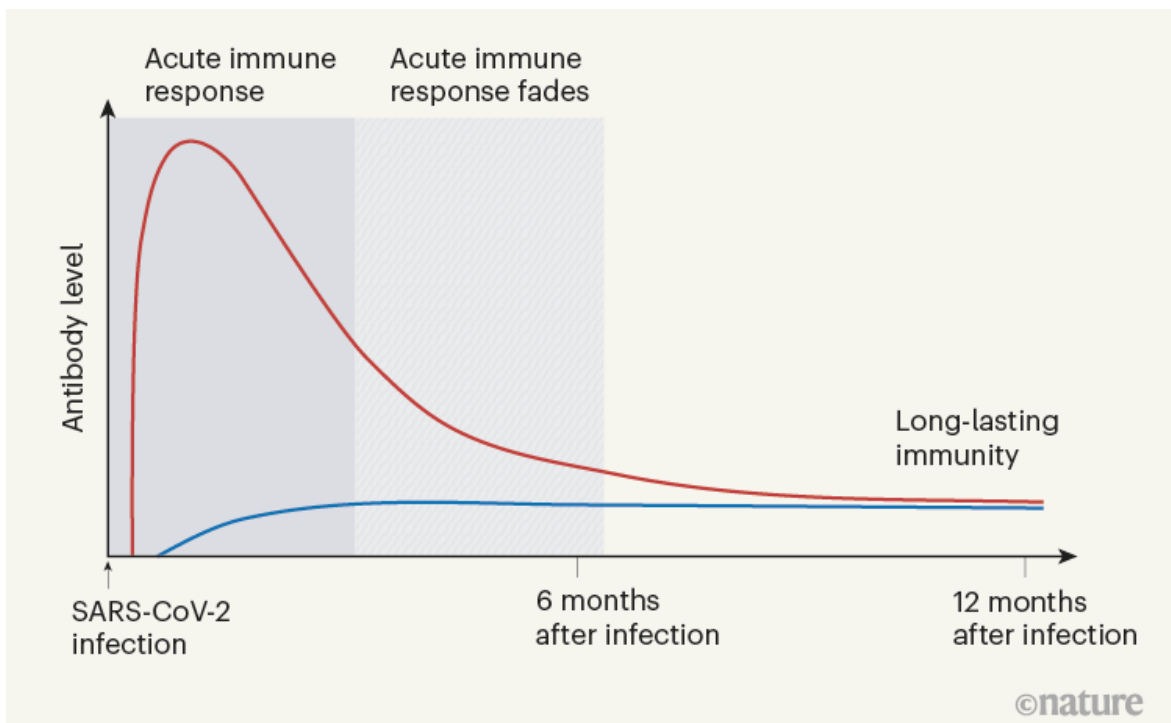
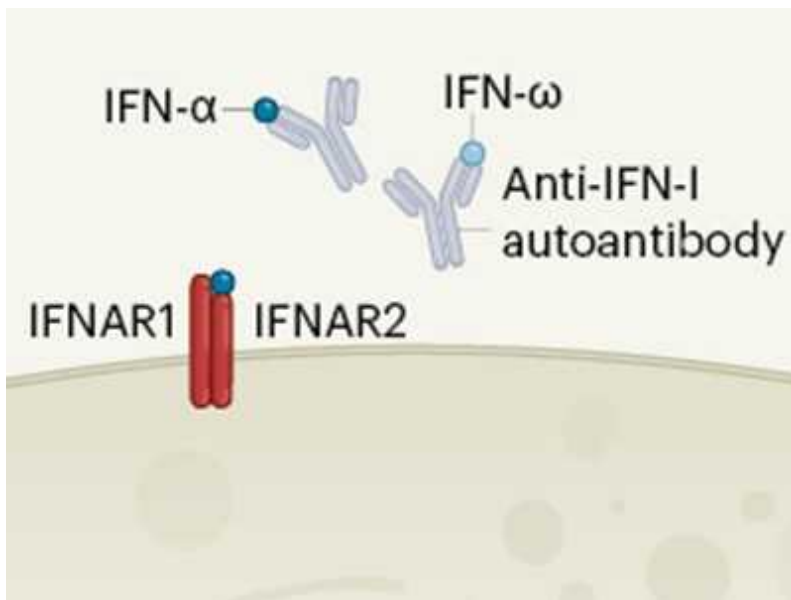


Figure 1 | The immune response to SARS-CoV-2 infection. Data are becoming available that shed light on longer-term aspects of the human immune response to coronavirus infection. One component of the defence response is the production of antibodies that target viral proteins (red line). During the initial, acute phase of the immune response, antibody levels peak rapidly; this peak is generated by short-lived immune cells called plasma cells. Turner *et al.*¹ present clinical evidence, from people who have had COVID-19, that long-lived, memory plasma cells that produce antibodies are generated in the bone marrow. These cells provide long-term antibody production that offers stable protection at a level of 10–20% of that during the acute phase (blue line). Memory plasma cells are a cell type that can be maintained for many years, if not a lifetime⁸. Wang *et al.*² have characterized antibody responses at between six months and a year in people who have been infected with SARS-CoV-2; their results also provide evidence for the generation of immunological memory.

For SARS-CoV, a coronavirus very like SARS-CoV-2 that was originally identified in 2003 and causes severe acute respiratory syndrome (SARS), the continued presence of high concentrations of neutralizing antibodies in blood serum for more than 17 years was reported⁹ in 2020. Wang and colleagues' results suggest that long-term immunity might also be expected

for SARS-CoV-2. The authors report a follow-up investigation of serum antibodies and memory B cells specific for SARS-CoV-2 approximately one year after infection. The individuals studied had previously been analysed by Wang and colleagues' group after six months¹⁰, but it is only now, after a year, that the transition from an acute immune reaction to the generation of immunological memory has become evident.

Wang *et al.* show that, between 6 and 12 months after infection, the concentration of neutralizing antibodies remains unchanged. That the acute immune reaction extends even beyond six months is suggested by the authors' analysis of SARS-CoV-2-specific memory B cells in the blood of the convalescent individuals over the course of the year. These memory B cells continuously enhance the reactivity of their SARS-CoV-2-specific antibodies through a process known as somatic hypermutation. The authors demonstrated this with *in vitro* tests of antibody neutralization of a broad collection of SARS-CoV-2 variant strains.



Interferon deficiency can lead to severe COVID

Finally, Wang and colleagues show that immunity can be boosted even further in convalescent individuals by vaccinating them after a year. This resulted in the generation of more plasma cells, together with an increase in the level of SARS-CoV-2 antibodies that was up to 50 times greater than before vaccination. Some of the plasma cells will probably be recruited to

become memory plasma cells, although this remains to be demonstrated formally, as does the induction of stable, long-term memory as a consequence of SARS-CoV-2 vaccination.

In evaluating vaccine efficacy, we should not expect the high antibody concentrations characteristic of acute immune reactions to be maintained in the memory phase¹¹. It is an old misconception, when advocating frequent revaccinations, that antibody concentrations during the acute immune reaction can be compared with those later on, to calculate an imaginary ‘half-life’ of antibody-mediated immunity. This ignores the biphasic character of the immune response (Fig. 1).

The good news is that the evidence thus far predicts that infection with SARS-CoV-2 induces long-term immunity in most individuals. This provides a welcome positive note as we wait for further data on memory responses to vaccination.

Nature **595**, 359-360 (2021)

doi: <https://doi.org/10.1038/d41586-021-01557-z>

References

1. 1.

Turner, J. S. *et al.* *Nature* <https://doi.org/10.1038/s41586-021-03647-4> (2021).

[Article](#) [Google Scholar](#)

2. 2.

Wang, Z. *et al.* *Nature* <https://doi.org/10.1038/s41586-021-03696-9> (2021).

[Article](#) [Google Scholar](#)

3. 3.

Crotty, S., Kersh, E. N., Cannons, J., Schwartzberg, P. L. & Ahmed, R. *Nature* **421**, 282–287 (2003).

[PubMed](#) [Article](#) [Google Scholar](#)

4. 4.

Löhning, M., Richter, A. & Radbruch, A. *Adv. Immunol.* **80**, 115–181 (2002).

[PubMed](#) [Article](#) [Google Scholar](#)

5. 5.

Manz, R. A., Thiel, A. & Radbruch, A. *Nature* **388**, 133–134 (1997).

[PubMed](#) [Article](#) [Google Scholar](#)

6. 6.

Chang, H.-D. & Radbruch, A. *Eur. J. Immunol.* <https://doi.org/10.1002/eji.202049012> (2021).

[Article](#) [Google Scholar](#)

7. 7.

Sette, A. & Crotty, S. *Cell* **184**, 861–880 (2021).

[PubMed](#) [Article](#) [Google Scholar](#)

8. 8.

Amanna, I. J., Carlson, N. E. & Slifka, M. K. *N. Engl. J. Med.* **357**, 1903–1915 (2007).

[PubMed](#) [Article](#) [Google Scholar](#)

9. 9.

Anderson, D. E. *et al.* *Emerg. Microbes Infect.* **9**, 900–902 (2020).

[PubMed](#) [Article](#) [Google Scholar](#)

10. 10.

Gaebler, C. *et al.* *Nature* **591**, 639–644 (2021).

[PubMed](#) [Article](#) [Google Scholar](#)

11. 11.

Hammarlund, E. *et al.* *Nature Commun.* **8**, 1781 (2017).

[PubMed](#) [Article](#) [Google Scholar](#)

[Download references](#)

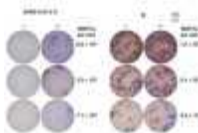
Competing Interests

The authors declare no competing interests.

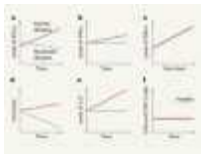
Related Articles



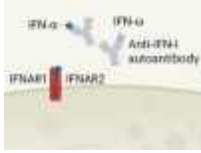
- [Read the paper: Naturally enhanced neutralizing breadth against SARS-CoV-2 one year after infection](#)



- [Read the paper: SARS-CoV-2 infection induces long-lived bone marrow plasma cells in humans](#)



- [COVID-19 poses a riddle for the immune system](#)



- [Interferon deficiency can lead to severe COVID](#)
- [See all News & Views](#)

Subjects

- [SARS-CoV-2](#)
- [Immunology](#)
- [Medical research](#)

nature careers

Jobs >

- [Postdoctoral Training Fellow](#)

Francis Crick Institute

London, United Kingdom

- [Senior Business Manager](#)

Francis Crick Institute

London, United Kingdom

- [Postdoctoral Research Fellow in Pharmacogenomics Pain Management](#)

The University of British Columbia (UBC)

Vancouver, Canada

- [Postdoctoral Research Fellow in Pain Management and C. elegans](#)

The University of British Columbia (UBC)

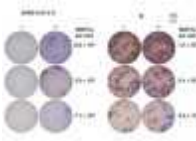
Vancouver, Canada

[Download PDF](#)

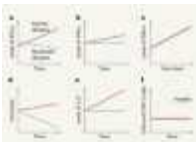
Related Articles



- [Read the paper: Naturally enhanced neutralizing breadth against SARS-CoV-2 one year after infection](#)



- [Read the paper: SARS-CoV-2 infection induces long-lived bone marrow plasma cells in humans](#)



- [COVID-19 poses a riddle for the immune system](#)



- [Interferon deficiency can lead to severe COVID](#)
- [See all News & Views](#)

Subjects

- [SARS-CoV-2](#)
- [Immunology](#)
- [Medical research](#)

This article was downloaded by **calibre** from <https://www.nature.com/articles/d41586-021-01557-z>

| [Section menu](#) | [Main menu](#) |

- Perspective
- [Published: 14 July 2021](#)

Designing the next generation of proton-exchange membrane fuel cells

- [Kui Jiao](#) [ORCID: orcid.org/0000-0002-1296-1330¹](#),
^{na1},
- [Jin Xuan](#) [ORCID: orcid.org/0000-0002-6718-9018²](#),
^{na1},
- [Qing Du](#) [ORCID: orcid.org/0000-0002-6246-3479¹](#),
^{na1},
- [Zhiming Bao](#) [ORCID: orcid.org/0000-0002-1574-6679¹](#),
- [Biao Xie](#) [ORCID: orcid.org/0000-0002-5536-5838¹](#),
- [Bowen Wang](#) [ORCID: orcid.org/0000-0002-4583-2287¹](#),
- [Yan Zhao](#) [ORCID: orcid.org/0000-0001-6722-6555³](#),
- [Linhao Fan](#) [ORCID: orcid.org/0000-0003-4291-7709¹](#),
- [Huizhi Wang](#) [ORCID: orcid.org/0000-0003-2287-0544³](#),
- [Zhongjun Hou](#) [ORCID: orcid.org/0000-0002-9081-036X⁴](#),
- [Sen Huo](#) [ORCID: orcid.org/0000-0002-8023-678X⁴](#),
- [Nigel P. Brandon⁵](#),
- [Yan Yin](#) [ORCID: orcid.org/0000-0003-1655-6831¹](#) &
- [Michael D. Guiver](#) [ORCID: orcid.org/0000-0003-2619-6809^{1,6}](#)

[Nature](#) volume **595**, pages 361–369 (2021) [Cite this article](#)

- 3320 Accesses
- 16 Altmetric
- [Metrics details](#)

Subjects

- [Electrocatalysis](#)
- [Fuel cells](#)

Abstract

With the rapid growth and development of proton-exchange membrane fuel cell (PEMFC) technology, there has been increasing demand for clean and sustainable global energy applications. Of the many device-level and infrastructure challenges that need to be overcome before wide commercialization can be realized, one of the most critical ones is increasing the PEMFC power density, and ambitious goals have been proposed globally. For example, the short- and long-term power density goals of Japan's New Energy and Industrial Technology Development Organization are 6 kilowatts per litre by 2030 and 9 kilowatts per litre by 2040, respectively. To this end, here we propose technical development directions for next-generation high-power-density PEMFCs. We present the latest ideas for improvements in the membrane electrode assembly and its components with regard to water and thermal management and materials. These concepts are expected to be implemented in next-generation PEMFCs to achieve high power density.

Access options

Subscribe to Journal

Get full journal access for 1 year

\$199.00

only \$3.90 per issue

[Subscribe](#)

All prices are NET prices.

VAT will be added later in the checkout.

Tax calculation will be finalised during checkout.

Rent or Buy article

Get time limited or full article access on ReadCube.

from \$8.99

[Rent or Buy](#)

All prices are NET prices.

Additional access options:

- [Log in](#)
- [Access through your institution](#)
- [Learn about institutional subscriptions](#)

Fig. 1: Expected application domains of BEVs and FCVs in future automotive transportation, and comparison of their technical characteristics[6,7,8,9,10,11,12,13](#).

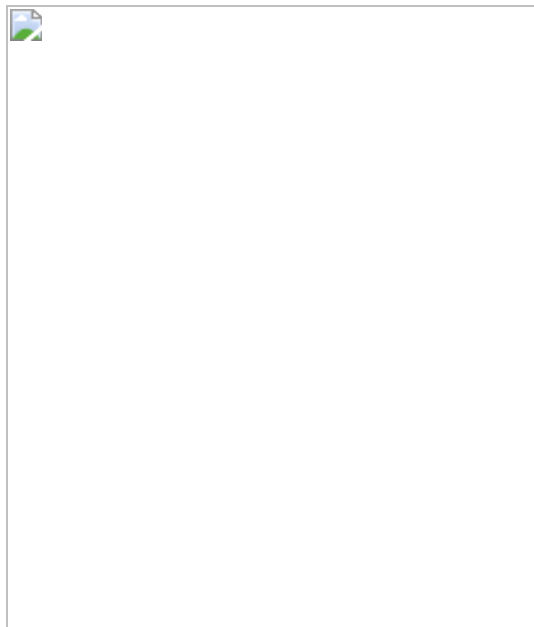


Fig. 2: Overview of progressive improvements in PEMFCs to meet future high-power-density requirements and a schematic explanation of the working principle.

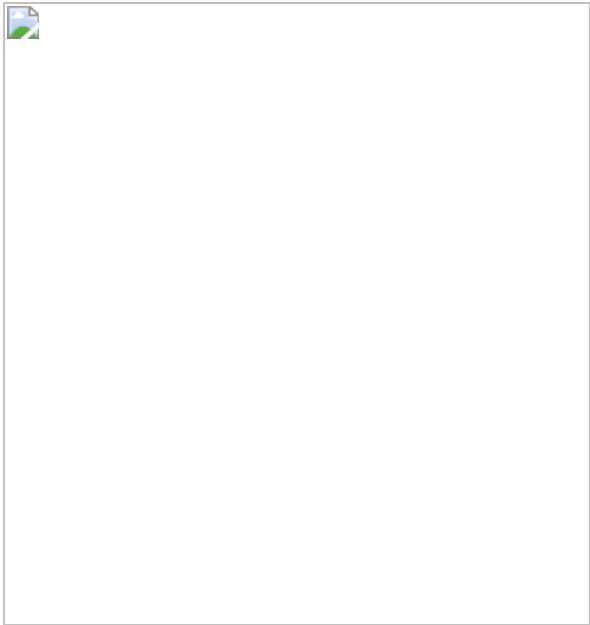


Fig. 3: State-of-the-art and next-generation MEA designs.

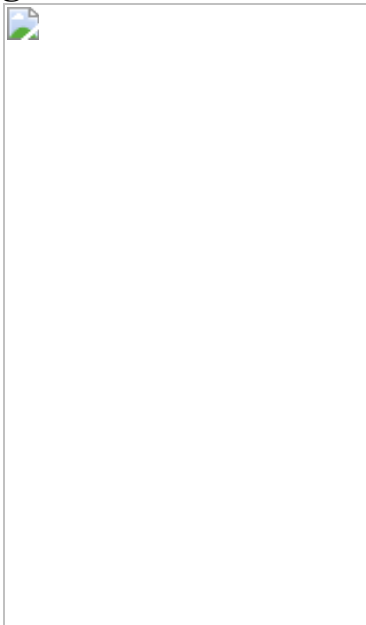
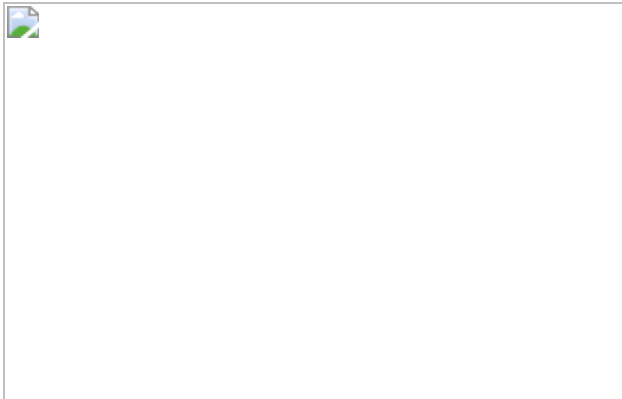


Fig. 4: Trends in the development of BPs for FCVs.



References

1. 1.

Jewell, J. et al. Limited emission reductions from fuel subsidy removal except in energy-exporting regions. *Nature* **554**, 229–233 (2018).

[ADS](#) [CAS](#) [Google Scholar](#)

2. 2.

Staffell, I. et al. The role of hydrogen and fuel cells in the global energy system. *Energy Environ. Sci.* **12**, 463–491 (2019).

[CAS](#) [Google Scholar](#)

3. 3.

Itaoka, K., Saito, A. & Sasaki, K. Public perception on hydrogen infrastructure in Japan: Influence of rollout of commercial fuel cell vehicles. *Int. J. Hydrogen Energy* **42**, 7290–7296 (2017).

[CAS](#) [Google Scholar](#)

4. 4.

Eberle, U., Müller, B. & Helmolt, R. Fuel cell electric vehicles and hydrogen infrastructure: status 2012. *Energy Environ. Sci.* **5**, 8780–

8798 (2012).

[Google Scholar](#)

5. 5.

Cano, Z. P. et al. Batteries and fuel cells for emerging electric vehicle markets. *Nat. Energy* **3**, 279–289 (2018).

[ADS](#) [Google Scholar](#)

6. 6.

Gröger, O., Gasteiger, H. A. & Suchsland, J. P. Electromobility: batteries or fuel cells? *J. Electrochem. Soc.* **162**, A2605–A2622 (2015). **This review compares batteries and fuel cells for automotive applications, suggesting that the high energy density of fuel cells makes them suitable for heavy-duty and long-distance transportation.**

[Google Scholar](#)

7. 7.

Hu, X. et al. Battery warm-up methodologies at subzero temperatures for automotive applications: recent advances and perspectives. *Progr. Energy Combust. Sci.* **77**, 100806 (2020).

[Google Scholar](#)

8. 8.

Introducing the all-new Toyota MIRAI. *Toyota Europe Newsroom* <https://newsroom.toyota.eu/introducing-the-all-new-toyota-MIRAI/> (2020).

9. 9.

Wilson, A., Kleen, G. & Papageorgopoulos, D. *Fuel Cell System Cost–2017. DOE Hydrogen and Fuel Cells Program Record 17007.*
https://www.hydrogen.energy.gov/pdfs/17007_fuel_cell_system_cost_2017.pdf (DOE Fuel Cell Technologies Office, 2017).

10. 10.

Wang, Y. et al. Fundamentals, materials, and machine learning of polymer electrolyte membrane fuel cell technology. *Energy AI* **1**, 100014 (2020).

[Google Scholar](#)

11. 11.

Frendo, O. et al. Data-driven smart charging for heterogeneous electric vehicle fleets. *Energy AI* **1**, 100007 (2020).

[Google Scholar](#)

12. 12.

Jin, D. & Jiao, K. Charging infrastructure intellectualization and future of different automotive powertrains. *Joule* **4**, 1634–1636 (2020).

[Google Scholar](#)

13. 13.

Harrison, M. Toyota electrification strategy in Europe today and tomorrow. *Toyota Motor Europe*
https://www.autonews.com/assets/pdf/ane-congress/presentations2019/matthew_harrison.pdf (2019).

14. 14.

Full specs of Toyota MIRAI 2021. *Toyota USA*
https://www.toyota.com/MIRAI/features/mileage_estimates/3002/3003 (2020).

15. 15.

Konno, N., Mizuno, S. & Nakaji, H. Development of compact and high-performance fuel cell stack. *SAE Mobilus* **4**, 123–129 (2015).

[Google Scholar](#)

16. 16.

Amamiya, I. & Tanaka, S. Current topics proposed by PEFC manufacturers, etc. – current status and topics of fuel cells for FCV. In *Hydrogen, Fuel Cell Project Evaluation, and Issue Sharing Week* (Japan New Energy and Industrial Technology Development Organization, 2019); available at <https://www.nedo.go.jp/content/100895101.pdf> (in Japanese).

17. 17.

Volume manufacturing of PEM FC stacks for transportation and in-line quality assurance (European Commission, 2019);
<https://cordis.europa.eu/project/id/671465>

18. 18.

Fuel Cells and Hydrogen 2 Joint Undertaking (FCH 2 JU). 2019 annual work plan and budget (FCH 2 JU, 2018);
https://ec.europa.eu/research/participants/data/ref/h2020/other/wp/jtis/h2020-wp19-fch_en.pdf

19. 19.

Ozden, A., Shahgaldi, S., Li, X. & Hamdullahpur, F. A review of gas diffusion layers for proton exchange membrane fuel cells – with a focus on characteristics, characterization techniques, materials and designs. *Progr. Energy Combust. Sci.* **74**, 50–102 (2019).

[Google Scholar](#)

20. 20.

Gerteisen, D. & Sadeler, C. Stability and performance improvement of a polymer electrolyte membrane fuel cell stack by a laser perforation of gas diffusion layers. *J. Power Sources* **195**, 5252–5257 (2010).

[ADS](#) [CAS](#) [Google Scholar](#)

21. 21.

Tian, X. et al. Engineering bunched Pt-Ni alloy nanocages for efficient oxygen reduction in practical fuel cells. *Science* **366**, 850–856 (2019).

[ADS](#) [CAS](#) [Google Scholar](#)

22. 22.

Chong, L. et al. Ultralow-loading platinum-cobalt fuel cell catalysts derived from imidazolate frameworks. *Science* **362**, 1276–1281 (2018).

[ADS](#) [CAS](#) [PubMed](#) [PubMed Central](#) [Google Scholar](#)

23. 23.

Chen, C. et al. Highly crystalline multimetallic nanoframes with three-dimensional electrocatalytic surfaces. *Science* **343**, 1339–1343 (2014).

[ADS](#) [CAS](#) [Google Scholar](#)

24. 24.

Li, M. et al. Ultrafine jagged platinum nanowires enable ultrahigh mass activity for the oxygen reduction reaction. *Science* **354**, 1414–1419 (2016). **This study achieves high specific and mass activity using ultrafine jagged platinum nanowires for oxygen reduction, suggesting a promising approach to realizing high-current-density fuel cells.**

[ADS](#) [CAS](#) [PubMed](#) [PubMed Central](#) [Google Scholar](#)

25. 25.

Huang, X. et al. High-performance transition metal-doped Pt₃Ni octahedra for oxygen reduction reaction. *Science* **348**, 1230–1234 (2015).

[ADS](#) [CAS](#) [Google Scholar](#)

26. 26.

Ott, S. et al. Ionomer distribution control in porous carbon-supported catalyst layers for high-power and low Pt-loaded proton exchange membrane fuel cells. *Nat. Mater.* **19**, 77–85 (2020). **This study shows that N-doped carbon supports can improve ionomer distribution in the catalyst layer, providing an important path to next-generation high-power-density fuel cells.**

[ADS](#) [CAS](#) [Google Scholar](#)

27. 27.

Yarlagadda, V. et al. Boosting fuel cell performance with accessible carbon mesopores. *ACS Energy Lett.* **3**, 618–621 (2018).

[CAS](#) [Google Scholar](#)

28. 28.

Poojary, S., Islam, M. N., Shrivastava, U. N., Roberts, E. P. L. & Karan, K. Transport and electrochemical interface properties of ionomers in low-Pt loading catalyst layers: effect of ionomer equivalent weight and relative humidity. *Molecules* **25**, 3387 (2020).

[CAS](#) [PubMed](#) [PubMed Central](#) [Google Scholar](#)

29. 29.

Yoon, K. R. et al. Mussel-inspired polydopamine-treated reinforced composite membranes with self-supported CeO_x radical scavengers for

highly stable PEM fuel cells. *Adv. Funct. Mater.* **29**, 1806929 (2019).

[Google Scholar](#)

30. 30.

Park, C. H. et al. Nanocrack-regulated self-humidifying membranes. *Nature* **532**, 480–483 (2016). **This study develops self-humidifying membranes with surface nanocrack coatings, providing an alternative solution for membranes that tolerate low-humidity conditions.**

[ADS](#) [Google Scholar](#)

31. 31.

Liu, X. et al. Magnetic field alignment of stable proton-conducting channels in an electrolyte membrane. *Nat. Commun.* **10**, 842 (2019). **This study develops composite membranes with through-plane-aligned proton channels, showing that thus oriented channels improve proton conductivity and durability, and that microporous channels strongly retain water.**

[ADS](#) [CAS](#) [PubMed](#) [PubMed Central](#) [Google Scholar](#)

32. 32.

Tanaka, S., Bradfield, W. W., Legrand, C. & Malan, A. G. Numerical and experimental study of the effects of the electrical resistance and diffusivity under clamping pressure on the performance of a metallic gas-diffusion layer in polymer electrolyte fuel cells. *J. Power Sources* **330**, 273–284 (2016).

[ADS](#) [CAS](#) [Google Scholar](#)

33. 33.

Tanaka, S. & Shudo, T. Corrugated mesh flow channel and novel microporous layers for reducing flooding and resistance in gas

diffusion layer-less polymer electrolyte fuel cells. *J. Power Sources* **268**, 183–193 (2014).

[ADS](#) [CAS](#) [Google Scholar](#)

34. 34.

Lee, J., Hinebaugh, J. & Bazylak, A. Synchrotron X-ray radiographic investigations of liquid water transport behavior in a PEMFC with MPL-coated GDLs. *J. Power Sources* **227**, 123–130 (2013).

[CAS](#) [Google Scholar](#)

35. 35.

Li, D. et al. Functional links between Pt single crystal morphology and nanoparticles with different size and shape: the oxygen reduction reaction case. *Energy Environ. Sci.* **7**, 4061–4069 (2014).

[CAS](#) [Google Scholar](#)

36. 36.

Karan, K. PEFC catalyst layer: recent advances in materials, microstructural characterization, and modeling. *Curr. Opin. Electrochem.* **5**, 27–35 (2017).

[CAS](#) [Google Scholar](#)

37. 37.

Kim, Y. S. & Pivovar, B. S. The membrane–electrode interface in PEFCs. *J. Electrochem. Soc.* **157**, B1616 (2010).

[CAS](#) [Google Scholar](#)

38. 38.

Holdcroft, S. Fuel cell catalyst layers: a polymer science perspective. *Chem. Mater.* **26**, 381–393 (2014).

[CAS](#) [Google Scholar](#)

39. 39.

Yin, Y. et al. Ionomer migration within PEMFC catalyst layers induced by humidity changes. *Electrochem. Commun.* **109**, 106590 (2019).

[CAS](#) [Google Scholar](#)

40. 40.

Crowtz, T. C. & Dahn, J. R. Screening bifunctional Pt based NSTF catalysts for durability with the rotating disk electrode: The effect of Ir and Ru. *J. Electrochem. Soc.* **165**, F854–F862 (2018).

[CAS](#) [Google Scholar](#)

41. 41.

Steinbach, A. J. et al. Ultrathin film NSTF ORR electrocatalysts for PEM fuel cells. *ECS Trans.* **80**, 659–676 (2017).

[CAS](#) [Google Scholar](#)

42. 42.

Steinbach, A. *Final Technical Report for Project Entitled Highly Active, Durable, and Ultra-Low PGM NSTF Thin Film ORR Catalysts and Support*. Technical Report DOE-3M-0007270 (US Department of Energy, 2020).

43. 43.

Murata, S., Imanishi, M., Hasegawa, S. & Namba, R. Vertically aligned carbon nanotube electrodes for high current density operating

proton exchange membrane fuel cells. *J. Power Sources* **253**, 104–113 (2014).

[ADS](#) [CAS](#) [Google Scholar](#)

44. 44.

Kraytsberg, A. & Ein-Eli, Y. Review of advanced materials for proton exchange membrane fuel cells. *Energy Fuels* **28**, 7303–7330 (2014).

[CAS](#) [Google Scholar](#)

45. 45.

Wang, Y., Ruiz Diaz, D. F., Chen, K. S., Wang, Z. & Adroher, X. C. Materials, technological status, and fundamentals of PEM fuel cells – A review. *Mater. Today* **32**, 178–203 (2020).

[CAS](#) [Google Scholar](#)

46. 46.

Zamel, N. & Li, X. Effect of contaminants on polymer electrolyte membrane fuel cells. *Progr. Energy Combust. Sci.* **37**, 292–329 (2011).

[CAS](#) [Google Scholar](#)

47. 47.

Kinumoto, T. et al. Durability of perfluorinated ionomer membrane against hydrogen peroxide. *J. Power Sources* **158**, 1222–1228 (2006).

[ADS](#) [CAS](#) [Google Scholar](#)

48. 48.

Pearman, B. P. et al. The chemical behavior and degradation mitigation effect of cerium oxide nanoparticles in perfluorosulfonic acid polymer electrolyte membranes. *Polym. Degrad. Stabil.* **98**, 1766–1772 (2013).

[CAS](#) [Google Scholar](#)

49. 49.

Durante, V. A. & Delaney, W. E. Highly stable fuel cell membranes and methods of making them. US patent 7,989,115 B2 (2011).

50. 50.

Zaidi, S. M. J., Mikhailenko, S. D., Robertson, G. P., Guiver, M. D. & Kaliaguine, S. Proton conducting composite membranes from polyether ether ketone and heteropolyacids for fuel cell applications. *J. Membr. Sci.* **173**, 17–34 (2000).

[CAS](#) [Google Scholar](#)

51. 51.

Miyatake, K., Chikashige, Y., Higuchi, E. & Watanabe, M. Tuned Polymer electrolyte membranes based on aromatic polyethers for fuel cell applications. *J. Am. Chem. Soc.* **129**, 3879–3887 (2007).

[CAS](#) [Google Scholar](#)

52. 52.

Yin, Y. et al. Synthesis and properties of highly sulfonated proton conducting polyimides from bis(3-sulfopropoxy)benzidine diamines. *J. Mater. Chem.* **14**, 1062–1070 (2004).

[CAS](#) [Google Scholar](#)

53. 53.

Wu, S. et al. The direct synthesis of wholly aromatic poly(p-phenylene)s bearing sulfonylbenzoyl side groups as proton exchange membranes. *Polymer* **47**, 6993–7000 (2006).

[CAS](#) [Google Scholar](#)

54. 54.

Rikukawa, M. & Sanui, K. Proton-conducting polymer electrolyte membranes based on hydrocarbon polymers. *Prog. Polym. Sci.* **25**, 1463–1502 (2000).

[CAS](#) [Google Scholar](#)

55. 55.

Smitha, B., Sridhar, S. & Khan, A. A. Solid polymer electrolyte membranes for fuel cell applications—a review. *J. Membr. Sci.* **259**, 10–26 (2005).

[CAS](#) [Google Scholar](#)

56. 56.

Miyake, J. et al. Design of flexible polyphenylene proton-conducting membrane for next-generation fuel cells. *Sci. Adv.* **3**, eaao0476 (2017).

[PubMed](#) [PubMed Central](#) [Google Scholar](#)

57. 57.

Kang, N. R., Pham, T. H. & Jannasch, P. Polyaromatic perfluorophenylsulfonic acids with high radical resistance and proton conductivity. *ACS Macro Lett.* **8**, 1247–1251 (2019).

[CAS](#) [Google Scholar](#)

58. 58.

Adamski, M. et al. Molecular branching as a simple approach to improving polymer electrolyte membranes. *J. Membr. Sci.* **595**, 117539 (2020).

[CAS](#) [Google Scholar](#)

59. 59.

Lee, K.-S., Spendelow, J. S., Choe, Y.-K., Fujimoto, C. & Kim, Y. S. An operationally flexible fuel cell based on quaternary ammonium-biphosphate ion pairs. *Nat. Energy* **1**, 16120 (2016).

[ADS](#) [CAS](#) [Google Scholar](#)

60. 60.

Lee, S. Y. et al. Morphological transformation during cross-linking of a highly sulfonated poly(phenylene sulfide nitrile) random copolymer. *Energy Environ. Sci.* **5**, 9795–9802 (2012).

[CAS](#) [Google Scholar](#)

61. 61.

Liu, X. et al. Oriented proton-conductive nano-sponge-facilitated polymer electrolyte membranes. *Energy Environ. Sci.* **13**, 297–309 (2020).

[CAS](#) [Google Scholar](#)

62. 62.

Zhang, X. et al. A paradigm shift for a new class of proton exchange membranes with ferrocyanide proton-conducting groups providing enhanced oxidative stability. *J. Membr. Sci.* **616**, 118536 (2020).

[CAS](#) [Google Scholar](#)

63. 63.

Steele, B. C. H. & Heinzel, A. Materials for fuel-cell technologies. *Nature* **414**, 345–352 (2001).

[ADS](#) [CAS](#) [PubMed](#) [PubMed Central](#) [Google Scholar](#)

64. 64.

Taherian, R. A review of composite and metallic bipolar plates in proton exchange membrane fuel cell: materials, fabrication, and material selection. *J. Power Sources* **265**, 370–390 (2014); retraction **265**, 370–390 (2014).

[ADS](#) [CAS](#) [Google Scholar](#)

65. 65.

Office of Energy Efficiency & Renewable Energy. DOE Technical targets for polymer electrolyte membrane fuel cell components
<https://www.energy.gov/eere/fuelcells/doe-technical-targets-polymer-electrolyte-membrane-fuel-cell-components#bipolarplate> (accessed 3 July 2021).

66. 66.

Wang, C. & Cullen, D. A. Novel structured metal bipolar plates for low cost manufacturing
https://www.hydrogen.energy.gov/pdfs/review20/fc105_wang_2020_p.pdf (TreadStone Technologies Inc., 2020).

67. 67.

James, B. D., Huya-Kouadio, J. M., Houchins, C. & DeSantis, D. A. Mass production cost estimation of direct H₂ PEM fuel cell systems for transportation applications: 2018 update
<https://www.energy.gov/sites/default/files/2020/02/f71/fcto-sa-2018-transportation-fuel-cell-cost-analysis-2.pdf> (Strateg. Anal. Inc., 2018). **This study evaluates the manufacturing cost of fuel cells from individual components to transportation systems. The paper supports the discussion on bipolar plates presented in this Perspective.**

68. 68.

Adrianowycz, O. et al. *Next Generation Bipolar Plates for Automotive PEM Fuel Cells*. Report DE-FC36-07GO17012 (Office of Scientific & Technical Information, 2010);
<https://digital.library.unt.edu/ark:/67531/metadc927369/>

69. 69.

Saito, N., Kikuchi, H. & Nakao, Y. *New Fuel Cell Stack for FCX Clarity*. Honda R&D Technical Review 21, 1 (Honda, 2009).

70. 70.

Inoue, M., Saito, N. & Uchibori, K. *Next-Generation Fuel Cell Stack for Honda FCX*. Honda R&D Technical Review 17, 2 (Honda, 2005).

71. 71.

Kikuchi, H., Kaji, H., Nishiyama, T., Okonogi, D. & Harata, H. *Development of New FC Stack for Clarity Fuel Cell*. Honda R&D Technical Review 28, 2 (Honda, 2016).

72. 72.

Kimura, Y., Oyama, S., Giga, A. & Okonogi, D. *Development of New FC Separator for Clarity Fuel Cell*. Honda R&D Technical Review 29, 2 (Honda, 2017).

73. 73.

Wilberforce, T. et al. A comprehensive study of the effect of bipolar plate (BP) geometry design on the performance of proton exchange membrane (PEM) fuel cells. *Renew. Sustain. Energy Rev.* **111**, 236–260 (2019).

[CAS](#) [Google Scholar](#)

74. 74.

Dubau, L. et al. A review of PEM fuel cell durability: materials degradation, local heterogeneities of aging and possible mitigation strategies. *WIREs Energy Environ.* **3**, 540–560 (2014).

[CAS](#) [Google Scholar](#)

75. 75.

Jiao, K. & Li, X. Water transport in polymer electrolyte membrane fuel cells. *Progr. Energy Combust. Sci.* **37**, 221–291 (2011).

[CAS](#) [Google Scholar](#)

76. 76.

Zhang, G. & Kandlikar, S. G. A critical review of cooling techniques in proton exchange membrane fuel cell stacks. *Int. J. Hydrogen Energy* **37**, 2412–2429 (2012).

[CAS](#) [Google Scholar](#)

77. 77.

Khandelwal, M. & Mench, M. M. Direct measurement of through-plane thermal conductivity and contact resistance in fuel cell material. *J. Power Sources* **161**, 1106–1115 (2006).

[ADS](#) [CAS](#) [Google Scholar](#)

78. 78.

Antunes, R. A., Oliveira, M. C. L., Ett, G. & Ett, V. Corrosion of metal bipolar plates for PEM fuel cells: a review. *Int. J. Hydrogen Energy* **35**, 3632–3647 (2010).

[CAS](#) [Google Scholar](#)

79. 79.

Saiki, K. *Strength Design Method of Metallic Separator for Fuel Cell*. Honda R&D Technical Review 29, 1 (Honda, 2017).

80. 80.

Norley, J. Graphite-based bipolar plates for PEM motive fuel cell applications. In *DOE Bipolar Plates Workshop* (GrafTech Int. Holdings Ltd, 2017);
https://www.energy.gov/sites/prod/files/2017/05/f34/fcto_bipolar_plates_wkshp_norley.pdf

81. 81.

Wu, J. et al. A review of PEM fuel cell durability: degradation mechanisms and mitigation strategies. *J. Power Sources* **184**, 104–119 (2008).

[ADS](#) [CAS](#) [Google Scholar](#)

82. 82.

Wang, Y. Porous-media flow fields for polymer electrolyte fuel cells. *J. Electrochem. Soc.* **156**, B1124 (2009).

[CAS](#) [Google Scholar](#)

83. 83.

Srouji, A. K., Zheng, L. J., Dross, R., Turhan, A. & Mench, M. M. Ultra-high current density water management in polymer electrolyte fuel cell with porous metallic flow field. *J. Power Sources* **239**, 433–442 (2013).

[CAS](#) [Google Scholar](#)

84. 84.

Yuan, W., Tang, Y., Yang, X. & Wan, Z. Porous metal materials for polymer electrolyte membrane fuel cells – a review. *Appl. Energy* **94**,

309–329 (2012).

[ADS](#) [CAS](#) [Google Scholar](#)

85. 85.

Park, J. E. et al. Gas diffusion layer/flow-field unified membrane-electrode assembly in fuel cell using graphene foam. *Electrochim. Acta* **323**, 134808 (2019). **This study proposes an integrated design of the gas diffusion layer and flow field with boosted fuel cell performance, demonstrating that such a design is promising for increasing the power density.**

[CAS](#) [Google Scholar](#)

[Download references](#)

Acknowledgements

This research was supported by the China-UK International Cooperation and Exchange Project (Newton Advanced Fellowship), supported by the National Natural Science Foundation of China (grant number 51861130359), the UK Royal Society (grant number NAF\R1\180146), UK EPSRC (grant number EP/S000933/1), and the Natural Science Foundation of Tianjin (China) for Distinguished Young Scholars (grant number 18JCJQJC46700).

Author information

Author notes

1. These authors contributed equally: Kui Jiao, Jin Xuan, Qing Du

Affiliations

1. State Key Laboratory of Engines, Tianjin University, Tianjin, China

Kui Jiao, Qing Du, Zhiming Bao, Biao Xie, Bowen Wang, Linhao Fan, Yan Yin & Michael D. Guiver

2. Department of Chemical Engineering, Loughborough University, Loughborough, UK

Jin Xuan

3. Department of Mechanical Engineering, Imperial College London, London, UK

Yan Zhao & Huizhi Wang

4. Shanghai Hydrogen Propulsion Technology Co. Ltd, Shanghai, China

Zhongjun Hou & Sen Huo

5. Department of Earth Science and Engineering, Imperial College London, London, UK

Nigel P. Brandon

6. Collaborative Innovation Center of Chemical Science and Engineering (Tianjin), Tianjin, China

Michael D. Guiver

Authors

1. Kui Jiao

[View author publications](#)

You can also search for this author in [PubMed](#) [Google Scholar](#)

2. Jin Xuan

[View author publications](#)

You can also search for this author in [PubMed](#) [Google Scholar](#)

3. Qing Du

[View author publications](#)

You can also search for this author in [PubMed](#) [Google Scholar](#)

4. Zhiming Bao

[View author publications](#)

You can also search for this author in [PubMed](#) [Google Scholar](#)

5. Biao Xie

[View author publications](#)

You can also search for this author in [PubMed](#) [Google Scholar](#)

6. Bowen Wang

[View author publications](#)

You can also search for this author in [PubMed](#) [Google Scholar](#)

7. Yan Zhao

[View author publications](#)

You can also search for this author in [PubMed](#) [Google Scholar](#)

8. Linhao Fan

[View author publications](#)

You can also search for this author in [PubMed](#) [Google Scholar](#)

9. Huizhi Wang

[View author publications](#)

You can also search for this author in [PubMed](#) [Google Scholar](#)

10. Zhongjun Hou

[View author publications](#)

You can also search for this author in [PubMed](#) [Google Scholar](#)

11. Sen Huo

[View author publications](#)

You can also search for this author in [PubMed](#) [Google Scholar](#)

12. Nigel P. Brandon

[View author publications](#)

You can also search for this author in [PubMed](#) [Google Scholar](#)

13. Yan Yin

[View author publications](#)

You can also search for this author in [PubMed](#) [Google Scholar](#)

14. Michael D. Guiver

[View author publications](#)

You can also search for this author in [PubMed](#) [Google Scholar](#)

Contributions

K.J., J.X., Q.D., Z.H. and M.D.G. conceived the idea for the study. All authors contributed to the writing and commented on the manuscript. K.J., Z.B., B.X., B.W., Y.Z., L.F. and M.D.G. contributed to the preparation of the figures.

Corresponding authors

Correspondence to [Kui Jiao](#) or [Zhongjun Hou](#) or [Michael D. Guiver](#).

Ethics declarations

Competing interests

The authors declare no competing interests.

Additional information

Peer review information *Nature* thanks Shangfeng Du, Julien Durst and the other, anonymous, reviewer(s) for their contribution to the peer review of this work.

Publisher's note Springer Nature remains neutral with regard to jurisdictional claims in published maps and institutional affiliations.

Supplementary information

Supplementary Information

This file contains Supplementary Information, including Supplementary Tables 1-2 and additional references.

Rights and permissions

Reprints and Permissions

About this article



Check for
updates

Cite this article

Jiao, K., Xuan, J., Du, Q. *et al.* Designing the next generation of proton-exchange membrane fuel cells. *Nature* **595**, 361–369 (2021).
<https://doi.org/10.1038/s41586-021-03482-7>

Download citation

- Received: 10 August 2020

- Accepted: 22 March 2021
- Published: 14 July 2021
- Issue Date: 15 July 2021
- DOI: <https://doi.org/10.1038/s41586-021-03482-7>

Comments

By submitting a comment you agree to abide by our [Terms](#) and [Community Guidelines](#). If you find something abusive or that does not comply with our terms or guidelines please flag it as inappropriate.

[Access through your institution](#)

[Change institution](#)

[Buy or subscribe](#)

Advertisement

This article was downloaded by **calibre** from <https://www.nature.com/articles/s41586-021-03482-7>

| [Section menu](#) | [Main menu](#) |

- Article
- [Published: 14 July 2021](#)

The ^{13}CO -rich atmosphere of a young accreting super-Jupiter

- [Yapeng Zhang](#) ORCID: [orcid.org/0000-0003-0097-4414¹](https://orcid.org/0000-0003-0097-4414),
- [Ignas A. G. Snellen](#) ORCID: [orcid.org/0000-0003-1624-3667¹](https://orcid.org/0000-0003-1624-3667),
- [Alexander J. Bohn](#) ORCID: [orcid.org/0000-0003-1401-9952¹](https://orcid.org/0000-0003-1401-9952),
- [Paul Mollière²](#),
- [Christian Ginski³](#),
- [H. Jens Hoeijmakers^{4,5}](#),
- [Matthew A. Kenworthy](#) ORCID: [orcid.org/0000-0002-7064-8270¹](https://orcid.org/0000-0002-7064-8270),
- [Eric E. Mamajek^{6,7}](#),
- [Tiffany Meshkat⁸](#),
- [Maddalena Reggiani](#) ORCID: [orcid.org/0000-0003-2911-0898⁹](https://orcid.org/0000-0003-2911-0898) &
- [Frans Snik¹](#)

Nature volume **595**, pages 370–372 (2021) [Cite this article](#)

- 819 Accesses
- 168 Altmetric
- [Metrics details](#)

Subjects

- [Exoplanets](#)

Abstract

Isotope abundance ratios have an important role in astronomy and planetary sciences, providing insights into the origin and evolution of the Solar System, interstellar chemistry and stellar nucleosynthesis^{1,2}. In contrast to deuterium/hydrogen ratios, carbon isotope ratios are found to be roughly constant (around 89) in the Solar System^{1,3}, but do vary on galactic scales with a $^{12}\text{C}/^{13}\text{C}$ isotopologue ratio of around 68 in the current local interstellar medium^{4,5,6}. In molecular clouds and protoplanetary disks, $^{12}\text{CO}/^{13}\text{CO}$ ratios can be altered by ice and gas partitioning⁷, low-temperature isotopic ion-exchange reactions⁸ and isotope-selective photodissociation⁹. Here we report observations of ^{13}CO in the atmosphere of the young, accreting super-Jupiter TYC 8998-760-1 b, at a statistical significance of more than six sigma. Marginalizing over the planet's atmospheric temperature structure, chemical composition and spectral calibration uncertainties suggests a $^{12}\text{CO}/^{13}\text{CO}$ ratio of $\{{31}\}_{-10}^{+17}$ (90% confidence), a substantial enrichment in ^{13}C with respect to the terrestrial standard and the local interstellar value. As the current location of TYC 8998-760-1 b at greater than or equal to 160 astronomical units is far beyond the CO snowline, we postulate that it accreted a substantial fraction of its carbon from ices enriched in ^{13}C through fractionation.

Access options

Subscribe to Journal

Get full journal access for 1 year

\$199.00

only \$3.90 per issue

[Subscribe](#)

All prices are NET prices.

VAT will be added later in the checkout.

Tax calculation will be finalised during checkout.

Rent or Buy article

Get time limited or full article access on ReadCube.

from \$8.99

[Rent or Buy](#)

All prices are NET prices.

Additional access options:

- [Log in](#)
- [Access through your institution](#)
- [Learn about institutional subscriptions](#)

Fig. 1: Observed SINFONI spectrum of exoplanet TYC 8998 b and cross-correlation signal of ^{13}CO .

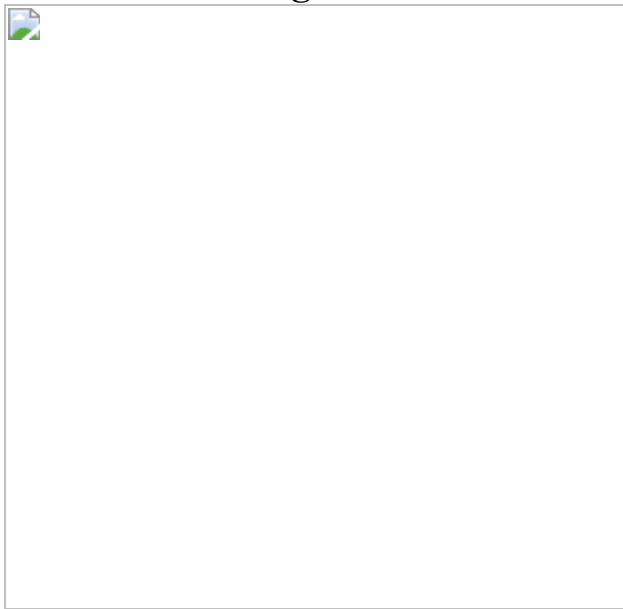
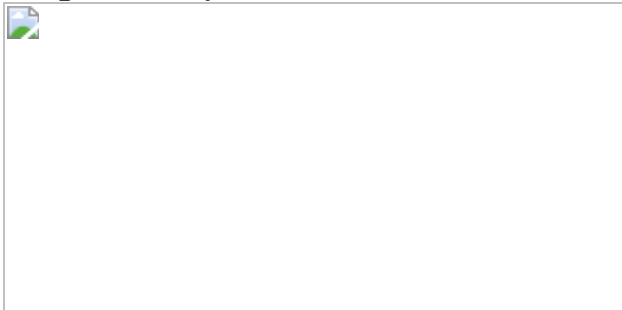


Fig. 2: Spectral retrieval results.



Fig. 3: Cartoon of the birth environments of planets in a protoplanetary disk.



Data availability

The data are publicly available from the ESO Science Archive with the programme ID 2103.C-5012(C).

Code availability

The data analysis was performed with custom Python scripts following the standard procedure. The code and reduced spectrum are available from <https://gitlab.strw.leidenuniv.nl/yzhang/yses1b-sinfoni>. The atmospheric retrieval models use petitRADTRANS, which is available from <https://petitradtrans.readthedocs.io/>, and the nested sampling tool PyMultiNest, which is available from <https://johannesbuchner.github.io/PyMultiNest/>.

References

1. 1.

Clayton, D. D. & Nittler, L. R. Astrophysics with presolar stardust. *Annu. Rev. Astron. Astrophys.* **42**, 39–78 (2004).

[ADS](#) [CAS](#) [Article](#) [Google Scholar](#)

2. 2.

Wilson, T. L. & Matteucci, F. Abundances in the interstellar medium. *Astron. Astrophys. Rev.* **4**, 1–33 (1992).

[ADS](#) [CAS](#) [Article](#) [Google Scholar](#)

3. 3.

Woods, P. M. & Willacy, K. Carbon isotope fractionation in protoplanetary disks. *Astrophys. J.* **693**, 1360–1378 (2009).

[ADS](#) [CAS](#) [Article](#) [Google Scholar](#)

4. 4.

Langer, W. D. & Penzias, A. A. $^{12}\text{C}/^{13}\text{C}$ isotope ratio in the local interstellar medium from observations of $^{13}\text{C}^{18}\text{O}$ in molecular clouds. *Astrophys. J.* **408**, 539–547 (1993).

[ADS](#) [CAS](#) [Article](#) [Google Scholar](#)

5. 5.

Milam, S. N., Savage, C., Brewster, M. A., Ziurys, L. M. & Wyckoff, S. The $^{12}\text{C}/^{13}\text{C}$ isotope gradient derived from millimeter transitions of CN: the case for galactic chemical evolution. *Astrophys. J.* **634**, 1126–1132 (2005).

[ADS](#) [CAS](#) [Article](#) [Google Scholar](#)

6. 6.

Prantzos, N., Aubert, O. & Audouze, J. Evolution of the carbon and oxygen isotopes in the Galaxy. *Astron. Astrophys.* **309**, 760–774 (1996).

[ADS](#) [CAS](#) [Google Scholar](#)

7. 7.

Smith, R. L., Pontoppidan, K. M., Young, E. D. & Morris, M. R. Heterogeneity in $^{12}\text{CO}/^{13}\text{CO}$ abundance ratios toward solar-type young stellar objects. *Astrophys. J.* **813**, 120 (2015).

[ADS](#) [Article](#) [Google Scholar](#)

8. 8.

Langer, W. D., Graedel, T. E., Frerking, M. A. & Armentrout, P. B. Carbon and oxygen isotope fractionation in dense interstellar clouds. *Astrophys. J.* **277**, 581–604 (1984).

[ADS](#) [CAS](#) [Article](#) [Google Scholar](#)

9. 9.

Bally, J. & Langer, W. D. Isotope-selective photodestruction of carbon monoxide. *Astrophys. J.* **255**, 143–148 (1982).

[ADS](#) [CAS](#) [Article](#) [Google Scholar](#)

10. 10.

Bohn, A. J. et al. The Young Suns Exoplanet Survey: detection of a wide-orbit planetary-mass companion to a solar-type Sco–Cen member. *Mon. Not. R. Astron. Soc.* **492**, 431–443 (2020).

[ADS](#) [Article](#) [Google Scholar](#)

11. 11.

Pecaut, M. J. & Mamajek, E. E. The star formation history and accretion-disc fraction among the K-type members of the Scorpius–Centaurus OB association. *Mon. Not. R. Astron. Soc.* **461**, 794–815 (2016).

[ADS](#) [CAS](#) [Article](#) [Google Scholar](#)

12. 12.

Bohn, A. J. et al. Two directly imaged, wide-orbit giant planets around the young, solar analog TYC 8998–760–1. *Astrophys. J.* **898**, L16 (2020).

[ADS](#) [Article](#) [Google Scholar](#)

13. 13.

Eisenhauer, F. et al. SINFONI—integral field spectroscopy at 50 milli-arcsecond resolution with the ESO VLT. In *Proc. SPIE* Vol. 4841 (eds Iye, M. & Moorwood, A. F.M.) 1548–1561 (SPIE, 2003).

14. 14.

Bonnet, H. et al. First light of SINFONI at the VLT. *Messenger* **117**, 17–24 (2004).

[ADS](#) [Google Scholar](#)

15. 15.

van Holstein, R. G. et al. A survey of the linear polarization of directly imaged exoplanets and brown dwarf companions with SPHERE-IRDIS. First polarimetric detections revealing disks around DH Tau B and GSC 6214–210 B. *Astron. Astrophys.* **647**, A21 (2021).

[Article](#) [Google Scholar](#)

16. 16.

Mollière, P. et al. petitRADTRANS. A Python radiative transfer package for exoplanet characterization and retrieval. *Astron. Astrophys.* **627**, A67 (2019).

[Article](#) [Google Scholar](#)

17. 17.

Buchner, J. et al. Astrophysics X-ray spectral modelling of the AGN obscuring region in the CDFS: Bayesian model selection and catalogue. *Astron. Astrophys.* **564**, A125 (2014).

[Article](#) [Google Scholar](#)

18. 18.

Mollière, P. & Snellen, I. A. G. Detecting isotopologues in exoplanet atmospheres using ground-based high-dispersion spectroscopy. *Astron. Astrophys.* **622**, A139 (2019).

[ADS](#) [Article](#) [Google Scholar](#)

19. 19.

Öberg, K. I., Murray-Clay, R. & Bergin, E. A. The effects of snowlines on C/O in planetary atmospheres. *Astrophys. J.* **743**, L16 (2011).

[ADS](#) [Article](#) [Google Scholar](#)

20. 20.

Mollière, P. et al. Retrieving scattering clouds and disequilibrium chemistry in the atmosphere of HR 8799e. *Astron. Astrophys.* **640**, A131 (2020).

[Article](#) [Google Scholar](#)

21. 21.

Benneke, B. & Seager, S. How to distinguish between cloudy mini-Neptunes and water/volatile- dominated super-Earths. *Astrophys. J.* **778**, 153 (2013).

[ADS](#) [Article](#) [Google Scholar](#)

22. 22.

Jørgensen, J. K. et al. The ALMA Protostellar Interferometric Line Survey (PILS). *Astron. Astrophys.* **595**, A117 (2016).

[Article](#) [Google Scholar](#)

23. 23.

Jørgensen, J. K. et al. The ALMA-PILS survey: isotopic composition of oxygen-containing complex organic molecules toward IRAS 16293–2422B. *Astron. Astrophys.* **620**, A170 (2018).

[Article](#) [Google Scholar](#)

24. 24.

Acharyya, K., Fuchs, G. W., Fraser, H. J., van Dishoeck, E. F. & Linnartz, H. Desorption of CO and O₂ interstellar ice analogs. *Astron. Astrophys.* **466**, 1005–1012 (2007).

[ADS](#) [CAS](#) [Article](#) [Google Scholar](#)

25. 25.

Miotello, A., Bruderer, S. & van Dishoeck, E. F. Protoplanetary disk masses from CO isotopologue line emission. *Astron. Astrophys.* **572**, A96 (2014).

[Article](#) [Google Scholar](#)

26. 26.

Cridland, A. J., Bosman, A. D. & van Dishoeck, E. F. Impact of vertical gas accretion on the carbon-to-oxygen ratio of gas giant atmospheres. *Astron. Astrophys.* **635**, A68 (2020).

[CAS](#) [Article](#) [Google Scholar](#)

27. 27.

Qi, C. et al. Imaging of the CO snow line in a solar nebula analog. *Science* **341**, 630–632 (2013).

[ADS](#) [CAS](#) [Article](#) [Google Scholar](#)

28. 28.

Morbidelli, A., Levison, H. F., Tsiganis, K. & Gomes, R. Chaotic capture of Jupiter’s Trojan asteroids in the early Solar System. *Nature* **435**, 462–465 (2005).

[ADS](#) [CAS](#) [Article](#) [Google Scholar](#)

29. 29.

Feuchtgruber, H. et al. The D/H ratio in the atmospheres of Uranus and Neptune from Herschel-PACS observations. *Astron. Astrophys.* **551**, A126 (2013).

[Article](#) [Google Scholar](#)

30. 30.

Morley, C. V. et al. Measuring the D/H ratios of exoplanets and brown dwarfs. *Astrophys. J.* **882**, L29 (2019).

[ADS](#) [CAS](#) [Article](#) [Google Scholar](#)

31. 31.

Horne, K. An optimal extraction algorithm for CCD spectroscopy. *Publ. Astron. Soc. Pacif.* **98**, 609–617 (1986).

[ADS](#) [CAS](#) [Article](#) [Google Scholar](#)

32. 32.

Husser, T.-O. et al. A new extensive library of PHOENIX stellar atmospheres and synthetic spectra. *Astron. Astrophys.* **553**, A6 (2013).

[Article](#) [Google Scholar](#)

33. 33.

Shokry, A. et al. Stellar parameters of Be stars observed with X-shooter. *Astron. Astrophys.* **609**, A108 (2018).

[Article](#) [Google Scholar](#)

34. 34.

McDonald, I., Zijlstra, A. A. & Boyer, M. L. Fundamental parameters and infrared excesses of Hipparcos stars. *Mon. Not. R. Astron. Soc.* **427**, 343–357 (2012).

[ADS](#) [Article](#) [Google Scholar](#)

35. 35.

Smette, A. et al. Molecfit: a general tool for telluric absorption correction. *Astron. Astrophys.* **576**, A77 (2015).

[Article](#) [Google Scholar](#)

36. 36.

Feroz, F., Hobson, M. P. & Bridges, M. MultiNest: an efficient and robust Bayesian inference tool for cosmology and particle physics. *Mon. Not. R. Astron. Soc.* **398**, 1601–1614 (2009).

[ADS](#) [Article](#) [Google Scholar](#)

37. 37.

Nowak, M. et al. Peering into the formation history of β Pictoris b with VLTI/GRAVITY long-baseline interferometry. *Astron. Astrophys.* **633**, A110 (2020).

[CAS](#) [Article](#) [Google Scholar](#)

38. 38.

Wakeford, H. R. et al. High-temperature condensate clouds in super-hot Jupiter atmospheres. *Mon. Not. R. Astron. Soc.* **464**, 4247–4254 (2017).

[ADS](#) [CAS](#) [Article](#) [Google Scholar](#)

39. 39.

Muzerolle, J., Hartmann, L. & Calvet, N. A Bry probe of disk accretion in T Tauri stars and embedded young stellar objects. *Astron. J.* **116**, 2965–2974 (1998).

[ADS](#) [Article](#) [Google Scholar](#)

40. 40.

Reid, I. N. et al. Meeting the cool neighbors. X. Ultracool dwarfs from the 2MASS all-sky data release. *Astron. J.* **136**, 1290–1311 (2008).

[ADS](#) [Article](#) [Google Scholar](#)

41. 41.

Bryan, M. L. et al. Constraints on the spin evolution of young planetary-mass companions. *New Astron.* **2**, 138–144 (2018).

[Google Scholar](#)

[Download references](#)

Acknowledgements

We thank E. van Dishoeck, A. Cridland and A. Miotello for discussions on carbon fractionation in protoplanetary disks. We thank K. Chubb for a ^{13}CO line list comparison. Based on observations collected at the European Southern Observatory (ESO) under ESO programme 2103.C-5012(C). Y.Z. and I.A.G.S. acknowledge funding from the European Research Council (ERC) under the European Union’s Horizon 2020 research and innovation programme under grant agreement number 694513. The research of A.J.B. and F.S. leading to these results has received funding from the European Research Council under ERC Starting Grant agreement 678194 (FALCONER). P.M. acknowledges support from the European Research Council under the European Union’s Horizon 2020 research and innovation programme under grant agreement number 832428. Part of this research was carried out at the Jet Propulsion Laboratory, California Institute of Technology, under a contract with the National Aeronautics and Space Administration.

Author information

Affiliations

1. Leiden Observatory, Leiden University, Leiden, The Netherlands
Yapeng Zhang, Ignas A. G. Snellen, Alexander J. Bohn, Matthew A. Kenworthy & Frans Snik
2. Max-Planck-Institut für Astronomie, Heidelberg, Germany
Paul Mollière
3. Anton Pannekoek Institute for Astronomy, University of Amsterdam, Amsterdam, The Netherlands
Christian Ginski

4. Observatoire de Genève, Université de Genève, Versoix, Switzerland

H. Jens Hoeijmakers

5. Lund Observatory, Department of Astronomy and Theoretical Physics,
Lunds Universitet, Lund, Sweden

H. Jens Hoeijmakers

6. Jet Propulsion Laboratory, California Institute of Technology,
Pasadena, CA, USA

Eric E. Mamajek

7. Department of Physics and Astronomy, University of Rochester,
Rochester, NY, USA

Eric E. Mamajek

8. IPAC, California Institute of Technology, Pasadena, CA, USA

Tiffany Meshkat

9. Institute of Astronomy, KU Leuven, Leuven, Belgium

Maddalena Reggiani

Authors

1. Yapeng Zhang

[View author publications](#)

You can also search for this author in [PubMed](#) [Google Scholar](#)

2. Ignas A. G. Snellen

[View author publications](#)

You can also search for this author in [PubMed](#) [Google Scholar](#)

3. Alexander J. Bohn

[View author publications](#)

You can also search for this author in [PubMed](#) [Google Scholar](#)

4. Paul Mollière

[View author publications](#)

You can also search for this author in [PubMed](#) [Google Scholar](#)

5. Christian Ginski

[View author publications](#)

You can also search for this author in [PubMed](#) [Google Scholar](#)

6. H. Jens Hoeijmakers

[View author publications](#)

You can also search for this author in [PubMed](#) [Google Scholar](#)

7. Matthew A. Kenworthy

[View author publications](#)

You can also search for this author in [PubMed](#) [Google Scholar](#)

8. Eric E. Mamajek

[View author publications](#)

You can also search for this author in [PubMed](#) [Google Scholar](#)

9. Tiffany Meshkat

[View author publications](#)

You can also search for this author in [PubMed](#) [Google Scholar](#)

10. Maddalena Reggiani

[View author publications](#)

You can also search for this author in [PubMed](#) [Google Scholar](#)

11. Frans Snik

[View author publications](#)

You can also search for this author in [PubMed](#) [Google Scholar](#)

Contributions

Y.Z. and I.A.G.S. performed the data analysis and wrote the manuscript. A.J.B. led the SINFONI proposal, planned the observations and commented on the manuscript, and is the principal investigator of the Young Suns Exoplanet Survey (YSES) that led to the discovery of the TYC 8998 system. P.M. developed the retrieval models and assisted the data analysis. C.G., M.A.K., E.E.M., T.M., M.R. and F.S. constitute the core team of YSES, contributed to the SINFONI proposal and commented on the manuscript. H.J.H. helped the preparations of the observations and commented on the manuscript.

Corresponding author

Correspondence to [Ignas A. G. Snellen](#).

Ethics declarations

Competing interests

The authors declare no competing interests.

Additional information

Peer review information *Nature* thanks Drake Deming and the other, anonymous, reviewer(s) for their contribution to the peer review of this work. Peer reviewer reports are available.

Publisher's note Springer Nature remains neutral with regard to jurisdictional claims in published maps and institutional affiliations.

Extended data figures and tables

Extended Data Fig. 1 Schematics of the observations of TYC 8998-760-1 b using SINFONI at the Very Large Telescope.

The background image is captured by the SPHERE instrument on the VLT (Credit: ESO/Bohn et al.). The small blue box marks the FOV of SINFONI observations targeting the planet b. Both the host star and planet c are outside the FOV. An example of the wavelength-collapsed image is shown in the enlarged blue box, showing negligible contribution from starlight.

Extended Data Fig. 2 Posteriors of retrieved parameters.

a, Posteriors of the retrieved parameters and temperature structure for the full (cyan) and reduced (red) models. The vertical dashed lines denote the 5%, 50% and 95% quantiles (90% uncertainties) of the distribution. **b**, $T-P$ profile. The shaded regions with decreasing colour saturation show 1σ , 2σ and 3σ temperature uncertainty envelopes, respectively. The black dashed line shows the flux average of the emission contribution function. The opaqueness of the temperature uncertainty envelopes has been scaled by this contribution function. **c**, Fitting statistics of the full and reduced retrieval model, where $\ln(Z)$ and $\ln(B_m)$ represent the logarithm of Bayesian evidence and Bayes factor, respectively.

Extended Data Fig. 3 Posteriors of the retrieved parameters for the data of individual nights.

Similar to Extended Data Fig. [2a](#).

Extended Data Fig. 4 Cross-correlation signal of ^{13}CO from individual nights and bandheads.

a, Observational residuals of the two nights separately. **b**, Cross-correlation signal from the individual nights. **c**, Filtered observational residuals of the

two ^{13}CO bandheads separately. **d**, Cross-correlation signal from the individual bandheads.

[Extended Data Fig. 5 Impact of telluric absorption lines and cross-correlation signal of \$^{13}\text{CO}\$ at the extended wavelength region.](#)

a, Comparison of the telluric transmission model with residuals. Some noise is attributed to imperfect telluric correction as noted by dotted grey lines. **b**, Cross-correlation function between the telluric model and the ^{13}CO model, showing no correlation between them.

[Extended Data Fig. 6 K-band spectrum of the brown dwarf 2M0355 taken by Keck/NIRSPEC and the cross-correlation signal of \$^{13}\text{CO}\$.](#)

The black line shows the observed spectrum and the orange line is the best-fit model obtained by retrieval analysis. Bottom: CCF between the ^{13}CO model and observational residuals. The peak at zero velocity clearly shows the detection of ^{13}CO .

Extended Data Table 1 Priors and inferred posteriors of the TYC 8998 b retrieval [Full size table](#)

Supplementary information

[Peer Review File](#)

Rights and permissions

[Reprints and Permissions](#)

About this article



Check for
updates

Cite this article

Zhang, Y., Snellen, I.A.G., Bohn, A.J. *et al.* The ^{13}CO -rich atmosphere of a young accreting super-Jupiter. *Nature* **595**, 370–372 (2021).
<https://doi.org/10.1038/s41586-021-03616-x>

Download citation

- Received: 30 October 2020
- Accepted: 05 May 2021
- Published: 14 July 2021
- Issue Date: 15 July 2021
- DOI: <https://doi.org/10.1038/s41586-021-03616-x>

Comments

By submitting a comment you agree to abide by our [Terms](#) and [Community Guidelines](#). If you find something abusive or that does not comply with our terms or guidelines please flag it as inappropriate.

[Access through your institution](#)

[Change institution](#)

[Buy or subscribe](#)

Advertisement

| [Section menu](#) | [Main menu](#) |

- Article
- [Published: 14 July 2021](#)

Real-time optimal quantum control of mechanical motion at room temperature

- [Lorenzo Magrini](#) [ORCID: orcid.org/0000-0002-7746-938X¹](#),
- [Philipp Rosenzweig](#) [ORCID: orcid.org/0000-0001-9740-5503²](#),
- [Constanze Bach¹](#),
- [Andreas Deutschmann-Olek](#) [ORCID: orcid.org/0000-0001-7602-9211²](#),
- [Sebastian G. Hofer](#) [ORCID: orcid.org/0000-0002-3560-2672¹](#),
- [Sungkun Hong^{3,4}](#),
- [Nikolai Kiesel¹](#),
- [Andreas Kugi](#) [ORCID: orcid.org/0000-0001-7995-1690^{2,5}](#) &
- [Markus Aspelmeyer](#) [ORCID: orcid.org/0000-0003-4499-7335^{1,6}](#)

[Nature](#) volume **595**, pages 373–377 (2021) [Cite this article](#)

- 2025 Accesses
- 144 Altmetric
- [Metrics details](#)

Subjects

- [Quantum mechanics](#)
- [Quantum optics](#)

Abstract

The ability to accurately control the dynamics of physical systems by measurement and feedback is a pillar of modern engineering¹. Today, the increasing demand for applied quantum technologies requires adaptation of this level of control to individual quantum systems^{2,3}. Achieving this in an optimal way is a challenging task that relies on both quantum-limited measurements and specifically tailored algorithms for state estimation and feedback⁴. Successful implementations thus far include experiments on the level of optical and atomic systems^{5,6,7}. Here we demonstrate real-time optimal control of the quantum trajectory⁸ of an optically trapped nanoparticle. We combine confocal position sensing close to the Heisenberg limit with optimal state estimation via Kalman filtering to track the particle motion in phase space in real time with a position uncertainty of 1.3 times the zero-point fluctuation. Optimal feedback allows us to stabilize the quantum harmonic oscillator to a mean occupation of 0.56 ± 0.02 quanta, realizing quantum ground-state cooling from room temperature. Our work establishes quantum Kalman filtering as a method to achieve quantum control of mechanical motion, with potential implications for sensing on all scales. In combination with levitation, this paves the way to full-scale control over the wavepacket dynamics of solid-state macroscopic quantum objects in linear and nonlinear systems.

Access options

Subscribe to Journal

Get full journal access for 1 year

\$199.00

only \$3.90 per issue

[Subscribe](#)

All prices are NET prices.
VAT will be added later in the checkout.
Tax calculation will be finalised during checkout.

Rent or Buy article

Get time limited or full article access on ReadCube.

from \$8.99

[Rent or Buy](#)

All prices are NET prices.

Additional access options:

- [Log in](#)
- [Access through your institution](#)
- [Learn about institutional subscriptions](#)

Fig. 1: Experimental setup.

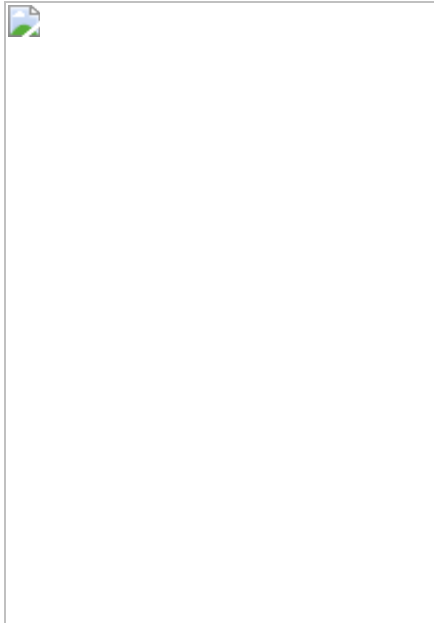


Fig. 2: Kalman filter and verification.

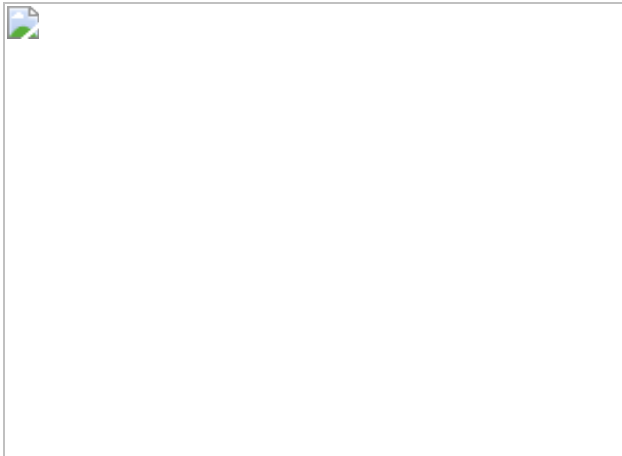
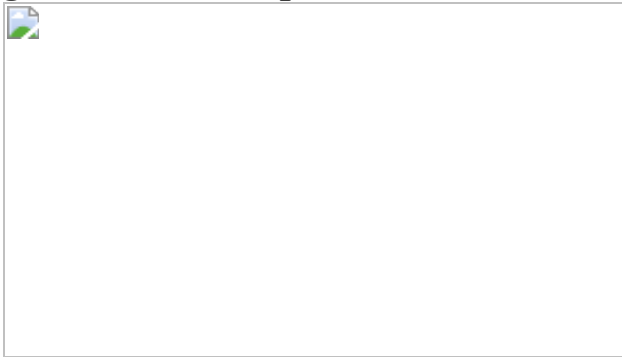


Fig. 3: Quantum optimal control.



Data availability

The data that support the plots within this paper and other findings of this study are available from the corresponding author upon reasonable request.

References

1. 1.

Åström, K. J. & Wittenmark, B. *Computer-controlled Systems: Theory and Design* (Courier Corporation, 2013).

2. 2.

Geremia, J., Stockton, J. K., Doherty, A. C. & Mabuchi, H. Quantum Kalman filtering and the Heisenberg limit in atomic magnetometry. *Phys. Rev. Lett.* **91**, 250801 (2003).

[ADS](#) [CAS](#) [PubMed](#) [PubMed Central](#) [Google Scholar](#)

3. 3.

Glaser, S. J. et al. Training Schrödinger's cat: quantum optimal control. *Eur. Phys. J. D* **69**, 279 (2015).

[ADS](#) [Google Scholar](#)

4. 4.

Wieseman, H. M. & Milburn, G. J. *Quantum Measurement and Control* (Cambridge Univ. Press, 2010).

5. 5.

Sayrin, C. et al. Real-time quantum feedback prepares and stabilizes photon number states. *Nature* **477**, 73–77 (2011).

[ADS](#) [CAS](#) [PubMed](#) [PubMed Central](#) [Google Scholar](#)

6. 6.

Yonezawa, H. et al. Quantum-enhanced optical-phase tracking. *Science* **337**, 1514–1517 (2012).

[ADS](#) [MathSciNet](#) [CAS](#) [PubMed](#) [PubMed Central](#) [MATH](#) [Google Scholar](#)

7. 7.

Jiménez-Martínez, R. et al. Signal tracking beyond the time resolution of an atomic sensor by Kalman filtering. *Phys. Rev. Lett.* **120**, 040503 (2018).

[ADS](#) [PubMed](#) [PubMed Central](#) [Google Scholar](#)

8. 8.

Carmichael, H. *An Open Systems Approach to Quantum Optics* (Springer, 1993).

9. 9.

Kalman, R. E. A new approach to linear filtering and prediction problems. *J. Basic Eng.* **82**, 35–45 (1960).

[MathSciNet](#) [Google Scholar](#)

10. 10.

Kalman, R. E. et al. Contributions to the theory of optimal control. *Bol. Soc. Mat. Mex.* **5**, 102–119 (1960).

[MathSciNet](#) [Google Scholar](#)

11. 11.

Sittig, D. F. & Cheung, K.-H. A parallel implementation of a multi-state Kalman filtering algorithm to detect ECG arrhythmias. *Int. J. Clin. Monit. Com.* **9**, 13–22 (1992).

[CAS](#) [Google Scholar](#)

12. 12.

Bar-Shalom, Y., Li, X. R. & Kirubarajan, T. *Estimation with Applications to Tracking and Navigation: Theory Algorithms and Software* (Wiley, 2004).

13. 13.

Ruppert, M. G., Karvinen, K. S., Wiggins, S. L. & Moheimani, S. O. R. A Kalman filter for amplitude estimation in high-speed dynamic mode atomic force microscopy. *IEEE Trans. Control Syst. Technol.* **24**, 276–284 (2016).

[Google Scholar](#)

14. 14.

Rossi, M., Mason, D., Chen, J., Tsaturyan, Y. & Schliesser, A. Measurement-based quantum control of mechanical motion. *Nature* **563**, 53–58 (2018).

[ADS](#) [CAS](#) [Google Scholar](#)

15. 15.

Rossi, M., Mason, D., Chen, J. & Schliesser, A. Observing and verifying the quantum trajectory of a mechanical resonator. *Phys. Rev. Lett.* **123**, 163601 (2019).

[ADS](#) [CAS](#) [PubMed](#) [PubMed Central](#) [Google Scholar](#)

16. 16.

Belavkin, V. P. Quantum filtering of Markov signals with white quantum noise. In *Quantum Communications and Measurement* (eds Belavkin, V. P. et al.) 381–391 (1995).

17. 17.

Iwasawa, K. et al. Quantum-limited mirror-motion estimation. *Phys. Rev. Lett.* **111**, 163602 (2013).

[ADS](#) [PubMed](#) [PubMed Central](#) [Google Scholar](#)

18. 18.

Wieczorek, W. et al. Optimal state estimation for cavity optomechanical systems. *Phys. Rev. Lett.* **114**, 223601 (2015).

[ADS](#) [PubMed](#) [PubMed Central](#) [Google Scholar](#)

19. 19.

Setter, A., Toroš, M., Ralph, J. F. & Ulbricht, H. Real-time Kalman filter: cooling of an optically levitated nanoparticle. *Phys. Rev. A* **97**, 033822 (2018).

[ADS](#) [CAS](#) [Google Scholar](#)

20. 20.

Liao, J. et al. FPGA implementation of a Kalman-based motion estimator for levitated nanoparticles. *IEEE Trans. Instrum. Meas.* **68**, 2374–2386 (2019).

[Google Scholar](#)

21. 21.

Sudhir, V. et al. Appearance and disappearance of quantum correlations in measurement-based feedback control of a mechanical oscillator. *Phys. Rev. X* **7**, 011001 (2017).

[Google Scholar](#)

22. 22.

Tebbenjohanns, F., Frimmer, M., Jain, V., Windey, D. & Novotny, L. Motional sideband asymmetry of a nanoparticle optically levitated in free space. *Phys. Rev. Lett.* **124**, 013603 (2020).

[ADS](#) [CAS](#) [PubMed](#) [PubMed Central](#) [Google Scholar](#)

23. 23.

Kamba, M., Kiuchi, H., Yotsuya, T. & Aikawa, K. Recoil-limited feedback cooling of single nanoparticles near the ground state in an optical lattice. *Phys. Rev. A* **103**, L051701 (2021).

[ADS](#) [CAS](#) [Google Scholar](#)

24. 24.

Windey, D. et al. Cavity-based 3D cooling of a levitated nanoparticle via coherent scattering. *Phys. Rev. Lett.* **122**, 123601 (2019).

[ADS](#) [CAS](#) [PubMed](#) [PubMed Central](#) [Google Scholar](#)

25. 25.

Delić, U. et al. Cavity cooling of a levitated nanosphere by coherent scattering. *Phys. Rev. Lett.* **122**, 123602 (2019).

[ADS](#) [PubMed](#) [PubMed Central](#) [Google Scholar](#)

26. 26.

de los Ríos Sommer, A., Meyer, N. & Quidant, R. Strong optomechanical coupling at room temperature by coherent scattering. *Nat. Commun.* **12**, 276 (2021).

[PubMed](#) [PubMed Central](#) [Google Scholar](#)

27. 27.

Delić, U. et al. Cooling of a levitated nanoparticle to the motional quantum ground state. *Science* **367**, 892–895 (2020).

[ADS](#) [PubMed](#) [PubMed Central](#) [Google Scholar](#)

28. 28.

Gieseler, J., Novotny, L. & Quidant, R. Thermal nonlinearities in a nanomechanical oscillator. *Nat. Phys.* **9**, 806–810 (2013).

[CAS](#) [Google Scholar](#)

29. 29.

Frimmer, M. et al. Controlling the net charge on a nanoparticle optically levitated in vacuum. *Phys. Rev. A* **95**, 061801 (2017).

[ADS](#) [Google Scholar](#)

30. 30.

Tebbenjohanns, F., Frimmer, M. & Novotny, L. Optimal position detection of a dipolar scatterer in a focused field. *Phys. Rev. A* **100**, 043821 (2019).

[ADS](#) [CAS](#) [Google Scholar](#)

31. 31.

Seberson, T. & Robicheaux, F. Distribution of laser shot-noise energy delivered to a levitated nanoparticle. *Phys. Rev. A* **102**, 033505 (2020).

[ADS](#) [CAS](#) [Google Scholar](#)

32. 32.

Vamivakas, A. N. et al. Phase-sensitive detection of dipole radiation in a fiber-based high numerical aperture optical system. *Opt. Lett.* **32**, 970–972 (2007).

[ADS](#) [CAS](#) [PubMed](#) [PubMed Central](#) [Google Scholar](#)

33. 33.

Clerk, A. A., Devoret, M. H., Girvin, S. M., Marquardt, F. & Schoelkopf, R. J. Introduction to quantum noise, measurement, and amplification. *Rev. Mod. Phys.* **82**, 1155–1208 (2010).

[ADS](#) [MathSciNet](#) [MATH](#) [Google Scholar](#)

34. 34.

Abbott, B. et al. Observation of a kilogram-scale oscillator near its quantum ground state. *New J. Phys.* **11**, 073032 (2009).

[Google Scholar](#)

35. 35.

Bushev, P. et al. Shot-noise-limited monitoring and phase locking of the motion of a single trapped ion. *Phys. Rev. Lett.* **110**, 133602 (2013).

[ADS](#) [CAS](#) [PubMed](#) [PubMed Central](#) [Google Scholar](#)

36. 36.

Doherty, A. C. & Jacobs, K. Feedback control of quantum systems using continuous state estimation. *Phys. Rev. A* **60**, 2700–2711 (1999).

[ADS](#) [CAS](#) [Google Scholar](#)

37. 37.

Poggio, M., Degen, C. L., Mamin, H. J. & Rugar, D. Feedback cooling of a cantilever's fundamental mode below 5 mK. *Phys. Rev. Lett.* **99**, 017201 (2007).

[ADS](#) [CAS](#) [PubMed](#) [PubMed Central](#) [Google Scholar](#)

38. 38.

Safavi-Naeini, A. H. et al. Observation of quantum motion of a nanomechanical resonator. *Phys. Rev. Lett.* **108**, 033602 (2012).

[ADS](#) [PubMed](#) [PubMed Central](#) [Google Scholar](#)

39. 39.

Braginskiĭ, V. B. & Vorontsov, Y. I. Quantum-mechanical limitations in macroscopic experiments and modern experimental technique. *Sov. Phys. Uspekhi* **17**, 644–650 (1975).

[ADS](#) [Google Scholar](#)

40. 40.

Ranjit, G., Cunningham, M., Casey, K. & Geraci, A. A. Zeptonewton force sensing with nanospheres in an optical lattice. *Phys. Rev. A* **93**, 053801 (2016).

[ADS](#) [Google Scholar](#)

41. 41.

Monteiro, F. et al. Force and acceleration sensing with optically levitated nanogram masses at microkelvin temperatures. *Phys. Rev. A* **101**, 053835 (2020).

[ADS](#) [CAS](#) [Google Scholar](#)

42. 42.

Moore, D. C. & Geraci, A. A. Searching for new physics using optically levitated sensors. *Quant. Sci. Tech.* **6**, 014008 (2021).

[Google Scholar](#)

43. 43.

Monteiro, F. et al. Search for composite dark matter with optically levitated sensors. *Phys. Rev. Lett.* **125**, 181102 (2020).

[ADS](#) [CAS](#) [PubMed](#) [PubMed Central](#) [Google Scholar](#)

44. 44.

Carney, D. et al. Mechanical quantum sensing in the search for dark matter. *Quant. Sci. Tech.* **6**, 024002 (2020).

[Google Scholar](#)

45. 45.

Leggett, A. J. Testing the limits of quantum mechanics: motivation, state of play, prospects. *J. Phys. Condens. Matter* **14**, R415–R451

(2002).

[ADS](#) [CAS](#) [Google Scholar](#)

46. 46.

Chen, Y. Macroscopic quantum mechanics: theory and experimental concepts of optomechanics. *J. Phys. At. Mol. Opt. Phys.* **46**, 104001 (2013).

[ADS](#) [CAS](#) [Google Scholar](#)

47. 47.

Genoni, M. G., Zhang, J., Millen, J., Barker, P. F. & Serafini, A. Quantum cooling and squeezing of a levitating nanosphere via time-continuous measurements. *New J. Phys.* **17**, 073019 (2015).

[ADS](#) [Google Scholar](#)

48. 48.

Ralph, J. F. et al. Dynamical model selection near the quantum-classical boundary. *Phys. Rev. A* **98**, 010102 (2018).

[ADS](#) [CAS](#) [Google Scholar](#)

49. 49.

Rakhubovsky, A. A. & Filip, R. Stroboscopic high-order nonlinearity in quantum optomechanics. Preprint at
<https://arXiv.org/abs/1904.00773v1> (2019).

[Download references](#)

Acknowledgements

We thank J. M. Leitão for his introduction to optimal control, and P. Vezio, H. Hepach and T. Westphal for discussions and their help in the laboratory. L.M. thanks A. Rauschenbeutel for the discussion inspiring the confocal detection scheme. This project was supported by the European Research Council (grant agreement no. 649008, ERC CoG QLev4G), by the ERA-NET programme QuantERA under grants QuaSeRT (contract no. 11299191) and TheBlinQC (project no. 731473) (via the EC, the Austrian ministries BMDW and BMBWF and research promotion agency FFG), by the European Union's Horizon 2020 research and innovation programme under grant no. 863132 (iQLev), and by the Austrian Science Fund (FWF, START Project TheLO, Y 952-N36). L.M. is supported by the Vienna Doctoral School of Physics (VDS-P) and by the FWF under project W1210 (CoQuS).

Author information

Affiliations

1. Vienna Center for Quantum Science and Technology (VCQ), Faculty of Physics, University of Vienna, Vienna, Austria

Lorenzo Magrini, Constanze Bach, Sebastian G. Hofer, Nikolai Kiesel & Markus Aspelmeyer

2. Automation and Control Institute (ACIN), TU Wien, Vienna, Austria

Philipp Rosenzweig, Andreas Deutschmann-Olek & Andreas Kugi

3. Institute for Functional Matter and Quantum Technologies (FMQ), University of Stuttgart, Stuttgart, Germany

Sungkun Hong

4. Center for Integrated Quantum Science and Technology (IQST), University of Stuttgart, Stuttgart, Germany

Sungkun Hong

5. Center for Vision, Automation & Control, Austrian Institute of Technology (AIT), Vienna, Austria

Andreas Kugi

6. Institute for Quantum Optics and Quantum Information (IQOQI), Austrian Academy of Sciences, Vienna, Austria

Markus Aspelmeyer

Authors

1. Lorenzo Magrini

[View author publications](#)

You can also search for this author in [PubMed](#) [Google Scholar](#)

2. Philipp Rosenzweig

[View author publications](#)

You can also search for this author in [PubMed](#) [Google Scholar](#)

3. Constanze Bach

[View author publications](#)

You can also search for this author in [PubMed](#) [Google Scholar](#)

4. Andreas Deutschmann-Olek

[View author publications](#)

You can also search for this author in [PubMed](#) [Google Scholar](#)

5. Sebastian G. Hofer

[View author publications](#)

You can also search for this author in [PubMed](#) [Google Scholar](#)

6. Sungkun Hong

[View author publications](#)

You can also search for this author in [PubMed](#) [Google Scholar](#)

7. Nikolai Kiesel

[View author publications](#)

You can also search for this author in [PubMed](#) [Google Scholar](#)

8. Andreas Kugi

[View author publications](#)

You can also search for this author in [PubMed](#) [Google Scholar](#)

9. Markus Aspelmeyer

[View author publications](#)

You can also search for this author in [PubMed](#) [Google Scholar](#)

Contributions

L.M. designed and built the experiment, P.R. designed and programmed the filter and controller. L.M. and C.B. performed the measurements. L.M., P.R. and C.B. analysed the data. The work was supervised by A.K. and M.A. All authors discussed the results and contributed to writing the paper.

Corresponding authors

Correspondence to [Lorenzo Magrini](#) or [Markus Aspelmeyer](#).

Ethics declarations

Competing interests

The authors declare no competing interests.

Additional information

Peer review information *Nature* thanks the anonymous reviewers for their contribution to the peer review of this work. Peer reviewer reports are available.

Publisher's note Springer Nature remains neutral with regard to jurisdictional claims in published maps and institutional affiliations.

Supplementary information

Supplementary Information

This file contains Supplementary Text, Supplementary Figures 1 – 13, Supplementary Equations 1 – 104 and Supplementary References.

Peer Review File

Rights and permissions

Reprints and Permissions

About this article



Check for
updates

Cite this article

Magrini, L., Rosenzweig, P., Bach, C. *et al.* Real-time optimal quantum control of mechanical motion at room temperature. *Nature* **595**, 373–377 (2021). <https://doi.org/10.1038/s41586-021-03602-3>

Download citation

- Received: 30 December 2020

- Accepted: 30 April 2021
- Published: 14 July 2021
- Issue Date: 15 July 2021
- DOI: <https://doi.org/10.1038/s41586-021-03602-3>

Comments

By submitting a comment you agree to abide by our [Terms](#) and [Community Guidelines](#). If you find something abusive or that does not comply with our terms or guidelines please flag it as inappropriate.

[Access through your institution](#)

[Change institution](#)

[Buy or subscribe](#)

Associated Content

[Measurement-based system provides quantum control of nanoparticles](#)

- Tania S. Monteiro

Advertisement

This article was downloaded by **calibre** from <https://www.nature.com/articles/s41586-021-03602-3>

- Article
- [Published: 14 July 2021](#)

Quantum control of a nanoparticle optically levitated in cryogenic free space

- [Felix Tebbenjohanns](#)^{1 na1},
- [M. Luisa Mattana](#)^{1 na1},
- [Massimiliano Rossi](#) [ORCID: orcid.org/0000-0001-8992-3378](#)^{1 na1},
- [Martin Frimmer](#)¹ &
- [Lukas Novotny](#) [ORCID: orcid.org/0000-0002-9970-8345](#)^{1,2}

[Nature](#) volume **595**, pages 378–382 (2021) [Cite this article](#)

- 1561 Accesses
- 84 Altmetric
- [Metrics details](#)

Subjects

- [Optomechanics](#)
- [Quantum mechanics](#)

Abstract

Tests of quantum mechanics on a macroscopic scale require extreme control over mechanical motion and its decoherence^{1,2,3}. Quantum control of mechanical motion has been achieved by engineering the radiation-pressure

coupling between a micromechanical oscillator and the electromagnetic field in a resonator^{4,5,6,7}. Furthermore, measurement-based feedback control relying on cavity-enhanced detection schemes has been used to cool micromechanical oscillators to their quantum ground states⁸. In contrast to mechanically tethered systems, optically levitated nanoparticles are particularly promising candidates for matter-wave experiments with massive objects^{9,10}, since their trapping potential is fully controllable. Here we optically levitate a femtogram (10^{-15} grams) dielectric particle in cryogenic free space, which suppresses thermal effects sufficiently to make the measurement backaction the dominant decoherence mechanism. With an efficient quantum measurement, we exert quantum control over the dynamics of the particle. We cool its centre-of-mass motion by measurement-based feedback to an average occupancy of 0.65 motional quanta, corresponding to a state purity of 0.43. The absence of an optical resonator and its bandwidth limitations holds promise to transfer the full quantum control available for electromagnetic fields to a mechanical system. Together with the fact that the optical trapping potential is highly controllable, our experimental platform offers a route to investigating quantum mechanics at macroscopic scales¹¹.

Access options

Subscribe to Journal

Get full journal access for 1 year

\$199.00

only \$3.90 per issue

[Subscribe](#)

All prices are NET prices.

VAT will be added later in the checkout.

Tax calculation will be finalised during checkout.

Rent or Buy article

Get time limited or full article access on ReadCube.

from \$8.99

[Rent or Buy](#)

All prices are NET prices.

Additional access options:

- [Log in](#)
- [Access through your institution](#)
- [Learn about institutional subscriptions](#)

Fig. 1: Experimental setup.

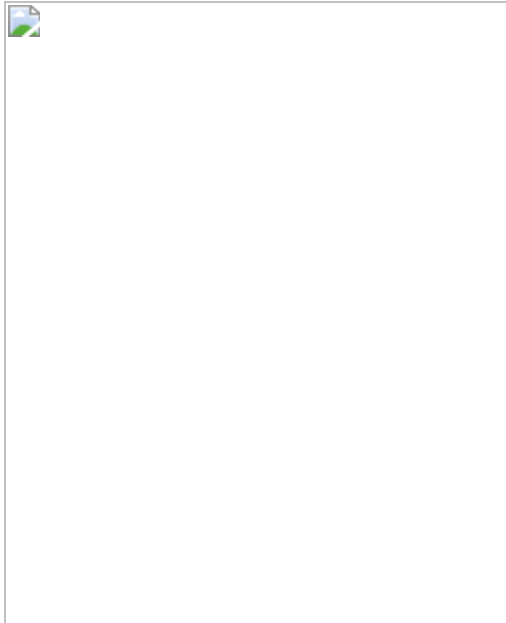


Fig. 2: Quantum ground-state verification via out-of-loop measurements.

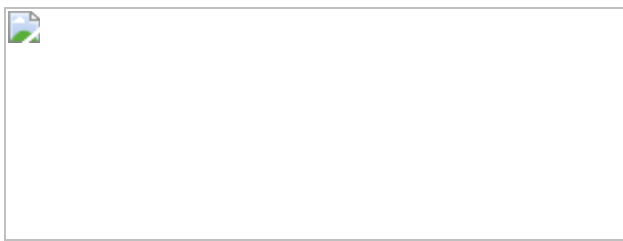
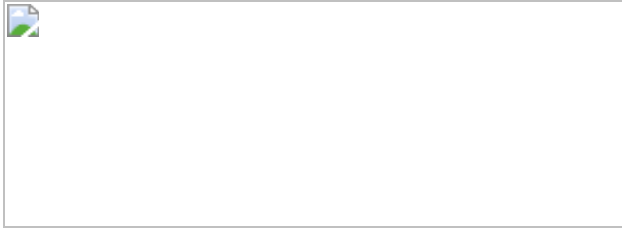


Fig. 3: In-loop analysis of the feedback system.



Data availability

Source data for Figs. 1b, 2, 3 and for Extended Data Figs. 2–7 are available in the ETH Zurich Research Collection (<https://doi.org/10.3929/ethz-b-000480147>).

References

1. 1.

Zurek, W. H. Decoherence and the transition from quantum to classical — revisited. In *Quantum Decoherence: Poincaré Seminar 2005* (eds Duplantier, B. et al.) 1–31 (Birkhäuser, 2007).

2. 2.

Chen, Y. Macroscopic quantum mechanics: theory and experimental concepts of optomechanics. *J. Phys. B* **46**, 104001 (2013).

[ADS](#) [CAS](#) [Google Scholar](#)

3. 3.

Hornberger, K., Gerlich, S., Haslinger, P., Nimmrichter, S. & Arndt, M. Colloquium: Quantum interference of clusters and molecules. *Rev. Mod. Phys.* **84**, 157–173 (2012).

[ADS](#) [CAS](#) [Google Scholar](#)

4. 4.

Teufel, J. D. et al. Sideband cooling of micromechanical motion to the quantum ground state. *Nature* **475**, 359–363 (2011).

[ADS](#) [CAS](#) [Google Scholar](#)

5. 5.

Chan, J. et al. Laser cooling of a nanomechanical oscillator into its quantum ground state. *Nature* **478**, 89–92 (2011).

[ADS](#) [CAS](#) [Google Scholar](#)

6. 6.

Qiu, L., Shomroni, I., Seidler, P. & Kippenberg, T. J. Laser cooling of a nanomechanical oscillator to its zero-point energy. *Phys. Rev. Lett.* **124**, 173601 (2020).

[ADS](#) [CAS](#) [Google Scholar](#)

7. 7.

Aspelmeyer, M., Kippenberg, T. J. & Marquardt, F. Cavity optomechanics. *Rev. Mod. Phys.* **86**, 1391–1452 (2014).

[ADS](#) [Google Scholar](#)

8. 8.

Rossi, M., Mason, D., Chen, J., Tsaturyan, Y. & Schliesser, A. Measurement-based quantum control of mechanical motion. *Nature* **563**, 53–58 (2018).

[ADS](#) [CAS](#) [Google Scholar](#)

9. 9.

Chang, D. E. et al. Cavity opto-mechanics using an optically levitated nanosphere. *Proc. Natl Acad. Sci. USA* **107**, 1005–1010 (2010).

[ADS](#) [CAS](#) [PubMed](#) [PubMed Central](#) [Google Scholar](#)

10. 10.

Romero-Isart, O., Juan, M. L., Quidant, R. & Cirac, J. I. Toward quantum superposition of living organisms. *New J. Phys.* **12**, 033015 (2010).

[ADS](#) [Google Scholar](#)

11. 11.

Leggett, A. J. Testing the limits of quantum mechanics: motivation, state of play, prospects. *J. Phys. Condens. Matter* **14**, R415 (2002).

[ADS](#) [CAS](#) [Google Scholar](#)

12. 12.

Braginskii, V. B. & Manukin, A. B. *Measurement of Weak Forces in Physics Experiments* (Univ. of Chicago Press, 1977).

13. 13.

Andrews, R. W. et al. Bidirectional and efficient conversion between microwave and optical light. *Nat. Phys.* **10**, 321–326 (2014).

[CAS](#) [Google Scholar](#)

14. 14.

Bagci, T. et al. Optical detection of radio waves through a nanomechanical transducer. *Nature* **507**, 81–85 (2014).

[Google Scholar](#)

15. 15.

Mirhosseini, M., Sipahigil, A., Kalaee, M. & Painter, O. Superconducting qubit to optical photon transduction. *Nature* **588**, 599–603 (2020).

[ADS](#) [CAS](#) [PubMed](#) [PubMed Central](#) [Google Scholar](#)

16. 16.

Cirac, J. I., Lewenstein, M., Mølmer, K. & Zoller, P. Quantum superposition states of Bose-Einstein condensates. *Phys. Rev. A* **57**, 1208–1218 (1998).

[ADS](#) [Google Scholar](#)

17. 17.

Bose, S., Jacobs, K. & Knight, P. L. Scheme to probe the decoherence of a macroscopic object. *Phys. Rev. A* **59**, 3204–3210 (1999).

[ADS](#) [CAS](#) [Google Scholar](#)

18. 18.

Marshall, W., Simon, C., Penrose, R. & Bouwmeester, D. Towards quantum superpositions of a mirror. *Phys. Rev. Lett.* **91**, 130401 (2003).

[ADS](#) [MathSciNet](#) [PubMed](#) [PubMed Central](#) [Google Scholar](#)

19. 19.

Romero-Isart, O. Quantum superposition of massive objects and collapse models. *Phys. Rev. A* **84**, 052121 (2011).

[ADS](#) [Google Scholar](#)

20. 20.

Ashkin, A. & Dziedzic, J. M. Feedback stabilization of optically levitated particles. *Appl. Phys. Lett.* **30**, 202 (1977).

[ADS](#) [Google Scholar](#)

21. 21.

Hebestreit, E., Frimmer, M., Reimann, R. & Novotny, L. Sensing Static forces with free-falling nanoparticles. *Phys. Rev. Lett.* **121**, 063602 (2018).

[ADS](#) [CAS](#) [PubMed](#) [PubMed Central](#) [Google Scholar](#)

22. 22.

Purdy, T. P., Peterson, R. W. & Regal, C. A. Observation of radiation pressure shot noise on a macroscopic object. *Science* **339**, 801–804 (2013).

[ADS](#) [CAS](#) [PubMed](#) [PubMed Central](#) [Google Scholar](#)

23. 23.

Jain, V. et al. Direct measurement of photon recoil from a levitated nanoparticle. *Phys. Rev. Lett.* **116**, 243601 (2016).

[ADS](#) [PubMed](#) [PubMed Central](#) [Google Scholar](#)

24. 24.

Kaltenbaek, R. et al. Macroscopic quantum resonators (MAQRO). *Exp. Astron.* **34**, 123–164 (2012).

[ADS](#) [Google Scholar](#)

25. 25.

Kiesel, N. et al. Cavity cooling of an optically levitated submicron particle. *Proc. Natl Acad. Sci. USA* **110**, 14180–14185 (2013).

[ADS](#) [CAS](#) [PubMed](#) [PubMed Central](#) [Google Scholar](#)

26. 26.

Windey, D. et al. Cavity-based 3D cooling of a levitated nanoparticle via coherent scattering. *Phys. Rev. Lett.* **122**, 123601 (2019).

[ADS](#) [CAS](#) [PubMed](#) [PubMed Central](#) [Google Scholar](#)

27. 27.

Delić, U. et al. Cavity cooling of a levitated nanosphere by coherent scattering. *Phys. Rev. Lett.* **122**, 123602 (2019).

[ADS](#) [PubMed](#) [PubMed Central](#) [Google Scholar](#)

28. 28.

Delić, U. et al. Cooling of a levitated nanoparticle to the motional quantum ground state. *Science* **367**, 892–895 (2020).

[ADS](#) [PubMed](#) [PubMed Central](#) [Google Scholar](#)

29. 29.

Li, T., Kheifets, S. & Raizen, M. G. Millikelvin cooling of an optically trapped microsphere in vacuum. *Nat. Phys.* **7**, 527–530 (2011).

[CAS](#) [Google Scholar](#)

30. 30.

Gieseler, J., Deutsch, B., Quidant, R. & Novotny, L. Subkelvin parametric feedback cooling of a laser-trapped nanoparticle. *Phys. Rev. Lett.* **109**, 103603 (2012).

[ADS](#) [Google Scholar](#)

31. 31.

Tebbenjohanns, F., Frimmer, M., Militaru, A., Jain, V. & Novotny, L. Cold damping of an optically levitated nanoparticle to microkelvin temperatures. *Phys. Rev. Lett.* **122**, 223601 (2019).

[ADS](#) [CAS](#) [Google Scholar](#)

32. 32.

Mancini, S., Vitali, D. & Tombesi, P. Optomechanical cooling of a macroscopic oscillator by homodyne feedback. *Phys. Rev. Lett.* **80**, 688 (1998).

[ADS](#) [CAS](#) [Google Scholar](#)

33. 33.

Wilson, D. et al. Measurement-based control of a mechanical oscillator at its thermal decoherence rate. *Nature* **524**, 325–329 (2015).

[ADS](#) [CAS](#) [Google Scholar](#)

34. 34.

Cohadon, P. F., Heidmann, A. & Pinard, M. Cooling of a mirror by radiation pressure. *Phys. Rev. Lett.* **83**, 3174–3177 (1999).

[ADS](#) [CAS](#) [Google Scholar](#)

35. 35.

Poggio, M., Degen, C. L., Mamin, H. J. & Rugar, D. Feedback cooling of a cantilever's fundamental mode below 5 mK. *Phys. Rev. Lett.* **99**, 017201 (2007).

[ADS](#) [CAS](#) [PubMed](#) [PubMed Central](#) [Google Scholar](#)

36. 36.

Tebbenjohanns, F., Frimmer, M., Jain, V., Windey, D. & Novotny, L. Motional sideband asymmetry of a nanoparticle optically levitated in free space. *Phys. Rev. Lett.* **124**, 013603 (2020).

[ADS](#) [CAS](#) [PubMed](#) [PubMed Central](#) [Google Scholar](#)

37. 37.

Tebbenjohanns, F., Frimmer, M. & Novotny, L. Optimal position detection of a dipolar scatterer in a focused field. *Phys. Rev. A* **100**, 043821 (2019).

[ADS](#) [CAS](#) [Google Scholar](#)

38. 38.

Millen, J., Fonseca, P. Z. G., Mavrogordatos, T., Monteiro, T. S. & Barker, P. F. Cavity cooling a single charged levitated nanosphere. *Phys. Rev. Lett.* **114**, 123602 (2015).

[ADS](#) [CAS](#) [Google Scholar](#)

39. 39.

Clerk, A. A., Devoret, M. H., Girvin, S. M., Marquardt, F. & Schoelkopf, R. J. Introduction to quantum noise, measurement, and amplification. *Rev. Mod. Phys.* **82**, 1155–1208 (2010).

[ADS](#) [MathSciNet](#) [MATH](#) [Google Scholar](#)

40. 40.

Safavi-Naeini, A. H. et al. Observation of quantum motion of a nanomechanical resonator. *Phys. Rev. Lett.* **108**, 033602 (2012).

[ADS](#) [PubMed](#) [PubMed Central](#) [Google Scholar](#)

41. 41.

Purdy, T. P., Grutter, K. E., Srinivasan, K. & Taylor, J. M. Quantum correlations from a room-temperature optomechanical cavity. *Science* **356**, 1265–1268 (2017).

[ADS](#) [MathSciNet](#) [CAS](#) [PubMed](#) [PubMed Central](#) [MATH](#) [Google Scholar](#)

42. 42.

Shkarin, A. B. et al. Quantum optomechanics in a liquid. *Phys. Rev. Lett.* **122**, 153601 (2019).

[ADS](#) [CAS](#) [PubMed](#) [PubMed Central](#) [Google Scholar](#)

43. 43.

Wiseman, H. M. & Milburn, G. J. *Quantum Measurement and Control* (Cambridge Univ. Press, 2010).

44. 44.

Sudhir, V. et al. Appearance and disappearance of quantum correlations in measurement-based feedback control of a mechanical oscillator. *Phys. Rev. X* **7**, 011001 (2017).

[Google Scholar](#)

45. 45.

Sayrin, C. et al. Real-time quantum feedback prepares and stabilizes photon number states. *Nature* **477**, 73–77 (2011).

[ADS](#) [CAS](#) [PubMed](#) [PubMed Central](#) [Google Scholar](#)

46. 46.

Vijay, R. et al. Stabilizing Rabi oscillations in a superconducting qubit using quantum feedback. *Nature* **490**, 77–80 (2012).

[ADS](#) [CAS](#) [PubMed](#) [PubMed Central](#) [Google Scholar](#)

47. 47.

Magrini, L. et al. Real-time optimal quantum control of mechanical motion at room temperature. *Nature* <https://doi.org/10.1038/s41586-021-03602-3> (2021).

48. 48.

Meng, C., Brawley, G. A., Bennett, J. S., Vanner, M. R. & Bowen, W. P. Mechanical squeezing via fast continuous measurement. *Phys. Rev. Lett.* **125**, 043604 (2020).

[ADS](#) [CAS](#) [PubMed](#) [PubMed Central](#) [Google Scholar](#)

49. 49.

Vanner, M. R. et al. Pulsed quantum optomechanics. *Proc. Natl Acad. Sci. USA* **108**, 16182 (2011).

[ADS](#) [CAS](#) [PubMed](#) [PubMed Central](#) [Google Scholar](#)

50. 50.

Gabrielse, G. et al. Thousandfold improvement in the measured antiproton mass. *Phys. Rev. Lett.* **65**, 1317–1320 (1990).

[ADS](#) [CAS](#) [PubMed](#) [PubMed Central](#) [Google Scholar](#)

51. 51.

Bateman, J., Nimmrichter, S., Hornberger, K. & Ulbricht, H. Near-field interferometry of a free-falling nanoparticle from a point-like source. *Nat. Commun.* **5**, 4788 (2014).

[ADS](#) [CAS](#) [PubMed](#) [PubMed Central](#) [Google Scholar](#)

52. 52.

Doherty, A. C., Tan, S. M., Parkins, A. S. & Walls, D. F. State determination in continuous measurement. *Phys. Rev. A* **60**, 2380–2392 (1999).

[ADS](#) [CAS](#) [Google Scholar](#)

53. 53.

Micke, P. et al. Closed-cycle, low-vibration 4 K cryostat for ion traps and other applications. *Rev. Sci. Instrum.* **90**, 065104 (2019).

[ADS](#) [CAS](#) [PubMed](#) [PubMed Central](#) [Google Scholar](#)

54. 54.

Frimmer, M. et al. Controlling the net charge on a nanoparticle optically levitated in vacuum. *Phys. Rev. A* **95**, 061801 (2017).

[ADS](#) [Google Scholar](#)

55. 55.

Ahn, J. et al. Optically levitated nanodumbbell torsion balance and GHz nanomechanical rotor. *Phys. Rev. Lett.* **121**, 033603 (2018).

[ADS](#) [CAS](#) [PubMed](#) [PubMed Central](#) [Google Scholar](#)

56. 56.

Hebestreit, E. et al. Calibration and energy measurement of optically levitated nanoparticle sensors. *Rev. Sci. Instrum.* **89**, 033111 (2018).

[ADS](#) [PubMed](#) [PubMed Central](#) [Google Scholar](#)

57. 57.

van der Laan, F. et al. Optically levitated rotor at its thermal limit of frequency stability. *Phys. Rev. A* **102**, 013505 (2020).

[ADS](#) [Google Scholar](#)

58. 58.

Underwood, M. et al. Measurement of the motional sidebands of a nanogram-scale oscillator in the quantum regime. *Phys. Rev. A* **92**, 061801(R) (2015).

[ADS](#) [Google Scholar](#)

59. 59.

Doherty, A. C. & Jacobs, K. Feedback control of quantum systems using continuous state estimation. *Phys. Rev. A* **60**, 2700–2711 (1999).

[ADS](#) [CAS](#) [Google Scholar](#)

60. 60.

Genes, C., Vitali, D., Tombesi, P., Gigan, S. & Aspelmeyer, M. Ground-state cooling of a micromechanical oscillator: Comparing cold damping and cavity-assisted cooling schemes. *Phys. Rev. A* **77**, 033804 (2008).

[ADS](#) [Google Scholar](#)

61. 61.

Pluchar, C. M., Agrawal, A. R., Schenk, E. & Wilson, D. J. Towards cavity-free ground-state cooling of an acoustic-frequency silicon nitride membrane. *Appl. Opt.* **59**, G107–G111 (2020).

[CAS](#) [PubMed](#) [PubMed Central](#) [Google Scholar](#)

62. 62.

Iwasaki, M. et al. Electric feedback cooling of single charged nanoparticles in an optical trap. *Phys. Rev. A* **99**, 051401 (2019).

[ADS](#) [CAS](#) [Google Scholar](#)

63. 63.

Conangla, G. P. et al. Optimal feedback cooling of a charged levitated nanoparticle with adaptive control. *Phys. Rev. Lett.* **122**, 223602 (2019).

[ADS](#) [CAS](#) [PubMed](#) [PubMed Central](#) [Google Scholar](#)

64. 64.

Kamba, M., Kiuchi, H., Yotsuya, T. & Aikawa, K. Recoil-limited feedback cooling of single nanoparticles near the ground state in an optical lattice. *Phys. Rev. A* **103**, L051701 (2021).

[ADS](#) [CAS](#) [Google Scholar](#)

65. 65.

Rodenburg, B., Neukirch, L. P., Vamivakas, A. N. & Bhattacharya, M. Quantum model of cooling and force sensing with an optically trapped nanoparticle. *Optica* **3**, 318–323 (2016).

[ADS](#) [CAS](#) [Google Scholar](#)

66. 66.

Wieczorek, W. et al. Optimal state estimation for cavity optomechanical systems. *Phys. Rev. Lett.* **114**, 223601 (2015).

[ADS](#) [PubMed](#) [PubMed Central](#) [Google Scholar](#)

67. 67.

Garbini, J. L., Bruland, K. J., Dougherty, W. M. & Sidles, J. A. Optimal control of force microscope cantilevers. I. Controller design. *J. Appl. Phys.* **80**, 1951–1958 (1996).

[ADS](#) [CAS](#) [Google Scholar](#)

[Download references](#)

Acknowledgements

This research was supported by the Swiss National Science Foundation (SNF) through the NCCR-QSIT programme (grant no. 51NF40-160591) and the R'Equip programme (grant no. 206021-189605), and by the European Union's Horizon 2020 research and innovation programme under grant no. 863132 (iQLev). We are grateful to F. van der Laan for his contributions to the particle characterization procedure. We thank O. Wipfli and C. Fischer for their suggestions in designing the cryogenic vacuum chamber, J. Piotrowski and D. Windey for their advice with the trap assembly, and Y. Li for her work on the control software. We thank our colleagues P. Back, E. Bonvin, J. Gao, A. Militaru, R. Reimann, J. Vijayan and J. Zielinska for input and discussions.

Author information

Author notes

1. These authors contributed equally: Felix Tebbenjohanns, M. Luisa Mattana, Massimiliano Rossi

Affiliations

1. Photonics Laboratory, ETH Zürich, Zürich, Switzerland

Felix Teffenjohanns, M. Luisa Mattana, Massimiliano Rossi, Martin Frimmer & Lukas Novotny

2. Quantum Center, ETH Zurich, Zürich, Switzerland

Lukas Novotny

Authors

1. Felix Tebbenjohanns
[View author publications](#)

You can also search for this author in [PubMed](#) [Google Scholar](#)

2. M. Luisa Mattana
[View author publications](#)

You can also search for this author in [PubMed](#) [Google Scholar](#)

3. Massimiliano Rossi
[View author publications](#)

You can also search for this author in [PubMed](#) [Google Scholar](#)

4. Martin Frimmer
[View author publications](#)

You can also search for this author in [PubMed](#) [Google Scholar](#)

5. Lukas Novotny
[View author publications](#)

You can also search for this author in [PubMed](#) [Google Scholar](#)

Contributions

F.T., M.L.M. and M.R. conducted the experiments and co-wrote the manuscript with M.F., who directed the project with L.N.

Corresponding author

Correspondence to [Lukas Novotny](#).

Additional information

Competing interests The authors declare no competing interests.

Peer review information *Nature* thanks Dalziel Wilson and the other, anonymous, reviewer(s) for their contribution to the peer review of this work. Peer reviewer reports are available.

Publisher's note Springer Nature remains neutral with regard to jurisdictional claims in published maps and institutional affiliations.

Extended data figures and tables

Extended Data Fig. 1 Experimental setup.

We optically trap a nanoparticle inside a cryogenic vacuum chamber using a telecom laser. In the forwards direction, we employ a libration and position detection system. In the backwards direction, we place both a homodyne and a heterodyne photodetector. AOM, acousto-optic modulator; DAQ, data acquisition card; EOM, electro-optic modulator; $\lambda/2$, half-wave plate; LO, local oscillator; PBS, polarizing beam-splitter; R, reflection; T, transmission.

Extended Data Fig. 2 Postselecting the data.

The compression cycles of the cryocooler are visible in our interferometric signal at baseband ($i_{\text{dc}}[t]$ in grey). We identify the cycles (red dotted lines) and postselect 300-ms-long intervals (indicator function in orange) of the time traces containing the particle motion (exemplary for $i_{\text{hom}}[t]$ in blue).

Extended Data Fig. 3 Transfer function of the electronic feedback chain.

a, b, Measured magnitude (**a**) and phase (**b**) response of the experimentally used delay filter. The dotted, dashed, and dot-dashed vertical lines mark the location of the resonance frequency of motion along the z , x , and y axes, respectively.

Extended Data Fig. 4 Detection noise characterization.

Variance of the laser noise as a function of local oscillator power in homodyne detection. The variance, expressed in dB, is normalized to the variance of the electronic noise floor of the detector (grey). The dotted blue line provides a guide for the eye for the linear dependence between variance and power of the beam.

Extended Data Fig. 5 Sideband asymmetry in out-of-loop heterodyne measurements.

a, b, Stokes (**a**) and anti-Stokes (**b**) sidebands, at different electronic feedback gains, normalized to the estimated background level (grey line). Each sideband pair is simultaneously fitted to a theoretical model. **c**, Mechanical occupations (green squares) at different feedback gains. The black solid line is a theoretical model based on an ideal delay filter with parameters estimated from the in-loop spectra. The error bars are obtained by propagating the fit uncertainties (1 s.d.) of the areas.

Extended Data Fig. 6 Sideband cross-correlations in out-of-loop heterodyne measurements.

a, b, Real (**a**) and imaginary (**b**) parts of cross-spectra, at different electronic feedback gains. Each pair is simultaneously fitted to a theoretical model and the results are shown as black lines. The grey line marks the zero as a reference. **c, d**, Fitted mechanical resonance frequency (**c**) and effective linewidth (**d**) at different electronic gains. **e**, Extracted mechanical occupations as a function of fitted effective linewidths. The black line is a theoretical model based on an ideal delay filter and on parameters estimated from the in-loop spectra. The error bars are obtained by the fit uncertainties (1 s.d.).

Extended Data Fig. 7 Fit results.

a, Reference displacement spectrum measured by the homodyne detector at the smallest feedback gain, with a fit to a model (black line). In light red we show the spectral features excluded from the fits. **b**, Fitted feedback gain, γ_{eff} , as a function of the experimentally tunable electronic gain g_{el} . Coloured

dots come from fitting the corresponding spectra shown in Fig. 3a. The black squares are the full-width at half-maximum extracted from the computed actual displacement spectra. The grey line is a guide for the eye, and represents the expected linear relation.

Extended Data Table 1 Notation

[Full size table](#)

Supplementary information

[Peer Review File](#)

Rights and permissions

[Reprints and Permissions](#)

About this article



Check for
updates

Cite this article

Tebbenjohanns, F., Mattana, M.L., Rossi, M. *et al.* Quantum control of a nanoparticle optically levitated in cryogenic free space. *Nature* **595**, 378–382 (2021). <https://doi.org/10.1038/s41586-021-03617-w>

[Download citation](#)

- Received: 04 March 2021
- Accepted: 05 May 2021
- Published: 14 July 2021

- Issue Date: 15 July 2021
- DOI: <https://doi.org/10.1038/s41586-021-03617-w>

Comments

By submitting a comment you agree to abide by our [Terms](#) and [Community Guidelines](#). If you find something abusive or that does not comply with our terms or guidelines please flag it as inappropriate.

[Access through your institution](#)

[Change institution](#)

[Buy or subscribe](#)

Associated Content

[Measurement-based system provides quantum control of nanoparticles](#)

- Tania S. Monteiro

Advertisement

This article was downloaded by **calibre** from <https://www.nature.com/articles/s41586-021-03617-w>

Exponential suppression of bit or phase errors with cyclic error correction

[Download PDF](#)

- Article
- Open Access
- [Published: 14 July 2021](#)

Exponential suppression of bit or phase errors with cyclic error correction

- [Google Quantum AI](#)

Nature volume **595**, pages 383–387 (2021) [Cite this article](#)

- 6210 Accesses
- 185 Altmetric
- [Metrics details](#)

Subjects

- [Quantum information](#)
- [Qubits](#)

Abstract

Realizing the potential of quantum computing requires sufficiently low logical error rates¹. Many applications call for error rates as low as 10^{-15} (refs. [2,3,4,5,6,7,8,9](#)), but state-of-the-art quantum platforms typically have physical error rates near 10^{-3} (refs. [10,11,12,13,14](#)). Quantum error correction^{[15,16,17](#)} promises to bridge this divide by distributing quantum logical information across many physical qubits in such a way that errors can be detected and corrected. Errors on the encoded logical qubit state can be exponentially suppressed as the number of physical qubits grows, provided that the physical error rates are below a certain threshold and stable over the course of a computation. Here we implement one-dimensional repetition codes embedded in a two-dimensional grid of superconducting qubits that demonstrate exponential suppression of bit-flip or phase-flip errors, reducing logical error per round more than

100-fold when increasing the number of qubits from 5 to 21. Crucially, this error suppression is stable over 50 rounds of error correction. We also introduce a method for analysing error correlations with high precision, allowing us to characterize error locality while performing quantum error correction. Finally, we perform error detection with a small logical qubit using the 2D surface code on the same device^{18,19} and show that the results from both one- and two-dimensional codes agree with numerical simulations that use a simple depolarizing error model. These experimental demonstrations provide a foundation for building a scalable fault-tolerant quantum computer with superconducting qubits.

[Download PDF](#)

Main

Many quantum error-correction (QEC) architectures are built on stabilizer codes²⁰, where logical qubits are encoded in the joint state of multiple physical qubits, which we refer to as data qubits. Additional physical qubits known as measure qubits are interlaced with the data qubits and are used to periodically measure the parity of chosen data qubit combinations. These projective stabilizer measurements turn undesired perturbations of the data qubit states into discrete errors, which we track by looking for changes in parity. The stream of parity values can then be decoded to determine the most likely physical errors that occurred. For the purpose of maintaining a logical quantum memory in the codes presented in this work, these errors can be compensated in classical software³. In the simplest model, if the physical error per operation p is below a certain threshold p_{th} determined by quantum computer architecture, chosen QEC code and decoder, then the probability of logical error per round of error correction (ε_L) should scale as:

$$\varepsilon_L \propto e^{-\Lambda} = C p^{\frac{d}{2}} \quad (1)$$

Here, $\Lambda \propto p_{\text{th}}/p$ is the exponential error suppression factor, C is a fitting constant and d is the code distance, defined as the minimum number of physical errors required to generate a logical error, and increases with the number of physical qubits^{3,21}. More realistic error models cannot be characterized by a single error rate p or a single threshold value p_{th} . Instead, quantum processors must be benchmarked by measuring Λ .

Many previous experiments have demonstrated the principles of stabilizer codes in various platforms such as nuclear magnetic resonance^{22,23}, ion traps^{24,25,26} and superconducting qubits^{19,21,27,28}. However, these results cannot be extrapolated to

exponential error suppression in large systems unless non-idealities such as crosstalk are well understood. Moreover, exponential error suppression has not previously been demonstrated with cyclic stabilizer measurements, which are a key requirement for fault-tolerant computing but introduce error mechanisms such as state leakage, heating and data qubit decoherence during measurement^{21,29}.

In this work, we run two stabilizer codes. In the repetition code, qubits alternate between measure and data qubits in a 1D chain, and the number of qubits for a given code distance is $n_{\text{qubits}} = 2d - 1$. Each measure qubit checks the parity of its two neighbours, and all measure qubits check the same basis so that the logical qubit is protected from either X or Z errors, but not both. In the surface code^{3,30,31,32}, qubits follow a 2D chequerboard pattern of measure and data qubits, with $n_{\text{qubits}} = 2d^2 - 1$. The measure qubits further alternate between X and Z types, providing protection against both types of errors. We use repetition codes up to $d = 11$ to test for exponential error suppression and a $d = 2$ surface code to test the forward compatibility of our device with larger 2D codes.

QEC with the Sycamore processor

We implement QEC using a Sycamore processor³³, which consists of a 2D array of transmon qubits³⁴ where each qubit is tunably coupled to four nearest neighbours—the connectivity required for the surface code. Compared with ref. ³³, this device has an improved design of the readout circuit, allowing for faster readout with less crosstalk and a factor of 2 reduction in readout error per qubit (see Supplementary Section I). Like its predecessor, this processor has 54 qubits, but we used at most 21 because only a subset of the processor was wired up. Figure 1a shows the layout of the $d = 11$ (21 qubit) repetition code and $d = 2$ (7 qubit) surface code on the Sycamore device, while Fig. 1b summarizes the error rates of the operations which make up the stabilizer circuits. Additionally, the mean coherence times for each qubit are $T_1 = 15 \mu\text{s}$ and $T_2 = 19 \mu\text{s}$.

Fig. 1: Stabilizer circuits on Sycamore.

 **figure1**

a, Layout of distance-11 repetition code and distance-2 surface code in the Sycamore processor. In the experiment, the two codes use overlapping sets of qubits, which are offset in the figure for clarity. **b**, Pauli error rates for single-qubit and CZ gates and identification error rates for measurement, each benchmarked in simultaneous operation. **c**, Circuit schematic for the phase-flip code. Data qubits are randomly initialized into $|+\rangle$ or $|-\rangle$, followed by repeated application of XX stabilizer measurements and finally X -basis measurements of the data qubits. Hadamard refers to the Hadamard gate, a quantum operation. **d**, Illustration of error detection events that occur when a measurement disagrees with the previous round. **e**, Fraction of measurements (out of 80,000) that detected an error versus measurement round for the $d = 11$ phase-flip code. The dark line is an average of the individual

traces (grey lines) for each of the 10 measure qubits. The first (last) round also uses data qubit initialization (measurement) values to identify detection events.

[Full size image](#)

The experiments reported here leverage two recent advancements in gate calibration on the Sycamore architecture. First, we use the reset protocol introduced in ref. [35](#), which removes population from excited states (including non-computational states) by sweeping the frequency of each measure qubit through that of its readout resonator. This reset operation is appended after each measurement in the QEC circuit and produces the ground state with error below 0.5%[35](#) in 280 ns. Second, we implement a 26-ns controlled-Z (CZ) gate using a direct swap between the joint states $\langle 1,1 \rangle$ and $\langle 0,2 \rangle$ of the two qubits (refs. [14,36](#)). As in ref. [33](#), the tunable qubit-qubit couplings allow these CZ gates to be executed with high parallelism, and up to 10 CZ gates are executed simultaneously in the repetition code. Additionally, we use the results of running QEC to calibrate phase corrections for each CZ gate ([Supplementary Information section III](#)). Using simultaneous cross-entropy benchmarking[33](#), we find that the median CZ gate Pauli error is 0.62% (median CZ gate average error of 0.50%).

We focused our repetition code experiments on the phase-flip code, where data qubits occupy superposition states that are sensitive to both energy relaxation and dephasing, making it more challenging to implement and more predictive of surface code performance than the bit-flip code. A five-qubit unit of the phase-flip code circuit is shown in Fig. [1c](#). This circuit, which is repeated in both space (across the 1D chain) and time, maps the pairwise X -basis parity of the data qubits onto the two measure qubits, which are measured then reset. During measurement and reset, the data qubits are dynamically decoupled to protect the data qubits from various sources of dephasing ([Supplementary Section XI](#)). In a single run of the experiment, we initialize the data qubits into a random string of $\langle + \rangle$ or $\langle - \rangle$ on each qubit. Then, we repeat stabilizer measurements across the chain over many rounds, and finally, we measure the state of the data qubits in the X basis.

Our first pass at analysing the experimental data is to turn measurement outcomes into error detection events, which are changes in the measurement outcomes from the same measure qubit between adjacent rounds. We refer to each possible spacetime location of a detection event (that is, a specific measure qubit and round) as a detection node.

In Fig. [1e](#), for each detection node in a 50-round, 21-qubit phase-flip code, we plot the fraction of experiments (80,000 total) where a detection event was observed on that node. This is the detection event fraction. We first note that the detection event fraction is reduced in the first and last rounds of detection compared with other rounds. At these two time boundary rounds, detection events are found by comparing

the first (last) stabilizer measurement with data qubit initialization (measurement). Thus, the data qubits are not subject to decoherence during measure qubit readout in the time boundary rounds, illustrating the importance of running QEC for multiple rounds in order to benchmark performance accurately ([Supplementary Information section VII](#)). Aside from these boundary effects, we observe that the average detection event fraction is 11% and is stable across all 50 rounds of the experiment, a key finding for the feasibility of QEC. Previous experiments had observed detections rising with number of rounds²¹, and we attribute our experiment's stability to the use of reset to remove leakage in every round³⁵.

Correlations in error detection events

We next characterize the pairwise correlations between detection events. With the exception of the spatial boundaries of the code, a single-qubit Pauli error in the repetition code should produce two detections which come in three categories²¹. First, an error on a data qubit usually produces a detection on the two neighbouring measure qubits in the same round—a spacelike error. The exception is a data qubit error between the two CZ gates in each round, which produces detection events offset by 1 unit in time and space—a spacetime-like error. Finally, an error on a measure qubit will produce detections in two subsequent rounds—a timelike error. These error categories are represented in the planar graph shown in Fig. 2a, where expected detection pairs are drawn as graph edges between detection nodes.

Fig. 2: Analysis of error detections.



a. Detection event graph. Errors in the code trigger two detections (except at the ends of the chain), each represented by a node. Edges represent the expected correlations due to data qubit errors (spacelike and spacetime-like) and measure qubit errors (timelike). **b.** Ordering of the measure qubits in the repetition code. **c.** Measured two-point correlations (p_{ij}) between detection events represented as a symmetric matrix. The axes correspond to possible locations of detection events, with major ticks

marking measure qubits (space) and minor ticks marking difference (Δ round) in rounds (time). For the purpose of illustration, we have averaged together the matrices for 4-round segments of the 50-round experiment shown in Fig. 1e and also set $p_{ij} = 0$ if $i = j$. A description of the uncertainties on the matrix values can be found in [Supplementary Information section IX](#). The upper triangle shows the full scale, where only the expected spacelike and timelike correlations are apparent. The lower triangle shows a truncated colour scale, highlighting unexpected detection pairs due to crosstalk and leakage. Note that observed crosstalk errors occur between next-nearest neighbours in the 2D array. d, Top: observed high-energy event in a time series of repetition code runs. Bottom: zoom-in on high-energy event, showing rapid rise and exponential decay of device-wide errors, and data that are removed when computing logical error probabilities.

[Full size image](#)

We check how well Sycamore conforms to these expectations by computing the correlation probabilities between arbitrary pairs of detection nodes. Under the assumptions that all correlations are pairwise and that error rates are sufficiently low, we estimate the probability of simultaneously triggering two detection nodes i and j as

$$\$ \$ \{ p \} _{ij} \approx \frac{\langle x_i x_j \rangle - \langle x_i \rangle \langle x_j \rangle}{\sqrt{(1 - 2\langle x_i \rangle^2)(1 - 2\langle x_j \rangle^2)}}, \$ \$ \quad (2)$$

where $x_i = 1$ if there is a detection event and $x_i = 0$ otherwise, and $\langle \cdot \rangle$ denotes an average over all experiments ([Supplementary Information section IX](#)). Note that p_{ij} is symmetric between i and j . In Fig. 2c, we plot the p_{ij} matrix for the data shown in Fig. 1e. In the upper triangle, we show the full scale of the data, where, as expected, the most visible correlations are either spacelike or timelike.

However, the sensitivity of this technique allows us to find features that do not fit the expected categories. In the lower triangle, we plot the same data but with the scale truncated by nearly an order of magnitude. The next most prominent correlations are spacetimelike, as we expect, but we also find two additional categories of correlations. First, we observe correlations between non-adjacent measure qubits in the same measurement round. Although these non-adjacent qubits are far apart in the repetition code chain, the qubits are in fact spatially close, owing to the embedding of the 1D chain in a 2D array. Optimization of gate operation frequencies mitigates crosstalk errors to a large extent³⁷, but suppressing these errors further is the subject of active research. Second, we find excess correlations between measurement rounds that differ by more than 1, which we attribute to leakage generated by a number of sources including gates¹² and thermalization^{38,39}. For the observed crosstalk and leakage

errors, the excess correlations are around 3×10^{-3} , an order of magnitude below the measured spacelike and timelike errors but well above the measurement noise floor of 2×10^{-4} .

Additionally, we observe sporadic events that greatly decrease performance for some runs of the repetition code. In Fig. 2d, we plot a time series of detection event fractions averaged over all measure qubits for each run of an experiment. We observe a sharp three-fold increase in detection event fraction, followed by an exponential decay with a time constant of 50 ms. These types of events affect less than 0.5% of all data taken ([Supplementary Information section V](#)), and we attribute them to high-energy particles such as cosmic rays striking the quantum processor and decreasing T_1 on all qubits^{40,41}. For the purpose of understanding the typical behaviour of our system, we remove data near these events (Fig. 2d). However, we note that mitigation of these events through improved device design⁴² and/or shielding⁴³ will be critical to implementing large-scale fault-tolerant computers with superconducting qubits.

Logical errors in the repetition code

We decode detection events and determine logical error probabilities following the procedure in ref. ²¹. Briefly, we use a minimum-weight perfect matching algorithm to determine which errors were most likely to have occurred given the observed detection events. Using the matched errors, we then correct the final measured state of the data qubits in post-processing. A logical error occurs if the corrected final state is not equal to the initial state. We repeat the experiment and analysis while varying the number of detection rounds from 1 to 50 with a fixed number of qubits, 21. We determine logical performance of smaller code sizes by analysing spatial subsets of the 21-qubit data (see [Supplementary Section VII](#)). These results are shown in Fig. 3a, where we observe a clear decrease in the logical error probability with increasing code size. The same data are plotted on a semilog scale in Fig. 3b, highlighting the exponential nature of the error reduction.

Fig. 3: Logical errors in the repetition code.

 **figure3**

a, Logical error probability versus number of detection rounds and number of qubits for the phase-flip code. Smaller code sizes are subsampled from the 21-qubit code as shown in the inset; small dots are data from subsamples and large dots are averages. **b**, Semilog plot of the averages from **a** showing even spacing in $\log(\text{error probability})$

between the code sizes. Error bars are estimated standard error from binomial sampling given the total number of statistics over all subsamples. The lines are exponential fits to data for rounds greater than 10. **c**, Logical error per round (ε_L) versus number of qubits, showing exponential suppression of error rate for both bit-flip and phase-flip, with extracted Λ factors. The fits for Λ and uncertainties were obtained using a linear regression on the log of the logical error per round versus the code distance. The fit excludes $n_{\text{qubits}} = 5$ to reduce the influence of spatial boundary effects ([Supplementary Information section VII](#)).

[Full size image](#)

To extract logical error per round (ε_L), we fitted the data for each number of qubits (averaged over spatial subsets) to $\sqrt{2P} \cdot \sqrt{\ln(\text{error})} = 1 - (1 - 2\sqrt{\lambda})^n$, which expresses an exponential decay in logical fidelity with number of rounds. In Fig. 3c, we show ε_L for the phase-flip and bit-flip codes versus number of qubits used. We find more than 100 \times suppression in ε_L for the phase-flip code from 5 qubits ($\varepsilon_L = 8.7 \times 10^{-3}$) to 21 qubits ($\varepsilon_L = 6.7 \times 10^{-5}$). Additionally, we fitted ε_L versus code distance to equation (1) to extract Λ , and find $\Lambda_X = 3.18 \pm 0.08$ for the phase-flip code and $\Lambda_Z = 2.99 \pm 0.09$ for the bit-flip code.

Error budgeting and projecting QEC performance

To better understand our repetition code results and project surface code performance for our device, we simulated our experiments with a depolarizing noise model, meaning that we probabilistically inject a random Pauli error (X , Y or Z) after each operation ([Supplementary Information section VIII](#)). The Pauli error probabilities for each type of operation are computed using mean error rates and are shown in Fig. 4a. We first simulate the bit-flip and phase-flip codes using the error rates in Fig. 4a, obtaining values of Λ that should be directly comparable to our experimentally measured values. Then we repeat the simulations while individually sweeping the Pauli error probability for each operation type and observing how $1/\Lambda$ changes. The relationship between $1/\Lambda$ and each of the error probabilities is approximately linear, and we use the simulated sensitivity coefficients to estimate how much each operation in the circuit increases $1/\Lambda$ (decreases Λ).

Fig. 4: Error budgeting repetition and surface codes.

 **figure4**

a, Depolarizing error probability (bit flip errors for M and R) for various operations in the stabilizer circuit, derived from averaging quantities in Fig. 1b. Note that the idle gate (I) and dynamical decoupling (DD) values depend on the code being run because the data qubits occupy different states. Op., operation; Rep., repetition. **b**, Estimated error budgets for the bit-flip and phase-flip codes, and projected error budget for the surface code, based on the depolarizing errors from **a**. The repetition code budgets slightly underestimate the experimental errors, and the discrepancy is labelled stray error. For the surface code, the estimated $1/\Lambda$ corresponds to the difference in ε_L between a $d = 3$ and $d = 5$ surface code, and is ~ 4 times higher than in the repetition codes owing to the more stringent threshold for the surface code. Rep., repetition **c**, For the $d = 2$ surface code, the fraction of runs that had no detection events versus number of rounds, plotted with the prediction from a similar error model as the repetition code (dashed line). Inset: physical qubit layout of the $d = 2$ surface code, seven qubits embedded in a 2D array. **d**, Probability of logical error in the surface code

among runs with no detection events versus number of rounds. Depolarizing model simulations that do not include leakage or crosstalk (dashed lines) show good agreement. Error bars for **c** (not visible) and **d** are estimated standard error from binomial sampling with 240,000 experimental shots, minus the shots removed by post-selection in **d**.

[Full size image](#)

The resulting error budgets for the phase-flip and bit-flip codes are shown in Fig. 4b. Overall, measured values of Λ are approximately 20% worse than simulated values, which we attribute to mechanisms such as the leakage and crosstalk errors that are shown in Fig. 2c but were not included in the simulations. Of the modelled contributions to $1/\Lambda$, the dominant sources of error are the CZ gate and data qubit decoherence during measurement and reset. In the same plot, we show the projected error budget for the surface code, which has a more stringent threshold than the repetition code because the higher-weight stabilizers in both X and Z bases lead to more possible logical errors for the same code distance. We find that the overall performance of Sycamore must be improved to observe error suppression in the surface code.

Finally, we test our model against a distance-2 surface code logical qubit¹⁹. We use seven qubits to implement one weight-4 X stabilizer and two weight-2 Z stabilizers as depicted in Fig. 1a. This encoding can detect any single error but contains ambiguity in mapping detections to corrections, so we discard any runs where we observe a detection event. We show the fraction of runs where no errors were detected in Fig. 4c for both logical X and Z preparations; we discard 27% of runs each round, in good agreement with the simulated prediction. Logical errors can still occur after post-selection if two or more physical errors flip the logical state without generating a detection event. In Fig. 4d, we plot the post-selected logical error probability in the final measured state of the data qubits, along with corresponding depolarizing model simulations. Linear fits of the experimental data give 2×10^{-3} error probability per round averaged between the X and Z basis, while the simulations predict 1.5×10^{-3} error probability per round. [Supplementary Information section VI](#) discusses potential explanations for the excess error in experiment, but the general agreement provides confidence in the projected error budget for surface codes in Fig. 4b.

Conclusion and outlook

In this work, we demonstrate stable error detection event fractions while executing 50 rounds of stabilizer measurements on a Sycamore device. By computing the probabilities of detection event pairs, we find that the physical errors detected on the device are localized in space and time to the 3×10^{-3} level. Repetition code logical

errors are exponentially suppressed when increasing the number of qubits from 5 to 21, with a total error suppression of more than $100\times$. Finally, we corroborate experimental results on both 1D and 2D codes with depolarizing model simulations and show that the Sycamore architecture is within a striking distance of the surface code threshold.

Nevertheless, many challenges remain on the path towards scalable quantum error correction. Our error budgets point to the salient research directions required to reach the surface code threshold: reducing CZ gate error and data qubit error during measurement and reset. Reaching this threshold will be an important milestone in quantum computing. However, practical quantum computation will require $\Lambda \approx 10$ for a reasonable physical-to-logical qubit ratio of 1,000:1 ([Supplementary Information section VI](#)). Achieving $\Lambda \approx 10$ will require substantial reductions in operational error rates and further research into mitigation of error mechanisms such as high-energy particles.

Methods

The Sycamore processor

In this work, we use a Sycamore quantum processor consisting of 54 superconducting transmon qubits and 88 tunable couplers in a 2D array. The available operational frequencies of the qubits range from 5 GHz to 7 GHz. The couplers are capable of tuning the qubit–qubit couplings between 0 MHz and 40 MHz, allowing for fast entangling gates while also mitigating unwanted stray interactions. The qubits and couplers in the Sycamore processor are fabricated using aluminium metallization and aluminium/aluminium-oxide Josephson junctions. Indium bump bonds are used to connect a chip containing control circuitry to the chip containing the qubits. The hybridized device is then wire-bonded to a superconducting circuit board and cooled below 20 mK in a dilution refrigerator.

Control and readout

Each qubit is connected to a microwave control line used to drive XY rotations, while qubits and couplers are each connected to flux control lines that tune their frequencies and are used to perform CZ and reset operations. Additionally, each qubit is coupled to a resonator with frequency around 4.5 GHz for dispersive readout, and six such resonators are frequency multiplexed and coupled to a microwave transmission line via a common Purcell filter. Microwave drive and flux lines are connected via multiple stages of wiring and filters to arbitrary waveform generators (AWGs) at room temperature. The AWGs for both microwave and flux control operate at 1 gigasample per second, and for the microwaves, signals are additionally upconverted with single

sideband mixing to reach the qubit frequencies. The outputs of the readout transmission lines are additionally connected to a series of amplifiers—impedance matched parametric amplifiers at 20 mK, high-electron-mobility transistor amplifiers at 3 K, and room-temperature amplifiers—before terminating in a downconverter and analogue–digital converter (ADC). Low-level operation of the AWGs is controlled by FPGAs. Construction and upload of control waveforms and discrimination of ADC signals are controlled by classical computers running servers that each control different types of equipment, and a client computer that controls the overall experiment.

Calibration

Upon initial cooldown, various properties of each qubit and coupler (including coherence times as a function of frequency, control couplings, and couplings between qubits and couplers) are characterized individually. An optimizer is then used to select operational frequencies for gates and readout for each qubit (or pair of qubits for the CZ gate). The optimizer’s objective function is the predicted fidelity of gate operations and is designed to incorporate coherence times, parasitic couplings between qubits, and microwave non-idealities such as crosstalk and carrier bleedthrough. More information about the optimization can be found in refs. [33,37](#) and in [Supplementary Information section XII](#). Next, the primary operations required for QEC (SQ gates, CZ, reset, readout) are calibrated individually. Finally, we perform a round of QEC specific calibrations for phase corrections (see [Supplementary Information section III](#)). Automated characterizations and calibrations are described using a directed acyclic graph, which determines the flow of experiments from basic characterizations to fine tuning^{[44](#)}.

Execution of the experiment

Circuits for the repetition codes and $d = 2$ surface code were specified using Cirq^{[45](#)}, then translated into control waveforms based on calibration data. The exact circuits that were run are available on request. For the bit-flip and phase-flip repetition codes, the 80,000 total experimental shots for each number of rounds were run in four separate experiments. Each experiment consisted of randomly selecting initial data qubit states, running for 4,000 shots, then repeating that process five times for 20,000 shots total. In between shots of the experiment, the qubits idle for 100 μ s and are also reset. The 400 total experiments (one bit-flip and one phase-flip code for each total number of error correction rounds between 1 and 50, and four experiments for each number of rounds) were shuffled before being run. Data for the distance-2 surface code was similarly acquired, but with 15,000 shots for each of the 16 possible data qubit states for 240,000 shots total, and shuffling was done within each number of

rounds over the data qubit states, but no shuffling was done over the number of rounds or data qubit basis.

Data analysis

As described in the main text, for each experimental shot, the array of raw parity measurements is first prepended with initial data qubit parities and appended with final measured data qubit parities. Then the parity values are turned into an array detection events by computing the XOR between each neighbouring round of measurements, resulting in an array that is one less in the ‘rounds’ dimension. For the repetition code data, cosmic rays are post-selected by first computing the total detection event fraction for each experimental shot, producing an array of 80,000 values between 0 and 1. Next, we apply a moving average to that array, with a rectangular window of length 20. Finally, we find where the moving average exceeds 0.2 and remove 100 shots before crossing the threshold and 600 shots following the crossing of the threshold. The analysis then proceeds through minimum-weight perfect matching and exponential fits of logical error rate per round and A , as described in the main text and in more detail in [Supplementary Section X](#). Cosmic ray post-selection is not done for the $d = 2$ surface code data, since the analysis as described in the main text already post-selects any shots where errors are detected.

Data availability

The data that support the plots within this paper and other findings of this study are available from the corresponding authors upon reasonable request.

References

1. 1.

Preskill, J. Quantum computing in the NISQ era and beyond. *Quantum* **2**, 79 (2018).

[Article](#) [Google Scholar](#)

2. 2.

Shor, P. W. Polynomial-time algorithms for prime factorization and discrete logarithms on a quantum computer. *SIAM Rev.* **41**, 303 (1999).

[ADS](#) [MathSciNet](#) [Article](#) [Google Scholar](#)

3. 3.

Fowler, A. G., Mariantoni, M., Martinis, J. M. & Cleland, A. N. Surface codes: towards practical large-scale quantum computation. *Phys. Rev. A* **86**, 032324 (2012).

[ADS](#) [Article](#) [Google Scholar](#)

4. 4.

Childs, A. M., Maslov, D., Nam, Y., Ross, N. J. & Su, Y. Toward the first quantum simulation with quantum speedup. *Proc. Natl Acad. Sci. USA* **115**, 9456–9461(2018).

[MathSciNet](#) [CAS](#) [Article](#) [Google Scholar](#)

5. 5.

Campbell, E., Khurana, A. & Montanaro, A. Applying quantum algorithms to constraint satisfaction problems. *Quantum* **3**, 167 (2019).

[Article](#) [Google Scholar](#)

6. 6.

Kivlichan, I. D. et al. Improved fault-tolerant quantum simulation of condensed-phase correlated electrons via Trotterizatio. *Quantum* **4**, 296 (2020).

[Article](#) [Google Scholar](#)

7. 7.

Gidney, C. & Ekerå, M. How to factor 2048 bit RSA integers in 8 hours using 20 million noisy qubits. *Quantum* **5**, 433 (2021).

[Article](#) [Google Scholar](#)

8. 8.

Lee, J. et al. Even more efficient quantum computations of chemistry through tensor hypercontraction. Preprint at <https://arxiv.org/abs/2011.03494> (2020).

9. 9.

Lemieux, J., Duclos-Cianci, G., Sénéchal, D. & Poulin, D. Resource estimate for quantum many-body ground-state preparation on a quantum computer. *Phys. Rev. A* **103**, 052408 (2021).

[ADS](#) [MathSciNet](#) [CAS](#) [Article](#) [Google Scholar](#)

10. 10.

Ballance, C., Harty, T., Linke, N., Sepiol, M. & Lucas, D. High-fidelity quantum logic gates using trapped-ion hyperfine qubits. *Phys. Rev. Lett.* **117**, 060504 (2016).

[ADS](#) [CAS](#) [Article](#) [Google Scholar](#)

11. 11.

Huang, W. et al. Fidelity benchmarks for two-qubit gates in silicon. *Nature* **569**, 532–536 (2019).

[ADS](#) [CAS](#) [Article](#) [Google Scholar](#)

12. 12.

Rol, M. et al. *Phys. Rev. Lett.* **123**, 120502 (2019).

[ADS](#) [CAS](#) [Article](#) [Google Scholar](#)

13. 13.

Jurcevic, P. et al., Demonstration of quantum volume 64 on a superconducting quantum computing system. *Quantum Sci. Technol.* **6**, 020520 (2021).

[Article](#) [Google Scholar](#)

14. 14.

Foxen, B. et al. Demonstrating a continuous set of two-qubit gates for near-term quantum algorithms. *Phys. Rev. Lett.* **125**, 120504 (2020).

[ADS](#) [CAS](#) [Article](#) [Google Scholar](#)

15. 15.

Shor, P. W. Scheme for reducing decoherence in quantum computer memory. *Phys. Rev. A* **52**, R2493 (1995).

[ADS](#) [CAS](#) [Article](#) [Google Scholar](#)

16. 16.

Calderbank, A. R. & Shor, P. W. Good quantum error-correcting codes exist. *Phys. Rev. A* **54**, 1098 (1996).

[ADS](#) [CAS](#) [Article](#) [Google Scholar](#)

17. 17.

Terhal, B. M. Quantum error correction for quantum memories. *Rev. Mod. Phys.* **87**, 307 (2015).

[ADS](#) [MathSciNet](#) [Article](#) [Google Scholar](#)

18. 18.

Horsman, C., Fowler, A. G., Devitt, S. & Van Meter, R. Surface code quantum computing by lattice surgery. *New J. Phys.* **14**, 123011 (2012).

[ADS](#) [MathSciNet](#) [Article](#) [Google Scholar](#)

19. 19.

Andersen, C. K. et al. Repeated quantum error detection in a surface code. *Nat. Phys.* **16**, 875–880 (2020).

[CAS](#) [Article](#) [Google Scholar](#)

20. 20.

Gottesman, D. *Stabilizer Codes and Quantum Error Correction*. PhD thesis, CalTech (1997); preprint at <https://arxiv.org/abs/quant-ph/9705052> (1997).

21. 21.

Kelly, J. et al. State preservation by repetitive error detection in a superconducting quantum circuit. *Nature* **519**, 66–69 (2015).

[ADS](#) [CAS](#) [Article](#) [Google Scholar](#)

22. 22.

Cory, D. G. et al. Experimental quantum error correction. *Phys. Rev. Lett.* **81**, 2152 (1998).

[ADS](#) [CAS](#) [Article](#) [Google Scholar](#)

23. 23.

Knill, E., Laamme, R., Martinez, R. & Negrevergne, C. Benchmarking quantum computers: the five-qubit error correcting code. *Phys. Rev. Lett.* **86**, 5811 (2001).

[ADS](#) [CAS](#) [Article](#) [Google Scholar](#)

24. 24.

Moussa, O., Baugh, J., Ryan, C. A. & Laamme, R. Demonstration of Sufficient control for two rounds of quantum error correction in a solid state ensemble quantum information processor. *Phys. Rev. Lett.* **107**, 160501 (2011).

[ADS](#) [Article](#) [Google Scholar](#)

25. 25.

Nigg, D. et al. Quantum computations on a topologically encoded qubit. *Science* **345**, 302–305 (2014).

[ADS](#) [MathSciNet](#) [CAS](#) [Article](#) [Google Scholar](#)

26. 26.

Egan, L. et al. Fault-tolerant operation of a quantum error-correction code. Preprint at <https://arxiv.org/abs/2009.11482> (2020).

27. 27.

Takita, M., Cross, A. W., Córcoles, A., Chow, J. M. & Gambetta, J. M. Experimental demonstration of fault-tolerant state preparation with superconducting qubits. *Phys. Rev. Lett.* **119**, 180501 (2017).

[ADS](#) [Article](#) [Google Scholar](#)

28. 28.

Wootton, J. R. Benchmarking near-term devices with quantum error correction. *Quantum Sci. Technol.* **5**, 044004 (2020).

[ADS](#) [Article](#) [Google Scholar](#)

29. 29.

Pino, J. et al. Demonstration of the trapped-ion quantum-CCD computer architecture. *Nature* **592**, 209–213 (2021).

[ADS](#) [CAS](#) [Article](#) [Google Scholar](#)

30. 30.

Bravyi, S. B. & Kitaev, A. Y. Quantum codes on a lattice with boundary. Preprint at <https://arxiv.org/abs/quant-ph/9811052> (1998).

31. 31.

Dennis, E., Kitaev, A., Landahl, A. & Preskill, J. Topological quantum memory. *J. Math. Phys.* **43**, 4452 (2002).

[ADS](#) [MathSciNet](#) [Article](#) [Google Scholar](#)

32. 32.

Kitaev, A. Y. Fault-tolerant quantum computation by anyons. *Ann. Phys.* **303**, 2–30 (2003).

[ADS](#) [MathSciNet](#) [Article](#) [Google Scholar](#)

33. 33.

Arute, F. et al. Quantum supremacy using a programmable superconducting processor. *Nature* **574**, 505–510 (2019).

[ADS](#) [CAS](#) [Article](#) [Google Scholar](#)

34. 34.

Koch, J. et al. Charge-insensitive qubit design derived from the Cooper pair box. *Phys. Rev. A* **76**, 042319 (2007).

[ADS](#) [Article](#) [Google Scholar](#)

35. 35.

McEwen, M. et al. Removing leakage-induced correlated errors in superconducting quantum error correction. *Nat. Commun.* **12**, 1761 (2021).

[ADS](#) [CAS](#) [Article](#) [Google Scholar](#)

36. 36.

Sung, Y. et al. Realization of high-fidelity CZ and ZZ-free iSWAP gates with a tunable coupler. Preprint at <https://arxiv.org/abs/2011.01261> (2020).

37. 37.

Klimov, P. V., Kelly, J., Martinis, J. M. & Neven, H. The Snake optimizer for learning quantum processor control parameters. Preprint at <https://arxiv.org/abs/2006.04594> (2020).

38. 38.

Chen, Z. et al. Measuring and suppressing quantum state leakage in a superconducting qubit. *Phys. Rev. Lett.* **116**, 020501 (2016).

[ADS](#) [Article](#) [Google Scholar](#)

39. 39.

Wood, C. J. & Gambetta, J. M. Quantification and characterization of leakage errors. *Phys. Rev. A* **97**, 032306 (2018).

[ADS](#) [CAS](#) [Article](#) [Google Scholar](#)

40. 40.

Vepsäläinen, A. et al. Impact of ionizing radiation on superconducting qubit coherence. *Nature* **584**, 551–556 (2020).

[ADS](#) [Article](#) [Google Scholar](#)

41. 41.

Wilen, C. et al. Correlated charge noise and relaxation errors in superconducting qubits. Preprint at <https://arxiv.org/abs/2012.06029> (2020).

42. 42.

Karatsu, K. et al. Mitigation of cosmic ray effect on microwave kinetic inductance detector arrays. *Appl. Phys. Lett.* **114**, 032601 (2019).

[ADS Article](#) [Google Scholar](#)

43. 43.

Cardani, L. et al. Reducing the impact of radioactivity on quantum circuits in a deep-underground facility. Preprint at <https://arxiv.org/abs/2005.02286> (2020).

44. 44.

Kelly, J., O'Malley, P., Neeley, M., Neven, H. & Martinis, J. M. Physical qubit calibration on a directed acyclic graph. Preprint at <https://arxiv.org/abs/1803.03226> (2018).

45. 45.

Cirq. <https://github.com/quantumlib/Cirq> (2021).

[Download references](#)

Acknowledgements

We thank J. Platt, J. Dean and J. Yagnik for their executive sponsorship of the Google Quantum AI team, and for their continued engagement and support. We thank S. Leichenauer and J. Platt for reviewing a draft of the manuscript and providing feedback.

Author information

Author notes

1. Harald Putterman

Present address: AWS Center for Quantum Computing, Pasadena, CA, USA

Affiliations

1. Google LLC, Mountain View, CA, USA

Zijun Chen, Kevin J. Satzinger, Juan Atalaya, Alexander N. Korotkov, Andrew Dunsworth, Daniel Sank, Chris Quintana, Matt McEwen, Rami Barends, Paul V.

Klimov, Sabrina Hong, Cody Jones, Andre Petukhov, Dvir Kafri, Sean Demura, Brian Burkett, Craig Gidney, Austin G. Fowler, Harald Puttermann, Igor Aleiner, Frank Arute, Kunal Arya, Ryan Babbush, Joseph C. Bardin, Andreas Bengtsson, Alexandre Bourassa, Michael Broughton, Bob B. Buckley, David A. Buell, Nicholas Bushnell, Benjamin Chiaro, Roberto Collins, William Courtney, Alan R. Derk, Daniel Eppens, Catherine Erickson, Edward Farhi, Brooks Foxen, Marissa Giustina, Ami Greene, Jonathan A. Gross, Matthew P. Harrigan, Sean D. Harrington, Jeremy Hilton, Alan Ho, Trent Huang, William J. Huggins, L. B. Ioffe, Sergei V. Isakov, Evan Jeffrey, Zhang Jiang, Kostyantyn Kechedzhi, Seon Kim, Alexei Kitaev, Fedor Kostritsa, David Landhuis, Pavel Laptev, Erik Lucero, Orion Martin, Jarrod R. McClean, Trevor McCourt, Xiao Mi, Kevin C. Miao, Masoud Mohseni, Shirin Montazeri, Wojciech Mruczkiewicz, Josh Mutus, Ofer Naaman, Matthew Neeley, Charles Neill, Michael Newman, Murphy Yuezen Niu, Thomas E. O'Brien, Alex Opremcak, Eric Ostby, Bálint Pató, Nicholas Redd, Pedram Roushan, Nicholas C. Rubin, Vladimir Shvarts, Doug Strain, Marco Szalay, Matthew D. Trevithick, Benjamin Villalonga, Theodore White, Z. Jamie Yao, Ping Yeh, Juhwan Yoo, Adam Zalcman, Hartmut Neven, Sergio Boixo, Vadim Smelyanskiy, Yu Chen, Anthony Megrant & Julian Kelly

2. Department of Electrical and Computer Engineering, University of California, Riverside, CA, USA

Alexander N. Korotkov

3. Department of Physics, University of California, Santa Barbara, CA, USA

Matt McEwen

4. Johannes Kepler University, Linz, Austria

Alexandru Paler

5. University of Texas at Dallas, Richardson, TX, USA

Alexandru Paler

6. Department of Electrical and Computer Engineering, University of Massachusetts, Amherst, MA, USA

Joseph C. Bardin

7. Pritzker School of Molecular Engineering, University of Chicago, Chicago, IL, USA

Alexandre Bourassa

8. Research Laboratory of Electronics, Massachusetts Institute of Technology,
Cambridge, MA, USA

Ami Greene

9. California Institute of Technology, Pasadena, CA, USA

Alexei Kitaev

Consortia

Google Quantum AI

- , Zijun Chen
- , Kevin J. Satzinger
- , Juan Atalaya
- , Alexander N. Korotkov
- , Andrew Dunsworth
- , Daniel Sank
- , Chris Quintana
- , Matt McEwen
- , Rami Barends
- , Paul V. Klimov
- , Sabrina Hong
- , Cody Jones
- , Andre Petukhov
- , Dvir Kafri
- , Sean Demura
- , Brian Burkett
- , Craig Gidney
- , Austin G. Fowler
- , Alexandru Paler
- , Harald Putterman
- , Igor Aleiner
- , Frank Arute
- , Kunal Arya
- , Ryan Babbush
- , Joseph C. Bardin
- , Andreas Bengtsson
- , Alexandre Bourassa

- , Michael Broughton
- , Bob B. Buckley
- , David A. Buell
- , Nicholas Bushnell
- , Benjamin Chiaro
- , Roberto Collins
- , William Courtney
- , Alan R. Derk
- , Daniel Eppens
- , Catherine Erickson
- , Edward Farhi
- , Brooks Foxen
- , Marissa Giustina
- , Ami Greene
- , Jonathan A. Gross
- , Matthew P. Harrigan
- , Sean D. Harrington
- , Jeremy Hilton
- , Alan Ho
- , Trent Huang
- , William J. Huggins
- , L. B. Ioffe
- , Sergei V. Isakov
- , Evan Jeffrey
- , Zhang Jiang
- , Kostyantyn Kechedzhi
- , Seon Kim
- , Alexei Kitaev
- , Fedor Kostritsa
- , David Landhuis
- , Pavel Laptev
- , Erik Lucero
- , Orion Martin
- , Jarrod R. McClean
- , Trevor McCourt
- , Xiao Mi
- , Kevin C. Miao
- , Masoud Mohseni
- , Shirin Montazeri
- , Wojciech Mruczkiewicz
- , Josh Mutus
- , Ofer Naaman

- , Matthew Neeley
- , Charles Neill
- , Michael Newman
- , Murphy Yuezhen Niu
- , Thomas E. O'Brien
- , Alex Opremcak
- , Eric Ostby
- , Bálint Pató
- , Nicholas Redd
- , Pedram Roushan
- , Nicholas C. Rubin
- , Vladimir Shvarts
- , Doug Strain
- , Marco Szalay
- , Matthew D. Trevithick
- , Benjamin Villalonga
- , Theodore White
- , Z. Jamie Yao
- , Ping Yeh
- , Juhwan Yoo
- , Adam Zalcman
- , Hartmut Neven
- , Sergio Boixo
- , Vadim Smelyanskiy
- , Yu Chen
- , Anthony Megrant
- & Julian Kelly

Contributions

Z.C., K.J.S., H.P., A.G.F., A.N.K. and J.K. designed the experiment. Z.C., K.J.S. and J.K. performed the experiment and analysed the data. C.Q., K.J.S., A. Petukhov and Y.C. developed the controlled-Z gate. M. McEwen, D.K., A. Petukhov and R. Barends developed the reset operation. M. McEwen and R. Barends performed experiments on leakage, reset and high-energy events in error correcting codes. D. Sank and Z.C. developed the readout operation. A.D., B.B., S.D. and A.M. led the design and fabrication of the processor. J.A. and A.N.K. developed and performed the p_{ij} analysis. C.J. developed the inverse Λ model and performed the simulations. A.G.F. and C.G. wrote the decoder and interface software. S. H., K.J.S. and J.K. developed the dynamical decoupling protocols. P.V.K. developed error mitigation techniques based on system frequency optimization. Z.C., K.J.S., S.H., P.V.K. and J.K. developed error correction calibration techniques. Z.C., K.J.S. and J.K. wrote the manuscript. S.B., V.

Smelyanskiy, Y.C., A.M. and J.K. coordinated the team-wide error correction effort. Work by H. Putterman was done prior to joining AWS. All authors contributed to revising the manuscript and writing the Supplementary Information. All authors contributed to the experimental and theoretical infrastructure to enable the experiment.

Corresponding authors

Correspondence to [Anthony Megrant](#) or [Julian Kelly](#).

Ethics declarations

Competing interests

The authors declare no competing interests.

Additional information

Peer review information *Nature* thanks Carmen Almudever, Benjamin Brown and the other, anonymous, reviewer(s) for their contribution to the peer review of this work. Peer reviewer reports are available.

Publisher's note Springer Nature remains neutral with regard to jurisdictional claims in published maps and institutional affiliations.

Supplementary information

[Supplementary Information](#)

This file contains Supplementary Information, including Supplementary Figures 1-28, Supplementary Tables 1-7, and additional references.

[Peer Review File](#)

Rights and permissions

Open Access This article is licensed under a Creative Commons Attribution 4.0 International License, which permits use, sharing, adaptation, distribution and reproduction in any medium or format, as long as you give appropriate credit to the original author(s) and the source, provide a link to the Creative Commons license, and indicate if changes were made. The images or other third party material in this article

are included in the article's Creative Commons license, unless indicated otherwise in a credit line to the material. If material is not included in the article's Creative Commons license and your intended use is not permitted by statutory regulation or exceeds the permitted use, you will need to obtain permission directly from the copyright holder. To view a copy of this license, visit <http://creativecommons.org/licenses/by/4.0/>.

[Reprints and Permissions](#)

About this article



Check for
updates

Cite this article

Google Quantum AI. Exponential suppression of bit or phase errors with cyclic error correction. *Nature* **595**, 383–387 (2021). <https://doi.org/10.1038/s41586-021-03588-y>

[Download citation](#)

- Received: 11 January 2021
- Accepted: 28 April 2021
- Published: 14 July 2021
- Issue Date: 15 July 2021
- DOI: <https://doi.org/10.1038/s41586-021-03588-y>

Comments

By submitting a comment you agree to abide by our [Terms](#) and [Community Guidelines](#). If you find something abusive or that does not comply with our terms or guidelines please flag it as inappropriate.

[Download PDF](#)

Advertisement

| [Section menu](#) | [Main menu](#) |

- Article
- [Published: 14 July 2021](#)

Amazonia as a carbon source linked to deforestation and climate change

- [Luciana V. Gatti](#) [ORCID: orcid.org/0000-0003-4908-8974^{1,2}](#),
- [Luana S. Basso¹](#),
- [John B. Miller³](#),
- [Manuel Gloor⁴](#),
- [Lucas Gatti Domingues^{1,2,5}](#),
- [Henrique L. G. Cassol](#) [ORCID: orcid.org/0000-0001-6728-4712¹](#),
- [Graciela Tejada¹](#),
- [Luiz E. O. C. Aragão^{1,6}](#),
- [Carlos Nobre⁷](#),
- [Wouter Peters](#) [ORCID: orcid.org/0000-0001-8166-2070^{8,9}](#),
- [Luciano Marani](#) [ORCID: orcid.org/0000-0001-7382-464X¹](#),
- [Egidio Arai¹](#),
- [Alber H. Sanches](#) [ORCID: orcid.org/0000-0001-7966-2880¹](#),
- [Sergio M. Corrêa](#) [ORCID: orcid.org/0000-0002-0038-0790^{1,10}](#),
- [Liana Anderson](#) [ORCID: orcid.org/0000-0001-9545-5136¹¹](#),
- [Celso Von Randow](#) [ORCID: orcid.org/0000-0003-1045-4316¹](#),
- [Caio S. C. Correia^{1,2}](#),
- [Stephane P. Crispim¹](#) &
- [Raiane A. L. Neves¹](#)

[Nature](#) volume 595, pages 388–393 (2021) [Cite this article](#)

- 3945 Accesses

- 1911 Altmetric
- [Metrics details](#)

Subjects

- [Carbon cycle](#)

Abstract

Amazonia hosts the Earth's largest tropical forests and has been shown to be an important carbon sink over recent decades^{1,2,3}. This carbon sink seems to be in decline, however, as a result of factors such as deforestation and climate change^{1,2,3}. Here we investigate Amazonia's carbon budget and the main drivers responsible for its change into a carbon source. We performed 590 aircraft vertical profiling measurements of lower-tropospheric concentrations of carbon dioxide and carbon monoxide at four sites in Amazonia from 2010 to 2018⁴. We find that total carbon emissions are greater in eastern Amazonia than in the western part, mostly as a result of spatial differences in carbon-monoxide-derived fire emissions.

Southeastern Amazonia, in particular, acts as a net carbon source (total carbon flux minus fire emissions) to the atmosphere. Over the past 40 years, eastern Amazonia has been subjected to more deforestation, warming and moisture stress than the western part, especially during the dry season, with the southeast experiencing the strongest trends^{5,6,7,8,9}. We explore the effect of climate change and deforestation trends on carbon emissions at our study sites, and find that the intensification of the dry season and an increase in deforestation seem to promote ecosystem stress, increase in fire occurrence, and higher carbon emissions in the eastern Amazon. This is in line with recent studies that indicate an increase in tree mortality and a reduction in photosynthesis as a result of climatic changes across Amazonia^{1,10}.

Access options

Subscribe to Journal

Get full journal access for 1 year

\$199.00

only \$3.90 per issue

[Subscribe](#)

All prices are NET prices.

VAT will be added later in the checkout.

Tax calculation will be finalised during checkout.

Rent or Buy article

Get time limited or full article access on ReadCube.

from \$8.99

[Rent or Buy](#)

All prices are NET prices.

Additional access options:

- [Log in](#)
- [Access through your institution](#)
- [Learn about institutional subscriptions](#)

Fig. 1: Regions of influence.



Fig. 2: Annual mean VPs.

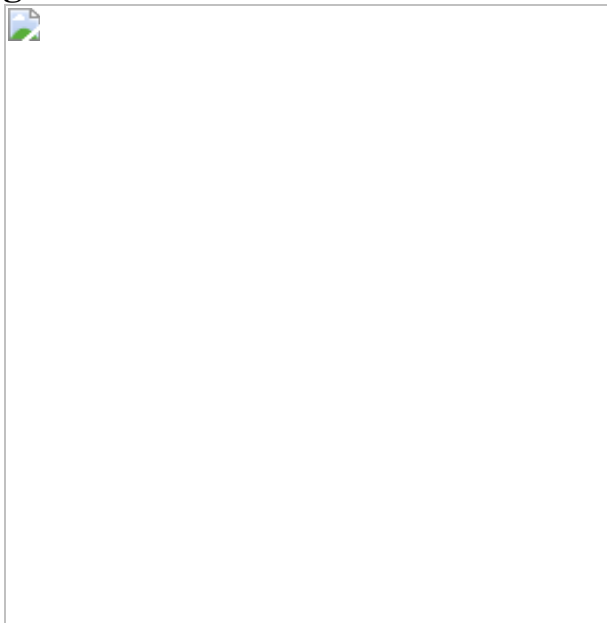


Fig. 3: Annual carbon fluxes.

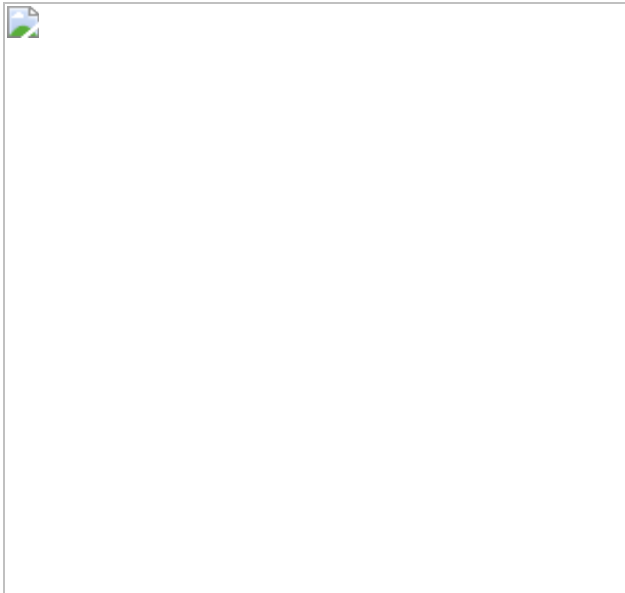


Fig. 4: 40-year precipitation and temperature trends.

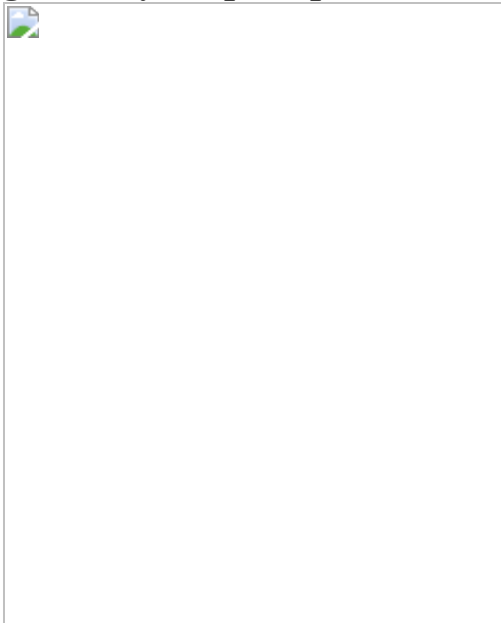
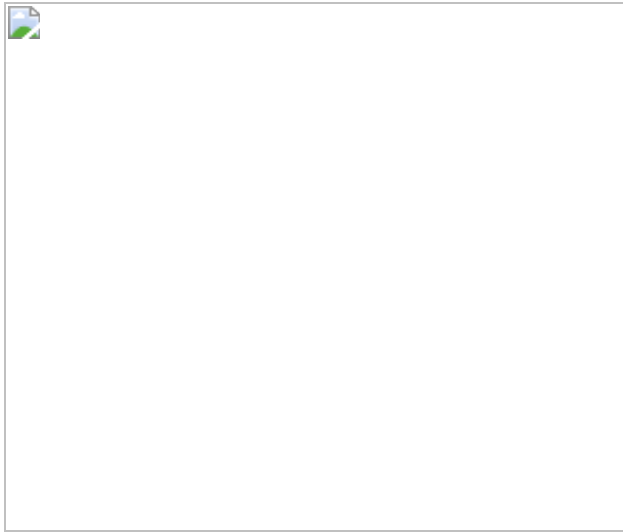


Fig. 5: Spatial results overview.



Data availability

The CO₂ VP data that support the findings of this study are available from PANGAEA Data Archiving, at <https://doi.org/10.1594/PANGAEA.926834>. [Source data](#) are provided with this paper.

References

1. 1.

Brienen, R. J. W. et al. Long-term decline of the Amazon carbon sink. *Nature* **519**, 344–348 (2015).

[ADS](#) [CAS](#) [Google Scholar](#)

2. 2.

Phillips, O. L. & Brienen, R. J. W. Carbon uptake by mature Amazon forests has mitigated Amazon nations' carbon emissions. *Carbon Balance Manag.* **12**, 1 (2017).

[PubMed](#) [PubMed Central](#) [Google Scholar](#)

3. 3.

Hubau, W. et al. Asynchronous carbon sink saturation in African and Amazonian tropical forests. *Nature* **579**, 80–87 (2020).

[ADS](#) [CAS](#) [Google Scholar](#)

4. 4.

Gatti, L. V. et al. Drought sensitivity of Amazonian carbon balance revealed by atmospheric measurements. *Nature* **506**, 76–80 (2014).

[ADS](#) [CAS](#) [Google Scholar](#)

5. 5.

Barkhordarian, A., Saatchi, S. S., Behrangi, A., Loikith, P. C. & Mechoso, C. R. A recent systematic increase in vapor pressure deficit over tropical South America. *Sci. Rep.* **9**, 15331 (2019).

[ADS](#) [PubMed](#) [PubMed Central](#) [Google Scholar](#)

6. 6.

Leite-Filho, A. T., de Sousa Pontes, V. Y. & Costa, M. H. Effects of deforestation on the onset of the rainy season and the duration of dry spells in southern Amazonia. *J. Geophys. Res. Atmos.* **124**, 5268–5281 (2019).

[ADS](#) [Google Scholar](#)

7. 7.

Fu, R. et al. Increased dry-season length over southern Amazonia in recent decades and its implication for future climate projection. *Proc. Natl Acad. Sci. USA* **110**, 18110–18115 (2013).

[ADS](#) [CAS](#) [PubMed](#) [PubMed Central](#) [Google Scholar](#)

8. 8.

Tan, P. H., Chou, C. & Tu, J. Y. Mechanisms of global warming impacts on robustness of tropical precipitation asymmetry. *J. Clim.* **21**, 5585–5602 (2008).

[ADS](#) [Google Scholar](#)

9. 9.

Spracklen, D. V., Arnold, S. R. & Taylor, C. M. Observations of increased tropical rainfall preceded by air passage over forests. *Nature* **489**, 282–285 (2012); corrigendum **494**, 390 (2013).

[ADS](#) [CAS](#) [Google Scholar](#)

10. 10.

Doughty, C. E. et al. Drought impact on forest carbon dynamics and fluxes in Amazonia. *Nature* **519**, 78–82 (2015).

[ADS](#) [CAS](#) [Google Scholar](#)

11. 11.

Malhi, Y. et al. The regional variation of aboveground live biomass in old-growth Amazonian forests. *Glob. Change Biol.* **12**, 1107–1138 (2006).

[ADS](#) [Google Scholar](#)

12. 12.

Cox, P. M., Betts, R. A., Jones, C. D., Spall, S. A. & Totterdell, I. J. Acceleration of global warming due to carbon-cycle feedbacks in a coupled climate model. *Nature* **408**, 184–187 (2000); erratum **408**, 750 (2000).

[ADS](#) [CAS](#) [Google Scholar](#)

13. 13.

Aragão, L. E. O. C. et al. 21st Century drought-related fires counteract the decline of Amazon deforestation carbon emissions. *Nat. Commun.* **9**, 536 (2018).

[ADS](#) [PubMed](#) [PubMed Central](#) [Google Scholar](#)

14. 14.

Staal, A. et al. Forest-rainfall cascades buffer against drought across the Amazon. *Nat. Clim. Chang.* **8**, 539–543 (2018).

[ADS](#) [Google Scholar](#)

15. 15.

Costa, M. H. & Foley, J. A. Trends in the hydrologic cycle of the Amazon Basin. *J. Geophys. Res. Atmos.* **104**, 14189–14198 (1999).

[ADS](#) [Google Scholar](#)

16. 16.

Aragão, L. E. O. C. The rainforest's water pump. *Nature* **489**, 217–218 (2012).

[ADS](#) [Google Scholar](#)

17. 17.

Proyecto MapBiomas Amazonía. Colección [2.0] de los mapas anuales de cobertura y uso del suelo. *Mapbiomas_Amazonia* <http://amazonia.mapbiomas.org/mapas-de-la-coleccion> (2020).

18. 18.

Baker, J. C. A. & Spracklen, D. V. Climate benefits of intact Amazon forests and the biophysical consequences of disturbance. *Front. For.*

Glob. Change **2**, 47 (2019).

19. 19.

Almeida, C. T., Oliveira-Júnior, J. F., Delgado, R. C., Cubo, P. & Ramos, M. C. Spatiotemporal rainfall and temperature trends throughout the Brazilian Legal Amazon, 1973–2013. *Int. J. Climatol.* **37**, 2013–2026 (2017).

[Google Scholar](#)

20. 20.

Marengo, J. A. et al. Changes in climate and land use over the Amazon region: current and future variability and trends. *Front. Earth Sci.* **6**, 228 (2018).

21. 21.

Costa, M. H. & Pires, G. F. Effects of Amazon and Central Brazil deforestation scenarios on the duration of the dry season in the arc of deforestation. *Int. J. Climatol.* **30**, 1970–1979 (2010).

[Google Scholar](#)

22. 22.

Nobre, C. A. et al. Land-use and climate change risks in the amazon and the need of a novel sustainable development paradigm. *Proc. Natl Acad. Sci. USA* **113**, 10759–10768 (2016).

[ADS](#) [CAS](#) [PubMed](#) [PubMed Central](#) [Google Scholar](#)

23. 23.

Silva, C. V. J. et al. Estimating the multi-decadal carbon deficit of burned Amazonian forests. *Environ. Res. Lett.* **15**, 114023 (2020).

[ADS](#) [CAS](#) [Google Scholar](#)

24. 24.

van der Werf, G. R. et al. Global fire emissions and the contribution of deforestation, savanna, forest, agricultural, and peat fires (1997–2009). *Atmos. Chem. Phys.* **10**, 11707–11735 (2010).

[ADS](#) [Google Scholar](#)

25. 25.

NASA/GISS. *Global Climate Change, Global Temperature* <https://climate.nasa.gov/vital-signs/global-temperature/> (accessed 6 March 2020).

26. 26.

Maeda, E. E. et al. Evapotranspiration seasonality across the Amazon Basin. *Earth Syst. Dyn.* **8**, 439–454 (2017).

[ADS](#) [Google Scholar](#)

27. 27.

Haghtalab, N., Moore, N., Heerspink, B. P. & Hyndman, D. W. Evaluating spatial patterns in precipitation trends across the Amazon basin driven by land cover and global scale forcings. *Theor. Appl. Climatol.* **140**, 411–427 (2020).

[ADS](#) [Google Scholar](#)

28. 28.

Leite-Filho, A. T., Costa, M. H. & Fu, R. The southern Amazon rainy season: the role of deforestation and its interactions with large-scale mechanisms. *Int. J. Climatol.* **40**, 2328–2341 (2020).

[Google Scholar](#)

29. 29.

Esquivel-Muelbert, A. et al. Compositional response of Amazon forests to climate change. *Glob. Change Biol.* **25**, 39–56 (2019).

[ADS](#) [Google Scholar](#)

30. 30.

Liu, J. et al. Contrasting carbon cycle responses of the tropical continents to the 2015–2016 El Niño. *Science* **358**, eaam5690 (2017).

[Google Scholar](#)

31. 31.

Alkama, R. & Cescatti, A. Biophysical climate impacts of recent changes in global forest cover. *Science* **351**, 600–604 (2016).

[ADS](#) [CAS](#) [Google Scholar](#)

32. 32.

INPE. *Amazon Deforestation Monitoring Project (PRODES)* <http://www.obt.inpe.br/OBT/assuntos/programas/amazonia/prodes> (2019).

33. 33.

Eva, H. D. et al. *A Proposal for Defining the Geographical Boundaries of Amazonia; Synthesis of the Results from an Expert Consultation Workshop Organized by the European Commission in Collaboration with the Amazon Cooperation Treaty Organization*. Report No. 21808-EN (European Commission, 2005).

34. 34.

Olson, D. M. et al. Terrestrial ecoregions of the world: a new map of life on Earth. *Bioscience* **51**, 933–938 (2001).

[Google Scholar](#)

35. 35.

Tans, P. P., Bakwin, P. S. & Guenter, D. W. A feasible Global Carbon Cycle Observing System: a plan to decipher today's carbon cycle based on observations. *Glob. Change Biol.* **2**, 309–318 (1996).

[ADS](#) [Google Scholar](#)

36. 36.

Marani, L. et al. Estimation methods of greenhouse gases fluxes and the human influence in the CO₂ removal capability of the Amazon Forest. *Rev. Virtual Química* **12**, 5 (2020).

[Google Scholar](#)

37. 37.

Miller, J. B. et al. Airborne measurements indicate large methane emissions from the eastern Amazon basin. *Geophys. Res. Lett.* **34**, L10809 (2007).

[ADS](#) [Google Scholar](#)

38. 38.

Gatti, L. V. et al. Vertical profiles of CO₂ above eastern Amazonia suggest a net carbon flux to the atmosphere and balanced biosphere between 2000 and 2009. *Tellus B* **62**, 581–594 (2010).

[ADS](#) [Google Scholar](#)

39. 39.

Basso, L. S. et al. Seasonality and interannual variability of CH₄ fluxes from the eastern Amazon Basin inferred from atmospheric mole fraction profiles. *J. Geophys. Res. Atmos.* **121**, 168–184 (2016).

[ADS](#) [CAS](#) [PubMed](#) [PubMed Central](#) [Google Scholar](#)

40. 40.

D'Amelio, M. T. S., Gatti, L. V., Miller, J. B. & Tans, P. Regional N₂O fluxes in Amazonia derived from aircraft vertical profiles. *Atmos. Chem. Phys.* **9**, 8785–8797 (2009).

[ADS](#) [Google Scholar](#)

41. 41.

Gatti Domingues, L. et al. A new background method for greenhouse gases flux calculation based in back-trajectories over the Amazon. *Atmosphere* **11**, 734 (2020).

[ADS](#) [Google Scholar](#)

42. 42.

Draxler, R. R. *HYSPLIT 4 User's Guide*. Technical Memorandum ERL ARL-230 (NOAA, 1999); https://www.arl.noaa.gov/wp_arl/wp-content/uploads/documents/reports/arl-230.pdf

43. 43.

Cassol, H. L. G. et al. Determination of region of influence obtained by aircraft vertical profiles using the density of trajectories from the HYSPLIT model. *Atmosphere* **11**, 1073 (2020).

[ADS](#) [Google Scholar](#)

44. 44.

Stavrakou, T. et al. How consistent are top-down hydrocarbon emissions based on formaldehyde observations from GOME-2 and OMI? *Atmos. Chem. Phys.* **15**, 11861–11884 (2015).

[ADS](#) [CAS](#) [Google Scholar](#)

45. 45.

Stein, A. F. et al. NOAA's HYSPLIT atmospheric transport and dispersion modeling system. *Bull. Am. Meteorol. Soc.* **96**, 2059–2077 (2015).

[ADS](#) [Google Scholar](#)

46. 46.

Berrisford, P. et al. Atmospheric conservation properties in ERA-Interim. *Q. J. R. Meteorol. Soc.* **137**, 1381–1399 (2011).

[ADS](#) [Google Scholar](#)

47. 47.

Adler, R. et al. The Global Precipitation Climatology Project (GPCP) monthly analysis (New Version 2.3) and a review of 2017 global precipitation. *Atmosphere* **9**, 138 (2018).

[ADS](#) [PubMed](#) [PubMed Central](#) [Google Scholar](#)

48. 48.

Huffman, G. J. et al. Global precipitation at one-degree daily resolution from multisatellite observations. *J. Hydrometeorol.* **2**, 36–50 (2001).

[ADS](#) [Google Scholar](#)

49. 49.

Santos, S. R. Q., Sansigolo, C. A., Neves, T. T. A. T. & Santos, A. P. Variabilidade sazonal da precipitação na Amazônia: Validação da série de precipitação mensal do GPCC. *Rev. Bras. Geogr. Física* **10**, 1721–1729 (2017).

[Google Scholar](#)

50. 50.

Landerer, F. *JPL TELLUS GRACE Level-3 Monthly LAND Water-Equivalent-Thickness Surface-Mass Anomaly Release 6.0 in netCDF/ASCII/GeoTIFF Formats*
https://podaac.jpl.nasa.gov/dataset/TELLUS_GRAC_L3_JPL_RL06_LND (2019).

51. 51.

Landerer, F. W. & Swenson, S. C. Accuracy of scaled GRACE terrestrial water storage estimates. *Wat. Resour. Res.* **48**, W04531 (2012).

[ADS](#) [Google Scholar](#)

52. 52.

Giglio, L., Boschetti, L., Roy, D. P., Humber, M. L. & Justice, C. O. The Collection 6 MODIS burned area mapping algorithm and product. *Remote Sens. Environ.* **217**, 72–85 (2018).

[ADS](#) [PubMed](#) [PubMed Central](#) [Google Scholar](#)

53. 53.

Vermote, E. F., El Saleous, N. Z. & Justice, C. O. Atmospheric correction of MODIS data in the visible to middle infrared: first results. *Remote Sens. Environ.* **83**, 97–111 (2002).

[ADS](#) [Google Scholar](#)

54. 54.

Justice, C. et al. An overview of MODIS Land data processing and product status. *Remote Sens. Environ.* **83**, 3–15 (2002).

[ADS](#) [Google Scholar](#)

55. 55.

Friedl, M. A. et al. MODIS Collection 5 global land cover: algorithm refinements and characterization of new datasets. *Remote Sens. Environ.* **114**, 168–182 (2010).

[ADS](#) [Google Scholar](#)

56. 56.

Huete, A. et al. Overview of the radiometric and biophysical performance of the MODIS vegetation indices. *Remote Sens. Environ.* **83**, 195–213 (2002).

[ADS](#) [Google Scholar](#)

57. 57.

Dalagnol, R., Wagner, F. H., Galvão, L. S., Oliveira, L. E. & Aragao, C. *The MANVI Product: MODIS (MAIAC) Nadir-Solar Adjusted Vegetation Indices (EVI and NDVI) for South America* https://zenodo.org/record/3159488#.YLeQtH4o_IU (2019).

58. 58.

de Almeida, C. A. et al. High spatial resolution land use and land cover mapping of the Brazilian Legal Amazon in 2008 using Landsat-5/TM and MODIS data. *Acta Amazon.* **46**, 291–302 (2016).

[Google Scholar](#)

59. 59.

Jiang, N. & Riley, M. L. Exploring the utility of the random forest method for forecasting ozone pollution in SYDNEY. *Int. J. Environ. Sustain. Dev.* **1**, 245–254 (2015).

[Google Scholar](#)

60. 60.

Stekhoven, D. J. & Buhlmann, P. MissForest–non-parametric missing value imputation for mixed-type data. *Bioinformatics* **28**, 112–118 (2012).

[CAS](#) [Google Scholar](#)

61. 61.

Junninen, H., Niska, H., Tuppurainen, K., Ruuskanen, J. & Kolehmainen, M. Methods for imputation of missing values in air quality data sets. *Atmos. Environ.* **38**, 2895–2907 (2004).

[ADS](#) [CAS](#) [Google Scholar](#)

62. 62.

R Core Team. *R: A Language and Environment for Statistical Computing* <http://www.R-project.org> (R Foundation for Statistical Computing, 2018).

63. 63.

Stohl, A., Forster, C., Frank, A., Seibert, P. & Wotawa, G. The Lagrangian particle dispersion model FLEXPART version 6.2. *Atmos. Chem. Phys.* **5**, 2461–2474 (2005).

[ADS](#) [CAS](#) [Google Scholar](#)

64. 64.

Freitas, S. R. et al. The Coupled Aerosol and Tracer Transport model to the Brazilian developments on the Regional Atmospheric Modeling System (CATT-BRAMS) – Part 1: model description and evaluation. *Atmos. Chem. Phys.* **9**, 2843–2861 (2009).

[ADS](#) [CAS](#) [Google Scholar](#)

[Download references](#)

Acknowledgements

We thank S. Denning and E. Mitchard for valuable reviews. This work was funded by many projects supporting the long-term measurements: State of São Paulo Science Foundation – FAPESP (16/02018-2, 11/51841-0, 08/58120-3, 18/14006-4, 18/14423-4, 18/18493-7, 19/21789-8, 11/17914-0), UK Environmental Research Council (NERC) AMAZONICA project (NE/F005806/1), NASA grants (11-CMS11-0025, NRMJ1000-17-00431), European Research Council (ERC) under Horizon 2020 (649087), 7FP EU (283080), MCTI/CNPq (2013), CNPq (134878/2009-4, 310130/2017-4, 305054/2016-3, 314416/2020-0). We thank the staff at NOAA/GML who provided advice and technical support for air sampling and measurements in Brazil, and the pilots and technical team at aircraft sites who collected the air samples. We thank J. F. Mueller for providing modelled biogenic CO fluxes.

Author information

Affiliations

1. General Coordination of Earth Science (CGCT), National Institute for Space Research (INPE), São José dos Campos, Brazil

Luciana V. Gatti, Luana S. Basso, Lucas Gatti Domingues, Henrique L. G. Cassol, Graciela Tejada, Luiz E. O. C. Aragão, Luciano Marani, Egidio Arai, Alber H. Sanches, Sergio M. Corrêa, Celso Von Randow, Caio S. C. Correia, Stephane P. Crispim & Raiane A. L. Neves

2. Nuclear and Energy Research Institute (IPEN), São Paulo, Brazil

Luciana V. Gatti, Lucas Gatti Domingues & Caio S. C. Correia

3. Global Monitoring Laboratory, National Oceanic and Atmospheric Administration (NOAA), Boulder, CO, USA

John B. Miller

4. School of Geography, University of Leeds, Leeds, UK

Manuel Gloor

5. National Isotope Centre, GNS Science, Lower Hutt, New Zealand

Lucas Gatti Domingues

6. College of Life and Environmental Sciences, University of Exeter, Exeter, UK

Luiiz E. O. C. Aragão

7. Institute of Advanced Studies (IEA), University of São Paulo (USP), São Paulo, Brazil

Carlos Nobre

8. Department of Meteorology and Air Quality, Wageningen University, Wageningen, The Netherlands

Wouter Peters

9. Centre for Isotope Research, University of Groningen, Groningen, The Netherlands

Wouter Peters

10. Rio de Janeiro State University (UERJ), Resende, Brazil

Sergio M. Corrêa

11. National Center for Monitoring and Early Warning of Natural Disasters (CEMADEN), São José dos Campos, Brazil

Liana Anderson

Authors

1. Luciana V. Gatti

[View author publications](#)

You can also search for this author in [PubMed](#) [Google Scholar](#)

2. Luana S. Basso

[View author publications](#)

You can also search for this author in [PubMed](#) [Google Scholar](#)

3. John B. Miller

[View author publications](#)

You can also search for this author in [PubMed](#) [Google Scholar](#)

4. Manuel Gloor

[View author publications](#)

You can also search for this author in [PubMed](#) [Google Scholar](#)

5. Lucas Gatti Domingues

[View author publications](#)

You can also search for this author in [PubMed](#) [Google Scholar](#)

6. Henrique L. G. Cassol

[View author publications](#)

You can also search for this author in [PubMed](#) [Google Scholar](#)

7. Graciela Tejada

[View author publications](#)

You can also search for this author in [PubMed](#) [Google Scholar](#)

8. Luiz E. O. C. Aragão
[View author publications](#)

You can also search for this author in [PubMed](#) [Google Scholar](#)

9. Carlos Nobre
[View author publications](#)

You can also search for this author in [PubMed](#) [Google Scholar](#)

10. Wouter Peters
[View author publications](#)

You can also search for this author in [PubMed](#) [Google Scholar](#)

11. Luciano Marani
[View author publications](#)

You can also search for this author in [PubMed](#) [Google Scholar](#)

12. Egidio Arai
[View author publications](#)

You can also search for this author in [PubMed](#) [Google Scholar](#)

13. Alber H. Sanches
[View author publications](#)

You can also search for this author in [PubMed](#) [Google Scholar](#)

14. Sergio M. Corrêa
[View author publications](#)

You can also search for this author in [PubMed](#) [Google Scholar](#)

15. Liana Anderson
[View author publications](#)

You can also search for this author in [PubMed](#) [Google Scholar](#)

16. Celso Von Rando

[View author publications](#)

You can also search for this author in [PubMed](#) [Google Scholar](#)

17. Caio S. C. Correia

[View author publications](#)

You can also search for this author in [PubMed](#) [Google Scholar](#)

18. Stephane P. Crispim

[View author publications](#)

You can also search for this author in [PubMed](#) [Google Scholar](#)

19. Raiane A. L. Neves

[View author publications](#)

You can also search for this author in [PubMed](#) [Google Scholar](#)

Contributions

L.V.G., M.G. and J.B.M. conceived the basin-wide measurement programme and approach; L.V.G. wrote the paper; all co-authors participated in scientific meetings to interpret the data, and commented on and reviewed the manuscript; L.G.D., A.H.S., L.S.B., H.L.G.C., G.T., L.M. and L.V.G. contributed to the region-of-influence study; L.V.G., H.L.G.C., E.A., L.S.B., S.M.C. and J.B.M. contributed to the climate data weighted analysis; L.G.D., C.S.C.C., S.M.C. and R.A.L.N. contributed to the greenhouse gas concentration analysis; G.T. provided deforestation analyses; J.B.M. and L.V.G. contributed to the estimation of biogenic CO₂.

Corresponding author

Correspondence to [Luciana V. Gatti](#).

Ethics declarations

Competing interests

The authors declare no competing interests.

Additional information

Peer review information *Nature* thanks Scott Denning, Edward Mitchard and the other, anonymous, reviewer(s) for their contribution to the peer review of this work. Peer reviewer reports are available.

Publisher's note Springer Nature remains neutral with regard to jurisdictional claims in published maps and institutional affiliations.

Extended data figures and tables

[Extended Data Fig. 1 VPs, time series and annual mean CO₂ concentrations.](#)

a, Time series of mean VPs of the CO₂ mole fractions of the flasks below 1.5 km a.s.l. (red circles) and above 3.8 km a.s.l. (blue circles) for sites SAN, ALF, RBA and TAB_TEF (590 VPs) and the background sites RPB, ASC and CPT. **b**, Annual mean VPs for the four sites (annual mean per height; see [Methods](#)). **c**, Annual mean ΔVP (see [Methods](#)) for each site and year. **d**, Annual mean differences between mean CO₂ mole fractions below 1.5 km a.s.l. and means above 3.8 km a.s.l. for each site and year (see [Methods](#)). **e**, Partial column annual means plotted against annual mean fluxes, by site.

[Source data](#)

[Extended Data Fig. 2 Regions of influence.](#)

a, Mean quarterly regions of influence for the ALF, SAN, RBA, TEF and TAB sites, averaged between 2010 and 2018, calculated using the density of back-trajectories (see [Methods](#)). **b**, Deforestation inside quarterly regions of

influence and the Amazon mask (purple line) using data from PRODES³² (see [Methods](#)). **c**, Annual mean regions of influence (trajectory densities) averaged between 2010 and 2018.

Extended Data Fig. 3 Seasonal carbon flux and driver variables.

Average monthly means of potential flux driver variables at sites TAB_TEF, SAN, RBA and ALF in 2010–2018. Grey bands denote the standard deviation of the monthly mean.

Extended Data Fig. 4 Time series of carbon flux and driver variables.

As in Extended Data Fig. 3, but showing the full time series of monthly means from 2010 to 2018 for SAN, ALF, TAB_TEF and RBA. Grey bands as in Extended Data Fig. 3, showing the 2010–2018 standard deviation for each month.

Extended Data Fig. 5 ALF NBE drivers.

a, ALF annual mean NBE (NBE = total C flux – fire C flux, in $\text{g C m}^{-2} \text{ d}^{-1}$) from 2010 to 2018. Error bars are uncertainties related to the background, travel time trajectories, emission ratios CO/CO₂ and natural CO flux (see [Methods](#)). **b**, Annual mean FC_{NBE}, annual mean temperature and GRACE (equivalent water thickness) satellite soil water storage anomalies.

Extended Data Fig. 6 Amazon carbon fluxes per region.

a, Separation of three regions inside the Amazon Mask ($7,256,362 \text{ km}^2$, purple line). Region 1: area of combined regions of influence for SAN and ALF; region 2: area of combined region of influence for RBA and TAB (2010–2012) and RBA and TEF (2013–2018), excluding region 1; region 3: the remaining area outside regions 1 and 2 and inside the purple line. **b**,

Annual mean fluxes for regions 1, 2 and 3 (total, blue line; fire, red line; NBE, green line).

Extended Data Fig. 7 Mean temperature and precipitation in Amazonia over the past 40 years.

a, Monthly mean temperature in Amazonia in 1979–2018, calculated using ERA Interim (ECMWF) monthly means (see [Methods](#)). Grey points are monthly mean temperatures from 1979 to 2018. Blue and red circles show decadal monthly mean temperatures for 1979–1988 and 2009–2018, respectively. Error bars denote one standard deviation for the decade. **b**, Blue circles are annual mean temperatures; green circles show mean temperatures for January, February and March; red circles show mean temperatures for August, September and October. **c**, As in **a**, but for precipitation calculated using GPCP version 2.3 (see [Methods](#)). **d**, Blue circles are annual total precipitation; green circles are total precipitation for January, February and March; and red circles are total precipitation for August, September and October.

Extended Data Fig. 8 Seasonal temperature and precipitation over the past 40 years.

Monthly precipitation (GPCP v2.3) and monthly mean temperature (ERA-Interim) for TAB, SAN, RBA, ALF and TEF, calculated using spatial weightings from 2010–2018 quarterly regions of influence (Extended Data Fig. [2a](#)) inside the Amazon mask. Symbols are as in Extended Data Fig. [7](#).

Extended Data Table 1 Analysis of temperature and precipitation data obtained over the past 40 years

[Full size table](#)

Extended Data Table 2 Summary of the main results for ALF, SAN, RBA and TAB_TEF

[Full size table](#)

Supplementary information

Supplementary Information

This file contains 8 Supplementary Figures and 2 Supplementary Tables – see the guide at the beginning of the file for details.

Peer Review File

Source data

Source Data Fig. 2

Source Data Fig. 3

Source Data Fig. 4

Source Data Extended Data Fig. 1

Rights and permissions

Reprints and Permissions

About this article



Check for
updates

Cite this article

Gatti, L.V., Basso, L.S., Miller, J.B. *et al.* Amazonia as a carbon source linked to deforestation and climate change. *Nature* **595**, 388–393 (2021). <https://doi.org/10.1038/s41586-021-03629-6>

Download citation

- Received: 11 September 2020
- Accepted: 10 May 2021
- Published: 14 July 2021
- Issue Date: 15 July 2021
- DOI: <https://doi.org/10.1038/s41586-021-03629-6>

Comments

By submitting a comment you agree to abide by our [Terms](#) and [Community Guidelines](#). If you find something abusive or that does not comply with our terms or guidelines please flag it as inappropriate.

[Access through your institution](#)

[Change institution](#)

[Buy or subscribe](#)

Associated Content

[**Southeast Amazonia is no longer a carbon sink**](#)

- Scott Denning

Advertisement

This article was downloaded by **calibre** from <https://www.nature.com/articles/s41586-021-03629-6>

- Article
- [Published: 14 July 2021](#)

A lithium-isotope perspective on the evolution of carbon and silicon cycles

- [Boriana Kalderon-Asael](#) [ORCID: orcid.org/0000-0002-5442-8219¹](#),
- [Joachim A. R. Katchinoff](#) [ORCID: orcid.org/0000-0003-1286-8344¹](#),
- [Noah J. Planavsky](#) [ORCID: orcid.org/0000-0001-5849-8508¹](#),
- [Ashleigh v. S. Hood²](#),
- [Mathieu Dellinger](#) [ORCID: orcid.org/0000-0002-1770-4333³](#),
- [Eric J. Bellefroid¹](#),
- [David S. Jones](#) [ORCID: orcid.org/0000-0001-8478-3599⁴](#),
- [Axel Hofmann⁵](#),
- [Frantz Ossa Ossa](#) [ORCID: orcid.org/0000-0003-1875-8082^{5,6}](#),
- [Francis A. Macdonald](#) [ORCID: orcid.org/0000-0001-8416-4894⁷](#),
- [Chunjiang Wang⁸](#),
- [Terry T. Isson](#) [ORCID: orcid.org/0000-0002-1040-0230^{1,9}](#),
- [Jack G. Murphy](#) [ORCID: orcid.org/0000-0002-7579-6213¹⁰](#),
- [John A. Higgins¹⁰](#),
- [A. Joshua West](#) [ORCID: orcid.org/0000-0001-6909-1471¹¹](#),
- [Malcolm W. Wallace²](#),
- [Dan Asael¹](#) &
- [Philip A. E. Pogge von Strandmann](#) [ORCID: orcid.org/0000-0001-7181-4165^{12,13}](#)

[Nature](#) volume **595**, pages 394–398 (2021) [Cite this article](#)

- 1079 Accesses

- 176 Altmetric
- [Metrics details](#)

Subjects

- [Carbon cycle](#)
- [Palaeoclimate](#)

Abstract

The evolution of the global carbon and silicon cycles is thought to have contributed to the long-term stability of Earth's climate^{1,2,3}. Many questions remain, however, regarding the feedback mechanisms at play, and there are limited quantitative constraints on the sources and sinks of these elements in Earth's surface environments^{4,5,6,7,8,9,10,11,12}. Here we argue that the lithium-isotope record can be used to track the processes controlling the long-term carbon and silicon cycles. By analysing more than 600 shallow-water marine carbonate samples from more than 100 stratigraphic units, we construct a new carbonate-based lithium-isotope record spanning the past 3 billion years. The data suggest an increase in the carbonate lithium-isotope values over time, which we propose was driven by long-term changes in the lithium-isotopic conditions of sea water, rather than by changes in the sedimentary alterations of older samples. Using a mass-balance modelling approach, we propose that the observed trend in lithium-isotope values reflects a transition from Precambrian carbon and silicon cycles to those characteristic of the modern. We speculate that this transition was linked to a gradual shift to a biologically controlled marine silicon cycle and the evolutionary radiation of land plants^{13,14}.

Access options

Subscribe to Journal

Get full journal access for 1 year

\$199.00

only \$3.90 per issue

[Subscribe](#)

All prices are NET prices.

VAT will be added later in the checkout.

Tax calculation will be finalised during checkout.

Rent or Buy article

Get time limited or full article access on ReadCube.

from \$8.99

[Rent or Buy](#)

All prices are NET prices.

Additional access options:

- [Log in](#)
- [Access through your institution](#)
- [Learn about institutional subscriptions](#)

Fig. 1: Isotope records in carbonates through time.

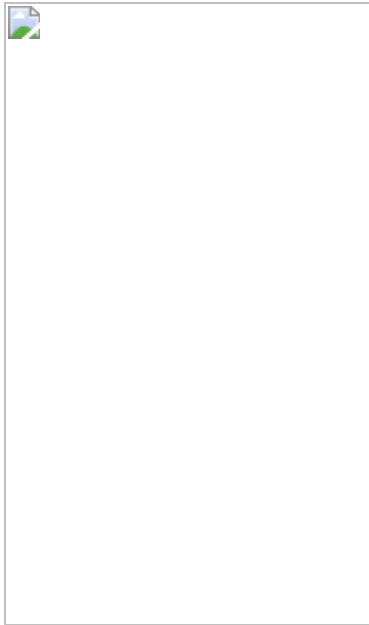


Fig. 2: Thin-section photomicrographs of representative well preserved carbonates from this study.

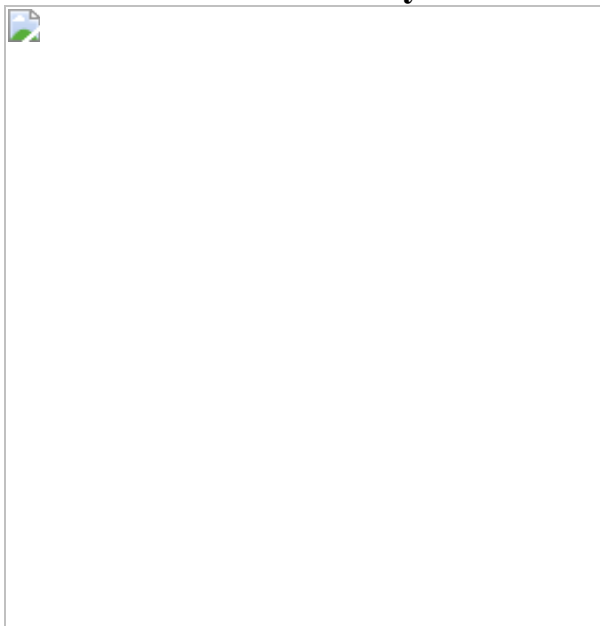


Fig. 3: Two-dimensional density heat map of Li-isotope mass-balance results.



Data availability

All geochemical data generated here are included in [Supplementary Table 2](#) and are available on Mendeley Data (<https://doi.org/10.17632/ztpkpbm43x.1>). Splits of samples are reposed in the Yale Peabody Museum of Natural History.

Code availability

A description of the global Li mass-balance model is available in [Supplementary Information](#). Additional code (in Python) has been posted on GitHub (<https://github.com/jkatch/Li-global-mass-balance>). A description of the Li-isotope diagenetic model is available in [Supplementary Information](#).

References

1. 1.

Jaffrés, J. B. D., Shields, G. A. & Wallmann, K. The oxygen isotope evolution of seawater: a critical review of a long-standing controversy and an improved geological water cycle model for the past 3.4 billion years. *Earth Sci. Rev.* **83**, 83–122 (2007).

[ADS](#) [Google Scholar](#)

2. 2.

Berner, R. A., Lasaga, A. C. & Garrels, R. M. Carbonate-silicate geochemical cycle and its effect on atmospheric carbon dioxide over the past 100 million years. *Am. J. Sci.* **283**, 641–683 (1983).

[ADS](#) [CAS](#) [Google Scholar](#)

3. 3.

West, A. J., Galy, A. & Bickle, M. Tectonic and climatic controls on silicate weathering. *Earth Planet. Sci. Lett.* **235**, 211–228 (2005).

[ADS](#) [CAS](#) [Google Scholar](#)

4. 4.

Issoon, T. T. et al. Evolution of the global carbon cycle and climate regulation on Earth. *Glob. Biogeochem. Cycles* **34**, 1–28 (2020).

[Google Scholar](#)

5. 5.

Hilton, R. G. & West, A. J. Mountains, erosion and the carbon cycle. *Nat. Rev. Earth Environ.* **1**, 284–299 (2020).

[ADS](#) [Google Scholar](#)

6. 6.

Mills, B., Lenton, T. M. & Watson, A. J. Proterozoic oxygen rise linked to shifting balance between seafloor and terrestrial weathering. *Proc. Natl Acad. Sci. USA* **111**, 9073–9078 (2014).

[ADS](#) [CAS](#) [PubMed](#) [PubMed Central](#) [Google Scholar](#)

7. 7.

Coogan, L. A., Gillis, K. M., Pope, M. & Spence, J. The role of low-temperature (off-axis) alteration of the oceanic crust in the global Li-cycle: insights from the Troodos ophiolite. *Geochim. Cosmochim. Acta* **203**, 201–215 (2017).

[ADS](#) [CAS](#) [Google Scholar](#)

8. 8.

Isson, T. T. & Planavsky, N. J. Reverse weathering as a long-term stabilizer of marine pH and planetary climate. *Nature* **560**, 471–475 (2018).

[ADS](#) [CAS](#) [PubMed](#) [PubMed Central](#) [Google Scholar](#)

9. 9.

Krissansen-Totton, J. & Catling, D. C. Constraining climate sensitivity and continental versus seafloor weathering using an inverse geological carbon cycle model. *Nat. Commun.* **8**, 15423 (2017).

[ADS](#) [CAS](#) [PubMed](#) [PubMed Central](#) [Google Scholar](#)

10. 10.

Krissansen-Totton, J. & Catling, D. C. A coupled carbon-silicon cycle model over Earth history: reverse weathering as a possible explanation of a warm mid-Proterozoic climate. *Earth Planet. Sci. Lett.* **537**, 116181 (2020).

[CAS](#) [Google Scholar](#)

11. 11.

Keller, C. K. & Wood, B. D. Possibility of chemical weathering before the advent of vascular land plants. *Nature* **364**, 223–225 (1993).

[ADS](#) [CAS](#) [Google Scholar](#)

12. 12.

Ibarra, D. E. et al. Modeling the consequences of land plant evolution on silicate weathering. *Am. J. Sci.* **319**, 1–43 (2019).

[ADS](#) [CAS](#) [Google Scholar](#)

13. 13.

McMahon, W. J. & Davies, N. S. Evolution of alluvial mudrock forced by early land plants. *Science* **359**, 1022–1024 (2018).

[ADS](#) [CAS](#) [PubMed](#) [PubMed Central](#) [Google Scholar](#)

14. 14.

Berner, R. A. & Kothavala, Z. GEOCARB III: a revised model of atmospheric CO₂ over Phanerozoic time. *Am. J. Sci.* **301**, 182–204 (2001).

[ADS](#) [CAS](#) [Google Scholar](#)

15. 15.

Dellinger, M. et al. Riverine Li isotope fractionation in the Amazon River basin controlled by the weathering regimes. *Geochim. Cosmochim. Acta* **164**, 71–93 (2015).

[ADS](#) [CAS](#) [Google Scholar](#)

16. 16.

Vigier, N. et al. Quantifying Li isotope fractionation during smectite formation and implications for the Li cycle. *Geochim. Cosmochim. Acta* **72**, 780–792 (2008).

[ADS](#) [CAS](#) [Google Scholar](#)

17. 17.

Sauzéat, L., Rudnick, R. L., Chauvel, C., Garçon, M. & Tang, M. New perspectives on the Li isotopic composition of the upper continental crust and its weathering signature. *Earth Planet. Sci. Lett.* **428**, 181–192 (2015).

[ADS](#) [Google Scholar](#)

18. 18.

Misra, S. & Froelich, P. N. Lithium isotope history of Cenozoic seawater: changes in silicate weathering and reverse weathering. *Science* **335**, 818–823 (2012).

[ADS](#) [CAS](#) [PubMed](#) [PubMed Central](#) [Google Scholar](#)

19. 19.

Pogge von Strandmann, P. A. E. & Henderson, G. M. The Li isotope response to mountain uplift. *Geology* **43**, 67–70 (2015).

[ADS](#) [Google Scholar](#)

20. 20.

Pogge von Strandmann, P. A. E. et al. Assessing bulk carbonates as archives for seawater Li isotope ratios. *Chem. Geol.* **530**, 119338 (2019).

[ADS](#) [CAS](#) [Google Scholar](#)

21. 21.

Washington, K. E. et al. Lithium isotope composition of modern and fossilized Cenozoic brachiopods. *Geology* **48**, 1058–1061 (2020).

[ADS](#) [CAS](#) [Google Scholar](#)

22. 22.

Fantle, M. S., Barnes, B. D. & Lau, K. V. The role of diagenesis in shaping the geochemistry of the marine carbonate record. *Annu. Rev. Earth Planet. Sci.* **48**, 549–583 (2020).

[ADS](#) [CAS](#) [Google Scholar](#)

23. 23.

Dellinger, M. et al. The effects of diagenesis on lithium isotope ratios of shallow marine carbonates. *Am. J. Sci.* **320**, 150–184 (2020).

[ADS](#) [CAS](#) [Google Scholar](#)

24. 24.

Hood, A. van S. & Wallace, M. W. Synsedimentary diagenesis in a Cryogenian reef complex: ubiquitous marine dolomite precipitation. *Sedim. Geol.* **255–256**, 56–71 (2012).

[ADS](#) [Google Scholar](#)

25. 25.

Blättler, C. L. & Higgins, J. A. Testing Urey’s carbonate–silicate cycle using the calcium isotopic composition of sedimentary carbonates. *Earth Planet. Sci. Lett.* **479**, 241–251 (2017).

[ADS](#) [Google Scholar](#)

26. 26.

Ahm, A. C. et al. An early diagenetic deglacial origin for basal Ediacaran “cap dolostones”. *Earth Planet. Sci. Lett.* **506**, 292–307 (2019).

[ADS](#) [CAS](#) [Google Scholar](#)

27. 27.

Hoffman, P. F. & Lamothe, K. G. Seawater-buffered diagenesis, destruction of carbon isotope excursions, and the composition of DIC in Neoproterozoic oceans. *Proc. Natl Acad. Sci. USA* **116**, 18874–18879 (2019).

[ADS](#) [CAS](#) [PubMed](#) [PubMed Central](#) [Google Scholar](#)

28. 28.

Ahm, A. S. C., Bjerrum, C. J., Blättler, C. L., Swart, P. K. & Higgins, J. A. Quantifying early marine diagenesis in shallow-water carbonate sediments. *Geochim. Cosmochim. Acta* **236**, 140–159 (2018).

[ADS](#) [CAS](#) [Google Scholar](#)

29. 29.

Higgins, J. A. et al. Mineralogy, early marine diagenesis, and the chemistry of shallow-water carbonate sediments. *Geochim. Cosmochim. Acta* **220**, 512–534 (2018).

[ADS](#) [CAS](#) [Google Scholar](#)

30. 30.

Hathorne, E. C. & James, R. H. Temporal record of lithium in seawater: a tracer for silicate weathering? *Earth Planet. Sci. Lett.* **246**, 393–406 (2006).

[ADS](#) [CAS](#) [Google Scholar](#)

31. 31.

Hall, J. M., Chan, L. H., McDonough, W. F. & Turekian, K. K. Determination of the lithium isotopic composition of planktic foraminifera and its application as a paleo-seawater proxy. *Mar. Geol.* **217**, 255–265 (2005).

[ADS](#) [CAS](#) [Google Scholar](#)

32. 32.

Crockford, P. W. et al. Reconstructing Neoproterozoic seawater chemistry from early diagenetic dolomite. *Geology* **49**, 442–446 (2021).

[ADS](#) [CAS](#) [Google Scholar](#)

33. 33.

Ullmann, C. V. et al. Partial diagenetic overprint of Late Jurassic belemnites from New Zealand: implications for the preservation potential of $\delta^{7}\text{Li}$ values in calcite fossils. *Geochim. Cosmochim. Acta* **120**, 80–96 (2013).

[ADS](#) [CAS](#) [Google Scholar](#)

34. 34.

Veizer, J. in *Encyclopedia of Paleoclimatology and Ancient Environments* (ed. Gornitz, V.) 923–926 (Springer, 2009).

35. 35.

Hood, A. van S. & Wallace, M. W. Neoproterozoic marine carbonates and their paleoceanographic significance. *Global Planet. Change* **160**, 28–45 (2018).

[ADS](#) [Google Scholar](#)

36. 36.

Jeffcoate, A. B., Elliott, T., Thomas, A. & Bouman, C. Precise, small sample size determinations of lithium isotopic compositions of geological reference materials and modern seawater by MC-ICP-MS. *Geostand. Geoanal. Res.* **28**, 161–172 (2004).

[CAS](#) [Google Scholar](#)

37. 37.

Galili, N. et al. The geologic history of seawater oxygen isotopes from marine iron oxides. *Science* **365**, 469–473 (2019).

[ADS](#) [CAS](#) [PubMed](#) [PubMed Central](#) [Google Scholar](#)

38. 38.

Coogan, L. A. & Dosso, S. An internally consistent, probabilistic, determination of ridge-axis hydrothermal fluxes from basalt-hosted systems. *Earth Planet. Sci. Lett.* **323–324**, 92–101 (2012).

[ADS](#) [Google Scholar](#)

39. 39.

O'Neill, C., Lenardic, A., Höink, T. & Coltice, N. in *Comparative Climatology of Terrestrial Planets* (eds Mackwell, S. J., Simon-Miller, A. A., Harder, J. W. & Bullock, M. A.) 473–486 (Univ. Arizona Press, 2013).

40. 40.

Korenaga, J. Initiation and evolution of plate tectonics on Earth: theories and observations. *Annu. Rev. Earth Planet. Sci.* **41**, 117–151 (2013).

[ADS](#) [CAS](#) [Google Scholar](#)

41. 41.

Rafiei, M. & Kennedy, M. Weathering in a world without terrestrial life recorded in the Mesoproterozoic Velkerri Formation. *Nat. Commun.* **10**, 3448 (2019).

[ADS](#) [CAS](#) [PubMed](#) [PubMed Central](#) [Google Scholar](#)

42. 42.

Clark, S. K. & Johnson, T. M. Effective isotopic fractionation factors for solute removal by reactive sediments: a laboratory microcosm and slurry study. *Environ. Sci. Technol.* **42**, 7850–7855 (2008).

[ADS](#) [CAS](#) [PubMed](#) [PubMed Central](#) [Google Scholar](#)

43. 43.

Conley, D. J. et al. Biosilicification drives a decline of dissolved Si in the oceans through geologic time. *Front. Mar. Sci.* **4**, 397 (2017).

[Google Scholar](#)

44. 44.

Pogge von Strandmann, P. A. E. et al. Global climate stabilisation by chemical weathering during the Hirnantian glaciation. *Geochem. Perspect. Lett.* **3**, 230–237 (2017).

[Google Scholar](#)

45. 45.

Lechler, M., Pogge von Strandmann, P. A. E., Jenkyns, H. C., Prosser, G. & Parente, M. Lithium-isotope evidence for enhanced silicate weathering during OAE 1a (Early Aptian Selli event). *Earth Planet. Sci. Lett.* **432**, 210–222 (2015).

[ADS](#) [CAS](#) [Google Scholar](#)

46. 46.

Pogge von Strandmann, P. A. E., Jenkyns, H. C. & Woodfine, R. G. Lithium isotope evidence for enhanced weathering during Oceanic Anoxic Event 2. *Nat. Geosci.* **6**, 668–672 (2013).

[ADS](#) [CAS](#) [Google Scholar](#)

47. 47.

Shields, G. & Veizer, J. Precambrian marine carbonate isotope database: version 1.1. *Geochem. Geophys. Geosyst.* **3**, <https://doi.org/10.1029/2001GC000266> (2002).

48. 48.

McArthur, J. M., Howarth, R. J. & Shields-Zhou, G. A. in *A Geologic Time Scale 2012* (eds Gradstein, F., Ogg, J., Schmitz, M. & Ogg, G.) 127–144 (Cambridge Univ. Press, 2012).

49. 49.

Holland, H. D. Why the atmosphere became oxygenated: a proposal. *Geochim. Cosmochim. Acta* **73**, 5241–5255 (2009).

[ADS](#) [CAS](#) [Google Scholar](#)

50. 50.

Tajika, E. & Matsui, T. Evolution of terrestrial proto-CO₂ atmosphere coupled with thermal history of the earth. *Earth Planet. Sci. Lett.* **113**, 251–266 (1992).

[ADS](#) [CAS](#) [Google Scholar](#)

[Download references](#)

Acknowledgements

N.J.P. acknowledges funding from the Alternative Earths NASA Astrobiology Institute and the Packard Foundation. P.A.E.P.v.S. was funded by a European Research Council (ERC) consolidator grant (682760 CONTROLPASTCO2). A.v.S.H. acknowledges funding from an Australian Research Council (ARC) Discovery Early Career Researcher Award (DECRA; DE190100988). B.K.-A. acknowledges financial support from the Yale Institute for Biospheric Studies. We thank J. Utrup, S. H. Butts and

the Yale Peabody Museum of Natural History for providing brachiopods and carbonate samples.

Author information

Affiliations

1. Earth and Planetary Sciences, Yale University, New Haven, CT, USA

Boriana Kalderon-Asael, Joachim A. R. Katchinoff, Noah J. Planavsky, Eric J. Bellefroid, Terry T. Isson & Dan Asael

2. The University of Melbourne, School of Earth Sciences, Parkville, Victoria, Australia

Ashleigh v. S. Hood & Malcolm W. Wallace

3. Department of Geography, Durham University, Durham, UK

Mathieu Dellinger

4. Amherst College Geology Department, Amherst, MA, USA

David S. Jones

5. Department of Geology, University of Johannesburg, Johannesburg, South Africa

Axel Hofmann & Frantz Ossa Ossa

6. Department of Geosciences, University of Tuebingen, Tuebingen, Germany

Frantz Ossa Ossa

7. Department of Earth Sciences, University of California Santa Barbara, Santa Barbara, CA, USA

Francis A. Macdonald

8. China University of Petroleum, College of Geosciences, Beijing,
China

Chunjiang Wang

9. Te Aka Mātuatua, University of Waikato, Tauranga, New Zealand

Terry T. Isson

10. Department of Geoscience, Princeton University, Princeton, NJ, USA

Jack G. Murphy & John A. Higgins

11. Department of Earth Sciences, University of Southern California, Los Angeles, CA, USA

A. Joshua West

12. London Geochemistry and Isotope Centre (LOGIC), Institute of Earth and Planetary Sciences, University College London and Birkbeck, University of London, London, UK

Philip A. E. Pogge von Strandmann

13. Institute of Geosciences, Johannes Gutenberg University, Mainz, Germany

Philip A. E. Pogge von Strandmann

Authors

1. Boriana Kalderon-Asael
[View author publications](#)

You can also search for this author in [PubMed](#) [Google Scholar](#)

2. Joachim A. R. Katchinoff

[View author publications](#)

You can also search for this author in [PubMed](#) [Google Scholar](#)

3. Noah J. Planavsky

[View author publications](#)

You can also search for this author in [PubMed](#) [Google Scholar](#)

4. Ashleigh v. S. Hood

[View author publications](#)

You can also search for this author in [PubMed](#) [Google Scholar](#)

5. Mathieu Dellinger

[View author publications](#)

You can also search for this author in [PubMed](#) [Google Scholar](#)

6. Eric J. Bellefroid

[View author publications](#)

You can also search for this author in [PubMed](#) [Google Scholar](#)

7. David S. Jones

[View author publications](#)

You can also search for this author in [PubMed](#) [Google Scholar](#)

8. Axel Hofmann

[View author publications](#)

You can also search for this author in [PubMed](#) [Google Scholar](#)

9. Frantz Ossa Ossa

[View author publications](#)

You can also search for this author in [PubMed](#) [Google Scholar](#)

10. Francis A. Macdonald

[View author publications](#)

You can also search for this author in [PubMed](#) [Google Scholar](#)

11. Chunjiang Wang

[View author publications](#)

You can also search for this author in [PubMed](#) [Google Scholar](#)

12. Terry T. Isson

[View author publications](#)

You can also search for this author in [PubMed](#) [Google Scholar](#)

13. Jack G. Murphy

[View author publications](#)

You can also search for this author in [PubMed](#) [Google Scholar](#)

14. John A. Higgins

[View author publications](#)

You can also search for this author in [PubMed](#) [Google Scholar](#)

15. A. Joshua West

[View author publications](#)

You can also search for this author in [PubMed](#) [Google Scholar](#)

16. Malcolm W. Wallace

[View author publications](#)

You can also search for this author in [PubMed](#) [Google Scholar](#)

17. Dan Asael

[View author publications](#)

You can also search for this author in [PubMed](#) [Google Scholar](#)

18. Philip A. E. Pogge von Strandmann

[View author publications](#)

You can also search for this author in [PubMed](#) [Google Scholar](#)

Contributions

B.K.-A., N.J.P., P.A.E.P.v.S. and J.A.R.K. designed the research. E.J.B., A.v.S.H., D.S.J., F.A.M., M.W.W., J.A.R.K., A.H., F.O.O., C.W., M.D. and N.J.P. collected samples. B.K.-A., P.A.E.P.v.S., J.A.R.K., M.D., J.G.M., D.A., F.A.M., A.J.W. and J.A.H. conducted geochemical analyses. J.A.R.K. wrote the Li-isotope mass-balance model. B.K.-A. wrote the Li-isotope diagenetic model. B.K.-A., N.J.P., P.A.E.P.v.S. and J.A.R.K. analysed the data and wrote the paper. All authors contributed to the preparation of the manuscript.

Corresponding authors

Correspondence to [Boriana Kalderon-Asael](#) or [Noah J. Planavsky](#) or [Philip A. E. Pogge von Strandmann](#).

Ethics declarations

Competing interests

The authors declare no competing interests.

Additional information

Peer review information *Nature* thanks Jeremy Caves Rugenstein and the other, anonymous, reviewer(s) for their contribution to the peer review of this work.

Publisher's note Springer Nature remains neutral with regard to jurisdictional claims in published maps and institutional affiliations.

Supplementary information

Supplementary Information

The file contains Supplementary Figures 1 – 29; Supplementary Tables 1 – 3; Supplementary Methods; Supplementary Discussion; Global lithium isotope mass balance; Diagenetic modelling and Supplementary References.

Supplementary Table 1

Description of the samples analysed in this study at a) Yale University; b) Oxford and University College London.

Supplementary Table 2

Geochemical data generated in this study: a) $\delta^{7\text{Li}}$ (in ‰), Li, Mg, Al, Ca, Ti, Mn, Rb, Sr, Pb concentrations (in ppm) and $\delta^{44/40\text{Ca}}$ (in ‰) of the samples analysed at Yale University; b) $\delta^{7\text{Li}}$ (in ‰), Li/Ca, Al/Ca, Mn/Ca, Sr/Ca and Mg/Ca elemental ratios of the samples analysed at Oxford and University College London.

Rights and permissions

Reprints and Permissions

About this article



Check for
updates

Cite this article

Kalderon-Asael, B., Katchinoff, J.A.R., Planavsky, N.J. *et al.* A lithium-isotope perspective on the evolution of carbon and silicon cycles. *Nature* **595**, 394–398 (2021). <https://doi.org/10.1038/s41586-021-03612-1>

[Download citation](#)

- Received: 14 March 2019
- Accepted: 04 May 2021
- Published: 14 July 2021
- Issue Date: 15 July 2021
- DOI: <https://doi.org/10.1038/s41586-021-03612-1>

Comments

By submitting a comment you agree to abide by our [Terms](#) and [Community Guidelines](#). If you find something abusive or that does not comply with our terms or guidelines please flag it as inappropriate.

[Access through your institution](#)

[Change institution](#)

[Buy or subscribe](#)

Advertisement

This article was downloaded by **calibre** from <https://www.nature.com/articles/s41586-021-03612-1>

Pleistocene sediment DNA reveals hominin and faunal turnovers at Denisova Cave
[Download PDF](#)

- Article
- Open Access
- [Published: 23 June 2021](#)

Pleistocene sediment DNA reveals hominin and faunal turnovers at Denisova Cave

- [Elena I. Zavala](#) [ORCID: orcid.org/0000-0001-7687-5370¹](#),
- [Zenobia Jacobs](#) [ORCID: orcid.org/0000-0001-5424-5837^{2,3}](#),
- [Benjamin Vernot¹](#),
- [Michael V. Shunkov](#) [ORCID: orcid.org/0000-0003-1388-2308⁴](#),
- [Maxim B. Kozlikin](#) [ORCID: orcid.org/0000-0001-5082-3345⁴](#),
- [Anatoly P. Derevianko⁴](#),
- [Elena Essel¹](#),
- [Cesare de Filippo¹](#),
- [Sarah Nagel¹](#),
- [Julia Richter¹](#),
- [Frédéric Romagné¹](#),
- [Anna Schmidt¹](#),
- [Bo Li](#) [ORCID: orcid.org/0000-0003-4186-4828^{2,3}](#),
- [Kieran O'Gorman](#) [ORCID: orcid.org/0000-0002-2231-2457²](#),
- [Viviane Slon^{1,5,6,7}](#),
- [Janet Kelso](#) [ORCID: orcid.org/0000-0002-3618-322X¹](#),
- [Svante Pääbo](#) [ORCID: orcid.org/0000-0002-4670-6311¹](#),
- [Richard G. Roberts](#) [ORCID: orcid.org/0000-0002-0128-4119^{2,3}](#) &
- [Matthias Meyer](#) [ORCID: orcid.org/0000-0002-4760-558X¹](#)

Nature volume 595, pages 399–403 (2021) [Cite this article](#)

- 15k Accesses
- 598 Altmetric

- [Metrics details](#)

Subjects

- [Archaeology](#)
- [Biological anthropology](#)
- [Evolutionary biology](#)
- [Evolutionary genetics](#)
- [Population genetics](#)

Abstract

Denisova Cave in southern Siberia is the type locality of the Denisovans, an archaic hominin group who were related to Neanderthals^{1,2,3,4}. The dozen hominin remains recovered from the deposits also include Neanderthals^{5,6} and the child of a Neanderthal and a Denisovan⁷, which suggests that Denisova Cave was a contact zone between these archaic hominins. However, uncertainties persist about the order in which these groups appeared at the site, the timing and environmental context of hominin occupation, and the association of particular hominin groups with archaeological assemblages^{5,8,9,10,11}. Here we report the analysis of DNA from 728 sediment samples that were collected in a grid-like manner from layers dating to the Pleistocene epoch. We retrieved ancient faunal and hominin mitochondrial (mt)DNA from 685 and 175 samples, respectively. The earliest evidence for hominin mtDNA is of Denisovans, and is associated with early Middle Palaeolithic stone tools that were deposited approximately 250,000 to 170,000 years ago; Neanderthal mtDNA first appears towards the end of this period. We detect a turnover in the mtDNA of Denisovans that coincides with changes in the composition of faunal mtDNA, and evidence that Denisovans and Neanderthals occupied the site repeatedly—possibly until, or after, the onset of the Initial Upper Palaeolithic at least 45,000 years ago, when modern human mtDNA is first recorded in the sediments.

[Download PDF](#)

Main

Denisova Cave consists of three chambers (designated Main, East and South Chambers) that contain deposits with stratigraphic sequences extending from the Middle Pleistocene to the Holocene epoch. The Pleistocene deposits have chronologies that have been constructed from the radiocarbon dating of bone, tooth and charcoal⁵ (to around 50 thousand years ago (ka)) and optical dating of sediments⁸ (to more than 300 ka). Optical ages for Main and East Chambers (Fig. [1a–c](#)) can be

aligned on a common time scale (Extended Data Fig. 1) but excavations are ongoing in South Chamber, where layers are only tentatively recognized. Mitochondrial DNA and nuclear DNA have been recovered from eight hominin fossils, enabling four to be assigned to Denisovans (Denisova 2, Denisova 3, Denisova 4 and Denisova 8)^{1,2,3,4}, three to Neanderthals (Denisova 5, Denisova 9 and Denisova 15)^{5,6,12}, and one to the child of a Neanderthal and a Denisovan (Denisova 11)⁷. However, there are too few fossils to enable the detailed reconstruction of the timing and sequence of hominin occupation, and the association of the early Middle Palaeolithic, middle Middle Palaeolithic and Initial Upper Palaeolithic assemblages identified at the site with specific hominin groups. Moreover, two Denisovan fossils (Denisova 3 and Denisova 4)—but no modern human remains—have been recovered from the Initial Upper Palaeolithic layers, so it is debated whether archaic hominins or modern humans created the associated ornaments and bone tools^{9,10,11}.

Fig. 1: Stratigraphic sequences in Denisova Cave, showing locations of sediment samples collected for mtDNA analysis and results obtained for ancient hominins.

 **figure1**

a, East Chamber, southeast profile. **b**, East Chamber, northwest profile. **c**, Main Chamber, southeast profile. **d**, Phylogenetic tree of mtDNA genomes used as references to distinguish specific hominin lineages, and estimated placement of the Neanderthal mtDNA lineage identified in sample M76 from Main Chamber layer 20. Filled circles in **a–c** indicate the locations of individual sediment samples, and colours correspond to the hominin mtDNA detected: red (Denisovan), blue (Neanderthal), yellow (ancient modern human), grey (unidentified ancient hominin) and white (no ancient hominins detected). Other symbols denote samples for which mtDNA could be

assigned to one of the specific hominin lineages in **d** (Denisovan, red open triangles; Neanderthal, blue open diamonds, crosses and star). Composite stratigraphic sections (modified from a previous publication⁸) to the left of each profile show modelled start and end ages (in ka) for sedimentary layers (uncertainties at 95.4% probability). Hominin specimen numbers are shown circled in the layer from which each fossil was recovered: Denisovan (red), Neanderthal (blue) and Neanderthal–Denisovan offspring (both colours)⁵. Dashed lines in profiles in **a** and **b** indicate areas in which layer assignment is uncertain⁸. Background shading denotes the associated archaeological assemblage: early Middle Palaeolithic (eMP) (dark green), middle Middle Palaeolithic (mMP) (light green), Initial Upper Palaeolithic (IUP) (dark orange) and Upper Palaeolithic (UP) (light orange).

[Full size image](#)

A pilot study of DNA preservation in sediments from Denisova Cave identified ancient hominin mtDNA in 12 out of 52 samples¹³, which suggested a path to reconstructing the occupational history of the site at higher resolution than is feasible from the scarce hominin fossil record. Here we report the analysis of 728 sediment samples, collected in a 10–15-cm grid-like pattern from the exposed Pleistocene deposits in all three chambers (Extended Data Figs. [2](#), [3a](#), [b](#), Supplementary Information sections [1](#), [2](#)). Using automated laboratory protocols, DNA was extracted from each sample, converted to single-stranded libraries and enriched for mammalian and hominin mtDNA^{13,14}, which we identified to the biological-family level using an established analysis pipeline¹³.

Patterns of DNA preservation

We identified ancient mammalian mtDNA in 685 samples (94%) from all sampled layers, including those older than 290 ka (Extended Data Figs. [4](#), [5a](#), Supplementary Data [1](#)). DNA retrieved from the deposits in all three chambers shows deamination-induced substitutions that are characteristic of ancient DNA^{15,16}. These substitutions significantly increase with age (Extended Data Figs. [3d](#), [4a](#)), which argues against extensive post-depositional leaching of DNA across layers^{13,17}. We also observed a significant reduction in average DNA fragment length and the number of mtDNA fragments recovered with increasing age (Extended Data Figs. [3e](#), f, [4b](#), [c](#)), although variability was greater across layers than for deamination, probably as a result of local differences in the geochemical environment. For example, the fewest ancient DNA fragments (none in some samples) were recovered from the youngest sampled unit (designated pdd-9) in South Chamber (Extended Data Fig. [3f](#)), which is extensively phosphatized⁸ and has slightly acidic pH values (between 6 and 6.5) (Supplementary Information section [3](#), Supplementary Data [2](#)).

Ancient hominin mtDNA

We detected ancient hominin mtDNA in 175 samples (24%), covering nearly all layers in all three chambers (Fig. 1a–c, Extended Data Figs. 3a, b, 5b). Four samples showed evidence for the presence of predominantly one haplotype and yielded sufficient mtDNA fragments to reconstruct mtDNA consensus sequences that are more than 80% complete (Supplementary Information sections 5, 6). Three of the sequences (samples E202 and E213 from East Chamber (layers 11.4 and 11.4/12.1) and sample M65 from Main Chamber (layer 19)) group with Neanderthals in phylogenetic trees built with previously published hominin mtDNAs (Supplementary Information section 7), specifically with Denisova 5, Denisova 15, Mezmaiskaya 1 and Scladina I-4A (Fig. 1d, Extended Data Fig. 6a). The fourth sequence (sample M71 from Main Chamber (layer 20)) is of the Denisovan type and falls basal to Denisova 2 and Denisova 8, albeit with low bootstrap support (Extended Data Fig. 6b). The most complete mtDNA sequence (over 99% of the genome reconstructed) for a Neanderthal from Main Chamber (M65) has a genetic age estimate of 140 ka (95.4% highest posterior density interval of 181–98 ka) (Supplementary Information section 7), consistent with the time of deposition of layer 19 (151 ± 17 to 128 ± 13 ka; here and below, uncertainties on optical ages are given at 95.4% probability)⁸.

For the remaining 171 samples, we assigned mtDNA fragments to specific hominin groups by counting the number of fragments that support lineage-specific states at diagnostic sites that distinguish between modern human, Neanderthal and Denisovan mtDNA genomes. We distinguished three Neanderthal lineages: the Sima de los Huesos lineage (representing Neanderthals who lived approximately 430 ka in Spain and whose mtDNA is most closely related to that of Denisovans)^{18,19}; the Hohlenstein–Stadel (HST) lineage, which falls basal to all other Neanderthal mtDNAs²⁰; and the ‘typical’ Neanderthal mtDNA, known from all other Neanderthals. The presence of ancient modern human mtDNA was evaluated by restricting the analysis to deaminated fragments to mitigate the effect of present-day human DNA contamination. We identified Denisovan and typical Neanderthal mtDNA in 79 and 47 samples, respectively (based on 54–9,093 unique hominin mtDNA fragments), and modern human mtDNA in 35 samples (based on 55–2,200 deaminated fragments) (Fig. 1a–c, Extended Data Fig. 3a, b). We detected DNA from two hominin groups in ten samples, either within a single library or across libraries that were prepared from independent subsamples in some cases (Extended Data Fig. 6c, Supplementary Information section 4). In addition, we identified one sample (M76 from Main Chamber (layer 20)) containing hominin mtDNA fragments that support the branch shared by HST and typical Neanderthal mtDNA, but neither of the branches defining those lineages. This signal cannot be created by mixing mtDNA fragments from Neanderthals, Denisovans and ancient or present-day modern humans. On the basis of simulations with ancestralized Neanderthal mtDNA, the mtDNA in this sample is

compatible with the presence of a previously unknown Neanderthal mtDNA lineage that diverged from typical Neanderthal mtDNA between 255 and 230 ka, 20 to 45 thousand years after the split of the HST and typical Neanderthal mtDNA lineages (Supplementary Information section 9).

The oldest hominin mtDNA recovered—identified as Denisovan—originates from a sample in Main Chamber layer 21, which began to accumulate 250 ± 44 ka. This provides the earliest genetic evidence for hominin occupation in Denisova Cave; Denisova 2 was found in layer 22.1, but is probably intrusive from an overlying layer and has an estimated age of 194–123 ka⁵. Among all 223 samples from the early Middle Palaeolithic layers in Main and East Chambers, 50 contained evidence for Denisovan mtDNA and only three (all from layer 20 in Main Chamber) for Neanderthal mtDNA. Two of these (M174 and M235) contain typical Neanderthal mtDNA and are from areas in which small-scale mixing with overlying sediments may have occurred⁸, the third (M76) is from the middle of the layer, and carries the previously unknown Neanderthal mtDNA lineage. These results point to Denisovans as the first and principal makers of the early Middle Palaeolithic assemblages, which are older than 170 ± 19 ka. Consistent with this interpretation, the detection of Neanderthal mtDNA in a sediment sample from early Middle Palaeolithic layer 14 in East Chamber in the pilot study¹³ was due to an incorrect assignment, which was later corrected to middle Middle Palaeolithic layer 11.4 in this chamber⁸ (Supplementary Information section 2). Our results also suggest that Neanderthals first occupied Denisova Cave towards the end of the early Middle Palaeolithic and may therefore have contributed to the production of these assemblages in their later stages.

Forty out of 173 samples from the middle Middle Palaeolithic layers in Main and East Chambers (deposited approximately 160–60 ka) yielded Neanderthal and/or Denisovan mtDNA, with both present in six samples (Fig. 1a–c). DNA from both groups also occurs in the deformed Middle Palaeolithic layers in South Chamber (Extended Data Fig. 3b). Notably, sediments deposited between 120 ± 11 and 97 ± 11 ka in Main and East Chambers produced no traces of Denisovan mtDNA, whereas 12 samples contained Neanderthal mtDNA. This suggests that only Neanderthals may have occupied the cave during that period, and possibly for most of Marine Isotope Stage (MIS) 5 (Fig. 2).

Fig. 2: Timeline of hominin and faunal mtDNA presence, archaeological phases and environmental records at Denisova Cave.

 **figure2**

a, Baikal Drilling Project 1996 composite biogenic silica record of diatom productivity in Lake Baikal, a proxy for regional annual temperature²⁸. **b, c**, Summary data for Main Chamber (**b**) and East Chamber (**c**). Start and end ages for layers and corresponding data are based on the common time scale in Extended Data Fig. 1. Time intervals in white represent gaps in the stratigraphic sequence, or were not sampled. Archaeological phases (early Middle Palaeolithic, middle Middle Palaeolithic, Initial Upper Palaeolithic and Upper Palaeolithic) follow the colour scheme in Fig. 1 and Extended Data Fig. 1. Genetic data for hominins are from Fig. 1 (excluding samples M174 and M235 from Main Chamber, which are thought to be out of context), and for dominant hyaenid and ursid populations from Extended Data Fig. 10. Symbols for specific hominin mtDNA lineages (Fig. 1d) are inset in white. Environmental conditions are inferred from pollen records and skeletal remains of vertebrate fauna⁸. Relative proportions of bovid, canid, equid, hyaenid and ursid mtDNA are from Extended Data Figs. 8, 9.

[Full size image](#)

Only ancient modern human mtDNA was detected in the Initial Upper Palaeolithic and Upper Palaeolithic layers in Main Chamber (layers 11.4 and above, deposited 44 ± 5

to 21 ± 8 ka), except for one sample from Initial Upper Palaeolithic layer 11.2 that yielded Neanderthal mtDNA (Fig. 1c). The association between Initial Upper Palaeolithic assemblages and the appearance of modern humans is further supported by the recovery of modern human mtDNA from a sample from Initial Upper Palaeolithic layer 11 in South Chamber, which was deposited after 47 ± 8 ka (Extended Data Fig. 3a). The situation in East Chamber is more complex: Denisovan, Neanderthal and ancient modern human mtDNAs were recovered from Initial Upper Palaeolithic layer 11.2, and Neanderthal and ancient modern human mtDNA from Initial Upper Palaeolithic layer 11.1 (Fig. 1a). Given these results and the recovery of two Denisovan fossils (Denisova 3 and Denisova 4) from layers associated with Initial Upper Palaeolithic assemblages, we cannot discount the possibility that—in addition to modern humans—Denisovans and Neanderthals may have been present during the period of Initial Upper Palaeolithic production^{9,10,11}.

For 34 out of 37 samples that yielded 100 or more deaminated hominin mtDNA fragments, we identified similarities with specific Neanderthal and Denisovan mtDNA genomes using a k -mer-based approach^{21,22} (denoted by symbols other than circles in Fig. 1a–c, Extended Data Fig. 3b, Supplementary Information section 8). This analysis revealed that the early Middle Palaeolithic layers in Main and East Chambers and the earliest middle Middle Palaeolithic layer in East Chamber, which span the period between 250 ± 44 and 146 ± 11 ka, contain Denisova-2- and Denisova-8-like mtDNA fragments. This contrasts with the Denisovan mtDNA recovered from middle Middle Palaeolithic layers deposited after 80 ± 9 ka, which yielded assignments to Denisova-3- and Denisova-4-like sequences, as did a sample from South Chamber. These results suggest a transition in mtDNA sequences sometime in the 146–80-ka interval, possibly reflecting different Denisovan populations. Our results also align well with the modelled ages of Denisova 2, Denisova 3 and Denisova 4, and with the relative age of Denisova 8 inferred from molecular dating⁵. Sediments deposited between about 130 and 100 ka (and possibly longer, given the subsequent time gap of 20 millennia)—during MIS 5—contain mtDNA and fossil evidence only of Neanderthals, with Denisova-11-like mtDNA sequences only appearing in sediments deposited after 80 ka.

Ancient faunal mtDNA

All large mammals present in the palaeontological record of Denisova Cave (currently available for Main and East Chambers only⁸) were also identified in the sediment DNA (Extended Data Fig. 7a, Supplementary Information section 10). In addition, ancient mtDNA from camelids was found in one sample from East Chamber (layer 12), consistent with the Pleistocene presence of *Camelus knoblochi* in the region²³. In contrast to large mammals, small mammals (such as Spalacidae, Leporidae and

Sciuridae) are largely absent from the genetic data (Extended Data Fig. 7b), which may be due to their lower biomass or underrepresentation among the capture probes. The sharp boundaries between the faunal mtDNA composition in some of the adjacent layers (for example, between layers 22.1 and 21/20 in Main Chamber) (Extended Data Fig. 8) provide additional evidence that post-depositional leaching of DNA is limited, if it occurs.

Despite the highly fragmentary nature of fossil remains at Denisova Cave⁸ and the varying quantities of DNA that may be deposited by different species, changes in the relative abundance of mammalian DNA over time are broadly consistent with changes in the skeletal records for some families, such as bovids, hyaenids, ursids and canids (Extended Data Fig. 7c,d). Genetic data also provide the opportunity to study faunal diversity at the species or population level, in cases in which comprehensive reference data are available (as is the case for elephantids, ursids and hyaenids) (Supplementary Information section 11). Elephantid mtDNA was assigned predominantly to woolly mammoth in all layers, whereas the relative abundance of ursid species shifted from predominantly cave bear mtDNA in layers deposited before 187 ± 14 ka to exclusively brown bear mtDNA after 112 ± 12 ka (Extended Data Fig. 10). We also detected the presence of three previously described mtDNA haplogroups of the genus *Crocuta* (spotted and cave hyaenas)²⁴. Layers deposited before 200 ka and after 120–80 ka contain mostly mtDNAs seen in African spotted hyaenas and European cave hyaenas (haplogroup A), whereas layers of intermediate age contain mtDNA predominantly from east Asian cave hyaenas (haplogroup D) and some from European cave hyaenas (haplogroup B) (Extended Data Fig. 10). The Altai Mountains may therefore have been a contact zone for both hominins and distinct lineages of hyaena and other fauna, as previously suggested by studies of mammalian skeletal remains²⁵.

At least two major turnovers of large mammals are evident from the sediment DNA (Fig. 2). First, marked changes in the relative proportions of mtDNA fragments of bovids, canids, equids, hyaenids and ursids, a turnover in hyaena mtDNA haplogroups and a shift from cave bears to brown bears occurred about 190 ka, contemporaneous with the climatic transition from an interglacial period (MIS 7) to a glacial period (MIS 6). The earliest traces of Neanderthal mtDNA also appear around this time. A second turnover took place between about 130 and 100 (or 80) ka, during and after the climatic transition from MIS 6 to MIS 5: mtDNA proportions of bovids, canids, felids and ursids declined, whereas those of cervids and equids increased, and cave bears and two hyaena haplogroups disappeared (Extended Data Fig. 10). This period is notable also for the absence of Denisovan mtDNA in the cave sediments. These changes suggest that turnovers in hominin and faunal populations may have been linked, and related to ecological factors²⁵.

Discussion

The identification of archaic hominin mtDNA in 175 sediment samples exceeds by an order of magnitude the number of hominin fossils retrieved from the deposits in Denisova Cave and provides a genetic profile of the presence of hominins in nearly all of the Pleistocene layers (Fig. 2). These data are complemented by faunal mtDNA sequences from 685 samples, which provide information about the diversity of other large mammals and changes in their relative abundance. However, we caution that the inferred sequence of hominin and faunal occupation is constrained by several factors: the existence of two major gaps in the stratigraphic record (170–156 and 97–80 ka), the time-averaging inherent in the accumulation of each sediment layer, the post-depositional disturbance of some layers owing to burrowing animals or small-scale mixing^{8,26}, and the precision of the optical ages used to construct the site chronology.

Beyond reconstructing the occupational history of Denisova Cave, our results have wider implications for understanding the human past. First, fragments of Denisovan mtDNA recovered from the middle Middle Palaeolithic layers deposited in Denisova Cave after 80 ka consistently show the highest similarity to the mtDNA of Denisova 3 and Denisova 4, as do mtDNA fragments retrieved from sediments at Baishiya Karst Cave on the northeastern flank of the Tibetan Plateau that are broadly contemporaneous in age (70–45 ka)²⁷. This pattern suggests that this lineage was the most abundant mtDNA type carried by Denisovans after 80 ka. Palaeontological studies²⁵ have suggested that Pleistocene mammals migrated from southeast Asia, along the eastern foothills of the Himalayas, to the northwest Altai. These faunal migrations may have spurred the dispersal of Denisovans into the region in which their remains were first discovered. Second, the presence of Neanderthal mtDNA before 170 ka further constrains the timing of an early event in Neanderthal history—the replacement of the mtDNA lineage found in Neanderthals who lived 430 ka in Spain by mtDNA that introgressed from early ancestors of modern humans^{18,19}—to between 430 and 170 ka. High-resolution profiling of sediment DNA can therefore provide an effective means of filling gaps in our knowledge of human evolutionary history and palaeoecology, independent of the discovery of skeletal remains.

Methods

No statistical methods were used to predetermine sample size. The experiments were not randomized, and investigators were not blinded to allocation during experiments and outcome assessment.

Collection of sediment samples

We collected a total of 728 sediment samples in a 10–15-cm grid-like pattern from the exposed Pleistocene deposits in Main ($n = 274$), East ($n = 252$) and South ($n = 202$)

Chambers (Extended Data Figs. 2b–d, 3a, b). We deviated from this pattern only if rocks were in the way or if a sample was clearly located on the boundary between layers. Gloves, face masks and hair nets were worn to minimize contamination by modern DNA. At the time of sample collection, a small area of the exposed profile at each sample location was first cleaned back to a depth of approximately 1 cm using a sterilized scalpel blade. Each sample was then collected using a new scalpel blade, which was inserted into the deposit, and the sediment extracted was carefully placed in a separate zip-lock plastic bag for each sample. This process was repeated at each location until sufficient sediment (several grams) had been collected. Each zip-lock bag was sealed immediately with duct tape and labelled with its sample number and prefix M, E or S to denote Main, East or South Chamber, respectively. Sample positions and corresponding layers were recorded in a field notebook, and layer assignments were checked for accuracy by M.B.K. in the field and also against high-resolution photographs. Sample numbers and locations are displayed in Supplementary Figs. 1–3. All materials were acquired as part of an agreement of scientific cooperation between the Institute of Archaeology and Ethnography, Siberian Branch of the Russian Academy of Sciences and the Max Planck Institute for Evolutionary Anthropology for projects in the field of palaeogenetics in North Asia, signed on 25 December 2018 and valid for a duration of five years. The Institute of Archaeology and Ethnography, Siberian Branch of the Russian Academy of Sciences oversees the excavations at Denisova Cave and obtained all of the permits necessary for conducting archaeological fieldwork and research associated with this project from the Ministry of Culture of the Russian Federation.

Common time scale for Main and East Chambers

We constructed a common time scale for the Pleistocene stratigraphic sequences in Main and East Chambers, but excluded South Chamber because of various stratigraphic complications that preclude definitive layer assignments to most of the Pleistocene deposit exposed at the time of sample collection (Supplementary Information section 2).

The stratified sequences in each chamber are numbered by layer, but layers with the same number cannot be traced stratigraphically between the chambers and are not necessarily equivalent in age. To correlate stratigraphic layers between chambers, a previous study⁸ constructed a separate Bayesian statistical age model for each chamber using their large dataset of optical ages, and then established isochrons (lines of equal age) between the chambers, using the modelled start and end ages for each depositional phase (figure 3 and extended data table 1 in ref. ⁸). Bayesian age models were constructed separately for each chamber because there is no a priori reason to assume that sediments have accumulated continuously, or at the same rate, in each of

the chambers. Time gaps in the stratigraphic sequence may therefore differ between the chambers owing to erosional events or periods of little or no sediment deposition.

Here we created a common time scale for the Pleistocene stratigraphic sequences in Main and East Chambers, using the modelled start and end ages for each depositional phase and the modelled time gaps (Extended Data Fig. 1). To construct this time scale, only point estimates of modelled age and not their associated uncertainties were taken into consideration; for example, if the start and end ages for a specific phase are 100 ± 10 and 50 ± 5 ka, respectively, then the corresponding time depth (size of coloured box in Extended Data Fig. 1a, b) is estimated to extend from 100 to 50 ka. The modelled ages for Main and East Chambers were projected horizontally onto a linear scale to derive a common time scale for the depositional phases in these two chambers (Extended Data Fig. 1c). We use the common timeline to display the mtDNA data and to show (Extended Data Fig. 1d) the Bayesian modelled ages (95.4% highest posterior density interval) for individual hominin fossils⁵.

Sampling, DNA extraction, library preparation and shotgun sequencing

Sampling, DNA extraction and library preparation were performed in a dedicated clean room at the Max Planck Institute for Evolutionary Anthropology (Leipzig). Sediment subsamples of between 29 and 191 mg were transferred into 2-ml tubes using antistatic spatulas. Before use, each spatula was soaked in 12% bleach for approximately 15 min with occasional mixing, washed thoroughly with water, dried and UV-treated with a dose of 7 J cm^{-2} in a UV-C crosslinker from both sides. One ml of extraction buffer²⁹ was added to subsamples with less than 100 mg of sediment, and 2 ml to samples with 100 mg or more. The resulting lysates were incubated overnight at 37°C on rotation. Aliquots of 150 μl of lysate were purified on a BRAVO NGS workstation B (Agilent Technologies) following a previously described bead-based protocol²⁹ using binding buffer ‘D’. The remaining lysate was stored at -20°C . Negative controls containing no sample material were included for both the lysis and purification steps. Supplementary Data 1 provides sample information.

The entire volume of DNA extract (30 μl) from each sample was converted into a single-stranded DNA library using the BRAVO NGS workstation B as previously described³⁰. Approximately six million molecules of a control oligonucleotide were added into each sample during the library preparation to evaluate the potential presence of inhibitors, which may reduce the efficiency of the process³¹. The number of sample and control library molecules obtained in each reaction was determined using two real-time PCR assays³⁰. All libraries were tagged with two indices, amplified to PCR plateau, and purified as described in the aforementioned protocol³⁰.

Aliquots of 1 µl from each library were pooled into sets of up to 92 samples (including controls) and sequenced on an Illumina MiSeq v3 platform in 76 cycle paired-end reads using micro or nano flowcells. Base calling was completed using Bustard (Illumina). The resulting shotgun data were evaluated only for the presence of the expected index pairs, which was confirmed in all sequencing runs.

Hybridization capture for mammalian and hominin mtDNA

Each library was enriched separately with two mtDNA probe sets, one targeting 242 mammalian mtDNA genomes¹³ and the other using the revised Cambridge Reference Sequences (rCRS³²) for targeting hominin mtDNA, in two successive rounds of on-bead hybridization capture following a previously published protocol¹³ with minor adjustments. All capture reactions were performed in sets of 384 samples (including extraction and library negative controls), using the BRAVO NGS workstation B. For some samples, 30 PCR cycles were performed in post-capture amplification of the enriched libraries (thus reaching PCR plateau for all libraries). For others, PCR cycles were reduced to between 12 and 16.

Captured libraries were pooled by combining 5-µl aliquots from each library in sets of approximately 92 libraries (including controls) for mammalian mtDNA enriched libraries, and sets of approximately 180 libraries (including controls) for human mtDNA enriched libraries. Each pool was sequenced on the Illumina HiSeq 2500 platform. Base calling was completed using Bustard (Illumina). The resulting capture data were evaluated as described in Supplementary Information sections 3, 4 for the presence of ancient mammalian and/or hominin DNA.

Identification of mammalian taxa

The initial processing of the mammalian capture data was performed using a previously described pipeline¹³. In brief, overlapping paired-end reads were merged into full-length molecule sequences using leeHom³³ (<https://bioinf.eva.mpg.de/>) and mapped to the 242 mammalian mitochondrial genomes included in the capture probe design¹³. Reads that could not be overlap-merged, unmapped sequences and sequences shorter than 35 base pairs (bp) were removed. Only a single sequence was retained from duplicates showing perfect sequence identity, and sequences with fewer than two duplicates were removed. All unique sequences were then assigned to mammalian taxa at the family level using BLAST³⁴ and the lowest common ancestor algorithm implemented in MEGAN³⁵. Sequences assigned to each family were mapped to the mitochondrial genomes of all species available within each family (Supplementary Data 3), requiring a mapping quality score of at least 25, and residual duplicate sequences were removed using bam-rmdup (<https://github.com/mpieva/biohazard->

[tools](#)) based on the sharing of identical alignment start and end coordinates. The mtDNA genome that produced the largest number of aligned sequences after removal of PCR duplicates was then used to determine the number of DNA fragments assigned to the respective family, as well as the frequency of cytosine (C) to thymine (T) substitutions at fragment ends.

Identification of ‘ancient taxa’ (that is, taxa for which ancient DNA sequences were retrieved) was performed according to the following criteria: (1) number of fragments assigned to a given taxon had to comprise at least 1% of the total number of taxonomically identified fragments; (2) at least 10 putatively deaminated fragments (that is, fragments showing C-to-T substitutions at the 5' and/or 3' terminal bases) had to be present; (3) frequency of C-to-T substitutions was required to be significantly higher than 10% based on 95% binomial confidence intervals at one or both termini; and (4) the fragments had to yield a coverage of at least 500 bp of the mtDNA reference genome. Supplementary Data [1](#) provides information on each sample and controls. Statistical testing was performed using R version 3.5.1.

Identification of ancient hominin DNA fragments

The processing of the hominin mtDNA capture data was performed as previously described^{[13](#)}, using an analysis pipeline that differed from the processing of the mammalian mtDNA capture data (Supplementary Information section [3](#)) only in that full-length molecule sequences were mapped to the rCRS of the human mitochondrial genome, and duplicates were removed based on alignment start and end coordinates using bam-rmdup (<https://github.com/mpieva/biohazard-tools>) before sequences were assigned to mammalian taxa.

To ensure that all libraries were sequenced to a sufficient depth, libraries that produced less than three sequence duplicates, on average, were sequenced deeper, and the final data were merged for analysis. The presence of ancient hominin DNA was determined according to the following criteria: (1) number of fragments assigned to hominins had to comprise at least 1% of the total number of taxonomically identified fragments; (2) at least 10 putatively deaminated fragments (that is, fragments showing a C-to-T substitution at the three 5' and/or 3' terminal bases) had to be present; and (3) frequency of C-to-T substitutions was required to be significantly higher than 10% based on 95% binomial confidence intervals at both termini. For some samples, multiple subsamples were taken and from some lysates, multiple libraries were prepared. The resulting data were analysed on a per-library basis, as well as merged by lysate (subsample). Supplementary Data [1](#) provides results of individual and merged data, and information on each sample and control. Statistical testing was performed using R version 3.5.1.

Reporting summary

Further information on research design is available in the [Nature Research Reporting Summary](#) linked to this paper.

Data availability

The mitochondrial consensus sequences reported from Main Chamber layers 19 (M65) and 20 (M71), and from East Chamber layers 11.4 (E202) and 11.4/12.1 (E213), are available in the Dryad digital repository (<https://doi.org/10.5061/dryad.k3j9kd567>), and the raw data for each mammalian mtDNA and human mtDNA enriched library are available in the European Nucleotide Archive under accession number [PRJEB44036](#). Any other relevant data are available from the corresponding authors upon reasonable request.

References

1. 1.

Krause, J. et al. The complete mitochondrial DNA genome of an unknown hominin from southern Siberia. *Nature* **464**, 894–897 (2010).

[ADS](#) [CAS](#) [PubMed](#) [Article](#) [Google Scholar](#)

2. 2.

Meyer, M. et al. A high-coverage genome sequence from an archaic Denisovan individual. *Science* **338**, 222–226 (2012).

[ADS](#) [CAS](#) [PubMed](#) [PubMed Central](#) [Article](#) [Google Scholar](#)

3. 3.

Sawyer, S. et al. Nuclear and mitochondrial DNA sequences from two Denisovan individuals. *Proc. Natl Acad. Sci. USA* **112**, 15696–15700 (2015).

[ADS](#) [CAS](#) [PubMed](#) [PubMed Central](#) [Article](#) [Google Scholar](#)

4. 4.

Slon, V. et al. A fourth Denisovan individual. *Sci. Adv.* **3**, e1700186 (2017).

[ADS](#) [PubMed](#) [PubMed Central](#) [Article](#) [Google Scholar](#)

5. 5.

Douka, K. et al. Age estimates for hominin fossils and the onset of the Upper Palaeolithic at Denisova Cave. *Nature* **565**, 640–644 (2019).

[ADS](#) [CAS](#) [PubMed](#) [Article](#) [Google Scholar](#)

6. 6.

Prüfer, K. et al. The complete genome sequence of a Neanderthal from the Altai Mountains. *Nature* **505**, 43–49 (2014).

[ADS](#) [PubMed](#) [Article](#) [Google Scholar](#)

7. 7.

Slon, V. et al. The genome of the offspring of a Neanderthal mother and a Denisovan father. *Nature* **561**, 113–116 (2018).

[ADS](#) [CAS](#) [PubMed](#) [PubMed Central](#) [Article](#) [Google Scholar](#)

8. 8.

Jacobs, Z. et al. Timing of archaic hominin occupation of Denisova Cave in southern Siberia. *Nature* **565**, 594–599 (2019).

[ADS](#) [CAS](#) [PubMed](#) [Article](#) [Google Scholar](#)

9. 9.

Shunkov, M. V., Kozlikin, M. B. & Derevianko, A. P. Dynamics of the Altai Paleolithic industries in the archaeological record of Denisova Cave. *Quat. Int.* **559**, 34–46 (2020).

[Article](#) [Google Scholar](#)

10. 10.

Shunkov, M. V., Fedorchenko, A. Y., Kozlikin, M. B. & Derevianko, A. P. Initial Upper Palaeolithic ornaments and formal bone tools from the East Chamber of Denisova Cave in the Russian Altai. *Quat. Int.* **559**, 47–67 (2020).

[Article](#) [Google Scholar](#)

11. 11.

Derevianko, A. P., Shunkov, M. V. & Kozlikin, M. B. Who were the Denisovans? *Archaeol. Ethnol. Anthropol. Eurasia* **48**, 3–32 (2020).

[Article](#) [Google Scholar](#)

12. 12.

Sawyer, S. *Insights into Neandertals and Denisovans from Denisova Cave*. PhD thesis, Univ. Leipzig (2016).

13. 13.

Slon, V. et al. Neandertal and Denisovan DNA from Pleistocene sediments. *Science* **356**, 605–608 (2017).

[ADS](#) [CAS](#) [PubMed](#) [Article](#) [Google Scholar](#)

14. 14.

Slon, V. et al. Mammalian mitochondrial capture, a tool for rapid screening of DNA preservation in faunal and undiagnostic remains, and its application to Middle Pleistocene specimens from Qesem Cave (Israel). *Quat. Int.* **398**, 210–218 (2016).

[Article](#) [Google Scholar](#)

15. 15.

Briggs, A. W. et al. Patterns of damage in genomic DNA sequences from a Neandertal. *Proc. Natl Acad. Sci. USA* **104**, 14616–14621 (2007).

[ADS](#) [CAS](#) [PubMed](#) [PubMed Central](#) [Article](#) [Google Scholar](#)

16. 16.

Sawyer, S., Krause, J., Guschanski, K., Savolainen, V. & Pääbo, S. Temporal patterns of nucleotide misincorporations and DNA fragmentation in ancient DNA. *PLoS ONE* **7**, e34131 (2012).

[ADS](#) [CAS](#) [PubMed](#) [PubMed Central](#) [Article](#) [Google Scholar](#)

17. 17.

Haile, J. et al. Ancient DNA chronology within sediment deposits: are paleobiological reconstructions possible and is DNA leaching a factor? *Mol. Biol. Evol.* **24**, 982–989 (2007).

[CAS](#) [PubMed](#) [Article](#) [Google Scholar](#)

18. 18.

Meyer, M. et al. A mitochondrial genome sequence of a hominin from Sima de los Huesos. *Nature* **505**, 403–406 (2014).

[ADS](#) [CAS](#) [PubMed](#) [Article](#) [Google Scholar](#)

19. 19.

Meyer, M. et al. Nuclear DNA sequences from the Middle Pleistocene Sima de los Huesos hominins. *Nature* **531**, 504–507 (2016).

[ADS](#) [CAS](#) [PubMed](#) [Article](#) [Google Scholar](#)

20. 20.

Peyrégne, S. et al. Nuclear DNA from two early Neandertals reveals 80,000 years of genetic continuity in Europe. *Sci. Adv.* **5**, eaaw5873 (2019).

[ADS](#) [PubMed](#) [PubMed Central](#) [Article](#) [Google Scholar](#)

21. 21.

Bray, N. L., Pimentel, H., Melsted, P. & Pachter, L. Near-optimal probabilistic RNA-seq quantification. *Nat. Biotechnol.* **34**, 525–527 (2016).

[CAS](#) [PubMed](#) [Article](#) [Google Scholar](#)

22. 22.

Vernot, B. et al. Unearthing Neanderthal population history using nuclear and mitochondrial DNA from cave sediments. *Science* **372**, eabf1667 (2021).

[CAS](#) [PubMed](#) [Article](#) [Google Scholar](#)

23. 23.

Titov, V. V. Habitat conditions for *Camelus knoblochi* and factors in its extinction. *Quat. Int.* **179**, 120–125 (2008).

[Article](#) [Google Scholar](#)

24. 24.

Westbury, M. V. et al. Hyena paleogenomes reveal a complex evolutionary history of cross-continental gene flow between spotted and cave hyena. *Sci. Adv.* **6**, eaay0456 (2020).

[ADS](#) [CAS](#) [PubMed](#) [PubMed Central](#) [Article](#) [Google Scholar](#)

25. 25.

Agadjanian, A. K. & Shunkov, M. V. Paleolithic man of Denisova Cave and zoogeography of Pleistocene mammals of northwestern Altai. *Paleontol. J.* **52**, 66–89 (2018).

[Article](#) [Google Scholar](#)

26. 26.

Morley, M. W. et al. Hominin and animal activities in the microstratigraphic record from Denisova Cave (Altai Mountains, Russia). *Sci. Rep.* **9**, 13785 (2019).

[ADS](#) [PubMed](#) [PubMed Central](#) [Article](#) [Google Scholar](#)

27. 27.

Zhang, D. et al. Denisovan DNA in Late Pleistocene sediments from Baishiya Karst Cave on the Tibetan Plateau. *Science* **370**, 584–587 (2020).

[CAS](#) [PubMed](#) [Article](#) [Google Scholar](#)

28. 28.

Prokopenko, A. A., Hinnov, L. A., Williams, D. F. & Kuzmin, M. I. Orbital forcing of continental climate during the Pleistocene: a complete astronomically tuned climatic record from Lake Baikal, SE Siberia. *Quat. Sci. Rev.* **25**, 3431–3457 (2006).

[ADS](#) [Article](#) [Google Scholar](#)

29. 29.

Rohland, N., Glocke, I., Aximu-Petri, A. & Meyer, M. Extraction of highly degraded DNA from ancient bones, teeth and sediments for high-throughput sequencing. *Nat. Protocols* **13**, 2447–2461 (2018).

[CAS](#) [PubMed](#) [Article](#) [Google Scholar](#)

30. 30.

Gansauge, M. T., Aximu-Petri, A., Nagel, S. & Meyer, M. Manual and automated preparation of single-stranded DNA libraries for the sequencing of DNA from ancient biological remains and other sources of highly degraded DNA. *Nat. Protocols* **15**, 2279–2300 (2020).

[CAS](#) [PubMed](#) [Article](#) [Google Scholar](#)

31. 31.

Glocke, I. & Meyer, M. Extending the spectrum of DNA sequences retrieved from ancient bones and teeth. *Genome Res.* **27**, 1230–1237 (2017).

[CAS](#) [PubMed](#) [PubMed Central](#) [Article](#) [Google Scholar](#)

32. 32.

Andrews, R. M. et al. Reanalysis and revision of the Cambridge reference sequence for human mitochondrial DNA. *Nat. Genet.* **23**, 147 (1999).

[CAS](#) [PubMed](#) [Article](#) [Google Scholar](#)

33. 33.

Renaud, G., Stenzel, U. & Kelso, J. leeHom: adaptor trimming and merging for Illumina sequencing reads. *Nucleic Acids Res.* **42**, e141 (2014).

[PubMed](#) [PubMed Central](#) [Article](#) [Google Scholar](#)

34. 34.

Altschul, S. F., Gish, W., Miller, W., Myers, E. W. & Lipman, D. J. Basic local alignment search tool. *J. Mol. Biol.* **215**, 403–410 (1990).

[CAS](#) [PubMed](#) [PubMed Central](#) [Article](#) [Google Scholar](#)

35. 35.

Huson, D. H., Auch, A. F., Qi, J. & Schuster, S. C. MEGAN analysis of metagenomic data. *Genome Res.* **17**, 377–386 (2007).

[CAS](#) [PubMed](#) [PubMed Central](#) [Article](#) [Google Scholar](#)

[Download references](#)

Acknowledgements

This project was funded by the Max Planck Society, the European Research Council (grant agreement no. 694707 to S.P.) and the Australian Research Council (fellowships FT150100138 to Z.J., FT140100384 to B.L. and FL130100116 to R.G.R.). K.O. was supported by an Australian Government Research Training Program Award. M.V.S., M.B.K. and A.P.D. were supported by RFBR, project no. 20-29-01011. V.S. acknowledges funding from the Alon Fellowship. We thank S. Grote, L. Jauregui, S. Lin, F. Mafessoni and L. Skov for help with the organization of laboratory work and data visualization; J. Lihanova, F. Müller, B. Schellbach and A. Weihmann for help with sample preparation and sequencing; and V. Vaneev for field assistance.

Funding

Open access funding provided by Max Planck Society.

Author information

Affiliations

1. Max Planck Institute for Evolutionary Anthropology, Leipzig, Germany

Elena I. Zavala, Benjamin Vernot, Elena Essel, Cesare de Filippo, Sarah Nagel, Julia Richter, Frédéric Romagné, Anna Schmidt, Viviane Slon, Janet Kelso, Svante Pääbo & Matthias Meyer

2. Centre for Archaeological Science, School of Earth, Atmospheric and Life Sciences, University of Wollongong, Wollongong, New South Wales, Australia

Zenobia Jacobs, Bo Li, Kieran O’Gorman & Richard G. Roberts

3. Australian Research Council Centre of Excellence for Australian Biodiversity and Heritage, University of Wollongong, Wollongong, New South Wales, Australia

Zenobia Jacobs, Bo Li & Richard G. Roberts

4. Institute of Archaeology and Ethnography, Russian Academy of Sciences, Siberian Branch, Novosibirsk, Russia

Michael V. Shunkov, Maxim B. Kozlikin & Anatoly P. Derevianko

5. Department of Anatomy and Anthropology, Sackler Faculty of Medicine, Tel Aviv University, Tel Aviv, Israel

Viviane Slon

6. Department of Human Molecular Genetics and Biochemistry, Sackler Faculty of Medicine, Tel Aviv University, Tel Aviv, Israel

Viviane Slon

7. The Shmunis Family Anthropology Institute, The Dan David Center for Human Evolution and Biohistory Research, Tel Aviv University, Tel Aviv, Israel

Viviane Slon

Authors

1. Elena I. Zavala

[View author publications](#)

You can also search for this author in [PubMed](#) [Google Scholar](#)

2. Zenobia Jacobs

[View author publications](#)

You can also search for this author in [PubMed](#) [Google Scholar](#)

3. Benjamin Vernot

[View author publications](#)

You can also search for this author in [PubMed](#) [Google Scholar](#)

4. Michael V. Shunkov

[View author publications](#)

You can also search for this author in [PubMed](#) [Google Scholar](#)

5. Maxim B. Kozlikin

[View author publications](#)

You can also search for this author in [PubMed](#) [Google Scholar](#)

6. Anatoly P. Derevianko

[View author publications](#)

You can also search for this author in [PubMed](#) [Google Scholar](#)

7. Elena Essel

[View author publications](#)

You can also search for this author in [PubMed](#) [Google Scholar](#)

8. Cesare de Fillipo

[View author publications](#)

You can also search for this author in [PubMed](#) [Google Scholar](#)

9. Sarah Nagel

[View author publications](#)

You can also search for this author in [PubMed](#) [Google Scholar](#)

10. Julia Richter

[View author publications](#)

You can also search for this author in [PubMed](#) [Google Scholar](#)

11. Frédéric Romagné

[View author publications](#)

You can also search for this author in [PubMed](#) [Google Scholar](#)

12. Anna Schmidt

[View author publications](#)

You can also search for this author in [PubMed](#) [Google Scholar](#)

13. Bo Li

[View author publications](#)

You can also search for this author in [PubMed](#) [Google Scholar](#)

14. Kieran O'Gorman

[View author publications](#)

You can also search for this author in [PubMed](#) [Google Scholar](#)

15. Viviane Slon

[View author publications](#)

You can also search for this author in [PubMed](#) [Google Scholar](#)

16. Janet Kelso

[View author publications](#)

You can also search for this author in [PubMed](#) [Google Scholar](#)

17. Svante Pääbo

[View author publications](#)

You can also search for this author in [PubMed](#) [Google Scholar](#)

18. Richard G. Roberts

[View author publications](#)

You can also search for this author in [PubMed](#) [Google Scholar](#)

19. Matthias Meyer

[View author publications](#)

You can also search for this author in [PubMed](#) [Google Scholar](#)

Contributions

E.I.Z., Z.J., S.P., R.G.R. and M.M. designed the study. Z.J., B.L., K.O. and R.G.R. collected samples in the field. M.V.S., M.B.K., A.P.D., Z.J. and R.G.R. provided archaeological, stratigraphical and geochronological context and interpretation. E.I.Z., E.E., S.N., J.R. and A.S. performed laboratory experiments. E.I.Z., Z.J., B.V., C.d.F., F.R., V.S. and J.K. performed, aided in or supervised data analysis and visualization. E.I.Z., Z.J., R.G.R. and M.M. wrote the manuscript with input from all authors.

Corresponding authors

Correspondence to [Elena I. Zavala](#) or [Zenobia Jacobs](#) or [Richard G. Roberts](#) or [Matthias Meyer](#).

Ethics declarations

Competing interests

The authors declare no competing interests.

Additional information

Peer review information *Nature* thanks Katerina Douka, Peter Heintzman and David Reich for their contribution to the peer review of this work. Peer reviewer reports are available.

Publisher's note Springer Nature remains neutral with regard to jurisdictional claims in published maps and institutional affiliations.

Extended data figures and tables

[Extended Data Fig. 1 Chronologies for sedimentary layers and hominin fossils.](#)

a, b, Schematic stratigraphic sequences for East Chamber (**a**) and Main Chamber (**b**), with ages and layer assignments from a previous publication⁸. Archaeological associations for each layer are colour-coded to differentiate between the four main artefact phases (early Middle Palaeolithic, dark green; middle Middle Palaeolithic, light green; Initial Upper Palaeolithic, dark orange; Upper Palaeolithic, light orange). White areas indicate layers with no archaeology, dark grey areas denote modelled time gaps and light grey areas denote time gaps between point estimates of age for successive layers that have overlapping age uncertainties. Trowel symbols indicate the layers from which sediment-derived Denisovan (red) and Neanderthal (blue) mtDNAs were recovered in a pilot study¹³ (corrected for the misattribution of a sample in East Chamber to layer 14 instead of layer 11.4). **c**, Common time scale constructed for Main and East Chambers (Methods) to facilitate comparison between layers and display mtDNA data. **d**, Age ranges (95.4% highest posterior density (HPD)) for fossils of Neanderthals (blue), Denisovans (red) and the Neanderthal–Denisovan offspring (Denisova 11, both colours), plotted on the common time scale. Fossil ages were estimated using a Bayesian model incorporating radiocarbon, optical and uranium-series ages, stratigraphic information and genetic data generated from hominin DNA sequences⁵.

[Extended Data Fig. 2 Locations of sediment DNA samples.](#)

a, Plan of cave interior, showing location of each chamber. Red lines denote stratigraphic profiles sampled in 2017. Grid coordinates for the excavation squares are shown along the top and left side of the plan, and the corresponding squares (each consisting of a Cyrillic letter and a number) are shown at the top of the stratigraphic profiles in Fig. [1a–c](#), Extended Data Figs. [3a, b](#), [5, 8, 9](#), Supplementary Figs. [1, 2, 3b, d](#). **b**, Southeast profile of Main Chamber after excavations in 2016. **c**, Southeast profile of East Chamber after excavation in 2015. **d**, Northwest profile of East Chamber after excavation in 2016. White circles represent samples collected for sediment DNA analysis. Individual sample numbers are provided in Supplementary Figs. [1](#) (Main) and [2](#) (East); sample numbers referred to in the text are indicated in **b**, **c**. Sample locations in South Chamber are indicated in Extended Data Fig. [3a, b](#), Supplementary Fig. [3](#).

Extended Data Fig. 3 Ancient hominin and mammalian mtDNA data for sediment samples in South Chamber.

a, b, Sample locations in upper section (**a**) and lower section (**b**) of southeast profile, using the same symbols for hominins as in Fig. [1](#). Layer 11 (associated with the Initial Upper Palaeolithic) and layer 22 are numbered, but other layers are denoted as either deformed Middle Palaeolithic (dMP) or as phosphate deformation deposits (pdd-9 and -12). The dMP and pdd deposits have been substantially affected by post-depositional deformation and phosphatization, respectively (Supplementary Information section [2](#)). **c**, Proportion of mtDNA fragments assigned to different families of large mammal in each layer, arranged in relative stratigraphic order. Values were obtained by averaging across the percentages of fragments assigned to each family in all samples from a specified layer. **d**, The 5' C-to-T substitution frequencies (putative deamination rates, in per cent) of mtDNA fragments assigned to bovid, canid, hyaenid and ursid in each layer. Individual values are shown as vertical bars, and the mean and s.d. values by black symbols. **e**, Average size (base pairs (bp)) of mammalian mtDNA fragments in each layer; individual values are shown as vertical bars and the mean and s.d. values by black symbols. **f**, Number of unique mtDNA fragments in each layer assigned to mammalian taxa per milligram of sediment from each library; individual values are shown as vertical bars and the mean and s.d. values by black symbols. Spearman's correlation test (one-sided) was used to test for correlation between stratigraphic depth (layer) and 5' C-to-T substitution frequency (minimum $n = 112$, positive correlation, maximum $P = 1.8 \times 10^{-5}$), number of unique ancient mtDNA fragments (minimum $n = 79$, negative correlation, maximum $P = 1.7 \times 10^{-5}$), and average fragment size (minimum $n = 79$, negative correlation, maximum $P = 1.8 \times 10^{-8}$).

Extended Data Fig. 4 Ancient mammalian mtDNA preservation in Main and East Chambers.

a, The 5' C-to-T substitution frequencies (putative deamination rates, in per cent) of mtDNA fragments assigned to bovid, canid, hyaenid and ursid, plotted as a function of time. **b**, **c**, Average size of mammalian mtDNA fragments (**b**) and number of unique mtDNA fragments assigned to taxa per milligram of sediment from each library (**c**), plotted as a function of time. Individual values for Main and East Chambers are shown as brown and green circles, respectively, and the mean and s.d. values by black symbols. The latter symbols are positioned on the time axis at the mean age for the relevant layer, and the time intervals for the corresponding layers in Main and East Chambers are denoted by brown and green shading, respectively (Extended Data Fig. 1). Spearman's correlation test (one-sided) was used to test for correlation between stratigraphic depth (layer) and 5' C-to-T substitution frequency (minimum $n = 133$, positive correlation, maximum $P = 2.7 \times 10^{-8}$), number of unique ancient mtDNA fragments (minimum $n = 222$, negative correlation, maximum $P = 0.02$), and average fragment size (minimum $n = 222$, negative correlation, maximum $P = 2.0 \times 10^{-25}$).

Extended Data Fig. 5 Abundance of ancient mammalian and hominin mtDNA in Main and East Chambers.

a, **b**, Number of unique mtDNA fragments assigned to mammalian taxa (**a**) and number of deaminated fragments assigned to hominins (**b**) per milligram of sediment from each library, for samples in Main Chamber (southeast profile) and East Chamber (southeast and northwest profiles). Ancient mammalian fragments encompass all mtDNA fragments assigned to families deemed to contain ancient DNA on the basis of signals of cytosine deamination. Intensity of shading in filled circles reflects relative abundance; samples that yielded no ancient mtDNA are shown as white circles. Background shading in **a** denotes layers that were deposited under relatively cold (blue) or relatively warm (orange) conditions⁸, and in **b** denotes layers associated with early Middle Palaeolithic (dark green), middle Middle Palaeolithic (light green), Initial Upper Palaeolithic (dark orange) and Upper Palaeolithic (light orange) archaeological assemblages⁸.

Extended Data Fig. 6 Phylogenetic trees for mtDNA sequences assigned to specific hominin lineages, and consistency of hominin mtDNA recovery from individual sediment samples.

a, **b**, Neighbour-joining tree constructed with newly constructed Neanderthal mtDNA consensus sequences (in bold) and published Neanderthal mtDNA genomes (protein-coding genes only) (**a**) and published Denisovan and Sima de los Huesos mtDNA genomes and a newly reconstructed Denisovan mtDNA consensus (protein-coding genes only) (**b**). Taxa were clustered on the basis of pairwise differences, with support for each node based on a bootstrap test with 500 replicates. Positions with missing

data or gaps were removed, resulting in 9,219 and 7,495 positions used for analysis in **a** and **b**, respectively. **c**, Recovery of ancient hominin mtDNA fragments and identification of hominin lineages in cases in which several libraries were prepared from the same sediment sample. Each rectangle represents one library and shows the corresponding number of deaminated fragments. Libraries produced from the same sediment subsample are shown by adjacent rectangles; libraries from different subsamples are kept separate.

Extended Data Fig. 7 Proportions of mammalian mtDNA fragments and skeletal remains in Main and East Chambers.

a, b, Proportion (in per cent) of ancient DNA fragments (red) and skeletal remains (blue)⁸ assigned to various families of large (**a**) and small (**b**) mammals, combined for all samples in Main and East Chambers and ranked in descending order of mtDNA percentage. **c, d**, Proportion (in per cent) of ancient mtDNA fragments and skeletal remains assigned to families of large mammals for individual layers in Main Chamber (**c**) and East Chamber (**d**), arranged in relative stratigraphic order. The mtDNA values were obtained by averaging across the percentages of fragments assigned to each family in all samples from a specified layer.

Extended Data Fig. 8 Proportions of ancient mtDNA fragments of large mammals in Main Chamber.

Pie charts showing proportions of mtDNA fragments assigned to specific mammalian families for each sample; empty circles denote samples that yielded no ancient mtDNA.

Extended Data Fig. 9 Proportions of ancient mtDNA fragments of large mammals in East Chamber.

a, b, Pie charts showing proportions of mtDNA fragments assigned to specific mammalian families for each sample in the southeast (**a**) and northwest (**b**) profiles.

Extended Data Fig. 10 Numbers and proportions of ancient mtDNA fragments assigned to different mtDNA groups of ursids, hyaenids and elephantids in Main and East Chambers.

Black-and-white circles denote the total number of samples assigned to a specific mtDNA clade, plotted as a function of time (mean age for the relevant layer). The corresponding bars are colour-coded on the basis of the proportion (in per cent) of

samples assigned to each group, and extend over the time intervals for the respective layers in Main and East Chambers.

Supplementary information

Supplementary Information

This file contains a Supplementary Discussion, Supplementary References, Supplementary Tables 1-10 and Supplementary Figures 1-44.

Reporting Summary

Supplementary Data 1

Summary of DNA lysates, extracts and libraries and results of mammalian and human mtDNA capture.

Supplementary Data 2

Summary of results from pH testing.

Supplementary Data 3

mtDNA genomes used as references for different analyses.

Peer Review File

Rights and permissions

Open Access This article is licensed under a Creative Commons Attribution 4.0 International License, which permits use, sharing, adaptation, distribution and reproduction in any medium or format, as long as you give appropriate credit to the original author(s) and the source, provide a link to the Creative Commons license, and indicate if changes were made. The images or other third party material in this article are included in the article's Creative Commons license, unless indicated otherwise in a credit line to the material. If material is not included in the article's Creative Commons license and your intended use is not permitted by statutory regulation or exceeds the permitted use, you will need to obtain permission directly from the copyright holder. To view a copy of this license, visit <http://creativecommons.org/licenses/by/4.0/>.

Reprints and Permissions

About this article



Check for
updates

Cite this article

Zavala, E.I., Jacobs, Z., Vernot, B. *et al.* Pleistocene sediment DNA reveals hominin and faunal turnovers at Denisova Cave. *Nature* **595**, 399–403 (2021).
<https://doi.org/10.1038/s41586-021-03675-0>

[Download citation](#)

- Received: 02 February 2021
- Accepted: 27 May 2021
- Published: 23 June 2021
- Issue Date: 15 July 2021
- DOI: <https://doi.org/10.1038/s41586-021-03675-0>

Comments

By submitting a comment you agree to abide by our [Terms](#) and [Community Guidelines](#). If you find something abusive or that does not comply with our terms or guidelines please flag it as inappropriate.

[Download PDF](#)

Advertisement

This article was downloaded by **calibre** from <https://www.nature.com/articles/s41586-021-03675-0>

Mechanism of disease and therapeutic rescue of *Dok7* congenital myasthenia
[Download PDF](#)

- Article
- Open Access
- [Published: 23 June 2021](#)

Mechanism of disease and therapeutic rescue of *Dok7* congenital myasthenia

- [Julien Oury](#)¹,
- [Wei Zhang](#)¹,
- [Nadia Leloup](#)²,
- [Akiko Koide](#)^{2,3},
- [Alexis D. Corrado](#)²,
- [Gayatri Ketavarapu](#) [ORCID: orcid.org/0000-0001-5029-8595](#)²,
- [Takamitsu Hattori](#)^{2,4},
- [Shohei Koide](#) [ORCID: orcid.org/0000-0001-5473-4358](#)^{2,4} &
- [Steven J. Burden](#) [ORCID: orcid.org/0000-0002-3550-6891](#)¹

[Nature](#) volume 595, pages 404–408 (2021) [Cite this article](#)

- 4023 Accesses
- 155 Altmetric
- [Metrics details](#)

Subjects

- [Developmental disorders](#)
- [Neuromuscular disease](#)

Abstract

Congenital myasthenia (CM) is a devastating neuromuscular disease, and mutations in DOK7, an adaptor protein that is crucial for forming and maintaining neuromuscular synapses, are a major cause of CM^{1,2}. The most common disease-causing mutation

(*DOK7*^{1124_1127 dup}) truncates DOK7 and leads to the loss of two tyrosine residues that are phosphorylated and recruit CRK proteins, which are important for anchoring acetylcholine receptors at synapses. Here we describe a mouse model of this common form of CM (*Dok7*^{CM} mice) and a mouse with point mutations in the two tyrosine residues (*Dok7*^{2YF}). We show that *Dok7*^{CM} mice had severe deficits in neuromuscular synapse formation that caused neonatal lethality. Unexpectedly, these deficits were due to a severe deficiency in phosphorylation and activation of muscle-specific kinase (MUSK) rather than a deficiency in DOK7 tyrosine phosphorylation. We developed agonist antibodies against MUSK and show that these antibodies restored neuromuscular synapse formation and prevented neonatal lethality and late-onset disease in *Dok7*^{CM} mice. These findings identify an unexpected cause for disease and a potential therapy for both *DOK7* CM and other forms of CM caused by mutations in *AGRIN*, *LRP4* or *MUSK*, and illustrate the potential of targeted therapy to rescue congenital lethality.

[Download PDF](#)

Main

Congenital myasthenia is a group of diseases caused by mutations in genes that are important for the formation, function, and maintenance of neuromuscular synapses^{1,2}. Mostly, mutations in these genes are recessive and diminish gene activity, thereby causing synaptic deficits that lead to early onset structural and functional deficits in the neuromuscular synapse, which are responsible for muscle weakness throughout life.

The formation and maintenance of neuromuscular synapses requires the assembly of highly specialized presynaptic and postsynaptic membranes, which involves the coordinated action of several key molecules^{3,4,5}. AGRIN, which is released from motor nerve terminals, binds to the lipoprotein receptor-related protein 4 (LRP4) in muscle, stimulating the formation of a complex between LRP4 and muscle-specific kinase (MUSK), a receptor tyrosine kinase that acts as a master regulator of synaptic differentiation^{4,5,6,7,8,9}. LRP4, once clustered in the postsynaptic membrane as a consequence of MUSK activation, also signals directly back to motor axons to stimulate presynaptic differentiation¹⁰. Mutations in *AGRIN*, *LRP4* and *MUSK*, as well as in the genes that encode subunits of acetylcholine receptors (AChRs), also cause CM^{2,11}.

Activation of MUSK also depends on the adaptor protein DOK7¹². Mutations in *Dok7* are responsible for 10–20% of all cases of CM^{13,14,15}. The disease is debilitating—causing weakness in limb, neck and facial muscles—and one-quarter of patients with

DOK7 CM require non-invasive ventilation at some point during their lifetime. Few treatments abate the clinical symptoms¹⁶. The N-terminal region of DOK7 contains pleckstrin homology (PH) and phosphotyrosine-binding (PTB) domains (Fig. 1a), which function to dimerize DOK7 and bind a phosphorylated tyrosine motif in the MUSK juxtamembrane (JM) region¹⁷. A failure of DOK7 to bind MUSK leads to a failure of AGRIN to stimulate MUSK phosphorylation^{12,18}, demonstrating that DOK7 is essential to stabilize phosphorylation of MUSK, probably by promoting its dimerization¹⁹. In addition, AGRIN-stimulated MUSK phosphorylation leads to phosphorylation of two tyrosine residues in the C-terminal region of DOK7, which triggers the recruitment of CRK and CRK-L—proteins that participate in the clustering of AChRs^{15,20}.

Fig. 1: The C-terminal region of DOK7 is essential for synaptic differentiation and to sustain MUSK tyrosine phosphorylation.

 **figure1**

a, *Dok7^{1124_1127,dup}* (*Dok7^{CM}*) leads to a frame-shift and premature termination, including loss of Y396 and Y406. **b**, Expected and observed numbers of progeny, and χ^2 values, from intercrossing *Dok7* heterozygous mutant mice. **c, d**, Staining of AChRs (red) and axons and nerve terminals (green) in diaphragm muscles from wild-type and

Dok7 mutant E18.5 mice (**c**). Scale bars, 10 µm. Scatter plots (**d**) show the number of synapses, synaptic size, and density of synaptic AChRs from $n = 5\text{--}8$ mice of each genotype. **e, f**, Western blot (top) and quantification (bottom) of DOK7 expression in E18.5 mice. $n = 8$ mice in **e**, 11 in **f**. t-DOK7, truncated DOK7; IP, immunoprecipitation. **g, h**, Western blot (top) and quantification (bottom) of MUSK tyrosine phosphorylation (pTyr) in E18.5 mice. $n = 7$ mice in **g**, 5 in **h**. Plots show data for individual mice and mean ± s.e.m.; NS, not significant; *** $P < 0.00005$; two-sided Student's *t*-test.

[Source data](#)

[Full size image](#)

The most common cause of *Dok7* CM is a four-base-pair duplication (residues 1124–1127, TGCC), which leads to a frameshift and premature termination of DOK7^{13,21}. Some individuals with *Dok7* CM are homozygous for this mutant allele, whereas others carry this mutant allele in combination with a different mutant allele of *Dok7*. The truncated form of DOK7 retains the PH and PTB domains and binds to the tyrosine-phosphorylated JM region of MUSK¹³, but lacks the two tyrosine residues that are phosphorylated and recruit CRK proteins, suggesting that the loss of these tyrosine residues is responsible for the synaptic deficits in this common form of *Dok7* CM^{2,15,20}.

Synapse formation requires DOK7 C-terminal region

To study how loss of the C-terminal region of DOK7 leads to defects in the structure and function of neuromuscular synapses, we generated a mouse model of the most common form of *Dok7* CM (*Dok7*^{1124_1127 dup}; referred to as *Dok7*^{CM} mice) and a second mouse mutant (*Dok7*^{Y396F,Y406F}; referred to as *Dok7*^{2YF} mice), in which the two tyrosine residues in the C-terminal region are mutated to phenylalanine (Fig. [1a](#)).

Homozygous *Dok7*^{CM} mice were present at the expected numbers at embryonic day 18.5 (E18.5), but were rarely found alive a day later, at birth, when neuromuscular synapses are essential for respiration and survival (Fig. [1b](#)). We stained diaphragm muscles from E18.5 embryos with probes that allowed us to visualize presynaptic and postsynaptic differentiation and found fivefold fewer synapses in *Dok7*^{CM} mice than in wild-type mice (Fig. [1c,d](#)). Moreover, the synapses that did form were immature, as both synaptic size and the density of synaptic AChRs were reduced fivefold (Fig. [1c,d](#), Extended Data Fig. [1a](#)). By contrast, homozygous *Dok7*^{2YF} mice were born at the expected frequency (Fig. [1b](#)) and thrived as fertile adult mice. Moreover, their neuromuscular synapses appeared largely normal (Fig. [1c,d](#), Extended Data Fig. [1b](#)).

Thus, unexpectedly, loss of the two tyrosine residues in the C-terminal region of DOK7 is not the cause of the lethality and severe synaptic deficits in *Dok7^{CM}* mice.

***Dok7^{CM}* lowers DOK7 levels and MUSK phosphorylation**

To determine how loss of the DOK7 C-terminal region caused the synaptic defects, we measured expression of *Dok7* mRNA and truncated DOK7 protein in *Dok7^{CM}* mice using antibodies against the DOK7 PTB domain that detected the truncated and wild-type proteins equally (Extended Data Fig. 2). *Dok7* mRNA levels were normal in muscle from *Dok7^{CM}* mice, whereas the truncated DOK7 protein was expressed at threefold lower levels than the wild-type DOK7 protein (Fig. 1e, Extended Data Fig. 3). By contrast, DOK7(2YF) was expressed at normal levels (Fig. 1f) and, as expected^{15,20}, was not tyrosine phosphorylated (Extended Data Fig. 4).

Because DOK7 functions as a dimer to dimerize MUSK, thereby stabilizing MUSK tyrosine phosphorylation¹⁹, we determined whether MUSK tyrosine phosphorylation was diminished in *Dok7^{CM}* mice. MUSK phosphorylation was reduced sevenfold in *Dok7^{CM}* mice but was normal in *Dok7^{2YF}* mice (Fig. 1g,h).

CRK proteins are recruited directly to MUSK

We anticipated that recruitment of CRK proteins to the synapse would be absent or severely reduced in both *Dok7^{CM}* and *Dok7^{2YF}* mutant mice. Indeed, CRK recruitment to the synapse and to the MUSK complex was substantially diminished (2.8-fold) in *Dok7^{CM}* mice (Fig. 2a,b), but to our surprise was only modestly reduced (by 28%) in *Dok7^{2YF}* mice (Fig. 2a,b). These findings suggest that CRK is recruited to a tyrosine phosphorylated synaptic protein(s) in addition to DOK7.

Fig. 2: Recruitment of CRK to the synapse and to the MUSK–DOK7 complex is impaired in *Dok7^{CM/CM}* mice.

 **figure2**

a, Staining for CRK-L (green) and AChRs (red) in muscle sections from E18.5 mice. Scale bars, 5 μ m. Representative images from three experiments. **b**, Top, co-immunoprecipitation of CRK with MUSK from muscles of E18.5 mice. Bottom, CRK levels normalized to MUSK levels for mice of each genotype ($n = 8$ for *Dok7*^{CM/CM} and $n = 4$ for *Dok7*^{2YF/2YF} mice). **c**, Amino acid sequence of the MUSK JM region showing binding site for DOK7 and potential binding site for CRK. **d**, Left, affinity capture of DOK7 and CRK-I with phosphorylated and non-phosphorylated peptides detected by immunoblotting. The peptide sequences are shown. Right, quantification. Plots show individual data and mean \pm s.e.m.; * $P < 0.05$, ** $P < 0.0005$, *** $P < 0.00005$; two-sided Student's *t*-test.

[Source data](#)

[Full size image](#)

The three activation loop tyrosines and Y553 in MUSK become phosphorylated after stimulation by AGRIN^{12,18,22,23}. We found that Y553 in the MUSK JM region is within not only a PTB-binding site that recruits DOK7, but also a potential SH2-binding motif for CRK proteins (Fig. 2c). Both CRKI and DOK7 bound the MUSK JM site in a phosphorylation-dependent manner (Fig. 2d). Mutation of amino acids that compose the SH2-binding motif, but not the PTB-binding site, impaired binding of CRKI (Fig. 2d). Thus, CRK can bind not only to the phosphorylated C-terminal region of DOK7 but also directly to the tyrosine-phosphorylated JM region of MUSK. This redundancy for recruiting CRK to the synapse is likely to explain the near-normal association of CRK with the MUSK complex in *Dok7^{2YF}* mice and the difference in the phenotypes of *Dok7^{CM}* and *Dok7^{2YF}* mice.

Agonist antibodies against MUSK

If diminished MUSK phosphorylation caused disease in *Dok7 CM*, we reasoned that stimulation of MUSK might rescue the synaptic defects and overcome lethality. We explored this idea by generating agonist antibodies targeting MUSK and treating *Dok7^{CM}* mice with the agonist antibodies.

We screened a phage-display library for antibodies that bound the Fz-like domain in the extracellular region of mouse and human MUSK. We targeted the Fz-like domain because this domain is not essential for MUSK function and antibodies against the Fz-like domain cause no obvious harm in mice^{24,25}.

We identified high-affinity antibodies that bound the Fz-like domain in human and mouse MUSK and stimulated MUSK phosphorylation independent of AGRIN (Fig. 3a,b, Extended Data Fig. 5), thereby overcoming the shortcomings of previously described agonist antibodies that recognized mouse but not human MUSK²⁵.

Fig. 3: Antibodies against MUSK Fz domain stimulate MUSK phosphorylation in cultured myotubes and bind MUSK in vivo.

 **figure3**

a, MUSK phosphorylation, normalized to MUSK expression, in C2 myotubes treated for 30 min with biotinylated Fabs each tetramerized with streptavidin. Top, western blot; bottom, quantification. **b**, MUSK phosphorylation in C2 myotubes treated with 0.5 nM AGRIN or 10 nM antibodies, with either mouse IgG2a or human IgG1 Fc regions. Top, western blot; bottom, quantification. **c**, Left, staining for AChRs (red) and human IgG (cyan) in diaphragm muscles of P30 wild-type mice two days after intraperitoneal injection of antibody X17. Right, X17 signal intensities normalized to AChR plotted against antibody dose ($n = 3$ mice per concentration). Plots show mean \pm s.e.m. (with individual data points in **a**, **b**).

[Source data](#)

[Full size image](#)

We injected the MUSK agonist antibody X17, in a mouse IgG2a format with mutations that reduce Fc domain effector function²⁶, interperitoneally into wild-type mice and found that 10 mg kg^{-1} of X17 had a half-life of 5 days in blood and that it saturated synaptic MUSK (Fig. 3c, Extended Data Fig. 6a). Chronic injection of X17 (10 mg kg^{-1} at postnatal day 4 (P4), P24 and P44) in wild-type mice over two months had no effect on the organization of neuromuscular synapses, weight gain or motor behaviour (Extended Data Fig. 6).

X17 rescues synapse formation and lethality

Although *Dok7^{CM}* mice on a C57BL/6 background died at birth, we found that *Dok7^{CM}* mice on a mixed genetic background survived for one to two weeks after birth (Extended Data Table 1), which facilitated experiments to study the therapeutic efficacy of X17. We injected these *Dok7^{CM}* mice with 10 mg kg⁻¹ of X17 or an isotype-matched negative control antibody at P4, when they showed signs of disease (they were runted and had synaptic deficits) (Extended Data Fig. 7). *Dok7^{CM}* mice injected with the control antibody continued to lose weight and died within a week (Fig. 4a,b). Injection of X17 reversed the weight loss and rescued the *Dok7^{CM}* mice from this early lethality (Fig. 4a,b). Over the next few weeks, the weight gain was continuous in nine of the twelve *Dok7^{CM}* mice injected with X17; the weight gain slowed in three of the X17-injected mice, and they died at P23–P24. Another antibody, X3, rescued *Dok7^{CM}* mice from early postnatal lethality when injected at 20 mg kg⁻¹ but not at 10 mg kg⁻¹ (Extended Data Fig. 8), suggesting that a higher initial dose of a MUSK agonist antibody may be more effective during early postnatal development, when synapses are undergoing critical steps in maturation.

Fig. 4: An agonist antibody against MUSK restores synapse development and rescues lethality in young *Dok7^{CM}* mice and reverses disease relapse in adult *Dok7^{CM}* mice.

 **figure4**

a, *Dok7^{CM/CM}* mice on a C57BL/6-CBA mixed background ($n = 12$) were injected with X17 at P4, P24 and P44, and the experiment was ended when the mice were at P60. Mice ($n = 6$) injected with the isotype control died within two weeks of birth. **b**, X17 restored weight gain in *Dok7^{CM/CM}* mice. **c**, Left, diaphragm muscles from P60

mice stained for AChRs (red) and neurofilament and synapsin to label motor axons and nerve terminals (green). Scale bar, 10 µm. Right, quantification ($n = 3$ mice, >50 synapses per mouse). **d**, Staining for AChRs (red), CRK-L (green) and synapsin (cyan) in myofibres isolated from muscles of wild-type mice (left) and *Dok7^{CM/CM}* mice injected with X17 (right). Representative images of ten synapses per mouse from three mice. Scale bars, 5 µm. **e**, Grip strength and latency to fall from a rotating rotarod of *Dok7^{CM/CM}* mice treated with X17 ($n = 9$), compared with wild-type mice ($n = 18$). **f**, Weight changes in *Dok7^{CM/CM}* mice treated either with mIgG2a-X17 at P4, P24 and P44 or with hIgG1-X17 at P4 and P18, with antibody treatment then discontinued for 2–3 months. When *Dok7^{CM/CM}* mice began to lose weight and showed motor deficits, they were re-injected with hIgG1-X17 and their weights monitored. Red dots indicate death at the end of the experiment. **g**, Latency to fall for four wild-type and three *Dok7^{CM/CM}* mice. **h**, Change in rotarod performance one week after X17 treatment of *Dok7^{CM/CM}* mice (fold-change from performance before X17), compared with that of wild-type mice not injected with X17. All plots except **b**, **f** show individual data points and mean ± s.e.m.; NS, not significant; * $P < 0.05$, ** $P < 0.005$, *** $P < 0.0005$, **** $P < 0.00005$; two-sided Student's *t*-test.

[Source data](#)

[Full size image](#)

We investigated whether chronic dosing could lead to long-term survival. Repeated injections of X17 in the nine surviving *Dok7^{CM}* mice at P24 and P44 led to survival of these mice for at least two months (Fig. 4a, b), at which point we assessed their motor performance and the structure of their neuromuscular synapses. X17 rescued synapse formation and maturation, as the neuromuscular synapses of these mice had developed the complex pretzel-like shape characteristic of fully mature mouse neuromuscular synapses (Fig. 4c). Moreover, X17 rescued the recruitment of CRK proteins to the neuromuscular synapse (Fig. 4d).

Antibody X17 rescued the motor function of *Dok7^{CM}* mice, as assessed by grip strength and rotarod assays (Fig. 4e). Moreover, *Dok7^{CM}* mice injected with X17 were fertile and produced offspring at the expected frequency. Together, these findings indicate that reduced MUSK tyrosine phosphorylation is central to disease in *Dok7^{CM}* mice. Even if the C-terminal region of DOK7 has an additional role in synapse formation, this function can be overridden by stimulating MUSK.

Therapeutic reversal in adult *Dok7 CM* mice

We next sought to determine whether X17 could reverse neuromuscular deficits that develop during adulthood, a question particularly relevant to developing a human therapy as *DOK7* CM in humans would probably be treated during adult life. We treated *Dok7^{CM}* mice with X17 either at P4, P24 and P44 or at P4 and P18 but then discontinued antibody treatment. Both groups of *Dok7^{CM}* mice continued to maintain their weight and mobility for 2–3 months (Fig. 4f), indicating that the effects of the antibody lasted for longer than its lifetime in the blood. However, mice ultimately began to lose weight and display motor deficits (Fig. 4f,g, Supplementary Video 1). When the mice were losing weight at a rate of about 0.4 g per day, we injected X17 once again and monitored their weight and mobility. Two days after the resumption of X17 treatment, the *Dok7^{CM}* mice began to regain weight (by about 0.4 g per day over the next week) (Fig. 4f). Within one week of reinitiating antibody treatment, the motor performance of the *Dok7^{CM}* mice had been restored (Fig. 4g, Supplementary Video 1). The mice continued to gain weight and their motor performance continued to improve for at least one additional week after antibody treatment, when the experiment was ended (Fig. 4f,g).

Discussion

Stimulation of MUSK with an agonist antibody rescued synapse formation and motor function, prevented lethality and allowed *Dok7^{CM}* mice to thrive postnatally as fertile adults. Moreover, the motor deficits that developed in adult *Dok7^{CM}* mice after withdrawal of antibody treatment were readily reversed by reinitiating antibody treatment. Thus this therapeutic strategy, which avoids the complex requirements for gene therapy²⁷, might be beneficial for humans with *DOK7* CM or other neuromuscular diseases.

Most previous studies of DOK7 have relied upon analysis of transfected muscle and non-muscle cells that overexpress DOK7^{12,15,20}. In this context, which bypasses the normal requirement for AGRIN and LRP4 to stimulate MUSK, the *in vivo* consequences of *Dok7* mutations might have been masked by the overexpression of DOK7.

Inbred C57BL/6 mice containing the *Dok7^{CM}* mutation showed more severe functional deficits than humans with the same mutation. The mutant phenotype was less severe in mice with a mixed genetic background, as outbred mice survived for up to three weeks postnatally, whereas inbred mutant mice died at birth. Modifiers in the hybrid strains may lessen disease severity, or C57BL/6 mice may contain genes that worsen the phenotype. In either case, the modestly prolonged lifespan of *Dok7^{CM}* mice on the mixed background offers a mouse model that presents a longer temporal window in which to assess therapeutic approaches.

These experiments demonstrate full rescue from congenital lethality by targeted therapy. Our findings point to an unforeseen therapeutic approach, as this strategy does not directly target the mutant protein but rather targets a wild-type protein that has diminished activity caused by the mutation of an upstream gene, in this case *DOK7*. Epistatic rescue in this way could also provide therapy for CM caused by mutations in *AGRIN*, *LRP4* or *MUSK*, in addition to *DOK7*, as well as for other neuromuscular diseases. Moreover, this strategy has the potential for widespread use to treat genetic disorders in humans for which the disease mechanism is understood and suitable targets have been identified.

Methods

Mice

To generate *Dok7^{CM}* mice, we microinjected in vitro-transcribed single guide RNA (sgRNA; 5' CTGCTCAGTCTGGCCCCCCC 3', 5 ng/μl) and in vitro-transcribed Cas9 RNA (10 ng/μl), together with a DNA repair template (5' ATGCCGGCAATCTGGACGTCTGGCGGGCCGGTGAGGAATT CGTTCTCTGC TCAGTCTGCCTGCCCCCTGGAGGCCAGCGCACCTGAGCCCAGACTGTGTGCC TGCCCACCTGGGGCGGCCGAGTA 3', 10 ng/μl) containing the TGCC duplication, into the pronuclei of C57BL/6 mouse zygotes²⁸. We analysed 14 mice that were born from injected zygotes by sequencing tail DNA (primer: 5' GCAGTTACAGGAGGTTGG 3'). One mouse carried a *Dok7* allele with the desired TGCC duplication. We crossed the founder mouse with wild-type C57BL/6 mice to generate the *Dok7^{CM}* line. DNA sequencing confirmed the sequence of the *Dok7* mutation. Mice were subsequently genotyped using primers (forward: 5' GCGGCCTCGGCAGTTACAG 3'; reverse: 5' GCTTACCTTGAGTCCGCCACAGA 3'). We analysed five genomic loci that scored the highest probability for off-target recognition (<http://crispr.mit.edu>). We found no evidence for mutations in these genes (Extended Data Table 2).

An earlier study described a similar mouse model, generated using classic embryonic stem cell gene targeting, for this common form of *DOK7* CM²⁷. Although the lethality of these mutant mice could be rescued by an adenoviral-associated vector expressing wild-type DOK7, establishing a gene therapy approach to treat *DOK7* CM²⁷, this study did not examine the cause of disease in the *Dok7^{I124_I127,dup}* mouse model.

To generate *Dok7^{YF}* mice, we injected an sgRNA (5' TTCGAGGTGTGTCATAG 3', 15 ng/μl) and in vitro-transcribed Cas9 RNA (30 ng/μl), together with the DNA repair template (5' ATGCCGGCAGCAACCTGGACGTGTGGCGGGCCGGTGAGGAATT CGTTCTC

TGCTCAGTCTGCCTGCCCTGGAGCCAGCGCACCTGAGCCCAGACTGTGT GCCTGCCACCTGGGGCGGCCGAGTA 3', 30 ng/μl) to convert tyrosine 396 and tyrosine 406 to phenylalanine, into the cytoplasm of C57BL/6 mouse zygotes. We analysed 33 mice that were born from injected zygotes by sequencing tail DNA (primer: 5' TGGCATTGCCACAGGCAG 3'). One mouse carried a *Dok7* allele with the desired tyrosine-to-phenylalanine substitutions. We crossed the founder mouse with wild-type C57BL/6 mice to generate the *Dok7^{2YF}* line. DNA sequencing from these lines confirmed the sequence of the *Dok7* mutation. Mice were housed and maintained according to Institutional Animal Use and Care Committee (IACUC) guidelines.

Growth of cultured cells

C2C12 mouse muscle cells, purchased from and authenticated by ATCC (Cat CRL-1772), were grown at 37 °C in growth medium (GM): Dulbecco's modified Eagle's medium (DMEM) containing 4.5 g/l glucose, l-glutamine and sodium pyruvate (Corning cellgro), supplemented with 10% fetal bovine serum (FBS; GemCell). Myoblast fusion and myotube differentiation were induced when myoblasts were 70% confluent by switching to differentiation medium (DM): DMEM with 4.5 g/l glucose and 1 mM l-glutamine, supplemented with 2% heat-inactivated horse serum. Immortalized myoblasts were isolated from wild-type and *Dok7^{2YF}* embryos and grown as described previously²⁹.

HEK 293 cells were purchased from and authenticated by ATCC (ATCC Cat CRL-1573). Cells were grown at 37 °C in the same medium as described above for C2C12 myoblasts and transfected using Lipofectamine 3000 Transfection Reagent Kit (Thermofisher Scientific). All cell lines tested negative for mycoplasma contamination using the e-Myco Plus PCR detection kit.

Antibody treatment of C2 myotubes

Three days after C2C12 myotubes had formed, the cultures were treated for 30 min with 10 nM biotinylated Fabs in complex with 2.5 nM streptavidin, 10 nM IgGs, or 0.5 nM recombinant neural AGRIN-B8 (R&D Systems). Myotubes were homogenized at 4 °C in lysis buffer (50 mM sodium chloride, 30 mM triethanolamine, pH 7.5, 50 mM sodium fluoride, 5 mM EDTA, 5 mM EGTA, 2 mM sodium orthovanadate, 1 mM *N*-ethylmaleimide, 1 mM sodium tetrathionate, 10 μM pepstatin, plus complete protease inhibitor mix (Roche)). NP-40 was added to a final concentration of 1%, and the extract was incubated with rocking for 30 min at 4 °C. Insoluble proteins were removed by centrifugation at 12,000 rpm for 20 min at 4 °C. The supernatant was precleared for 1 h at 4 °C with Protein G-agarose beads (Sigma-Aldrich) before incubation overnight at 4 °C with antibodies against MUSK (MUSK 1A)³⁰.

Complexes were incubated for 4 h with Protein G-agarose beads. The beads were subsequently washed (three times for 9 min) in lysis buffer containing 1% NP-40. Proteins were eluted from the beads with 1% SDS in lysis buffer.

Isolation of MUSK and DOK7 from muscle

Whole leg muscles or cultured muscle cells were homogenized at 4 °C in lysis buffer (50 mM sodium chloride, 30 mM triethanolamine pH 7.5, 50 mM sodium fluoride, 5 mM EDTA, 5 mM EGTA, 2 mM sodium orthovanadate, 1 mM *N*-ethylmaleimide, 1 mM sodium tetrathionate, 10 µM pepstatin, plus complete protease inhibitor mix (Roche)). NP-40 was added to a final concentration of 1%, and the extract was incubated with rocking for 30 min at 4 °C. Insoluble proteins were removed by centrifugation at 12,000 rpm for 20 min at 4 °C. The supernatant was pre-cleared for 1 h at 4 °C with Protein G-agarose beads (Sigma-Aldrich) before overnight incubation at 4 °C with antibodies against MUSK (MUSK 1A)³⁰ or goat anti-DOK7 (R&D Systems, AF 6398), followed by incubation for 4 h with Protein G-agarose beads. The beads were subsequently washed (three times for 9 min) in lysis buffer containing 1% NP-40. Proteins were eluted from the beads with 1% SDS in lysis buffer.

Western blotting

Proteins were fractionated by SDS-PAGE and transferred to PVDF membranes. Blots were probed with antibodies against MUSK (R&D Systems, AF562), phosphotyrosine (Millipore, 05-321) or DOK7 (1916), as described previously^{18,19,20,24}. Antibodies against CRK (BD Bioscience, 610035) and CRK-L (Santa Cruz Biotechnology, sc-365092) have been described previously²⁰. We quantified the band intensities with a ChemiDoc imaging system (BioRad), as described previously²⁴. The graphs show the mean values from at least three separate experiments. A two-sided Student's *t*-test was used to determine statistical significance and was conducted using GraphPad Prism 9.0 software.

Whole-mount muscle immunohistochemistry

Diaphragm muscles were dissected from E18.5 embryos and postnatal mice in oxygenated L-15 medium. The muscles were pinned onto Sylgard-coated dissection dishes, fixed for 1.5 h in 1% PFA and blocked for 1 h in PBS with 3% BSA (Sigma IgG free) and 0.5% Triton X-100 (PBT). Diaphragm muscles were stained with Alexa 488-conjugated anti-BGT (Invitrogen) to label AChRs and with antibodies against neurofilament-L (Synaptic Systems, 171002), β-TUBIII (Synaptic Systems 302302) or synapsin 1/2 (Synaptic Systems, 106002) to label motor axons and nerve terminals, respectively³¹. The antibodies were force-pipetted into the muscle, and the muscles

were incubated overnight at 4 °C on an orbital shaker in a humidified chamber. Diaphragm muscles were washed 10 times over the course of 5 h with PT (PBS with Triton X-100) at room temperature and rinsed in PBS before the muscle was whole-mounted in 50% glycerol. Muscles from at least three mice of each genotype were analysed for each experiment. Images were acquired with a Zeiss LSM 800 confocal microscope using ZEN software. Adjustments to detector gain and laser intensity were made to avoid saturation. The number and size of synapses, the density of synaptic AChRs, the width of the endplate zone, the extent of denervation and the co-localization index (synapsin/AChRs) were quantified using FIJI/ImageJ software, as described previously³². A two-sided Student's *t*-test was used to determine statistical significance and was conducted using GraphPad Prism 9.0 software.

Staining single muscle fibres

Tibialis anterior muscles were dissected in oxygenated L-15 medium, pinned to a Sylgard-coated dish and fixed in 2% PFA (in PBS) for 2 h. After several rinses in PBS, one to three myofibres were manually teased with fine forceps. Fixed myofibres were blocked for 2 h at room temperature in PBS containing 5% BSA, 1% normal goat serum, and 0.04% saponin. Fibres were then incubated with primary antibodies overnight at 4 °C, washed three times for 5 min with PBS containing 0.04% saponin, incubated with secondary antibodies for 2 h at room temperature, washed again, and mounted in VectaShield (Vector Laboratories). Antibodies against CRK-L (Santa Cruz Biotechnology, sc-365092) were used and the postsynaptic membrane was visualized by staining with Alexa Fluor 488–anti-BGT (Invitrogen).

Cryosection immunohistochemistry

Limb muscles were embedded in optimal cutting temperature (OCT) medium and frozen on a dry-ice platform. Ten-micrometre sections, collected onto poly-l-lysine-coated glass slides, were fixed in 1–4% PFA for 10 min, washed in PBS with 3% BSA (PB) three times for 5 min, permeabilized with PB + 0.5% X-Triton (PBT) for 10 min, washed in PB and incubated overnight at 4 °C with primary antibodies against CRK-L (Santa Cruz Biotechnology, sc-365092) in PBT in a humidified chamber. Sections were washed in PB three times for 5 min before overnight incubation at 4 °C with secondary antibodies and Alexa Fluor 488–anti-BGT (Invitrogen), diluted in PBS, in a humidified chamber. Sections were washed three times for 5 min in PB, then PBS, before mounting in Vectashield anti-fade mounting medium.

Behaviour

All-limb grip strength was measured using a grip-strength apparatus (Bioseb). Mice were allowed to grip the grid with both forelimbs and hindlimbs, and the mouse was

pulled back steadily, until the mouse lost grip on the grid. The grip strength meter digitally displayed the maximum force applied (in grams) as the grasp was released. The mean measurement from six consecutive trials was taken as an index of all-limb grip strength. Mice were given an interval of 10–15 s between trials. Body weight was determined after all grip-strength measurements to analyse for potential co-variability. To enhance the robustness and reliability of the grip-strength assessment, all measurements were taken by the same experimenter³³.

Motor function of male and female mice at P60 was assessed on a rotarod (AccuRotor four-channel, Omnitech Electronics). Mice were placed on the rotarod (3.0-cm rotating cylinder) rotating at 2.5 rpm, and the speed of rotation was increased linearly to 40 rpm over the course of 5 min. The time to fall from the rod was measured. Each mouse was subjected to three trials with 5-min intervals, and we recorded the longest latency to fall from the three trials. A two-sided Student's *t*-test was used to determine statistical significance and was conducted using GraphPad Prism 9.0 software.

Development of synthetic antibodies

The full-length extracellular region (E22 to T494 of mouse MUSK and E22 to T495 of human MUSK), including the Fz domain and the C-terminal flanking sequence (D307 to T494 of mouse MUSK and K314 to T495 of human MUSK) were expressed as a C-terminal fusion with the Avi and His₆ tags using the secretion signal sequence of mouse IgkVIII in EXPI293 cells with the ExpiFectamine 293 Transfection kit (Thermo Fisher Scientific) using standard procedures provided by the vendor. The proteins were purified from the filtered culture supernatant using a HiTrap Nickel column (GE Healthcare) and biotinylated in vitro using the BirA enzyme in the presence of 0.5 mM biotin and 10 mM ATP. The biotinylated proteins were further purified using a Superdex S75 10/300 column (GE Healthcare).

Sorting of an antibody phage-display library was performed as described previously³⁴. In brief, a phage-display library was first sorted with all four antigens at 100 nM in the first round, followed by sorting with a single antigen at 100, 50 and 20 nM in the second, third and fourth rounds, respectively. To enrich for clones that bind to both human and mouse Fz domains, we used multiple sorting strategies in which alternate antigens were used in successive rounds (for example, human Fz; mouse ECD; human ECD). Individual clones were screened using phage enzyme-linked immunosorbent assay (ELISA) with the four antigens³⁴, and the DNA sequences of clones bound to all of the antigens were determined.

The Fab proteins with the Avi tag at the C terminus of the heavy chain of selected clones were produced from *Escherichia coli* and biotinylated as described previously³⁴. The mouse IgG2a-LALAPG sample of clone X17 was produced using a

modified version of the pFUSE-mIgG2a-Fc vector (InvivoGen) containing the LALAPG mutations in the Fc region²⁶ and human CH1 domain and the pFUSE-CL Ig vector (InvivoGen). This chimeric antibody consisted of a human Fab and mouse Fc sequences. In addition, we exchanged the mouse Fc sequences with those from human IgG1, containing LALA mutations, to generate hIgG1-X17, hIgG1-X2 and hIgG1-X3 antibodies.

Affinity measurements

The affinities of antibody clones in the Fab and IgG formats were measured using a bead-binding assay^{35,36,37}. A biotinylated human antigen protein was immobilized on Dynabeads M280 streptavidin beads (Thermo Fisher Scientific) by rapidly mixing 100 µl of tenfold diluted beads in PBSB (PBS containing 0.5% bovine serum albumin (BSA, GeminiBio)) and 100 µl of 50 nM protein. The beads were then blocked with 2 µM biotin, washed twice with PBSB and resuspended in 1 ml PBSB. This reaction was appropriately scaled for the number of measurements when necessary. Five microlitres of the diluted beads and 20 µl of an antibody sample were mixed in a well of a 96-well polypropylene plate (Greiner Bio-One, catalogue number 650261) and incubated at room temperature for 30 min with gentle shaking. Samples were transferred to the wells of a 96-well filter plate (Millipore MultiScreen HTS HV, 0.45 mm, Thermo Fisher); the liquid was removed using a vacuum manifold and the wells were washed three times with 200 µl ice-cold PBSB using the vacuum manifold. The beads were stained with anti-human Fab antibody labelled with Alexa Fluor 647 (Jackson Immuno Research, Alexa Fluor 647 AffiniPure Goat Anti-Human IgG, F(ab')₂ fragment specific, 109-605-097). Following washing, the beads were suspended in 70 µl PBSB and analysed using an iQue screener (Sartorius) or an Intellicyt HTFC system. The resulting titration curves were analysed by nonlinear least-squared fitting of a 1:1 binding model using the GraphPad Prism software.

Half-life of antibody in blood

Mice were injected intraperitoneally with antibodies. Mouse blood samples were centrifuged, and supernatants were diluted 2,000-fold in PBSB. Antibody levels were measured using the bead assay described above except that the binding reaction was performed at 4 °C. The half-life was determined by nonlinear least squares fitting of the median fluorescence intensities with a single exponential curve.

Phosphopeptide pull-down assay

HEK 293 cells were transfected with plasmids encoding HA-tagged DOK7 and HA-tagged CRKI at 37 °C for 48h (Lipofectamine 3000, Thermofisher Scientific). After 48 h, the transfected cells were homogenized at 4 °C in lysis buffer; NP-40 was added

to a final concentration of 1%, and the extract was incubated with rocking for 30 min at 4 °C. Insoluble proteins were removed by centrifugation at 12,000 rpm for 20 min at 4 °C. The supernatants were precleared for 1 h at 4 °C with streptavidin-agarose beads (Sigma-Aldrich).

Four biotinylated phosphopeptides ((1) ELLLDRLHPNPMYQRMPLLL, (2) ELLLDRLHPNPMp(Y)QRMPLLL, (3) ELLLDRLHPAPMp(Y)QRMPLLL, and (4) ELLLDRLHPNPMp(Y)AAAPLLL (Thermofisher Scientific)) were immobilized on streptavidin-agarose beads and incubated overnight at 4 °C in lysis buffer (50 mM sodium chloride, 30 mM triethanolamine, pH 7.5, 50 mM sodium fluoride, 5 mM EDTA, 5 mM EGTA, 2 mM sodium orthovanadate, 1 mM *N*-ethylmaleimide, 1 mM sodium tetrathionate, and 10 µM pepstatin, plus complete protease inhibitor mix (Roche)), containing 1% NP-40. The cell extracts, pre-cleared on streptavidin-agarose beads, were incubated overnight at 4 °C with biotinylated phosphopeptides immobilized on streptavidin-agarose beads. The beads were subsequently washed (three times for 9 min) in lysis buffer containing 1% NP-40. Proteins were eluted from the beads with 1% SDS in lysis buffer. Western blotting was performed using antibodies against HA tag (Abcam, ab49969).

Quantitative PCR with reverse transcription (RT-qPCR)

Total RNA was isolated from muscles of E18.5 wild-type and *Dok7*^{CM} embryos using TRIZOL reagent (Invitrogen) and reverse transcribed with Superscript-III First strand kit (Invitrogen). Real-time qPCR was performed on a LightCycler 480 (Roche) using SYBR Green Master kit (Roche). PCRs were performed using primer pairs: 5'-CTGGTAAAAAGGACCTCTCGAAG-3' and 5'-CCAGTTCACTAATGACACAAACG-3' for *Hprt*, 5'-TCAGCCTCAGAACAGAGCGTGTTG-3' and 5'-GCCTCAGAACAGAGGAAGTGGATAG-3' for *Dok7*. Samples were run in triplicate and *Dok7* expression level was normalized to *Hprt* expression.

Statistics and reproducibility

No statistical method was used to predetermine sample size. No data were excluded from the analyses. The experiments were not randomized. The investigators were not blinded to the genotype of the mice with the exception of the motor performance experiments.

Reporting summary

Further information on research design is available in the [Nature Research Reporting Summary](#) linked to this paper.

Data availability

Raw data generated from this study are available upon a reasonable request. [Source data](#) are provided with this paper.

References

1. 1.

Müller, J. S., Mihaylova, V., Abicht, A. & Lochmüller, H. Congenital myasthenic syndromes: spotlight on genetic defects of neuromuscular transmission. *Expert Rev. Mol. Med.* **9**, 1–20 (2007).

[Article](#) [Google Scholar](#)

2. 2.

Engel, A. G., Shen, X. M., Selcen, D. & Sine, S. M. Congenital myasthenic syndromes: pathogenesis, diagnosis, and treatment. *Lancet Neurol.* **14**, 420–434 (2015).

[Article](#) [Google Scholar](#)

3. 3.

Sanes, J. R. & Lichtman, J. W. Induction, assembly, maturation and maintenance of a postsynaptic apparatus. *Nat. Rev. Neurosci.* **2**, 791–805 (2001).

[CAS](#) [Article](#) [Google Scholar](#)

4. 4.

Burden, S. J., Yumoto, N. & Zhang, W. The role of MuSK in synapse formation and neuromuscular disease. *Cold Spring Harb. Perspect. Biol.* **5**, a009167 (2013).

[Article](#) [Google Scholar](#)

5. 5.

Tintignac, L. A., Brenner, H. R. & Rüegg, M. A. Mechanisms regulating neuromuscular junction development and function and causes of muscle wasting. *Physiol. Rev.* **95**, 809–852 (2015).

[CAS](#) [Article](#) [Google Scholar](#)

6. 6.

Jennings, C. G., Dyer, S. M. & Burden, S. J. Muscle-specific trk-related receptor with a kringle domain defines a distinct class of receptor tyrosine kinases. *Proc. Natl Acad. Sci. USA* **90**, 2895–2899 (1993).

[ADS](#) [CAS](#) [Article](#) [Google Scholar](#)

7. 7.

DeChiara, T. M. et al. The receptor tyrosine kinase MuSK is required for neuromuscular junction formation in vivo. *Cell* **85**, 501–512 (1996).

[CAS](#) [Article](#) [Google Scholar](#)

8. 8.

Kim, N. et al. Lrp4 is a receptor for Agrin and forms a complex with MuSK. *Cell* **135**, 334–342 (2008).

[CAS](#) [Article](#) [Google Scholar](#)

9. 9.

Zhang, B. et al. LRP4 serves as a coreceptor of agrin. *Neuron* **60**, 285–297 (2008).

[CAS](#) [Article](#) [Google Scholar](#)

10. 10.

Yumoto, N., Kim, N. & Burden, S. J. Lrp4 is a retrograde signal for presynaptic differentiation at neuromuscular synapses. *Nature* **489**, 438–442 (2012).

[ADS](#) [CAS](#) [Article](#) [Google Scholar](#)

11. 11.

McMacken, G., Abicht, A., Evangelista, T., Spendiff, S. & Lochmüller, H. The increasing genetic and phenotypical diversity of congenital myasthenic syndromes. *Neuropediatrics* **48**, 294–308 (2017).

[CAS](#) [Article](#) [Google Scholar](#)

12. 12.

Okada, K. et al. The muscle protein Dok-7 is essential for neuromuscular synaptogenesis. *Science* **312**, 1802–1805 (2006).

[ADS](#) [CAS](#) [Article](#) [Google Scholar](#)

13. 13.

Beeson, D. et al. Dok-7 mutations underlie a neuromuscular junction synaptopathy. *Science* **313**, 1975–1978 (2006).

[ADS](#) [CAS](#) [Article](#) [Google Scholar](#)

14. 14.

Müller, J. S. et al. Phenotypical spectrum of DOK7 mutations in congenital myasthenic syndromes. *Brain* **130**, 1497–1506 (2007).

[Article](#) [Google Scholar](#)

15. 15.

Hamuro, J. et al. Mutations causing DOK7 congenital myasthenia ablate functional motifs in Dok-7. *J. Biol. Chem.* **283**, 5518–5524 (2008).

[CAS](#) [Article](#) [Google Scholar](#)

16. 16.

Burke, G. et al. Salbutamol benefits children with congenital myasthenic syndrome due to DOK7 mutations. *Neuromuscul. Disord.* **23**, 170–175 (2013).

[Article](#) [Google Scholar](#)

17. 17.

Yamanashi, Y., Tezuka, T. & Yokoyama, K. Activation of receptor protein-tyrosine kinases from the cytoplasmic compartment. *J. Biochem.* **151**, 353–359 (2012).

[CAS](#) [Article](#) [Google Scholar](#)

18. 18.

Herbst, R. & Burden, S. J. The juxtamembrane region of MuSK has a critical role in agrin-mediated signaling. *EMBO J.* **19**, 67–77 (2000).

[CAS](#) [Article](#) [Google Scholar](#)

19. 19.

Bergamin, E., Hallock, P. T., Burden, S. J. & Hubbard, S. R. The cytoplasmic adaptor protein Dok7 activates the receptor tyrosine kinase MuSK via dimerization. *Mol. Cell* **39**, 100–109 (2010).

[CAS](#) [Article](#) [Google Scholar](#)

20. 20.

Hallock, P. T. et al. Dok-7 regulates neuromuscular synapse formation by recruiting Crk and Crk-L. *Genes Dev.* **24**, 2451–2461 (2010).

[CAS](#) [Article](#) [Google Scholar](#)

21. 21.

Cossins, J. et al. The spectrum of mutations that underlie the neuromuscular junction synaptopathy in DOK7 congenital myasthenic syndrome. *Hum. Mol. Genet.* **21**, 3765–3775 (2012).

[CAS](#) [Article](#) [Google Scholar](#)

22. 22.

Watty, A. et al. The in vitro and in vivo phosphotyrosine map of activated MuSK. *Proc. Natl Acad. Sci. USA* **97**, 4585–4590 (2000).

[ADS](#) [CAS](#) [Article](#) [Google Scholar](#)

23. 23.

Till, J. H. et al. Crystal structure of the MuSK tyrosine kinase: insights into receptor autoregulation. *Structure* **10**, 1187–1196 (2002).

[CAS](#) [Article](#) [Google Scholar](#)

24. 24.

Remédio, L. et al. Diverging roles for Lrp4 and Wnt signaling in neuromuscular synapse development during evolution. *Genes Dev.* **30**, 1058–1069 (2016).

[Article](#) [Google Scholar](#)

25. 25.

Cantor, S. et al. Preserving neuromuscular synapses in ALS by stimulating MuSK with a therapeutic agonist antibody. *eLife* **7**, e34375 (2018).

[Article](#) [Google Scholar](#)

26. 26.

Lo, M. et al. Effector-attenuating substitutions that maintain antibody stability and reduce toxicity in mice. *J. Biol. Chem.* **292**, 3900–3908 (2017).

[CAS](#) [Article](#) [Google Scholar](#)

27. 27.

Arimura, S. et al. Neuromuscular disease. DOK7 gene therapy benefits mouse models of diseases characterized by defects in the neuromuscular junction. *Science* **345**, 1505–1508 (2014).

[ADS](#) [CAS](#) [Article](#) [Google Scholar](#)

28. 28.

Price, N. L. et al. Specific disruption of Abca1 targeting largely mimics the effects of miR-33 knockout on macrophage cholesterol efflux and atherosclerotic plaque development. *Circ. Res.* **124**, 874–880 (2019).

[CAS](#) [Article](#) [Google Scholar](#)

29. 29.

Smith, C. L., Mittaud, P., Prescott, E. D., Fuhrer, C. & Burden, S. J. Src, Fyn, and Yes are not required for neuromuscular synapse formation but are necessary for stabilization of agrin-induced clusters of acetylcholine receptors. *J. Neurosci.* **21**, 3151–3160 (2001).

[CAS](#) [Article](#) [Google Scholar](#)

30. 30.

Fichtner, M. L. et al. Affinity maturation is required for pathogenic monovalent IgG4 autoantibody development in myasthenia gravis. *J. Exp. Med.* **217**, e20200513 (2020). <https://doi.org/10.1084/jem.20200513>.

[CAS](#) [Article](#) [PubMed](#) [PubMed Central](#) [Google Scholar](#)

31. 31.

Kim, N. & Burden, S. J. MuSK controls where motor axons grow and form synapses. *Nat. Neurosci.* **11**, 19–27 (2008).

[CAS](#) [Article](#) [Google Scholar](#)

32. 32.

Jaworski, A. & Burden, S. J. Neuromuscular synapse formation in mice lacking motor neuron- and skeletal muscle-derived Neuregulin-1. *J. Neurosci.* **26**, 655–661 (2006).

[CAS](#) [Article](#) [Google Scholar](#)

33. 33.

Oury, J. et al. MACF1 links Rapsyn to microtubule- and actin-binding proteins to maintain neuromuscular synapses. *J. Cell Biol.* **218**, 1686–1705 (2019).

[CAS](#) [Article](#) [Google Scholar](#)

34. 34.

Miller, K. R. et al. T cell receptor-like recognition of tumor in vivo by synthetic antibody fragment. *PLoS ONE* **7**, e43746 (2012).

[ADS](#) [CAS](#) [Article](#) [Google Scholar](#)

35. 35.

Hattori, T. et al. Multiplex bead binding assays using off-the-shelf components and common flow cytometers. *J. Immunol. Methods* **490**, 112952 (2021).

[CAS](#) [Article](#) [Google Scholar](#)

36. 36.

Nady, N. et al. ETO family protein Mtgr1 mediates Prdm14 functions in stem cell maintenance and primordial germ cell formation. *eLife* **4**, e10150 (2015).

[Article](#) [Google Scholar](#)

37. 37.

Nishikori, S. et al. Broad ranges of affinity and specificity of anti-histone antibodies revealed by a quantitative peptide immunoprecipitation assay. *J. Mol. Biol.* **424**, 391–399 (2012).

[CAS](#) [Article](#) [Google Scholar](#)

38. 38.

Wu, T. T., Johnson, G. & Kabat, E. A. Length distribution of CDRH3 in antibodies. *Proteins* **16**, 1–7 (1993).

[CAS](#) [Article](#) [Google Scholar](#)

[Download references](#)

Acknowledgements

We thank T. Nottoli and the Yale Genome Editing Center for their assistance in generating the *Dok7* mutant mice.; K. O'Connor for the gift of antibody MUSK IA; A. Mar and B. Gamallo-Lana for assistance with the motor performance tests; B. G. Pil for assistance with genotyping and maintaining mice; M. Usmani for assistance with antibody characterization; and D. Littman and R. Lehmann for reading and providing comments on the manuscript. This work was supported by NINDS grants (RO1 NS075124 and R37 NS36193 to S.J.B.), and funds from the Colton Center for Autoimmunity (to S.J.B. and S.K.).

Author information

Affiliations

1. Helen L. and Martin S. Kimmel Center for Biology and Medicine at the Skirball Institute of Biomolecular Medicine, NYU Grossman School of Medicine, New York, NY, USA

Julien Oury, Wei Zhang & Steven J. Burden

2. Perlmutter Cancer Center, NYU Langone Health, New York, NY, USA

Nadia Leloup, Akiko Koide, Alexis D. Corrado, Gayatri Ketavarapu, Takamitsu Hattori & Shohei Koide

3. Department of Medicine, NYU Grossman School of Medicine, New York, NY, USA

Akiko Koide

4. Department of Biochemistry and Molecular Pharmacology, NYU Grossman School of Medicine, New York, NY, USA

Takamitsu Hattori & Shohei Koide

Authors

1. Julien Oury

[View author publications](#)

You can also search for this author in [PubMed](#) [Google Scholar](#)

2. Wei Zhang

[View author publications](#)

You can also search for this author in [PubMed](#) [Google Scholar](#)

3. Nadia Leloup

[View author publications](#)

You can also search for this author in [PubMed](#) [Google Scholar](#)

4. Akiko Koide

[View author publications](#)

You can also search for this author in [PubMed](#) [Google Scholar](#)

5. Alexis D. Corrado

[View author publications](#)

You can also search for this author in [PubMed](#) [Google Scholar](#)

6. Gayatri Ketavarapu

[View author publications](#)

You can also search for this author in [PubMed](#) [Google Scholar](#)

7. Takamitsu Hattori

[View author publications](#)

You can also search for this author in [PubMed](#) [Google Scholar](#)

8. Shohei Koide

[View author publications](#)

You can also search for this author in [PubMed](#) [Google Scholar](#)

9. Steven J. Burden

[View author publications](#)

You can also search for this author in [PubMed](#) [Google Scholar](#)

Contributions

W.Z. generated the *Dok7* mutant mice. W.Z. and J.O. analysed the *Dok7* mutant mice. J.O. measured MUSK phosphorylation in cultured muscle cells treated with the MUSK antibodies and studied *Dok7^{CM}* mutant mice treated with the agonist antibodies. N.L. designed and constructed antigen vectors, produced antigens, performed antibody library sorting, characterized clones, produced Fab proteins, performed affinity measurements and constructed IgG vectors. A.K. supervised the design and execution of the antibody library screen and clone analysis. A.D.C. performed sequence analysis, produced IgG proteins, and performed affinity measurements and half-life analysis. G.K. performed affinity measurements and half-life analysis. T.H. supervised the antigen design and vector construction, and production and characterization of the IgG proteins. S.K. performed sequence analysis. S.J.B. and S.K. supervised all aspects of this work.

Corresponding authors

Correspondence to [Shohei Koide](#) or [Steven J. Burden](#).

Ethics declarations

Competing interests

S.J.B. is an inventor on a patent (no. 9,329,182) for ‘Method of treating motor neuron disease with an antibody that agonizes MUSK’. S.J.B., S.K., J.O., A.K. and N.L. are

inventors on a patent application (no. 1474662.02232) for ‘Therapeutic MUSK Antibodies’ filed by New York University. These patents have been licensed to Argenx BVBA. S.J.B. and S.K. received research funding from Argenx BVBA. S.K. is a scientific advisory board member and holds equity in and receives consulting fees from Black Diamond Therapeutics, and receives research funding from Puretech Health.

Additional information

Peer review information *Nature* thanks the anonymous reviewers for their contribution to the peer review of this work.

Publisher’s note Springer Nature remains neutral with regard to jurisdictional claims in published maps and institutional affiliations.

Extended data figures and tables

[Extended Data Fig. 1 Characterization of neuromuscular synapses in *Dok7* mutant mice.](#)

a, b, Left, diaphragm muscles from E18.5 (**a**) and P135 (**b**) wild-type and *Dok7* mutant mice were stained with Alexa 488–anti-BGT to label AChRs (red) and antibodies against neurofilament and synapsin to label motor axons and nerve terminals (green). Scale bars, 50 µm (**a**), 10 µm (**b**). **a**, Right, endplate width, denervation and co-localization of synapses in wild-type, *Dok7*^{CM/CM} and *Dok7*^{2YF/2YF} mice. The width of the endplate band (dashed lines) was increased by 45% in *Dok7*^{CM/CM} mice but was normal in *Dok7*^{2YF/2YF} mice. In *Dok7*^{CM/CM} mice, 17% of AChR clusters were completely unopposed by nerve terminals, indicating denervated myofibres. Many synapses in *Dok7*^{CM/CM} mice were partially innervated, as nearly half of the AChR-rich area at synapses was not juxtaposed by nerve terminals. **b**, Right, in *Dok7*^{2YF/2YF} mice, synapses mature from a plaque-like to a complex, pretzel-like shape, characteristic of mature mouse neuromuscular synapses. Synapses in *Dok7*^{2YF/2YF} mice, however, often appeared elongated. The number of synapses and the density of synaptic AChRs were similar in wild-type and *Dok7*^{2YF/2YF} mice. Synaptic size was increased by 20% in *Dok7*^{2YF/2YF} mice when compared with wild-type mice. Data shown as mean ± s.e.m. from 3 mice (>50 synapses per mouse). n.s., not significant; **P* < 0.05, ****P* < 0.00005; two-sided Student’s *t*-test.

[Source data](#)

Extended Data Fig. 2 Wild-type and truncated DOK7 are detected with similar efficiency by antibodies against the PH and PTB domains in DOK7.

a, HEK 293 cells were transiently transfected with a plasmid expressing either HA-tagged DOK7 or HA-tagged truncated DOK7 encoded by *Dok7^{II24_II27 TGCC dup}*. Proteins in cell lysates (triplicates) were separated by SDS-PAGE, and western blots were probed with either a rabbit antibody against the PTB domain in DOK7 or a monoclonal antibody against HA (left). We measured the grey levels of the bands for wild-type and truncated DOK7 proteins and normalized the level detected by western blotting with the rabbit antibody against DOK7 with the level detected by western blotting with the antibody against HA. The ratio for wild-type DOK7 was equivalent to the ratio for truncated DOK7 (left), indicating that the rabbit antibody against DOK7 detected wild-type and truncated DOK7 proteins with similar efficiency by western blotting. **b**, Wild-type and truncated DOK7 were immunoprecipitated with similar efficiency by a goat antibody against the PTB domain in DOK7. HEK 293 cells were transiently co-transfected with plasmids expressing HA-tagged DOK7 and HA-tagged truncated DOK7 encoded by *Dok7^{II24_II27 TGCC dup}*. DOK7 proteins were immunoprecipitated from cell lysates (triplicates) with either a monoclonal antibody against HA or a goat antibody against the PTB domain in DOK7, and western blots were probed with the monoclonal antibody against HA (left). We measured the grey levels, subtracted the level for the background band in the control, non-transfected samples, and normalized the value for each protein immunoprecipitated with the goat antibody against DOK7 to the value for the same protein immunoprecipitated with the antibody against HA. This ratio was equivalent for wild-type and truncated DOK7 proteins, indicating that the goat antibody against DOK7 immunoprecipitated wild-type and truncated proteins with similar efficiency (right). Plots show individual values from three and four experiments for **a** and **b**, respectively, and the mean ± s.e.m. (n.s., not significant); two-sided Student's *t*-test.

[Source data](#)

Extended Data Fig. 3 *Dok7* RNA expression is normal in *Dok7^{CM/CM}* mice.

a, RT-PCR amplification of *Dok7* RNA shows that *Dok7* mRNA levels are similar in muscle from E18.5 wild-type and *Dok7^{CM/CM}* mice. *GAPDH* was used as a loading control. **b**, *Dok7* mRNA levels were quantified by qPCR, which showed that *Dok7* mRNA levels are normal in *Dok7^{CM/CM}* mice (*n* = 3 mice). **c**, DOK7 was immunoprecipitated from muscles of E18.5 wild-type and *Dok7^{CM/CM}* mice, and the blots were probed with antibodies against DOK7 (left). Truncated DOK7, encoded by

Dok7^{CM/CM}, migrates at the predicted size, but is expressed at threefold lower levels than wild-type DOK7 (right; $n = 10$ mice). Data shown as individual data points and mean \pm s.e.m.; n.s., not significant; *** $P < 0.00005$; two-sided Student's *t*-test.

[Source data](#)

Extended Data Fig. 4 Y396 and Y406 are the main, if not sole, tyrosine residues in DOK7 that are phosphorylated by AGRIN stimulation.

We generated muscle cell lines from wild-type and *Dok7*^{2YF/2YF} mice and treated the cultured myotubes with AGRIN for 30 min. MUSK was immunoprecipitated, and western blots were probed with antibodies against MUSK or phosphotyrosine (pTyr). AGRIN stimulates DOK7 tyrosine phosphorylation in wild-type but not *Dok7*^{2YF/2YF} myotubes (data from two experiments).

Extended Data Fig. 5 MUSK antibody clones.

a, Amino acid sequences of the complementarity-determining regions (CDRs) of antibodies against MUSK developed in this study. CDR definitions are based on Wu and Kabat³⁸, except that CDR-H1 includes four additional residues at the N terminus to show diversified positions. **b**, Amino acid sequences of the VL and VH domains of clone X17. **c**, **d**, Binding titration of antibodies against MUSK in the Fab format to immobilized hFz, hECD, mFz and mECD, as tested using a bead-based binding assay. Curves show the best fit of the 1:1 binding model. The table lists apparent K_D values (mean \pm s.d., $n = 3$). The datasets in **c** and **d** were obtained different instruments, which resulted in different signal ranges. **e**, Binding titration of antibodies against MUSK in the IgG format, as in **c**.

[Source data](#)

Extended Data Fig. 6 Chronic injection of MUSK agonist antibody X17 in wild-type mice has no effect on the organization of neuromuscular synapses, weight gain or motor behaviour.

a, Blood half-life measurements of X17-mIgG2a-LALAPG. Nonlinear least-squares fitting of the median fluorescence intensities with a single exponential curve for three mice is shown. The half-life was determined to be 4.9 ± 0.2 days. **b**, Wild-type mice on a C57BL/6-CBA mixed background, injected at P4, P24 and P44 with X17 ($n = 4$), survived until P60, when the experiment was ended. The scatter plot shows the survival time for nine non-injected wild-type mice and four wild-type mice injected with X17 with mean \pm s.e.m. (n.s., not significant). **c**, Wild-type mice injected with

X17 ($n = 4$) gained weight like uninjected wild-type mice ($n = 9$). **d**, Left, diaphragm muscles from P60 wild-type mice and wild-type mice injected with X17 were stained with Alexa 488–anti-BGT to label AChRs (red) and antibodies against neurofilament and synapsin to label motor axons and nerve terminals (green). In wild-type mice treated with X17, synapses matured from a simple, plaque-like shape to a complex, pretzel-like shape, characteristic of mature mouse neuromuscular synapses. Scale bar, 10 μm . Right, injection of X17 in wild-type mice had no effect on synapse number, size or AChR density. We analysed more than 50 synapses per diaphragm muscle from two mice in each category. **e**, Motor performance of wild-type mice injected with X17, as assessed by grip strength and the latency to fall from a rotating rotarod, was similar to that of non-injected wild-type mice. The scatter plots show the values for 18 wild-type mice and 4 wild-type mice injected with X17 and the mean \pm s.e.m; two-sided Student's *t*-test.

[Source data](#)

[Extended Data Fig. 7 The C-terminal region of DOK7 is essential for complete differentiation and maturation of the neuromuscular synapse in *Dok7^{CM/CM}* mice on a mixed genetic background.](#)

a–c, Left, diaphragm muscles from wild-type and *Dok7^{CM/CM}* mice on a C57BL/6-CBA mixed background at E18.5 and P10 were stained with Alexa 488–anti-BGT to label AChRs (red) and antibodies against neurofilament and synapsin to label motor axons and nerve terminals (green). Scale bars, 50 μm (**a**), 10 μm (**b, c**). **a**, Right, at E18.5, the endplate band (dashed white lines on left) is 30% wider in *Dok7^{CM/CM}* than wild-type mice. Moreover, nerve terminals were absent from 15% of AChR clusters and the colocalization index (synapsin/AChR) was reduced 3.5-fold in *Dok7^{CM/CM}* mice. $n = 3$ mice. **b**, Right, the number of synapses, synaptic size and density of synaptic AChRs were reduced 3.2-, 4.5- and 8-fold, respectively, in E18.5 *Dok7^{CM/CM}* mice. $n = 3$ mice (>50 synapses per mouse). **c**, Right, at P10, the number of synapses, synaptic size and density of synaptic AChRs were reduced over tenfold in *Dok7^{CM/CM}* mice. In addition, nerve terminals were absent from 20% of the AChR clusters in *Dok7^{CM/CM}* mice. $n = 3$ mice (>50 synapses per mouse). **d**, DOK7 was immunoprecipitated from muscles of E18.5 wild-type and *Dok7^{CM/CM}* mice, and the blots were probed with antibodies against DOK7 (left). Truncated DOK7, encoded by *Dok7^{CM/CM}*, migrated at the predicted size, but was expressed at threefold lower levels than wild-type DOK7 (right). Because DOK7 expression and MUSK phosphorylation were diminished to the same extent in the C57BL/6-CBA mixed breed and C57BL/6 inbred mice, other factors presumably led to increased survival in the mixed genetic background. $n = 8$ mice per genotype. **e**, MUSK was immunoprecipitated from muscles of E18.5 wild-type and *Dok7^{CM/CM}* mice, and the blots were probed with

antibodies against MUSK, phosphotyrosine, and CRK (left). The levels of phosphotyrosine and CRK that co-isolated with the MUSK complex were normalized to MUSK expression (right). CRK association with the MUSK complex was 2.8-fold lower in *Dok7*^{CM/CM} mice than wild-type mice. MUSK tyrosine phosphorylation was fivefold lower in *Dok7*^{CM/CM} mice than wild-type mice. $n = 3$ mice per genotype. Scatter plots show individual data points and mean \pm s.e.m.; * $P < 0.05$, ** $P < 0.005$, *** $P < 0.0005$, **** $P < 0.00005$; two-sided Student's *t*-test.

[Source data](#)

[Extended Data Fig. 8 Antibodies X2 and X3, like X17, rescue *Dok7*^{CM/CM} mice from early lethality.](#)

a, *Dok7*^{CM/CM} mice on a C57BL/6-CBA mixed background were injected at P4 with 10 mg kg⁻¹ mIgG2a-X3. At this dose, X3 failed to rescue the mice from lethality. **b**, By contrast, dosing with 20 mg kg⁻¹ mIgG2a-X3 at P4 rescued the mice from early lethality. These mice were subsequently injected with 10 mg kg⁻¹ mIgG2a-X3 at P18, which led to survival until P60, when the experiment was ended. **c**, Injecting *Dok7*^{CM/CM} mice with 20 mg kg⁻¹ hIgG1-X2 at P4 likewise rescued *Dok7*^{CM/CM} mice from early lethality; subsequent injection of 10 mg kg⁻¹ hIgG1-X2 at P18 led to survival of *Dok7*^{CM/CM} mice until P60, when the experiment was ended.

[Source data](#)

Extended Data Table 1 *Dok7*^{CM/CM} mice on a mixed genetic background survive for approximately two weeks postnatally

[Full size table](#)

Extended Data Table 2 Sequence analysis of potential off-target sites failed to identify mutations in these genes

[Full size table](#)

Supplementary information

[Supplementary Figures](#)

This file contains the uncropped western blots for Figures 1–3 and Extended Data Figures 2, 3, 4 and 8.

[Reporting Summary](#)

[Video 1 MuSK agonist antibody X17 reverses impaired mobility of *Dok7*^{CM/CM} mice](#)

A *Dok7*^{CM/CM} mouse was injected with hIgG1-X17 at P4, P24 and P44. Antibody treatment was then discontinued. The video shows the movement of this *Dok7*^{CM/CM} mouse as well as a wildtype mouse at P100. At P100, the *Dok7*^{CM/CM} mouse moved infrequently and displayed motor deficits, notably dragging of his hindlimbs. Treatment with hIgG1-X17 was reinitiated at P100, and the second video was recorded 7 days later. At P107, the *Dok7*^{CM/CM} mouse showed improved use of the hindlimb muscles and movement throughout the cage.

Source data

[Source Data Fig. 1](#)

[Source Data Fig. 2](#)

[Source Data Fig. 3](#)

[Source Data Fig. 4](#)

[Source Data Extended Data Fig. 1](#)

[Source Data Extended Data Fig. 2](#)

[Source Data Extended Data Fig. 3](#)

[Source Data Extended Data Fig. 5](#)

[Source Data Extended Data Fig. 6](#)

[Source Data Extended Data Fig. 7](#)

[Source Data Extended Data Fig. 8](#)

[Source Data Extended Data Table 1](#)

Rights and permissions

Open Access This article is licensed under a Creative Commons Attribution 4.0 International License, which permits use, sharing, adaptation, distribution and reproduction in any medium or format, as long as you give appropriate credit to the original author(s) and the source, provide a link to the Creative Commons license, and indicate if changes were made. The images or other third party material in this article are included in the article's Creative Commons license, unless indicated otherwise in a credit line to the material. If material is not included in the article's Creative Commons license and your intended use is not permitted by statutory regulation or exceeds the permitted use, you will need to obtain permission directly from the copyright holder. To view a copy of this license, visit <http://creativecommons.org/licenses/by/4.0/>.

Reprints and Permissions

About this article



Check for
updates

Cite this article

Oury, J., Zhang, W., Leloup, N. *et al.* Mechanism of disease and therapeutic rescue of *Dok7* congenital myasthenia. *Nature* **595**, 404–408 (2021).
<https://doi.org/10.1038/s41586-021-03672-3>

Download citation

- Received: 15 January 2021
- Accepted: 25 May 2021
- Published: 23 June 2021
- Issue Date: 15 July 2021
- DOI: <https://doi.org/10.1038/s41586-021-03672-3>

Comments

By submitting a comment you agree to abide by our [Terms](#) and [Community Guidelines](#). If you find something abusive or that does not comply with our terms or guidelines please flag it as inappropriate.

[Download PDF](#)

Advertisement

This article was downloaded by **calibre** from <https://www.nature.com/articles/s41586-021-03672-3>

| [Section menu](#) | [Main menu](#) |

- Article
- [Published: 30 June 2021](#)

Microbiota regulate social behaviour via stress response neurons in the brain

- [Wei-Li Wu](#) [ORCID: orcid.org/0000-0003-2610-1881](#)^{1,2,3},
- [Mark D. Adame](#)¹,
- [Chia-Wei Liou](#)^{2,3},
- [Jacob T. Barlow](#)¹,
- [Tzu-Ting Lai](#)²,
- [Gil Sharon](#)¹,
- [Catherine E. Schretter](#) [ORCID: orcid.org/0000-0002-3957-6838](#)¹,
- [Brittany D. Needham](#)¹,
- [Madelyn I. Wang](#) [ORCID: orcid.org/0000-0001-7576-1179](#)¹,
- [Weiyi Tang](#) [ORCID: orcid.org/0000-0002-1279-1001](#)¹,
- [James Ousey](#)⁴,
- [Yuan-Yuan Lin](#)²,
- [Tzu-Hsuan Yao](#)²,
- [Reem Abdel-Haq](#) [ORCID: orcid.org/0000-0002-7418-5736](#)¹,
- [Keith Beadle](#)¹,
- [Viviana Gradinaru](#) [ORCID: orcid.org/0000-0001-5868-348X](#)¹,
- [Rustem F. Ismagilov](#)^{1,4} &
- [Sarkis K. Mazmanian](#) [ORCID: orcid.org/0000-0003-2713-1513](#)¹

[Nature](#) volume 595, pages 409–414 (2021) [Cite this article](#)

- 13k Accesses

- 374 Altmetric
- [Metrics details](#)

Subjects

- [Microbial communities](#)
- [Emotion](#)

Abstract

Social interactions among animals mediate essential behaviours, including mating, nurturing, and defence^{1,2}. The gut microbiota contribute to social activity in mice^{3,4}, but the gut–brain connections that regulate this complex behaviour and its underlying neural basis are unclear^{5,6}. Here we show that the microbiome modulates neuronal activity in specific brain regions of male mice to regulate canonical stress responses and social behaviours. Social deviation in germ-free and antibiotic-treated mice is associated with elevated levels of the stress hormone corticosterone, which is primarily produced by activation of the hypothalamus–pituitary–adrenal (HPA) axis. Adrenalectomy, antagonism of glucocorticoid receptors, or pharmacological inhibition of corticosterone synthesis effectively corrects social deficits following microbiome depletion. Genetic ablation of glucocorticoid receptors in specific brain regions or chemogenetic inactivation of neurons in the paraventricular nucleus of the hypothalamus that produce corticotrophin-releasing hormone (CRH) reverse social impairments in antibiotic-treated mice. Conversely, specific activation of CRH-expressing neurons in the paraventricular nucleus induces social deficits in mice with a normal microbiome. Via microbiome profiling and *in vivo* selection, we identify a bacterial species, *Enterococcus faecalis*, that promotes social activity and reduces corticosterone levels in mice following social stress. These studies suggest that specific gut bacteria can restrain the activation of the HPA axis, and show that the microbiome can affect social behaviours through discrete neuronal circuits that mediate stress responses in the brain.

Access options

[Subscribe to Journal](#)

Get full journal access for 1 year

\$199.00

only \$3.90 per issue

[Subscribe](#)

All prices are NET prices.

VAT will be added later in the checkout.

Tax calculation will be finalised during checkout.

Rent or Buy article

Get time limited or full article access on ReadCube.

from \$8.99

[Rent or Buy](#)

All prices are NET prices.

Additional access options:

- [Log in](#)
- [Access through your institution](#)
- [Learn about institutional subscriptions](#)

Fig. 1: The gut microbiome regulates social behaviour and serum corticosterone levels in mice.

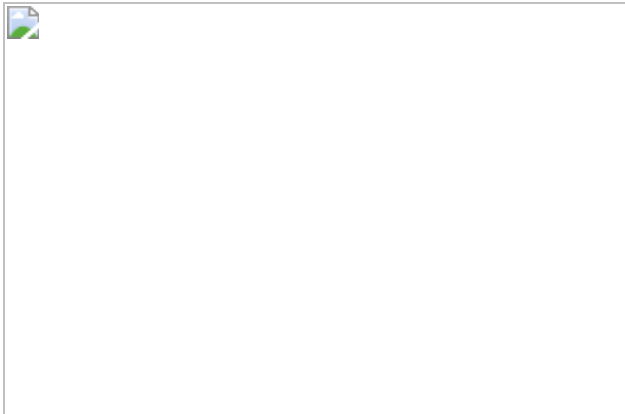


Fig. 2: Microbiome modulation of glucocorticoid signalling alters social behaviour.

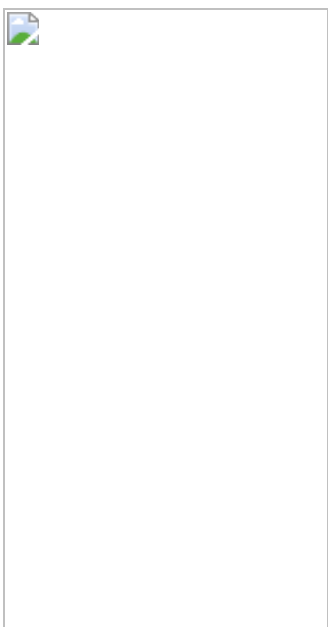


Fig. 3: CRH neurons and glucocorticoid receptors affect social behaviour.

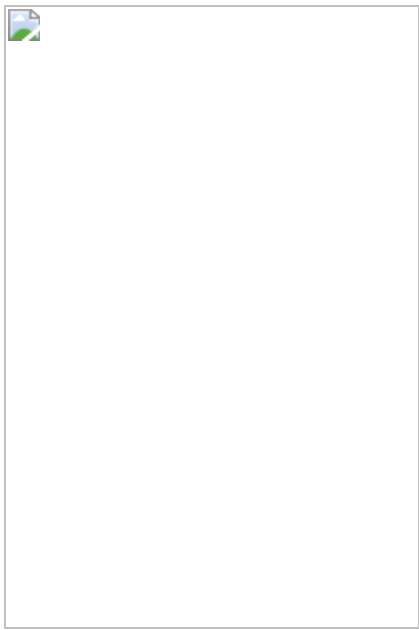
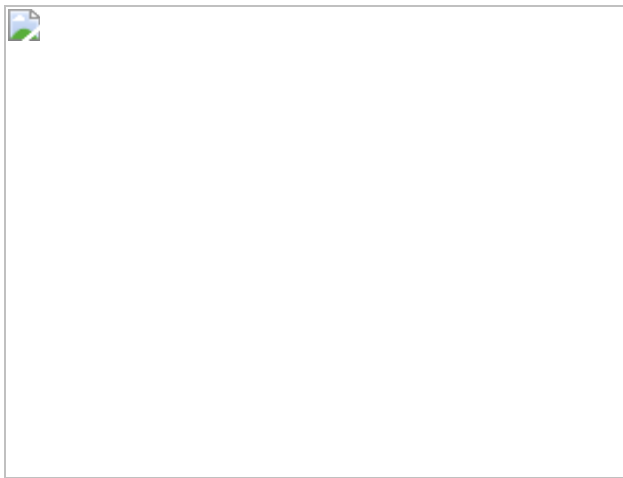


Fig. 4: *Enterococcus faecalis* restores social deficits and corticosterone levels in mice.



Data availability

All data generated and analysed during this study are included in this published article and its Supplementary Information files. Raw data for 16S rRNA gene sequencing and data analysis have been deposited in the ENA database under BioProject [PRJNA632893](#). [Source data](#) are provided with this paper.

References

1. 1.

Anderson, D. J. Circuit modules linking internal states and social behaviour in flies and mice. *Nat. Rev. Neurosci.* **17**, 692–704 (2016).

[CAS](#) [PubMed](#) [Article](#) [Google Scholar](#)

2. 2.

Chen, P. & Hong, W. Neural circuit mechanisms of social behavior. *Neuron* **98**, 16–30 (2018).

[CAS](#) [PubMed](#) [PubMed Central](#) [Article](#) [Google Scholar](#)

3. 3.

Buffington, S. A. et al. Microbial reconstitution reverses maternal diet-induced social and synaptic deficits in offspring. *Cell* **165**, 1762–1775 (2016).

[CAS](#) [PubMed](#) [PubMed Central](#) [Article](#) [Google Scholar](#)

4. 4.

Desbonnet, L., Clarke, G., Shanahan, F., Dinan, T. G. & Cryan, J. F. Microbiota is essential for social development in the mouse. *Mol. Psychiatry* **19**, 146–148 (2014).

[CAS](#) [PubMed](#) [Article](#) [Google Scholar](#)

5. 5.

Rogers, G. B. et al. From gut dysbiosis to altered brain function and mental illness: mechanisms and pathways. *Mol. Psychiatry* **21**, 738–748 (2016).

[CAS](#) [PubMed](#) [PubMed Central](#) [Article](#) [Google Scholar](#)

6. 6.

Sharon, G., Sampson, T. R., Geschwind, D. H. & Mazmanian, S. K. The central nervous system and the gut microbiome. *Cell* **167**, 915–932 (2016).

[CAS](#) [PubMed](#) [PubMed Central](#) [Article](#) [Google Scholar](#)

7. 7.

Dinan, T. G. & Cryan, J. F. The impact of gut microbiota on brain and behaviour: implications for psychiatry. *Curr. Opin. Clin. Nutr. Metab. Care* **18**, 552–558 (2015).

[PubMed](#) [Article](#) [Google Scholar](#)

8. 8.

Diaz Heijtz, R. et al. Normal gut microbiota modulates brain development and behavior. *Proc. Natl Acad. Sci. USA* **108**, 3047–3052 (2011).

[ADS](#) [PubMed](#) [Article](#) [Google Scholar](#)

9. 9.

Sudo, N. et al. Postnatal microbial colonization programs the hypothalamic-pituitary-adrenal system for stress response in mice. *J. Physiol. (Lond.)* **558**, 263–275 (2004).

[CAS](#) [Article](#) [Google Scholar](#)

10. 10.

Bercik, P. et al. The intestinal microbiota affect central levels of brain-derived neurotropic factor and behavior in mice. *Gastroenterology* **141**, 599–609.e3 (2011).

[CAS](#) [PubMed](#) [Article](#) [Google Scholar](#)

11. 11.

Arentsen, T., Raith, H., Qian, Y., Forssberg, H. & Diaz Heijtz, R. Host microbiota modulates development of social preference in mice. *Microb. Ecol. Health Dis.* **26**, 29719 (2015).

[PubMed](#) [Google Scholar](#)

12. 12.

Clarke, G. et al. The microbiome-gut-brain axis during early life regulates the hippocampal serotonergic system in a sex-dependent manner. *Mol. Psychiatry* **18**, 666–673 (2013).

[CAS](#) [PubMed](#) [Article](#) [Google Scholar](#)

13. 13.

Neufeld, K. M., Kang, N., Bienenstock, J. & Foster, J. A. Reduced anxiety-like behavior and central neurochemical change in germ-free mice. *Neurogastroenterol. Motil.* **23**, 255–e119 (2011).

[CAS](#) [PubMed](#) [Article](#) [Google Scholar](#)

14. 14.

Hsiao, E. Y. et al. Microbiota modulate behavioral and physiological abnormalities associated with neurodevelopmental disorders. *Cell* **155**, 1451–1463 (2013).

[CAS](#) [PubMed](#) [PubMed Central](#) [Article](#) [Google Scholar](#)

15. 15.

Hanstok, T. L., Clayton, E. H., Li, K. M. & Mallet, P. E. Anxiety and aggression associated with the fermentation of carbohydrates in the hindgut of rats. *Physiol. Behav.* **82**, 357–368 (2004).

[CAS](#) [PubMed](#) [Article](#) [Google Scholar](#)

16. 16.

Crumeyrolle-Arias, M. et al. Absence of the gut microbiota enhances anxiety-like behavior and neuroendocrine response to acute stress in rats. *Psychoneuroendocrinology* **42**, 207–217 (2014).

[CAS](#) [PubMed](#) [Article](#) [Google Scholar](#)

17. 17.

Golubeva, A. V. et al. Microbiota-related changes in bile acid & tryptophan metabolism are associated with gastrointestinal dysfunction in a mouse model of autism. *EBioMedicine* **24**, 166–178 (2017).

[PubMed](#) [PubMed Central](#) [Article](#) [Google Scholar](#)

18. 18.

Buffington, S. A. et al. Dissecting the contribution of host genetics and the microbiome in complex behaviors. *Cell* **184**, 1740–1756.e6 (2021).

[CAS](#) [PubMed](#) [Article](#) [Google Scholar](#)

19. 19.

Sgritta, M. et al. Mechanisms underlying microbial-mediated changes in social behavior in mouse models of autism spectrum disorder. *Neuron* **101**, 246–259.e6 (2019).

[CAS](#) [PubMed](#) [Article](#) [Google Scholar](#)

20. 20.

Gorrindo, P. et al. Gastrointestinal dysfunction in autism: parental report, clinical evaluation, and associated factors. *Autism Res.* **5**, 101–108 (2012).

[PubMed](#) [PubMed Central](#) [Article](#) [Google Scholar](#)

21. 21.

Buie, T. et al. Recommendations for evaluation and treatment of common gastrointestinal problems in children with ASDs. *Pediatrics* **125** (Suppl 1), S19–S29 (2010).

[PubMed](#) [Article](#) [Google Scholar](#)

22. 22.

Kang, D. W. et al. Reduced incidence of *Prevotella* and other fermenters in intestinal microflora of autistic children. *PLoS ONE* **8**, e68322 (2013).

[ADS](#) [CAS](#) [PubMed](#) [PubMed Central](#) [Article](#) [Google Scholar](#)

23. 23.

Adams, J. B., Johansen, L. J., Powell, L. D., Quig, D. & Rubin, R. A. Gastrointestinal flora and gastrointestinal status in children with autism—comparisons to typical children and correlation with autism severity. *BMC Gastroenterol.* **11**, 22 (2011).

[PubMed](#) [PubMed Central](#) [Article](#) [Google Scholar](#)

24. 24.

Theis, K. R. et al. Symbiotic bacteria appear to mediate hyena social odors. *Proc. Natl Acad. Sci. USA* **110**, 19832–19837 (2013).

[ADS](#) [CAS](#) [PubMed](#) [PubMed Central](#) [Article](#) [Google Scholar](#)

25. 25.

Nielsen, B. L. et al. Sexual responses of male rats to odours from female rats in oestrus are not affected by female germ-free status. *Behav. Brain Res.* **359**, 686–693 (2019).

[CAS](#) [PubMed](#) [Article](#) [Google Scholar](#)

26. 26.

Donaldson, Z. R. & Young, L. J. Oxytocin, vasopressin, and the neurogenetics of sociality. *Science* **322**, 900–904 (2008).

[ADS](#) [CAS](#) [PubMed](#) [Article](#) [Google Scholar](#)

27. 27.

Urban, D. J. & Roth, B. L. DREADDs (designer receptors exclusively activated by designer drugs): chemogenetic tools with therapeutic utility. *Annu. Rev. Pharmacol. Toxicol.* **55**, 399–417 (2015).

[CAS](#) [PubMed](#) [Article](#) [Google Scholar](#)

28. 28.

Füzesi, T., Daviu, N., Wamsteeker Cusulin, J. I., Bonin, R. P. & Bains, J. S. Hypothalamic CRH neurons orchestrate complex behaviours after stress. *Nat. Commun.* **7**, 11937 (2016).

[ADS](#) [PubMed](#) [PubMed Central](#) [Article](#) [CAS](#) [Google Scholar](#)

29. 29.

Barlow, J. T., Bogatyrev, S. R. & Ismagilov, R. F. A quantitative sequencing framework for absolute abundance measurements of mucosal and luminal microbial communities. *Nat. Commun.* **11**, 2590 (2020).

[ADS](#) [CAS](#) [PubMed](#) [PubMed Central](#) [Article](#) [Google Scholar](#)

30. 30.

Kwong, W. K. et al. Dynamic microbiome evolution in social bees. *Sci. Adv.* **3**, e1600513 (2017).

[ADS](#) [PubMed](#) [PubMed Central](#) [Article](#) [Google Scholar](#)

31. 31.

Sharon, G. et al. Commensal bacteria play a role in mating preference of *Drosophila melanogaster*. *Proc. Natl Acad. Sci. USA* **107**, 20051–20056 (2010).

[ADS](#) [CAS](#) [PubMed](#) [PubMed Central](#) [Article](#) [Google Scholar](#)

32. 32.

Foster, J. A., Rinaman, L. & Cryan, J. F. Stress & the gut-brain axis: regulation by the microbiome. *Neurobiol. Stress* **7**, 124–136 (2017).

[PubMed](#) [PubMed Central](#) [Article](#) [Google Scholar](#)

33. 33.

Paxinos, G. & Franklin, K. B. J. *The Mouse Brain in Stereotaxic Coordinates* 2nd edn (Academic, 2001).

34. 34.

Hagihara, H., Toyama, K., Yamasaki, N. & Miyakawa, T. Dissection of hippocampal dentate gyrus from adult mouse. *J. Vis. Exp.* **(33)**:1543 (2009).

[Google Scholar](#)

35. 35.

Yoshioka, W. et al. Fluorescence laser microdissection reveals a distinct pattern of gene activation in the mouse hippocampal region. *Sci. Rep.* **2**, 783 (2012).

[PubMed](#) [PubMed Central](#) [Article](#) [CAS](#) [Google Scholar](#)

36. 36.

Spandidos, A., Wang, X., Wang, H. & Seed, B. PrimerBank: a resource of human and mouse PCR primer pairs for gene expression detection and quantification. *Nucleic Acids Res.* **38**, D792–D799 (2010).

[CAS](#) [PubMed](#) [Article](#) [Google Scholar](#)

37. 37.

Wamsteeker Cusulin, J. I., Füzesi, T., Watts, A. G. & Bains, J. S. Characterization of corticotropin-releasing hormone neurons in the paraventricular nucleus of the hypothalamus of *Crh-IRES-Cre* mutant mice. *PLoS ONE* **8**, e64943 (2013).

[ADS](#) [CAS](#) [PubMed](#) [PubMed Central](#) [Article](#) [Google Scholar](#)

38. 38.

Bolyen, E. et al. Reproducible, interactive, scalable and extensible microbiome data science using QIIME 2. *Nat. Biotechnol.* **37**, 852–857 (2019).

[CAS](#) [PubMed](#) [PubMed Central](#) [Article](#) [Google Scholar](#)

39. 39.

Rognes, T., Flouri, T., Nichols, B., Quince, C. & Mahé, F. VSEARCH: a versatile open source tool for metagenomics. *PeerJ* **4**, e2584 (2016).

[PubMed](#) [PubMed Central](#) [Article](#) [Google Scholar](#)

40. 40.

Amir, A. et al. Deblur rapidly resolves single-nucleotide community sequence patterns. *mSystems* **2**, e00191-16 (2017).

[PubMed](#) [PubMed Central](#) [Article](#) [Google Scholar](#)

41. 41.

McDonald, D. et al. An improved Greengenes taxonomy with explicit ranks for ecological and evolutionary analyses of bacteria and archaea. *ISME J.* **6**, 610–618 (2012).

[CAS](#) [PubMed](#) [Article](#) [Google Scholar](#)

42. 42.

Janssen, S. et al. Phylogenetic placement of exact amplicon sequences improves associations with clinical information. *mSystems* **3**, e00021-18 (2018).

[CAS](#) [PubMed](#) [PubMed Central](#) [Article](#) [Google Scholar](#)

43. 43.

Bokulich, N. A. et al. Optimizing taxonomic classification of marker-gene amplicon sequences with QIIME 2's q2-feature-classifier plugin. *Microbiome* **6**, 90 (2018).

[PubMed](#) [PubMed Central](#) [Article](#) [Google Scholar](#)

44. 44.

Lozupone, C. & Knight, R. UniFrac: a new phylogenetic method for comparing microbial communities. *Appl. Environ. Microbiol.* **71**, 8228–8235 (2005).

[ADS](#) [CAS](#) [PubMed](#) [PubMed Central](#) [Article](#) [Google Scholar](#)

45. 45.

Bogatyrev, S. R. & Ismagilov, R. F. Quantitative microbiome profiling in luminal and tissue samples with broad coverage and dynamic range via a single-step 16S rRNA gene DNA copy quantification and amplicon barcoding. Preprint at <https://doi.org/10.1101/2020.01.22.914705> (2020).

46. 46.

Bogatyrev, S. R., Rolando, J. C. & Ismagilov, R. F. Self-reinoculation with fecal flora changes microbiota density and composition leading to

an altered bile-acid profile in the mouse small intestine. *Microbiome* **8**, 19 (2020).

[PubMed](#) [PubMed Central](#) [Article](#) [Google Scholar](#)

47. 47.

Balamurugan, R., Rajendiran, E., George, S., Samuel, G. V. & Ramakrishna, B. S. Real-time polymerase chain reaction quantification of specific butyrate-producing bacteria, *Desulfovibrio* and *Enterococcus faecalis* in the feces of patients with colorectal cancer. *J. Gastroenterol. Hepatol.* **23**, 1298–1303 (2008).

[CAS](#) [PubMed](#) [Article](#) [Google Scholar](#)

48. 48.

Bolyen, E. et al. Reproducible, interactive, scalable and extensible microbiome data science using QIIME 2. *Nat. Biotechnol.* **37**, 852–857 (2019).

[CAS](#) [PubMed](#) [PubMed Central](#) [Article](#) [Google Scholar](#)

49. 49.

Callahan, B. J. et al. DADA2: high-resolution sample inference from Illumina amplicon data. *Nat. Methods* **13**, 581–583 (2016).

[CAS](#) [PubMed](#) [PubMed Central](#) [Article](#) [Google Scholar](#)

50. 50.

Quast, C. et al. The SILVA ribosomal RNA gene database project: improved data processing and web-based tools. *Nucleic Acids Res.* **41**, D590–D596 (2013).

[CAS](#) [PubMed](#) [PubMed Central](#) [Article](#) [Google Scholar](#)

51. 51.

Shih, H. T. & Mok, H. K. ETHOM: rvent-recording computer software for the study of animal behavior. *Acta Zool. Taiwan.* **11**, 47–61 (2000).

[Google Scholar](#)

[Download references](#)

Acknowledgements

We thank H.-N. Huang for support and planning in the initial staged of this study; H. Chu, J. Boktor, members of the Mazmanian laboratory and B. E. Deverman for critically reviewing the manuscript; Y. Garcia-Flores for administrative assistance; T. M. Thron, OLAR at Caltech, and LAC at NCKU for animal husbandry; D. J. Anderson and L. C. Hsieh-Wilson for stereotaxic instruments; L.-C. Lo and H. Huang for technical assistance; and J.-W. Chen for biological materials. M. Costa-Mattioli, M. Sgritta and K. Imanbayev provided advice on vagotomy. The BIF at Caltech provided use of confocal microscopes. The CLOVER Center at Caltech provided viral vectors. This work was supported by funds from the Ministry of Science and Technology in Taiwan (MOST 107-2320-B-006-072-MY3; 108-2321-B-006-025-MY2; 109-2314-B-006-046), the Higher Education Sprout Project, Ministry of Education to the Headquarters of University Advancement (NCKU) to W.-L.W.; an NIH Biotechnology Leadership Pre-doctoral Training Program (BLP) Fellowship (T32GM112592) to J.T.B.; the National Science Foundation Graduate Research Fellowship Program (NSF GRFP No. DGE-1745301) to J.O.; a grant from the Jacobs Institute for Molecular Engineering for Medicine (Caltech), the Kenneth Rainin Foundation Innovator Award (2018-1207) to R.F.I.; and Lynda and Blaine Fetter, Charlie Trimble, the Heritage Medical Research Institute, and the NIH (MH100556) to S.K.M.

Author information

Affiliations

1. Division of Biology and Biological Engineering, California Institute of Technology, Pasadena, CA, USA

Wei-Li Wu, Mark D. Adame, Jacob T. Barlow, Gil Sharon, Catherine E. Schretter, Brittany D. Needham, Madelyn I. Wang, Weiyi Tang, Reem Abdel-Haq, Keith Beadle, Viviana Grdinaru, Rustem F. Ismagilov & Sarkis K. Mazmanian

2. Department of Physiology, College of Medicine, National Cheng Kung University, Tainan, Taiwan

Wei-Li Wu, Chia-Wei Liou, Tzu-Ting Lai, Yuan-Yuan Lin & Tzu-Hsuan Yao

3. Institute of Basic Medical Sciences, College of Medicine, National Cheng Kung University, Tainan, Taiwan

Wei-Li Wu & Chia-Wei Liou

4. Division of Chemistry and Chemical Engineering, California Institute of Technology, Pasadena, CA, USA

James Ousey & Rustem F. Ismagilov

Authors

1. Wei-Li Wu

[View author publications](#)

You can also search for this author in [PubMed](#) [Google Scholar](#)

2. Mark D. Adame

[View author publications](#)

You can also search for this author in [PubMed](#) [Google Scholar](#)

3. Chia-Wei Liou

[View author publications](#)

You can also search for this author in [PubMed](#) [Google Scholar](#)

4. Jacob T. Barlow

[View author publications](#)

You can also search for this author in [PubMed](#) [Google Scholar](#)

5. Tzu-Ting Lai

[View author publications](#)

You can also search for this author in [PubMed](#) [Google Scholar](#)

6. Gil Sharon

[View author publications](#)

You can also search for this author in [PubMed](#) [Google Scholar](#)

7. Catherine E. Schretter

[View author publications](#)

You can also search for this author in [PubMed](#) [Google Scholar](#)

8. Brittany D. Needham

[View author publications](#)

You can also search for this author in [PubMed](#) [Google Scholar](#)

9. Madelyn I. Wang

[View author publications](#)

You can also search for this author in [PubMed](#) [Google Scholar](#)

10. Weiyi Tang

[View author publications](#)

You can also search for this author in [PubMed](#) [Google Scholar](#)

11. James Ousey

[View author publications](#)

You can also search for this author in [PubMed](#) [Google Scholar](#)

12. Yuan-Yuan Lin

[View author publications](#)

You can also search for this author in [PubMed](#) [Google Scholar](#)

13. Tzu-Hsuan Yao

[View author publications](#)

You can also search for this author in [PubMed](#) [Google Scholar](#)

14. Reem Abdel-Haq

[View author publications](#)

You can also search for this author in [PubMed](#) [Google Scholar](#)

15. Keith Beadle

[View author publications](#)

You can also search for this author in [PubMed](#) [Google Scholar](#)

16. Viviana Gradinaru

[View author publications](#)

You can also search for this author in [PubMed](#) [Google Scholar](#)

17. Rustem F. Ismagilov

[View author publications](#)

You can also search for this author in [PubMed](#) [Google Scholar](#)

18. Sarkis K. Mazmanian

[View author publications](#)

You can also search for this author in [PubMed](#) [Google Scholar](#)

Contributions

W.-L.W., M.D.A., C.-W.L., J.T.B., T.-T.L., G.S., C.E.S., M.I.W., W.T., J.O., Y.-Y.L., T.-H.Y. and R.A.-H. performed the experiments and/or analysed data. J.T.B., G.S., B.D.N. and R.F.I. provided consultations regarding microbiome analysis. K.B. and V.G. provided novel viral vectors. W.-L.W. and S.K.M. designed the research. S.K.M. supervised the research. W.-L.W. and S.K.M. integrated the data, interpreted the results, and wrote the manuscript. All authors discussed the results and commented on the manuscript.

Corresponding author

Correspondence to [Wei-Li Wu](#).

Ethics declarations

Competing interests

W-L.W., M.D.A., B.D.N., and S.K.M. have filed a provisional patent on this work. All other authors declare no competing interests.

Additional information

Peer review information *Nature* thanks Ioana Carcea and the other, anonymous, reviewer(s) for their contribution to the peer review of this work.

Publisher's note Springer Nature remains neutral with regard to jurisdictional claims in published maps and institutional affiliations.

Extended data figures and tables

[Extended Data Fig. 1 Social behaviours, non-social activity, c-Fos expression and corticosterone levels in GF and/or ABX-treated mice.](#)

a–c, Social activity in SPF and GF test mice (subject), in the context of SPF (**a**) or GF (**b**) novel mice. **a**, Anogenital sniff *** $P < 0.0001$, nose–nose sniff *** $P < 0.0001$, active approach *** $P = 0.0003$, push-crawl ** $P = 0.0055$; **b**, anogenital sniff *** $P < 0.0001$, nose–nose sniff ** $P = 0.003$, active approach ** $P = 0.0023$; **c**, novel mouse effect $P = 0.1133$ (data from Fig. [1b](#), [c](#)). $n = 20$ SPF, 19 GF (vs SPF); 8 SPF, 8 GF (vs GF) mice. **d**, **e**, Social activity in vehicle (VEH)- and ABX-treated test mice (subject), in the context of SPF (**d**) or ABX-treated (**e**) novel mice. **d**, Anogenital sniff *** $P = 0.0005$, nose–nose sniff ** $P = 0.0028$, active approach *** $P = 0.0004$, push-crawl $P = 0.4601$. $n = 26$ mice per group. **e**, $P = 0.7039$, $n = 10$ VEH, 9 ABX mice. **f**, Non-social activity in the reciprocal social interaction (RSI) paradigm in SPF, GF and ABX-treated mice (subject), in the context of SPF or GF novel mice. GF vs SPF novel mouse: $P = 0.8086$, $n = 20$ SPF, 19 GF mice. GF vs GF novel mouse: $P = 0.1205$, $n = 8$ mice per group. ABX vs SPF novel mouse: $P = 0.5044$, $n = 26$ mice per group. **g**, Non-social behaviour in a novel cage without the presence of a novel mouse. Grooming $P = 0.482$, digging $P = 0.8689$, rearing $P = 0.4608$ or total $P = 0.1743$. $n = 8$ SPF, 10 GF mice. **h**, Timeline schematic of guide cannula stereotaxic surgery, intracerebroventricular (ICV) injection of vehicle, ampicillin (A) and metronidazole (M), social behaviour, and sample collection. Social activity was tested in SPF mice injected ICV with antibiotics (subject), in the context of SPF novel mice. Social activity $P = 0.5294$, nose-to-nose $P = 0.1784$, nose-to-tail $P = 0.4477$. $n = 12$ mice per group. **i**, **j**, Timeline schematic of intraperitoneal (i.p.) injection of vehicle, ampicillin and metronidazole, open-field (OF) test, social behaviour, and sample collection. RSI (**i**) and open-field (**j**) test were tested in antibiotic-injected SPF mice (subject), in the context of SPF novel mice. Social activity $P = 0.5583$ (**i**); locomotion $P = 0.3705$ (**j**). $n = 6$ VEH, 4 ampicillin, 6 metronidazole mice. **k**, Social activity was tested in SPF, GF, VEH-treated and ABX-treated female mice (subject), in the context of SPF female novel mice. GF ** $P = 0.0053$ and ABX * $P = 0.0191$. $n = 10$ SPF, 9 GF, 5 VEH, 5 ABX mice. **l**, The length of isolation shown in Fig. [1b](#) did not affect social activity in GF or SPF controls. Microbiota effect *** $P < 0.0001$. $n = 4$ SPF (4–5 h), 7 SPF (5–6 h), 5 SPF (6–7 h), 2 SPF (7–8 h), 5 SPF (8–9 h), 10 GF (4–5 h), 3 GF (5–6 h), 4 GF (6–7 h), 6 GF (7–8 h), 4 GF (8–9 h) mice (data from Fig. [1b](#), [c](#)). **m**, Age of GF mice had no effect on social activity. $P = 0.379$. $n = 6$ (11–12 w),

5 (13 w), 8 (14–15 w) GF mice (data from Fig. [1b,d](#)). **n–q**, The distance travelled and social activity in the three-chamber social test for SPF and GF male mice (**n**, **o**) and VEH- and ABX-treated mice (**p**, **q**), in the context of SPF novel mice. $n = 9$ SPF, 10 GF, 10 VEH, 10 ABX mice. Distance moved in the sociability phase (**n**, GF $**P = 0.0047$; **p**, ABX $P = 0.1246$), time in chamber (**o**, left, SPF mouse (M) vs object (O) $***P < 0.0001$, GF M vs O $***P = 0.0005$; **q**, left, VEH M vs O $P = 0.1220$, ABX M vs O $**P = 0.0063$), and frequency entering chamber (**o**, right, SPF M vs O $P = 0.1420$, GF M vs O $P = 0.0872$; **q**, right, VEH M vs O $P = 0.2194$, ABX M vs O $***P = 0.0008$). $n = 9$ SPF, 10 GF, 10 VEH, 10 ABX mice. **r**, Left, schematic of brain regions with high c-Fos expression after RSI (relevant to Fig. [1e–l](#)). Right, representative images (from 6 SPF, 6 GF, 5 VEH, 5 ABX mice) of c-Fos staining in BLA in SPF, GF, VEH, and ABX after RSI. Scale bars, 200 μm . **s**, Quantification of c-Fos⁺ cells in BLA of GF and ABX mice. SPF vs GF $P = 0.1014$, VEH vs ABX $P = 0.1095$. $n = 6$ SPF, 6 GF, 5 VEH, 5 ABX mice. **t**, Quantification of c-Fos⁺ cells in various brain regions of SPF and GF mice. PVN $P = 0.4239$, adBNST $P = 0.2571$, DG $P = 0.0818$, BLA $P = 0.2552$. $n = 5$ SPF, 6 GF mice. **u**, Serum corticosterone levels in ABX-treated mice at isolation (iso), 0 h and 1 h post-RSI. VEH: Iso vs 0 h $\#P = 0.0129$, Iso vs 1 h $\#\#P = 0.0027$, 0 h vs 1 hr $\#\#P = 0.0023$; ABX: Iso vs 0 h $P = 0.0624$, Iso vs 1 h $\#\#P = 0.0016$, 0 h vs 1 h $\#\#P = 0.0062$. $n = 5$ mice per group. **v**, Serum corticosterone levels after novel cage exposure in GF and ABX-treated mice. ABX vs GF $**P = 0.0085$, SPF vs GF $*P = 0.0125$. $n = 11$ VEH, 11 ABX, 5 SPF, 4 GF mice. **w**, **x**, Serum corticosterone levels at different times of death in SPF and GF (**w**) and VEH and ABX mice (**x**) tested in Fig. [1m–o](#). GF $***P = 0.0005$ (**w**), ABX $**P = 0.0011$ (**x**). **w**, $n = 2$ SPF (0–1 h), 5 SPF (1–2 h), 4 SPF (2–3 h), 4 SPF (3–4 h), 3 SPF (4–5 h), 9 GF (0–1 h), 3 GF (1–2 h), 4 GF (2–3 h), 6 GF (3–4 h), 4 GF (4–5 h) mice (data from Fig. [1m](#), **n**). **x**, $n = 9$ VEH (0–100 m), 17 VEH (100–200 m), 22 ABX (0–100 m), 4 ABX (100–200 m) mice (data from Fig. [1o](#)). **y**, Social activity in SPF, GF and exGF test mice (subject), in the context of SPF novel mice. SPF vs GF $***P < 0.0001$, SPF vs exGF $***P = 0.0001$, GF vs exGF $****P < 0.0001$. $n = 20$ SPF, 19 GF, 8 exGF mice (SPF and GF data from Fig. [1b,c](#)). **z**, Serum corticosterone levels after RSI in exGF mice. SPF vs GF $**P = 0.0012$, GF vs exGF $*P = 0.0467$. $n = 13$ SPF, 18 GF, 8 exGF mice (SPF and GF data from Fig. [1b,c](#)). Data shown as individual points

with mean \pm s.e.m. Data analysed by two-tailed unpaired *t*-test (**a**, **b**, **d–g**, **k**, **n**, **p**, **s**, **t**); one-tailed paired *t*-test (**o**, **q**); one-way ANOVA (**i**, **j**, **m**, **y**, **z**), repeated measures (**h**) with Bonferroni's multiple comparison post hoc test; two-way ANOVA (**c**, **l**, **v–x**), repeated measures (**u**) with Bonferroni's multiple comparison post hoc test. * $P < 0.05$, ** $P < 0.01$, *** $P < 0.001$, **** $P < 0.0001$, ND: no difference. For more statistical details, see [Supplementary Information](#).

[Source data](#)

[Extended Data Fig. 2 The depletion of microbiota in GF and/or ABX-treated mice was demonstrated by absolute bacteria quantification, plating, microbiome analysis and profiling.](#)

a, Bacterial DNA was detected using Femto DNA quantification methods. Bacterial DNA was completely absent from faecal samples collected from GF mice housed in closed IVC cages for one week (** $P = 0.0038$) and from adult mice treated with ABX for three weeks (** $P = 0.0083$). $n = 4$ mice per group. **b**, **c**, Colony-forming units (CFU) quantified by scoring colonies from faecal samples plated on brucella blood agar following three weeks ABX treatment. **b**, Aerobes were depleted at the first week of ABX treatment. VEH vs ABX: 1 w ** $P = 0.001$, 2 w *** $P = 0.0001$, 3 w **** $P < 0.0001$. **c**, Anaerobes were completely depleted by the third week of ABX treatment. VEH vs ABX: 1 w $P = 0.2237$, 2 w * $P = 0.0179$, 3 w **** $P < 0.0001$. $n = 4$ mice per group. **d**, Representative images of caecum enlargement and brucella blood agar plating of caecal contents from VEH and ABX-treated mice. Plating of caecal contents showed that culturable bacteria were completely absent after 3 weeks of ABX treatment. **e**, **f**, Box plots of number of total reads (**e**) and total reads that matched sequences in 16S reference database (**f**) in VEH- and AVNM-treated mice, compared to negative controls. $n = 8$ VEH, 8 AVNM, 3 negative control. **g**, **h**, Box plots of alpha diversity as measured by number of observed ASVs (**g**) and Faith's phylogenetic diversity (**h**) in VEH- and AVNM-treated mice, compared to negative controls. $n = 8$ VEH, 8 AVNM, 3 negative control. **g**, VEH vs AVNM *** $P = 0.00093097$; VEH vs negative control * $P = 0.03169856$. (**h**) VEH vs AVNM ** $P = 0.00113133$; VEH vs negative control * $P = 0.01430588$. **i**, **j**, Principle coordinate analysis plots based on

unweighted (**i**) and weighted (**j**) UniFrac distances between faecal samples from VEH- and AVNM-treated mice, compared to negative controls (rarified to 728 reads per sample). $n = 8$ VEH, 7 AVNM, 3 negative control. **i**, VEH vs AVNM *** $P = 0.0002$; VEH vs negative control ** $P = 0.0071$. **j**, VEH vs AVNM *** $P = 0.0005$; VEH vs negative control ** $P = 0.0055$. **k**, Relative abundance of major phyla in VEH- and AVNM-treated mice, compared to negative controls. $n = 8$ VEH, 7 AVNM, 3 negative control. **i–k**, One AVNM mouse was found to be contaminated and excluded for the generation of the graphs. Data shown as individual points with mean \pm s.e.m. (**a–c**); box plots (**e–h**) show median (centre line) and interquartile range (IQR) (box limits); whiskers show either $1.5 \times$ IQR of the lower and upper quartiles or range. Data analysed by two-tailed unpaired *t*-test (**a**); two-way ANOVA, repeated measures (**b, c**) with Bonferroni's multiple comparison post hoc test; Kruskal–Wallis test (**g, h**); permutational multivariate analysis of variance (PERMANOVA) (**i, j**). * $P < 0.05$, ** $P < 0.01$, *** $P < 0.001$, **** $P < 0.0001$, ND: no difference. For more statistical details, see [Supplementary Information](#).

[Source data](#)

[Extended Data Fig. 3 Anxiety-like behaviour, locomotion, water intake, and olfactory investigative behaviour in GF and/or ABX-treated mice.](#)

a–h, Anxiety-like behaviour and locomotion were tested using the open-field test, light–dark box and elevated plus maze in SPF, GF, VEH-treated and ABX-treated mice. **a**, Locomotor activity measured in open-field test in GF mice showed no difference in distance travelled in open-field chamber. $P = 0.8371$. $n = 9$ SPF, 8 GF mice per group. **b**, Centre zone duration in open-field test in GF mice. GF mice spent longer in the centre of the open-field chamber than SPF mice. * $P = 0.0108$. $n = 9$ SPF, 8 GF mice per group. **c**, Light chamber duration measured in light–dark box for GF mice. GF mice spent longer in the light chamber than SPF mice. * $P = 0.0442$. $n = 9$ mice per group. **d**, Open arm duration measured in elevated plus maze for GF mice. GF mice spent longer in the open arm than SPF mice. * $P = 0.0261$. $n = 9$ mice per group. **e**, Locomotor activity measured in open-field test for ABX mice showed no difference in distance travelled in

the open-field chamber. $P = 0.3606$. $n = 10$ mice per group. **f**, Duration in the centre zone measured in open-field test shows no difference in centre duration for ABX mice. $P = 0.3372$. $n = 10$ mice per group. **g**, Duration in the light chamber measured in light–dark box shows no difference in light chamber duration for ABX mice. $P = 0.9381$. $n = 10$ mice per group. **h**, Duration spent in open arm measured in elevated plus maze shows no difference in open arm duration for ABX mice. $P = 0.8743$. $n = 10$ mice per group. **i**, ABX mice show no change in the distance travelled in the open-field chamber. VEH vs ABX $P = 0.6223$. $n = 15$ mice per group. **j**, Water intake was monitored in GF mice housed in IVC cages for one week. GF mice showed no difference in water consumed. SPF vs GF $P = 0.7591$. $n = 5$ mice per group. **k**, The olfactory habituation/dishabituation test involves exposure to a series of odours: baseline (water), volatile non-social odours (almond and banana extracts), and social odours (C57BL/6 and BTBR cages). Time-course of sniffing time shows no difference for GF mice when exposed to water, almond extract, or banana extract. GF mice displayed increased sniffing time when exposed to the social odour from C57BL/6J mice, but not from BTBR mice. SPF vs GF: B6 Cage(1-1) $*P = 0.0172$, B6 Cage(1-2) $*P = 0.0402$. $n = 10$ SPF, 11 GF mice per group. **l**, Percentage investigation time in response to the first exposure to social odour was measured in the olfactory habituation/dishabituation test in SPF and GF mice. The percentage of investigation time decreased at the second and third exposures to the same social odour in both SPF and GF mice. The investigation time decreased when switched to BTBR odour in GF mice. SPF: B6 Cage 1-1 vs 1-2 $**P = 0.0020$, B6 Cage 1-1 vs 1-3 $***P = 0.0002$, BTBR Cage 1-1 vs 1-2 $***P = 0.0002$, BTBR Cage 1-1 vs 1-3 $***P < 0.0001$; GF: B6 Cage 1-1 vs 1-2 $*P = 0.0120$, B6 Cage 1-1 vs 1-3 $*P = 0.0397$, BTBR Cage 1-1 vs 1-2 $***P < 0.0001$, BTBR Cage 1-1 vs 1-3 $***P < 0.0001$, B6 Cage 1-1 vs BTBR Cage 1-1 $*P = 0.0143$. $n = 10$ SPF, 11 GF mice per group. Data shown as individual points with mean \pm s.e.m. Data analysed by two-tailed unpaired *t*-test (**a–h**) and two-way ANOVA, repeated measures (**i–l**) with Bonferroni's multiple comparison post hoc test. $*P < 0.05$, $**P < 0.01$, $***P < 0.001$, $****P < 0.0001$, ND: no difference. For more statistical details, see [Supplementary Information](#).

[Source data](#)

Extended Data Fig. 4 IEG expression in the brains of GF mice and stress-related gene expression in the hippocampus and hypothalamus of ABX-treated mice.

a–d, IEG expression was measured in GF mice taken from the isolator and temporarily mixed with other mice from different cages. SPF mice were sampled and handled following the same procedure. Mice were immediately killed and the brains were collected and analysed. Brains were dissected into hippocampus (**a**), hypothalamus (**b**), midbrain (**c**), and brainstem (**d**). IEG expression in each region was analysed by qRT–PCR. $n = 6$ mice per group. **a**, In the hippocampus, *Arc* ($*P = 0.024$), *Fos* ($**P = 0.0036$), *cJun* ($*P = 0.0152$), *JunB* ($**P = 0.0077$), *Egr1* ($P = 0.0532$), *Egr2* ($*P = 0.0328$), *Gadd45b* ($***P = 0.0005$), *Gadd45g* ($*P = 0.0435$), and *Bdnf* ($*P = 0.0142$) were upregulated in GF mice. *Map2* $P = 0.3874$. $n = 6$ mice per group. **b**, In the hypothalamus, *Arc* ($*P = 0.0108$), *Fos* ($***P = 0.0001$), and *Egr1* ($**P = 0.0022$) were upregulated in GF mice, with no change in *Map2* gene expression. *cJun* $P = 0.3859$, *JunB* $P = 0.106$, *Egr2* $P = 0.0864$, *Gadd45b* $P = 0.8544$, *Gadd45g* $P = 0.4398$, *Bdnf* $P = 0.1517$, *Map2* $P = 0.8255$. $n = 6$ mice per group. **c**, No changes in IEG expression were found in the midbrains of GF mice. *Arc* $P = 0.4733$, *Fos* $P = 0.455$, *cJun* $P = 0.6153$, *JunB* $P = 0.6154$, *Egr1* $P = 0.4102$, *Egr2* $P = 0.283$, *Gadd45b* $P = 0.424$, *Gadd45g* $P = 0.0852$, *Bdnf* $P = 0.9779$, *Map2* $P = 0.4018$. $n = 3$ mice per group. **d**, In the brainstem, *cJun* ($*P = 0.0479$), *JunB* ($*P = 0.0244$), *Egr1* ($P = 0.0502$), *Gadd45b* ($**P = 0.0022$), *Gadd45g* ($**P = 0.0075$), and *Bdnf* ($*P = 0.0127$) were downregulated in GF mice. No change in *Map2* was detected in all four brain regions in GF mice. *Arc* $P = 0.8297$, *Fos* $P = 0.5208$, *Egr2* $P = 0.5391$, *Map2* $P = 0.1266$. $n = 6$ mice per group. **e**, Timeline schematic of ABX treatment, single housing, behavioural manipulations, and tissue sampling. Tissues collected include hippocampal dentate gyrus (DG; red), hippocampal Ammon's horn, and hypothalamus. **f**, Gene expression analysis in Ammon's horn and DG was performed by qRT–PCR. *Mgr1b* is enriched in Ammon's horn. *Dsp* and *Tdo2* are specific to the DG. Analysis confirmed the specific dissection of the hippocampus into Ammon's horn and DG. All $****P < 0.0001$. $n = 24$ mice per group. **g**, **h**, Gene expression of glucocorticoid receptor (*Nr3c1*) and mineralocorticoid receptor (*Nr3c2*) in the hippocampus analysed by qRT–

PCR. There was no difference between vehicle and ABX mice in DG (**g**, *Nr3c1* $P = 0.1016$, *Nr3c2* $P = 0.8947$) or Ammon's horn (**h**, *Nr3c1* $P = 0.1379$, *Nr3c2* $P = 0.9764$) after RSI. $n = 6$ mice per group. **i**, Expression of stress-related genes (*Crhr1* $P = 0.4032$, *Crhr2* $P = 0.6778$, *Ucn* $P = 0.2477$, *Ucn2* $P = 0.0636$, and *Ucn3* $P = 0.0797$) and neuropeptide genes (*Avp* $P = 0.9861$ and *Oxt* $P = 0.1445$) were unchanged after reciprocal social interaction in ABX mice. $n = 5$ vehicle, 6 ABX mice per group. **j, k**, Expression of *Nr3c1* and *Nr3c2* does not differ between vehicle and ABX mice in DG (**j**, *Nr3c1* $P = 0.6206$, *Nr3c2* $P = 0.5075$) or Ammon's horn (**k**, *Nr3c1* $P = 0.4873$, *Nr3c2* $P = 0.0931$) after novel cage exposure. $n = 6$ mice per group. **l**, *Ucn* gene expression is upregulated after novel cage exposure in ABX mice ($*P = 0.013$). Other stress-related genes (*Crh1* $P = 0.649$, *Crhr2* $P = 0.3875$, *Ucn2* $P = 0.1409$, and *Ucn3* $P = 0.511$) and neuropeptide genes (*Avp* $P = 0.5809$ and *Oxt* $P = 0.8216$) were unchanged. $n = 6$ mice per group. Data shown as individual points with mean \pm s.e.m. Data analysed by two-tailed unpaired *t*-test (**a–d, f–l**). $*P < 0.05$, $**P < 0.01$, $***P < 0.001$, $****P < 0.0001$, ND: no difference. For more statistical details, see [Supplementary Information](#).

[Source data](#)

[Extended Data Fig. 5 Expression of oxytocin, vasopressin, and their receptors in the hypothalamus of GF mice and Fluorogold labelling of neurons in the PVN and median eminence \(ME\) of GF and/or ABX-treated mice.](#)

a, b, Representative images (from 8 SPF and 6 GF mice) of vasopressin (**a**, AVP; red) and oxytocin (**b**, OXT; green) staining in brain sections after reciprocal social interaction. Scale bars, 100 μm . **c, d**, Quantification of AVP (**c**) and OXT (**d**) distribution in PVN of SPF and GF mice. No difference in the number of AVP neurons in PVN was detected in GF mice ($P = 0.3869$). OXT-positive cells were lower in GF mice ($**P = 0.0049$). $n = 8$ SPF, 6 GF mice per group. **e**, Gene expression of AVP, OXT, and their receptors analysed by qRT–PCR. No difference was found between naive SPF and GF mice. *Avp* $P = 0.3992$, *Avpr1a* $P = 0.6361$, *Avpr1b* $P = 0.5471$, *Avpr2* $P = 0.2168$, *Oxt* $P = 0.9281$, *Oxtr* $P = 0.3252$. $n = 4$ mice per group. **f–i**, GF and SPF mice were intraperitoneally injected with Fluorogold and

killed six days later. PVN and ME were retrogradely labelled. **f**, Representative Fluorogold retrograde tracing and immunohistochemistry images of the PVN. Green, anti-Fluorescent Gold (Fluorogold); magenta: anti-NeuN. $n = 4$ mice per group. **g**, Number of Fluorogold⁺ cells in the PVN shows no difference between GF and SPF mice. SPF vs GF $P = 0.2362$. $n = 4$ mice per group. **h**, Representative Fluorogold retrograde tracing and immunohistochemistry images of the ME. Green: anti-Fluorescent Gold (Fluorogold); magenta: anti-NeuN. $n = 3$ mice per group. **i**, Integrated density of Fluorogold in the ME shows no difference between GF and SPF mice. $P = 0.3723$. $n = 3$ mice per group. **j, k**, ABX- or vehicle-treated *Crh-ires-Cre;Ai14D* mice were intraperitoneally injected with Fluorogold and killed six days later. PVN neurons were retrogradely labelled with Fluorogold. **j**, Representative Fluorogold retrograde tracing and immunohistochemistry images of the PVN. Green: anti-Fluorescent Gold (Fluorogold); red: corticotropin-releasing hormone (CRH); magenta: anti-NeuN. $n = 4$ mice per group. **k**, Number of Fluorogold⁺ cells in the PVN shows no difference between ABX and vehicle mice. $P = 0.4545$. $n = 4$ mice per group. Scale bars, 200 μm . Data analysed by two-tailed unpaired *t*-test (**c–e, i, k**) and two-way ANOVA, repeated measures (**g**) with Bonferroni's multiple comparison post hoc test. ** $P < 0.01$; ND: no difference. For more statistical details, see [Supplementary Information](#).

Source data

Extended Data Fig. 6 Perturbation of glucocorticoid and vagus-dependent signalling in GF and/or ABX-treated mice.

a, b, Social activity was tested using the RSI paradigm in VEH-sham, ABX-sham, and ABX-ADX mice injected with corticosterone (subject), in the context of SPF novel mice. Acute administration of corticosterone produced no difference between groups in social activity (**a**, $P = 0.5697$) or non-social activity (**b**, $P = 0.6781$). $n = 5$ VEH-sham, 7 ABX-sham, and 4 ABX-ADX mice per group (subject only). **c, d**, Non-social activity was recorded using the RSI paradigm in SPF and GF (**c**), VEH-sham, ABX-sham, and ABX-ADX mice (**d**) (subject), in the context of SPF novel mice. **c**, Non-social activity was analysed during the social interaction test in SPF and GF mice injected with metyrapone. Equally decreased non-social

activity was detected in GF and SPF mice injected with metyrapone. SPF-CMC vs SPF-MET * $P = 0.041$, GF-CMC vs GF-MET * $P = 0.0274$. $n = 5$ SPF-CMC, 5 GF-CMC, 6 SPF-MET, 5 GF-MET mice per group (subject only). **d**, Non-social activity was analysed during the social interaction test in VEH-sham, ABX-sham, and ABX-ADX test mice injected with CMC, RU-486, or metyrapone (subject), in the context of SPF novel mice. Lower non-social activity was detected in ABX-ADX animals injected with RU-486 and ABX animals injected with metyrapone. First CMC: VEH-sham vs ABX-sham ** $P = 0.0034$; RU-486: VEH-sham vs ABX-ADX * $P = 0.0215$; MET: VEH-sham vs ABX-sham *** $P = 0.0006$, VEH-sham vs ABX-ADX * $P = 0.0145$. $n = 11$ mice for VEH-sham, 18 ABX-sham and 11 ABX-ADX sham mice per group (subject only). **e**, The completeness of subdiaphragmatic vagotomy (SDV) was validated by fasting-induced food consumption for 2 h following intraperitoneal CCK-8 injection. Food intake was normalized by body weight. SDV mice showed increased food intake compared to sham mice. SPF naive control vs SPF naive CCK-8 ** $P = 0.0038$, ABX-sham CCK-8 vs ABX-SDV CCK-8 ** $P = 0.0084$. $n = 6$ control saline, 6 control CCK-8, 7 ABX-sham, and 4 ABX-SDV mice per group. **f**, Measurement of serum corticosterone concentrations showed no difference after social interaction in ABX-SDV mice, compared to ABX-sham mice. $P = 0.8436$. $n = 9$ ABX-sham, 8 ABX-SDV mice per group. **g**, Quantification of c-Fos⁺ cells in anterodorsal bed nucleus of stria terminalis (adBNST) and dentate gyrus (DG) of ABX-sham and ABX-SDV mice. Increased c-Fos⁺ cells were detected in adBNST (left, * $P = 0.0451$), but not in DG (right, $P = 0.2577$), after social interaction in ABX-SDV mice, compared to ABX-sham mice. $n = 5$ sham, 5 SDV mice per group. Data shown as individual points with mean ± s.e.m. Data analysed by one-way ANOVA with Bonferroni's multiple comparison post hoc test (**a**, **b**); two-way ANOVA (**c**), repeated measures with mixed effect (**d**), with Bonferroni's multiple comparison post hoc test; two-tailed unpaired *t*-test (**e–g**). * $P < 0.05$, ** $P < 0.01$, *** $P < 0.001$, **** $P < 0.0001$, ND: no difference. For more statistical details, see [Supplementary Information](#).

[Source data](#)

[Extended Data Fig. 7 Knockout of glucocorticoid receptors in specific brain regions in ABX-treated and SPF mice.](#)

a, d, g Diagrams of virus injection into the DG ($Nr3c1^{ADG}$; relevant to Fig. 2*h, i*), BNST ($Nr3c1^{ABNST}$; relevant to Fig. 2*j, k*) and hypothalamus ($Nr3c1^{AHYPO}$; relevant to Fig. 2*l, m*). **b, e, h**, Non-social activity recorded using the RSI paradigm in ABX mice (subject), in the context of SPF novel mice. **b**, No difference in non-social activity was detected in ABX $Nr3c1^{ADG}$ mice. Control vs $Nr3c1^{ADG}$ $P = 0.1191$. $n = 7$ mice per group (subject only). **e**, Minimal difference in non-social activity was detected in ABX $Nr3c1^{ABNST}$ mice. A decrease in non-social activity was detected only at the second CMC injection (* $P = 0.0363$). $n = 7$ mice per group (subject only). **h**, No difference in non-social activity was detected in $Nr3c1^{AHYPO}$ mice. Control vs $Nr3c1^{AHYPO}$ $P = 0.0652$. $n = 6$ control, 5 $Nr3c1^{HYPO}$ mice per group (subject only). **c**, Quantification of c-Fos⁺ cells in various brain regions of ABX $Nr3c1^{ADG}$ and control mice. Decreased c-Fos⁺ cells were detected in the PVN and adBNST after social interaction in ABX $Nr3c1^{ADG}$ mice compared to control mice. There was no change in c-Fos expression in the DG of ABX $Nr3c1^{ADG}$ mice. PVN *** $P < 0.0001$, adBNST ** $P = 0.0022$, DG $P = 0.9714$. $n = 7$ mice per group. **f**, Quantification of c-Fos⁺ cells in various brain regions of ABX $Nr3c1^{ABNST}$ and control mice. Decreased c-Fos⁺ cells were detected in the PVN and adBNST after social interaction in ABX $Nr3c1^{ABNST}$ mice compared to control mice. There was no change in c-Fos staining in the DG. PVN *** $P < 0.0001$, adBNST *** $P = 0.0002$, DG $P = 0.4187$. $n = 7$ mice per group. **i**, Quantification of c-Fos⁺ cells in various brain regions of ABX $Nr3c1^{AHYPO}$ and control mice. Increased c-Fos⁺ cells were detected in DG and adBNST after social interaction in ABX $Nr3c1^{AHYPO}$ mice compared to control mice. There was no change in c-Fos expression in the PVN. PVN $P = 0.1163$, adBNST $P = 0.0688$, DG * $P = 0.0389$. $n = 6$ control, 5 $Nr3c1^{AHYPO}$ mice per group. **j**, Neuronal activity was measured by c-Fos staining of various brain sections. Representative images of c-Fos staining after social interaction in PVN, adBNST, and DG in $Nr3c1^{ADG}$ (from 7 animals each group), $Nr3c1^{ABNST}$ (from 7 animals each group) and $Nr3c1^{AHYPO}$ mice (from 6 control and 5 $Nr3c1^{AHYPO}$ animals), and their corresponding control groups. Scale bars, 100 μ m. **k, l**, Social activity (**k**) and non-social activity (**l**) were tested using the RSI paradigm in SPF test mice (subject), in the context of SPF novel mice. SPF $Nr3c1^{ADG}$ mice did not display altered social activity

($P = 0.4323$) or non-social activity ($P = 0.8234$) compared to control mice with vehicle injection. $n = 5$ mice per group (subject only). **m**, Serum corticosterone concentrations show no change after social interaction in SPF $Nr3c1^{ADG}$ mice. $P = 0.9935$. $n = 5$ mice per group. **n, o**, Social activity (**n**) and non-social activity (**o**) were tested using the RSI paradigm in SPF test mice (subject) in the context of SPF novel mice. SPF $Nr3c1^{ABNST}$ mice showed reduced social activity compared to control mice with vehicle injection (* $P = 0.0473$). No change was observed in non-social activity between SPF control and $Nr3c1^{ABNST}$ mice ($P = 0.4742$). $n = 5$ mice per group (subject only). **p**, Serum corticosterone concentrations show no change after social interaction in SPF $Nr3c1^{ABNST}$ mice. $P = 0.9312$. $n = 5$ mice per group. **q, r**, Social activity (**q**) and non-social activity (**r**) were tested using the RSI paradigm in SPF test mice (subject), in the context of SPF novel mice. SPF $Nr3c1^{HYPO}$ mice did not display altered social activity ($P = 0.1823$) or non-social activity ($P = 0.2339$) compared to control mice with vehicle injection. $n = 5$ mice per group (subject only). **s**, Serum corticosterone concentrations show no change after social interaction in SPF $Nr3c1^{HYPO}$ mice. $P = 0.0701$. $n = 5$ mice per group. Data shown as individual points with mean \pm s.e.m. Data analysed by two-way ANOVA, repeated measures (**b, e**) with mixed effect (**h**) with Bonferroni's multiple comparison post hoc test; two-tailed unpaired *t*-test (**c, f, i, k-s**). * $P < 0.05$, ** $P < 0.01$, *** $P < 0.001$, **** $P < 0.0001$, ND: no difference. For more statistical details, see [Supplementary Information](#).

[Source data](#)

[Extended Data Fig. 8 Manipulations of CRH neurons and glucocorticoid-sensing neurons in ABX-treated and SPF mice.](#)

a, Diagram of AAV-hSyn-DIO-hM4Di-mCherry (hM4Di) or AAV-hSyn-DIO-mCherry (mCherry) virus injection into the PVN of *Crh-ires-Cre* mice. **b**, Non-social activity in ABX-treated mCherry and hM4Di mice, with and without CNO (subject). hM4Di effect $P = 0.4909$. $n = 10$ mCherry, 11 hM4Di mice. **c, d**, Neuronal activity was measured by c-Fos staining of brain sections. Representative images (from 10 mCherry and 11 hM4Di mice) of c-Fos, mCherry and DAPI staining in the adBNST (**c**) and DG (**d**)

in hM4Di and mCherry mice upon CNO injection after social interaction. Scale bars, 100 μ m. **e, f**, Quantification of c-Fos⁺ cells in various brain regions of ABX hM4Di and mCherry mice. There was no change in c-Fos in the adBNST (**e**, $P = 0.301$) or DG (**f**, $P = 0.5745$) of ABX hM4Di mice upon CNO injection. $n = 10$ mCherry, 11 hM4Di mice per group. **g**, Top, timeline scheme of stereotaxic surgery, ABX treatment, drug administration, social behaviour, and sample collection. *Crh-ires-Cre* mice were stereotactically injected with viruses into the BNST one week before ABX treatment at the age of 7–8 weeks. After three weeks of ABX treatment, social behaviour was tested in VEH- or CNO-injected mice. Bottom, diagram of virus injection into the BNST of *Crh-ires-Cre* mice to deliver AAV-hSyn-DIO-hM4Di-mCherry (hM4Di) or AAV-hSyn-DIO-mCherry (mCherry). **h**, Social activity was tested using the RSI paradigm in ABX test mice (subject), in the context of SPF novel mice. With VEH and CNO injection, there was no difference in social activity between mice injected with hM4Di and mice injected with mCherry. mCherry vs hM4Di $P = 0.4722$. $n = 10$ mCherry, 9 hM4Di mice per group (subject only). **i**, Non-social activity was recorded using the RSI paradigm in ABX mice (subject), in the context of SPF novel mice. With VEH and CNO injection, there was no difference in non-social activity between mice injected with hM4Di and mice injected with mCherry at the BNST. mCherry vs hM4Di $P = 0.1921$. $n = 10$ mCherry, 9 hM4Di mice per group (subject only). **j**, Serum corticosterone concentrations show no change after social interaction in ABX hM4Di mice when injected with CNO. $P = 0.2063$. $n = 8$ mice per group. **k, l**, Quantification of c-Fos⁺ cells in various brain regions of ABX hM4Di and mCherry mice. No change in c-Fos⁺ cells was detected in the PVN (**k**, $P = 0.4792$) or adBNST (**l**, $P = 0.3054$) after social interaction in ABX hM4Di mice with CNO injection, compared to mCherry mice. $n = 10$ mCherry, 8 hM4Di mice per group. **m**, Neuronal activity was measured by c-Fos staining of brain sections. Representative images (from 10 mCherry, 8 hM4Di mice) of c-Fos, mCherry and DAPI staining in the PVN and adBNST of hM4Di and mCherry mice with CNO injection after social interaction. Scale bars, 100 μ m. **a–m**, All mice received antibiotics. **n**, Diagram of AAV-hSyn-DIO-hM3Dq-mCherry (hM3Dq) or AAV-hSyn-DIO-mCherry (mCherry) injection into the PVN. **o**, Relevant to Fig. [3h–j](#). Non-social activity was recorded using the RSI paradigm in SPF mice (subject), in the context of SPF novel mice. With VEH injection, there was

no difference in non-social activity between mice injected with AAV-hSyn-DIO-hM3Dq-mCherry (hM3Dq) and mice injected with AAV-hSyn-DIO-mCherry (mCherry). Injection of CNO increased non-social activity in hM3Dq mice but not mCherry mice. SPF mCherry CNO vs SPF hM3Dq CNO *** $P < 0.0001$. $n = 10$ mCherry, 11 hM3Dq mice per group (subject only). **p**, Relevant to Fig. [3k–m](#). Diagram of guide cannula implantation into the PVN to deliver VEH or CRF. **q**, Non-social activity was recorded using the RSI paradigm in SPF mice (subject), in the context of SPF novel mice. Injection of CRF (low) increased non-social activity, whereas injection of CRF (high) did not alter non-social activity compared to VEH mice. VEH vs CRF(low) * $P = 0.0427$, CRF(low) vs CRF(high) * $P = 0.0134$. $n = 16$ VEH, 7 CRF (low), 9 CRF (high) mice per group (subject only). **r, s**, Relevant to Fig. [3n–p](#). Diagram of guide cannula implantation into the DG (**r**) or BNST (**s**) to deliver VEH, CORT, or DEX. **t**, Relevant to Fig. [3k–m](#). Correct guide cannula implantation into the PVN was validated by histological sectioning and DAPI staining for visualization of the PVN to confirm CRF injection. The customized guide cannula set includes guide cannula, injector, dummy, and cap (left). The guide cannula was implanted 0.5 mm above the PVN. The tip of the guide cannula track can be visualized in the thalamus region in each implanted mouse. The injector was designed to reach 0.5 mm below the tip of the guide cannula. As the injector was made of 33G fine needle, the needle track of the injector was not visible in the brain slice and is depicted in the image (middle). Enlarged image to show the guide cannula track and the depicted needle track above the PVN (right). Scale bars, 500 μm . Data shown as individual points with mean \pm s.e.m. Data analysed by two-way ANOVA, repeated measures (**b, h, i, o**) with Bonferroni's multiple comparison post hoc test; two-tailed unpaired (**e, f, k, l**) or paired *t*-test (**j**); one-way ANOVA with Bonferroni's multiple comparison post hoc test (**q**). * $P < 0.05$, *** $P < 0.0001$, ND: no difference. For more statistical details, see [Supplementary Information](#).

Source data

Extended Data Fig. 9 Retrograde neural tracing of the PVN and adBNST of GF and ABX-treated mice.

a, CTB-488 was stereotactically injected into the PVN of GF and SPF C57BL/6J mice. The brains were removed seven days after injection. CTB-488 retrograde tracing was visualized by confocal imaging of brain sections counterstained with an antibody against NeuN. GF mice were treated with ABX after surgery. **b**, Quantification of CTB-488⁺ cells in various brain regions of SPF and GF mice. adBNST ($P = 0.229$); LS ($P = 0.1373$); MeA ($P = 0.358$). No difference in CTB-488 retrograde-labelled cells was detected between SPF and GF mice. $n = 4$ mice per group. **c**, Representative images (from 4 animals each group) of CTB-488 (green) labelling and NeuN (magenta) staining in the adBNST, MeA, and LS of SPF and GF mice. Scale bars, 100 μm . **d**, CTB-488 and Fluorogold were stereotactically injected into the PVN and adBNST, respectively, in vehicle and ABX *Crhires-Cre;Ai14D* mice. Brains were removed 7 days after injection. Retrograde tracers were visualized by confocal imaging of brain sections counterstained with antibodies. **e**, Quantification of CTB-488⁺ cells in various brain regions of vehicle and ABX mice. No difference in CTB-488 retrograde-labelled cells was detected between vehicle and ABX mice. adBNST $P = 0.2064$, LS $P = 0.4332$, MeA $P = 0.4366$. $n = 4$ mice per group. **f**, Quantification of Fluorogold (FG)⁺ cells in various brain regions of vehicle and ABX mice. No difference in Fluorogold retrograde-labelled cells was detected between vehicle and ABX mice. adBNST $P = 0.8922$, LS $P = 0.8715$, MeA $P = 0.7284$. $n = 4$ mice per group. **g**, Representative images (from 4 animals each group) of CTB-488 (green) labelling, Fluorogold (blue) staining, and CRH⁺ tdTomato (red) cells in the adBNST, MeA, LS, and PVN of vehicle and ABX mice. Scale bars, 100 μm . Data shown as individual points with mean \pm s.e.m. Data analysed by two-tailed unpaired *t*-test (**b**, **e**, **f**). ND: no difference. For more statistical details, see [Supplementary Information](#).

[Source data](#)

[Extended Data Fig. 10 Microbiome analysis of AVNM and AVM mice, and identification and effects of *E. faecalis*.](#)

a, Quantification of c-Fos⁺ cells in PVN of AVNM and AVM mice. Decreased c-Fos⁺ cells are detected in PVN after social interaction in AVM

mice compared to AVNM mice. *** $P = 0.0003$. $n = 8$ mice per group. **b**, Total microbial loads of faecal pellets from GF mice receiving faecal microbial transplants from AVM- or AVNM-treated mice. All measurements performed with digital PCR and normalized to faecal pellet weights. $n = 11$ GF-AVM, 9 GF-AVNM mice per group. **c**, Correlation between the \log_{10} abundance of *Enterococcus* as determined by taxon-specific dPCR and 16S rRNA gene amplicon sequencing with dPCR anchoring (relative abundance of *Enterococcus* measured by sequencing \times total 16S rRNA gene copies measured by dPCR). $n = 8$ mice per group. **d**, Percentage abundance of taxa from faecal pellets of GF mice that received faecal microbial transplants from AVM- or AVNM-treated mice. $n = 9$ GF-AVNM, 11 GF-AVM mice per group. **e**, Social activity shown in Fig. 4*i* in vehicle (VEH) and ABX mice (subject) in the first RSI test. * $P = 0.0321$. $n = 8$ VEH, 15 ABX mice (data from Fig. 4*i*). **f**, *Enterococcus faecalis*-specific 16S rRNA gene copy number in faecal pellets from ABX mice colonized with *E.f.* for 3 weeks and VEH or ABX mice gavaged with control buffer. All measurements performed with qPCR and normalized to faecal bacteria 16S rRNA gene. High *E.f.* values in ABX + *E.f.* compared to VEH + Ctrl mice probably reflect reduced competition by other bacteria following antibiotic treatment. The dashed line represents *E.f.* expression in VEH + Ctrl mice. VEH + Ctrl vs ABX + *E.f.* ** $P = 0.002$, ABX + Ctrl vs ABX + *E.f.* ** $P = 0.0015$. $n = 3$ mice per group, subset selected from Extended Data Fig. 10*g*. **g**, Social activity (relevant to Fig. 4*i*) following three weeks of *E. faecalis* colonization using the RSI paradigm in VEH + Ctrl, ABX + Ctrl, and ABX + *E.f.* mice (subject). ABX + Ctrl vs ABX + *E.f.* * $P = 0.0336$. $n = 8$ VEH + Ctrl, 8 ABX + Ctrl, 7 ABX + *E.f.* mice. Note, ABX + Ctrl mice are half the same group used in **i**, and therefore show a baseline reduction in social activity (data from Fig. 4*i*). **h**, Social activity was tested using the RSI paradigm in SPF and GF mice and in GF mice colonized with *E.f.* at the perinatal stage (subject), in the context of SPF novel mice. GF mice colonized with *E.f.* display increased social activity, compared to GF control mice. SPF vs GF * $P = 0.028$, GF vs GF + *E.f.* ** $P = 0.0066$. $n = 6$ SPF, 11 GF, 10 GF + *E.f.* mice per group (subject only). **i–k**, Quantification of c-Fos⁺ cells in various brain regions of GF and GF + *E.f.* mice. Decreased c-Fos⁺ cells were detected in PVN (**i**, * $P = 0.0167$), adBNST (**j**, * $P = 0.0467$), and DG (**k**, ** $P = 0.0076$) after social interaction in GF + *E.f.* mice compared to GF mice. $n = 9$ mice per

group for PVN; $n = 10$ mice per group for DG; $n = 10$ GF, 9 GF + *E.f.* mice per group for adBNST. **I**, Serum corticosterone concentrations show no change after social interaction in GF + *E.f.* mice compared to GF mice. SPF vs GF $P = 0.959$, SPF vs GF + *E.f.* $P = 0.0585$, GF vs GF + *E.f.* $P = 0.2642$. $n = 6$ SPF, 11 GF, 10 GF + *E.f.* mice per group. Data shown as individual points with mean \pm s.e.m. Data analysed by two-tailed unpaired *t*-test (**a, e, i–k**); one-way ANOVA with Bonferroni's multiple comparison post hoc test (**f–h, l**). * $P < 0.05$, ** $P < 0.01$, *** $P < 0.001$, ND: no difference. For more statistical details, see [Supplementary Information](#).

[Source data](#)

Supplementary information

[Supplementary Information](#)

This file contains statistical tests and exact P values for each figure.

[Reporting Summary](#)

[Video 1](#)

Social interaction test of CNO-injected *Crh^{PVN}* expressing hM3Dq.

[Video 2](#)

Social interaction test of saline-injected *Crh^{PVN}* expressing hM3Dq.

Source data

[Source Data Fig. 1](#)

[Source Data Fig. 2](#)

[Source Data Fig. 3](#)

[Source Data Fig. 4](#)

[Source Data Extended Data Fig. 1](#)

[Source Data Extended Data Fig. 2](#)

[Source Data Extended Data Fig. 3](#)

[Source Data Extended Data Fig. 4](#)

[Source Data Extended Data Fig. 5](#)

[Source Data Extended Data Fig. 6](#)

[Source Data Extended Data Fig. 7](#)

[Source Data Extended Data Fig. 8](#)

[Source Data Extended Data Fig. 9](#)

[Source Data Extended Data Fig. 10](#)

Rights and permissions

[Reprints and Permissions](#)

About this article



Check for
updates

Cite this article

Wu, WL., Adame, M.D., Liou, CW. *et al.* Microbiota regulate social behaviour via stress response neurons in the brain. *Nature* **595**, 409–414 (2021). <https://doi.org/10.1038/s41586-021-03669-y>

[Download citation](#)

- Received: 05 January 2019
- Accepted: 25 May 2021
- Published: 30 June 2021
- Issue Date: 15 July 2021
- DOI: <https://doi.org/10.1038/s41586-021-03669-y>

Comments

By submitting a comment you agree to abide by our [Terms](#) and [Community Guidelines](#). If you find something abusive or that does not comply with our terms or guidelines please flag it as inappropriate.

[Access through your institution](#)

[Change institution](#)

[Buy or subscribe](#)

Advertisement

This article was downloaded by **calibre** from <https://www.nature.com/articles/s41586-021-03669-y>.

- Article
- [Published: 14 July 2021](#)

A metabolomics pipeline for the mechanistic interrogation of the gut microbiome

- [Shuo Han](#) [ORCID: orcid.org/0000-0003-1181-351X](#)^{1 na1},
- [Will Van Treuren](#)^{1,2 na1},
- [Curt R. Fischer](#) [ORCID: orcid.org/0000-0003-3386-9813](#)^{3,4},
- [Bryan D. Merrill](#) [ORCID: orcid.org/0000-0002-9967-5539](#)^{1,2},
- [Brian C. DeFelice](#) [ORCID: orcid.org/0000-0001-8243-0300](#)⁴,
- [Juan M. Sanchez](#)⁴,
- [Steven K. Higginbottom](#)¹,
- [Leah Guthrie](#)¹,
- [Lalla A. Fall](#)^{3,5},
- [Dylan Dodd](#) [ORCID: orcid.org/0000-0001-6210-6239](#)^{1,5},
- [Michael A. Fischbach](#) [ORCID: orcid.org/0000-0003-3079-8247](#)^{4,6}
&
- [Justin L. Sonnenburg](#) [ORCID: orcid.org/0000-0003-2299-6817](#)^{1,4,7}

[Nature](#) volume **595**, pages 415–420 (2021) [Cite this article](#)

- 4704 Accesses
- 116 Altmetric
- [Metrics details](#)

Subjects

- [Bioinformatics](#)
- [Metabolomics](#)
- [Microbiome](#)

Abstract

Gut microorganisms modulate host phenotypes and are associated with numerous health effects in humans, ranging from host responses to cancer immunotherapy to metabolic disease and obesity. However, difficulty in accurate and high-throughput functional analysis of human gut microorganisms has hindered efforts to define mechanistic connections between individual microbial strains and host phenotypes. One key way in which the gut microbiome influences host physiology is through the production of small molecules^{1,2,3}, yet progress in elucidating this chemical interplay has been hindered by limited tools calibrated to detect the products of anaerobic biochemistry in the gut. Here we construct a microbiome-focused, integrated mass-spectrometry pipeline to accelerate the identification of microbiota-dependent metabolites in diverse sample types. We report the metabolic profiles of 178 gut microorganism strains using our library of 833 metabolites. Using this metabolomics resource, we establish deviations in the relationships between phylogeny and metabolism, use machine learning to discover a previously undescribed type of metabolism in *Bacteroides*, and reveal candidate biochemical pathways using comparative genomics. Microbiota-dependent metabolites can be detected in diverse biological fluids from gnotobiotic and conventionally colonized mice and traced back to the corresponding metabolomic profiles of cultured bacteria. Collectively, our microbiome-focused metabolomics pipeline and interactive metabolomics profile explorer are a powerful tool for characterizing microorganisms and interactions between microorganisms and their host.

Access options

Subscribe to Journal

Get full journal access for 1 year

\$199.00

only \$3.90 per issue

[Subscribe](#)

All prices are NET prices.

VAT will be added later in the checkout.

Tax calculation will be finalised during checkout.

Rent or Buy article

Get time limited or full article access on ReadCube.

from \$8.99

[Rent or Buy](#)

All prices are NET prices.

Additional access options:

- [Log in](#)
- [Access through your institution](#)
- [Learn about institutional subscriptions](#)

Fig. 1: A microbiome-focused metabolomics pipeline enables the mechanistic interrogation of microbiome metabolism.

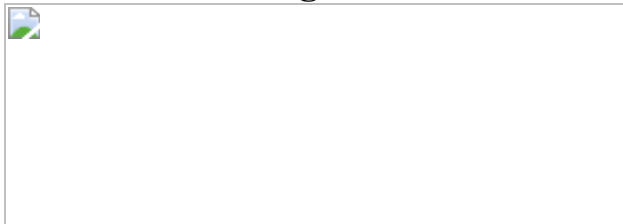


Fig. 2: Relationships between phylogeny, taxonomy and metabolome.



Fig. 3: Discovery of nitrogen-assimilation strategies in *Bacteroides* and previously undescribed gene–phenotype relationships.

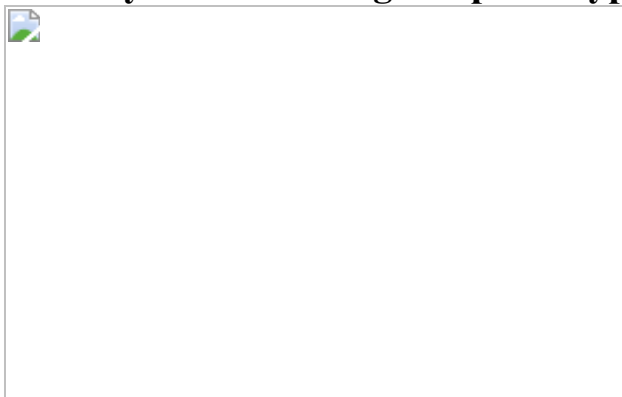
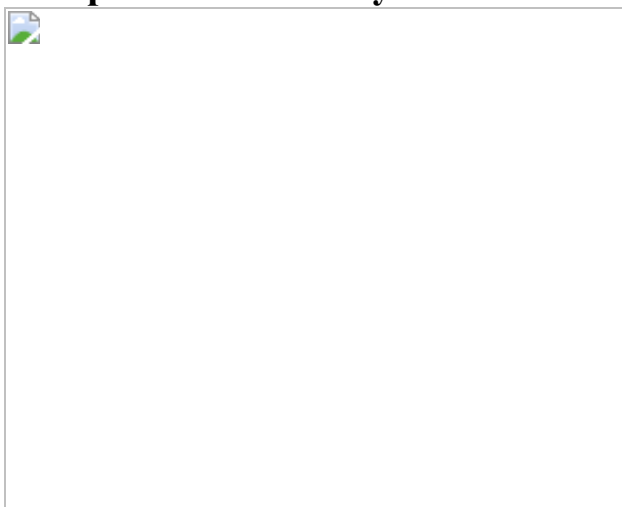


Fig. 4: Metabolic contribution by individual gut microorganisms in a multi-species community.



Data availability

All raw data from metabolomics are publicly available from the Metabolomics Workbench under study number ST001683 for in vivo data and study number ST001688 for in vitro data. MS/MS libraries generated using the qTOF and QE instruments are publicly accessible in the MoNA spectrum database (<https://mona.fiehnlab.ucdavis.edu>) and can be queried using the keywords ‘Sonnenburg Lab MS2 Library’.

Code availability

Custom Python code was written to enable the construction of the MS/MS libraries, the processing and visualization of the in vitro and in vivo LC–MS data, the optical density and growth curve data, the bioinformatics analysis of 16S and whole genomes, and the analysis of the metabolomic data. Full code for each of these steps is available at <https://doi.org/10.5281/zenodo.4890994>. The JavaScript code supporting the interactive, web-based Metabolomics Data Explorer is available at <https://doi.org/10.5281/zenodo.4890999>.

References

1. 1.

Koppel, N., Maini Rekdal, V. & Balskus, E. P. Chemical transformation of xenobiotics by the human gut microbiota. *Science* **356**, eaag2770 (2017).

[Google Scholar](#)

2. 2.

Koh, A., De Vadder, F., Kovatcheva-Datchary, P. & Bäckhed, F. From dietary fiber to host physiology: short-chain fatty acids as key bacterial metabolites. *Cell* **165**, 1332–1345 (2016).

[CAS](#) [Google Scholar](#)

3. 3.

Donia, M. S. & Fischbach, M. A. Small molecules from the human microbiota. *Science* **349**, 1254766 (2015).

[PubMed](#) [PubMed Central](#) [Google Scholar](#)

4. 4.

Rooks, M. G. & Garrett, W. S. Gut microbiota, metabolites and host immunity. *Nat. Rev. Immunol.* **16**, 341–352 (2016).

[CAS](#) [PubMed](#) [PubMed Central](#) [Google Scholar](#)

5. 5.

Cani, P. D. Microbiota and metabolites in metabolic diseases. *Nat. Rev. Endocrinol.* **15**, 69–70 (2019).

[CAS](#) [Google Scholar](#)

6. 6.

Sonnenburg, J. L. & Bäckhed, F. Diet-microbiota interactions as moderators of human metabolism. *Nature* **535**, 56–64 (2016).

[ADS](#) [CAS](#) [PubMed](#) [PubMed Central](#) [Google Scholar](#)

7. 7.

Kasahara, K. & Rey, F. E. The emerging role of gut microbial metabolism on cardiovascular disease. *Curr. Opin. Microbiol.* **50**, 64–70 (2019).

[CAS](#) [Google Scholar](#)

8. 8.

Lynch, J. B. & Hsiao, E. Y. Microbiomes as sources of emergent host phenotypes. *Science* **365**, 1405–1409 (2019).

[ADS](#) [CAS](#) [Google Scholar](#)

9. 9.

Nemet, I. et al. A cardiovascular disease-linked gut microbial metabolite acts via adrenergic receptors. *Cell* **180**, 862–877.e22 (2020).

[CAS](#) [PubMed](#) [PubMed Central](#) [Google Scholar](#)

10. 10.

Koh, A. et al. Microbially produced imidazole propionate impairs insulin signaling through mTORC1. *Cell* **175**, 947–961.e17 (2018).

[CAS](#) [Google Scholar](#)

11. 11.

Rinschen, M. M., Ivanisevic, J., Giera, M. & Siuzdak, G. Identification of bioactive metabolites using activity metabolomics. *Nat. Rev. Mol. Cell Biol.* **20**, 353–367 (2019)

[CAS](#) [PubMed](#) [PubMed Central](#) [Google Scholar](#)

12. 12.

Blaženović, I., Kind, T., Ji, J. & Fiehn, O. Software tools and approaches for compound identification of LC-MS/MS data in metabolomics. *Metabolites* **8**, 31 (2018).

[PubMed](#) [PubMed Central](#) [Google Scholar](#)

13. 13.

Guijas, C. et al. METLIN: a technology platform for identifying knowns and unknowns. *Anal. Chem.* **90**, 3156–3164 (2018).

[CAS](#) [PubMed](#) [PubMed Central](#) [Google Scholar](#)

14. 14.

Wishart, D. S. et al. HMDB 4.0: the human metabolome database for 2018. *Nucleic Acids Res.* **46** (D1), D608–D617 (2018).

[CAS](#) [Google Scholar](#)

15. 15.

Kanehisa, M., Sato, Y., Furumichi, M., Morishima, K. & Tanabe, M. New approach for understanding genome variations in KEGG. *Nucleic Acids Res.* **47** (D1), D590–D595 (2019).

[CAS](#) [Google Scholar](#)

16. 16.

Sampson, T. R. & Mazmanian, S. K. Control of brain development, function, and behavior by the microbiome. *Cell Host Microbe* **17**, 565–576 (2015).

[CAS](#) [PubMed](#) [PubMed Central](#) [Google Scholar](#)

17. 17.

Lloyd-Price, J. et al. Multi-omics of the gut microbial ecosystem in inflammatory bowel diseases. *Nature* **569**, 655–662 (2019).

[ADS](#) [CAS](#) [PubMed](#) [PubMed Central](#) [Google Scholar](#)

18. 18.

Goldford, J. E. et al. Emergent simplicity in microbial community assembly. *Science* **361**, 469–474 (2018).

[ADS](#) [CAS](#) [PubMed](#) [PubMed Central](#) [Google Scholar](#)

19. 19.

Kamneva, O. K. Genome composition and phylogeny of microbes predict their co-occurrence in the environment. *PLOS Comput. Biol.* **13**, e1005366 (2017).

[ADS](#) [PubMed](#) [PubMed Central](#) [Google Scholar](#)

20. 20.

Borenstein, E., Kupiec, M., Feldman, M. W. & Ruppin, E. Large-scale reconstruction and phylogenetic analysis of metabolic environments. *Proc. Natl Acad. Sci. USA* **105**, 14482–14487 (2008).

[ADS](#) [CAS](#) [PubMed](#) [PubMed Central](#) [Google Scholar](#)

21. 21.

Plata, G., Henry, C. S. & Vitkup, D. Long-term phenotypic evolution of bacteria. *Nature* **517**, 369–372 (2015).

[ADS](#) [CAS](#) [Google Scholar](#)

22. 22.

Tofalo, R., Cocchi, S. & Suzzi, G. Polyamines and gut microbiota. *Front. Nutr.* **6**, 16 (2019).

[PubMed](#) [PubMed Central](#) [Google Scholar](#)

23. 23.

Qi, H. et al. *Lactobacillus* maintains healthy gut mucosa by producing l-ornithine. *Commun. Biol.* **2**, 171 (2019).

[PubMed](#) [PubMed Central](#) [Google Scholar](#)

24. 24.

Zúñiga, M., Pérez, G. & González-Candelas, F. Evolution of arginine deiminase (ADI) pathway genes. *Mol. Phylogenet. Evol.* **25**, 429–444 (2002).

[Google Scholar](#)

25. 25.

Tabor, C. W. & Tabor, H. Polyamines in microorganisms. *Microbiol. Rev.* **49**, 81–99 (1985).

[CAS](#) [PubMed](#) [PubMed Central](#) [Google Scholar](#)

26. 26.

Varel, V. H. & Bryant, M. P. Nutritional features of *Bacteroides fragilis* subsp. *fragilis*. *Appl. Microbiol.* **28**, 251–257 (1974).

[CAS](#) [PubMed](#) [PubMed Central](#) [Google Scholar](#)

27. 27.

Mars, R. A. T. et al. Longitudinal multi-omics reveals subset-specific mechanisms underlying irritable bowel syndrome. *Cell* **182**, 1460–1473.e17 (2020).

[CAS](#) [PubMed](#) [PubMed Central](#) [Google Scholar](#)

28. 28.

Wastyk, H. C. et al. Gut microbiota-targeted diets modulate human immune status. Preprint at <https://doi.org/10.1101/2020.09.30.321448> (2020).

29. 29.

Kotagale, N. R., Taksande, B. G. & Inamdar, N. N. Neuroprotective offerings by agmatine. *Neurotoxicology* **73**, 228–245 (2019).

[CAS](#) [Google Scholar](#)

30. 30.

Winter, T. N., Elmquist, W. F. & Fairbanks, C. A. OCT2 and MATE1 provide bidirectional agmatine transport. *Mol. Pharm.* **8**, 133–142 (2011).

[CAS](#) [Google Scholar](#)

31. 31.

Chin, R. M. et al. The metabolite α -ketoglutarate extends lifespan by inhibiting ATP synthase and TOR. *Nature* **510**, 397–401 (2014).

[ADS](#) [CAS](#) [PubMed](#) [PubMed Central](#) [Google Scholar](#)

32. 32.

Zhou, W. et al. Longitudinal multi-omics of host–microbe dynamics in prediabetes. *Nature* **569**, 663–671 (2019).

[ADS](#) [CAS](#) [PubMed](#) [PubMed Central](#) [Google Scholar](#)

33. 33.

Watrous, J. D. et al. Directed non-targeted mass spectrometry and chemical networking for discovery of eicosanoids and related oxylipins. *Cell Chem. Biol.* **26**, 433–442.e4 (2019).

[CAS](#) [PubMed](#) [PubMed Central](#) [Google Scholar](#)

34. 34.

Dumas, M. E. et al. Metabolic profiling reveals a contribution of gut microbiota to fatty liver phenotype in insulin-resistant mice. *Proc. Natl*

Acad. Sci. USA **103**, 12511–12516 (2006).

[ADS](#) [CAS](#) [PubMed](#) [PubMed Central](#) [Google Scholar](#)

35. 35.

Langille, M. G. I. et al. Predictive functional profiling of microbial communities using 16S rRNA marker gene sequences. *Nat. Biotechnol.* **31**, 814–821 (2013).

[CAS](#) [PubMed](#) [PubMed Central](#) [Google Scholar](#)

36. 36.

Sberro, H. et al. Large-scale analyses of human microbiomes reveal thousands of small, novel genes. *Cell* **178**, 1245–1259.e14 (2019).

[CAS](#) [PubMed](#) [PubMed Central](#) [Google Scholar](#)

37. 37.

Quinn, R. A. et al. Global chemical effects of the microbiome include new bile-acid conjugations. *Nature* **579**, 123–129 (2020).

[ADS](#) [CAS](#) [PubMed](#) [PubMed Central](#) [Google Scholar](#)

38. 38.

Zimmermann, M., Zimmermann-Kogadeeva, M., Wegmann, R. & Goodman, A. L. Mapping human microbiome drug metabolism by gut bacteria and their genes. *Nature* **570**, 462–467 (2019).

[CAS](#) [PubMed](#) [PubMed Central](#) [Google Scholar](#)

39. 39.

Wu, G. D. et al. Comparative metabolomics in vegans and omnivores reveal constraints on diet-dependent gut microbiota metabolite production. *Gut* **65**, 63–72 (2016).

[CAS](#) [Google Scholar](#)

40. 40.

Kim, S. G. et al. Microbiota-derived lantibiotic restores resistance against vancomycin-resistant *Enterococcus*. *Nature* **572**, 665–669 (2019).

[ADS](#) [CAS](#) [PubMed](#) [PubMed Central](#) [Google Scholar](#)

41. 41.

Maini Rekdal, V., Bess, E. N., Bisanz, J. E., Turnbaugh, P. J. & Balskus, E. P. Discovery and inhibition of an interspecies gut bacterial pathway for Levodopa metabolism. *Science* **364**, eaau6323 (2019).

[Google Scholar](#)

42. 42.

Wikoff, W. R. et al. Metabolomics analysis reveals large effects of gut microflora on mammalian blood metabolites. *Proc. Natl Acad. Sci. USA* **106**, 3698–3703 (2009).

[ADS](#) [CAS](#) [PubMed](#) [PubMed Central](#) [Google Scholar](#)

43. 43.

Showalter, M. R. et al. Obesogenic diets alter metabolism in mice. *PLoS ONE* **13**, e0190632 (2018).

[PubMed](#) [PubMed Central](#) [Google Scholar](#)

44. 44.

Cajka, T., Smilowitz, J. T. & Fiehn, O. Validating quantitative untargeted lipidomics across nine liquid chromatography-high-resolution mass spectrometry platforms. *Anal. Chem.* **89**, 12360–12368 (2017).

[CAS](#) [Google Scholar](#)

45. 45.

Tsugawa, H. et al. MS-DIAL: data-independent MS/MS deconvolution for comprehensive metabolome analysis. *Nat. Methods* **12**, 523–526 (2015).

[CAS](#) [PubMed](#) [PubMed Central](#) [Google Scholar](#)

46. 46.

Kösters, M. et al. pymzML v2.0: introducing a highly compressed and seekable gzip format. *Bioinformatics* **34**, 2513–2514 (2018).

[Google Scholar](#)

47. 47.

Wu, M. et al. Genetic determinants of in vivo fitness and diet responsiveness in multiple human gut *Bacteroides*. *Science* **350**, aac5992 (2015).

[PubMed](#) [PubMed Central](#) [Google Scholar](#)

48. 48.

Shepherd, E. S., DeLoache, W. C., Pruss, K. M., Whitaker, W. R. & Sonnenburg, J. L. An exclusive metabolic niche enables strain engraftment in the gut microbiota. *Nature* **557**, 434–438 (2018).

[ADS](#) [CAS](#) [PubMed](#) [PubMed Central](#) [Google Scholar](#)

49. 49.

Tritsch, G. L. & Moore, G. E. Spontaneous decomposition of glutamine in cell culture media. *Exp. Cell Res.* **28**, 360–364 (1962).

[CAS](#) [Google Scholar](#)

50. 50.

Dodd, D. et al. A gut bacterial pathway metabolizes aromatic amino acids into nine circulating metabolites. *Nature* **551**, 648–652 (2017).

[ADS](#) [CAS](#) [PubMed](#) [PubMed Central](#) [Google Scholar](#)

51. 51.

Bolger, A. M., Lohse, M. & Usadel, B. Trimmomatic: a flexible trimmer for Illumina sequence data. *Bioinformatics* **30**, 2114–2120 (2014).

[CAS](#) [PubMed](#) [PubMed Central](#) [Google Scholar](#)

52. 52.

Bankevich, A. et al. SPAdes: a new genome assembly algorithm and its applications to single-cell sequencing. *J. Comput. Biol.* **19**, 455–477 (2012).

[MathSciNet](#) [CAS](#) [PubMed](#) [PubMed Central](#) [Google Scholar](#)

53. 53.

Seemann, T. Prokka: rapid prokaryotic genome annotation. *Bioinformatics* **30**, 2068–2069 (2014).

[CAS](#) [Google Scholar](#)

54. 54.

Medema, M. H., Takano, E. & Breitling, R. Detecting sequence homology at the gene cluster level with MultiGeneBlast. *Mol. Biol. Evol.* **30**, 1218–1223 (2013).

[CAS](#) [PubMed](#) [PubMed Central](#) [Google Scholar](#)

[Download references](#)

Acknowledgements

We thank C. Khosla, Y. Dai and the Stanford ChEM-H Metabolomics Knowledge Center for use of the LC–MS-qTOF instrument; A. Shiver, K. C. Huang and A. Cheng for sharing bacterial strains; T. Meyers and T. Cowan for sharing chemical standards; H. C. Wastyk and G. K. Fragiadakis for sharing their metabolite data before publication; J. K. Yang for consultation on web design tools; and T. Le for discussion on MS methods. This work is supported by R01-DK085025, DP1-AT009892, R01-DK101674, gifts from M. and J. Pasquesi, H. Buhr and J. Feiber, a Stanford Discovery Innovation Fund Award (J.L.S.), Chan Zuckerberg Biohub (M.A.F. and J.L.S.), DP1-DK113598 and P01-HL147823 (M.A.F.), K08DK110335 (D.D.), Stanford Dean’s Postdoctoral Fellowship and NRSA F32AG062119 (S.H.), NSF-GRFP DGE-114747 (W.V.T.) and 5T32AI007328-32 (L.G.).

Author information

Author notes

1. These authors contributed equally: Shuo Han, Will Van Treuren

Affiliations

1. Department of Microbiology and Immunology, Stanford University School of Medicine, Stanford, CA, USA

Shuo Han, Will Van Treuren, Bryan D. Merrill, Steven K. Higginbottom, Leah Guthrie, Dylan Dodd & Justin L. Sonnenburg

2. Microbiology and Immunology Graduate Program, Stanford University School of Medicine, Stanford, CA, USA

Will Van Treuren & Bryan D. Merrill

3. ChEM-H, Stanford University, Stanford, CA, USA

Curt R. Fischer & Lalla A. Fall

4. Chan Zuckerberg Biohub, San Francisco, CA, USA

Curt R. Fischer, Brian C. DeFelice, Juan M. Sanchez, Michael A. Fischbach & Justin L. Sonnenburg

5. Department of Pathology, Stanford University School of Medicine, Stanford, CA, USA

Lalla A. Fall & Dylan Dodd

6. Department of Bioengineering, Stanford University, Stanford, CA, USA

Michael A. Fischbach

7. Center for Human Microbiome Studies, Stanford, CA, USA

Justin L. Sonnenburg

Authors

1. Shuo Han

[View author publications](#)

You can also search for this author in [PubMed](#) [Google Scholar](#)

2. Will Van Treuren

[View author publications](#)

You can also search for this author in [PubMed](#) [Google Scholar](#)

3. Curt R. Fischer

[View author publications](#)

You can also search for this author in [PubMed](#) [Google Scholar](#)

4. Bryan D. Merrill

[View author publications](#)

You can also search for this author in [PubMed](#) [Google Scholar](#)

5. Brian C. DeFelice

[View author publications](#)

You can also search for this author in [PubMed](#) [Google Scholar](#)

6. Juan M. Sanchez

[View author publications](#)

You can also search for this author in [PubMed](#) [Google Scholar](#)

7. Steven K. Higginbottom

[View author publications](#)

You can also search for this author in [PubMed](#) [Google Scholar](#)

8. Leah Guthrie

[View author publications](#)

You can also search for this author in [PubMed](#) [Google Scholar](#)

9. Lalla A. Fall

[View author publications](#)

You can also search for this author in [PubMed](#) [Google Scholar](#)

10. Dylan Dodd

[View author publications](#)

You can also search for this author in [PubMed](#) [Google Scholar](#)

11. Michael A. Fischbach

[View author publications](#)

You can also search for this author in [PubMed](#) [Google Scholar](#)

12. Justin L. Sonnenburg

[View author publications](#)

You can also search for this author in [PubMed](#) [Google Scholar](#)

Contributions

S.H., W.V.T., D.D., M.A.F. and J.L.S. designed this study. S.H., W.V.T. and S.K.H. performed all bacterial culture and gnotobiotic mouse experiments. S.H. constructed MS qTOF and QE *m/z*-RT and MS2 spectrum libraries, performed MS experimental validation and MS-DIAL data analysis, conducted comparative genomics and metabolomic distance analyses, constructed the *in vivo* metabolomics pipeline and database, and designed the Metabolomics Data Explorer. W.V.T. constructed the bacterial strain library, performed phylogenetic analysis, built the *in vitro* bioinformatics pipeline and database, performed phylogenetic versus metabolomic distance comparisons, and built random forest models. C.R.F. and L.G. conducted chemoinformatics analyses of reference library compounds. B.D.M. built the strain-resolved comparative genomics database. S.H., B.C.D. and J.M.S. developed qTOF and QE MS2 methods and collected data. D.D., L.A.F. and C.R.F. set up the MS1 MS methods. S.H., D.D. and L.A.F. built the authentic compound collection and developed metabolomics sample preparation methods. All authors provided intellectual contributions. S.H., W.V.T. and J.L.S. wrote the paper, and all authors provided feedback. S.H. and W.V.T. contributed equally with author order determined by coin-flip.

Corresponding authors

Correspondence to [Dylan Dodd](#) or [Michael A. Fischbach](#) or [Justin L. Sonnenburg](#).

Ethics declarations

Competing interests

M.A.F. is a co-founder and director of Federation Bio and Viralogic, a co-founder of Revolution Medicines, and a member of the scientific advisory boards of NGM Bio and Zymergen.

Additional information

Peer review information *Nature* thanks Gary Siuzdak and the other, anonymous, reviewer(s) for their contribution to the peer review of this work.

Publisher's note Springer Nature remains neutral with regard to jurisdictional claims in published maps and institutional affiliations.

Extended data figures and tables

[Extended Data Fig. 1 Summary statistics for the MS reference library metabolites, their detection and validation.](#)

a, Chemical similarity network of the compound library. Network nodes, library compounds coloured by their superclasses. Node size, monoisotopic mass. Edges between nodes, substructure similarity values above a *z*-score threshold of 1 s.d. from the mean. **b**, Scatter plots and histograms of chemical properties of 833 library metabolites. **c**, Venn diagram of library compounds that are detected by each of the three methods. **d**, Venn diagram of compounds (by PubChem CID) identified in the reference compound library (Supplementary Table 1), in vitro conditions ([Supplementary Table 7](#), ‘count.ps’) and in vivo conditions ([Supplementary Table 8](#), ‘istd_corr_ion_count_matrix’). In vitro conditions include all medium types, and in vivo conditions include all sample types: urine, serum, faeces and caecal contents, and all colonization states. **e**, Scatterplot of all pairwise similarity scores (biological sample versus library) of the same compound searched against the MoNA spectrum database. All library standards (median similarity score = 992) and 97.3% of the corresponding compounds from biological samples (median similarity score = 923) had similarity scores of ≥ 600 , and 2.7% of those compounds from biological samples scored below 600. Confidence levels were determined based on both

similarity scores and visual validation of the MS/MS spectra. **f**, Schematic of the data collection and analysis workflow of the metabolomics pipeline. Panel created with Biorender.com.

Extended Data Fig. 2 Schematic of a custom bioinformatics analysis pipeline that generates a metabolite fold-change matrix.

The pipeline integrates data across multiple experimental runs and minimizes intra-replicate, intra-experiment and inter-experiment variability. The four steps detailed here are explained in depth in the [Supplementary Methods](#) (see ‘Custom bioinformatics: in vitro pipeline’ section). Step 1, a database recording sample metadata (organism, media, growth data, and so on) and MS-DIAL output files are integrated into data matrices that are specific to each analytical method. Step 2, all data are grouped by replicate (biological sample groups (BSGs)) and analysed to remove replicates with low intra-replicate correlation. Replicates are then grouped by experiment (EXPs) to assess inter-experiment variability. Transformations reducing inter-experiment variability are identified and compared. For metabolites that are detected by multiple methods, their ion counts are compared on a per-replicate and per-experiment basis to identify one or more methods that consistently detect these metabolites. Step 3, using an internal standard-based correction, ion counts for individual samples are adjusted and transformed into different fold-change data matrices. Step 4, data matrices corresponding to each method are combined into a single data matrix representing all detected metabolites.

Extended Data Fig. 3 High-throughput identification and analysis of diverse metabolites in complex biological matrices.

a, Number of unique compounds (by PubChem CID) within distinct chemical superclasses detected in the *m/z*-RT reference library ($n = 815$, 11 superclasses), in vitro dataset ($n = 458$, 9 superclasses) or in vivo dataset ($n = 551$, 9 superclasses), excluding internal standards. Nine of the eleven chemical superclasses in the reference library are represented in the metabolites detected in vitro and in vivo. The two remaining library

superclasses (organosulfur and organometallic compounds) not represented in the experimental data contain one compound each. **b**, Diverse classes of metabolites identified in the conventional mouse caecum. Representative metabolites shown are significantly elevated (≥ 4 -fold, corrected $P < 0.05$) in conventional mice versus germ-free controls in one experiment with $n = 3$ (conventional) and $n = 4$ (germ-free) mice. P values were calculated using two-tailed Student's t -tests with Benjamini–Hochberg correction for multiple comparisons. **c**, Examples of precursors, intermediates and products from the tryptophan fermentation pathway that were identified by our methods both in vitro (*C. sporogenes* culture supernatant) and in vivo (*C. sporogenes* mono-colonization caecal contents). Extracted ion chromatogram peaks representing relative ion counts for each metabolite are shown. **d, e**, Histograms of changes in RT (**d**) and total ion count (**e**) for 132 spike-in metabolites in five complex biological matrices using three analytical methods. All spiked-in metabolites show minimal change in RT, falling within a conservative ± 0.1 -min search window from their RTs as determined in the library control condition (**d**). The majority of spiked-in metabolites (for example, 97% in faeces) exhibit less than fourfold change in ion counts relative to those detected in the library control condition (**e**). Representative examples of RT shifts (**d**) and changes in total ion counts (**e**) in individual metabolites in the mouse faecal matrix are shown. Data are mean \pm s.e.m. of one experiment with $n = 3$ biological replicates. **f**, Histograms of linear ranges of 377 reference library metabolites measured in serial dilutions. A representative linear range of 5-hydroxyindole is shown. **g**, Violin plots (median, quartiles) of differences in RTs measured by three analytical methods between distinct MS instruments: the qTOF 6454, with which the library was built, was compared with a second instrument: a qTOF 6530 for a shared panel of 219 reference library metabolites (top) or a Orbitrap QE for a shared panel of 773 reference library metabolites (bottom). Mean RT differences (in min) between two instruments by each method (C18-positive, C18-negative, HILIC-positive, respectively) were as follows: qTOF versus qTOF, pre-correction: 0.238, 0.044, -0.110; post-correction: -0.023, -0.020, 0.015; qTOF versus QE, pre-correction: 0.151, 0.027, 0.196; post-correction: -0.040, -0.021, 0.026). Per method, RT correction was performed by polynomial transformation of the library based on inter-instrumental RT shifts of 10–20 robustly detected metabolites. Per method, using the corrected library with a RT tolerance window of 0.2 min,

around 99% of the 219 metabolites tested on the second qTOF and about 94% of the 773 metabolites tested on the QE were correctly identified.

Extended Data Fig. 4 Conserved and unique metabolomic signatures across bacterial taxa.

a, Schematic of our high-throughput bacterial culture and sample collection workflow. Panel created with Biorender.com. **b**, Intra-replicate Pearson correlation coefficients (triplicates and greater) stratified by fourteen independent bacterial culture experiments and three analytical methods. For each experiment, Pearson correlation r values were calculated for all supernatant and medium sample replicate groups: $n = 346$ (C18-positive), $n = 344$ (C18-negative) and $n = 344$ (HILIC-positive). Total ion count data were corrected by internal standards and log-transformed, standardized and scaled, before computing Pearson correlation values. Box, median, 25th and 75th percentiles; whiskers, Tukey's method. **c**, Left, number of medium-specific or common metabolites detected in the same bacterial strain grown in two different media (29 strains cultured in two or more of the 12 different media). Each dot represents the total number of metabolites from a single comparison between two media in which a strain has been grown: $n = 58$ (co-detected in two media), $n = 116$ (detected in one of the two media), $n = 33$ (detected in the mega medium) and $n = 16$ (detected in polyamine-free medium). Box, median, 25th and 75th percentiles; whiskers, minimum and maximum. Right, agmatine production levels by *B. eggerthii*. Data are mean \pm s.e.m. from 2–3 independent experiments, each with $n = 3$ biological replicates. P values, two-tailed t -test with Benjamini–Hochberg correction for multiple comparisons. **d**, Heat map of metabolomic profiles of 158 bacterial strains grown in mega medium, clustered by 16S phylogenetic distance. Individual metabolites are hierarchically clustered (Ward's method) using Euclidean distance between the fold-change (\log_2 -transformed) values across all taxonomies. Metabolites shown are detected in at least 50% of the 158 taxonomies to enable Ward clustering. **e, f**, Production or consumption patterns of tyramine and pantothenic acid across 158 strains grown in mega medium. Data are mean \pm s.e.m. from 1–3 independent experiments (identified by dot colour), each with $n \geq 3$ biological replicates.

Extended Data Fig. 5 Metabolic profile variation among related bacteria.

a, Pairwise metabolomic profile comparisons between two closely related strains grown in mega medium: *C. sporogenes* ATCC 15579 and *C. cadaveris* HM-1039 (subpanel 1), and among four strains of *Bacteroides fragilis* (subpanels 2–7): HM-710, HM-711, HM-714 and HM-20. Each dot represents an averaged fold-change value (\log_2 -transformed) from 1–3 independent experiments, each with $n = 3$ biological replicates. Pearson correlation r values of pairwise metabolomic profile comparisons, performed on standardized and scaled data: ATCC 15579 versus HM-1039 ($r = 0.063$), HM-711 versus HM-710 ($r = 0.859$), HM-714 versus HM-710 ($r = 0.866$), HM-714 versus HM-711 ($r = 0.880$), HM-20 versus HM-710 ($r = 0.829$), HM-20 versus HM-711 ($r = 0.845$) and HM-20 versus HM-714 ($r = 0.807$). **b**, Metabolic similarities and variations among closely related species of *C. sporogenes* and *C. cadaveris*, and among different strains of the same species of *B. fragilis* grown in mega medium. Taxonomies shown are clustered by 16S phylogenetic distance, and are coloured according to the distinct phyla. Data are mean \pm s.e.m. from 1–3 independent experiments, each with $n = 3$ biological replicates.

Extended Data Fig. 6 Relationships between phylogeny, taxonomy and metabolome.

a, Metabolomic profiles of 158 bacterial strains grown in mega medium. Individual taxonomies are clustered by metabolomic profile distances (fold change, \log_2 -transformed) across all metabolites. Individual metabolites are hierarchically clustered (Ward's method) using Euclidean distance between the fold-change (\log_2 -transformed) values across all taxonomies.

Metabolites shown are detected in at least 50% of the 158 taxonomies to enable Ward clustering. **b**, Metabolic similarities between two phylogenetically distant species grown in mega medium. Taxonomies are clustered by metabolomic profile distances (fold change, \log_2 -transformed) across all metabolites. Data are mean \pm s.e.m. of one experiment with $n = 3$ biological replicates. **c**, Scatter plot of pairwise metabolomic profile comparison between two phylogenetically distant species. Each dot

represents an averaged fold-change value (\log_2 -transformed) of one experiment with $n = 3$ biological replicates. Pearson correlation of pairwise metabolomic profile comparison between these two species, performed on standardized and scaled fold-change data, $r = 0.7090$. **d**, Venn diagram of unique and overlapping compounds (by PubChem CID) identified in the culture supernatant of 158 mega-medium grown strains and caecal contents of conventional mice.

Extended Data Fig. 7 Multiple data transformations identify nonlinear relationship between phylogenetic and metabolomic distance.

a, Heat map showing the comparison of phylogenetic and metabolomic tree topologies. Cells record the number of tips for which the neighbourhoods share more overlap than expected ($P < 0.05$; one-sided permutation test). Data are stratified by fractional overlap of neighbourhoods and permutation probability (see [Supplementary Methods](#), ‘Distance comparisons’). **b**, Histogram of chemical similarity scores (based on Tanimoto 2D structures) between each unique pair of compounds (by PubChem CID) detected in the in vitro dataset. For this pairwise comparison, 359 non-co-eluting compounds were used. **c**, Metabolomic distance tree with each metabolite weighted based on their chemical similarity (left) or unweighted control metabolomic distance tree (right). The weighted and unweighted matrices were calculated using uniquely detected, non-co-eluting compounds in the in vitro dataset, for which a unique PubChem CID identifier can be assigned to each compound. Two-sided Mantel test for comparison between the weighted and unweighted distance matrices: $r^2 = 0.863$, $P = 0.001$. **d**, Left, correlation of phylogenetic and metabolomic distance across pairs of strains coloured by lowest shared taxonomic rank with a LOESS fit shown. Dashed vertical line occurs at $x = 0.11$ as referenced in the text. Right, Metabolomic distance between pairs of strains binned by the lowest shared taxonomic rank. Species ($n = 111$), genus ($n = 1,386$), family ($n = 159$), order ($n = 1,222$), class ($n = 34$), phylum ($n = 1,442$) and kingdom ($n = 8,442$). Box, median, 25th and 75th percentiles; whiskers, Tukey’s method. **e–i**, Internal-standard-corrected fold-change data (**e–g**) and internal-standard-corrected total ion count data (**h, i**) were log-transformed

and used to calculate pairwise metabolomic distances between microbial taxa. These distances were compared to the corresponding pairwise phylogenetic distances generated from a tree built with the V4 region of 16S (left) or the full-length 16S gene (right). Data are plotted with a LOESS fit. Set 1, microorganisms grown in at least one experiment simultaneously. Set 2, microorganisms grown in the same experiment only. **j**, Phylogenetic tree constructed using the full 16S sequences of a subset of the strains grown in mega medium. Only strains with available full 16S sequences are shown ([Supplementary Table 6](#)). **k**, Left, schematic of the pathway that synthesizes citrulline and ornithine, or synthesizes agmatine and/or putrescine. Right, the top six matches identified by the comparative genomics tool MultiGeneBlast within a 40-kb search window, when searched against a genomic database of our strain collection with sequenced genomes. Horizontal dashed lines between genes represent multiple other genes present within the search window.

Extended Data Fig. 8 Asparagine and glutamine can be used as sole nitrogen sources by most tested Bacteroidetes.

a, Top, an example decision tree from a forest that can differentiate Bacteroidetes versus bacteria from the other four represented phyla with >97% accuracy. For each decision node, phylum-level increases and decreases based on metabolite levels are shown (relative fold change compared to the bacterial medium controls, \log_2 -transformed).

Actinobacteria ($n = 20$), Bacteroidetes ($n = 57$), Firmicutes ($n = 83$), Fusobacteria ($n = 3$) and Proteobacteria ($n = 10$). Dashed line, metabolite threshold. Box, median, 25th and 75th percentiles; whiskers: Tukey's method. Bottom, the 10 most important features differentiating the five tested phyla. Data are shown as median metabolite \log_2 -fold-change values for each phylum; metabolites and phyla are ordered by Ward linkage distance. **b**, Representative growth curves from two independent experiments, each with $n = 3$ biological replicates for a subset of *Bacteroides* spp. using modified SMM with the indicated nitrogen source. Legend colours for the sole nitrogen source are the same in **b–d**. **c**, Representative growth curves of one experiment with $n = 5$ biological replicates for 60 Bacteroidetes using modified SMM with the indicated

nitrogen sources. **d**, Growth curves of wild-type and mutant *B. thetaiotaomicron* (*Bt*) grown in defined minimal media with either cysteine (top) (one experiment, $n = 3$ biological replicates) or sodium sulfide (Na_2S , bottom) as sole reduced sulfur sources (one experiment, $n = 3$ biological replicates). **e**, Amino acid production and consumption levels in gnotobiotic mice mono-colonized with *B. thetaiotaomicron* (one experiment, $n = 5$ mice). Box, median, 25th and 75th percentiles; whiskers, Tukey's method. Numeric labels in **b** and **c** correspond to the following: 1, *B. acidifaciens* DSMZ 15896; 2, *B. caccae* ATCC 43185; 3, *B. caccae* BEI HM-728; 4, *B. cellulosilyticus* BEI HM-726; 5, *B. cellulosilyticus* DSMZ 14838; 6, *B. coprophilus* DSMZ 18228; 7, *B. dorei* BEI HM-29; 8, *B. dorei* BEI HM-717; 9, *B. dorei* BEI HM-718; 10, *B. dorei* BEI HM-719; 11, *B. dorei* DSMZ 17855; 12, *B. eggerthii* ATCC 27754; 13, *B. eggerthii* DSMZ 20697; 14, *B. finegoldii* BEI HM-727; 15, *B. finegoldii* DSMZ 17565; 16, *B. fragilis* BEI HM-20; 17, *B. fragilis* BEI HM-710; 18, *B. fragilis* BEI HM-711; 19, *B. fragilis* BEI HM-714; 20, *B. fragilis* NCTC 9343; 21, *B. intestinalis* DSMZ 17393; 22, *B. ovatus* ATCC 8483; 23, *B. ovatus* BEI HM-222; 24, *B. pectinophilus* ATCC 43243; 25, *B. plebeius* DSMZ 17135; 26, *B. salyersiae* BEI HM-725; 27, *Bacteroides* sp. BEI HM-18; 28, *Bacteroides* sp. BEI HM-189; 29, *Bacteroides* sp. BEI HM-19; 30, *Bacteroides* sp. BEI HM-22; 31, *Bacteroides* sp. BEI HM-23; 32, *Bacteroides* sp. BEI HM-258; 33, *Bacteroides* sp. BEI HM-27; 34, *Bacteroides* sp. BEI HM-28; 35, *Bacteroides* sp. BEI HM-58; 36, *B. stercoris* ATCC 43183; 37, *B. stercoris* BEI HM-1036; 38, *B. thetaiotaomicron* 3730; 39, *B. thetaiotaomicron* 3731; 40, *B. thetaiotaomicron* 633; 41, *B. thetaiotaomicron* 7330; 42, *B. thetaiotaomicron* 7853; 43, *B. thetaiotaomicron* 8702; 44, *B. thetaiotaomicron* 8713; 45, *B. thetaiotaomicron* 8736; 46, *B. thetaiotaomicron* 940; 47, *B. thetaiotaomicron* VPI 5482; 48, *B. thetaiotaomicron* WH302; 49, *B. thetaiotaomicron* WH305; 50, *B. uniformis* ATCC 8492; 51, *B. vulgatus* ATCC 8482; 52, *B. vulgatus* BEI HM-720; 53, *B. xylanisolvans* DSMZ 18836; 54, *P. distasonis* ATCC 8503; 55, *P. distasonis* BEI HM-169; 56, *P. johnsonii* BEI HM-731; 57, *P. johnsonii* DSMZ 18315; 58, *P. merdae* ATCC 43184; 59, *P. merdae* BEI HM-729; 60, *P. merdae* BEI HM-730.

Extended Data Fig. 9 Metabolic contribution by individual gut microorganisms in a multi-species community.

a, α -Ketoglutaric acid levels in faeces of mice mono-colonized with *Anaerostipes* sp. BEI HM-220. Data are mean \pm s.e.m. of two independent experiments, each with $n = 4$ mice (germ-free) or $n = 5$ or 7 mice (*Anaerostipes* mono-colonized). **b**, Left, MDMs were associated with specific bacterial phyla leveraging both *in vivo* and *in vitro* metabolomic data. Right, number of bacterial strains grown in mega medium by phylum that produce MDMs identified in the caecal contents of mice colonized with *B. thetaiotaomicron* (*Bt*, $n = 5$) or *C. sporogenes* (*Cs*, $n = 3$), or with a six-member community ($n = 3$). Numbers of strains that produce at least one of these metabolites *in vitro* by phylum: Bacteroidetes, $n = 52$; Firmicutes, $n = 60$; Proteobacteria, $n = 8$; Actinobacteria, $n = 16$; and Fusobacteria, $n = 3$. Each metabolite shown was significantly produced both *in vitro* and *in vivo* (≥ 4 -fold, corrected $P < 0.05$). Uniquely detected (non-co-eluting) metabolites are shown ([Supplementary Table 9](#)). **c**, Spearman correlation between metabolomic profiles (standardized and scaled, \log_2 -transformed, fold-change data) of individual *B. thetaiotaomicron*- or *C. sporogenes*-mono-colonized host biofluids (caecal contents, faeces, serum or urine) and individual bacterial culture (158 strains grown in mega medium). Coloured dots, Spearman's ρ values calculated by comparing metabolomic profiles of individual bacterial culture versus individual biofluid of either *B. thetaiotaomicron*- or *C. sporogenes*-mono-colonized mice. Black dots, Spearman's ρ calculated using metabolomic profiles of *B. thetaiotaomicron* or *C. sporogenes*, the same strains used for mono-colonization in mice. **d**, Venn diagram of overlapping metabolites that are significantly produced (≥ 4 -fold, corrected $P < 0.05$) in culture and in the caecum of colonized mice. **e**, Principal component analysis separates metabolomic profiles of identified metabolites by sample type in each colonization state. P values on metabolomic profile comparisons between different sample types of the same colonization state were determined using PERMANOVA: six-member community ($P = 0.073$) and all other colonization states ($P = 0.001$). **f**, Principal component analysis separates metabolomic profiles of identified metabolites by colonization states. P values on metabolomic profile comparisons between different colonization states of the same sample type were determined using PERMANOVA: $P = 0.001$ for all four sample types.

g, h, Example chemical structures of significantly produced metabolites (≥ 4 -fold, corrected $P < 0.05$) in serum (**g**) or urine (**h**) by each colonization state corresponding to Fig. [4b](#). **a, b, d, g, h**, P values were determined using two-tailed Student's t -tests with Benjamini–Hochberg correction for multiple comparisons.

Extended Data Fig. 10 Metabolic contribution of multi-species communities in gnotobiotic mice.

a, Proposed host–microbial co-metabolism pathways that could lead to the synthesis of specific host–microbial co-metabolites in the urine and serum of mice colonized with the six-member community. **b, c**, Metabolite levels in urine (**b**) and caecal contents (**c**) of mice colonized with the six-member community (+Cs) or the five-member community (−Cs). Metabolites shown represent a panel of significantly elevated or reduced metabolites (≥ 4 -fold, corrected $P < 0.05$) in the six-member community. Superscript ‘1’ in metabolite names, co-eluting metabolites as annotated in the MS reference library ([Supplementary Table 1](#)). Superscript ‘2’ in metabolite names, co-eluting isomeric metabolites with truncated names in the figure (2-hydroxy-3-methylpentanoic acid, 2-hydroxy-4-methylpentanoic acid; and α -galactose 1-phosphate, α -glucose 1-phosphate, glucose-6-phosphate, mannose 6-phosphate). Data are mean \pm s.e.m. of one experiment with $n = 6$ (urine, six-member community), $n = 7$ (urine, five-member community) and $n = 3$ (caecal, both six-member and five-member communities). **b, c**, P values were calculated using two-tailed Student's t -tests with Benjamini–Hochberg correction for multiple comparisons.

* $P < 0.05$, ** $P < 0.01$, *** $P < 0.001$. **b**, Venn diagram (right) of significantly elevated and reduced metabolites in individual host biofluids (caecal contents, serum and urine) using the same threshold in **b** (left).

Supplementary information

Supplementary Information

This file contains Supplementary Methods and a full guide to Supplementary Tables 1-9. The Supplementary Methods include mass

spectrometry LC/MS methods, data analysis, bacterial sequencing and phylogenetics, distance comparisons and classifiers, the Mega Medium (MM) preparation protocol and Salyer's Minimal Medium (SMM) preparation protocol.

Reporting Summary

Supplementary Table 1

Mass spectrometry compound m/z-RT reference library.

Supplementary Table 2

MS/MS validation of biological metabolites and library standards, matrix effects on ion count and RT, and linear range of individual metabolites.

Supplementary Table 3

MS/MS spectra library constructed on qTOF and QE instruments.

Supplementary Table 4

Inter-instrumental retention time shift and correction.

Supplementary Table 5

In vitro sample metadata.

Supplementary Table 6

Culture and strain information.

Supplementary Table 7

In vitro data matrices.

Supplementary Table 8

The in vivo database and in vivo pipeline output data matrices.

Supplementary Table 9

List of “phylum-associated” metabolites.

Rights and permissions

Reprints and Permissions

About this article



Check for
updates

Cite this article

Han, S., Van Treuren, W., Fischer, C.R. *et al.* A metabolomics pipeline for the mechanistic interrogation of the gut microbiome. *Nature* **595**, 415–420 (2021). <https://doi.org/10.1038/s41586-021-03707-9>

Download citation

- Received: 16 July 2020
- Accepted: 08 June 2021
- Published: 14 July 2021
- Issue Date: 15 July 2021
- DOI: <https://doi.org/10.1038/s41586-021-03707-9>

Comments

By submitting a comment you agree to abide by our [Terms](#) and [Community Guidelines](#). If you find something abusive or that does not comply with our terms or guidelines please flag it as inappropriate.

[Access through your institution](#)

[Change institution](#)

[Buy or subscribe](#)

Associated Content

[Deciphering metabolism, one microbe at a time](#)

- William F. Kindschuh
- Tal Korem

Advertisement

This article was downloaded by **calibre** from <https://www.nature.com/articles/s41586-021-03707-9>

| [Section menu](#) | [Main menu](#) |

SARS-CoV-2 infection induces long-lived bone marrow plasma cells in humans
[Download PDF](#)

- Article
- [Published: 24 May 2021](#)

SARS-CoV-2 infection induces long-lived bone marrow plasma cells in humans

- [Jackson S. Turner](#)¹,
- [Wooseob Kim](#) [ORCID: orcid.org/0000-0002-9199-1000](#)¹,
- [Elizaveta Kalaidina](#)²,
- [Charles W. Goss](#)³,
- [Adriana M. Rauseo](#)⁴,
- [Aaron J. Schmitz](#) [ORCID: orcid.org/0000-0002-8077-6751](#)¹,
- [Lena Hansen](#)^{1,5},
- [Alem Haile](#)⁶,
- [Michael K. Klebert](#)⁶,
- [Iskra Pusic](#)⁷,
- [Jane A. O'Halloran](#) [ORCID: orcid.org/0000-0001-8265-9471](#)⁴,
- [Rachel M. Presti](#) [ORCID: orcid.org/0000-0002-5469-0727](#)^{4,8} &
- [Ali H. Ellebedy](#) [ORCID: orcid.org/0000-0002-6129-2532](#)^{1,8,9}

[Nature](#) volume 595, pages 421–425 (2021) [Cite this article](#)

- 420k Accesses
- 2 Citations
- 8325 Altmetric
- [Metrics details](#)

Subjects

- [Antibodies](#)

- [Immunological memory](#)
- [Plasma cells](#)
- [SARS-CoV-2](#)

Abstract

Long-lived bone marrow plasma cells (BMPCs) are a persistent and essential source of protective antibodies^{1,2,3,4,5,6,7}. Individuals who have recovered from COVID-19 have a substantially lower risk of reinfection with SARS-CoV-2^{8,9,10}. Nonetheless, it has been reported that levels of anti-SARS-CoV-2 serum antibodies decrease rapidly in the first few months after infection, raising concerns that long-lived BMPCs may not be generated and humoral immunity against SARS-CoV-2 may be short-lived^{11,12,13}. Here we show that in convalescent individuals who had experienced mild SARS-CoV-2 infections ($n = 77$), levels of serum anti-SARS-CoV-2 spike protein (S) antibodies declined rapidly in the first 4 months after infection and then more gradually over the following 7 months, remaining detectable at least 11 months after infection. Anti-S antibody titres correlated with the frequency of S-specific plasma cells in bone marrow aspirates from 18 individuals who had recovered from COVID-19 at 7 to 8 months after infection. S-specific BMPCs were not detected in aspirates from 11 healthy individuals with no history of SARS-CoV-2 infection. We show that S-binding BMPCs are quiescent, which suggests that they are part of a stable compartment. Consistently, circulating resting memory B cells directed against SARS-CoV-2 S were detected in the convalescent individuals. Overall, our results indicate that mild infection with SARS-CoV-2 induces robust antigen-specific, long-lived humoral immune memory in humans.

[Download PDF](#)

Main

Reinfections by seasonal coronaviruses occur 6 to 12 months after the previous infection, indicating that protective immunity against these viruses may be short-lived^{14,15}. Early reports documenting rapidly declining antibody titres in the first few months after infection in individuals who had recovered from COVID-19 suggested that protective immunity against SARS-CoV-2 might be similarly transient^{11,12,13}. It was also suggested that infection with SARS-CoV-2 could fail to elicit a functional germinal centre response, which would interfere with the generation of long-lived plasma cells^{3,4,5,7,16}. More recent reports analysing samples that were collected approximately 4 to 6 months after infection indicate that SARS-CoV-2 antibody titres decline more slowly than in the initial months after infection^{8,17,18,19,20,21}. Durable serum antibody titres are maintained by long-lived plasma cells—non-replicating,

antigen-specific plasma cells that are detected in the bone marrow long after the clearance of the antigen^{1,2,3,4,5,6,7}. We sought to determine whether they were detectable in convalescent individuals approximately 7 months after SARS-CoV-2 infection.

Biphasic decay of anti-S antibody titres

Blood samples were collected approximately 1 month after the onset of symptoms from 77 individuals who were convalescing from COVID-19 (49% female, 51% male, median age 49 years), the majority of whom had experienced mild illness (7.8% hospitalized, Extended Data Tables 1, 2). Follow-up blood samples were collected three times at approximately three-month intervals. Twelve convalescent participants received either the BNT162b2 (Pfizer) or the mRNA-1273 (Moderna) SARS-CoV-2 vaccine between the last two time points; these post-vaccination samples were not included in our analyses. In addition, bone marrow aspirates were collected from 18 of the convalescent individuals at 7 to 8 months after infection and from 11 healthy volunteers with no history of SARS-CoV-2 infection or vaccination. Follow-up bone marrow aspirates were collected from 5 of the 18 convalescent individuals and from 1 additional convalescent donor approximately 11 months after infection (Fig. 1a, Extended Data Tables 3, 4). We first performed a longitudinal analysis of circulating anti-SARS-CoV-2 serum antibodies. Whereas anti-SARS-CoV-2 spike protein (S) IgG antibodies were undetectable in blood from control individuals, 74 out of the 77 convalescent individuals had detectable serum titres approximately 1 month after the onset of symptoms. Between 1 and 4 months after symptom onset, overall anti-S IgG titres decreased from a mean \log_e -transformed half-maximal dilution of 6.3 to 5.7 (mean difference 0.59 ± 0.06 , $P < 0.001$). However, in the interval between 4 and 11 months after symptom onset, the rate of decline slowed, and mean titres decreased from 5.7 to 5.3 (mean difference 0.44 ± 0.10 , $P < 0.001$; Fig. 1a). In contrast to the anti-S antibody titres, IgG titres against the 2019–2020 inactivated seasonal influenza virus vaccine were detected in all control individuals and individuals who were convalescing from COVID-19, and declined much more gradually, if at all over the course of the study, with mean titres decreasing from 8.0 to 7.9 (mean difference 0.16 ± 0.06 , $P = 0.042$) and 7.9 to 7.8 (mean difference 0.02 ± 0.08 , $P = 0.997$) across the 1-to-4-month and 4-to-11-month intervals after symptom onset, respectively (Fig. 1b).

Fig. 1: SARS-CoV-2 infection elicits durable serum anti-S antibody titres.

 **figure1**

a, Study design. Seventy-seven convalescent individuals who had experienced mild SARS-CoV-2 infections (aged 21–69 years) were enrolled and blood was collected approximately 1 month, 4 months, 7 months and 11 months after the onset of symptoms. Bone marrow aspirates were collected from 18 of the convalescent individuals 7 to 8 months after infection and from 11 healthy volunteers (aged 23–60 years) with no history of SARS-CoV-2 infection. Follow-up bone marrow aspirates were collected from 5 of the 18 convalescent donors and 1 additional convalescent donor approximately 11 months after infection. **b**, Blood IgG titres against SARS-CoV-2 S (left) and influenza virus vaccine (right) measured by enzyme-linked immunosorbent assay (ELISA) in convalescent individuals (white circles) at the indicated time after onset of symptoms, and in control individuals (black circles). The dotted lines indicate the limit of detection (LOD). Mean titres and pairwise differences at each time point were estimated using a linear mixed model analysis.

[Full size image](#)

Induction of S-binding long-lived BMPCs

The relatively rapid early decline in the levels of anti-S IgG, followed by a slower decrease, is consistent with a transition from serum antibodies being secreted by short-lived plasmablasts to secretion by a smaller but more persistent population of long-lived plasma cells generated later in the immune response. The majority of this latter population resides in the bone marrow^{1,2,3,4,5,6}. To investigate whether individuals who had recovered from COVID-19 developed a virus-specific long-lived BMPC compartment, we examined bone marrow aspirates obtained approximately 7 and 11 months after infection for anti-SARS-CoV-2 S-specific BMPCs. We magnetically

enriched BMPCs from the aspirates and then quantified the frequencies of those secreting IgG and IgA directed against the 2019–2020 influenza virus vaccine, the tetanus–diphtheria vaccine and SARS-CoV-2 S by enzyme-linked immunosorbent spot assay (ELISpot) (Fig. 2a). Frequencies of influenza- and tetanus–diphtheria-vaccine-specific BMPCs were comparable between control individuals and convalescent individuals. IgG- and IgA-secreting S-specific BMPCs were detected in 15 and 9 of the 19 convalescent individuals, respectively, but not in any of the 11 control individuals (Fig. 2b). Notably, none of the control individuals or convalescent individuals had detectable S-specific antibody-secreting cells in the blood at the time of bone marrow sampling, indicating that the detected BMPCs represent bone-marrow-resident cells and not contamination from circulating plasmablasts. Frequencies of anti-S IgG BMPCs were stable among the 5 convalescent individuals who were sampled a second time approximately 4 months later, and frequencies of anti-S IgA BMPCs were stable in 4 of these 5 individuals but had decreased to below the limit of detection in one individual (Fig. 2c). Consistent with their stable BMPC frequencies, anti-S IgG titres in the 5 convalescent individuals remained consistent between 7 and 11 months after symptom onset. IgG titres measured against the receptor-binding domain (RBD) of the S protein—a primary target of neutralizing antibodies—were detected in 4 of the 5 convalescent individuals and were also stable between 7 and 11 months after symptom onset (Fig. 2d). Frequencies of anti-S IgG BMPCs showed a modest but significant correlation with circulating anti-S IgG titres at 7–8 months after the onset of symptoms in convalescent individuals, consistent with the long-term maintenance of antibody levels by these cells ($r = 0.48$, $P = 0.046$). In accordance with previous reports^{22,23,24}, frequencies of influenza-vaccine-specific IgG BMPCs and antibody titres exhibited a strong and significant correlation ($r = 0.67$, $P < 0.001$; Fig. 2e). Nine of the aspirates from control individuals and 12 of the 18 aspirates that were collected 7 months after symptom onset from convalescent individuals yielded a sufficient number of BMPCs for additional analysis by flow cytometry. We stained these samples intracellularly with fluorescently labelled S and influenza virus haemagglutinin (HA) probes to identify and characterize antigen-specific BMPCs. As controls, we also intracellularly stained peripheral blood mononuclear cells (PBMCs) from healthy volunteers one week after vaccination against SARS-CoV-2 or seasonal influenza virus (Fig. 3a, Extended Data Fig. 1a–c). Consistent with the ELISpot data, low frequencies of S-binding BMPCs were detected in 10 of the 12 samples from convalescent individuals, but not in any of the 9 control samples (Fig. 3b). Although both recently generated circulating plasmablasts and S- and HA-binding BMPCs expressed BLIMP-1, the BMPCs were differentiated by their lack of expression of Ki-67—indicating a quiescent state—as well as by higher levels of CD38 (Fig. 3c).

Fig. 2: SARS-CoV-2 infection elicits S-binding long-lived BMPCs.

 **figure2**

a, Representative images of ELISpot wells coated with the indicated antigens or anti-immunoglobulin (Ig) and developed in blue and red for IgG and IgA, respectively, after incubation of magnetically enriched BMPCs from control individuals and convalescent individuals. **b**, Frequencies of BMPCs secreting IgG (left) or IgA (right) antibodies specific for the indicated antigens, indicated as percentages of total IgG- or IgA-secreting BMPCs in control individuals (black circles) or convalescent individuals 7 months (white circles) or 11 months (grey circles) after symptom onset. Horizontal lines indicate the median. *P* values from two-sided Kruskal–Wallis tests with Dunn’s correction for multiple comparisons between control individuals and convalescent individuals. Each symbol represents one sample ($n = 18$ convalescent, $n = 11$ control). **c**, Paired frequencies of S-binding BMPCs among IgG-secreting (left) and IgA-secreting (right) BMPCs from convalescent individuals 7 months and 11 months after symptom onset. **d**, Paired anti-S (left) and anti-RBD (right) IgG serum antibody titres from convalescent individuals 7 months and 11 months after symptom onset. Data in **c** and **d** (left) are also shown in **b** and Fig. [1b](#), respectively. Each symbol represents one sample ($n = 5$). Dotted lines indicate the limit of detection. **e**, Frequencies of BMPCs secreting IgG antibodies specific for SARS-CoV-2 S (left) and influenza virus vaccine (right) plotted against respective IgG titres in paired blood

samples from control individuals (black circles) or convalescent individuals 7 months after symptom onset (white circles). P and r values from two-sided Spearman's correlations. Each symbol represents one sample ($n = 18$ convalescent, $n = 11$ control).

[Full size image](#)

Fig. 3: SARS-CoV-2 S-binding BMPCs are quiescent and distinct from circulating plasmablasts.

 [figure3](#)

a, Representative plots of intracellular S staining in $CD20^{\text{lo}}CD38^{+}\text{IgD}^{\text{lo}}CD19^{+/\text{lo}}CD3^{-}$ live singlet BMPCs (gating in Extended Data Fig. 1a) from magnetically enriched BMPCs from control individuals (left) or convalescent individuals 7 months after symptom onset (right). **b**, Frequencies of S-binding BMPCs in total BMPCs from control individuals (black circles) or convalescent individuals 7 months after symptom onset (white circles). Horizontal lines indicate the median. P value from two-sided Mann–Whitney U test. Each symbol represents one sample ($n = 12$ convalescent, $n = 9$ control). **c**, Histograms of BLIMP-1 (left), Ki-67 (centre), and CD38 (right) staining in S^{+} (blue) and HA^{+} (black) BMPCs from magnetically enriched BMPCs 7 months after symptom onset, and in S^{+} plasmablasts (red) and naive B cells (grey) from healthy donor PBMCs 1 week after SARS-CoV-2 S immunization.

[Full size image](#)

Robust S-binding memory B cell response

Memory B cells form the second arm of humoral immune memory. After re-exposure to an antigen, memory B cells rapidly expand and differentiate into antibody-secreting plasmablasts. We examined the frequency of SARS-CoV-2-specific circulating memory B cells in individuals who were convalescing from COVID-19 and in healthy control individuals. We stained PBMCs with fluorescently labelled S probes and determined the frequency of S-binding memory B cells among isotype-switched IgD^{lo}CD20⁺ memory B cells by flow cytometry. For comparison, we co-stained the cells with fluorescently labelled influenza virus HA probes (Fig. 4a, Extended Data Fig. 1d). S-binding memory B cells were identified in convalescent individuals in the first sample that was collected approximately one month after the onset of symptoms, with comparable frequencies to influenza HA-binding memory B cells (Fig. 4b). S-binding memory B cells were maintained for at least 7 months after symptom onset and were present at significantly higher frequencies relative to healthy controls—comparable to the frequencies of influenza HA-binding memory B cells that were identified in both groups (Fig. 4c).

Fig. 4: SARS-CoV-2 infection elicits a robust memory B cell response.



a. Representative plots of surface influenza virus HA and S staining in CD20⁺CD38^{lo/int}IgD^{lo}CD19⁺CD3⁻ live singlet memory B cells (gating in Extended Data Fig. 1d) from PBMCs from control individuals (left) and convalescent

individuals 7 months after symptom onset (right). **b**, Kinetics of S- (top) and HA- (bottom) binding memory B cells in PBMCs from convalescent individuals, collected at the indicated days after symptom onset. Data from the 7-month time point are also shown in **c**. **c**, Frequencies of S- (left) and HA- (right) binding memory B cells in PBMCs from control individuals (black circles) and convalescent individuals 7 months after symptom onset (white circles). The dotted line in the left plot indicates the limit of sensitivity, which was defined as the median + 2 \times s.d. of the controls. Each symbol represents one sample ($n = 18$ convalescent, $n = 11$ control). Horizontal lines indicate the median. P values from two-sided Mann–Whitney U tests.

[Full size image](#)

Discussion

This study sought to determine whether infection with SARS-CoV-2 induces antigen-specific long-lived BMPCs in humans. We detected SARS-CoV-2 S-specific BMPCs in bone marrow aspirates from 15 out of 19 convalescent individuals, and in none from the 11 control participants. The frequencies of anti-S IgG BMPCs modestly correlated with serum IgG titres at 7–8 months after infection. Phenotypic analysis by flow cytometry showed that S-binding BMPCs were quiescent, and their frequencies were largely consistent in 5 paired aspirates collected at 7 and 11 months after symptom onset. Notably, we detected no S-binding cells among plasmablasts in blood samples collected at the same time as the bone marrow aspirates by ELISpot or flow cytometry in any of the convalescent or control samples. Together, these data indicate that mild SARS-CoV-2 infection induces a long-lived BMPC response. In addition, we showed that S-binding memory B cells in the blood of individuals who had recovered from COVID-19 were present at similar frequencies to those directed against influenza virus HA. Overall, our results are consistent with SARS-CoV-2 infection eliciting a canonical T-cell-dependent B cell response, in which an early transient burst of extrafollicular plasmablasts generates a wave of serum antibodies that decline relatively quickly. This is followed by more stably maintained levels of serum antibodies that are supported by long-lived BMPCs.

Although this overall trend captures the serum antibody dynamics of the majority of participants, we observed that in three participants, anti-S serum antibody titres increased between 4 and 7 months after the onset of symptoms, after having initially declined between 1 and 4 months. This could be stochastic noise, could represent increased net binding affinity as early plasmablast-derived antibodies are replaced by those from affinity-matured BMPCs, or could represent increases in antibody concentration from re-encounter with the virus (although none of the participants in our cohort tested positive a second time). Although anti-S IgG titres in the convalescent cohort were relatively stable in the interval between 4 and 11 months

after symptom onset, they did measurably decrease, in contrast to anti-influenza virus vaccine titres. It is possible that this decline reflects a final waning of early plasmablast-derived antibodies. It is also possible that the lack of decline in influenza titres was due to boosting through exposure to influenza antigens. Our data suggest that SARS-CoV-2 infection induces a germinal centre response in humans because long-lived BMPCs are thought to be predominantly germinal-centre-derived⁷. This is consistent with a recent study that reported increased levels of somatic hypermutation in memory B cells that target the RBD of SARS-CoV-2 S in convalescent individuals at 6 months compared to 1 month after infection²⁰.

To our knowledge, the current study provides the first direct evidence for the induction of antigen-specific BMPCs after a viral infection in humans. However, we do acknowledge several limitations. Although we detected anti-S IgG antibodies in serum at least 7 months after infection in all 19 of the convalescent donors from whom we obtained bone marrow aspirates, we failed to detect S-specific BMPCs in 4 donors. Serum anti-S antibody titres in those four donors were low, suggesting that S-specific BMPCs may potentially be present at very low frequencies that are below the limit of detection of the assay. Another limitation is that we do not know the fraction of the S-binding BMPCs detected in our study that encodes neutralizing antibodies. SARS-CoV-2 S protein is the main target of neutralizing antibodies^{17,25,26,27,28,29,30} and a correlation between serum anti-S IgG binding and neutralization titres has been documented^{17,31}. Further studies will be required to determine the epitopes that are targeted by BMPCs and memory B cells, as well as their clonal relatedness. Finally, although our data document a robust induction of long-lived BMPCs after infection with SARS-CoV-2, it is critical to note that our convalescent individuals mostly experienced mild infections. Our data are consistent with a report showing that individuals who recovered rapidly from symptomatic SARS-CoV-2 infection generated a robust humoral immune response³². It is possible that more-severe SARS-CoV-2 infections could lead to a different outcome with respect to long-lived BMPC frequencies, owing to dysregulated humoral immune responses. This, however, has not been the case in survivors of the 2014 Ebola virus outbreak in West Africa, in whom severe viral infection induced long-lasting antigen-specific serum IgG antibodies³³.

Long-lived BMPCs provide the host with a persistent source of preformed protective antibodies and are therefore needed to maintain durable immune protection. However, the longevity of serum anti-S IgG antibodies is not the only determinant of how durable immune-mediated protection will be. Isotype-switched memory B cells can rapidly differentiate into antibody-secreting cells after re-exposure to a pathogen, offering a second line of defence³⁴. Encouragingly, the frequency of S-binding circulating memory B cells at 7 months after infection was similar to that of B cells directed against contemporary influenza HA antigens. Overall, our data provide strong evidence that SARS-CoV-2 infection in humans robustly establishes the two arms of

humoral immune memory: long-lived BMPCs and memory B cells. These findings provide an immunogenicity benchmark for SARS-CoV-2 vaccines and a foundation for assessing the durability of primary humoral immune responses that are induced in humans after viral infections.

Methods

Data reporting

No statistical methods were used to predetermine sample size. The experiments were not randomized and the investigators were not blinded during outcome assessment.

Sample collection, preparation and storage

All studies were approved by the Institutional Review Board of Washington University in St Louis. Written consent was obtained from all participants. Seventy-seven participants who had recovered from SARS-CoV-2 infection and eleven control individuals without a history of SARS-CoV-2 infection were enrolled (Extended Data Tables 1, 4). Blood samples were collected in EDTA tubes and PBMCs were enriched by density gradient centrifugation over Ficoll 1077 (GE) or Lymphopure (BioLegend). The remaining red blood cells were lysed with ammonium chloride lysis buffer, and cells were immediately used or cryopreserved in 10% dimethyl sulfoxide in fetal bovine serum (FBS). Bone marrow aspirates of approximately 30 ml were collected in EDTA tubes from the iliac crest of 18 individuals who had recovered from COVID-19 and the control individuals. Bone marrow mononuclear cells were enriched by density gradient centrifugation over Ficoll 1077, and the remaining red blood cells were lysed with ammonium chloride buffer (Lonza) and washed with phosphate-buffered saline (PBS) supplemented with 2% FBS and 2 mM EDTA. Bone marrow plasma cells were enriched from bone marrow mononuclear cells using the CD138 Positive Selection Kit II (Stemcell) and immediately used for ELISpot or cryopreserved in 10% dimethyl sulfoxide in FBS.

Antigens

Recombinant soluble spike protein (S) and its receptor-binding domain (RBD) derived from SARS-CoV-2 were expressed as previously described³⁵. In brief, mammalian cell codon-optimized nucleotide sequences coding for the soluble version of S (GenBank: MN908947.3, amino acids (aa) 1–1,213) including a C-terminal thrombin cleavage site, T4 foldon trimerization domain and hexahistidine tag cloned into the mammalian expression vector pCAGGS. The S protein sequence was modified to remove the polybasic cleavage site (RRAR to A) and two stabilizing mutations were introduced

(K986P and V987P, wild-type numbering). The RBD, along with the signal peptide (aa 1–14) plus a hexahistidine tag were cloned into the mammalian expression vector pCAGGS. Recombinant proteins were produced in Expi293F cells (Thermo Fisher Scientific) by transfection with purified DNA using the ExpiFectamine 293 Transfection Kit (Thermo Fisher Scientific). Supernatants from transfected cells were collected 3 (for S) or 4 (for RBD) days after transfection, and recombinant proteins were purified using Ni-NTA agarose (Thermo Fisher Scientific), then buffer-exchanged into PBS and concentrated using Amicon Ultracel centrifugal filters (EMD Millipore). For flow cytometry staining, recombinant S was labelled with Alexa Fluor 647- or DyLight 488-NHS ester (Thermo Fisher Scientific); excess Alexa Fluor 647 and DyLight 488 were removed using 7-kDa and 40-kDa Zeba desalting columns, respectively (Pierce). Recombinant HA from A/Michigan/45/2015 (aa 18–529, Immune Technology) was labelled with DyLight 405-NHS ester (Thermo Fisher Scientific); excess DyLight 405 was removed using 7-kDa Zeba desalting columns. Recombinant HA from A/Brisbane/02/2018 (aa 18–529) and B/Colorado/06/2017 (aa 18–546) (both Immune Technology) were biotinylated using the EZ-Link Micro NHS-PEG4-Biotinylation Kit (Thermo Fisher Scientific); excess biotin was removed using 7-kDa Zeba desalting columns.

ELISpot

Plates were coated with Flucelvax Quadrivalent 2019/2020 seasonal influenza virus vaccine (Sequiris), tetanus–diphtheria vaccine (Grifols), recombinant S or anti-human Ig. Direct ex vivo ELISpot was performed to determine the number of total, vaccine-binding or recombinant S-binding IgG- and IgA-secreting cells present in BMPC and PBMC samples using IgG/IgA double-colour ELISpot Kits (Cellular Technology) according to the manufacturer's instructions. ELISpot plates were analysed using an ELISpot counter (Cellular Technology).

ELISA

Assays were performed in 96-well plates (MaxiSorp, Thermo Fisher Scientific) coated with 100 µl of Flucelvax 2019/2020 or recombinant S in PBS, and plates were incubated at 4 °C overnight. Plates were then blocked with 10% FBS and 0.05% Tween-20 in PBS. Serum or plasma were serially diluted in blocking buffer and added to the plates. Plates were incubated for 90 min at room temperature and then washed 3 times with 0.05% Tween-20 in PBS. Goat anti-human IgG–HRP (Jackson ImmunoResearch, 1:2,500) was diluted in blocking buffer before adding to wells and incubating for 60 min at room temperature. Plates were washed 3 times with 0.05% Tween-20 in PBS, and then washed 3 times with PBS before the addition of *o*-phenylenediamine dihydrochloride peroxidase substrate (Sigma-Aldrich). Reactions were stopped by the addition of 1 M HCl. Optical density measurements were taken at

490 nm. The half-maximal binding dilution for each serum or plasma sample was calculated using nonlinear regression (GraphPad Prism v.8). The limit of detection was defined as 1:30.

Statistics

Spearman's correlation coefficients were estimated to assess the relationship between 7-month anti-S and anti-influenza virus vaccine IgG titres and the frequencies of BMPCs secreting IgG specific for S and for influenza virus vaccine, respectively. Means and pairwise differences of antibody titres at each time point were estimated using a linear mixed model analysis with a first-order autoregressive covariance structure. Time since symptom onset was treated as a categorical fixed effect for the 4 different sample time points spaced approximately 3 months apart. *P* values were adjusted for multiple comparisons using Tukey's method. All analyses were conducted using SAS v.9.4 (SAS Institute) and Prism v.8.4 (GraphPad), and *P* values of less than 0.05 were considered significant.

Flow cytometry

Staining for flow cytometry analysis was performed using cryo-preserved magnetically enriched BMPCs and cryo-preserved PBMCs. For BMPC staining, cells were stained for 30 min on ice with CD45-A532 (HI30, Thermo Fisher Scientific, 1:50), CD38-BB700 (HIT2, BD Horizon, 1:500), CD19-PE (HIB19, 1:200), CXCR5-PE-Dazzle 594 (J252D4, 1:50), CD71-PE-Cy7 (CY1G4, 1:400), CD20-APC-Fire750 (2H7, 1:400), CD3-APC-Fire810 (SK7, 1:50) and Zombie Aqua (all BioLegend) diluted in Brilliant Stain buffer (BD Horizon). Cells were washed twice with 2% FBS and 2 mM EDTA in PBS (P2), fixed for 1 h using the True Nuclear permeabilization kit (BioLegend), washed twice with perm/wash buffer, stained for 1h with DyLight 405-conjugated recombinant HA from A/Michigan/45/2015, DyLight 488- and Alexa 647-conjugated S, Ki-67-BV711 (Ki-67, 1:200, BioLegend) and BLIMP-1-A700 (646702, 1:50, R&D), washed twice with perm/wash buffer, and resuspended in P2. For memory B cell staining, PBMCs were stained for 30 min on ice with biotinylated recombinant HAs diluted in P2, washed twice, then stained for 30 min on ice with Alexa 647-conjugated S, IgA-FITC (M24A, Millipore, 1:500), IgG-BV480 (goat polyclonal, Jackson ImmunoResearch, 1:100), IgD-SB702 (IA6-2, Thermo Fisher Scientific, 1:50), CD38-BB700 (HIT2, BD Horizon, 1:500), CD20-Pacific Blue (2H7, 1:400), CD4-BV570 (OKT4, 1:50), CD24-BV605 (ML5, 1:100), streptavidin-BV650, CD19-BV750 (HIB19, 1:100), CD71-PE (CY1G4, 1:400), CXCR5-PE-Dazzle 594 (J252D4, 1:50), CD27-PE-Cy7 (O323, 1:200), IgM-APC-Fire750 (MHM-88, 1:100), CD3-APC-Fire810 (SK7, 1:50) and Zombie NIR (all BioLegend) diluted in Brilliant Stain buffer (BD Horizon), and washed twice with P2. Cells were acquired on an Aurora using SpectroFlo v.2.2 (Cytek). Flow cytometry data were analysed using

FlowJo v.10 (Treestar). In each experiment, PBMCs were included from convalescent individuals and control individuals.

Reporting summary

Further information on research design is available in the [Nature Research Reporting Summary](#) linked to this paper.

Data availability

Relevant data are available from the corresponding author upon reasonable request.

References

1. 1.

Benner, R., Meima, F., van der Meulen, G. M. & van Muiswinkel, W. B. Antibody formation in mouse bone marrow. I. Evidence for the development of plaque-forming cells in situ. *Immunology* **26**, 247–255 (1974).

[CAS](#) [PubMed](#) [PubMed Central](#) [Google Scholar](#)

2. 2.

Manz, R. A., Thiel, A. & Radbruch, A. Lifetime of plasma cells in the bone marrow. *Nature* **388**, 133–134 (1997).

[ADS](#) [CAS](#) [Article](#) [Google Scholar](#)

3. 3.

Slifka, M. K., Antia, R., Whitmire, J. K. & Ahmed, R. Humoral immunity due to long-lived plasma cells. *Immunity* **8**, 363–372 (1998).

[CAS](#) [Article](#) [Google Scholar](#)

4. 4.

Hammarlund, E. et al. Duration of antiviral immunity after smallpox vaccination. *Nat. Med.* **9**, 1131–1137 (2003).

[CAS](#) [Article](#) [Google Scholar](#)

5. 5.

Halliley, J. L. et al. Long-lived plasma cells are contained within the CD19⁻CD38^{hi}CD138⁺ subset in human bone marrow. *Immunity* **43**, 132–145 (2015).

[CAS](#) [Article](#) [Google Scholar](#)

6. 6.

Mei, H. E. et al. A unique population of IgG-expressing plasma cells lacking CD19 is enriched in human bone marrow. *Blood* **125**, 1739–1748 (2015).

[CAS](#) [Article](#) [Google Scholar](#)

7. 7.

Nutt, S. L., Hodgkin, P. D., Tarlinton, D. M. & Corcoran, L. M. The generation of antibody-secreting plasma cells. *Nat. Rev. Immunol.* **15**, 160–171 (2015).

[CAS](#) [Article](#) [Google Scholar](#)

8. 8.

Hall, V. J. et al. SARS-CoV-2 infection rates of antibody-positive compared with antibody-negative health-care workers in England: a large, multicentre, prospective cohort study (SIREN). *Lancet* **397**, 1459–1469 (2021).

[CAS](#) [Article](#) [Google Scholar](#)

9. 9.

Houlihan, C. F. et al. Pandemic peak SARS-CoV-2 infection and seroconversion rates in London frontline health-care workers. *Lancet* **396**, e6–e7 (2020).

[CAS](#) [Article](#) [Google Scholar](#)

10. 10.

Lumley, S. F. et al. Antibodies to SARS-CoV-2 are associated with protection against reinfection. Preprint at <https://doi.org/10.1101/2020.11.18.20234369> (2020).

11. 11.

Long, Q.-X. et al. Clinical and immunological assessment of asymptomatic SARS-CoV-2 infections. *Nat. Med.* **26**, 1200–1204 (2020).

[CAS](#) [Article](#) [Google Scholar](#)

12. 12.

Ibarrondo, F. J. et al. Rapid decay of anti-SARS-CoV-2 antibodies in persons with mild Covid-19. *N. Engl. J. Med.* **383**, 1085–1087 (2020).

[Article](#) [Google Scholar](#)

13. 13.

Seow, J. et al. Longitudinal observation and decline of neutralizing antibody responses in the three months following SARS-CoV-2 infection in humans. *Nat. Microbiol.* **5**, 1598–1607 (2020).

[CAS](#) [Article](#) [Google Scholar](#)

14. 14.

Edridge, A. W. D. et al. Seasonal coronavirus protective immunity is short-lasting. *Nat. Med.* **26**, 1691–1693 (2020).

[Article](#) [Google Scholar](#)

15. 15.

Callow, K. A., Parry, H. F., Sergeant, M. & Tyrrell, D. A. The time course of the immune response to experimental coronavirus infection of man. *Epidemiol. Infect.* **105**, 435–446 (1990).

[CAS](#) [Article](#) [Google Scholar](#)

16. 16.

Kaneko, N. et al. Loss of Bcl-6-expressing T follicular helper cells and germinal centers in COVID-19. *Cell* **183**, 143–157 (2020).

[CAS](#) [Article](#) [Google Scholar](#)

17. 17.

Wajnberg, A. et al. Robust neutralizing antibodies to SARS-CoV-2 infection persist for months. *Science* **370**, 1227–1230 (2020).

[ADS](#) [CAS](#) [Article](#) [Google Scholar](#)

18. 18.

Isho, B. et al. Persistence of serum and saliva antibody responses to SARS-CoV-2 spike antigens in COVID-19 patients. *Sci. Immunol.* **5**, eabe5511 (2020).

[Article](#) [Google Scholar](#)

19. 19.

Dan, J. M. et al. Immunological memory to SARS-CoV-2 assessed for up to 8 months after infection. *Science* **371**, eabf4063 (2021).

[CAS](#) [Article](#) [Google Scholar](#)

20. 20.

Gaebler, C. et al. Evolution of antibody immunity to SARS-CoV-2. *Nature* **591**, 639–644 (2021).

[ADS](#) [CAS](#) [Article](#) [Google Scholar](#)

21. 21.

Rodda, L. B. et al. Functional SARS-CoV-2-specific immune memory persists after mild COVID-19. *Cell* **184**, 169–183 (2021).

[CAS](#) [Article](#) [Google Scholar](#)

22. 22.

Davis, C. W. et al. Influenza vaccine-induced human bone marrow plasma cells decline within a year after vaccination. *Science* **370**, 237–241 (2020).

[ADS](#) [CAS](#) [Article](#) [Google Scholar](#)

23. 23.

Turesson, I. Distribution of immunoglobulin-containing cells in human bone marrow and lymphoid tissues. *Acta Med. Scand.* **199**, 293–304 (1976).

[CAS](#) [Article](#) [Google Scholar](#)

24. 24.

Pritz, T. et al. Plasma cell numbers decrease in bone marrow of old patients. *Eur. J. Immunol.* **45**, 738–746 (2015).

[CAS](#) [Article](#) [Google Scholar](#)

25. 25.

Shi, R. et al. A human neutralizing antibody targets the receptor-binding site of SARS-CoV-2. *Nature* **584**, 120–124 (2020).

[ADS](#) [CAS](#) [Article](#) [Google Scholar](#)

26. 26.

Cao, Y. et al. Potent neutralizing antibodies against SARS-CoV-2 identified by high-throughput single-cell sequencing of convalescent patients' B cells. *Cell* **182**, 73–84 (2020).

[CAS](#) [Article](#) [Google Scholar](#)

27. 27.

Robbiani, D. F. et al. Convergent antibody responses to SARS-CoV-2 in convalescent individuals. *Nature* **584**, 437–442 (2020).

[ADS](#) [CAS](#) [Article](#) [Google Scholar](#)

28. 28.

Kreer, C. et al. Longitudinal isolation of potent near-germline SARS-CoV-2-neutralizing antibodies from COVID-19 patients. *Cell* **182**, 843–854 (2020).

[CAS](#) [Article](#) [Google Scholar](#)

29. 29.

Alsoussi, W. B. et al. A potently neutralizing antibody protects mice against SARS-CoV-2 infection. *J. Immunol.* **205**, 915–922 (2020).

[CAS](#) [Article](#) [Google Scholar](#)

30. 30.

Wang, C. et al. A human monoclonal antibody blocking SARS-CoV-2 infection. *Nat. Commun.* **11**, 2251 (2020).

[ADS](#) [CAS](#) [Article](#) [Google Scholar](#)

31. 31.

Wang, K. et al. Longitudinal dynamics of the neutralizing antibody response to severe acute respiratory syndrome coronavirus 2 (SARS-CoV-2) Infection. *Clin. Infect. Dis.* **2020**, ciaa1143 (2020).

[Article](#) [Google Scholar](#)

32. 32.

Chen, Y. et al. Quick COVID-19 healers sustain anti-SARS-CoV-2 antibody production. *Cell* **183**, 1496–1507 (2020).

[CAS](#) [Article](#) [Google Scholar](#)

33. 33.

Davis, C. W. et al. Longitudinal analysis of the human B Cell response to ebola virus infection. *Cell* **177**, 1566–1582 (2019).

[CAS](#) [Article](#) [Google Scholar](#)

34. 34.

Ellebedy, A. H. et al. Defining antigen-specific plasmablast and memory B cell subsets in human blood after viral infection or vaccination. *Nat. Immunol.* **17**, 1226–1234 (2016).

[CAS](#) [Article](#) [Google Scholar](#)

35. 35.

Stadlbauer, D. et al. SARS-CoV-2 seroconversion in humans: a detailed protocol for a serological assay, antigen production, and test setup. *Curr. Protoc. Microbiol.* **57**, e100 (2020).

[CAS](#) [Article](#) [Google Scholar](#)

[Download references](#)

Acknowledgements

We thank the donors for providing specimens; T. Lei for assistance with preparing specimens; and L. Kessels, A. J. Winingham, the staff of the Infectious Diseases Clinical Research Unit at Washington University School of Medicine and the nursing team of the bone marrow biopsy suite at Washington University School of Medicine and Barnes Jewish Hospital for sample collection and providing care for donors. The SARS-CoV-2 S and RBD protein expression plasmids were provided by F. Krammer. The Ellebedy laboratory was supported by National Institute of Allergy and Infectious Diseases (NIAID) grants U01AI141990 and 1U01AI150747, NIAID Centers of Excellence for Influenza Research and Surveillance contracts HHSN272201400006C and HHSN272201400008C and NIAID Collaborative Influenza Vaccine Innovation Centers contract 75N93019C00051. J.S.T. was supported by NIAID 5T32CA009547. L.H. was supported by Norwegian Research Council grant 271160 and National Graduate School in Infection Biology and Antimicrobials grant 249062. This study used samples obtained from the Washington University School of Medicine's COVID-19 biorepository, which is supported by the NIH—National Center for Advancing Translational Sciences grant UL1 TR002345. The content is solely the responsibility of the authors and does not necessarily represent the view of the NIH. The WU353, WU367 and WU368 studies were reviewed and approved by the Washington University Institutional Review Board (approval nos. 202003186, 202009100 and 202012081, respectively).

Author information

Affiliations

1. Department of Pathology and Immunology, Washington University School of Medicine, St Louis, MO, USA

Jackson S. Turner, Wooseob Kim, Aaron J. Schmitz, Lena Hansen & Ali H. Ellebedy

2. Division of Allergy and Immunology, Department of Internal Medicine, Washington University School of Medicine, St Louis, MO, USA

Elizaveta Kalaidina

3. Division of Biostatistics, Washington University School of Medicine, St Louis, MO, USA

Charles W. Goss

4. Division of Infectious Diseases, Department of Internal Medicine, Washington University School of Medicine, St Louis, MO, USA

Adriana M. Rauseo, Jane A. O'Halloran & Rachel M. Presti

5. Influenza Centre, Department of Clinical Science, University of Bergen, Bergen, Norway

Lena Hansen

6. Clinical Trials Unit, Washington University School of Medicine, St Louis, MO, USA

Alem Haile & Michael K. Klebert

7. Division of Oncology, Department of Internal Medicine, Washington University School of Medicine, St Louis, MO, USA

Iskra Pusic

8. Center for Vaccines and Immunity to Microbial Pathogens, Washington University School of Medicine, St Louis, MO, USA

Rachel M. Presti & Ali H. Ellebedy

9. The Andrew M. and Jane M. Bursky Center for Human Immunology & Immunotherapy Programs, Washington University School of Medicine, St Louis, MO, USA

Ali H. Ellebedy

Authors

1. Jackson S. Turner

[View author publications](#)

You can also search for this author in [PubMed](#) [Google Scholar](#)

2. Wooseob Kim

[View author publications](#)

You can also search for this author in [PubMed](#) [Google Scholar](#)

3. Elizaveta Kalaidina

[View author publications](#)

You can also search for this author in [PubMed](#) [Google Scholar](#)

4. Charles W. Goss

[View author publications](#)

You can also search for this author in [PubMed](#) [Google Scholar](#)

5. Adriana M. Rauseo

[View author publications](#)

You can also search for this author in [PubMed](#) [Google Scholar](#)

6. Aaron J. Schmitz

[View author publications](#)

You can also search for this author in [PubMed](#) [Google Scholar](#)

7. Lena Hansen

[View author publications](#)

You can also search for this author in [PubMed](#) [Google Scholar](#)

8. Alem Haile

[View author publications](#)

You can also search for this author in [PubMed](#) [Google Scholar](#)

9. Michael K. Klebert

[View author publications](#)

You can also search for this author in [PubMed](#) [Google Scholar](#)

10. Iskra Pusic

[View author publications](#)

You can also search for this author in [PubMed](#) [Google Scholar](#)

11. Jane A. O'Halloran

[View author publications](#)

You can also search for this author in [PubMed](#) [Google Scholar](#)

12. Rachel M. Presti
[View author publications](#)

You can also search for this author in [PubMed](#) [Google Scholar](#)

13. Ali H. Ellebedy
[View author publications](#)

You can also search for this author in [PubMed](#) [Google Scholar](#)

Contributions

A.H.E. conceived and designed the study. J.S.T. and A.H.E. designed experiments and composed the manuscript. A.H., M.K.K., I.P., J.A.O. and R.M.P. wrote and maintained the Institutional Review Board protocol, recruited and phlebotomized participants and coordinated sample collection. J.S.T., W.K., E.K., A.J.S. and L.H. processed specimens. A.J.S. expressed S and RBD proteins. J.S.T., W.K. and E.K. performed ELISA and ELISpot. J.S.T. performed flow cytometry. J.S.T., A.M.R., C.W.G. and A.H.E. analysed data. All authors reviewed the manuscript.

Corresponding author

Correspondence to [Ali H. Ellebedy](#).

Ethics declarations

Competing interests

The Ellebedy laboratory received funding under sponsored research agreements that are unrelated to the data presented in the current study from Emergent BioSolutions and from AbbVie. J.S.T., A.J.S. and A.H.E. are recipients of a licensing agreement with Abbvie that is unrelated to the data presented in the current study. A.H.E. is a consultant for Mubadala Investment Company and the founder of ImmuneBio Consulting. All other authors declare no competing interests.

Additional information

Peer review information *Nature* thanks Stanley Perlman, Andreas Radbruch and the other, anonymous, reviewer(s) for their contribution to the peer review of this work. Peer reviewer reports are available.

Publisher's note Springer Nature remains neutral with regard to jurisdictional claims in published maps and institutional affiliations.

Extended data figures and tables

[Extended Data Fig. 1 Flow cytometry identification of SARS-CoV-2-elicited plasma cells and memory B cells.](#)

a, d, Flow cytometry gating strategies for BMPCs in magnetically enriched BMPCs and plasmablasts in PBMCs (**a**) and isotype-switched memory B cells and plasmablasts in PBMCs (**d**). **b**, Representative plots of intracellular SARS-CoV-2 S and influenza virus HA staining in BMPCs from samples from control individuals (left) and individuals who were convalescing from COVID-19 (right) 7 months after symptom onset. **c**, Representative plots of intracellular S staining in plasmablasts in PBMCs one week after vaccination against seasonal influenza virus or SARS-CoV-2.

Extended Data Table 1 Demographics of patients with COVID-19

[Full size table](#)

Extended Data Table 2 Symptoms of patients with COVID-19

[Full size table](#)

Extended Data Table 3 Symptoms and follow up samples (months 4–11) of convalescent individuals

[Full size table](#)

Extended Data Table 4 Healthy control demographics

[Full size table](#)

Supplementary information

[Reporting Summary](#)

[Peer Review File](#)

Rights and permissions

[Reprints and Permissions](#)

About this article



Cite this article

Turner, J.S., Kim, W., Kalaidina, E. *et al.* SARS-CoV-2 infection induces long-lived bone marrow plasma cells in humans. *Nature* **595**, 421–425 (2021).
<https://doi.org/10.1038/s41586-021-03647-4>

[Download citation](#)

- Received: 20 December 2020
- Accepted: 14 May 2021
- Published: 24 May 2021
- Issue Date: 15 July 2021
- DOI: <https://doi.org/10.1038/s41586-021-03647-4>

Further reading

- [**Had COVID? You'll probably make antibodies for a lifetime**](#)

- Ewen Callaway

Nature (2021)

Comments

By submitting a comment you agree to abide by our [Terms](#) and [Community Guidelines](#). If you find something abusive or that does not comply with our terms or guidelines please flag it as inappropriate.

[Download PDF](#)

Associated Content

Collection

Coronavirus

Had COVID? You'll probably make antibodies for a lifetime

- Ewen Callaway

A long-term perspective on immunity to COVID

- Andreas Radbruch
- Hyun-Dong Chang

Advertisement

This article was downloaded by **calibre** from <https://www.nature.com/articles/s41586-021-03647-4>

| [Section menu](#) | [Main menu](#) |

Naturally enhanced neutralizing breadth against SARS-CoV-2 one year after infection
[Download PDF](#)

- Article
- Open Access
- [Published: 14 June 2021](#)

Naturally enhanced neutralizing breadth against SARS-CoV-2 one year after infection

- [Zijun Wang¹](#),
[na1](#),
- [Frauke Muecksch](#) [ORCID: orcid.org/0000-0002-0132-5101²](#),
[na1](#),
- [Dennis Schaefer-Babajew](#) [ORCID: orcid.org/0000-0002-5380-2950¹](#),
[na1](#),
- [Shlomo Finkin](#) [ORCID: orcid.org/0000-0003-4474-2658¹](#),
[na1](#),
- [Charlotte Viant¹](#),
[na1](#),
- [Christian Gaebler](#) [ORCID: orcid.org/0000-0001-7295-8128¹](#),
[na1](#),
- [Hans- Heinrich Hoffmann³](#),
- [Christopher O. Barnes⁴](#),
- [Melissa Cipolla¹](#),
- [Victor Ramos](#) [ORCID: orcid.org/0000-0001-7353-3420¹](#),
- [Thiago Y. Oliveira](#) [ORCID: orcid.org/0000-0002-2654-0879¹](#),
- [Alice Cho¹](#),
- [Fabian Schmidt²](#),
- [Justin Da Silva²](#),
- [Eva Bednarski²](#),
- [Lauren Aguado](#) [ORCID: orcid.org/0000-0002-0036-4803³](#),
- [Jim Yee](#) [ORCID: orcid.org/0000-0003-1595-6585⁵](#),
- [Mridushi Daga¹](#),
- [Martina Turroja](#) [ORCID: orcid.org/0000-0001-9640-0559¹](#),
- [Katrina G. Millard](#) [ORCID: orcid.org/0000-0003-2247-3178¹](#),
- [Mila Jankovic¹](#),
- [Anna Gazumyan^{1,6}](#),
- [Zhen Zhao](#) [ORCID: orcid.org/0000-0002-9742-5982⁵](#),
- [Charles M. Rice³](#),

- [Paul D. Bieniasz](#) ORCID: [orcid.org/0000-0002-2368-3719^{2,6}](https://orcid.org/0000-0002-2368-3719),
- [Marina Caskey](#) ORCID: [orcid.org/0000-0003-1727-8693¹](https://orcid.org/0000-0003-1727-8693),
- [Theodora Hatzioannou](#) ORCID: [orcid.org/0000-0002-7889-0766²](https://orcid.org/0000-0002-7889-0766) &
- [Michel C. Nussenzweig](#) ORCID: [orcid.org/0000-0003-0592-8564^{1,6}](https://orcid.org/0000-0003-0592-8564)

Nature volume **595**, pages 426–431 (2021) [Cite this article](#)

- 67k Accesses
- 1 Citations
- 1679 Altmetric
- [Metrics details](#)

Subjects

- [Antibodies](#)
- [Antimicrobial responses](#)
- [SARS-CoV-2](#)

Abstract

More than one year after its inception, the coronavirus disease 2019 (COVID-19) pandemic caused by severe acute respiratory syndrome coronavirus 2 (SARS-CoV-2) remains difficult to control despite the availability of several working vaccines. Progress in controlling the pandemic is slowed by the emergence of variants that appear to be more transmissible and more resistant to antibodies^{1,2}. Here we report on a cohort of 63 individuals who have recovered from COVID-19 assessed at 1.3, 6.2 and 12 months after SARS-CoV-2 infection, 41% of whom also received mRNA vaccines^{3,4}. In the absence of vaccination, antibody reactivity to the receptor binding domain (RBD) of SARS-CoV-2, neutralizing activity and the number of RBD-specific memory B cells remain relatively stable between 6 and 12 months after infection. Vaccination increases all components of the humoral response and, as expected, results in serum neutralizing activities against variants of concern similar to or greater than the neutralizing activity against the original Wuhan Hu-1 strain achieved by vaccination of naive individuals^{2,5,6,7,8}. The mechanism underlying these broad-based responses involves ongoing antibody somatic mutation, memory B cell clonal turnover and development of monoclonal antibodies that are exceptionally resistant to SARS-CoV-2 RBD mutations, including those found in the variants of concern^{4,9}. In addition, B cell clones expressing broad and potent antibodies are selectively retained in the repertoire over time and expand markedly after vaccination. The data suggest that

immunity in convalescent individuals will be very long lasting and that convalescent individuals who receive available mRNA vaccines will produce antibodies and memory B cells that should be protective against circulating SARS-CoV-2 variants.

[Download PDF](#)

Main

We initially characterized immune responses to SARS-CoV-2 in a cohort of patients who have recovered from COVID-19 infection (hereafter referred to as convalescent individuals) 1.3 and 6.2 months after infection^{3,4}. Between 8 February and 26 March 2021, 63 participants between the ages of 26 and 73 years old (median 47 years old) returned for a 12-month follow-up visit. Among those, 26 (41%) had received at least one dose of either the Moderna (mRNA-1273) or Pfizer-BioNTech (BNT162b2) vaccines, on average 40 days (range 2–82 days) before their study visit and 311 days (range 272–373 days) after the onset of acute illness (Supplementary Table 1).

Participants were almost evenly split between the sexes (43% female) and of the individuals who returned for the 12-month follow-up, only 10% had been hospitalized and the remainder had experienced relatively mild initial infections. Only 14% of the individuals reported persistent long-term symptoms after 12 months, reduced from 44% at the 6-month time point⁴. Symptom persistence was not associated with the duration and severity of acute disease or with vaccination status (Extended Data Fig. 1a–c). All participants tested negative for active infection at the 12-month time point as measured by a saliva-based PCR assay⁴. The demographics and clinical characteristics of the participants are shown in Supplementary Tables 1, 2.

Plasma SARS-CoV-2 antibody reactivity

Antibody reactivity in plasma to the RBD and nucleoprotein (N) were measured by enzyme-linked immunosorbent assay (ELISA)³. We limited our analysis to RBD because plasma RBD antibodies are strongly correlated with neutralizing activity^{3,10,11,12}. Convalescent participants who had not been vaccinated maintained most of their anti-RBD IgM (103%), IgG (82%) and IgA (72%) titres between 6 and 12 months after infection (Fig. 1a, Extended Data Fig. 2a–k). Consistent with previous reports^{5,6,7,8}, vaccination increased the plasma RBD antibody levels, with IgG titres increasing by nearly 30-fold compared with unvaccinated individuals (Fig. 1a, right). The two individuals who did not show an increase in antibody titre had been vaccinated only two days before sample collection. In contrast to anti-RBD antibody titres that were relatively stable, anti-N antibody titres decreased significantly between 6 and 12 months in this assay, independently of vaccination status (Fig. 1b, Extended Data Fig. 2l–n).

Fig. 1: Plasma ELISAs and neutralizing activity.

 figure1

a–d, Plasma IgG antibody binding to SARS-CoV-2 RBD (**a**) and N protein (**b**) shown as area under the curve (AUC; numbers in red are mean geometric AUC), and plasma neutralizing activity (NT_{50}) in unvaccinated (**c**) and vaccinated (vac) (**d**) individuals 12 months after SARS-CoV-2 infection ($n = 63$). $n = 63$ individuals, 37 convalescent unvaccinated (black) and 26 convalescent vaccinated (blue) individuals. **a, b**, Two-sided Kruskal–Wallis test with subsequent Dunn’s multiple comparisons. **c, d**, Lines connect longitudinal samples from the same individual. Two-sided Friedman test with subsequent Dunn’s multiple comparisons. Two individuals who received their first dose of vaccine 24–48 h before sample collection are represented in purple. **e**, Plasma neutralizing activity against indicated SARS-CoV-2 variants of concern ($n = 30$, 15 convalescent and 15 convalescent vaccinated individuals). The B.1.526 variant used here contains the E484K substitution. Substitutions, deletions and insertions in S variants used here are described in Methods. Two-tailed Mann–Whitney test. Red numbers in **c–e** indicate the geometric mean NT_{50} at the indicated time point. All experiments were performed at least in duplicate.

[Full size image](#)

Plasma neutralizing activity in 63 participants was measured using a human immunodeficiency virus 1 (HIV-1) pseudotyped with the SARS-CoV-2 spike (S)

protein^{3,4,13} (Fig. 1c, d, Extended Data Fig. 2o). Twelve months after infection, the geometric mean half-maximal neutralizing titre (NT₅₀) for the 37 individuals who had not been vaccinated was 75, which was not significantly different from the NT₅₀ for the same individuals at 6.2 months after infection (Fig. 1c). By contrast, the vaccinated individuals showed a geometric mean NT₅₀ of 3,684, which was nearly 50-fold higher than that of unvaccinated individuals and slightly higher than the 30-fold increase in anti-RBD IgG antibodies (Fig. 1a,c,d). Neutralizing activity was directly correlated with IgG anti-RBD (Extended Data Fig. 2p) but not with anti-N titres (Extended Data Fig. 2q,r). We conclude that neutralizing titres remain relatively unchanged between 6 and 12 months after SARS-CoV-2 infection, and that vaccination further boosts this activity by nearly 50-fold.

To determine the neutralizing activity against circulating variants of concern or interest, we performed neutralization assays on HIV-1 virus pseudotyped with the S protein of the following SARS-CoV-2 variants of concern or interest: B.1.1.7 (Alpha), B.1.351 (Beta), B.1.526 (Iota) and P.1 (Gamma)^{1,14,15}. Twelve months after infection, neutralizing activity against the variants was generally lower than against wild-type SARS-CoV-2 virus in the same assay, with the greatest loss of activity against B.1.351 (Fig. 1e). After vaccination the geometric mean NT₅₀ increased to 11,493, 48,341, 22,109 and 26,553 against B.1.351, B.1.1.7, B.1.526 and P.1, respectively. These titres are an order of magnitude higher than the neutralizing titres that have been reported against wild-type SARS-CoV-2 at the peak of the initial response in infected individuals and in naive individuals receiving both doses of mRNA vaccines^{2,3,4,5,6,7,8} (Fig. 1d). Similar results were also obtained using authentic SARS-CoV-2 WA1/2020 and B.1.351 (Extended Data Fig. 2s).

Memory B cells

The memory B cell compartment serves as an immune reservoir containing a diverse collection of antibodies^{16,17}. Although antibodies to the N-terminal domain and other parts of S can also be neutralizing, we limited our analysis to memory B cells that produce anti-RBD antibodies because they are the most numerous and potent^{18,19}. To count RBD-specific memory B cells, we performed flow cytometry using biotin-labelled RBD³ (Fig. 2a, Extended Data Fig. 3a,b). Without vaccination, the number of RBD-specific memory B cells present 12 months after infection was 1.35-fold lower than the earlier 6.2-month time point ($P = 0.027$, Fig. 2a). By contrast, and consistent with previous reports^{5,8,20}, individuals who recovered from COVID-19 and received mRNA vaccines showed an average increase of 8.6-fold in the number of circulating RBD-specific memory B cells (Fig. 2a). We also counted B cells expressing antibodies that bound to both wild-type and K417N/E484K/N501Y mutant RBDs using flow cytometry (Extended Data Fig. 3c). The number of B cells cross-reacting with variant

RBD was directly proportional to and 1.6- to 3.2-fold lower than the number of B cells binding to wild-type RBD (Fig. 2a).

Fig. 2: SARS-CoV-2 RBD-specific B cell memory.

 [figure2](#)

a, Number of antigen-binding memory B cells per 2×10^6 B cells (Extended Data Fig. 5b, c) obtained at 1.3, 6.2 and 12 months after infection from 40 randomly selected individuals (vaccinated, $n = 20$; non-vaccinated, $n = 20$). Each dot represents one individual. Red horizontal bars indicate geometric mean values. Two-sided Kruskal–Wallis test with subsequent Dunn’s multiple comparisons. WT, wild type. **b**, The distribution of antibody sequences from 6 individuals 1.3 (top) or 6.2 (middle) or 12 (bottom) months after infection^{3,4}. The number in the inner circle indicates the number of sequences analysed for the individual whose identifier is denoted above the circle. Pie slice size is proportional to the number of clonally related sequences. The outer black arc indicates the frequency of clonally expanded sequences detected in each participant. Coloured slices indicate persisting clones (same IGV and IGJ genes, with highly similar CDR3 sequences) found at both time points in the same participant. Grey slices indicate clones unique to the time point. White indicates sequences isolated once, and white slices indicate singlets found at both time points. **c**, Number of somatic nucleotide mutations (SHM) in the IGVH and IGVL genes (Supplementary Table 3) obtained after 1.3 or 6.2 or 12 months (1.3 month, $n = 889$; 6.2 month, $n = 975$; 12 month, $n = 1,105$ (unvaccinated, $n = 417$; vaccinated, $n = 688$)). Red horizontal bars indicate mean values. Two-sided Kruskal–Wallis test with subsequent Dunn’s multiple comparisons.

[Full size image](#)

The memory B cell compartment accumulates mutations and undergoes clonal evolution over the initial six months after infection^{4,9,21,22}. To determine whether the memory compartment continues to evolve between 6 and 12 months after infection, we obtained 1,105 paired antibody heavy- and light-chain sequences from 10 individuals who were also assessed at the earlier time points, 6 of whom were vaccinated (Fig. 2b, Extended Data Fig. 3d, Supplementary Table 3). There were few significant differences among the expressed IGHV and IGLV genes between

vaccinated and un-vaccinated groups, or between the 1.3-, 6-month and 1-year time points^{3,4} (Extended Data Fig. 4a–c). *IGHV* 3-30 and *IGHV* 3-53 remained over-represented independently of vaccination status^{10,18} (Extended Data Fig. 4a).

All individuals assayed at 12 months showed expansion of RBD-binding memory cell clones that expressed closely related *IGHV* and *IGLV* genes (Fig. 2b, Extended Data Fig. 3d, e). The relative fraction of cells belonging to these clones varied from 7% to 54% of the repertoire, with no significant difference between vaccinated and non-vaccinated groups. The overall clonal composition differed between 6 and 12 months after infection in all individuals, suggesting ongoing clonal evolution (Fig. 2b, Extended Data Fig. 3d). Among the 89 clones found 12 months after infection, 61% were not previously detected and 39% were present at one of the earlier time points (Fig. 2b, Extended Data Fig. 3d). In vaccinated individuals, the increase in size of the memory compartment was paralleled by an increase in the absolute number of B cells representing all persistent clones (Extended Data Fig. 5a). Thus, RBD-specific memory B cell clones were re-expanded upon vaccination in all six convalescent individuals examined (Fig. 2b, Extended Data Figs. 3d, 5a).

Somatic hypermutation of antibody genes continued between 6 and 12 months after infection (Fig. 2c). Slightly higher levels of antibody-gene mutation were found in individuals who had not been vaccinated compared with vaccinated individuals, possibly owing to recruitment of newly formed memory cells into the expanded memory compartment of the vaccinated individuals (Fig. 2c, Extended Data Fig. 5b). There was no significant difference in numbers of mutations between conserved and newly arising clones at the 12-month time point in vaccinated individuals (Extended Data Fig. 5c). Moreover, phylogenetic analysis revealed that sequences found at 6 and 12 months after infection were intermingled and similarly distant from their unmutated common ancestors (Extended Data Fig. 6). We conclude that clonal re-expansion of memory cells in response to vaccination is not associated with additional accumulation of large numbers of somatic mutations as might be expected if the clones were re-entering and proliferating in germinal centres.

Neutralizing activity of monoclonal antibodies

To determine whether the antibodies obtained from memory B cells 12 months after infection bind to RBD, we performed ELISAs (Fig. 3a). We tested 174 antibodies, including: (1) 53 that were randomly selected from those that appeared only once and only after 1 year; (2) 91 that appeared as expanded clones or singlets at more than one time point; and (3) 30 representatives of newly arising expanded clones (Supplementary Tables 4, 5). Among the 174 antibodies tested, 173 bound to RBD, indicating that the flow cytometry method used to identify B cells expressing anti-RBD antibodies was efficient (Supplementary Tables 4, 5). The geometric mean

ELISA half-maximal concentration (EC_{50}) of the antibodies obtained 12 months after infection was 2.6 ng ml^{-1} , which was significantly lower than after 6 months, independently of vaccination status and suggestive of an increase in affinity (Fig. 3a, Extended Data Fig. 7a, b, Supplementary Tables 4, 5). Consistent with this observation, there was an overall increase in the apparent avidity of plasma antibodies between 1.3 and 12 months^{3,4} ($P < 0.0001$) (Extended Data Fig. 7c).

Fig. 3: Anti-SARS-CoV-2 RBD monoclonal antibodies.

 [figure3](#)

a, EC_{50} for SARS-CoV-2 RBD of antibodies isolated at 1.3 ($n = 152$) 6.2 ($n = 153$) and 12 ($n = 174$) months after infection^{3,4}, determined by ELISA. Two-sided Kruskal–Wallis test with subsequent Dunn’s multiple comparisons (1.3 months versus 6.2 months, $P = 0.27$; 1.3 months versus 12 months, $P = 0.0075$; 6.2 versus 12 months, $P < 0.0001$). **b**, SARS-CoV-2-neutralizing activity of monoclonal antibodies measured using a SARS-CoV-2 pseudovirus neutralization assay^{3,13}. IC_{50} values for antibodies isolated at 1.3, 6.2 and 12 months after infection against wild-type SARS-CoV-2 (Wuhan-Hu-1 strain⁴¹) are shown. Each dot represents one antibody. Pie charts illustrate the fraction of non-neutralizing ($IC_{50} > 1,000 \text{ ng ml}^{-1}$) antibodies (grey slices), inner circle shows the number of antibodies tested per group. Horizontal bars and red numbers indicate geometric mean values. Statistical significance was determined through the two-sided Kruskal–Wallis test with subsequent Dunn’s multiple comparisons.

[Full size image](#)

All 174 RBD binding antibodies obtained from the 12-month time point were tested for neutralizing activity in a SARS-CoV-2 pseudotype-neutralization assay. When compared with the earlier time points from the same individuals, the geometric mean half-maximal inhibitory concentration (IC_{50}) improved from 171 ng ml^{-1} (at 1.3 months) to 116 ng ml^{-1} (at 6 months) to 79 ng ml^{-1} (at 12 months), with no significant

difference between vaccinated and non-vaccinated individuals (Fig. 3b, Extended Data Fig. 7d, Supplementary Table 4). This increased potency was most evident in the antibodies expressed by expanded clones of B cells that were conserved for the entire observation period independently of vaccination status ($P = 0.014$) (Fig. 3b, right, Extended Data Fig. 7e–h, Supplementary Table 5). The overall increase in neutralizing activity among conserved clones was owing to accumulation of clones expressing antibodies with potent neutralizing activity and simultaneous loss of clones expressing antibodies with no measurable activity ($P = 0.028$) (Fig. 3b, bottom right). Consistent with this observation, antibodies obtained from clonally expanded B cells 12 months after infection were more potent than antibodies obtained from unique B cells at the same time point ($P = 0.029$) (Fig. 3b).

Epitopes and breadth of neutralization

To determine whether the loss of non-neutralizing antibodies over time was due to preferential loss of antibodies targeting specific epitopes, we performed biolayer interferometry (BLI) experiments in which a preformed antibody–RBD complex was exposed to a second monoclonal antibody targeting one of three classes of structurally defined epitopes^{3,23} (schematic in Fig. 4a). We assayed 60 randomly selected antibodies with comparable neutralizing activity from the 1.3- and 12-month time points. The 60 antibodies were evenly distributed between the two time points and between neutralizers and non-neutralizers (Fig. 4). Antibody affinities for RBD were similar among neutralizers and non-neutralizers obtained at the same time point (Fig. 4b, Extended Data Fig. 8). When the two sets of unrelated antibodies obtained 1.3 and 12 months after infection were compared, they showed increasing affinity over time independent of their neutralizing activity (Fig. 4b, Extended Data Fig. 8). In competition experiments, 2 out of 30 non-neutralizing antibodies inhibited binding of the class 1 (C105), 2 (C121 and C144) or 3 (C135) antibodies tested; the remaining 28 non-neutralizing antibodies must therefore bind to epitopes that do not overlap with the epitopes of these classes of antibodies (Fig. 4c, Extended Data Fig. 9). By contrast, 28 out of 30 neutralizing antibodies blocked class 1 or 2 antibodies whose target epitopes are structural components of the RBD that interact with its cellular receptor, angiotensin-converting enzyme 2 (ACE2)^{23,24} (Fig. 4c, Extended Data Fig. 9). In addition, whereas 9 of the 15 neutralizing antibodies obtained after 1.3 months blocked both class 1 and 2 antibodies, only 1 of the 15 obtained after 12 months did so. In contrast to the earlier time point, 13 of 15 neutralizing antibodies obtained after 12 months interfered only with C121, a class 2 antibody^{3,23} (Fig. 4c, Extended Data Fig. 9). We conclude that neutralizing antibodies are retained and non-neutralizing antibodies targeting RBD surfaces that do not interact with ACE2 are removed from the repertoire over time.

Fig. 4: Epitope targeting and evolution of anti-SARS-CoV-2 RBD antibodies.

 **figure4**

a, Schematic of the BLI experiment (left) and IC₅₀ values for randomly selected neutralizing and non-neutralizing antibodies (Ab1 and Ab2) isolated at 1.3 and 12 months after infection ($n = 15$ antibodies per group, $n = 60$ antibodies in total). Red horizontal bars indicate geometric mean. Two-sided Mann–Whitney test. **b**,

Dissociation constants (K_D) of the $n = 30$ neutralizing (green) and $n = 30$ non-neutralizing (red) antibodies shown in **a**. Horizontal bars indicate geometric mean values. Two-sided Kruskal–Wallis test with subsequent Dunn’s multiple comparisons. BLI traces are shown in Extended Data Fig. 8. **c**, Heat map of relative inhibition of binding of a monoclonal antibody (Ab2) to preformed complexes of RBD with another monoclonal antibody (Ab1) (grey, no binding; orange, intermediate binding; red, high binding). Data are normalized by subtraction of the autologous antibody control. BLI traces are shown in Extended Data Fig. 9. **d**, Neutralization of the indicated mutant RBD proteins with antibodies shown in **a–c**. Pie charts illustrate the fraction of antibodies that are poorly or non-neutralizing (IC_{50} of 100–1,000 ng ml $^{-1}$, red), intermediate neutralizing (IC_{50} of 10–100 ng ml $^{-1}$, pink) and potently neutralizing (IC_{50} of 0–10 ng ml $^{-1}$, white) for each mutant. The number in the inner circle shows the number of antibodies tested. **e**, Graphs show affinities (y-axis) plotted against neutralization activity (x-axis) for 18 clonal antibody pairs isolated 1.3 (top) and 12 months (bottom) after infection ($n = 36$ antibodies). Spearman correlation test. **f**, BLI affinity measurements for same $n = 36$ paired antibodies as in **e**. Two-tailed Wilcoxon test. **g**, IC_{50} values for $n = 30$ paired neutralizing antibodies isolated at indicated time points versus indicated mutant SARS-CoV-2 pseudoviruses. Antibodies are divided into groups I, II and III (left), on the basis of neutralizing activity: I, potent clonal pairs that do not improve over time; II, clonal pairs that show increased activity over time; and III, clonal pairs showing decreased neutralization activity after 12 months. Antibody class assignment based on initial (1.3 month after infection) sensitivity to mutation is indicated on the right. Red stars indicate antibodies that neutralize all tested RBD mutants. Colour gradient indicates IC_{50} values ranging from 0 (white) to 1,000 ng ml $^{-1}$ (red).

[Full size image](#)

To determine whether there was an increase in neutralization breadth over time, the neutralizing activity of the 60 antibodies was assayed against a panel of RBD mutants covering residues associated with circulating variants of concern: R346S, K417N, N440K, A475V, E484K and N501Y (Fig. 4d, Supplementary Table 6). Increased activity was evident against K417N, N440K, A475V, E484K and N501Y (Fig. 4d, Supplementary Table 6). These data indicate that evolution of the antibody repertoire results in acquisition of neutralization breadth over time.

The increase in breadth and overall potency of memory B cell antibodies could be owing to shifts in the repertoire, clonal evolution or both. To determine whether changes in specific clones are associated with increases in affinity and breadth, we measured the relative affinity and neutralizing breadth of matched pairs of antibodies expressed by expanded clones of B cells that were maintained in the repertoire over

the entire observation period^{3,4}. SARS-CoV-2-neutralizing activity of the antibodies present at 1.3 or 12 months was not significantly correlated with affinity at either time point when each time point was considered independently (Fig. 4e). However, there was a significant increase in overall affinity over time, including in the 4 pairs of antibodies with no measurable neutralizing activity (Fig. 4f and Supplementary Table 7). Neutralizing breadth was assayed for 15 randomly selected pairs of antibodies targeting epitopes assigned to the 3 dominant classes of neutralizing antibodies^{3,23,25,26}. Seven of the selected antibodies showed equivalent or decreased activity against wild-type SARS-CoV-2 after 12 months (Fig. 4g, Supplementary Table 8). However, neutralizing breadth increased between 1.3 and 12 months for all 15 pairs, even when neutralizing activity against the wild-type was unchanged or decreased (Fig. 4g, Supplementary Table 8). Only 1 out of the 15 antibodies obtained after 1.3 months neutralized all the mutants tested (Fig. 4g). By contrast, 10 out of the 15 antibodies obtained from the same clones 12 months after infection neutralized all variants tested, with IC₅₀ values as low as 1 ng ml⁻¹ against the RBD triple mutant K417N/E484K/N501Y found in B.1.351 (Fig. 4g, Supplementary Table 8). Similar results were obtained with authentic WA1/2020 and B.1.351 (Extended Data Fig. 7i). In conclusion, continued clonal evolution of anti-SARS-CoV-2 antibodies over 12 months favours increasing potency and breadth, resulting in monoclonal antibodies with exceptional activity against a wide group of variants.

Discussion

During immune responses, activated B cells interact with cognate T cells and begin dividing before selection into the plasma cell, memory or germinal centre B cell compartments, partly on the basis of their affinity for antigen^{17,27,28,29,30,31}. Whereas B cells expressing high-affinity antibodies are favoured to enter the long-lived plasma cell compartment, the memory compartment is more diverse and can develop directly from activated B cells or from a germinal centre^{17,27,28,29,30,31}. Memory cells emanating from a germinal centre carry more mutations than those that develop directly from activated B cells because they undergo additional cycles of division³².

Consistent with the longevity of bone marrow plasma cells, infection with SARS-CoV-2 leads to persistent anti-RBD antibodies in serum, and corresponding neutralizing responses. Nearly 93% of the plasma neutralizing activity is retained between 6 and 12 months after infection^{33,34}. Vaccination boosts the neutralizing response by 1.5 orders of magnitude by inducing additional plasma cell differentiation from the memory B cell compartment^{5,7,35}. Recruitment of evolved memory B cells producing antibodies with broad and potent neutralizing activity into the plasma cell compartment is likely to account for the high serologic activity of vaccinated convalescent individuals against variants of concern^{20,35,36}.

Less is known about selection and maintenance of the memory B cell compartment. SARS-CoV-2 infection produces a memory compartment that continues to evolve more than 12 months after infection with accumulation of somatic mutations, emergence of new clones and increasing affinity, all of which are consistent with long-term persistence of germinal centres. The increase in activity against SARS-CoV-2 mutants parallels the increase in affinity and is consistent with the finding that increasing the apparent affinity of anti-SARS-CoV-2 antibodies by dimerization or by creating bi-specific antibodies also increases resistance to RBD mutations^{[37,38,39,40](#)}.

Continued antibody evolution in germinal centres requires antigen, which can be retained in these structures over long periods of time^{[29](#)}. In addition, SARS-CoV-2 protein and nucleic acids have been reported to remain in the gut for at least two months after infection^{[4](#)}. Regardless of the source of the antigen, antibody evolution favours epitopes overlapping with the ACE2-binding site on the RBD, possibly because these are epitopes that are preferentially exposed on trimeric S protein or virus particles.

Vaccination after SARS-CoV-2 infection increases the number of RBD-binding memory cells by more than an order of magnitude by recruiting new B cell clones into memory and expanding persistent clones. The persistent clones expand without accumulating large numbers of additional mutations, indicating that clonal expansion of human memory B cells does not require re-entry into germinal centres and occurs in the activated B cell compartment^{[17,27,28,29,30,31](#)}.

The notable evolution of neutralizing breadth after infection with SARS-CoV-2 and the robust enhancement of serologic responses and B cell memory achieved with mRNA vaccination suggests that convalescent individuals who are vaccinated should enjoy high levels of protection against emerging variants without a need to modify existing vaccines. If memory responses evolve in a similar manner in naive individuals who receive vaccines, additional appropriately timed boosting with available vaccines should lead to protective immunity against circulating variants.

Methods

Data reporting

No statistical methods were used to predetermine sample size. The experiments were not randomized and the investigators were not blinded to allocation during experiments and outcome assessment.

Study participants

Previously enrolled study participants were asked to return for a 12-month follow-up visit at the Rockefeller University Hospital in New York between 8 February and 26 March 2021. Eligible participants were adults with a history of participation in both prior study visits of our longitudinal cohort study of COVID-19 recovered individuals^{3,4}. All participants had a confirmed history of SARS-CoV-2 infection, either diagnosed during the acute infection by PCR with reverse transcription (RT-PCR) or retrospectively confirmed by seroconversion. Exclusion criteria included presence of symptoms suggestive of active SARS-CoV-2 infection. Most study participants were residents of the Greater New York City tri-state region and were asked to return approximately 12 months after the time of onset of COVID-19 symptoms. Participants presented to the Rockefeller University Hospital for blood sample collection and were asked about potential symptom persistence since their 6.2-month study visit, laboratory-confirmed episodes of reinfection with SARS-CoV-2, and whether they had received any COVID-19-related treatment or SARS-CoV-2 vaccination in the interim. Study participants who had received COVID-19 vaccinations, were exclusively recipients of one of the two currently EUA-approved mRNA vaccines, Moderna (mRNA-1273) or Pfizer-BioNTech (BNT162b2), and individuals who received both doses did so according to current interval guidelines, namely 28 days (range 28–30 days) for Moderna and 21 days (range 21–23 days) for Pfizer-BioNTech. Detailed characteristics of the symptomatology and severity of the acute infection, symptom kinetics, and the immediate convalescent phase (7 weeks post-symptom onset until 6.2-month visit) have previously been reported⁴. Participants who presented with persistent symptoms attributable to COVID-19 were identified on the basis of chronic shortness of breath or fatigue, deficit in athletic ability and/or three or more additional long-term symptoms such as persistent unexplained fevers, chest pain, new-onset cardiac sequelae, arthralgias, impairment of concentration/mental acuity, impairment of sense of smell/taste, neuropathy or cutaneous findings as previously described⁴. Clinical data collection and management were carried out using the software iRIS by iMedRIS. All participants at Rockefeller University provided written informed consent before participation in the study and the study was conducted in accordance with Good Clinical Practice. For detailed participant characteristics see Supplementary Table 2. The study was performed in compliance with all relevant ethical regulations and the protocol (DRO-1006) for studies with human participants was approved by the Institutional Review Board of the Rockefeller University.

SARS-CoV-2 molecular tests

Saliva was collected into guanidine thiocyanate buffer as previously described⁴². RNA was extracted using either a column-based (Qiagen QIAamp DSP Viral RNA Mini Kit, catalogue (cat.) no. 61904) or a magnetic bead-based method as previously described⁴³. Reverse-transcribed cDNA was amplified using primers and

probes validated by the CDC or by Columbia University Personalized Medicine Genomics Laboratory, respectively and approved by the FDA under the Emergency Use Authorization. Viral RNA was considered detected if C_t for two viral primers/probes were <40 .

Blood samples processing and storage

Peripheral blood mononuclear cells obtained from samples collected at Rockefeller University were purified as previously reported by gradient centrifugation and stored in liquid nitrogen in the presence of FCS and DMSO^{3,4}. Heparinized plasma and serum samples were aliquoted and stored at -20°C or less. Prior to experiments, aliquots of plasma samples were heat-inactivated (56°C for 1 h) and then stored at 4°C .

ELISAs

ELISAs^{44,45} to evaluate antibodies binding to SARS-CoV-2 RBD and N were performed by coating of high-binding 96-half-well plates (Corning 3690) with $50\ \mu\text{l}$ per well of a $1\ \mu\text{g ml}^{-1}$ protein solution in PBS overnight at 4°C . Plates were washed 6 times with washing buffer ($1\times$ PBS with 0.05% Tween-20 (Sigma-Aldrich)) and incubated with $170\ \mu\text{l}$ per well blocking buffer ($1\times$ PBS with 2% BSA and 0.05% Tween-20 (Sigma)) for 1 h at room temperature. Immediately after blocking, monoclonal antibodies or plasma samples were added in PBS and incubated for 1 h at room temperature. Plasma samples were assayed at a 1:66 starting dilution and 7 (IgA and IgM anti-RBD) or 11 (IgG anti-RBD) additional threefold serial dilutions. Monoclonal antibodies were tested at $10\ \mu\text{g ml}^{-1}$ starting concentration and 10 additional fourfold serial dilutions. Plates were washed 6 times with washing buffer and then incubated with anti-human IgG, IgM or IgA secondary antibody conjugated to horseradish peroxidase (HRP) (Jackson Immuno Research 109-036-088 109-035-129 and Sigma A0295) in blocking buffer at a 1:5,000 dilution (IgM and IgG) or 1:3,000 dilution (IgA). Plates were developed by addition of the HRP substrate, TMB (ThermoFisher) for 10 min (plasma samples) or 4 min (monoclonal antibodies). The developing reaction was stopped by adding $50\ \mu\text{l}$ 1 M H_2SO_4 and absorbance was measured at 450 nm with an ELISA microplate reader (FluoStar Omega 5.11, BMG Labtech) with Omega MARS software for analysis. For plasma samples, a positive control (plasma from participant COV72, diluted 66.6-fold and seven additional threefold serial dilutions in PBS) was added to every assay plate for validation. The average of its signal was used for normalization of all of the other values on the same plate with Excel software before calculating the area under the curve using Prism v.9.1(GraphPad). For monoclonal antibodies, the EC_{50} was determined using four-parameter nonlinear regression (GraphPad Prism v.9.1).

Proteins

Mammalian expression vectors encoding the RBDs of SARS-CoV-2 (GenBank MN985325.1; S protein residues 319-539) or K417N, E484K, N501Y RBD mutants with an N-terminal human IL-2 or Mu phosphatase signal peptide were previously described⁴⁶. SARS-CoV-2 nucleocapsid protein (N) was purchased from Sino Biological (40588-V08B).

SARS-CoV-2 pseudotyped reporter virus

A panel of plasmids expressing RBD-mutant SARS-CoV-2 S proteins in the context of pSARS-CoV-2-S_{Δ19} has previously been described^{2,9,26}. Variant pseudoviruses resembling variants of concern B.1.1.7 (first isolated in the UK), B.1.351 (first isolated in South Africa), B.1.526 (first isolated in New York City) and P.1 (first isolated in Brazil) were generated by introduction of substitutions using synthetic gene fragments (IDT) or overlap extension PCR mediated mutagenesis and Gibson assembly. Specifically, the variant-specific deletions and substitutions introduced were: B.1.1.7: ΔH69/V70, ΔY144, N501Y, A570D, D614G, P681H, T761I, S982A, D1118H; B.1.351: D80A, D215G, L242H, R246I, K417N, E484K, N501Y, D614G, A701V; B.1.526: L5F, T95I, D253G, E484K, D614G, A701V; P.1: L18F, R20N, P26S, D138Y, R190S, K417T, E484K, N501Y, D614G, H655Y.

The E484K and K417N/E484K/N501Y (KEN) substitution, as well as the deletions and substitutions corresponding to variants of concern were incorporated into an S protein that also includes the R683G substitution, which disrupts the furin cleavage site and increases particle infectivity. Neutralizing activity against mutant pseudoviruses were compared to a wild-type SARS-CoV-2 S sequence (NC_045512), carrying R683G where appropriate.

SARS-CoV-2 pseudotyped particles were generated as previously described^{3,13}. In brief, 293T cells were transfected with pNL4-3ΔEnv-nanoluc and pSARS-CoV-2-S_{Δ19}, particles were collected 48 h after transduction, filtered and stored at -80 °C.

Microneutralization assay with authentic SARS-CoV-2

Microneutralization assays of SARS-CoV-2 virus were performed as previously described³. The day before infection, Vero E6 cells were seeded at 1 × 10⁴ cells per well into 96-well plates. The diluted plasma and antibodies were mixed with SARS-CoV-2 WA1/2020 or the B.1.351 variant and incubated for 1 h at 37 °C. The antibody–virus mix was then directly

applied to Vero E6 cells and incubated for 22 h at 37 °C. Cells were subsequently fixed by adding an equal volume of 70% formaldehyde to the wells, followed by permeabilization with 1% Triton X-100 for 10 min. After washing, cells were incubated for 1 h at 37 °C with blocking solution of 5% goat serum in PBS (catalogue no. 005–000-121; Jackson ImmunoResearch). A rabbit polyclonal anti-SARS-CoV-2 nucleocapsid antibody (catalogue no. GTX135357; GeneTex) was added to the cells at 1:1,000 dilution in blocking solution and incubated at 4 °C overnight. Goat anti-rabbit AlexaFluor 594 (catalogue no. A-11012; Life Technologies) was used as a secondary antibody at a dilution of 1:2,000. Nuclei were stained with Hoechst 33342 (catalogue no. 62249; Thermo Fisher Scientific) at 1 µg ml⁻¹. Images were acquired with a fluorescence microscope and analysed using ImageXpress Micro XLS (Molecular Devices). All experiments were performed in a biosafety level 3 laboratory.

Pseudotyped virus neutralization assay

Fourfold serially diluted plasma from COVID-19-convalescent individuals or monoclonal antibodies were incubated with SARS-CoV-2 pseudotyped virus for 1 h at 37 °C. The mixture was subsequently incubated with 293T_{Ace2} cells³ (for comparisons of plasma or monoclonal antibodies from convalescent individuals) or HT1080Ace2 cl14 cells¹³ (for analyses involving mutant or variant pseudovirus panels), as indicated, for 48 h after which cells were washed with PBS and lysed with Luciferase Cell Culture Lysis 5× reagent (Promega). Nanoluc luciferase activity in lysates was measured using the Nano-Glo Luciferase Assay System (Promega) with the Glomax Navigator (Promega). The obtained relative luminescence units were normalized to those derived from cells infected with SARS-CoV-2 pseudotyped virus in the absence of plasma or monoclonal antibodies. The NT₅₀ or half-maximal and 90% inhibitory concentrations for monoclonal antibodies (IC₅₀ and IC₉₀) were determined using four-parameter nonlinear regression (least squares regression method without weighting; constraints: top, 1; bottom, 0) (GraphPad Prism).

Biotinylation of viral protein for use in flow cytometry

Purified and Avi-tagged SARS-CoV-2 RBD or SARS-CoV-2 RBD KEN mutant (K417N, E484K, N501Y) was biotinylated using the Biotin–Protein Ligase–BIRA kit according to manufacturer’s instructions (Avidity) as previously described³. Ovalbumin (Sigma, A5503-1G) was biotinylated using the EZ-Link Sulfo-NHS-LC-Biotinylation kit according to the manufacturer’s instructions (Thermo Scientific). Biotinylated ovalbumin was conjugated to streptavidin-BV711 (BD biosciences, 563262) and RBD to streptavidin-PE (BD Biosciences, 554061) and streptavidin-AF647 (Biolegend, 405237)³.

Flow cytometry and single-cell sorting

Single-cell sorting by flow cytometry has previously been described³. In brief, peripheral blood mononuclear cells were enriched for B cells by negative selection using a pan-B-cell isolation kit according to the manufacturer’s instructions (Miltenyi Biotec, 130-101-638). The enriched B cells were incubated in FACS buffer (1× PBS, 2% FCS, 1 mM EDTA) with the following anti-human antibodies (all at 1:200 dilution): anti-CD20-PECy7 (BD Biosciences, 335793), anti-CD3-APC-eFluro 780 (Invitrogen, 47-0037-41), anti-CD8-APC-eFluor 780 (Invitrogen, 47-0086-42), anti-CD16-APC-eFluor 780 (Invitrogen, 47-0168-41), anti-CD14-APC-eFluor 780 (Invitrogen, 47-0149-42), as well as Zombie NIR (BioLegend, 423105) and fluorophore-labelled RBD and ovalbumin (Ova) for 30 min on ice. Single CD3⁻CD8⁻CD14⁻CD16⁻CD20⁺Ova⁻RBD⁻PE⁺RBD⁻AF647⁺ B cells were sorted into individual wells of 96-well plates containing 4 µl of lysis buffer (0.5 × PBS, 10 mM DTT, 3,000 units per ml RNasin Ribonuclease Inhibitors (Promega, N2615) per well using a FACS Aria III and FACSDiva software (Becton Dickinson) for acquisition and FlowJo for analysis. The sorted cells were frozen on dry ice, and then stored at –80 °C or immediately used for subsequent RNA reverse transcription. For B cell phenotype analysis, in addition to above antibodies, B cells were also stained with following anti-human antibodies: anti- IgG-PECF594 (BD biosciences, 562538), anti-IgM-AF700 (Biolegend, 314538), anti-IgA-Viogreen (Miltenyi Biotec, 130-113-481).

Antibody sequencing, cloning and expression

Antibodies were identified and sequenced as previously described³. In brief, RNA from single cells was reverse transcribed (SuperScript III Reverse Transcriptase, Invitrogen, 18080-044) and the cDNA stored at -20 °C or used for subsequent amplification of the variable IGH, IGL and IGK genes by nested PCR and Sanger sequencing. Sequence analysis was performed using MacVector. Amplicons from the first PCR reaction were used as templates for sequence- and ligation-independent cloning into antibody expression vectors. Recombinant monoclonal antibodies were produced and purified as previously described³.

Biolayer interferometry

BLI assays were performed as previously described³. In brief, we used the Octet Red instrument (ForteBio) at 30 °C with shaking at 1,000 r.p.m. Epitope-binding assays were performed with protein A biosensor (ForteBio 18-5010), following the manufacturer's protocol 'classical sandwich assay'. (1) Sensor check: sensors immersed 30 s in buffer alone (kinetics buffer 10x (ForteBio 18-1105) diluted 1x in PBS1x). (2) Capture first antibody: sensors immersed 10 min with Ab1 at 30 µg ml⁻¹. (3) Baseline: sensors immersed 30 s in buffer alone. (4) Blocking: sensors immersed 5 min with IgG isotype control at 50 µg ml⁻¹. (6) Antigen association: sensors immersed 5 min with RBD at 100 µg ml⁻¹. (7) Baseline: sensors immersed 30 s in buffer alone. (8) Association Ab2: sensors immersed 5 min with Ab2 at 30 µg ml⁻¹. Curve fitting was performed using the Fortebio Octet Data analysis software (ForteBio). Affinity measurement of anti-SARS-CoV-2 IgGs binding were corrected by subtracting the signal obtained from traces performed with IgGs in the absence of WT RBD. The kinetic analysis using protein A biosensor (ForteBio 18-5010) was performed as follows: (1) baseline: 60 s immersion in buffer. (2) loading: 200 s immersion in a solution with 30 µg ml⁻¹ IgGs. (3) baseline: 200 s immersion in buffer. (4) Association: 300 s immersion in solution with wild-type RBD at 200, 100, 50 or 25 µg/ml. (5) dissociation: 600 s immersion in buffer. Curve fitting was performed using a fast 1:1 binding model and data analysis software (ForteBio). Mean K_D values were determined by averaging all binding curves that matched the theoretical fit with an R^2 value ≥ 0.8 .

Plasma antibody avidity assay

The plasma SARS-CoV-2 antibody avidity assay were performed as previously described⁴⁷.

Computational analyses of antibody sequences

Antibody sequences were trimmed based on quality and annotated using Igblastn v.1.14. with IMGT domain delineation system. Annotation was performed systematically using Change-O toolkit v.0.4.540⁴⁸. Heavy and light chains derived from the same cell were paired, and clonotypes were assigned based on their V and J genes using in-house R and Perl scripts (Fig. 2d). All scripts and the data used to process antibody sequences are publicly available on GitHub (<https://github.com/stratust/igpipeline>).

The frequency distributions of human V genes in anti-SARS-CoV-2 antibodies from this study was compared to 131,284,220 IgH and IgL sequences generated by ref. ⁴⁹ and downloaded from cAb-Rep⁵⁰, a database of human shared BCR clonotypes available at <https://cab-rep.c2b2.columbia.edu/>. On the basis of the 91 distinct V genes that make up the 6,902 analysed sequences from Ig repertoire of the 10 participants present in this study, we selected the IgH and IgL sequences from the database that are partially coded by the same V genes and counted them according to the constant region. The frequencies shown in Extended Data Fig. 4) are relative to the source and isotype analysed. We used the two-sided binomial test to check whether the number of sequences belonging to a specific IgHV or IgLV gene in the repertoire is different according to the frequency of the same IgV gene in the database. Adjusted *P* values were calculated using the false discovery rate (FDR) correction. Significant differences are denoted with stars.

Nucleotide somatic hypermutation and CDR3 length were determined using in-house R and Perl scripts. For somatic hypermutations,IGHV and IGLV nucleotide sequences were aligned against their closest germlines using Igblastn and the number of differences were considered nucleotide mutations. The average mutations for V genes were calculated by dividing

the sum of all nucleotide mutations across all participants by the number of sequences used for the analysis.

Immunoglobulins grouped into the same clonal lineage had their respective IgH and IgL sequences merged and subsequently aligned, using TranslatorX v.1.1⁵¹, with the unmutated ancestral sequence obtained from IMGT/V-QUEST reference directory⁵². GCTree (<https://github.com/matsengrp/gctree>)⁵³ was further used to perform the phylogenetic trees construction. Each node represents a unique IgH and IgL combination and the size of each node is proportional to the number of identical sequences. The numbered nodes represent the unobserved ancestral genotypes between the germline sequence and the sequences on the downstream branch.

Data presentation

Figures were arranged in Adobe Illustrator 2020.

Reporting summary

Further information on research design is available in the [Nature Research Reporting Summary](#) linked to this paper.

Data availability

Data are provided in Supplementary Tables 1–8. The raw sequencing data have been deposited at Github (<https://github.com/stratust/igpipeline>). This study also uses data from <https://doi.org/10.5061/dryad.35ks2> and from <https://doi.org/10.1038/s41586-019-0934-8>.

Code availability

Computer code to process the antibody sequences and/or associated with Fig. 2 and Extended Data Fig. 5 is available at GitHub (<https://github.com/stratust/igpipeline>).

References

1. 1.

Davies, N. G. et al. Estimated transmissibility and impact of SARS-CoV-2 lineage B.1.1.7 in England. *Science* **372**, eabg3055 (2021).

[CAS](#) [PubMed](#) [PubMed Central](#) [Google Scholar](#)

2. 2.

Wang, Z. et al. mRNA vaccine-elicited antibodies to SARS-CoV-2 and circulating variants. *Nature* **592**, 616–622 (2021).

[ADS](#) [CAS](#) [Google Scholar](#)

3. 3.

Robbiani, D. F. et al. Convergent antibody responses to SARS-CoV-2 in convalescent individuals. *Nature* **584**, 437–442 (2020).

[ADS](#) [CAS](#) [PubMed](#) [PubMed Central](#) [Google Scholar](#)

4. 4.

Gaebler, C. et al. Evolution of antibody immunity to SARS-CoV-2. *Nature* **591**, 639–644 (2021).

[ADS](#) [CAS](#) [PubMed](#) [PubMed Central](#) [Google Scholar](#)

5. 5.

Goel, R. R. et al. Distinct antibody and memory B cell responses in SARS-CoV-2 naïve and recovered individuals following mRNA vaccination. *Sci. Immunol.* **6**, eabi6950 (2021). 10

[PubMed](#) [PubMed Central](#) [Google Scholar](#)

6. 6.

Saadat, S. et al. Binding and neutralization antibody titers after a single vaccine dose in health care workers previously infected with SARS-CoV-2. *J. Am. Med. Assoc.* **325**, 1467–1469 (2021).

[CAS](#) [Google Scholar](#)

7. 7.

Krammer, F. et al. Antibody responses in seropositive persons after a single dose of SARS-CoV-2 mRNA vaccine. *N. Engl. J. Med.* **384**, 1372–1374 (2021).

[CAS](#) [Google Scholar](#)

8. 8.

Reynolds, C. J. et al. Prior SARS-CoV-2 infection rescues B and T cell responses to variants after first vaccine dose. *Science* eabh1282 (2021).

9. 9.

Muecksch, F. et al. Development of potency, breadth and resilience to viral escape mutations in SARS-CoV-2 neutralizing antibodies. Preprint at <https://doi.org/10.1101/2021.03.07.434227> (2021).

10. 10.

Brouwer, P. J. M. et al. Potent neutralizing antibodies from COVID-19 patients define multiple targets of vulnerability. *Science* **369**, 643–650 (2020).

[ADS](#) [CAS](#) [PubMed](#) [PubMed Central](#) [Google Scholar](#)

11. 11.

Cao, Y. et al. Potent neutralizing antibodies against SARS-CoV-2 identified by high-throughput single-cell sequencing of convalescent patients' B cells. *Cell* **182**, 73–84 (2020).

[CAS](#) [PubMed](#) [PubMed Central](#) [Google Scholar](#)

12. 12.

Ju, B. et al. Human neutralizing antibodies elicited by SARS-CoV-2 infection. *Nature* **584**, 115–119 (2020).

[ADS](#) [CAS](#) [Google Scholar](#)

13. 13.

Schmidt, F. et al. Measuring SARS-CoV-2 neutralizing antibody activity using pseudotyped and chimeric viruses. *J. Exp. Med.* **217**, e20201181 (2020).

[PubMed](#) [PubMed Central](#) [Google Scholar](#)

14. 14.

Tegally, H. et al. Detection of a SARS-CoV-2 variant of concern in South Africa. *Nature* **592**, 438–443 (2021).

[ADS](#) [CAS](#) [Google Scholar](#)

15. 15.

West, A. P. et al. Detection and characterization of the SARS-CoV-2 lineage B.1.526 in New York. Preprint at <https://doi.org/10.1101/2021.02.14.431043> (2021).

16. 16.

Inoue, T. et al. Exit from germinal center to become quiescent memory B cells depends on metabolic reprogramming and provision of a survival signal. *J. Exp. Med.* **218**, e20200866 (2021).

[CAS](#) [Google Scholar](#)

17. 17.

Viant, C. et al. Antibody affinity shapes the choice between memory and germinal center B cell fates. *Cell* **183**, 1298–1311 (2020).

[CAS](#) [Google Scholar](#)

18. 18.

Rogers, T. F. et al. Isolation of potent SARS-CoV-2 neutralizing antibodies and protection from disease in a small animal model. *Science* **369**, 956–963 (2020).

[ADS](#) [CAS](#) [PubMed](#) [PubMed Central](#) [Google Scholar](#)

19. 19.

Kreer, C. et al. Longitudinal isolation of potent near-germline SARS-CoV-2-neutralizing antibodies from COVID-19 patients. *Cell* **182**, 1663–1673 (2020).

[CAS](#) [PubMed](#) [PubMed Central](#) [Google Scholar](#)

20. 20.

Stamatatos, L. et al. mRNA vaccination boosts cross-variant neutralizing antibodies elicited by SARS-CoV-2 infection. *Science* eabg9175 (2021).

21. 21.

Sokal, A. et al. Maturation and persistence of the anti-SARS-CoV-2 memory B cell response. *Cell* **184**, 1201–1213 (2021).

[CAS](#) [PubMed](#) [PubMed Central](#) [Google Scholar](#)

22. 22.

Sakharkar, M. et al. Prolonged evolution of the human B cell response to SARS-CoV-2 infection. *Sci. Immunol.* **6**, eabg6916 (2021).

[PubMed](#) [PubMed Central](#) [Google Scholar](#)

23. 23.

Barnes, C. O. et al. SARS-CoV-2 neutralizing antibody structures inform therapeutic strategies. *Nature* **588**, 682–687 (2020).

[ADS](#) [CAS](#) [PubMed](#) [PubMed Central](#) [Google Scholar](#)

24. 24.

Hoffmann, M. et al. SARS-CoV-2 cell entry depends on ACE2 and TMPRSS2 and is blocked by a clinically proven protease inhibitor. *Cell* **181**, 271–280 (2020).

[CAS](#) [PubMed](#) [PubMed Central](#) [Google Scholar](#)

25. 25.

Greaney, A. J. et al. Mutational escape from the polyclonal antibody response to SARS-CoV-2 infection is largely shaped by a single class of antibodies. Preprint at <https://doi.org/10.1101/2021.03.17.435863> (2021).

26. 26.

Weisblum, Y. et al. Escape from neutralizing antibodies by SARS-CoV-2 spike protein variants. *eLife* **9**, e61312 (2020).

[CAS](#) [PubMed](#) [PubMed Central](#) [Google Scholar](#)

27. 27.

Elsner, R. A. & Shlomchik, M. J. Germinal center and extrafollicular b cell responses in vaccination, immunity, and autoimmunity. *Immunity* **53**, 1136–1150 (2020).

[CAS](#) [Google Scholar](#)

28. 28.

Lau, A. W. & Brink, R. Selection in the germinal center. *Curr. Opin. Immunol.* **63**, 29–34 (2020).

[CAS](#) [Google Scholar](#)

29. 29.

Victora, G. D. & Nussenzweig, M. C. Germinal centers. *Annu. Rev. Immunol.* **30**, 429–457 (2012).

[CAS](#) [Google Scholar](#)

30. 30.

Inoue, T., Moran, I., Shinnakasu, R., Phan, T. G. & Kurosaki, T. Generation of memory B cells and their reactivation. *Immunol. Rev.* **283**, 138–149 (2018).

[CAS](#) [Google Scholar](#)

31. 31.

Taylor, J. J., Pape, K. A., Steach, H. R. & Jenkins, M. K. Humoral immunity. Apoptosis and antigen affinity limit effector cell differentiation of a single naïve B cell. *Science* **347**, 784–787 (2015)

[ADS](#) [CAS](#) [PubMed](#) [PubMed Central](#) [Google Scholar](#)

32. 32.

McKean, D. et al. Generation of antibody diversity in the immune response of BALB/c mice to influenza virus hemagglutinin. *Proc. Natl Acad. Sci. USA* **81**, 3180–3184 (1984).

[ADS](#) [CAS](#) [PubMed](#) [PubMed Central](#) [Google Scholar](#)

33. 33.

Petersen, M. S. et al. SARS-CoV-2 natural antibody response persists up to 12 months in a nationwide study from the Faroe Islands. Preprint at <https://doi.org/10.1101/2021.04.19.21255720> (2021).

34. 34.

Li, C. et al. Twelve-month specific IgG response to SARS-CoV-2 receptor-binding domain among COVID-19 convalescent plasma donors in Wuhan. Preprint at <https://doi.org/10.1101/2021.04.05.437224> (2021).

35. 35.

Turner, J. et al. SARS-CoV-2 mRNA vaccines induce a robust germinal centre reaction in humans. *Research Square* <https://www.researchsquare.com/article/rs-310773/v1> (2021).

36. 36.

Greaney, A. J. et al. The SARS-CoV-2 mRNA-1273 vaccine elicits more RBD-focused neutralization, but with broader antibody binding within the RBD. Preprint at <https://doi.org/10.1101/2021.04.14.439844> (2021).

37. 37.

Wang, Z. et al. Enhanced SARS-CoV-2 neutralization by dimeric IgA. *Sci. Transl. Med.* **13**, eabf1555 (2021).

[CAS](#) [Google Scholar](#)

38. 38.

Schoof, M. et al. An ultrapotent synthetic nanobody neutralizes SARS-CoV-2 by stabilizing inactive spike. *Science* **370**, 1473–1479 (2020).

[ADS](#) [CAS](#) [PubMed](#) [PubMed Central](#) [Google Scholar](#)

39. 39.

De Gasparo, R. et al. Bispecific IgG neutralizes SARS-CoV-2 variants and prevents escape in mice. *Nature* **593**, 424–428 (2021).

[ADS](#) [Google Scholar](#)

40. 40.

Xu, J. et al. Multimeric nanobodies from camelid engineered mice and llamas potently neutralize SARS-CoV-2 variants. Preprint at <https://doi.org/10.1101/2021.03.04.433768> (2021).

41. 41.

Wu, F. et al. A new coronavirus associated with human respiratory disease in China. *Nature* **579**, 265–269 (2020).

[ADS](#) [CAS](#) [PubMed](#) [PubMed Central](#) [Google Scholar](#)

42. 42.

Chomczynski, P. & Sacchi, N. Single-step method of RNA isolation by acid guanidinium thiocyanate-phenol-chloroform extraction. *Anal. Biochem.* **162**, 156–159 (1987).

[CAS](#) [PubMed](#) [PubMed Central](#) [Google Scholar](#)

43. 43.

DeAngelis, M. M., Wang, D. G. & Hawkins, T. L. Solid-phase reversible immobilization for the isolation of PCR products. *Nucleic Acids Res.* **23**, 4742–4743 (1995).

[CAS](#) [PubMed](#) [PubMed Central](#) [Google Scholar](#)

44. 44.

Grifoni, A. et al. Targets of T cell responses to SARS-CoV-2 coronavirus in humans with COVID-19 disease and unexposed individuals. *Cell* **181**, 1489–1501 (2020).

[CAS](#) [PubMed](#) [PubMed Central](#) [Google Scholar](#)

45. 45.

Amanat, F. et al. A serological assay to detect SARS-CoV-2 seroconversion in humans. *Nat. Med.* **26**, 1033–1036 (2020).

[CAS](#) [PubMed](#) [PubMed Central](#) [Google Scholar](#)

46. 46.

Barnes, C. O. et al. Structures of human antibodies bound to SARS-CoV-2 spike reveal common epitopes and recurrent features of antibodies. *Cell* **182**, 828–842 (2020).

[CAS](#) [PubMed](#) [PubMed Central](#) [Google Scholar](#)

47. 47.

Racine-Brzostek, S. E. et al. TOP-Plus is a versatile biosensor platform for monitoring SARS-CoV-2 antibody durability. *Clin. Chem.* hvab069 (2021).

48. 48.

Gupta, N. T. et al. Change-O: a toolkit for analyzing large-scale B cell immunoglobulin repertoire sequencing data. *Bioinformatics* **31**, 3356–3358 (2015).

[CAS](#) [PubMed](#) [PubMed Central](#) [Google Scholar](#)

49. 49.

Soto, C. et al. High frequency of shared clonotypes in human B cell receptor repertoires. *Nature* **566**, 398–402 (2019).

[ADS](#) [CAS](#) [PubMed](#) [PubMed Central](#) [Google Scholar](#)

50. 50.

Guo, Y., Chen, K., Kwong, P. D., Shapiro, L. & Sheng, Z. cAb-Rep: a database of curated antibody repertoires for exploring antibody diversity and predicting antibody prevalence. *Front. Immunol.* **10**, 2365 (2019).

[CAS](#) [PubMed](#) [PubMed Central](#) [Google Scholar](#)

51. 51.

Abascal, F., Zardoya, R. & Telford, M. J. TranslatorX: multiple alignment of nucleotide sequences guided by amino acid translations. *Nucleic Acids Res.* **38**, W7–W13 (2010).

[CAS](#) [PubMed](#) [PubMed Central](#) [Google Scholar](#)

52. 52.

Lefranc, M. P. IMGT, the International ImMunoGeneTics Information System. *Cold Spring Harb. Protoc.* **2011**, 595–603 (2011).

[Google Scholar](#)

53. 53.

DeWitt, W. S., III, Mesin, L., Victora, G. D., Minin, V. N. & Matsen, F. A., IV. Using genotype abundance to improve phylogenetic inference. *Mol. Biol. Evol.* **35**, 1253–1265 (2018).

[CAS](#) [PubMed](#) [PubMed Central](#) [Google Scholar](#)

[Download references](#)

Acknowledgements

We thank all study participants who devoted time to our research; The Rockefeller University Hospital nursing staff and Clinical Research Support Office and nursing staff; M. O. Frank, M. Bergh and R. B. Darnell for SARS-CoV-2 saliva PCR testing; P. J. Bjorkman and all members of the

M.C.N. laboratory for helpful discussions and M. Jankovic for laboratory support. This work was supported by NIH grant P01-AI138398-S1 (M.C.N., C.M.R. and P.J.B.) and 2U19AI111825 (M.C.N. and C.M.R.); George Mason University Fast Grants to C.M.R., 3 R01-AI091707-10S1 to C.M.R.; The G. Harold and Leila Y. Mathers Charitable Foundation to C.M.R.; NIH grant R37-AI64003 to P.D.B.; NIH grant R01AI78788 to T.H. We thank J. Vielmetter and the Protein Expression Center in the Beckman Institute at Caltech for expression assistance. C.O.B. is supported by the HHMI Hanna Gray and Burroughs Wellcome PDEP fellowships. C.G. was supported by the Robert S. Wenzel Post-Doctoral Fellowship, in part by the National Center for Advancing Translational Sciences (National Institutes of Health Clinical and Translational Science Award program, grant UL1 TR001866), and by the Shapiro–Silverberg Fund for the Advancement of Translational Research. P.D.B. and M.C.N. are Howard Hughes Medical Institute Investigators. F.M. is supported by the Bulgari Women & Science Fellowship in COVID-19 Research.

Author information

Author notes

1. These authors contributed equally: Zijun Wang, Frauke Muecksch, Dennis Schaefer-Babajew, Shlomo Finkin, Charlotte Viant, Christian Gaebler

Affiliations

1. Laboratory of Molecular Immunology, The Rockefeller University, New York, NY, USA

Zijun Wang, Dennis Schaefer-Babajew, Shlomo Finkin, Charlotte Viant, Christian Gaebler, Melissa Cipolla, Victor Ramos, Thiago Y. Oliveira, Alice Cho, Mridushi Daga, Martina Turroja, Katrina G. Millard, Mila Jankovic, Anna Gazumyan, Marina Caskey & Michel C. Nussenzweig

2. Laboratory of Retrovirology, The Rockefeller University, New York, NY, USA

Frauke Muecksch, Fabian Schmidt, Justin Da Silva, Eva Bednarski, Paul D. Bieniasz & Theodora Hatzioannou

3. Laboratory of Virology and Infectious Disease, The Rockefeller University, New York, NY, USA

Hans- Heinrich Hoffmann, Lauren Aguado & Charles M. Rice

4. Division of Biology and Biological Engineering, California Institute of Technology, Pasadena, CA, USA

Christopher O. Barnes

5. Department of Pathology and Laboratory Medicine, Weill Cornell Medicine, New York, NY, USA

Jim Yee & Zhen Zhao

6. Howard Hughes Medical Institute, New York, NY, USA

Anna Gazumyan, Paul D. Bieniasz & Michel C. Nussenzweig

Authors

1. Zijun Wang

[View author publications](#)

You can also search for this author in [PubMed](#) [Google Scholar](#)

2. Frauke Muecksch

[View author publications](#)

You can also search for this author in [PubMed](#) [Google Scholar](#)

3. Dennis Schaefer-Babajew

[View author publications](#)

You can also search for this author in [PubMed](#) [Google Scholar](#)

4. Shlomo Finkin

[View author publications](#)

You can also search for this author in [PubMed](#) [Google Scholar](#)

5. Charlotte Viant

[View author publications](#)

You can also search for this author in [PubMed](#) [Google Scholar](#)

6. Christian Gaebler

[View author publications](#)

You can also search for this author in [PubMed](#) [Google Scholar](#)

7. Hans- Heinrich Hoffmann

[View author publications](#)

You can also search for this author in [PubMed](#) [Google Scholar](#)

8. Christopher O. Barnes

[View author publications](#)

You can also search for this author in [PubMed](#) [Google Scholar](#)

9. Melissa Cipolla

[View author publications](#)

You can also search for this author in [PubMed](#) [Google Scholar](#)

10. Victor Ramos

[View author publications](#)

You can also search for this author in [PubMed](#) [Google Scholar](#)

11. Thiago Y. Oliveira

[View author publications](#)

You can also search for this author in [PubMed](#) [Google Scholar](#)

12. Alice Cho

[View author publications](#)

You can also search for this author in [PubMed](#) [Google Scholar](#)

13. Fabian Schmidt

[View author publications](#)

You can also search for this author in [PubMed](#) [Google Scholar](#)

14. Justin Da Silva

[View author publications](#)

You can also search for this author in [PubMed](#) [Google Scholar](#)

15. Eva Bednarski

[View author publications](#)

You can also search for this author in [PubMed](#) [Google Scholar](#)

16. Lauren Aguado

[View author publications](#)

You can also search for this author in [PubMed](#) [Google Scholar](#)

17. Jim Yee

[View author publications](#)

You can also search for this author in [PubMed](#) [Google Scholar](#)

18. Mridushi Daga

[View author publications](#)

You can also search for this author in [PubMed](#) [Google Scholar](#)

19. Martina Turroja

[View author publications](#)

You can also search for this author in [PubMed](#) [Google Scholar](#)

20. Katrina G. Millard

[View author publications](#)

You can also search for this author in [PubMed](#) [Google Scholar](#)

21. Mila Jankovic

[View author publications](#)

You can also search for this author in [PubMed](#) [Google Scholar](#)

22. Anna Gazumyan

[View author publications](#)

You can also search for this author in [PubMed](#) [Google Scholar](#)

23. Zhen Zhao

[View author publications](#)

You can also search for this author in [PubMed](#) [Google Scholar](#)

24. Charles M. Rice

[View author publications](#)

You can also search for this author in [PubMed](#) [Google Scholar](#)

25. Paul D. Bieniasz

[View author publications](#)

You can also search for this author in [PubMed](#) [Google Scholar](#)

26. Marina Caskey

[View author publications](#)

You can also search for this author in [PubMed](#) [Google Scholar](#)

27. Theodora Hatzioannou

[View author publications](#)

You can also search for this author in [PubMed](#) [Google Scholar](#)

28. Michel C. Nussenzweig
[View author publications](#)

You can also search for this author in [PubMed](#) [Google Scholar](#)

Contributions

P.D.B., T.H., C.M.R. and M.C.N. conceived, designed and analysed the experiments. M. Caskey and C.G. designed clinical protocols. Z.W., F.M., D.S.-B., S.F., C.V., H.-H.H., C.O.B., A.C., F.S., J.D.S., E.B., L.A., J.Y., M.J. and Z.Z. carried out experiments. A.G. and M. Cipolla produced antibodies. D.S.-B., M.D., M.T., K.G.M., C.G. and M. Caskey recruited participants, executed clinical protocols and processed samples. T.Y.O. and V.R. performed bioinformatic analysis. Z.W., F.M., D.S.-B., C.G. and M.C.N. wrote the manuscript with input from all co-authors.

Corresponding authors

Correspondence to [Paul D. Bieniasz](#) or [Marina Caskey](#) or [Theodora Hatzioannou](#) or [Michel C. Nussenzweig](#).

Ethics declarations

Competing interests

The Rockefeller University has filed a provisional patent application in connection with this work on which M.C.N. is an inventor (US patent 63/021,387). The patent has been licensed by Rockefeller University to Bristol Meyers Squib. Z.Z. received seed instruments and sponsored research funding from ET Healthcare.

Additional information

Peer review information *Nature* thanks Thushan de Silva, Pei-Yong Shi and the other, anonymous, reviewer(s) for their contribution to the peer review of this work.

Publisher's note Springer Nature remains neutral with regard to jurisdictional claims in published maps and institutional affiliations.

Extended data figures and tables

Extended Data Fig. 1 Clinical correlations.

a–d, Association of persistence of symptoms (Sx) 12 months after infection with various clinical and serological parameters in our cohort of individuals who recovered from COVID-19 ($n = 63$). **a, b**, Acute disease severity as assessed with the WHO Ordinal Scale of Clinical Improvement (**a**, $P = 0.99$) and duration of acute phase symptoms (**b**, $P = 0.63$) in individuals reporting persistent symptoms (+) compared to individuals who are symptom-free (−) 12 months post-infection. **c**, Proportion of individuals reporting persistent symptoms (black area) compared to individuals who are symptom-free (grey area) 12 months after infection grouped by vaccination status ($P = 0.72$). **d**, Anti-RBD IgG ($P = 0.75$), anti-N IgG ($P = 0.15$), the RBD/N IgG ratio ($P = 0.73$), and NT₅₀ titers ($P = 0.38$) at 12 months after infection in individuals reporting persistent symptoms (+) compared to individuals who are symptom-free (−) 12 months post-infection. Statistical significance was determined using the two-tailed Mann–Whitney test in **a, b, d**, and using the two-sided Fisher’s exact test in **c**.

Extended Data Fig. 2 Plasma activity.

a–h, ELISA results for plasma against SARS-CoV-2 RBD 12 months after infection ($n = 63$). Non-vaccinated individuals are depicted with black circles and lines, and vaccinated individuals are depicted in blue throughout. Two outlier individuals who received their first dose of vaccine 24–48 h before sample collection is depicted as purple circles. **a–n**, IgM (**a–d**) IgG (**e–g**) and IgA (**h–k**) antibody binding to SARS-CoV-2 RBD and IgG binding to N (**l–n**) 12 months after infection. **a, e, h, i**, ELISA curves from non-vaccinated (black lines) individuals, as well as individuals who received one or two doses (blue lines) of a COVID-19 mRNA vaccine (left panels). Area under the curve (AUC) over time in non-vaccinated (**b, f, i, m**) and vaccinated individuals (**c, g, j, n**). Lines connect longitudinal samples. **d, k**, Boxplots showing AUC values of all 63 individuals, as indicated. **o**, ranked average NT₅₀ at 1.3 months (light grey) and 6.2 months (dark grey), as well as at 12 months for non-vaccinated (orange)

individuals, and individuals who received one or two doses (blue circles) of a COVID-19 mRNA vaccine, respectively. Two individuals who received their first dose of vaccine 24–48 h before sample collection is depicted in purple. **p–r**, Correlation of serological parameters in non-vaccinated (black circles and black statistics) and vaccinated (blue circles and blue statistics) individuals. Two individuals who received their first dose of vaccine 24–48 h before sample collection is depicted as purple circles. Correlation of 12-month titers of anti-RBD IgG and NT₅₀ (**p**), anti-RBD IgG and N IgG (**q**), and anti-N IgG and NT₅₀ (**r**). **s**, Plasma neutralizing activity against authentic virus isolates WA1/2020 and B.1.351, as indicated ($n = 6$). Statistical significance was determined using two-sided Friedman test with subsequent Dunn's multiple comparisons (**b**, **c**, **f**, **g**, **i**, **j**, **m**, **n**), or two-sided Kruskal–Wallis test with subsequent Dunn's multiple comparisons (**d**, **k**) or using the Spearman correlation test for the non-vaccinated and vaccinated subgroups independently (**p–r**) or using two-tailed Mann–Whitney test (**s**). Red numbers indicate the geometric mean NT₅₀ at the indicated time point. All experiments were performed at least in duplicate.

Extended Data Fig. 3 Flow cytometry.

a, Gating strategy. Gating was on singlets that were CD20⁺ and CD3-CD8-CD16-Ova-. Anti-IgG, IgM, and IgA antibodies were used for B cell phenotype analysis. Sorted cells were RBD-PE⁺ and RBD/KEN-AF647⁺. **b**, **c**, Flow cytometry showing the percentage of RBD-double positive (**b**) and 647-K417N/E484K/N501Y mutant RBD cross-reactive (**c**) memory B cells from 1.3 or 6- and 12-months post-infection in 10 selected participants. **d**, As in Fig. 2b, Pie charts show the distribution of antibody sequences from 4 individuals after 1.3³ (upper panel) or 6.2⁴ months (middle panel) or 12 months (lower panel). **e**, Circos plot depicts the relationship between antibodies that share V and J gene segment sequences at both IGH and IGL. Purple, green, and grey lines connect related clones, clones and singles, and singles to each other, respectively. **f**, Graph summarizes cell number (indicated in **b**, **c**) (per 2 million B cells) of immunoglobulin class of antigens binding memory B cells in samples obtained at 1.3, 6.2 and 12 months. Each dot is one individual. (Vaccinees, $n = 20$, and non-vaccinees, $n = 20$). Red horizontal bars indicate mean values. Statistical significance

was determined using two-sided Kruskal–Wallis test with subsequent Dunn’s multiple comparisons.

Extended Data Fig. 4 Frequency distribution of human V genes.

Graph shows comparison of the frequency distributions of human V genes of anti-SARS-CoV-2 antibodies from donors at 1.3³, 6.2⁴, 12 months after infection. **a**, Graph shows relative abundance of human IGVH genes Sequence Read Archive accession SRP010970 (green), convalescent vaccinees (blue), and convalescent non-vaccinees (orange). Statistical significance was determined by two-sided binomial test. **b, c**, Same as in **a**, but showing comparison between antibodies from donors at 1.3 months³ (**b**), 6.2 month⁴ (**c**) and 12 months after infection. Two-sided binomial tests with unequal variance were used to compare the frequency distributions., significant differences are denoted with stars (* $P < 0.05$, ** $P < 0.01$, *** $P < 0.001$, **** = $P < 0.0001$).

Extended Data Fig. 5 Analysis of anti-RBD antibodies.

a, Number of clonally expanded B cells (per 10 million B cells) at indicated time points in 10 individuals. Colours indicate shared clones appearing at different time points. Statistical significance was determined using two-tailed Wilcoxon matched-pairs signed rank test. Vaccinees are marked in red. Statistical significance was determined using Wilcoxon matched-pairs signed rank tests. Vaccinees are marked in red. **b**, Number of somatic nucleotide mutations in the IGVH (top) and IGVL (bottom) in antibodies obtained after 1.3 or 6.2 or 12 months from the indicated individual. **c**, Same as **b**, but graphs show comparison between new clones and conserved clones in 6 vaccinated convalescent individuals at 12 months after infection. **d**, The amino acid length of the CDR3 s at the IGVH and IGVL for each individual. Right panel shows all antibodies combined. (1.3m: $n = 889$; 6.2m: $n = 975$; 12m: $n = 1105$, (non-vax: $n = 417$; vax: $n = 688$)). The horizontal bars indicate the mean. Statistical significance was determined using two-sided Kruskal–Wallis test with subsequent Dunn’s multiple comparisons (**a, b, d**), or two-tailed Mann–Whitney U-tests (**c**).

Extended Data Fig. 6 Evolution of anti-SARS-CoV-2 RBD antibody clone.

Clonal evolution of RBD-binding memory B cells from ten convalescent individuals, **a**, Phylogenetic tree graph shows clones from convalescent non-vaccinees, **b**, Same as **a**, but from convalescent vaccinees. Numbers refer to mutations compared to the preceding vertical node. Colours indicate time point; grey, orange and red represent 1.3, 6 and 12 months respectively, black dots indicate inferred nodes, and size is proportional to sequence copy number; GL = germline sequence.

Extended Data Fig. 7 WT RBD binding and pseudovirus neutralization.

a, b, Binding curves (**a**) and EC₅₀ dot plot (**b**) of mAbs isolated from non-vaccinated (black curves and dots) and from vaccinated (blue curves and dots) convalescents individuals 12 months after infection ($P = 0.74$). **c**, Avidity (dissociation rate) measuring plasma reactivity to RBD at the 1.3- and 12 month follow-up visit ($n = 33$). **d–f**, IC₅₀ values of mAbs isolated 12 months after infection from non-vaccinated and vaccinated individuals; all 12 month antibodies irrespective of clonality (**d**), singlets only (**e**), and only antibodies belonging to a clone or shared over time (**f**). Statistical significance in **b, d–f** was determined using the two-tailed Mann–Whitney test; two-tailed Wilcoxon test (**c**). The geometric mean EC₅₀ and IC₅₀ are indicated in red. **g**, Heat map shows the neutralizing activity of clonally related antibodies against wt-SARS-CoV-2 over time. White tiles indicate no clonal relative at the respective time point. Clones are ranked from left to right by the potency of the 12 month progeny antibodies which are denoted below the tiles. **h**, IC₅₀ values of shared clones of mAbs cloned from B cells from the initial 1.3- and 6.2-, as well as 12 month follow-up visit, divided by participant, as indicated. Lines connect clonal antibodies shared between time points. Antibodies with IC₅₀ > 1,000 ng/ml are plotted at 1,000 ng/ml in **d–h**. **i**, IC₅₀ values of 5 neutralizing antibody pairs against indicated authentic SARS-CoV-2 WA1/2020 and B.1.351 viruses ($n = 10$). Average EC₅₀ and IC₅₀ values of two independent experiments are shown.

Extended Data Fig. 8 Biolayer interferometry affinity measurements.

a, b, Graphs depict affinity measurements of neutralizing (green) and non-neutralizing (red) antibodies isolated 1.3 months (**a**) or 12 months (**b**) after infection.

Extended Data Fig. 9 Biolayer interferometry antibody competition experiment.

a, b, Anti-SARS-CoV-2 RBD antibodies isolated 1.3 (**a**) or 12 months (**b**) after infection were assayed for competition with structurally characterized anti-RBD antibodies by biolayer interferometry experiments as in Fig. [4a](#). Graphs represent the binding of the second antibody (2nd Ab) to preformed first antibody (1st Ab)-RBD complexes. Dotted line denotes when 1st Ab and 2nd Ab are the same. For each antibody group identified in Fig. [4c](#) the left graphs represent the binding of the class-representative C144, C121, C135 or C105^{[3,23](#)} (2nd Ab) to the candidate antibody (1st Ab)-RBD complex. The right graphs represent the binding of the candidate antibody (2nd Ab) to the complex of C144-RBD, C121-RBD, C135-RBD or C105-RBD (1st Ab). Antibodies belonging to the same groups are indicated to the left of the respective curves.

Supplementary information

Reporting Summary

Supplementary Table 1

Cohort summary.

Supplementary Table 2

Individual participant characteristics.

Supplementary Table 3

Sequences of anti-SARS-CoV-2 RBD IgG antibodies.

Supplementary Table 4

Sequences, half maximal effective concentrations (EC50s) and inhibitory concentrations (IC50s) of the cloned monoclonal antibodies.

Supplementary Table 5

Binding and Neutralization activity of mAbs against mutant SARS-CoV-2 pseudoviruses.

Supplementary Table 6

Neutralization activity of mAbs against mutant SARS-CoV-2 pseudoviruses
- Random potently neutralizing antibodies isolated at 1.3 and 12 months.

Supplementary Table 7

Antibody affinities and neutralization - Clonal pairs isolated at 1.3 and 12 months.

Supplementary Table 8

Neutralization activity of mAbs against mutant SARS-CoV-2 pseudoviruses
- Clonal pairs isolated at 1.3 and 12 months.

Rights and permissions

Open Access This article is licensed under a Creative Commons Attribution 4.0 International License, which permits use, sharing, adaptation, distribution and reproduction in any medium or format, as long as you give appropriate credit to the original author(s) and the source, provide a link to the Creative Commons license, and indicate if changes

were made. The images or other third party material in this article are included in the article's Creative Commons license, unless indicated otherwise in a credit line to the material. If material is not included in the article's Creative Commons license and your intended use is not permitted by statutory regulation or exceeds the permitted use, you will need to obtain permission directly from the copyright holder. To view a copy of this license, visit <http://creativecommons.org/licenses/by/4.0/>.

[Reprints and Permissions](#)

About this article



Check for
updates

Cite this article

Wang, Z., Muecksch, F., Schaefer-Babajew, D. *et al.* Naturally enhanced neutralizing breadth against SARS-CoV-2 one year after infection. *Nature* **595**, 426–431 (2021). <https://doi.org/10.1038/s41586-021-03696-9>

[Download citation](#)

- Received: 02 May 2021
- Accepted: 04 June 2021
- Published: 14 June 2021
- Issue Date: 15 July 2021
- DOI: <https://doi.org/10.1038/s41586-021-03696-9>

Further reading

- [A long-term perspective on immunity to COVID](#)

- Andreas Radbruch
- & Hyun-Dong Chang

Nature (2021)

Comments

By submitting a comment you agree to abide by our [Terms](#) and [Community Guidelines](#). If you find something abusive or that does not comply with our terms or guidelines please flag it as inappropriate.

[Download PDF](#)

Associated Content

[A long-term perspective on immunity to COVID](#)

- Andreas Radbruch
- Hyun-Dong Chang

[Is one vaccine dose enough if you've had COVID? What the science says](#)

- Elie Dolgin

Advertisement

This article was downloaded by **calibre** from <https://www.nature.com/articles/s41586-021-03696-9>

- Article
- [Published: 16 June 2021](#)

ctDNA guiding adjuvant immunotherapy in urothelial carcinoma

- [Thomas Powles](#) ORCID: orcid.org/0000-0001-7760-4724^{1 na1},
- [Zoe June Assaf](#)^{2 na1},
- [Nicole Davarpanah](#)²,
- [Romain Banchereau](#)²,
- [Bernadett E. Szabados](#)³,
- [Kobe C. Yuen](#)²,
- [Petros Grivas](#)^{4,5,6},
- [Maha Hussain](#)⁷,
- [Stephane Oudard](#)⁸,
- [Jürgen E. Gschwend](#)⁹,
- [Peter Albers](#)¹⁰,
- [Daniel Castellano](#)¹¹,
- [Hiroyuki Nishiyama](#)¹²,
- [Siamak Daneshmand](#)¹³,
- [Shruti Sharma](#)¹⁴,
- [Bernhard G. Zimmermann](#)¹⁴,
- [Himanshu Sethi](#)¹⁴,
- [Alexey Aleshin](#)¹⁴,
- [Maurizio Perdicchio](#)¹⁵,
- [Jingbin Zhang](#)¹⁶,
- [David S. Shames](#)²,
- [Viraj Degaonkar](#)²,
- [Xiaodong Shen](#)²,

- [Corey Carter²](#),
- [Carlos Bais²](#),
- [Joaquim Bellmunt](#) ORCID: orcid.org/0000-0003-2328-3421^{17 na2} &
- [Sanjeev Mariathasan](#) ^{2 na2}

[Nature](#) volume **595**, pages 432–437 (2021)[Cite this article](#)

- 10k Accesses
- 422 Altmetric
- [Metrics details](#)

Subjects

- [Bladder cancer](#)
- [Predictive markers](#)

Abstract

Minimally invasive approaches to detect residual disease after surgery are needed to identify patients with cancer who are at risk for metastatic relapse. Circulating tumour DNA (ctDNA) holds promise as a biomarker for molecular residual disease and relapse¹. We evaluated outcomes in 581 patients who had undergone surgery and were evaluable for ctDNA from a randomized phase III trial of adjuvant atezolizumab versus observation in operable urothelial cancer. This trial did not reach its efficacy end point in the intention-to-treat population. Here we show that ctDNA testing at the start of therapy (cycle 1 day 1) identified 214 (37%) patients who were positive for ctDNA and who had poor prognosis (observation arm hazard ratio = 6.3 (95% confidence interval: 4.45–8.92); $P < 0.0001$). Notably, patients who were positive for ctDNA had improved disease-free survival and overall survival in the atezolizumab arm versus the observation arm (disease-free survival hazard ratio = 0.58 (95% confidence interval: 0.43–0.79); $P = 0.0024$, overall survival hazard ratio = 0.59 (95% confidence interval: 0.41–0.86)). No difference in disease-free survival or overall survival between treatment arms was noted for patients who were negative

for ctDNA. The rate of ctDNA clearance at week 6 was higher in the atezolizumab arm (18%) than in the observation arm (4%) ($P = 0.0204$). Transcriptomic analysis of tumours from patients who were positive for ctDNA revealed higher expression levels of cell-cycle and keratin genes. For patients who were positive for ctDNA and who were treated with atezolizumab, non-relapse was associated with immune response signatures and basal–squamous gene features, whereas relapse was associated with angiogenesis and fibroblast TGF β signatures. These data suggest that adjuvant atezolizumab may be associated with improved outcomes compared with observation in patients who are positive for ctDNA and who are at a high risk of relapse. These findings, if validated in other settings, would shift approaches to postoperative cancer care.

Access options

Subscribe to Journal

Get full journal access for 1 year

\$199.00

only \$3.90 per issue

[Subscribe](#)

All prices are NET prices.

VAT will be added later in the checkout.

Tax calculation will be finalised during checkout.

Rent or Buy article

Get time limited or full article access on ReadCube.

from \$8.99

[Rent or Buy](#)

All prices are NET prices.

Additional access options:

- [Log in](#)
- [Access through your institution](#)
- [Learn about institutional subscriptions](#)

Fig. 1: Kaplan–Meier estimates among patients evaluated for post-surgical ctDNA status.



Fig. 2: Changes in ctDNA status from baseline to on-treatment (IMvigor010) or post-treatment (ABACUS) time points.

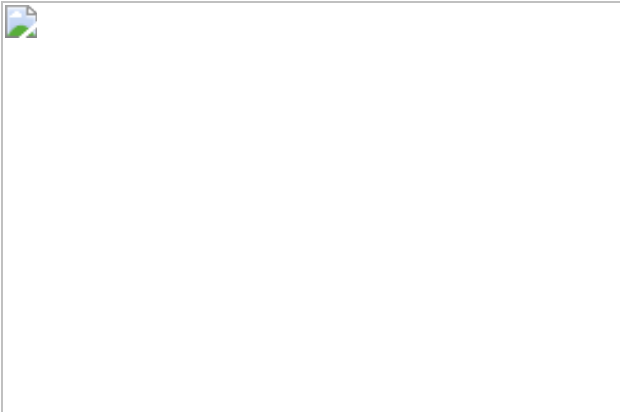


Fig. 3: Transcriptional correlates of ctDNA positivity and biomarkers for response to atezolizumab within the ctDNA⁺ population.

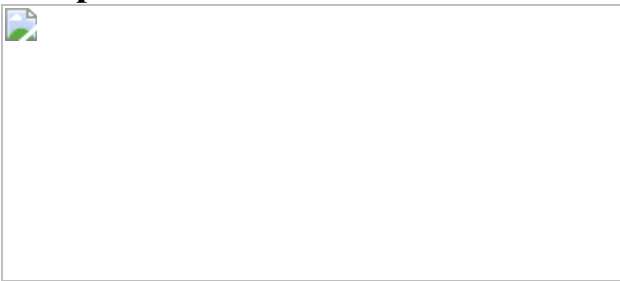
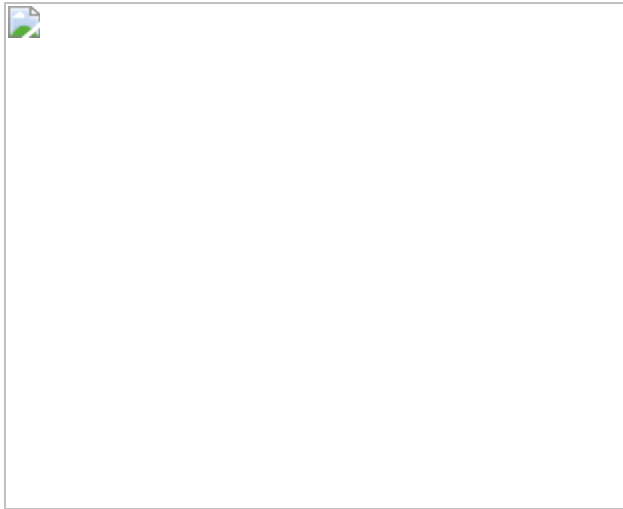


Fig. 4: TCGA subtypes and correlates of relapse.



Data availability

All clinical, ctDNA and raw RNA-seq data for IMvigor010 are deposited to the European Genome-Phenome Archive under accession number [EGAS00001004997](#). All clinical and ctDNA data for the ABACUS trial are deposited to the European Genome-Phenome Archive under accession number [EGAS00001004445](#). Public datasets that were used during data processing included 1000 Genomes Project (<https://www.internationalgenome.org/>), ExAC (<http://exac.broadinstitute.org/>), ESP (<https://esp.gs.washington.edu/drupal/>), dbSNP (<https://www.ncbi.nlm.nih.gov/snp/>) and Molecular Signature Database (<http://www.gsea-msigdb.org/gsea/msigdb/>)³³. Qualified researchers may request access to individual patient-level data through the clinical study data request platform (<https://vivli.org/>). Further details on Roche's criteria for eligible studies are available at <https://vivli.org/members/ourmembers>. For further details on Roche's Global Policy on the Sharing of Clinical Information and how to request access to related clinical study documents, see https://www.roche.com/research_and_development/who_we_are_how_we_work/clinical_trials/our_commitment_to_data_sharing.htm.

Code availability

The fully documented code for the R statistical computing environment for analyses related to IMvigor010 are deposited to the European Genome-Phenome Archive under accession number [EGAS00001004997](#), and for analyses related to the ABACUS trial under accession number [EGAS00001004445](#).

References

1. 1.

Chin, R. I. et al. Detection of solid tumor molecular residual disease (MRD) using circulating tumor DNA (ctDNA). *Mol. Diagn. Ther.* **23**, 311–331 (2019).

[CAS](#) [Article](#) [Google Scholar](#)

2. 2.

Christensen, E. et al. Early detection of metastatic relapse and monitoring of therapeutic efficacy by ultra-deep sequencing of plasma cell-free DNA in patients with urothelial bladder carcinoma. *J. Clin. Oncol.* **37**, 1547–1557 (2019).

[CAS](#) [Article](#) [Google Scholar](#)

3. 3.

Abbosh, C. et al. Phylogenetic ctDNA analysis depicts early-stage lung cancer evolution. *Nature* **545**, 446–451 (2017).

[ADS](#) [CAS](#) [Article](#) [Google Scholar](#)

4. 4.

Thomsen, M. B. H. et al. Comprehensive multiregional analysis of molecular heterogeneity in bladder cancer. *Sci. Rep.* **7**, 11702 (2017).

[ADS](#) [Article](#) [Google Scholar](#)

5. 5.

Snyder, A., Morrissey, M. P. & Hellmann, M. D. Use of circulating tumor DNA for cancer immunotherapy. *Clin. Cancer Res.* **25**, 6909–6915 (2019).

[CAS](#) [Article](#) [Google Scholar](#)

6. 6.

Corcoran, R. B. & Chabner, B. A. Application of cell-free DNA analysis to cancer treatment. *N. Engl. J. Med.* **379**, 1754–1765 (2018).

[CAS](#) [Article](#) [Google Scholar](#)

7. 7.

Turner, N. C. et al. Circulating tumour DNA analysis to direct therapy in advanced breast cancer (plasmaMATCH): a multicentre, multicohort, phase 2a, platform trial. *Lancet Oncol.* **21**, 1296–1308 (2020).

[CAS](#) [Article](#) [Google Scholar](#)

8. 8.

Nuzzo, P. V. et al. Detection of renal cell carcinoma using plasma and urine cell-free DNA methylomes. *Nat. Med.* **26**, 1041–1043 (2020).

[CAS](#) [Article](#) [Google Scholar](#)

9. 9.

Tie, J. et al. Circulating tumor DNA analysis detects minimal residual disease and predicts recurrence in patients with stage II colon cancer. *Sci. Transl. Med.* **8**, 346ra92 (2016).

[Article](#) [Google Scholar](#)

10. 10.

Garcia-Murillas, I. et al. Assessment of molecular relapse detection in early-stage breast cancer. *JAMA Oncol.* **5**, 1473–1478 (2019).

[Article](#) [Google Scholar](#)

11. 11.

Bratman, S. V. et al. Personalized circulating tumor DNA analysis as a predictive biomarker in solid tumor patients treated with pembrolizumab. *Nat. Cancer* **1**, 873–881 (2020).

[Article](#) [Google Scholar](#)

12. 12.

Nabet, B. Y. et al. Noninvasive early identification of therapeutic benefit from immune checkpoint inhibition. *Cell* **183**, 363–376.e13 (2020).

[CAS](#) [Article](#) [Google Scholar](#)

13. 13.

Zhang, Q. et al. Prognostic and predictive impact of circulating tumor DNA in patients with advanced cancers treated with immune checkpoint blockade. *Cancer Discov.* **10**, 1842–1853 (2020).

[CAS](#) [Article](#) [Google Scholar](#)

14. 14.

Chan, A. T. C. et al. Analysis of plasma Epstein–Barr virus DNA in nasopharyngeal cancer after chemoradiation to identify high-risk patients for adjuvant chemotherapy: a randomized controlled trial. *J. Clin. Oncol.* **36**, 3091–3100 (2018).

[CAS](#) [Article](#) [Google Scholar](#)

15. 15.

Taieb, J. et al. Analysis of circulating tumour DNA (ctDNA) from patients enrolled in the IDEA-FRANCE phase III trial: prognostic and predictive value for adjuvant treatment duration. *Ann. Oncol.* **30**, v867 (2019).

[Article](#) [Google Scholar](#)

16. 16.

Bellmunt, J. et al. Adjuvant atezolizumab versus observation in muscle-invasive urothelial carcinoma (IMvigor010): a multicentre, open-label, randomised, phase 3 trial. *Lancet Oncol.* **22**, 525–537 (2021).

[Article](#) [Google Scholar](#)

17. 17.

Stein, J. P. et al. Radical cystectomy in the treatment of invasive bladder cancer: long-term results in 1,054 patients. *J. Clin. Oncol.* **19**, 666–675 (2001).

[CAS](#) [Article](#) [Google Scholar](#)

18. 18.

Balar, A. V. et al. Atezolizumab as first-line treatment in cisplatin-ineligible patients with locally advanced and metastatic urothelial carcinoma: a single-arm, multicentre, phase 2 trial. *Lancet* **389**, 67–76 (2017).

[CAS](#) [Article](#) [Google Scholar](#)

19. 19.

Rosenberg, J. E. et al. Atezolizumab in patients with locally advanced and metastatic urothelial carcinoma who have progressed following

treatment with platinum-based chemotherapy: a single-arm, multicentre, phase 2 trial. *Lancet* **387**, 1909–1920 (2016).

[CAS](#) [Article](#) [Google Scholar](#)

20. 20.

Horn, L. et al. First-line atezolizumab plus chemotherapy in extensive-stage small-cell lung cancer. *N. Engl. J. Med.* **379**, 2220–2229 (2018).

[CAS](#) [Article](#) [Google Scholar](#)

21. 21.

Powles, T. et al. Atezolizumab versus chemotherapy in patients with platinum-treated locally advanced or metastatic urothelial carcinoma (IMvigor211): a multicentre, open-label, phase 3 randomised controlled trial. *Lancet* **391**, 748–757 (2018).

[CAS](#) [Article](#) [Google Scholar](#)

22. 22.

Powles, T. et al. Clinical efficacy and biomarker analysis of neoadjuvant atezolizumab in operable urothelial carcinoma in the ABACUS trial. *Nat. Med.* **25**, 1706–1714 (2019).

[CAS](#) [Article](#) [Google Scholar](#)

23. 23.

Hellmann, M. D. et al. Nivolumab plus ipilimumab in lung cancer with a high tumor mutational burden. *N. Engl. J. Med.* **378**, 2093–2104 (2018).

[CAS](#) [Article](#) [Google Scholar](#)

24. 24.

Mariathasan, S. et al. TGF β attenuates tumour response to PD-L1 blockade by contributing to exclusion of T cells. *Nature* **554**, 544–548 (2018).

[ADS](#) [CAS](#) [Article](#) [Google Scholar](#)

25. 25.

Robertson, A. G. et al. Comprehensive molecular characterization of muscle-invasive bladder cancer. *Cell* **171**, 540–556.e25 (2017).

[CAS](#) [Article](#) [Google Scholar](#)

26. 26.

Bajorin, D. F. et al. First results from the phase 3 CheckMate 274 trial of adjuvant nivolumab vs placebo in patients who underwent radical surgery for high-risk muscle-invasive urothelial carcinoma (MIUC). *J. Clin. Oncol.* **39**, 391 (2021).

[Article](#) [Google Scholar](#)

27. 27.

Tan, L. et al. Prediction and monitoring of relapse in stage III melanoma using circulating tumor DNA. *Ann. Oncol.* **30**, 804–814 (2019).

[CAS](#) [Article](#) [Google Scholar](#)

28. 28.

Reinert, T. et al. Analysis of plasma cell-free DNA by ultradeep sequencing in patients with stages I to III colorectal cancer. *JAMA Oncol.* **5**, 1124–1131 (2019).

[Article](#) [Google Scholar](#)

29. 29.

Coombes, R. C. et al. Personalized detection of circulating tumor DNA antedates breast cancer metastatic recurrence. *Clin. Cancer Res.* **25**, 4255–4263 (2019).

[CAS](#) [Article](#) [Google Scholar](#)

30. 30.

Wu, T. D. & Nacu, S. Fast and SNP-tolerant detection of complex variants and splicing in short reads. *Bioinformatics* **26**, 873–881 (2010).

[CAS](#) [Article](#) [Google Scholar](#)

31. 31.

Wu, T. D., Reeder, J., Lawrence, M., Becker, G. & Brauer, M. J. GMAP and GSNAP for genomic sequence alignment: enhancements to speed, accuracy, and functionality. *Methods Mol. Biol.* **1418**, 283–334 (2016).

[Article](#) [Google Scholar](#)

32. 32.

Wu, D. & Smyth, G. K. Camera: a competitive gene set test accounting for inter-gene correlation. *Nucleic Acids Res.* **40**, e133 (2012).

[CAS](#) [Article](#) [Google Scholar](#)

33. 33.

Subramanian, A. et al. Gene set enrichment analysis: a knowledge-based approach for interpreting genome-wide expression profiles. *Proc. Natl Acad. Sci. USA* **102**, 15545–15550 (2005).

[ADS](#) [CAS](#) [Article](#) [Google Scholar](#)

[Download references](#)

Acknowledgements

The study was sponsored by F. Hoffmann-La Roche Ltd/Genentech, Inc. We thank the patients who participated in the trial and the clinical site investigators, the Barts Health Experimental Cancer Medicine Centre (CRUK), A. Yiu and M. Ravasz from Fios Genomics for additional help with transcriptomic analysis, S. Flynn, K. Zvonar and D. Rishipathak of the Genentech Biomarker Operations Team for providing support in the generation and analysis of the data, and E. E. Kadel III from the Genentech Biomarker Development team for data integration. Medical writing assistance for this manuscript was provided by H. Grewal and Z. Augur of Anshin Biosolutions, M. Malhotra of Natera and A. J. Pratt of Health Interactions, Inc., and was funded by F. Hoffmann-La Roche Ltd. M. Jacobson and J. Ball contributed to research funding for the ABACUS cohort.

Author information

Author notes

1. These authors contributed equally: Thomas Powles, Zoe June Assaf
2. These authors jointly supervised this work: Joaquim Bellmunt, Sanjeev Mariathasan

Affiliations

1. Barts Cancer Institute, Queen Mary University of London ECMC, Barts Health, London, UK

Thomas Powles

2. Roche/Genentech, South San Francisco, CA, USA

Zoe June Assaf, Nicole Davarpanah, Romain Banchereau, Kobe C. Yuen, David S. Shames, Viraj Degaonkar, Xiaodong Shen, Corey Carter, Carlos Bais & Sanjeev Mariathasan

3. Barts Cancer Institute, Queen Mary University of London, London, UK

Bernadett E. Szabados

4. University of Washington, Seattle, WA, USA

Petros Grivas

5. Seattle Cancer Care Alliance, Seattle, WA, USA

Petros Grivas

6. Fred Hutchinson Cancer Research Center, Seattle, WA, USA

Petros Grivas

7. Robert H. Lurie Comprehensive Cancer Center, Northwestern University, Chicago, IL, USA

Maha Hussain

8. Georges Pompidou European Hospital, University of Paris, Paris, France

Stephane Oudard

9. Rechts der Isar Medical Center, Department of Urology, Technical University Munich, Munich, Germany

Jürgen E. Gschwend

10. Heinrich-Heine University Düsseldorf, Medical Faculty, Department of Urology, University Hospital Düsseldorf, Düsseldorf, Germany

Peter Albers

11. University Hospital 12 de Octubre, Medical Oncology Department
CIBER-ONC, Madrid, Spain

Daniel Castellano

12. Department of Urology, Faculty of Medicine University of Tsukuba,
Ibaraki, Japan

Hiroyuki Nishiyama

13. USC Norris Comprehensive Cancer Center, Los Angeles, CA, USA

Siamak Daneshmand

14. Natera, Inc, San Carlos, CA, USA

Shruti Sharma, Bernhard G. Zimmermann, Himanshu Sethi & Alexey
Aleshin

15. F. Hoffmann-La Roche Ltd, Basel, Switzerland

Maurizio Perdicchio

16. Hoffmann-La Roche Ltd, Mississauga, Ontario, Canada

Jingbin Zhang

17. Beth Israel Deaconess Medical Center, PSMAR-IMIM Lab, Harvard
Medical School, Boston, MA, USA

Joaquim Bellmunt

Authors

1. Thomas Powles

[View author publications](#)

You can also search for this author in [PubMed](#) [Google Scholar](#)

2. Zoe June Assaf

[View author publications](#)

You can also search for this author in [PubMed](#) [Google Scholar](#)

3. Nicole Davarpanah

[View author publications](#)

You can also search for this author in [PubMed](#) [Google Scholar](#)

4. Romain Banchereau

[View author publications](#)

You can also search for this author in [PubMed](#) [Google Scholar](#)

5. Bernadett E. Szabados

[View author publications](#)

You can also search for this author in [PubMed](#) [Google Scholar](#)

6. Kobe C. Yuen

[View author publications](#)

You can also search for this author in [PubMed](#) [Google Scholar](#)

7. Petros Grivas

[View author publications](#)

You can also search for this author in [PubMed](#) [Google Scholar](#)

8. Maha Hussain

[View author publications](#)

You can also search for this author in [PubMed](#) [Google Scholar](#)

9. Stephane Oudard

[View author publications](#)

You can also search for this author in [PubMed](#) [Google Scholar](#)

10. Jürgen E. Gschwend

[View author publications](#)

You can also search for this author in [PubMed](#) [Google Scholar](#)

11. Peter Albers

[View author publications](#)

You can also search for this author in [PubMed](#) [Google Scholar](#)

12. Daniel Castellano

[View author publications](#)

You can also search for this author in [PubMed](#) [Google Scholar](#)

13. Hiroyuki Nishiyama

[View author publications](#)

You can also search for this author in [PubMed](#) [Google Scholar](#)

14. Siamak Daneshmand

[View author publications](#)

You can also search for this author in [PubMed](#) [Google Scholar](#)

15. Shruti Sharma

[View author publications](#)

You can also search for this author in [PubMed](#) [Google Scholar](#)

16. Bernhard G. Zimmermann

[View author publications](#)

You can also search for this author in [PubMed](#) [Google Scholar](#)

17. Himanshu Sethi

[View author publications](#)

You can also search for this author in [PubMed](#) [Google Scholar](#)

18. Alexey Aleshin

[View author publications](#)

You can also search for this author in [PubMed](#) [Google Scholar](#)

19. Maurizio Perdicchio

[View author publications](#)

You can also search for this author in [PubMed](#) [Google Scholar](#)

20. Jingbin Zhang

[View author publications](#)

You can also search for this author in [PubMed](#) [Google Scholar](#)

21. David S. Shames

[View author publications](#)

You can also search for this author in [PubMed](#) [Google Scholar](#)

22. Viraj Degaonkar

[View author publications](#)

You can also search for this author in [PubMed](#) [Google Scholar](#)

23. Xiaodong Shen

[View author publications](#)

You can also search for this author in [PubMed](#) [Google Scholar](#)

24. Corey Carter

[View author publications](#)

You can also search for this author in [PubMed](#) [Google Scholar](#)

25. Carlos Bais

[View author publications](#)

You can also search for this author in [PubMed](#) [Google Scholar](#)

26. Joaquim Bellmunt

[View author publications](#)

You can also search for this author in [PubMed](#) [Google Scholar](#)

27. Sanjeev Mariathasan

[View author publications](#)

You can also search for this author in [PubMed](#) [Google Scholar](#)

Contributions

T.P., N.D., R.B., P.G., M.H., S.O., J.E.G., P.A., D.C., H.N., S.D., S.S., B.G.Z., H.S., J.Z., D.S.S., V.D., X.S., C.C., C.B., J.B. and S.M. conceived and designed the study. Z.J.A., N.D., B.G.Z., A.A. and S.M. developed the methodology. N.D., V.D. and S.M. conducted the literature search. T.P., N.D., H.S., A.A., M.P., J.B. and S.M. collected the data. T.P., Z.J.A., N.D., R.B., B.E.S., K.C.Y., H.S., A.A., M.P., D.S.S., V.D., C.C., C.B., J.B. and S.M. analysed and interpreted the data. Z.J.A., S.S., A.A. and J.Z. contributed to the development of the statistical analysis plan and/or conducted the statistical analysis. S.M. and J.B. are co-senior authors. All authors drafted and revised the manuscript. All authors critically revised the manuscript for intellectual content. Z.J.A., N.D. and S.M. wrote the original draft. H.S. provided administrative, technical or material support. T.P., P.G., M.H., J.E.G., D.C. and J.B. selected candidates and recruited and treated patients. T.P., M.H., J.E.G., D.C. and J.B. were part of the steering committee. All authors approved the final version of the submitted report and agree to be accountable for all aspects. All authors verify that this study was done per protocol and vouch for data accuracy and completeness.

Corresponding authors

Correspondence to [Thomas Powles](#) or [Sanjeev Mariathasan](#).

Ethics declarations

Competing interests

T.P. received honoraria from advisory/consultancy roles with AstraZeneca, BMS, Exelixis, Incyte, Ipsen, Merck, MSD, Novartis, Pfizer, Seattle Genetics, Merck Serono (EMD Serono), Astellas, Johnson & Johnson, Eisai and Roche; institutional research funding support from AstraZeneca, Roche, BMS, Exelixis, Ipsen, Merck, MSD, Novartis, Pfizer, Seattle Genetics, Merck Serono (EMD Serono), Astellas and Johnson & Johnson; and travel, accommodation and expenses support from Roche, Pfizer, MSD, AstraZeneca and Ipsen. Z.J.A. discloses employment with Genentech, previous employment with Natera and stock and other ownership interests with Roche. N.D., D.S.S., V.D. and K.C.Y. disclose employment with Genentech and stock and other ownership interests with Roche. R.B. and X.S. disclose employment with and own stock or other ownership interests in Genentech. B.E.S. discloses honoraria from Merck, Roche, Pfizer and Ellipses; advisory/consulting fees from Merck, Ellipses and Onc; expert testimony or speakers' bureau fees from Merck and Pfizer; travel, accommodation or expenses support from Roche and Pfizer. P.G. received consulting fees from AstraZeneca, Bayer, BMS, Clovis Oncology, Driver, Dyania Health, EMD Serono, Exelixis, Foundation Medicine, GlaxoSmithKline, Genentech, Genzyme, Heron Therapeutics, Immunomedics, Janssen, Merck, Mirati Therapeutics, Pfizer, Roche, Seattle Genetics and QED Therapeutics; and institutional research funding support from AstraZeneca, Bavarian Nordic, Bayer, BMS, Clovis Oncology, Debiopharm, Genentech, GlaxoSmithKline, Immunomedics, Kure It Cancer Research, Merck, Mirati Therapeutics, OncogeneX, Pfizer and QED Therapeutics. M.H. received honoraria or advisory fees from Pfizer, AstraZeneca, Bayer, Genentech, PER, Projects in Knowledge, Astellas Pharma, Sanofi/Genzyme, Research to Practice, BMS and Daiichi Sankyo; research funding support from AstraZeneca, Genentech, Pfizer and Bayer; and travel, accommodation or expenses support from Pfizer, Bayer, Astellas Pharma and Genentech/Roche; and also has two pending patents and one licensed patent with Imbio. S.O. received advisory/consulting fees and honorarium from Astellas, Bayer, BMS, Eisai, Janssen, MSD, Novartis, Pfizer and Sanofi; research funding support from Ipsen and Sanofi; and travel, accommodation or expenses support from Bayer, BMS, Eisai, MSD, Novartis and Pfizer. J.E.G. received consulting fees or honoraria from

Amgen, AstraZeneca, Bayer, Janssen-Cilag, Merck, MSD, Pfizer, Roche and BMS. P.A. received advisory/consulting fees and honoraria from MSD Oncology, Sanofi and Roche/Genentech. D.C. received consulting fees from Astellas Pharma, AstraZeneca, Bayer, Boehringer Ingelheim, BMS, Ipsen, Janssen Oncology, Lilly, MSD Oncology, Novartis, Pfizer, Pierre Fabre, Roche/Genentech and Sanofi; research funding support from Janssen Oncology; and travel, accommodation or expenses support from AstraZeneca Spain, BMS, Pfizer and Roche. H.N. received research funding support from Ono and Chugai; consulting fees from Bayer, Chugai, BMS, Astellas, MSD, Janssen and AstraZeneca; and participated in speakers' bureaus for Chugai, MSD, Astellas and AstraZeneca. S.D. received honoraria from Ferring, Olympus, Pacific Edge, Photocure, QED, MDxHealth and Spectrum Pharmaceuticals; advisory fees from Ferring, Photocure, QED and Taris; and research funding, travel, accommodation or expenses support from Photocure. S.S., H.S. and A.A disclose employment with Natera. B.G.Z. discloses employment with and owns stock or other ownership interests in Natera. M.P. discloses employment with F. Hoffmann-La Roche. J.Z. discloses employment with Hoffmann-La Roche. C.C., C.B. and S.M. disclose employment with Genentech. J.B. received advisory/consulting fees from Astellas Pharma, AstraZeneca/MedImmune, BMS, Genentech, Merck, Novartis, Pfizer and Pierre Fabre; honoraria from UpToDate; research funding support from Millennium, Sanofi and Pfizer/EMD Serono; owns stock or other ownership interests in Rainer; and travel, accommodation or expenses support from Pfizer, MSD Oncology and Ipsen.

Additional information

Peer review information *Nature* thanks the anonymous reviewers for their contribution to the peer review of this work.

Publisher's note Springer Nature remains neutral with regard to jurisdictional claims in published maps and institutional affiliations.

Extended data figures and tables

Extended Data Fig. 1 The IMvigor010 ctDNA biomarker-evaluable population (BEP).

a, Inclusion criteria for the ctDNA BEP. Of the 809 patients enrolled in IMvigor010, 581 passed the predetermined quality control criteria. **b–e**, Kaplan–Meier estimates comparing patients treated with atezolizumab (blue) to observation (red) for DFS in the ITT population (**b**), stratified for nodal status, PD-L1 status and tumour stage, DFS in the ctDNA BEP population (**c**), stratified for nodal status, PD-L1 status and tumour stage, OS in the ITT (**d**), stratified for nodal status, PD-L1 status and tumour stage, and OS in the ctDNA BEP population (**e**), stratified for nodal status, PD-L1 status and tumour stage. Formal testing in IMvigor010 of OS as the secondary end point was not permitted based on the hierarchical study design. Note that stratification factors in this analysis were chosen to match exactly those used in the IMvigor010 primary clinical analysis¹⁶. **f, g**, Kaplan–Meier analyses of DFS showing different ctDNA dynamics from C1D1 to C3D1 where ‘Pos’ indicates ctDNA(+) and ‘Neg’ indicates ctDNA(–), in the atezolizumab arm (blue colours) (**f**) and in the observation arm (red colours) (**g**).

Extended Data Fig. 2 Baseline clinical features in the ctDNA BEP.

a, b, Forest plots comparing atezolizumab to observation in all ctDNA-evaluable patients, including DFS (**a**) and OS (**b**). Subgroups are defined by baseline clinical features and tissue immune biomarkers including nodal status, tumour stage, the number of lymph nodes resected, previous neoadjuvant chemotherapy, PD-L1 status by tissue immunohistochemistry (IHC), TMB status by tissue whole-exome sequencing (WES), as well as transcriptomic signatures including tGE3, TBRS, angiogenesis and TCGA subtypes. Forest plots show HRs for recurrence or death estimated using a univariable Cox proportional-hazards model, and 95% confidence intervals of HRs are represented by horizontal bars. **c**, Bar plot depicting association of baseline prognostic factors with ctDNA-positive (red) and ctDNA-negative (grey) status, wherein nodal-positive patients were enriched for

ctDNA-positive status (nodal-positive patients were 47.5% ctDNA positive, and nodal-negative patients were 25.2% ctDNA positive).

Extended Data Fig. 3 Forest plots for DFS and OS in ctDNA-positive and ctDNA-negative subgroups defined by clinical and immune features.

a–d, Forest plots comparing atezolizumab to observation including DFS in ctDNA(+) patients (**a**), OS in ctDNA(+) patients (**b**), DFS in ctDNA(–) patients (**c**) and OS in ctDNA(–) patients (**d**). Subgroups are defined by baseline clinical features and tissue immune biomarkers including nodal status, tumour stage, the number of lymph nodes resected, previous neoadjuvant chemotherapy, PD-L1 status by tissue IHC, TMB status by tissue WES, as well as transcriptomic signatures including tGE3, F-TBRS, angiogenesis and TCGA subtypes. Forest plots show HRs for death estimated using a univariable Cox proportional-hazards model, and 95% confidence intervals of HRs are represented by horizontal bars.

Extended Data Fig. 4 Continuous ctDNA metrics and association with clinical outcome within ctDNA(+) patients.

Only the observation arm ctDNA(+) patients are shown to demonstrate the prognostic value of baseline ctDNA. **a**, Scatter plot showing ctDNA concentration as measured by sample mean tumor molecules per mL of plasma (sample MTM/ml) versus DFS in months. The solid points indicate an event, and the empty points indicate censoring. **b**, Kaplan–Meier plot for DFS comparing patients with high ctDNA concentrations (dark red, greater than or equal to median sample MTM/ml) versus low ctDNA levels (light red, less than the median sample MTM/ml). **c**, Forest plot for DFS comparing patients with high versus low ctDNA levels using different quantile thresholds for splitting sample MTM/ml, including 10%, 25%, 50% (median), 75% and 90% quantiles. **d**, Scatter plot showing OS in months (*x* axis) versus ctDNA concentration as measured by sample MTM/ml. The solid points indicate an event, and the empty points indicate censoring. **e**, Kaplan–Meier plot for OS comparing patients with high ctDNA concentrations (dark red, greater than or equal to median sample

MTM/ml) versus low ctDNA concentrations (light red, less than the median sample MTM/ml). **f**, Forest plot for OS comparing patients with high versus low ctDNA concentrations using different quantile thresholds for splitting ctDNA sample MTM/ml, including 10%, 25%, 50% (median), 75% and 90% quantiles. Forest plots show HRs for recurrence or death estimated using a univariable Cox proportional-hazards model, and 95% confidence intervals of HRs are represented by horizontal bars.

Extended Data Fig. 5 Reductions in ctDNA levels occurred at a higher rate in the atezolizumab arm than in the observation arm and were associated with improvements in clinical outcome in the atezolizumab arm.

a–e, Reduction is assessed in C1D1 ctDNA(+) patients in the C1/C3 BEP and is defined as a decrease in sample MTM/ml from C1D1 to C3D1. The proportion of patients who are ctDNA(+) at C1D1 who have reduced ctDNA by C3D1 for the atezolizumab arm (blue) and the observation arm (red) (**a**). Kaplan–Meier analyses comparing patients who have reduced ctDNA ('reduction', dark blue or dark red) compared with those who have ctDNA levels that increase ('non-reduction', light blue or light red) for DFS in the atezolizumab arm (**b**), DFS in the observation arm (**c**), OS in the atezolizumab arm (**d**) and OS in the observation arm (**e**). **f–i**, Patients shown are from the atezolizumab arm C1/C3 BEP and are ctDNA(+) at baseline and have different types of ctDNA dynamics based on the percent change in sample MTM/ml from C1 to C3. Note that the scale for the per cent change goes from –100% (clearance) to infinity, where negative values indicate reductions, and positive values indicate increases. Kaplan–Meier analysis of DFS (**f**) and OS (**h**) in which ctDNA reduction is split into patients who clear ctDNA ('reduction with clearance', dark blue, solid lines) and those who have decreased ctDNA without clearance ('reduction without clearance', dark blue, dashed lines). Patients with an increase in ctDNA are also shown ('increase', light blue, solid lines). Forest plots for DFS (**g**) and comparing patients with reduction (anywhere from clearance (–100% change) to minor decreases in ctDNA (<0% change)) (**i**) using different thresholds for percent change in sample MTM/ml, including –100% (reduction with clearance versus reduction without clearance),

–50%, –25% and –10% changes. Forest plots show HRs for recurrence or death estimated using a univariable Cox proportional-hazards model, and 95% confidence intervals of HRs are represented by horizontal bars.

Extended Data Fig. 6 The ABACUS ctDNA study in the neoadjuvant setting supports the association of ctDNA with clinical outcomes.

a, ABACUS consort diagram depicting how patients in the ctDNA BEP ($n = 40$) were identified from the overall ABACUS study population ($n = 95$). ABACUS is a phase II prospective neoadjuvant ctDNA data from a prospective phase II study of neoadjuvant atezolizumab before cystectomy in muscle invasive urothelial cancer. **b**, Kaplan–Meier estimates comparing recurrence-free survival (RFS) of ctDNA-positive patients (red) to ctDNA-negative patients (blue) as assessed at the baseline (C1D1) time point before neoadjuvant treatment. **c**, Kaplan–Meier estimates for ctDNA-positive (red) versus ctDNA-negative patients (blue) at the post-neoadjuvant time point.

Extended Data Fig. 7 Tissue biomarkers in ctDNA(±) populations.

a–e, Kaplan–Meier analyses for ctDNA(+) patients in the atezolizumab (blue) and observation (red) arms in subgroups defined by high levels (dark colours) and low levels (light colours) of immune biomarkers of response to immunotherapy including PD-L1 by IHC (**a**), TMB from WES (**b**), tGE3 gene expression signature (**c**), and subgroups defined by immune biomarkers of resistance to immunotherapy including pan-TBRS (F-TBRS) gene expression signature (**d**) and angiogenesis gene expression signature (**e**). **f**, Hallmark gene set enrichment analysis in ctDNA(+) patients in the observation arm comparing non-relapsers (blue) to relapsers (red).

Extended Data Fig. 8 Tissue biomarkers in ctDNA(–) patients.

Kaplan–Meier analyses for ctDNA(–) patients in the atezolizumab (blue) and observation (red) arms for DFS (left column) and OS (right column) in

subgroups defined by high levels (dark colours) and low levels (light colours) of immune biomarkers of response to immunotherapy including PD-L1 by IHC, TMB from WES, tGE3 gene expression signature, and subgroups defined by immune biomarkers of resistance to immunotherapy including the pan-TBRS (F-TBRS) gene expression signature and the angiogenesis gene expression signature.

Extended Data Fig. 9 TCGA subgroups and Kaplan–Meier analyses for ctDNA(+) and ctDNA(−) patients.

a, Bar plot showing that TCGA subgroups are similarly distributed in ctDNA(+) (left) and ctDNA(−) (right) populations. **b**, Bar plot showing that TCGA subgroup distribution is associated with PD-L1 status (IC01, left; IC2/3; right). **c–g**, Kaplan–Meier analyses showing ctDNA(+) (dark colours) and ctDNA(−) (light colours) patients on atezolizumab (blue) and observation (red) for DFS in TCGA subgroups including luminal papillary (**c**), luminal infiltrated (**d**), luminal (**e**), basal/squamous (**f**) and neuronal (**g**). **h**, Kaplan–Meier analyses for OS in the neuronal TCGA subgroup.

Extended Data Fig. 10 ctDNA and C1D1 collection time and time until relapse.

Note that collection time analyses are shown for patients with muscle-invasive bladder cancer only, because patients with upper-tract urothelial carcinoma often received two surgeries. **a**, Scatter plot showing ctDNA levels (sample mean MTM) versus C1D1 collection time (days from surgery). **b**, Box plot showing the C1D1 collection time (y axis) for the ctDNA-negative (*x* axis, left box plot, $n = 339$) and ctDNA-positive (*x* axis, right box plot, $n = 199$) patients. No difference was found between the collection times for the ctDNA-negative patients and the ctDNA-positive patients (Wilcoxon $P = 0.18$, two sided). The box plot middle line is the median, the lower and upper hinges correspond to the first and third quartiles, the upper whisker extends from the hinge to the largest value no further than $1.5 \times$ IQR from the hinge and the lower whisker extends from the hinge to the smallest value at most $1.5 \times$ IQR of the hinge, while data beyond the end of the whiskers are outlying points that are plotted

individually. **c**, Bar plot showing the fraction of patients who were ctDNA positive (dark grey fill) for patients with C1D1 collection times less than the median collection time (*x* axis, left bar plot) and greater than the median collection time (*x* axis, right bar plot). **d**, Histogram showing the distribution of times between surgery and C1D1. **e**, Histogram plot showing the distribution of durations between a C1D1 ctDNA(+) test and radiological relapse.

Supplementary information

Supplementary Information

This file contains the final IMvigor010 statistical analysis plan for ctDNA analyses.

Reporting Summary

Supplementary Tables

This file contains Supplementary Tables 1-7.

Rights and permissions

Reprints and Permissions

About this article



Check for
updates

Cite this article

Powles, T., Assaf, Z.J., Davarpanah, N. *et al.* ctDNA guiding adjuvant immunotherapy in urothelial carcinoma. *Nature* **595**, 432–437 (2021).

<https://doi.org/10.1038/s41586-021-03642-9>

[Download citation](#)

- Received: 08 December 2020
- Accepted: 13 May 2021
- Published: 16 June 2021
- Issue Date: 15 July 2021
- DOI: <https://doi.org/10.1038/s41586-021-03642-9>

Comments

By submitting a comment you agree to abide by our [Terms](#) and [Community Guidelines](#). If you find something abusive or that does not comply with our terms or guidelines please flag it as inappropriate.

[Access through your institution](#)

[Change institution](#)

[Buy or subscribe](#)

Associated Content

[Using ctDNA to guide immunotherapy for urothelial cancer](#)

- Annette Fenner

Advertisement

This article was downloaded by **calibre** from <https://www.nature.com/articles/s41586-021-03642-9>

- Article
- [Published: 23 June 2021](#)

A transcriptional switch governs fibroblast activation in heart disease

- [Michael Alexanian](#)¹,
- [Pawel F. Przytycki](#) [ORCID: orcid.org/0000-0002-3360-6936](#)¹,
- [Rudi Micheletti](#)²,
- [Arun Padmanabhan](#)^{1,3},
- [Lin Ye](#)¹,
- [Joshua G. Travers](#) [ORCID: orcid.org/0000-0002-5660-2620](#)⁴,
- [Barbara Gonzalez-Teran](#) [ORCID: orcid.org/0000-0002-4336-8644](#)¹,
- [Ana Catarina Silva](#)¹,
- [Qiming Duan](#) [ORCID: orcid.org/0000-0002-6204-3028](#)¹,
- [Sanjeev S. Ranade](#)¹,
- [Franco Felix](#) [ORCID: orcid.org/0000-0002-4297-7149](#)¹,
- [Ricardo Linares-Saldana](#) [ORCID: orcid.org/0000-0003-2657-825X](#)⁵,
- [Li Li](#)⁵,
- [Clara Youngna Lee](#) [ORCID: orcid.org/0000-0002-9402-4155](#)¹,
- [Nandhini Sadagopan](#)^{1,3},
- [Angelo Pelonero](#) [ORCID: orcid.org/0000-0002-7684-3771](#)¹,
- [Yu Huang](#)¹,
- [Gaia Andreoletti](#)⁶,
- [Rajan Jain](#)⁵,
- [Timothy A. McKinsey](#)⁴,
- [Michael G. Rosenfeld](#)²,
- [Casey A. Gifford](#)¹,
- [Katherine S. Pollard](#) [ORCID: orcid.org/0000-0002-9870-6196](#)^{1,6,7,8,9},

- [Saptarsi M. Haldar](#) ORCID: orcid.org/0000-0001-7968-9696^{1,3} nAff13 &
- [Deepak Srivastava](#) ORCID: orcid.org/0000-0002-3480-5953^{1,10,11,12}

[Nature](#) volume 595, pages 438–443 (2021) [Cite this article](#)

- 8586 Accesses
- 240 Altmetric
- [Metrics details](#)

Subjects

- [Genetics](#)
- [Molecular biology](#)

Abstract

In diseased organs, stress-activated signalling cascades alter chromatin, thereby triggering maladaptive cell state transitions. Fibroblast activation is a common stress response in tissues that worsens lung, liver, kidney and heart disease, yet its mechanistic basis remains unclear^{1,2}. Pharmacological inhibition of bromodomain and extra-terminal domain (BET) proteins alleviates cardiac dysfunction^{3,4,5,6,7}, providing a tool to interrogate and modulate cardiac cell states as a potential therapeutic approach. Here we use single-cell epigenomic analyses of hearts dynamically exposed to BET inhibitors to reveal a reversible transcriptional switch that underlies the activation of fibroblasts. Resident cardiac fibroblasts demonstrated robust toggling between the quiescent and activated state in a manner directly correlating with BET inhibitor exposure and cardiac function. Single-cell chromatin accessibility revealed previously undescribed DNA elements, the accessibility of which dynamically correlated with cardiac performance. Among the most dynamic elements was an enhancer that regulated the transcription factor MEOX1, which was specifically expressed in activated fibroblasts, occupied putative regulatory elements of a broad fibrotic gene

program and was required for TGF β -induced fibroblast activation. Selective CRISPR inhibition of the single most dynamic *cis*-element within the enhancer blocked TGF β -induced *Meox1* activation. We identify MEOX1 as a central regulator of fibroblast activation associated with cardiac dysfunction and demonstrate its upregulation after activation of human lung, liver and kidney fibroblasts. The plasticity and specificity of BET-dependent regulation of MEOX1 in tissue fibroblasts provide previously unknown *trans*- and *cis*-targets for treating fibrotic disease.

Access options

Subscribe to Journal

Get full journal access for 1 year

\$199.00

only \$3.90 per issue

[Subscribe](#)

All prices are NET prices.

VAT will be added later in the checkout.

Tax calculation will be finalised during checkout.

Rent or Buy article

Get time limited or full article access on ReadCube.

from \$8.99

[Rent or Buy](#)

All prices are NET prices.

Additional access options:

- [Log in](#)

- [Access through your institution](#)
- [Learn about institutional subscriptions](#)

Fig. 1: Heart failure reversibility with BET inhibition correlates with myofibroblast state.

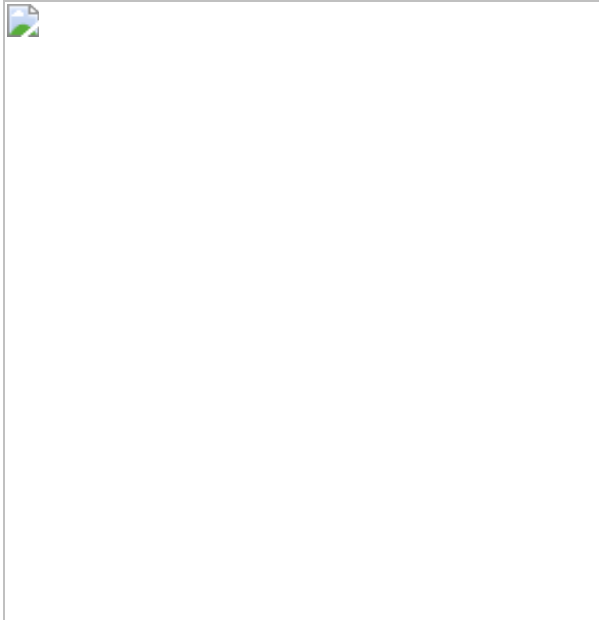


Fig. 2: Reversibility of chromatin states in fibroblasts reveals DNA elements that correlate with heart function.

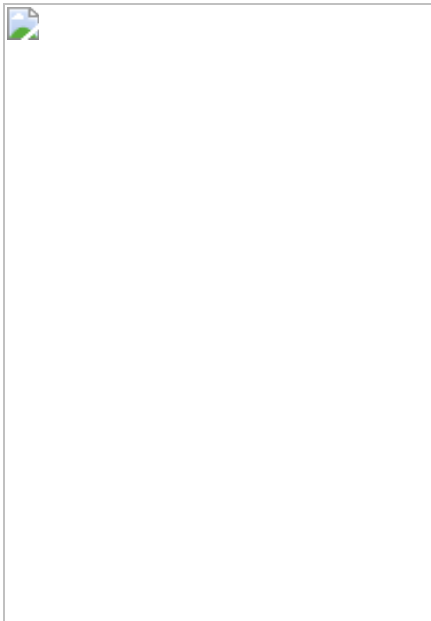


Fig. 3: Chromatin accessibility and nascent transcription identify a *cis*-element controlling *Meox1* expression.

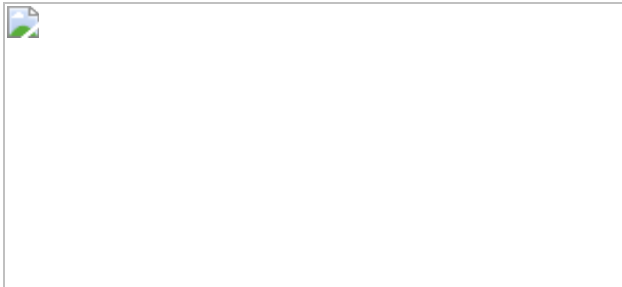
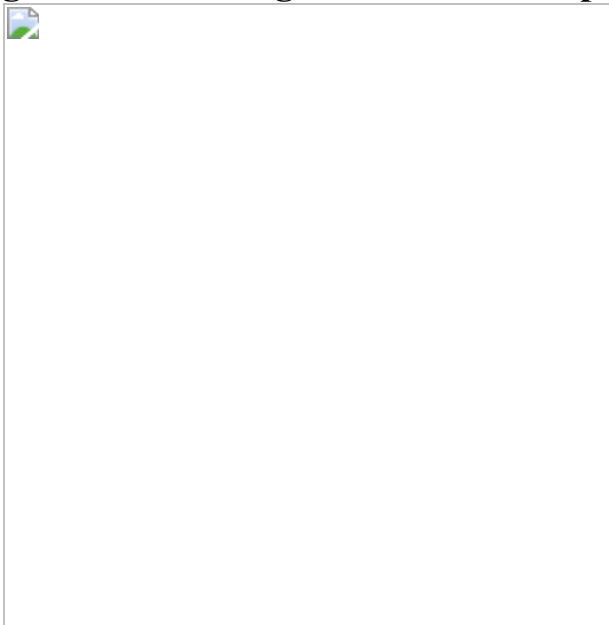


Fig. 4: MEOX1 regulates fibroblast plasticity and profibrotic function.



Data availability

All source data, including sequencing reads and single-cell expression matrices have been deposited in the NCBI's Gene Expression Omnibus under accession number [GSE155882](#).

Code availability

All scRNA-seq analyses were performed using standard protocols with the Seurat R package (v.2.3.4). Custom codes relevant to the scATAC-seq analysis are available on GitHub (<https://github.com/PFPrzytycki/FibroSwitch>).

References

1. 1.

Rockey, D. C., Bell, P. D. & Hill, J. A. Fibrosis—a common pathway to organ injury and failure. *N. Engl. J. Med.* **372**, 1138–1149 (2015).

[CAS](#) [Article](#) [Google Scholar](#)

2. 2.

Jun, J.-I. & Lau, L. F. Resolution of organ fibrosis. *J. Clin. Invest.* **128**, 97–107 (2018).

[Article](#) [Google Scholar](#)

3. 3.

Anand, P. et al. BET bromodomains mediate transcriptional pause release in heart failure. *Cell* **154**, 569–582 (2013).

[CAS](#) [Article](#) [Google Scholar](#)

4. 4.

Spiltoir, J. I. et al. BET acetyl-lysine binding proteins control pathological cardiac hypertrophy. *J. Mol. Cell. Cardiol.* **63**, 175–179 (2013).

[CAS](#) [Article](#) [Google Scholar](#)

5. 5.

Duan, Q. et al. BET bromodomain inhibition suppresses innate inflammatory and profibrotic transcriptional networks in heart failure. *Sci. Transl. Med.* **9**, eaah5084 (2017).

[Article](#) [Google Scholar](#)

6. 6.

Stratton, M. S. et al. Dynamic chromatin targeting of BRD4 stimulates cardiac fibroblast activation. *Circ. Res.* **125**, 662–677 (2019).

[CAS](#) [Article](#) [Google Scholar](#)

7. 7.

Antolic, A. et al. BET bromodomain proteins regulate transcriptional reprogramming in genetic dilated cardiomyopathy. *JCI Insight* **5**, e138687 (2020).

[Article](#) [Google Scholar](#)

8. 8.

Virani, S. S. et al. Heart disease and stroke statistics—2020 update: a report from the American Heart Association. *Circulation* **141**, e139–e596 (2020).

[PubMed](#) [Google Scholar](#)

9. 9.

Filippakopoulos, P. et al. Selective inhibition of BET bromodomains. *Nature* **468**, 1067–1073 (2010).

[CAS](#) [Article](#) [ADS](#) [Google Scholar](#)

10. 10.

Kanisicak, O. et al. Genetic lineage tracing defines myofibroblast origin and function in the injured heart. *Nat. Commun.* **7**, 12260 (2016).

[CAS](#) [Article](#) [ADS](#) [Google Scholar](#)

11. 11.

Buenrostro, J. D., Wu, B., Chang, H. Y. & Greenleaf, W. J. ATAC-seq: a method for assaying chromatin accessibility genome-wide. *Curr. Protoc. Mol. Biol.* **109**, 21.29.1–21.29.9 (2015).

[Article](#) [Google Scholar](#)

12. 12.

Przytycki, P. F. & Pollard, K. S. CellWalker integrates single-cell and bulk data to resolve regulatory elements across cell types in complex tissues. *Genome Biol.* **22**, 61 (2021).

[CAS](#) [Article](#) [Google Scholar](#)

13. 13.

Mahat, D. B. et al. Base-pair-resolution genome-wide mapping of active RNA polymerases using precision nuclear run-on (PRO-seq). *Nat. Protocols* **11**, 1455–1476 (2016).

[Article](#) [Google Scholar](#)

14. 14.

De Santa, F. et al. A large fraction of extragenic RNA pol II transcription sites overlap enhancers. *PLoS Biol.* **8**, e1000384 (2010).

[Article](#) [Google Scholar](#)

15. 15.

Gilbert, L. A. et al. CRISPR-mediated modular RNA-guided regulation of transcription in eukaryotes. *Cell* **154**, 442–451 (2013).

[CAS](#) [Article](#) [Google Scholar](#)

16. 16.

Whyte, W. A. et al. Master transcription factors and mediator establish super-enhancers at key cell identity genes. *Cell* **153**, 307–319 (2013).

[CAS](#) [Article](#) [Google Scholar](#)

17. 17.

Skuntz, S. et al. Lack of the mesodermal homeodomain protein MEOX1 disrupts sclerotome polarity and leads to a remodeling of the cranio-cervical joints of the axial skeleton. *Dev. Biol.* **332**, 383–395 (2009).

[CAS](#) [Article](#) [Google Scholar](#)

18. 18.

Lu, D. et al. Meox1 accelerates myocardial hypertrophic decompensation through Gata4. *Cardiovasc. Res.* **114**, 300–311 (2018).

[CAS](#) [Article](#) [Google Scholar](#)

19. 19.

Wei, Z. et al. Molecular mechanism of mesenchyme homeobox 1 in transforming growth factor β 1-induced *P311* gene transcription in fibrosis. *Front. Mol. Biosci.* **7**, 59 (2020).

[CAS](#) [Article](#) [ADS](#) [Google Scholar](#)

20. 20.

Litviňuková, M. et al. Cells of the adult human heart. *Nature* **588**, 466–472 (2020).

[Article](#) [ADS](#) [Google Scholar](#)

21. 21.

Domcke, S. et al. A human cell atlas of fetal chromatin accessibility. *Science* **370**, eaba7612 (2020).

[CAS](#) [Article](#) [Google Scholar](#)

22. 22.

Sivakumar, P. et al. RNA sequencing of transplant-stage idiopathic pulmonary fibrosis lung reveals unique pathway regulation. *ERJ Open Res.* **5**, 00117-2019 (2019).

[Article](#) [Google Scholar](#)

[Download references](#)

Acknowledgements

We thank members of the Srivastava laboratory, J. van Bemmel, M. Costa, N. Palpant, W. J. Shim, P. Grote, E. P. Nora, A. A. Rao, A. J. Combes, P. Benaglio and K. N. Ivey and J. Yang for discussion and feedback; and J. Qi, D. Li and L. Sigua for providing JQ1. We acknowledge the UCSF Center for Advanced Technology (CAT), Gladstone Genomics Core and Flow Cytometry Core for their technical support and the Gladstone Animal Facility for support with mouse colonies. M.A. was supported by the Swiss National Science Foundation (P400PM_186704 and P2LAP3_178056). P.F.P. and K.S.P. were supported by NIH P01 HL098707, HL098179, Gladstone Institutes and the San Simeon Fund. R.M. was supported by the NIH R01 AG070154. A. Padmanabhan was supported by the NIH (K08HL157700), Tobacco-Related Disease Research Program (578649), A. P. Giannini Foundation (P0527061), Michael Antonov Charitable Foundation and Sarnoff Cardiovascular Research foundation. J.G.T. was supported by NIH F32 HL147463. B.G.T. was supported by the American Heart Association (18POST34080175). R.J. was supported by the Burroughs Wellcome Fund and funds from the Allen Foundation and American Heart Association. T.A.M. was supported by NIH R01 HL116848, NIH R01 HL147558, NIH R01 DK119594 and NIH R01 HL150225. T.A.M. and J.G.T. were supported by the American Heart

Association (16SFRN31400013). M.G.R. is an investigator with HHMI and was supported by NIH R01 HL150521. S.M.H. was supported by NIH R01 HL127240. D.S. was supported by NIH P01 HL146366, NIH R01 HL057181, NIH R01 HL015100, and by the Roddenberry Foundation, the L.K. Whittier Foundation, Dario and Irina Sattui and the Younger Family Fund. D.S. and T.A.M. were supported by NIH R01 HL127240. This work was also supported by NIH/NCRR grant C06 RR018928 to the Gladstone Institutes.

Author information

Author notes

1. Saptarsi M. Haldar

Present address: Amgen Research, Cardiometabolic Disorders, South San Francisco, CA, USA

Affiliations

1. Gladstone Institutes, San Francisco, CA, USA

Michael Alexanian, Pawel F. Przytycki, Arun Padmanabhan, Lin Ye, Barbara Gonzalez-Teran, Ana Catarina Silva, Qiming Duan, Sanjeev S. Ranade, Franco Felix, Clara Youngna Lee, Nandhini Sadagopan, Angelo Pelonero, Yu Huang, Casey A. Gifford, Katherine S. Pollard, Saptarsi M. Haldar & Deepak Srivastava

2. Howard Hughes Medical Institute, Department and School of Medicine, University of California, San Diego, La Jolla, CA, USA

Rudi Micheletti & Michael G. Rosenfeld

3. Department of Medicine, Cardiology Division, UCSF School of Medicine, San Francisco, CA, USA

Arun Padmanabhan, Nandhini Sadagopan & Saptarsi M. Haldar

4. Department of Medicine, Division of Cardiology and Consortium for Fibrosis Research & Translation, University of Colorado Anschutz Medical Campus, Aurora, CO, USA

Joshua G. Travers & Timothy A. McKinsey

5. Cardiovascular Institute and Department of Medicine, Perelman School of Medicine, University of Pennsylvania, Philadelphia, PA, USA

Ricardo Linares-Saldana, Li Li & Rajan Jain

6. Institute for Computational Health Sciences, University of California, San Francisco, CA, USA

Gaia Andreoletti & Katherine S. Pollard

7. Chan-Zuckerberg Biohub, San Francisco, CA, USA

Katherine S. Pollard

8. Department of Epidemiology & Biostatistics, University of California, San Francisco, CA, USA

Katherine S. Pollard

9. Institute for Human Genetics, University of California, San Francisco, CA, USA

Katherine S. Pollard

10. Department of Pediatrics, UCSF School of Medicine, San Francisco, CA, USA

Deepak Srivastava

11. Roddenberry Center for Stem Cell Biology and Medicine at Gladstone, San Francisco, CA, USA

Deepak Srivastava

12. Department of Biochemistry and Biophysics, University of California, San Francisco, CA, USA

Deepak Srivastava

Authors

1. Michael Alexanian

[View author publications](#)

You can also search for this author in [PubMed](#) [Google Scholar](#)

2. Pawel F. Przytycki

[View author publications](#)

You can also search for this author in [PubMed](#) [Google Scholar](#)

3. Rudi Micheletti

[View author publications](#)

You can also search for this author in [PubMed](#) [Google Scholar](#)

4. Arun Padmanabhan

[View author publications](#)

You can also search for this author in [PubMed](#) [Google Scholar](#)

5. Lin Ye

[View author publications](#)

You can also search for this author in [PubMed](#) [Google Scholar](#)

6. Joshua G. Travers

[View author publications](#)

You can also search for this author in [PubMed](#) [Google Scholar](#)

7. Barbara Gonzalez-Teran
[View author publications](#)

You can also search for this author in [PubMed](#) [Google Scholar](#)

8. Ana Catarina Silva
[View author publications](#)

You can also search for this author in [PubMed](#) [Google Scholar](#)

9. Qiming Duan
[View author publications](#)

You can also search for this author in [PubMed](#) [Google Scholar](#)

10. Sanjeev S. Ranade
[View author publications](#)

You can also search for this author in [PubMed](#) [Google Scholar](#)

11. Franco Felix
[View author publications](#)

You can also search for this author in [PubMed](#) [Google Scholar](#)

12. Ricardo Linares-Saldana
[View author publications](#)

You can also search for this author in [PubMed](#) [Google Scholar](#)

13. Li Li
[View author publications](#)

You can also search for this author in [PubMed](#) [Google Scholar](#)

14. Clara Youngna Lee
[View author publications](#)

You can also search for this author in [PubMed](#) [Google Scholar](#)

15. Nandhini Sadagopan

[View author publications](#)

You can also search for this author in [PubMed](#) [Google Scholar](#)

16. Angelo Pelonero

[View author publications](#)

You can also search for this author in [PubMed](#) [Google Scholar](#)

17. Yu Huang

[View author publications](#)

You can also search for this author in [PubMed](#) [Google Scholar](#)

18. Gaia Andreoletti

[View author publications](#)

You can also search for this author in [PubMed](#) [Google Scholar](#)

19. Rajan Jain

[View author publications](#)

You can also search for this author in [PubMed](#) [Google Scholar](#)

20. Timothy A. McKinsey

[View author publications](#)

You can also search for this author in [PubMed](#) [Google Scholar](#)

21. Michael G. Rosenfeld

[View author publications](#)

You can also search for this author in [PubMed](#) [Google Scholar](#)

22. Casey A. Gifford

[View author publications](#)

You can also search for this author in [PubMed](#) [Google Scholar](#)

23. Katherine S. Pollard

[View author publications](#)

You can also search for this author in [PubMed](#) [Google Scholar](#)

24. Saptarsi M. Haldar

[View author publications](#)

You can also search for this author in [PubMed](#) [Google Scholar](#)

25. Deepak Srivastava

[View author publications](#)

You can also search for this author in [PubMed](#) [Google Scholar](#)

Contributions

M.A., S.M.H. and D.S. conceived the study, interpreted the data and wrote the manuscript. Y.H. performed heart surgeries and echocardiography. M.A., A. Padmanabhan and C.Y.L. performed JQ1 injections. M.A., A. Padmanabhan and Q.D. collected heart tissues and isolated cardiac cells for subsequent scRNA-seq or scATAC-seq. S.S.R. prepared chromium libraries. M.A. and G.A. analysed bulk RNA-seq. M.A., C.A.G. and G.A. analysed scRNA-seq. A.C.S., R.L.-S., L.L. and R.J. performed and analysed Picrosirius red staining. P.F.P. and K.S.P. analysed scATAC-seq and developed computational methods. R.M. and M.G.R. performed and analysed PRO-seq and 4C. M.A. and L.Y. generated all of the immortalized fibroblast lines. M.A., L.Y., F.F. and N.S. performed knockdown experiments and RT-qPCR analyses. M.A. and A.C.S. performed α SMA immunofluorescence. J.G.T. and T.A.M. performed collagen-contraction and proliferation studies on primary cardiac fibroblasts. M.A., B.G.T. and A. Pelonero performed and analysed ChIP-seq.

Corresponding authors

Correspondence to [Saptarsi M. Haldar](#) or [Deepak Srivastava](#).

Ethics declarations

Competing interests

D.S. is a scientific co-founder, shareholder and director of Tenaya Therapeutics. S.M.H. is an executive, officer and shareholder of Amgen, a scientific co-founder and shareholder of Tenaya Therapeutics, and serves on the scientific advisory board of DZHK (German Centre for Cardiovascular Research). K.S.P. is a shareholder of Tenaya Therapeutics. T.A.M. is on the scientific advisory board of Artemes Bio, Inc., received funding from Italfarmaco for an unrelated project, and has a subcontract from Eikonizo Therapeutics related to an SBIR grant from the National Institutes of Health (HL154959).

Additional information

Peer review information *Nature* thanks Jeffery Molkentin and the other, anonymous, reviewer(s) for their contribution to the peer review of this work. Peer reviewer reports are available.

Publisher's note Springer Nature remains neutral with regard to jurisdictional claims in published maps and institutional affiliations.

Extended data figures and tables

[Extended Data Fig. 1 Single-cell transcriptional landscape of non-cardiomyocytes in heart failure during intermittent exposure to BET bromodomain inhibition.](#)

a, Venn diagram showing overlap of TAC-induced and JQ1-suppressed genes ($\log_2[\text{FC}] > 0.5$; adjusted $P < 0.05$; false-discovery rate-adjusted, Benjamini–Hochberg correction) between bulk RNA-seq from undissociated left ventricle tissue⁵ and extracted cardiomyocytes. **b**, Heat map showing the top-5 markers per cluster in the scRNA-seq data. Total cells, $n = 35,551$ in 9 clusters. **c**, UMAP plots showing cluster identity of all

cells ($n = 35,551$) and expression of *Dcn*, *Postn*, *Ctgf*, *Lyz2* and *Fabp4*. **d, e**, UMAP plot coloured by sample identity of myeloid (**d**, $n = 7,986$) and endothelial (**e**, $n = 10,672$) cells.

Extended Data Fig. 2 Reversible effect of JQ1 exposure on the transcriptional signature of baseline and stressed fibroblasts.

a, Expression of known fibroblast stress-related genes shown as a UMAP feature plots in fibroblasts (total cells, $n = 13,937$). **b**, Expression by sample of known fibroblast stress-related genes shown as violin plots in fibroblasts. *y* axes, normalized UMI levels. **c**, Dot plots showing expression (avg.exp.scale) and cell percentages (pct.exp) of the top differentially expressed marker genes between samples. **d**, Percentages of the 260 genes upregulated in fibroblasts in TAC versus sham that are significantly downregulated in TAC JQ1 versus TAC (blue bar) and upregulated in TAC JQ1 withdrawn versus TAC JQ1 (yellow bar). **e**, Percentages of the 194 genes significantly downregulated in TAC versus sham that are significantly upregulated in TAC JQ1 versus TAC (blue bar) and downregulated in TAC JQ1 withdrawn versus TAC JQ1 (yellow bar). **f**, Violin plots showing the normalized expression score across fibroblast samples of the 194 genes significantly downregulated in TAC versus sham and associated top GO terms (Fisher's exact test).

Extended Data Fig. 3 Fibroblast subclusters associated to stress-related gene programs are depleted in sham and TAC JQ1 cells.

a, UMAP plot of fibroblasts coloured by sample identity. $n = 13,937$. **b**, Left, UMAP plot of fibroblast subclusters coloured by cluster identity. Right, a tree diagram showing the cluster relationship. Total cells, $n = 13,937$. **c**, Histograms showing the percentage of each sample in each fibroblast cluster. **d**, Heat map showing the top 10 markers per fibroblast cluster in the scRNA-seq data. Total cells, $n = 13,937$ in 9 clusters. **e**, *Postn* expression in fibroblasts by cluster as violin plots. *y* axes, normalized UMI levels. **f**, Comparative GO term analysis (Fisher's exact test) between

fibroblast clusters for fibroblast stress-related biological processes. Top GO terms when analysing the genes driving fibroblast clusters 2, 3 and 5.

Extended Data Fig. 4 Defining a catalogue of cell-population-enriched distal elements in fibroblasts, myeloid cells and endothelial cells using scATAC-seq.

a, Schematic highlighting the approach to integrate scRNA-seq data with scATAC-seq data¹². See [Supplementary Methods](#) for details. **b**, Total scATAC-seq proximal and distal peaks identified in all cells. **c**, scATAC-seq t-SNE plot showing clusters and cell number of fibroblasts, myeloid cells and endothelial cells after integration with scRNA-seq data. **d**, Venn diagrams showing sample replicate convergence of cell-enriched distal elements found with scATAC-seq.

Extended Data Fig. 5 scATAC-seq defines chromatin accessibility in heart failure during intermittent exposure to BET bromodomain inhibition.

a, Chromatin accessibility at distal elements between samples in fibroblasts, myeloid cells and endothelial cells. Box plots show the 25th, 50th and 75th percentiles, with whiskers extending to the furthest value no further than 1.5× the interquartile range. The 10% most extreme points were trimmed for better visualization (these never included points within the whiskers of the box plot). Numbers above the box plots indicate significant *P* values, statistical significance (two-sided Wilcoxon rank-sum test) is shown for: sham versus TAC; sham versus TAC JQ1; TAC versus TAC JQ1 and TAC JQ1 versus TAC JQ1 withdrawn. **b**, Dynamic accessibility (mean and 95% confidence interval) of distal elements in fibroblasts (*n* = 4,394), myeloid cells (*n* = 1,325) and endothelial cells (*n* = 1,626) clustered by trend across samples. Accessibility trend and top GO terms (binomial test) associated with clusters 2, 6, 9, 11, 12 and 14 are shown for fibroblasts. For myeloid and endothelial cells, only the top GO terms (binomial test) associated with cluster 2 are shown. **c**, Enrichment scores for transcription-factor motif accessibility in distal elements between samples for the 10 most expressed

transcription factors in TAC in fibroblasts, myeloid cells and endothelial cells. TF, transcription factor.

Extended Data Fig. 6 Nascent transcription in TGF β -treated cells identifies stress-responsive distal and gene elements.

a, Schematic of the isolation and immortalization of mouse adult cardiac fibroblasts. **b**, Expression by qPCR of canonical markers of activated fibroblasts in unstimulated (Unstim) and TGF β -treated cells. Unpaired, two-tailed Student's *t*-test. **c**, Pearson correlation of the two independent biological replicates of PRO-seq in unstimulated and TGF β -treated cells. **d,e**, Heat map of PRO-seq coverage of differentially transcribed distal regions (**d**) and protein-coding genes (**e**, right) between unstimulated and TGF β -treated fibroblasts. Wald test with Benjamini–Hochberg correction. Signal for replicates 1 and 2 is shown. **e**, Right, top associated GO terms (Fisher's exact test). **f**, PRO-seq tag density (± 5 kb gene body) in unstimulated and TGF β -treated cells in the genes differentially transcribed in unstimulated versus TGF β -treated. Top, genes upregulated after TGF β treatment. Bottom, genes downregulated after TGF β treatment. **g**, PRO-seq tag density (± 5 kb gene body) in unstimulated and TGF β -treated cells in the set of genes upregulated (left, $n = 260$) or downregulated (right, $n = 194$) in TAC versus sham in fibroblasts *in vivo*. **h**, Co-accessibility (CoAc) change in fibroblasts of *Postn* peak 10/11 element with the promoters of genes within 1 Mb of the peak. Change in co-accessibility with the *Postn* promoter is highlighted in red. $n = 27$ genes within 1 Mb. Box plots show the 25th, 50th and 75th percentiles, with whiskers extending to the furthest value no further than 1.5 \times the interquartile range. **i**, *Postn* expression measured by qPCR in unstimulated and TGF β -treated in the CRISPRi control line. Unpaired, two-tailed *t*-test. **j**, *Postn* peak 8, 10/11 and 19 eRNA expression measured by qPCR in unstimulated and TGF β -treated fibroblasts in a CRISPRi control line and lines targeting peak 8, peak 10/11 or peak 19. Values are normalized to the CRISPRi control line in the unstimulated condition. One-way ANOVA followed by Sidak's correction, statistical significance is shown between the unstimulated samples and TGF β -treated samples. **k**, ChIP-qPCR data showing enrichment over chromatin input of H3K9me3 in control and *Postn* peak 10/11 CRISPRi lines in the unstimulated (left) and TGF β -treated (right) condition. Regions

amplifying peak 10, peak 11 and *Postn* promoters are shown. One-way ANOVA followed by Sidak's correction, statistical significance is shown between control and *Postn* peak 10/11 CRISPRi lines. **b, i–k**, Numbers above histograms show significant *P* values. Data are mean ± s.e.m.

Extended Data Fig. 7 Characterization of a catalogue of super-enhancers in fibroblasts, myeloid cells and endothelial cells.

a, Distribution of accessibility in fibroblasts, myeloid cells and endothelial cells in the TAC state identifies a class of distal regions (super-enhancers (SE)) for which the accessibility falls over the inflection point of the curve. **b, c**, Volcano plots showing correlation coefficients and corresponding *P* values (refer to the analysis depicted in Fig. 2e) of 239 super-enhancers in myeloid (**b**) and 267 super-enhancers in endothelial (**c**) cells. **d**, Distribution of H3K27ac in unstimulated and TGF β -treated fibroblasts identifies a class of distal regions (super-enhancers) for which the accessibility falls over the inflection point of the curve. **e**, Fraction of H3K27ac in unstimulated and TGF β -treated fibroblasts for the enhancers identified *in vivo* having a negative (left, $n = 264$) or positive (right, $n = 206$) correlation with heart function (based on analysis depicted in Fig. 2e). Box plots show the 25th, 50th and 75th percentiles, with whiskers extending to the furthest value no further than 1.5 \times the interquartile range.

Extended Data Fig. 8 Dynamic changes in chromatin accessibility at the *Meox1* super-enhancer.

a, Comparison of left ventricle ejection fraction with chromatin accessibility at the *Meox1* super-enhancer in fibroblasts, myeloid cells and endothelial cells. **b**, UMAP plot of *Meox1* expression in all non-cardiomyocytes ($n = 35,551$). **c**, Chromatin accessibility at the *Meox1* super-enhancer between samples in fibroblasts, myeloid cells and endothelial cells. Box plots show the 25th, 50th and 75th percentiles, with whiskers extending to the furthest value no further than 1.5 \times the interquartile range. Sample sizes (from left to right for each cell type): fibroblasts ($n = 676, 979, 1,906, 1,654$), myeloid cells ($n = 631, 1,080, 1,021, 712$), endothelial cells ($n = 731, 1,666, 1,030, 851$). Numbers above

box plots show significant P values, statistical significance (two-sided Wilcoxon rank-sum test) is shown for: sham versus TAC, sham versus TAC JQ1, TAC versus TAC JQ1 and TAC JQ1 versus TAC JQ1 withdrawn. **d**, scATAC-seq average signal across cells in fibroblast samples at the *Meox1* super-enhancer identifies multiple dynamic peaks in heart failure with pulsatile exposure to BET inhibition. **e**, Chromatin accessibility trend between samples (mean and 95% confidence interval) in all identified *Meox1* super-enhancer peaks.

Extended Data Fig. 9 Brd4-dependent regulation of Meox1 expression.

a, *Meox1* expression measured by qPCR in unstimulated and TGF β -treated fibroblasts, treated with or without JQ1. **b**, Expression measured by qPCR of individual BET genes in unstimulated or TGF β -treated fibroblasts treated with siRNA targeting control (siCtrl), *Brd2* (si*Brd2*), *Brd3* (si*Brd3*) or *Brd4* (si*Brd4*). Statistical significance is shown between unstimulated samples and TGF β -treated samples. **c**, *Meox1* expression measured by qPCR in unstimulated or TGF β -treated fibroblasts treated with siRNA targeting control, *Brd2*, *Brd3* or *Brd4*. Statistical significance is shown between the TGF β and control siRNA sample and the other TGF β -treated samples. **a–c**, All analysed samples were biological replicates. Numbers above graphs show significant P values (one-way ANOVA followed by Tukey post hoc test). Data are mean \pm s.e.m.

Extended Data Fig. 10 The peak 9/10 Meox1 enhancer is strongly transcribed after TGF β stimulation.

a, Volcano plot showing the $\log_2[FC]$ of the PRO-seq signal of all identified distal scATAC-seq peaks in fibroblasts ($n = 9,211$) between unstimulated and TGF β -treated fibroblasts. *Meox1* peaks 9 (red) and 10 (orange) are highlighted. **b**, Co-accessibility change in fibroblasts of *Meox1* peak 9/10 element with the promoters of genes within 1 Mb of the peak. Change in co-accessibility with the *Meox1* promoter is highlighted in red. $n = 115$ genes within 1 Mb. Box plots show the 25th, 50th and 75th percentiles, with whiskers extending to the furthest value no further than 1.5 \times the

interquartile range. **c, d**, Chromosome conformation capture (4C) using the *Meox1* peak 9/10 region (**c**) or *Meox1* promoter (**d**) as anchor point. 4C coverage in unstimulated and TGF β -treated fibroblasts are shown in a 922-kb (top) and 328-kb (bottom) genomic regions. The last track represents the called TGF β -induced loops with the anchor point (coloured in purple). **e**, *Meox1* expression measured by qPCR in unstimulated and TGF β -treated fibroblasts in the CRISPRi control line. Unpaired, two-tailed *t*-test. **f**, *Meox1* peak 5, 9/10 and 13 eRNA expression measured by qPCR in unstimulated and TGF β -treated fibroblasts in a CRISPRi control line and lines targeting peak 5, peak 9/10 or peak 13. Values are normalized to the CRISPRi control line in the unstimulated condition. One-way ANOVA followed by Sidak's correction, statistical significance is shown between unstimulated samples and TGF β -treated samples. **g**, ChIP–qPCR data showing enrichment over chromatin input of H3K9me3 in control and *Meox1* peak 9/10 CRISPRi lines in the unstimulated (left) and TGF β -treated (right) conditions. Regions amplifying peak 9, peak 10 and *Meox1* promoters are shown. One-way ANOVA followed by Sidak's correction, statistical significance is shown between CRISPRi control and targeted lines. **h**, Droplet digital (dd)PCR amplifying a wild-type or mutated region of *Meox1* peak 9/10 DNA. Parental fibroblast cell line, wild type (clone 20, isogenic control exposed to CRISPR Cas9 and gRNAs) and peak 9/10 knockout (KO) (clone 16) cell lines are shown. **i**, Schematic showing the *Meox1* locus with the scATAC-seq average signal across fibroblasts in TAC. SMAD2/3 motifs (Jaspar, MA1622.1) in the peak 9/10 region and in the *Meox1* promoter (± 1 kb from the transcription start site (TSS)) are highlighted. **j**, Expression measured by qPCR of *Smad2* (left) and *Smad3* (right) in unstimulated or TGF β -treated fibroblasts with siRNA targeting control and *Smad2* (left) or *Smad3* (right). One-way ANOVA followed by Tukey post hoc test. **k**, *Meox1* expression measured by qPCR in unstimulated or TGF β -treated fibroblasts with siRNA targeting either control or *Smad2*. One-way ANOVA followed by Tukey post hoc test. **e–g, j, k**, Numbers above histograms show significant *P* values. Data are mean \pm s.e.m.

Extended Data Fig. 11 MEOX1 is a regulator of fibroblast activation.

a, b, *Meox1* expression measured by qPCR in mouse primary cardiac fibroblasts (**a**) and immortalized cardiac fibroblasts (**b**) in the unstimulated condition, or after treatment with TGF β and control siRNA or TGF β and *Meox1* siRNA. One-way ANOVA followed by Tukey post hoc test. **c**, Left, immunofluorescence staining of α SMA in unstimulated and TGF β -treated cells treated with a control or a *Meox1*-targeting siRNA. Nuclei are marked by Hoechst. Scale bars, 100 μ m. Right, quantification of α SMA staining (two independent experiments). The fold change in intensity is normalized to the cell number. One-way ANOVA followed by Tukey post hoc test. **d**, Expression of *Acta2* (which encodes α SMA) measured by qPCR in the unstimulated condition, or after treatment with TGF β and control siRNA or TGF β and *Meox1* siRNA. One-way ANOVA followed by Tukey post hoc test. **e**, Left, representative images of EdU incorporation in the unstimulated condition, or after treatment with TGF β and control siRNA or TGF β and *Meox1* siRNA. DAPI (blue), EdU (red) and CellMask (green). Scale bars, 200 μ m. Right, quantification (two independent experiments). One-way ANOVA followed by Tukey post hoc test. **f**, *Meox1* expression measured by qPCR in wild-type and *Meox1* overexpression (o/e) mouse immortalized cardiac fibroblasts. Unpaired, two-tailed *t*-test. **g**, Pearson correlation of the three replicates of MEOX1 anti-haemagglutinin (HA) ChIP-seq in unstimulated and TGF β -treated cells. **h**, MEOX1 anti-HA ChIP-seq coverage in all protein-coding genes (\pm 2 kb gene body) in unstimulated and TGF β -treated fibroblasts. **i**, Pearson correlation of the two independent biological replicates of PRO-seq for TGF β and control siRNA or TGF β and *Meox1* siRNA treatments. **j**, PRO-seq coverage in the unstimulated condition, and after treatment with TGF β and control siRNA or TGF β and *Meox1* siRNA at the distal elements defined as more transcribed in TGF β versus unstimulated (2,101 sites) (see Fig. [2a](#)) that are either bound by MEOX1 (496 regions, top) or not (1,605 regions, bottom). **k**, PRO-seq coverage in the unstimulated condition, or after treatment with TGF β and control siRNA or TGF β and *Meox1* siRNA at the distal elements with high H3K27ac enrichment in the unstimulated condition bound by MEOX1 (379 regions). **l**, PRO-seq coverage of differentially transcribed genes (Wald test followed by Benjamini–Hochberg correction) in TGF β -treated fibroblasts with control or *Meox1* siRNA. Signal for replicates 1 and 2 is shown. **m**, PRO-seq tag density (\pm 5 kb gene body) after treatment with TGF β and control siRNA or TGF β and *Meox1* siRNA in genes upregulated in TGF β

and control siRNA versus TGF β and *Meox1* siRNA (left); and genes upregulated in TGF β and *Meox1* siRNA versus TGF β and control siRNA (right). **n**, Violin plot showing the normalized expression scores of genes upregulated in TGF β and control siRNA versus TGF β and *Meox1* siRNA in PRO-seq that were captured in the scRNA-seq data. Expression of sham and TAC fibroblast samples is shown. **o**, Number of MEOX1-bound genes in MEOX1 ChIP-seq (in TGF β -treated cells) in ± 2 kb gene body, ± 100 kb gene body or ± 500 kb gene body in genes differentially transcribed in PRO-seq: upregulated in TGF β versus unstimulated (left); downregulated in TGF β versus unstimulated (centre left); upregulated in TGF β and control siRNA versus TGF β and *Meox1* siRNA (centre right); upregulated in TGF β and *Meox1* siRNA versus TGF β and control siRNA (right). **p**, Coverage of MEOX1 ChIP (TGF β -treated cells), H3K27ac ChIP-seq (unstimulated and TGF β -treated cells) and PRO-seq (unstimulated condition, or treatment with TGF β and control siRNA or TGF β and *Meox1* siRNA) at the *Postn* locus. The *Postn* peak 10/11 region is highlighted in red. **a–f**, Numbers above graphs show significant *P* values. Data are means \pm s.e.m.

Extended Data Fig. 12 MEOX1 is expressed in human activated fibroblasts.

a, *POSTN* (left) and *MEOX1* (right) expression in human adult fibroblast clusters. *y* axes, normalized UMI levels²⁰. **b**, Track showing scATAC-seq average signal across fibroblasts in the human fetal heart²¹ in the *MEOX1* locus. The syntenic region of peak 9/10 is highlighted in red. **c**, Bulk RNA-seq data of human *MEOX1* expression (fragments per kilobase of transcript per million mapped reads, FPKM) in heart tissue in control individuals (Ctrl) and individuals with dilated cardiomyopathy (DCM) or hypertrophic cardiomyopathy (HCM) (GSE141910). Unpaired, two-tailed *t*-test with Benjamini–Hochberg correction. **d**, Bulk RNA-seq data of human *MEOX1* expression (raw counts) in lung tissue between control individuals and individuals with idiopathic pulmonary fibrosis (IPF) (GSE134692)²². Unpaired, two-tailed *t*-test. **c, d**, Numbers above the graphs show significant *P* values.

Supplementary information

Supplementary Information

This file contains the Supplementary Methods and Data and Supplementary References.

Reporting Summary

Supplementary Tables

This file contains Supplementary Tables 1-20 and a Supplementary Table Guide.

Peer Review File

Rights and permissions

Reprints and Permissions

About this article



Check for
updates

Cite this article

Alexanian, M., Przytycki, P.F., Micheletti, R. *et al.* A transcriptional switch governs fibroblast activation in heart disease. *Nature* **595**, 438–443 (2021).
<https://doi.org/10.1038/s41586-021-03674-1>

Download citation

- Received: 17 July 2020
- Accepted: 26 May 2021

- Published: 23 June 2021
- Issue Date: 15 July 2021
- DOI: <https://doi.org/10.1038/s41586-021-03674-1>

Comments

By submitting a comment you agree to abide by our [Terms](#) and [Community Guidelines](#). If you find something abusive or that does not comply with our terms or guidelines please flag it as inappropriate.

[Access through your institution](#)

[Change institution](#)

[Buy or subscribe](#)

Advertisement

This article was downloaded by **calibre** from <https://www.nature.com/articles/s41586-021-03674-1>

| [Section menu](#) | [Main menu](#) |

- Article
- [Published: 30 June 2021](#)

Shape of promoter antisense RNAs regulates ligand-induced transcription activation

- [Fan Yang](#) [ORCID: orcid.org/0000-0003-4440-6128](#)¹ nat,
- [Bogdan Tanasa](#)² nat,
- [Rudi Micheletti](#)¹,
- [Kenneth A. Ohgii](#)¹,
- [Aneel K. Aggarwal](#) [ORCID: orcid.org/0000-0003-4389-0173](#)³ &
- [Michael G. Rosenfeld](#) [ORCID: orcid.org/0000-0002-1572-156X](#)¹

[Nature](#) volume **595**, pages 444–449 (2021) [Cite this article](#)

- 6122 Accesses
- 16 Altmetric
- [Metrics details](#)

Subjects

- [Epigenetics](#)
- [Non-coding RNAs](#)
- [Transcription](#)

Abstract

The size of the transcriptional program of long non-coding RNAs in the mammalian genome has engendered discussions about their biological roles¹, particularly the promoter antisense (PAS) transcripts^{2,3}. Here we report the development of an assay—referred to as chromatin isolation by RNA–Cas13a complex—to quantitatively detect the distribution of RNA in the genome. The assay revealed that PAS RNAs serve as a key gatekeeper of a broad transcriptional pause release program, based on decommissioning the 7SK small nuclear RNA-dependent inhibitory P-TEFb complex. Induction of PAS RNAs by liganded ERα led to a significant loss of H3K9me3 and the release of basally recruited HP1α and KAP1 on activated target gene promoters. This release was due to PAS RNA-dependent recruitment of H3K9me3 demethylases, which required interactions with a compact stem-loop structure in the PAS RNAs, an apparent feature of similarly regulated PAS RNAs. Activation of the ERα-bound MegaTrans enhancer, which is essential for robust pause release, required the recruitment of phosphorylated KAP1, with its transfer to the cognate promoters permitting 17β-oestradiol-induced pause release and activation of the target gene. This study reveals a mechanism, based on RNA structure, that mediates the function of PAS RNAs in gene regulation.

Access options

Subscribe to Journal

Get full journal access for 1 year

\$199.00

only \$3.90 per issue

[Subscribe](#)

All prices are NET prices.

VAT will be added later in the checkout.

Tax calculation will be finalised during checkout.

Rent or Buy article

Get time limited or full article access on ReadCube.

from \$8.99

[Rent or Buy](#)

All prices are NET prices.

Additional access options:

- [Log in](#)
- [Access through your institution](#)
- [Learn about institutional subscriptions](#)

Fig. 1: E₂ induction of Pol II pause release and PAS RNA transcription.

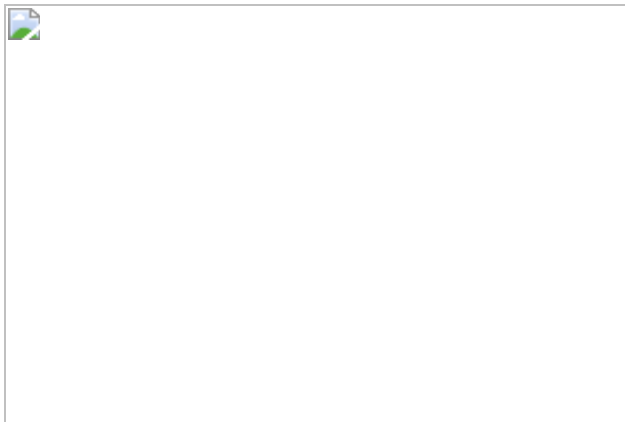


Fig. 2: The effect of the shape of PAS RNA on transcription activation.

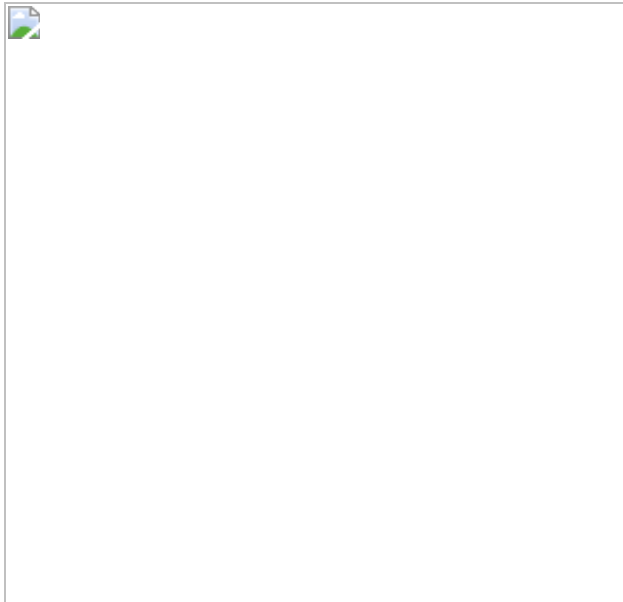


Fig. 3: H3K9me3 erasure at the promoter by PAS RNA.

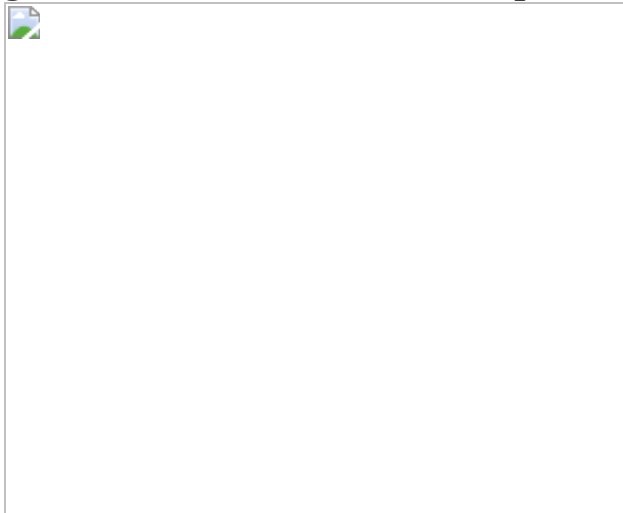


Fig. 4: PAS RNA stabilization of KDM4B and KDM4C at the promoter.



Data availability

The reagents, antibodies, primers and oligo DNA used in this study are listed in Supplementary Table 1. RNA sequences used in the RNA tethering experiments are available in Supplementary Table 2. The sequencing datasets generated from this study are deposited in the Gene Expression Omnibus (GEO) database using accession ID [GSE139199](#). The GRO-seq datasets used in this study were downloaded from [GSE41324](#). The ATAC-seq datasets used in this study were downloaded from [GSE99544](#). The H3K27ac ChIP-seq datasets used in this study were downloaded from [GSE62229](#). [Source data](#) are provided with this paper.

Code availability

The code used in this study is available at:

https://github.com/tanasa/the_scripts_analysis_ChIP_seq_PRO_seq.

References

1. 1.

Engreitz, J. M. et al. Local regulation of gene expression by lncRNA promoters, transcription and splicing. *Nature* **539**, 452–455 (2016).

[CAS](#) [PubMed](#) [PubMed Central](#) [Article](#) [ADS](#) [Google Scholar](#)

2. 2.

Sigova, A. A. et al. Divergent transcription of long noncoding RNA/mRNA gene pairs in embryonic stem cells. *Proc. Natl Acad. Sci. USA* **110**, 2876–2881 (2013).

[CAS](#) [PubMed](#) [PubMed Central](#) [Article](#) [ADS](#) [Google Scholar](#)

3. 3.

Flynn, R. A., Almada, A. E., Zamudio, J. R. & Sharp, P. A. Antisense RNA polymerase II divergent transcripts are P-TEFb dependent and substrates for the RNA exosome. *Proc. Natl Acad. Sci. USA* **108**, 10460–10465 (2011).

[CAS](#) [PubMed](#) [PubMed Central](#) [Article](#) [ADS](#) [Google Scholar](#)

4. 4.

Gupta, R. A. et al. Long non-coding RNA HOTAIR reprograms chromatin state to promote cancer metastasis. *Nature* **464**, 1071–1076 (2010).

[CAS](#) [PubMed](#) [PubMed Central](#) [Article](#) [ADS](#) [Google Scholar](#)

5. 5.

Chu, H. P. et al. TERRA RNA antagonizes ATRX and protects telomeres. *Cell* **170**, 86–101 (2017).

[CAS](#) [PubMed](#) [PubMed Central](#) [Article](#) [Google Scholar](#)

6. 6.

McHugh, C. A. et al. The Xist lncRNA interacts directly with SHARP to silence transcription through HDAC3. *Nature* **521**, 232–236 (2015).

[CAS](#) [PubMed](#) [PubMed Central](#) [Article](#) [ADS](#) [Google Scholar](#)

7. 7.

Sarma, K. et al. ATRX directs binding of PRC2 to Xist RNA and Polycomb targets. *Cell* **159**, 869–883 (2014).

[CAS](#) [PubMed](#) [PubMed Central](#) [Article](#) [Google Scholar](#)

8. 8.

Silva, A. M. et al. Long noncoding RNAs: a missing link in osteoporosis. *Bone Res.* **7**, 10 (2019).

[PubMed](#) [PubMed Central](#) [Article](#) [CAS](#) [Google Scholar](#)

9. 9.

Ulitsky, I. & Bartel, D. P. lincRNAs: genomics, evolution, and mechanisms. *Cell* **154**, 26–46 (2013).

[CAS](#) [PubMed](#) [PubMed Central](#) [Article](#) [Google Scholar](#)

10. 10.

Gebert, L. F. R. & MacRae, I. J. Regulation of microRNA function in animals. *Nat. Rev. Mol. Cell Biol.* **20**, 21–37 (2019).

[CAS](#) [PubMed](#) [PubMed Central](#) [Article](#) [Google Scholar](#)

11. 11.

Aravin, A. et al. A novel class of small RNAs bind to MILI protein in mouse testes. *Nature* **442**, 203–207 (2006).

[CAS](#) [PubMed](#) [Article](#) [ADS](#) [Google Scholar](#)

12. 12.

Girard, A., Sachidanandam, R., Hannon, G. J. & Carmell, M. A. A germline-specific class of small RNAs binds mammalian Piwi proteins. *Nature* **442**, 199–202 (2006).

[PubMed](#) [Article](#) [ADS](#) [Google Scholar](#)

13. 13.

Vagin, V. V. et al. A distinct small RNA pathway silences selfish genetic elements in the germline. *Science* **313**, 320–324 (2006).

[CAS](#) [PubMed](#) [Article](#) [ADS](#) [Google Scholar](#)

14. 14.

Treiber, T., Treiber, N. & Meister, G. Regulation of microRNA biogenesis and its crosstalk with other cellular pathways. *Nat. Rev. Mol. Cell Biol.* **20**, 5–20 (2019).

[CAS](#) [PubMed](#) [Article](#) [Google Scholar](#)

15. 15.

Sesto, N., Wurtzel, O., Archambaud, C., Sorek, R. & Cossart, P. The excludon: a new concept in bacterial antisense RNA-mediated gene regulation. *Nat. Rev. Microbiol.* **11**, 75–82 (2013).

[CAS](#) [PubMed](#) [Article](#) [Google Scholar](#)

16. 16.

Arab, K. et al. Long noncoding RNA TARID directs demethylation and activation of the tumor suppressor TCF21 via GADD45A. *Mol. Cell* **55**, 604–614 (2014).

[CAS](#) [PubMed](#) [Article](#) [Google Scholar](#)

17. 17.

Bester, A. C. et al. An integrated genome-wide CRISPRa approach to functionalize lncRNAs in drug resistance. *Cell* **173**, 649–664 (2018).

[CAS](#) [PubMed](#) [PubMed Central](#) [Article](#) [Google Scholar](#)

18. 18.

Canzio, D. et al. Antisense lncRNA transcription mediates DNA demethylation to drive stochastic protocadherin α promoter choice. *Cell* **177**, 639–653 (2019).

[CAS](#) [PubMed](#) [PubMed Central](#) [Article](#) [Google Scholar](#)

19. 19.

Ross-Innes, C. S. et al. Differential oestrogen receptor binding is associated with clinical outcome in breast cancer. *Nature* **481**, 389–393 (2012).

[CAS](#) [PubMed](#) [PubMed Central](#) [Article](#) [ADS](#) [Google Scholar](#)

20. 20.

He, H. H. et al. Differential DNase I hypersensitivity reveals factor-dependent chromatin dynamics. *Genome Res.* **22**, 1015–1025 (2012).

[CAS](#) [PubMed](#) [PubMed Central](#) [Article](#) [Google Scholar](#)

21. 21.

Wardell, S. E., Kazmin, D. & McDonnell, D. P. Research resource: transcriptional profiling in a cellular model of breast cancer reveals functional and mechanistic differences between clinically relevant SERM and between SERM/estrogen complexes. *Mol. Endocrinol.* **26**, 1235–1248 (2012).

[CAS](#) [PubMed](#) [PubMed Central](#) [Article](#) [Google Scholar](#)

22. 22.

Liu, Z. et al. Enhancer activation requires trans-recruitment of a mega transcription factor complex. *Cell* **159**, 358–373 (2014).

[CAS](#) [PubMed](#) [PubMed Central](#) [Article](#) [Google Scholar](#)

23. 23.

Nair, S. J. et al. Phase separation of ligand-activated enhancers licenses cooperative chromosomal enhancer assembly. *Nat. Struct. Mol. Biol.* **26**, 193–203 (2019).

[CAS](#) [PubMed](#) [PubMed Central](#) [Article](#) [Google Scholar](#)

24. 24.

Li, W. et al. Functional roles of enhancer RNAs for oestrogen-dependent transcriptional activation. *Nature* **498**, 516–520 (2013).

[CAS](#) [PubMed](#) [PubMed Central](#) [Article](#) [ADS](#) [Google Scholar](#)

25. 25.

Hah, N. et al. A rapid, extensive, and transient transcriptional response to estrogen signaling in breast cancer cells. *Cell* **145**, 622–634 (2011).

[CAS](#) [PubMed](#) [PubMed Central](#) [Article](#) [Google Scholar](#)

26. 26.

Danko, C. G. et al. Signaling pathways differentially affect RNA polymerase II initiation, pausing, and elongation rate in cells. *Mol. Cell* **50**, 212–222 (2013).

[CAS](#) [PubMed](#) [PubMed Central](#) [Article](#) [Google Scholar](#)

27. 27.

Lis, J. T. A. A 50 year history of technologies that drove discovery in eukaryotic transcription regulation. *Nat. Struct. Mol. Biol.* **26**, 777–782

(2019).

[CAS](#) [PubMed](#) [PubMed Central](#) [Article](#) [Google Scholar](#)

28. 28.

Peterlin, B. M. & Price, D. H. Controlling the elongation phase of transcription with P-TEFb. *Mol. Cell* **23**, 297–305 (2006).

[CAS](#) [PubMed](#) [Article](#) [PubMed Central](#) [Google Scholar](#)

29. 29.

Chu, C., Qu, K., Zhong, F. L., Artandi, S. E. & Chang, H. Y. Genomic maps of long noncoding RNA occupancy reveal principles of RNA–chromatin interactions. *Mol. Cell* **44**, 667–678 (2011).

[CAS](#) [PubMed](#) [PubMed Central](#) [Article](#) [Google Scholar](#)

30. 30.

Engreitz, J. M. et al. The Xist lncRNA exploits three-dimensional genome architecture to spread across the X chromosome. *Science* **341**, 1237973 (2013).

[PubMed](#) [PubMed Central](#) [Article](#) [CAS](#) [Google Scholar](#)

31. 31.

Simon, M. D. et al. The genomic binding sites of a noncoding RNA. *Proc. Natl Acad. Sci. USA* **108**, 20497–20502 (2011).

[CAS](#) [PubMed](#) [PubMed Central](#) [Article](#) [ADS](#) [Google Scholar](#)

32. 32.

Abudayyeh, O. O. et al. RNA targeting with CRISPR–Cas13. *Nature* **550**, 280–284 (2017).

[PubMed](#) [PubMed Central](#) [Article](#) [ADS](#) [CAS](#) [Google Scholar](#)

33. 33.

Cox, D. B. T. et al. RNA editing with CRISPR–Cas13. *Science* **358**, 1019–1027 (2017).

[CAS](#) [PubMed](#) [PubMed Central](#) [Article](#) [ADS](#) [Google Scholar](#)

34. 34.

West, J. A. et al. The long noncoding RNAs NEAT1 and MALAT1 bind active chromatin sites. *Mol. Cell* **55**, 791–802 (2014).

[CAS](#) [PubMed](#) [PubMed Central](#) [Article](#) [Google Scholar](#)

35. 35.

Larson, A. G. et al. Liquid droplet formation by HP1 α suggests a role for phase separation in heterochromatin. *Nature* **547**, 236–240 (2017).

[CAS](#) [PubMed](#) [PubMed Central](#) [Article](#) [ADS](#) [Google Scholar](#)

36. 36.

McNamara, R. P. et al. KAP1 recruitment of the 7SK snRNP complex to promoters enables transcription elongation by RNA polymerase II. *Mol. Cell* **61**, 39–53 (2016).

[CAS](#) [PubMed](#) [Article](#) [Google Scholar](#)

37. 37.

Bunch, H. et al. TRIM28 regulates RNA polymerase II promoter-proximal pausing and pause release. *Nat. Struct. Mol. Biol.* **21**, 876–883 (2014).

[CAS](#) [PubMed](#) [PubMed Central](#) [Article](#) [Google Scholar](#)

38. 38.

Liu, X. et al. In situ capture of chromatin interactions by biotinylated dCas9. *Cell* **170**, 1028–1043 (2017).

[CAS](#) [PubMed](#) [PubMed Central](#) [Article](#) [Google Scholar](#)

39. 39.

Mahat, D. B. et al. Base-pair-resolution genome-wide mapping of active RNA polymerases using precision nuclear run-on (PRO-seq). *Nat. Protoc.* **11**, 1455–1476 (2016).

[PubMed](#) [PubMed Central](#) [Article](#) [Google Scholar](#)

40. 40.

Yang, F., Zhang, H., Mei, Y. & Wu, M. Reciprocal regulation of HIF-1 α and lincRNA-p21 modulates the Warburg effect. *Mol. Cell* **53**, 88–100 (2014).

[CAS](#) [PubMed](#) [Article](#) [PubMed Central](#) [Google Scholar](#)

41. 41.

Shechner, D. M., Hacisuleyman, E., Younger, S. T. & Rinn, J. L. Multiplexable, locus-specific targeting of long RNAs with CRISPR-Display. *Nat. Methods* **12**, 664–670 (2015).

[CAS](#) [PubMed](#) [PubMed Central](#) [Article](#) [Google Scholar](#)

42. 42.

Konermann, S. et al. Genome-scale transcriptional activation by an engineered CRISPR–Cas9 complex. *Nature* **517**, 583–588 (2015).

[CAS](#) [PubMed](#) [Article](#) [ADS](#) [PubMed Central](#) [Google Scholar](#)

43. 43.

Smola, M. J., Rice, G. M., Busan, S., Siegfried, N. A. & Weeks, K. M. Selective 2'-hydroxyl acylation analyzed by primer extension and mutational profiling (SHAPE-MaP) for direct, versatile and accurate RNA structure analysis. *Nat. Protoc.* **10**, 1643–1669 (2015).

[CAS](#) [PubMed](#) [PubMed Central](#) [Article](#) [Google Scholar](#)

44. 44.

Langmead, B. & Salzberg, S. L. Fast gapped-read alignment with Bowtie 2. *Nat. Methods* **9**, 357–359 (2012).

[CAS](#) [PubMed](#) [PubMed Central](#) [Article](#) [Google Scholar](#)

45. 45.

Heinz, S. et al. Simple combinations of lineage-determining transcription factors prime *cis*-regulatory elements required for macrophage and B cell identities. *Mol. Cell* **38**, 576–589 (2010).

[CAS](#) [PubMed](#) [PubMed Central](#) [Article](#) [Google Scholar](#)

46. 46.

Robinson, M. D., McCarthy, D. J. & Smyth, G. K. edgeR: a Bioconductor package for differential expression analysis of digital gene expression data. *Bioinformatics* **26**, 139–140 (2010).

[CAS](#) [PubMed](#) [PubMed Central](#) [Article](#) [Google Scholar](#)

47. 47.

Busan, S. & Weeks, K. M. Accurate detection of chemical modifications in RNA by mutational profiling (MaP) with ShapeMapper 2. *RNA* **24**, 143–148 (2018).

[CAS](#) [PubMed](#) [PubMed Central](#) [Article](#) [Google Scholar](#)

48. 48.

Andrews, R. J., Baber, L. & Moss, W. N. Mapping the RNA structural landscape of viral genomes. *Methods* **183**, 57–67 (2020).

[CAS](#) [PubMed](#) [Article](#) [PubMed Central](#) [Google Scholar](#)

[Download references](#)

Acknowledgements

We are grateful to K. Jepsen (Director of IGM, UCSD) for Illumina sequencing, J. Hightower for assistance with figure preparation, M. Ghassemian from the UCSD Biomolecular/Proteomics Mass Spectrometry Facility for mass spectrometry analysis, P. Irving (UNC), and R. Andrews and W. Moss for their suggestions on SHAPE-MaP analysis and on the ScanFold pipeline, respectively. F.Y. was a recipient of the Prostate Cancer Research Program (PCRP) Postdoctoral Training Award of the Department of Defense (W81XWH-16-1-0548). M.G.R. is an investigator with the Howard Hughes Medical Institute. This work was supported by grants from the NIDDK and NHLBI (HL150521, DK018477 and DK039949) to M.G.R. and by NIH grant R35-GM131780 to A.K.A.

Author information

Author notes

1. These authors contributed equally: Fan Yang, Bogdan Tanasa

Affiliations

1. Howard Hughes Medical Institute, Department and School of Medicine, University of California, San Diego, La Jolla, CA, USA

Fan Yang, Rudi Micheletti, Kenneth A. Ohgi & Michael G. Rosenfeld

2. Department of Ophthalmology, Stanford University School of Medicine, Palo Alto, CA, USA

Bogdan Tanasa

3. Department of Pharmacological Sciences, Icahn School of Medicine at Mount Sinai, New York, NY, USA

Aneel K. Aggarwal

Authors

1. Fan Yang

[View author publications](#)

You can also search for this author in [PubMed](#) [Google Scholar](#)

2. Bogdan Tanasa

[View author publications](#)

You can also search for this author in [PubMed](#) [Google Scholar](#)

3. Rudi Micheletti

[View author publications](#)

You can also search for this author in [PubMed](#) [Google Scholar](#)

4. Kenneth A. Ohgi

[View author publications](#)

You can also search for this author in [PubMed](#) [Google Scholar](#)

5. Aneel K. Aggarwal

[View author publications](#)

You can also search for this author in [PubMed](#) [Google Scholar](#)

6. Michael G. Rosenfeld

[View author publications](#)

You can also search for this author in [PubMed](#) [Google Scholar](#)

Contributions

F.Y. and M.G.R. conceived the original ideas and designed the experimental strategies. F.Y. performed the majority of the experiments with participation from R.M. on PRO-seq experiments. B.T. performed all of the bioinformatics analyses with contribution from A.K.A. on 3D RNA structure modelling. K.A.O. prepared samples for deep sequencing. F.Y. and M.G.R. wrote the manuscript with input from B.T. and A.K.A.

Corresponding authors

Correspondence to [Fan Yang](#) or [Michael G. Rosenfeld](#).

Ethics declarations

Competing interests

The authors declare no competing interests.

Additional information

Peer review information *Nature* thanks Stephen Mack and the other, anonymous, reviewer(s) for their contribution to the peer review of this work.

Publisher's note Springer Nature remains neutral with regard to jurisdictional claims in published maps and institutional affiliations.

Extended data figures and tables

[Extended Data Fig. 1 PAS RNA and Pol II promoter proximal pause release induced by E2.](#)

a, Box plot analysis of the pausing ratio based on GRO-seq data set in GSE41324 ($n = 3$ independent experiments) for PR genes and 837

randomly selected genes (RSG), in the absence or presence of E₂ treatment. We hereafter use the abbreviations ‘PR’ for ‘the 837 upregulated genes with Pol II pause release’, and ‘RSG’ for ‘the 837 randomly selected genes’. **b**, Heat map representation of GRO-seq (GSE41324) normalized tag counts centred on the 837 PR promoters (± 3 kb) showing robust PAS RNA transcription at PR promoters induced by E₂. **c**, Box plots analysis of Pol II ChIP-seq data representing the effect of E₂ on Pol II occupancy over the gene bodies of the PR versus the gene bodies of RSG. **d**, Cumulative distribution of the Pol II pausing ratio based on Pol II ChIP-seq analysis for the PR genes in the absence or presence of E₂ treatment. Data were generated in two independent experiments. The *P* value was calculated with two-sided Kolmogorov–Smirnov test. **e**, Box plot analysis of the pausing ratio based on Pol II ChIP-seq data for PR genes and RSG, in the absence or presence of E₂ treatment. **f**, ChIP-seq tag distribution analysis representing the effect of E₂ on NELFA binding at the promoters of PR genes. **g**, Heat map of NELFA ChIP-seq analysis representing the effect of E₂ on NELFA binding at the promoters of PR genes. **h**, Heat map of NEAT1 ChIRC^{13a}-seq showing a subset of NEAT1 binding sites marked with promoter mark H3K4me3, revealing that lncRNA *NEAT1* localized to approximately 603 promoters in the absence of E₂ treatment. **i**, Genomic distribution of 7SK snRNA in the basal (-E₂) condition. Consistent with 7SK function regulating promoter-proximal pausing of Pol II, a large number of 7SK binding sites were localized on the promoter region of a large set of genes ($n = 6,885$, about 54.9% of its total binding sites). Unexpectedly, a large number of 7SK binding sites were also found to be located on intronic ($n = 1,351$, about 10.8% of its total binding sites) and intergenic ($n = 2,144$, approximately 17.1% of its total binding sites) regions. **j**, ChIRC^{13a}-seq tag profile representing the effect of E₂ treatment on 7SK binding at PR promoters. **k**, Heat map of 7SK ChIRC^{13a}-seq analysis representing the effect of E₂ on 7SK binding at the promoters of PR genes. **l**, Box plot analysis of HEXIM1 ChIP-seq data representing the effect of E₂ on HEXIM1 binding at PR promoters and RSG promoters. **m**, Heat map of HEXIM1 ChIP-seq data representing the effect of E₂ on HEXIM1 binding at the PR promoters. In **a**, **c**, **e**, **l**, the box plots denote the medians, the interquartile ranges and the whiskers. Data were generated in

two independent experiments. The *P* values were calculated with two-sided Wilcoxon test.

Extended Data Fig. 2 E₂-induced Pol II pause release occurs specifically on PR genes.

a, Box plot analysis of GRO-seq data set in GSE41324 showing the decrease of the pausing ratio at PR genes, in contrast to the 239 E₂-upregulated genes that do not show pause release, following E₂ treatment. These 239 genes, if without specification, are hereafter defined as non-PR genes. **b**, Cumulative distribution of the Pol II pausing ratio based on Pol II ChIP-seq analysis for the non-PR genes following E₂ treatment. Data were generated in two independent experiments. The *P* value was calculated with two-sided Kolmogorov–Smirnov test. **c**, Box plot analysis of GRO-seq data set in GSE41324 showing robust gene expression of PR and non-PR genes following E₂ treatment. **d**, Box plot analysis of GRO-seq data of the datasets in GSE41324 showing PAS RNA expression at the promoters of PR genes and at the promoters of non-PR genes, in the absence or presence of E₂ treatment. To compute PAS RNA expression, we counted the number of GRO-seq reads on 1-kb region in front of the TSS, on the opposite strand, as informed by the GRO-seq profiles around TSS regions. **e**, Box plot analysis of 7SK ChIRC^{13a}-seq data representing the effect of E₂ on 7SK binding at PR and non-PR promoters. **f–n**, Box plot analysis of NELFA (**f**), HEXIM1 (**g**), Suv39H1 (**h**), KDM4B (**i**), KDM4C (**j**), H3K9me3 (**k**), H3K27me3 (**l**), G9a (**m**) and HP1 α (**n**) ChIP-seq data representing the effect of E₂ on the corresponding factor binding at PR and non-PR promoters. The box plots denote the medians, the interquartile ranges and the whiskers. Data were generated in two independent experiments. The *P* values were calculated with two-sided Wilcoxon test.

Extended Data Fig. 3 Specificity of CRISPR–Cas13a-based PAS RNA degradation.

a–c, Genome browser views of Pol II ChIP-seq and GRO-seq on *TFF1* (**a**), *MYC* (**b**) and *ABAT* (**c**) genomic loci, in the absence or presence of E₂.

treatment. The red arrowhead indicates upregulation of PAS RNA. **d–f**, Real-time RT–PCR analysis of Bio-RIP data showing specificity of the CRISPR–Cas13a strategy mediated *ABAT*pasRNA (**d**), *MYC*pasRNA (**e**) and *TFF1*pasRNA (**f**) knockdown. Data shown as individual values, mean ± s.d. ($n = 3$). The P values were calculated with two-sided Student's t -test. **g**, Real-time PCR analysis of Bio-ChIP data showing that PAS RNA tethering by the CRISPR–dCas9 strategy did not affect functional assembly of CRISPR–dCas9 complex at the *ABAT* promoter. Data shown as individual values, mean ± s.d. ($n = 3$). The P values were calculated with two-sided Student's t -test.

[Source data](#)

Extended Data Fig. 4 Context-dependent gene activation by PAS RNA tethering.

a, c, e, g, Genome browser views of ATAC-seq, PRO-seq, Pol II ChIP-seq and H3K4me3 ChIP-seq on selected *FNIP1* (**a**), *IRF1* (**c**), *OR2J1* (**e**) and *DEFB129* (**g**) genomic regions in the absence or presence of E₂ treatment. **b, d, f, h**, Real-time RT–PCR data showing the effect of tethering a serial of pasRNAs or control RNAs to the *FNIP1* (**b**), *IRF1* (**d**), *OR2J1* (**f**) and *DEFB129* (**h**) promoters on the respective coding gene expression in the -E₂ condition by the CRISPR–dCas9 strategy. Data shown as individual values, mean ± s.d. ($n = 3$). The Shapiro–Wilk test was computed first to verify the normal distribution of the real-time RT–PCR data before P values were calculated with two-sided Welch's t -test. **i–k**, Real-time RT–PCR data showing the effect of using the CRISPR–dCas9/VP64 (CRISPRa) strategy targeting the *TMEM114* (**i**), *OR2J1* (**j**) and *DEFB129* (**k**) promoters on the respective coding gene expression in the -E₂ condition. Data shown as individual values, mean ± s.d. ($n = 3$). The P values were calculated with two-sided Student's t -test. **l**, Bar plot data showing the RPKM expression values of the genes to which dCas9–PAS RNAs were delivered. RPKM values were computed based on GRO-seq datasets in GSE41324 (combined replicates).

[Source data](#)

Extended Data Fig. 5 Higher-order structure of PAS RNA.

a, Box plot analysis of Gibbs free energy (dG) showing that PAS RNAs, in their native state, have a significantly lower minimum free energy (MFE) than synthetically random RNAs of the same length and their cognate mRNAs, suggesting that PAS RNAs may tend to form more secondary structures to maintain their stability. The synthetically random RNAs were generated with the packages kebabs and Rbioinf in R/Bioconductor version 3.12. PAS RNAs were compared with two independent synthetic random RNAs (500 nt, 1,000 nt) and their cognate mRNAs to calculate the difference of dG. The box plots denote the medians, the interquartile ranges and the whiskers. The *P* values were calculated with two-sided Wilcoxon test. **b**, Box plot analysis of z-scores showing that PAS RNAs have a higher percentage of negatively shifted z-score windows less than -1 than synthetically random RNAs of the same length and their cognate mRNAs, suggesting more local regions of potential structure in PAS RNAs. In the calculation of z-scores, we used the methodology described in ScanFold (<https://github.com/moss-lab/ScanFold>) that uses scanning windows of 120-nt length, and a step size of 40 nt, and generates 30 shuffled versions of the corresponding RNA sequence, using the same dinucleotide frequency. The box plots denote the medians, the interquartile ranges and the whiskers. PAS RNAs were compared with two independent sets of synthetic random RNAs (500 nt, 1,000 nt) and their cognate mRNAs to calculate the difference of z-scores. The *P* values were calculated with two-sided Wilcoxon test. **c–e**, Predicted MFE-based secondary structure of *ABAT*pasRNA (**c**), *MYC*pasRNA (**d**) and *TFF1*pasRNA (**e**) by RNAfold webserver. Owing to the long length, only a partial sequence of *MYC*pasRNA and *TFF1*pasRNA was used for computational analysis. **f–i**, Predicted MFE-based secondary structure by RNAfold webserver and genome browser views of *FAM110A*pasRNA (**f**), *FAM102A*pasRNA (**g**) *HIGD1A*pasRNA (**h**) and *KCNK6*pasRNA (**i**). The red arrowhead indicates the upregulation of PAS RNA.

Extended Data Fig. 6 E2-dependent PR promoter activation.

a–e, Box plot analysis of ChIP-seq data for H3K4me3 (**a**), H3K9K14ac (**b**), H3K27ac (**c**), H3K56ac (**d**) and H3K122ac (**e**) at the PR and RSG

promoters, in the absence or presence of E₂ treatment. The box plots denote the medians, the interquartile ranges and the whiskers. Data were generated in two independent experiments. The *P* values were calculated with two-sided Wilcoxon test. **f**, Genome browser views of H3K4me3, H3K9K14ac, H3K27ac, H3K56ac and H3K122ac ChIP-seq on a selected *TFF1* genomic region in the absence or presence of E₂ treatment.

Extended Data Fig. 7 PAS RNAs license cognate coding gene transcription activation.

a–c, H3K27me3 ChIP-qPCR data showing the effect of *TFF1*pasRNA (**a**), *MYC*pasRNA (**b**) and *ABAT*pasRNA (**c**) knockdown on the accumulation of H3K27me3 on the respective cognate gene promoter following E₂ treatment. Data shown as individual values, mean ± s.d. (*n* = 3). The *P* values were calculated with two-sided Student's *t*-test. **d**, H3K9me3 ChIP-qPCR data showing the effect of tethering *ABAT*pasRNA using the CRISPR–dCas9 strategy to the *TRIB2*, *FNIP1* and *IRF1* promoters on H3K9me3 accumulation on the respective cognate coding gene promoter in the -E₂ condition. Data shown as individual values, mean ± s.d. (*n* = 3). The *P* values were calculated with one-sided Student's *t*-test. **e, g**, ChIP-seq tag distribution analysis representing the effect of E₂ on Suv39H1 binding (**e**) and H3K27me3 (**g**) accumulation at PR promoters. **f, h**, Box plot analysis representing the effect of E₂ on Suv39H1 (**f**) and H3K27me3 (**h**) occupancy at PR gene promoters and RSG promoters. The box plots denote the medians, the interquartile ranges and the whiskers. Data were generated in two independent experiments. The *P* values were calculated with two-sided Wilcoxon test. **i**, Immunoblot analysis showing no effect of *TFF1*pasRNA, *MYC*pasRNA and *ABAT*pasRNA knockdown on KDM4B and KDM4C expression following E₂ treatment. The experiment was repeated three times with similar results. See Supplementary Fig. 1 for gel source data. **j**, Cell lysates as described in Fig. 2m were subjected to co-immunoprecipitation with anti-Flag antibody (for flag-dCas9) followed by immunoblot analysis with antibodies as indicated. The experiment was repeated three times with similar results. See Supplementary Fig. 1 for gel source data. **k**, ChIP-seq tag distribution analysis displaying the effect of E₂

treatment on G9a (EHMT2) binding at the PR promoters. **I**, Box plot analysis representing the effect of E₂ on G9a binding at the PR and RSG promoters. The box plots denote the medians, the interquartile ranges and the whiskers. Data were generated in two independent experiments. The P values were calculated with two-sided Wilcoxon test. **m–o**, Real-time RT-PCR data showing the effect of combined knockdown of *Suv39H1* and *G9a* in *TFF1*pasRNA (**m**), *MYC*pasRNA (**n**) and *ABAT*pasRNA (**o**) knockdown MCF-7 cells by the CRISPR–Cas13a strategy on the respective cognate coding gene transcription following E₂ treatment. Data shown as individual values, mean ± s.d. (n = 3). The P values were calculated with one-sided Student's t-test. **p**, The profile analysis of H3K9me3 ChIP-seq, Pol II ChIP-seq and H3K9me3 ChIP-seq performed in sh*KDM4B/4C* MCF-7 cells in the -E₂ condition showing major H3K9me3 accumulation on +1 nucleosome after knockdown of KDM4B/4C.

[Source data](#)

[Extended Data Fig. 8 The effect of KDM4B/KDM4C on E₂-induced Pol II promoter pause release.](#)

a, ChIP-seq tag distribution analysis representing the effect of *KDM4B/4C* knockdown on H3K9me3 accumulation at the PR promoters. **b**, Heat map of H3K9me3 ChIP-seq data representing the effect of *KDM4B/4C* knockdown on H3K9me3 binding at the PR promoters. **c**, Genome browser views of KDM4B and KDM4C ChIP-seq in the presence or absence of E₂, and H3K9me3 ChIP-seq after knockdown of *KDM4B* and *KDM4C* on the *TFF1* genomic region. **d**, ChIP-seq tag distribution analysis representing the effect of E₂ on H3K36me3 accumulation at the PR promoters. **e**, Genome browser views of H3K36me3 ChIP-seq in the presence or absence of E₂ on the *TFF1* genomic region. **f**, Box plot analysis of the pausing ratio based on Pol II ChIP-seq data representing the effect of *KDM4B/4C* knockdown on the pausing ratio for PR genes and RSG following E₂ treatment. The box plots denote the medians, the interquartile ranges and the whiskers. Data were generated in two independent experiments. The P values were calculated with two-sided Wilcoxon test. **g**, ChIP-seq tag distribution

analysis representing the effect of *KDM4B/4C* knockdown on Pol II accumulation at PR promoters following E₂ treatment. **h**, Schematic structure of KDM4B and KDM4C proteins. Between the JMJC domain and the double PHD/Tudor domain is the predicted IDR region, analysed by the IUPred2A online tool. **i**, Immunoblot analysis of full-length KDM4C and the relevant KDM4C-mutant expression in sh*KDM4C* MCF-7 cells following E₂ treatment. The experiment was repeated three times with similar results. See Supplementary Fig. 1 for gel source data. **j–l**, Real-time RT–PCR data showing the effect of *KDM4B/4C* knockdown on the expression of *TFF1*pasRNA (**j**), *MYC*pasRNA (**k**) and *ABAT*pasRNA (**l**) following E₂ treatment. Data shown as individual values, mean ± s.d. (n = 3). The P values were calculated with two-sided Student's *t*-test.

[Source data](#)

[Extended Data Fig. 9 Functional importance of HP1 in Pol II pause release.](#)

a–c, Real-time RT–PCR data showing the effect of knockdown of *HP1α*, *HP1β* and *HP1γ* on *TFF1* (**a**), *MYC* (**b**) and *ABAT* (**c**) coding gene transcription. Data shown as individual values, mean ± s.d. (n = 3). The P values were calculated with two-sided Student's *t*-test. **d**, ChIP-seq tag distribution analysis representing the effect of E₂ on HP1α binding at the PR promoters. **e**, Box plot analysis of HP1α ChIP-seq data (n = 1 experiment) representing the effect of E₂ on HP1α binding at the PR and RSG promoters. The box plots denote the medians, the interquartile ranges and the whiskers. The P values were calculated with two-sided Wilcoxon test. **f**, Genome browser views of HP1α ChIP-seq (in the presence or absence of E₂), HP1α (4E) mutant Bio-ChIP and HP1α (4A) mutant Bio-ChIP on the *TFF1* genomic region. **g**, Domain map of human HP1α. Phosphorylatable serine residues, and the corresponding phosphor-mimetic glutamic acid residues and phosphor-compromised alanine residues at the N-terminal extension (NTE) of human HP1α regulating its chromodomain (CD)–H3K9me3 tail interaction are in bold. CSD, chromoshadow domain; CTE, C-terminal extension; H, hinge region. **h**, Bio-ChIP-seq tag distribution (n = 1 experiment) representing the effect of phosphorylation at

the NTE on HP1 α binding at the PR promoters. **i**, Box plot analysis of HP1 α Bio-ChIP-seq data ($n = 1$ experiment) showing the effect of phosphorylation at the NTE on HP1 α occupancy at the PR gene promoters and RSG promoters. The box plots denote the medians, the interquartile ranges and the whiskers. The P values were calculated with two-sided Wilcoxon test. **j**, Heat map of HP1 α Bio-ChIP-seq data showing the effect of phosphorylation at the NTE on HP1 α occupancy at the PR gene promoters and RSG promoters. **k**, The profiles of PRO-seq normalized tag counts, starting 3 kb upstream of the transcription start site (TSS) to 3 kb downstream of the TSS in shCTL MCF-7 cells or shHP1 α/β MCF-7 cells. **l**, Box plot analysis of PRO-seq data representing the effect of HP1 α/β knockdown on transcription of the PR genes and RSGs. The box plots denote the medians, the interquartile ranges and the whiskers. Data were generated in two independent experiments. The P values were calculated with two-sided Wilcoxon test. **m**, Genome browser views of PRO-seq in the presence or absence of HP1 α/β knockdown on the *TFF1* genomic region.

Source data

Extended Data Fig. 10 HP1-mediated stabilization of 7SK and NELFA at the promoter.

a–c, HP1 α ChIP-qPCR data showing the effect of *TFF1*pasRNA (**a**), *MYC*pasRNA (**b**) and *ABAT*pasRNA (**c**) knockdown on accumulation of HP1 α on the respective cognate coding gene promoter following E₂ treatment. Data shown as individual values, mean \pm s.d. ($n = 3$). The P values were calculated with two-sided Student's *t*-test. **d–f**, Real-time RT–PCR data showing the effect of knockdown of HP1 α and HP1 β in *TFF1*pasRNA (**d**), *MYC*pasRNA (**e**) and *ABAT*pasRNA (**f**) knockdown MCF-7 cells by the CRISPR–Cas13a strategy on the respective cognate coding gene transcription. Data shown as individual values, mean \pm s.d. ($n = 3$). The P values were calculated with two-sided Student's *t*-test. **g, j**, 7SK ChIRC^{13a}–seq (**g**) and NELFA ChIP-seq (**j**) tag distribution analysis representing the effect of HP1 α and HP1 β knockdown on 7SK (**g**) and NELFA (**j**) binding at the PR promoters. **h, k**, Box plot analysis of 7SK ChIRC^{13a}–seq ($n = 1$ experiment) (**h**) and NELFA ChIP-seq (**k**) ($n = 1$ experiment) data representing the effect of HP1 α and HP1 β knockdown on

7SK (**h**) and NELFA (**k**) binding at the PR and RSG promoters. The box plots denote the medians, the interquartile ranges and the whiskers. The *P* values were calculated with two-sided Wilcoxon test. **i, l**, Heat map of 7SK ChIRC^{13a}-seq (**i**) and NELFA ChIP-seq (**l**) data representing the effect of *HP1α* and *HP1β* knockdown on 7SK (**i**) and NELFA (**l**) binding at the PR promoters.

[Source data](#)

[**Extended Data Fig. 11 Dual role of KAP1 in transcriptional regulation.**](#)

a, Heat map showing mass spectrometry analysis of HP1-associated proteins. Identified KAP1 is shown on the right. **b**, Co-IP result showing interaction between HP1 and KAP1. The experiment was repeated three times with similar results. See Supplementary Fig. 1 for gel source data. **c**, ChIRC^{13a}-seq tag distribution representing the effect of *KAP1* knockdown on 7SK binding at the PR promoters. **d**, Box plot analysis of 7SK ChIRC^{13a}-seq data representing the effect of *KAP1* knockdown (*n* = 1 experiment) on 7SK binding at the PR and RSG promoters. The box plots denote the medians, the interquartile ranges and the whiskers. The *P* values were calculated with two-sided Wilcoxon test. **e**, Heat map of 7SK ChIRC^{13a}-seq data representing the effect of *KAP1* knockdown on 7SK binding at the PR promoters. **f**, ChIP-seq tag distribution analysis representing the effect of E₂ on KAP1 binding at the PR promoters. **g**, Box plot analysis of KAP1 ChIP-seq data representing the effect of E₂ on KAP1 binding at the PR and RSG promoters. The box plots denote the medians, the interquartile ranges and the whiskers. Data were generated in two independent experiments. The *P* values were calculated with two-sided Wilcoxon test. **h, j**, Box plot analysis of PRO-seq data (**h**) (*n* = 1 experiment) and Pol II S2P data (**j**) (*n* = 1 experiment) representing the effect of *KAP1* knockdown on the transcription of the PR genes and RSGs following E₂ treatment. The box plots denote the medians, the interquartile ranges and the whiskers. The *P* values were calculated with two-sided Wilcoxon test. **i**, The profiles of PRO-seq tag counts on PR genes from 3 kb

upstream of the TSS to 3 kb downstream of TSS in shCTL MCF-7 cells and sh*KAP1* MCF-7 cells following E₂ treatment.

Extended Data Fig. 12 Phospho-KAP1(S824) as a determinant for KAP1-mediated transcription activation.

a, ChIP-qPCR data showing the effect of E₂ on accumulation of phospho-KAP1(S824) on the selective coding gene promoter. Data shown as individual values, mean ± s.d. (*n* = 3). The *P* values were calculated with two-sided Student's *t*-test. **b**, Sequence alignment of KAP1 (wild type (WT), 835 amino acids (AA)), truncated KAP1 (WT, 754 AA) and truncated KAP1(S824A) mutant used in the KAP1 rescue experiment shown in **c–e**. **c–e**, Real-time RT–PCR data showing the effect of overexpression of full-length KAP1 or the relevant KAP1(S824A) mutants on *TFF1* (**c**), *MYC* (**d**) and *ABAT* (**e**) coding gene transcription in *KAP1* knockdown MCF-7 cells following E₂ treatment. Data shown as individual values, mean ± s.d. (*n* = 3). The *P* values were calculated with two-sided Student's *t*-test. **f**, ChIP-seq tag distribution analysis representing the effect of E₂ on KAP1 binding at the 1,224 E₂-responsive MegaTrans enhancers. **g**, Box plot analysis of PRO-seq data representing the effect of *KAP1* knockdown (*n* = 1 experiment) on the transcription of the 1,224 E₂-responsive MegaTrans enhancers and 5,694 ERα bound but less active enhancers (weak ERα enhancers) following E₂ treatment. The box plots denote the medians, the interquartile ranges and the whiskers. The *P* values were calculated with two-sided Wilcoxon test. **h**, Model: the 7SK/KAP1 snRNP-associated inactive P-TEFb complex was assembled at paused PR promoters by association with H3K9me3 reader protein HP1α via H3K9me3 recognition, which is deposited by Suv39H1 H3K9me3 methyltransferase, thus keeping promoter-proximal RNA Pol II at a poised state. Upon E₂ stimulation, ligand-induced transcription factor ERα/co-factors are rapidly recruited at these promoters to help poised RNA polymerase initiate transcription to accumulate PAS RNA transcripts at promoters. These transiently expressed RNA molecules, which share a similar compact stem-loop structure that is responsible for the recruitment/stabilization of KDM4B/4C H3K9me3 demethylases at promoters to erase H3K9me3, lead to decommissioning of the HP1α–

KAP1–7SK snRNP complex at paused promoters to activate P-TEFb and unleash RNA Pol II transcription; unexpectedly, in response to E₂, KAP1, which is a transcription repressor to stabilize the 7SK snRNP complex at paused PR promoters in basal state, is recruited to MegaTrans enhancers, phosphorylated at S824 by MegaTrans enhancer-recruited DNA-PKcs, and subsequently delivered to promoters through E₂-induced enhancer–promoter looping, thus ensuring subsequent Pol II pause release for robust transcriptional activation.

[Source data](#)

Supplementary information

[Supplementary Figure 1](#)

This file contains Supplementary Figure 1, including the uncropped images of Western blot and PCR based gels.

[Reporting Summary](#)

[Supplementary Information](#)

This file includes SHAPE-MaP data from two independent biological replicates of *ABAT* PAS RNA SHAPE-MaP, involving mutation rate, read depth and SHAPE reactivity of the two replicates. Of note, constrained secondary structure models (on Page 10) from both replicates show that *ABAT* PAS RNA forms a highly reproducible compact stem-loop structure that plays a critical role in *ABAT* PAS RNA mediated gene regulation.

[Supplemental Table 1](#)

This table lists reagents, peptides, antibodies, primers (for real time PCR, ChIP-qPCR and SHAPE-MaP) and oligo DNA (shRNAs and gRNAs) used in this study.

[Supplemental Table 2](#)

This table includes RNA sequences used in RNA tether experiments.

Source data

[Source Data Fig. 2](#)

[Source Data Fig. 3](#)

[Source Data Fig. 4](#)

[Source Data Extended Data Fig. 3](#)

[Source Data Extended Data Fig. 4](#)

[Source Data Extended Data Fig. 7](#)

[Source Data Extended Data Fig. 8](#)

[Source Data Extended Data Fig. 9](#)

[Source Data Extended Data Fig. 10](#)

[Source Data Extended Data Fig. 12](#)

Rights and permissions

[Reprints and Permissions](#)

About this article



Check for
updates

Cite this article

Yang, F., Tanasa, B., Micheletti, R. *et al.* Shape of promoter antisense RNAs regulates ligand-induced transcription activation. *Nature* **595**, 444–449 (2021). <https://doi.org/10.1038/s41586-021-03589-x>

[Download citation](#)

- Received: 19 November 2019
- Accepted: 28 April 2021
- Published: 30 June 2021
- Issue Date: 15 July 2021
- DOI: <https://doi.org/10.1038/s41586-021-03589-x>

Comments

By submitting a comment you agree to abide by our [Terms](#) and [Community Guidelines](#). If you find something abusive or that does not comply with our terms or guidelines please flag it as inappropriate.

[Access through your institution](#)

[Change institution](#)

[Buy or subscribe](#)

Advertisement

This article was downloaded by **calibre** from <https://www.nature.com/articles/s41586-021-03589-x>

- Article
- [Published: 30 June 2021](#)

G-protein activation by a metabotropic glutamate receptor

- [Alpay B. Seven](#)¹,
- [Ximena Barros-Álvarez](#) [ORCID: orcid.org/0000-0001-6678-9436](#)¹,
- [Marine de Lapeyrière](#)²,
- [Makaía M. Papasergi-Scott](#) [ORCID: orcid.org/0000-0003-3238-3213](#)¹,
- [Michael J. Robertson](#) [ORCID: orcid.org/0000-0003-2610-680X](#)¹,
- [Chensong Zhang](#)¹,
- [Robert M. Nwokonko](#)¹,
- [Yang Gao](#) [ORCID: orcid.org/0000-0002-8758-0954](#)¹,
- [Justin G. Meyerowitz](#) [ORCID: orcid.org/0000-0001-7194-8286](#)^{1,3},
- [Jean-Philippe Rocher](#)²,
- [Dominik Schelshorn](#)²,
- [Brian K. Kobilka](#) [ORCID: orcid.org/0000-0001-5958-3990](#)¹,
- [Jesper M. Mathiesen](#) [ORCID: orcid.org/0000-0003-4251-4416](#)⁴ &
- [Georgios Skiniotis](#) [ORCID: orcid.org/0000-0003-0238-7846](#)^{1,5}

[Nature](#) volume 595, pages 450–454 (2021) [Cite this article](#)

- 5560 Accesses
- 176 Altmetric
- [Metrics details](#)

Subjects

- [Cryoelectron microscopy](#)
- [G protein-coupled receptors](#)

Abstract

Family C G-protein-coupled receptors (GPCRs) operate as obligate dimers with extracellular domains that recognize small ligands, leading to G-protein activation on the transmembrane (TM) domains of these receptors by an unknown mechanism¹. Here we show structures of homodimers of the family C metabotropic glutamate receptor 2 (mGlu2) in distinct functional states and in complex with heterotrimeric G_i. Upon activation of the extracellular domain, the two transmembrane domains undergo extensive rearrangement in relative orientation to establish an asymmetric TM6–TM6 interface that promotes conformational changes in the cytoplasmic domain of one protomer. Nucleotide-bound G_i can be observed pre-coupled to inactive mGlu2, but its transition to the nucleotide-free form seems to depend on establishing the active-state TM6–TM6 interface. In contrast to family A and B GPCRs, G-protein coupling does not involve the cytoplasmic opening of TM6 but is facilitated through the coordination of intracellular loops 2 and 3, as well as a critical contribution from the C terminus of the receptor. The findings highlight the synergy of global and local conformational transitions to facilitate a new mode of G-protein activation.

Access options

Subscribe to Journal

Get full journal access for 1 year

\$199.00

only \$3.90 per issue

[Subscribe](#)

All prices are NET prices.
VAT will be added later in the checkout.
Tax calculation will be finalised during checkout.

Rent or Buy article

Get time limited or full article access on ReadCube.

from \$8.99

[Rent or Buy](#)

All prices are NET prices.

Additional access options:

- [Log in](#)
- [Access through your institution](#)
- [Learn about institutional subscriptions](#)

Fig. 1: Structures of mGlu2 alone and in complex with G_i.



Fig. 2: Active-state mGlu2 forms an asymmetric dimer.

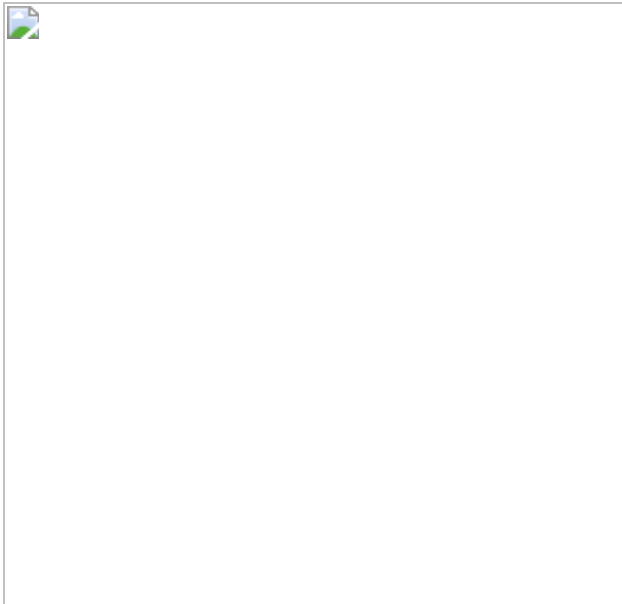


Fig. 3: G-protein coupling by mGlu2.



Fig. 4: mGlu2 conformational transitions upon activation.

Data availability

All data generated or analysed in this study are included in this article and the Supplementary Information. The cryo-EM density maps and

corresponding coordinates have been deposited in the Electron Microscopy Data Bank (EMDB) and the Protein Data Bank (PDB), respectively, under the following accession codes: [EMD-23994](#) and [7MTQ](#) (inactive-state mGlu2), [EMD-23995](#) and [7MTR](#) (Glu/ago-PAM-bound mGlu2), and [EMD-23996](#) and [7MTS](#) (mGlu2–G_i complex).

References

1. 1.

Koehl, A. et al. Structural insights into the activation of metabotropic glutamate receptors. *Nature* **566**, 79–84 (2019).

[ADS](#) [CAS](#) [PubMed](#) [PubMed Central](#) [Article](#) [Google Scholar](#)

2. 2.

Attwood, T. K. & Findlay, J. B. Fingerprinting G-protein-coupled receptors. *Protein Eng.* **7**, 195–203 (1994).

[CAS](#) [PubMed](#) [Article](#) [Google Scholar](#)

3. 3.

Weis, W. I. & Kobilka, B. K. The molecular basis of G protein-coupled receptor activation. *Annu. Rev. Biochem.* **87**, 897–919 (2018).

[CAS](#) [PubMed](#) [PubMed Central](#) [Article](#) [Google Scholar](#)

4. 4.

Niswender, C. M. & Conn, P. J. Metabotropic glutamate receptors: physiology, pharmacology, and disease. *Annu. Rev. Pharmacol. Toxicol.* **50**, 295–322 (2010).

[CAS](#) [PubMed](#) [PubMed Central](#) [Article](#) [Google Scholar](#)

5. 5.

Conn, P. J., Lindsley, C. W. & Jones, C. K. Activation of metabotropic glutamate receptors as a novel approach for the treatment of schizophrenia. *Trends Pharmacol. Sci.* **30**, 25–31 (2009).

[CAS](#) [PubMed](#) [Article](#) [Google Scholar](#)

6. 6.

Chappell, M. D. et al. Discovery of (1*S*,2*R*,3*S*,4*S*,5*R*,6*R*)-2-amino-3-[(3,4-difluorophenyl)sulfanyl]methyl]-4-hydroxy-bicyclo[3.1.0]hexane-2,6-dicarboxylic acid hydrochloride (LY3020371·HCl): a potent, metabotropic glutamate 2/3 receptor antagonist with antidepressant-like activity. *J. Med. Chem.* **59**, 10974–10993 (2016).

[CAS](#) [PubMed](#) [Article](#) [Google Scholar](#)

7. 7.

Monn, J. A. et al. Synthesis and pharmacological characterization of C4-(thiotriazolyl)-substituted-2-aminobicyclo[3.1.0]hexane-2,6-dicarboxylates. Identification of (1*R*,2*S*,4*R*,5*R*,6*R*)-2-amino-4-(1*H*-1,2,4-triazol-3-ylsulfanyl)bicyclo[3.1.0]hexane-2,6-dicarboxylic acid (LY2812223), a highly potent, functionally selective mGlu2 receptor agonist. *J. Med. Chem.* **58**, 7526–7548 (2015).

[ADS](#) [CAS](#) [PubMed](#) [Article](#) [Google Scholar](#)

8. 8.

Galici, R., Echemendia, N. G., Rodriguez, A. L. & Conn, P. J. A selective allosteric potentiator of metabotropic glutamate (mGlu) 2 receptors has effects similar to an orthosteric mGlu2/3 receptor agonist in mouse models predictive of antipsychotic activity. *J. Pharmacol. Exp. Ther.* **315**, 1181–1187 (2005).

[CAS](#) [PubMed](#) [Article](#) [Google Scholar](#)

9. 9.

Kingston, A. E. et al. LY341495 is a nanomolar potent and selective antagonist of group II metabotropic glutamate receptors. *Neuropharmacology* **37**, 1–12 (1998).

[CAS](#) [PubMed](#) [Article](#) [Google Scholar](#)

10. 10.

Bollinger, K. A. et al. Design and synthesis of mGlu2 NAMs with improved potency and CNS penetration based on a truncated picolinamide core. *ACS Med. Chem. Lett.* **8**, 919–924 (2017).

[CAS](#) [PubMed](#) [PubMed Central](#) [Article](#) [Google Scholar](#)

11. 11.

Papasergi-Scott, M. M. et al. Structures of metabotropic GABA_B receptor. *Nature* **584**, 310–314 (2020).

[ADS](#) [CAS](#) [PubMed](#) [PubMed Central](#) [Article](#) [Google Scholar](#)

12. 12.

Farinha, A. et al. Molecular determinants of positive allosteric modulation of the human metabotropic glutamate receptor 2. *Br. J. Pharmacol.* **172**, 2383–2396 (2015).

[CAS](#) [PubMed](#) [PubMed Central](#) [Article](#) [Google Scholar](#)

13. 13.

Lundström, L. et al. Structural determinants of allosteric antagonism at metabotropic glutamate receptor 2: mechanistic studies with new potent negative allosteric modulators. *Br. J. Pharmacol.* **164** (2b), 521–537 (2011).

[PubMed](#) [PubMed Central](#) [Article](#) [CAS](#) [Google Scholar](#)

14. 14.

Christopher, J. A. et al. Fragment and structure-based drug discovery for a class C GPCR: discovery of the mGlu5 negative allosteric modulator HTL14242 (3-chloro-5-[6-(5-fluoropyridin-2-yl)pyrimidin-4-yl]benzonitrile). *J. Med. Chem.* **58**, 6653–6664 (2015).

[CAS](#) [PubMed](#) [Article](#) [Google Scholar](#)

15. 15.

Gao, Y. et al. Asymmetric activation of the calcium sensing receptor homodimer. *Nature* <https://doi.org/10.1038/s41586-021-03691-0> (2021).

16. 16.

Xue, L. et al. Major ligand-induced rearrangement of the heptahelical domain interface in a GPCR dimer. *Nat. Chem. Biol.* **11**, 134–140 (2015).

[CAS](#) [PubMed](#) [Article](#) [Google Scholar](#)

17. 17.

Thibado, J. K. et al. Differences in interactions between transmembrane domains tune the activation of metabotropic glutamate receptors. *eLife* **10**, e67027 (2021).

[PubMed](#) [PubMed Central](#) [Article](#) [Google Scholar](#)

18. 18.

Goudet, C. et al. Heptahelical domain of metabotropic glutamate receptor 5 behaves like rhodopsin-like receptors. *Proc. Natl Acad. Sci. USA* **101**, 378–383 (2004).

[ADS](#) [CAS](#) [PubMed](#) [Article](#) [Google Scholar](#)

19. 19.

Trzaskowski, B. et al. Action of molecular switches in GPCRs - theoretical and experimental studies. *Curr. Med. Chem.* **19**, 1090–1109 (2012).

[CAS](#) [PubMed](#) [PubMed Central](#) [Article](#) [Google Scholar](#)

20. 20.

Maeda, S., Qu, Q., Robertson, M. J., Skiniotis, G. & Kobilka, B. K. Structures of the M1 and M2 muscarinic acetylcholine receptor/G-protein complexes. *Science* **364**, 552–557 (2019).

[ADS](#) [CAS](#) [PubMed](#) [PubMed Central](#) [Article](#) [Google Scholar](#)

21. 21.

Thal, D. M. et al. Crystal structures of the M1 and M4 muscarinic acetylcholine receptors. *Nature* **531**, 335–340 (2016).

[ADS](#) [CAS](#) [PubMed](#) [PubMed Central](#) [Article](#) [Google Scholar](#)

22. 22.

Pérez-Benito, L. et al. Molecular switches of allosteric modulation of the metabotropic glutamate 2 receptor. *Structure* **25**, 1153–1162.e4 (2017).

[PubMed](#) [Article](#) [CAS](#) [Google Scholar](#)

23. 23.

Fukuda, J. et al. Identification of a novel transmembrane domain involved in the negative modulation of mGluR1 using a newly discovered allosteric mGluR1 antagonist, 3-cyclohexyl-5-fluoro-6-methyl-7-(2-morpholin-4-ylethoxy)-4H-chromen-4-one. *Neuropharmacology* **57**, 438–445 (2009).

[CAS](#) [PubMed](#) [Article](#) [Google Scholar](#)

24. 24.

Mühlemann, A. et al. Determination of key amino acids implicated in the actions of allosteric modulation by 3,3'-difluorobenzaldazine on rat mGlu5 receptors. *Eur. J. Pharmacol.* **529**, 95–104 (2006).

[PubMed](#) [Article](#) [CAS](#) [Google Scholar](#)

25. 25.

Liu, J. et al. Allosteric control of an asymmetric transduction in a G-protein-coupled receptor heterodimer. *eLife* **6**, e26985 (2017).

[PubMed](#) [PubMed Central](#) [Article](#) [Google Scholar](#)

26. 26.

Goudet, C. et al. Asymmetric functioning of dimeric metabotropic glutamate receptors disclosed by positive allosteric modulators. *J. Biol. Chem.* **280**, 24380–24385 (2005).

[CAS](#) [PubMed](#) [Article](#) [Google Scholar](#)

27. 27.

Hlavackova, V. et al. Evidence for a single heptahelical domain being turned on upon activation of a dimeric GPCR. *EMBO J.* **24**, 499–509 (2005).

[CAS](#) [PubMed](#) [PubMed Central](#) [Article](#) [Google Scholar](#)

28. 28.

Kniazeff, J. et al. Closed state of both binding domains of homodimeric mGlu receptors is required for full activity. *Nat. Struct. Mol. Biol.* **11**, 706–713 (2004).

[CAS](#) [PubMed](#) [Article](#) [Google Scholar](#)

29. 29.

Ellaithy, A., Gonzalez-Maeso, J., Logothetis, D. A. & Levitz, J. Structural and biophysical mechanisms of class C G-protein-coupled receptor function. *Trends Biochem. Sci.* **45**, 1049–1064 (2020).

[CAS](#) [PubMed](#) [Article](#) [Google Scholar](#)

30. 30.

Dror, R. O. et al. Structural basis for nucleotide exchange in heterotrimeric G proteins. *Science* **348**, 1361–1365 (2015).

[ADS](#) [CAS](#) [PubMed](#) [PubMed Central](#) [Article](#) [Google Scholar](#)

31. 31.

Maeda, S. et al. Development of an antibody fragment that stabilizes GPCR/G-protein complexes. *Nat. Commun.* **9**, 3712 (2018).

[ADS](#) [PubMed](#) [PubMed Central](#) [Article](#) [CAS](#) [Google Scholar](#)

32. 32.

Koehl, A. et al. Structure of the μ -opioid receptor–G_i protein complex. *Nature* **558**, 547–552 (2018).

[ADS](#) [CAS](#) [PubMed](#) [PubMed Central](#) [Article](#) [Google Scholar](#)

33. 33.

Rasmussen, S. G. et al. Crystal structure of the $\beta 2$ adrenergic receptor–G_s protein complex. *Nature* **477**, 549–555 (2011).

[ADS](#) [CAS](#) [PubMed](#) [PubMed Central](#) [Article](#) [Google Scholar](#)

34. 34.

Petersen, T. N., Brunak, S., von Heijne, G. & Nielsen, H. SignalP 4.0: discriminating signal peptides from transmembrane regions. *Nat. Methods* **8**, 785–786 (2011).

[CAS](#) [PubMed](#) [Article](#) [Google Scholar](#)

35. 35.

Stoveken, H. M., Hajduczok, A. G., Xu, L. & Tall, G. G. Adhesion G-protein-coupled receptors are activated by exposure of a cryptic tethered agonist. *Proc. Natl Acad. Sci. USA* **112**, 6194–6199 (2015).

[ADS](#) [CAS](#) [PubMed](#) [PubMed Central](#) [Article](#) [Google Scholar](#)

36. 36.

Mastronarde, D. N. Automated electron microscope tomography using robust prediction of specimen movements. *J. Struct. Biol.* **152**, 36–51 (2005).

[Article](#) [Google Scholar](#)

37. 37.

Zheng, S. Q. et al. MotionCor2: anisotropic correction of beam-induced motion for improved cryo-electron microscopy. *Nat. Methods* **14**, 331–332 (2017).

[CAS](#) [PubMed](#) [PubMed Central](#) [Article](#) [Google Scholar](#)

38. 38.

Zhang, K. Gctf: Real-time CTF determination and correction. *J. Struct. Biol.* **193**, 1–12 (2016).

[ADS](#) [CAS](#) [PubMed](#) [PubMed Central](#) [Article](#) [Google Scholar](#)

39. 39.

Zivanov, J. et al. New tools for automated high-resolution cryo-EM structure determination in RELION-3. *eLife* **7**, e42166 (2018).

[PubMed](#) [PubMed Central](#) [Article](#) [Google Scholar](#)

40. 40.

Punjani, A., Rubinstein, J. L., Fleet, D. J. & Brubaker, M. A. cryoSPARC: algorithms for rapid unsupervised cryo-EM structure determination. *Nat. Methods* **14**, 290–296 (2017).

[CAS](#) [Article](#) [Google Scholar](#)

41. 41.

Ilca, S. L. et al. Multiple liquid crystalline geometries of highly compacted nucleic acid in a dsRNA virus. *Nature* **570**, 252–256 (2019).

[ADS](#) [CAS](#) [PubMed](#) [Article](#) [Google Scholar](#)

42. 42.

Pettersen, E. F. et al. UCSF Chimera—a visualization system for exploratory research and analysis. *J. Comput. Chem.* **25**, 1605–1612 (2004).

[CAS](#) [Article](#) [Google Scholar](#)

43. 43.

Sanchez-Garcia, R. et al. DeepEMhancer: a deep learning solution for cryo-EM volume post-processing. Preprint at <https://doi.org/10.1101/2021.01.12.426430> (2021).

44. 44.

Liebschner, D. et al. Macromolecular structure determination using X-rays, neutrons and electrons: recent developments in Phenix. *Acta*

Crystallogr. D **75**, 861–877 (2019).

[CAS](#) [Article](#) [Google Scholar](#)

45. 45.

Pettersen, E. F. et al. UCSF ChimeraX: structure visualization for researchers, educators, and developers. *Protein Sci.* **30**, 70–82 (2021).

[CAS](#) [Article](#) [Google Scholar](#)

46. 46.

Daniel, A., Eugene, P. & Cheng, Y. asarnow/pyem: UCSF pyem v0.5. <https://doi.org/10.5281/zenodo.3576630> (2019).

47. 47.

Krishna Kumar, K. et al. Structure of a signaling cannabinoid receptor 1–G protein complex. *Cell* **176**, 448–458.e12 (2019).

[CAS](#) [PubMed](#) [Article](#) [Google Scholar](#)

48. 48.

Waterhouse, A. et al. SWISS-MODEL: homology modelling of protein structures and complexes. *Nucleic Acids Res.* **46** (W1), W296–W303 (2018).

[CAS](#) [PubMed](#) [PubMed Central](#) [Article](#) [Google Scholar](#)

49. 49.

Robertson, M. J., van Zundert, G. C. P., Borrelli, K. & Skiniotis, G. GemSpot: a pipeline for robust modeling of ligands into cryo-EM maps. *Structure* **28**, 707–716.e3 (2020).

[CAS](#) [PubMed](#) [PubMed Central](#) [Article](#) [Google Scholar](#)

50. 50.

Emsley, P., Lohkamp, B., Scott, W. G. & Cowtan, K. Features and development of Coot. *Acta Crystallogr. D* **66**, 486–501 (2010).

[CAS](#) [PubMed](#) [PubMed Central](#) [Article](#) [Google Scholar](#)

51. 51.

Williams, C. J. et al. MolProbity: more and better reference data for improved all-atom structure validation. *Protein Sci.* **27**, 293–315 (2018).

[CAS](#) [PubMed](#) [PubMed Central](#) [Article](#) [Google Scholar](#)

52. 52.

Laurent, B. et al. Epoch: rapid analysis of protein pocket dynamics. *Bioinformatics* **31**, 1478–1480 (2015).

[CAS](#) [PubMed](#) [Article](#) [Google Scholar](#)

53. 53.

Friesner, R. A. et al. Extra precision glide: docking and scoring incorporating a model of hydrophobic enclosure for protein-ligand complexes. *J. Med. Chem.* **49**, 6177–6196 (2006).

[CAS](#) [PubMed](#) [Article](#) [Google Scholar](#)

54. 54.

Vedel, L., Bräuner-Osborne, H. & Mathiesen, J. M. A cAMP biosensor-based high-throughput screening assay for identification of G_s-coupled GPCR ligands and phosphodiesterase inhibitors. *J. Biomol. Screen.* **20**, 849–857 (2015).

[CAS](#) [PubMed](#) [Article](#) [Google Scholar](#)

55. 55.

Christopher, J. A. et al. Structure-based optimization strategies for G protein-coupled receptor (GPCR) allosteric modulators: a case study from analyses of new metabotropic glutamate receptor 5 (mGlu5) X-ray structures. *J. Med. Chem.* **62**, 207–222 (2019).

[CAS](#) [PubMed](#) [Article](#) [Google Scholar](#)

56. 56.

Doré, A. S. et al. Structure of class C GPCR metabotropic glutamate receptor 5 transmembrane domain. *Nature* **511**, 557–562 (2014).

[ADS](#) [PubMed](#) [Article](#) [CAS](#) [Google Scholar](#)

57. 57.

Michel, J., Tirado-Rives, J. & Jorgensen, W. L. Prediction of the water content in protein binding sites. *J. Phys. Chem. B* **113**, 13337–13346 (2009).

[CAS](#) [PubMed](#) [PubMed Central](#) [Article](#) [Google Scholar](#)

[Download references](#)

Acknowledgements

We thank E. Montabana at the Stanford-SLAC cryo-EM facility for support with data collection and J.-P. Aubry of the FACS facility (University of Geneva) for assistance with the FACS experiments. We also thank G. Eskici for discussions and support with coding. This work was supported, in part, by T32GM089626 (J.G.M.), R01 NS092695 (G.S., B.K.K. and J.M.M.) and R01 NS028471 (B.K.K.). B.K.K. is a Chan Zuckerberg Biohub Investigator.

Author information

Affiliations

1. Department of Molecular and Cellular Physiology, Stanford University School of Medicine, Stanford, CA, USA

Alpay B. Seven, Ximena Barros-Álvarez, Makaía M. Papasergi-Scott, Michael J. Robertson, Chensong Zhang, Robert M. Nwokonko, Yang Gao, Justin G. Meyerowitz, Brian K. Kobilka & Georgios Skiniotis

2. Addex Therapeutics, Geneva, Switzerland

Marine de Lapeyrière, Jean-Philippe Rocher & Dominik Schelshorn

3. Department of Anesthesiology, Perioperative, and Pain Medicine, Stanford University School of Medicine, Stanford, CA, USA

Justin G. Meyerowitz

4. Department of Drug Design and Pharmacology, Faculty of Health and Medical Sciences, University of Copenhagen, Copenhagen, Denmark

Jesper M. Mathiesen

5. Department of Structural Biology, Stanford University School of Medicine, Stanford, CA, USA

Georgios Skiniotis

Authors

1. Alpay B. Seven

[View author publications](#)

You can also search for this author in [PubMed](#) [Google Scholar](#)

2. Ximena Barros-Álvarez

[View author publications](#)

You can also search for this author in [PubMed](#) [Google Scholar](#)

3. Marine de Lapeyrière

[View author publications](#)

You can also search for this author in [PubMed](#) [Google Scholar](#)

4. Makaía M. Papasergi-Scott

[View author publications](#)

You can also search for this author in [PubMed](#) [Google Scholar](#)

5. Michael J. Robertson

[View author publications](#)

You can also search for this author in [PubMed](#) [Google Scholar](#)

6. Chensong Zhang

[View author publications](#)

You can also search for this author in [PubMed](#) [Google Scholar](#)

7. Robert M. Nwokonko

[View author publications](#)

You can also search for this author in [PubMed](#) [Google Scholar](#)

8. Yang Gao

[View author publications](#)

You can also search for this author in [PubMed](#) [Google Scholar](#)

9. Justin G. Meyerowitz

[View author publications](#)

You can also search for this author in [PubMed](#) [Google Scholar](#)

10. Jean-Philippe Rocher

[View author publications](#)

You can also search for this author in [PubMed](#) [Google Scholar](#)

11. Dominik Schelshorn

[View author publications](#)

You can also search for this author in [PubMed](#) [Google Scholar](#)

12. Brian K. Kobilka

[View author publications](#)

You can also search for this author in [PubMed](#) [Google Scholar](#)

13. Jesper M. Mathiesen

[View author publications](#)

You can also search for this author in [PubMed](#) [Google Scholar](#)

14. Georgios Skiniotis

[View author publications](#)

You can also search for this author in [PubMed](#) [Google Scholar](#)

Contributions

A.B.S. expressed and purified receptors, prepared cryo-EM samples, collected cryo-EM datasets, processed cryo-EM data and performed modelling. X.B.-A. purified G-protein complexes and assisted with modelling. M.d.L. performed and analysed ago-PAM binding-pose validation experiments. J.G.M. purified scFv16. M.J.R. assisted in modelling calculations of the ligand pose. R.M.N. assisted in mutagenesis experiments. M.M.P.-S. performed the GTP γ S activity assay and assisted with manuscript and figure preparation. J.-P.R. developed the chemical series leading to the identification of the ago-PAM. D.S. designed and analysed ago-PAM binding-pose validation experiments. J.M.M. performed and analysed cell-based in vitro functional G-protein-coupling assays. Y.G. assisted with data analysis. C.Z. assisted with the initial screening of cryo-EM samples. B.K.K. provided advice for G-protein complex formation and

analysed results. A.B.S. and G.S. wrote the manuscript with input from B.K.K., J.M.M., M.M.P.-S. and Y.G. G.S. supervised the project.

Corresponding authors

Correspondence to [Brian K. Kobilka](#) or [Jesper M. Mathiesen](#) or [Georgios Skiniotis](#).

Ethics declarations

Competing interests

B.K.K. is a co-founder of and consultant for ConfometRx, Inc.

Additional information

Peer review information *Nature* thanks Karen Gregory, Martin Lohse and the other, anonymous, reviewer(s) for their contribution to the peer review of this work. Peer reviewer reports are available.

Publisher's note Springer Nature remains neutral with regard to jurisdictional claims in published maps and institutional affiliations.

Extended data figures and tables

[Extended Data Fig. 1 Preparation of cryo-EM samples.](#)

a–c, Size-exclusion chromatography profiles of purified inactive-state mGlu2 (**a**), Glu/ago-PAM-bound state mGlu2 (**b**) and the mGlu2–G_i complex (**c**), repeated three times with similar results. Inset in **c** shows the size-exclusion profile of purified G_i heterotrimer. **d**, G_i protein nucleotide exchange stimulated by purified mGlu2 preparations in (1) inactive state, (2) Glu/ago-PAM-bound state and (3) active state preparation used for cryo-EM studies of the mGlu2–G_i complex, as determined in a GTPγS binding assay. mGlu2 purified in the presence of antagonist LY341495 and NAM

VU6001966 did not produce a substantial increase in G α_i GTP γ S binding above the intrinsic binding of G i alone. By contrast, mGlu2 purified in the presence of the agonist glutamate and ago-PAM ADX55164 produced a roughly 3.5-fold increase in G α_i GTP γ S binding. Data represent mean \pm s.e.m. of reactions performed in triplicate. **e**, Representative cryo-EM micrograph of mGlu2–G i –scFv complex from a single dataset with 45,371 micrographs.

Extended Data Fig. 2 Cryo-EM processing summary of mGlu2 in its inactive and Glu/ago-PAM-bound states.

a, Cryo-EM data processing workflow for the mGlu2 inactive state. **b**, Fourier shell correlation (FSC) curves for the mGlu2 inactive state cryo-EM maps of the ECD focused refinement and the global refinement. **c**, Angular distribution heat map of particles for reconstruction of the mGlu2 inactive state. **d**, Cryo-EM data processing workflow for the Glu/ago-PAM-bound state of mGlu2. **e**, FSC curves of the Glu/ago-PAM bound state of mGlu2 for the VFT focused refinement and the global refinement. **f**, Angular distribution heat map of particle projections in reconstruction of the Glu/ago-PAM-bound state of mGlu2. FSC curves and local refinement spectra were determined using CryoSPARC. Dashed lines represent the resolution at 0.143 FSC. All the processing steps were performed with Relion 3.1 (red) or CryoSPARC 3.1 (blue).

Extended Data Fig. 3 Cryo-EM processing summary for the mGlu2–G i complex.

a, Cryo-EM data processing workflow for the mGlu2–G i complex. **b**, FSC curves for the locally refined maps of the G $\beta\gamma$, 7TM–G $\alpha_i\beta\gamma$, CRD–7TM and VFT–CRD. Dashed lines represent the resolution at 0.143 FSC. **c**, Angular distribution heat map of particles for the mGlu2–G i global reconstruction. FSC curves and local refinement spectra were calculated using CryoSPARC. All the processing steps were performed with Relion 3.1 (red) or CryoSPARC 3.1 (blue).

Extended Data Fig. 4 Agreement between cryo-EM map and model.

a, EM density and model for the 7TM of the mGlu2 inactive state. The 7TM model of mGlu2 from the mGlu2–G_i complex is rigid-body-docked to the mGlu2 inactive-state map (7TM^A; green, 7TM^B; coral, additional density inside the allosteric pocket of the 7TM; purple). **b**, Magnified view of a density inside the allosteric pocket of 7TM^B that may correspond to negative allosteric modulator VU6001966. **c**, EM density, and model for the mGlu2–G_i complex; transmembrane helices of mGlu2 G-protein-coupled protomer (GC), transmembrane helices of non-G-protein-coupled protomer (NGC), ECL2, glutamate, ago-PAM ADX55164, 1,2-dipalmitoyl-*sn*-glycero-3-phosphoethanolamine as a representative phospholipid and α5 helix of Gα_i. Densities were visualized with UCSF ChimeraX and zoned at 4 Å with a uniform threshold.

Extended Data Fig. 5 Comparison of structures across family C GPCRs.

The overall architecture of mGlu2 is similar to that of other family C GPCRs. The differences in the angle between VFT and CRD, and the angle between CRD and 7TMs leads to variations in the 7TM configuration. **a–d**, Models of single protomers of family C GPCRs are overlaid based on VFT superposition. Comparison of the inactive-state model of mGlu2 from this study with the mGlu5 apo state model (PDB: 6N52) (**a**), the mGlu5 active state model (PDB: 6N51) (**b**), the CaSR inactive state model (**c**) and the CaSR active state model (**d**, see ref. [15](#)). **e**, Top-down view of mGlu2 7TM bundles shows that TM6 helices are distal to the 7TM interface in the inactive state (left) but form the active-state interface (right). **f–h**, The inactive state configuration of 7TMs of family C GPCRs are variable. Top-down view of the 7TMs of inactive-state (left) and active-state (right) family C GPCRs: mGlu5 (apo PDB: 6N52, active PDB: 6N51) (**f**), GABA_B (inactive PDB: 6W2X, active PDB: 7C7Q) (**g**) and CaSR (**h**, ref. [15](#)). The receptors display variable 7TM configuration.

Extended Data Fig. 6 Ago-PAM modulation of mGlu2.

a, The mGlu2 ago-PAM ADX55164, used to stabilize the active receptor conformation, potentiates the functional response of mGlu2 to l-glutamate. Receptor activation is measured by co-transfection of the mGlu2 with the neuronal glutamate transporter EAAT3 to remove extracellular glutamate and a chimeric G_{q/05} to enable intracellular calcium release as a readout. **b**, In a similar assay, mutation of the ECL2 tip (residues 712–714; ERR-AAA) and the Y767A mutation on the TM6–TM6 interface blunt glutamate-induced signalling (left) and compared to wild-type mGlu2, the ago-PAM ADX55164 has higher potency and higher E_{max} for the ERR-AAA mutant, consistent with a partial uncoupling of the ECD from the 7TM (right). **c**, Schematic of interactions between mGlu2 residues and ago-PAM ADX55164 bound within the 7TM core. Green, hydrophobic; blue, polar; purple, positively charged; magenta arrow, hydrogen bond; green line, π–π stacking; grey, glycine. **d**, **e**, Magnified views of the cryo-EM map of G-protein-coupled active-state mGlu2 GC (coral) (**d**) and NGC (green) (**e**) protomers show that ago-PAM (blue) binds only to the GC protomer, whereas the analogous pocket is not accessible by the membrane (pocket opening highlighted with orange box) on the NGC protomer. A phospholipid density between two 7TMs is shown in grey. The head group of the lipid molecule does not seem to interact with mGlu2 or G_i and the density might represent a lipid molecule with different head groups. All family C GPCR dimeric structures display elongated densities between two protomers, most likely corresponding to either cholesterol or phospholipids. Additionally, GABA_B structures displayed a phospholipid molecule inside the 7TM, indicating the importance of lipid molecules in family C GPCR dimerization and activity. Data in **a** and **b** represent mean ± s.e.m. from four and five independent experiments measured in duplicate, respectively.

Extended Data Fig. 7 Ago-PAM binding-pose validation for mGlu2.

Residues within the binding pocket of ago-PAM ADX55164 were mutated to study their role in PAM activity. **a**, Mutant and wild-type receptor responses to increasing concentrations of glutamate in the absence (brown)

or presence (green) of 200 nM ADX55164 were tested in an intracellular calcium release assay following co-transfection with the EAAT3 and G_{q/05}. Responses were normalized to the maximum response of the wild-type receptor. The concentrations of glutamate are plotted on the *x* axis [log (M)]. The amount of receptor DNA transfected was increased up to tenfold to obtain mutant expression levels similar to that of the wild-type; however, for some mutants, such expression levels could not be reached. Data shown represent the mean ± s.e.m. from five independent experiments. **b**, Mutant and wild-type receptor surface expression levels were monitored by fluorescence microscopy using an N-terminal Flag-tag present on all constructs and an anti-Flag Cy3 antibody. Data in **b** represent images from three independent experiments. R720A, S731A and L732A mutants did not produce glutamate or ADX55164 responses and did not show surface expression in immunofluorescence studies (not shown). **c**, The change in pEC₅₀ of mutant and wild-type receptors upon addition of 200 nM ADX55164 plotted from individual experiments along with individual data points for estimation of surface expression of mutants compared to the wild-type (100%) by flow cytometry. Statistics were derived from at least 4 independent experiments by one-way ANOVA and comparison of each mutant to the wild-type. A statistical difference from the wild-type is indicated by an asterisk (*). *P* values were corrected for multiple comparisons using Dunnett's test and are provided in Supplementary Table 1.

Extended Data Fig. 8 Comparison of water coordination, 7TM activation and the G-protein interface across GPCRs.

a, EM density for the region of the observed water molecule coordinated inside the allosteric pocket of PAM-less 7TM of mGlu2 (labelled residues are conserved in mGlu5, and blue dashed lines represent hydrogen bonds between the water molecule and mGlu2). **b**, Comparison of the water molecule coordinated inside the allosteric pocket of mGlu5 (PDB: 4OO9, yellow; water, brown) and the PAM-less 7TM of mGlu2 (mGlu2–G_i structure, green; water, red). The homologous Tyr647 residue in mGlu5 (Tyr659) coordinates a water molecule in the NAM-stabilized mGlu5 allosteric pocket^{14,55,56} and has a role in ligand pharmacology by affecting

allosteric modulator cooperativity²³. The mGlu2–G_i map also reveals a density that corresponds to a water molecule within the PAM-less 7TM bundle, coordinated between residues Tyr647, Thr769, Ser801 and Gly802, similar to the water-molecule coordination in the allosteric pocket of NAM-stabilized mGlu5 structures^{14,55,56}. The PAM-bound 7TM bundle shows a weaker density for this water molecule. Using JAWS simulations⁵⁷, a statistical thermodynamics-based approach to determine water-molecule positioning, a water molecule was observed to be bound in the pocket containing the putative water site in both protomers. The conservation of these four residues and resolution of water molecules in mGlu2 and mGlu5 indicates the importance of water for mGlu ligand pharmacology. **c**, Superposition of M1 muscarinic receptor (M1R) inactive (PDB: 5CXV) and active (PDB: 6OIJ) states reveals TM6 movement (agonist: iperoxo, orange). **d**, Tryptophan toggle switch in M1R. **e, f**, Comparison of the overall G_i protein coupling arrangement on the cannabinoid receptor 1 (CB1), a representative family A GPCR (**e**) and mGlu2 (**f**). The non-G-protein-coupled protomer model is not shown for clarity. **g**, Magnified view of cryo-EM map of G-protein-coupled active-state mGlu2.

Extended Data Fig. 9 Functional analysis of mGlu2 mutants for G_i activation.

a, Truncation of the mGlu2 C terminus or mutation of critical residues of mGlu2 involved in the formation of the observed G-protein interface substantially decreases receptor activation by l-Glu as tested in an intracellular calcium release assay following co-transfection with the EAAT3 and G_{q/05}. Data in **a** represent mean ± s.e.m. from five independent experiments. **b**, An Epac1-based FRET cAMP biosensor capable of reporting intracellular cAMP levels was used to investigate the effect of mutating critical residues of mGlu2 in the G_i-interacting interface. FRET between the fluorescent proteins decreases after cAMP binding to a fusion protein consisting of an Epac1-domain (residues 14–881) flanked by fluorescent proteins mCerulean and mCitrine. **c**, Representative kinetic traces of LY354740 (mGlu2 agonist)-induced inhibition of forskolin-stimulated cAMP formation through G_i activation by wild-type mGlu2 and

mutants. The effect of the NAM MNI-137 and non-transfected cell traces are shown for comparison. Indicated are time points for mGlu2 ligand addition and for taking cAMP values for generation of the concentration-response curves (CRC) shown in Fig. 3b. Data in c represent mean \pm s.d. from one representative experiment performed in triplicate.

Extended Data Fig. 10 Intermediate states of mGlu2–G_i activation.

a, Cryo-EM maps of mGlu2 in two distinct intermediate states with open-closed VFTs and inactive 7TM conformation. The protomer contributing TM3 to the interface (7TM^A) displays an open VFT and the protomer contributing TM4 to the interface (7TM^B) displays a closed VFT in one intermediate state (left), and the opposite in the other intermediate state (right). **b**, Reference-free cryo-EM 2D class average of the mGlu2–G_i protein complex shows heterotrimeric G-protein pre-coupling to mGlu2 in the inactive state (top), compared to an average of the nucleotide-free G_i coupled to mGlu2 (bottom). The α -helical domain of G α is ordered in the pre-coupled state, indicating a GDP-bound G protein. This observation suggests that VFT activation and the approximately 180° rearrangement of the 7TMs to establish the TM6–TM6 interface would be necessary for G-protein activation. **c**, Cryo-EM model of G-protein-coupled active state model of mGlu2 and G protein overlaid to either of the 7TMs of mGlu2 in the inactive-state model. The α N helix of the G α protein in both conformations would clash with the membrane, while G β would also clash with the adjacent protomer if the G_i is bound to TM^B of the inactive state (clash represented by red stars).

Extended Data Table 1 Cryo-EM data collection, refinement and validation statistics

[Full size table](#)

Supplementary information

Supplementary Tables

This file contains Supplementary Tables 1-4.

Reporting Summary

Peer Review File

Rights and permissions

[Reprints and Permissions](#)

About this article



Check for
updates

Cite this article

Seven, A.B., Barros-Álvarez, X., de Lapeyrière, M. *et al.* G-protein activation by a metabotropic glutamate receptor. *Nature* **595**, 450–454 (2021). <https://doi.org/10.1038/s41586-021-03680-3>

[Download citation](#)

- Received: 23 December 2020
- Accepted: 01 June 2021
- Published: 30 June 2021
- Issue Date: 15 July 2021
- DOI: <https://doi.org/10.1038/s41586-021-03680-3>

Comments

By submitting a comment you agree to abide by our [Terms](#) and [Community Guidelines](#). If you find something abusive or that does not comply with our terms or guidelines please flag it as inappropriate.

[Access through your institution](#)

[Change institution](#)

[Buy or subscribe](#)

Advertisement

This article was downloaded by **calibre** from <https://www.nature.com/articles/s41586-021-03680-3>

| [Section menu](#) | [Main menu](#) |

- Article
- [Published: 30 June 2021](#)

Asymmetric activation of the calcium-sensing receptor homodimer

- [Yang Gao](#) ORCID: [orcid.org/0000-0002-8758-0954^{1,2}](https://orcid.org/0000-0002-8758-0954),
- [Michael J. Robertson](#) ORCID: [orcid.org/0000-0003-2610-680X^{1,2}](https://orcid.org/0000-0003-2610-680X),
- [Sabrina N. Rahman⁴](#),
- [Alpay B. Seven^{1,2}](#),
- [Chensong Zhang^{1,2}](#),
- [Justin G. Meyerowitz](#) ORCID: [orcid.org/0000-0001-7194-8286^{1,2,3}](https://orcid.org/0000-0001-7194-8286),
- [Ouliana Panova^{1,2}](#),
- [Fadil M. Hannan](#) ORCID: [orcid.org/0000-0002-2975-5170^{5,6}](https://orcid.org/0000-0002-2975-5170),
- [Rajesh V. Thakker](#) ORCID: [orcid.org/0000-0002-1438-3220⁵](https://orcid.org/0000-0002-1438-3220),
- [Hans Bräuner-Osborne⁴](#),
- [Jesper M. Mathiesen](#) ORCID: [orcid.org/0000-0003-4251-4416⁴](https://orcid.org/0000-0003-4251-4416) &
- [Georgios Skiniotis](#) ORCID: [orcid.org/0000-0003-0238-7846^{1,2}](https://orcid.org/0000-0003-0238-7846)

[Nature](#) volume **595**, pages 455–459 (2021) [Cite this article](#)

- 3548 Accesses
- 1 Citations
- 35 Altmetric
- [Metrics details](#)

Subjects

- [Calcium and vitamin D](#)
- [Cryoelectron microscopy](#)
- [G protein-coupled receptors](#)
- [Membrane proteins](#)
- [Parathyroid diseases](#)

Abstract

The calcium-sensing receptor (CaSR), a cell-surface sensor for Ca^{2+} , is the master regulator of calcium homeostasis in humans and is the target of calcimimetic drugs for the treatment of parathyroid disorders¹. CaSR is a family C G-protein-coupled receptor² that functions as an obligate homodimer, with each protomer composed of a Ca^{2+} -binding extracellular domain and a seven-transmembrane-helix domain (7TM) that activates heterotrimeric G proteins. Here we present cryo-electron microscopy structures of near-full-length human CaSR in inactive or active states bound to Ca^{2+} and various calcilytic or calcimimetic drug molecules. We show that, upon activation, the CaSR homodimer adopts an asymmetric 7TM configuration that primes one protomer for G-protein coupling. This asymmetry is stabilized by 7TM-targeting calcimimetic drugs adopting distinctly different poses in the two protomers, whereas the binding of a calcilytic drug locks CaSR 7TMs in an inactive symmetric configuration. These results provide a detailed structural framework for CaSR activation and the rational design of therapeutics targeting this receptor.

Access options

Subscribe to Journal

Get full journal access for 1 year

\$199.00

only \$3.90 per issue

[Subscribe](#)

All prices are NET prices.
VAT will be added later in the checkout.
Tax calculation will be finalised during checkout.

Rent or Buy article

Get time limited or full article access on ReadCube.

from \$8.99

[Rent or Buy](#)

All prices are NET prices.

Additional access options:

- [Log in](#)
- [Access through your institution](#)
- [Learn about institutional subscriptions](#)

Fig. 1: Structural rearrangements of human CaSR upon activation.

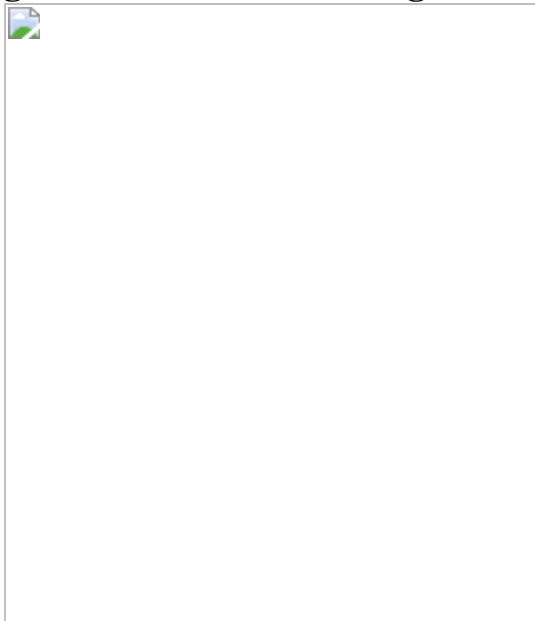


Fig. 2: Asymmetric configuration of active-state CaSR 7TMs and interactions between the CRD and the 7TMs.

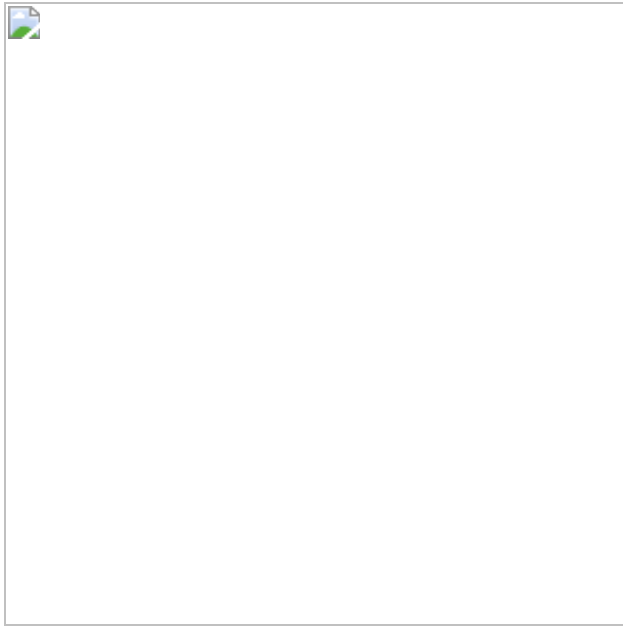


Fig. 3: Structural basis of CaSR-targeting by allosteric calcimimetic and calcilytic drug molecules.

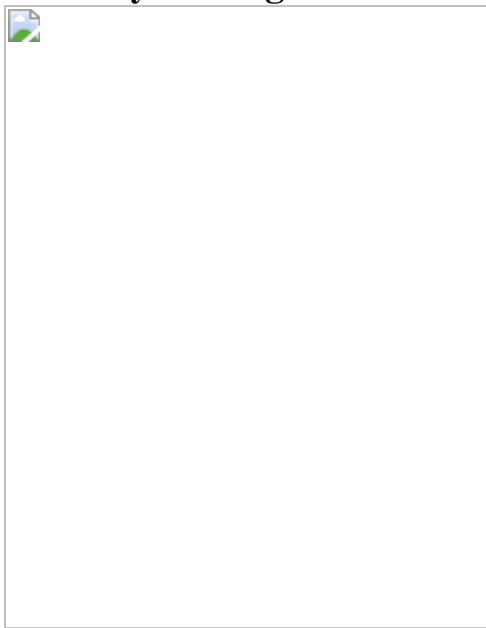
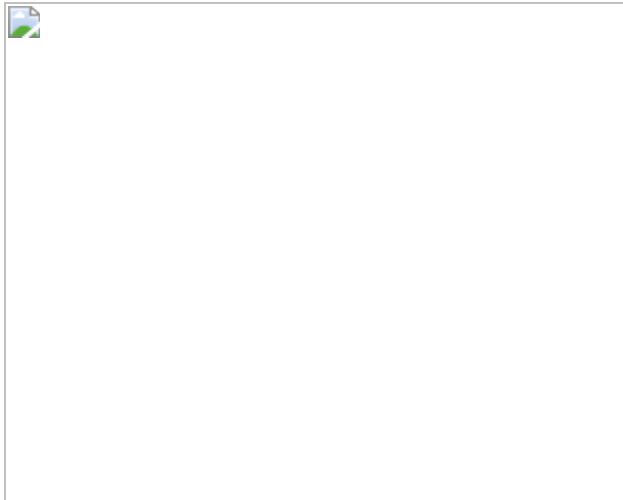


Fig. 4: Symmetric configuration of CaSR–NAM–Ca²⁺–Trp 7TMs and the TM6 toggle switch.



Data availability

All data generated or analysed during this study are included in the Article and its Supplementary Information. Cryo-EM maps of active-state CaSR–cinacalcet, active-state CaSR–etelcalcetide–evocalcet, inactive-state CaSR–NPS2143 and CaSR–NPS2143–Ca²⁺–Trp have been deposited in the Electron Microscopy Data Bank under accession codes [EMD-23653](#), [EMD-23654](#), [EMD-23655](#) and [EMD-23652](#), respectively. The atomic coordinates of active-state CaSR–cinacalcet, active-state CaSR–etelcalcetide–evocalcet, inactive-state CaSR–NPS2143 and CaSR–NPS2143–Ca²⁺–Trp have been deposited in the Protein Data Bank under the accession codes [7M3F](#), [7M3G](#), [7M3J](#) and [7M3E](#), respectively.

References

1. 1.

Hannan, F. M., Kallay, E., Chang, W., Brandi, M. L. & Thakker, R. V. The calcium-sensing receptor in physiology and in calcitropic and noncalcitropic diseases. *Nat. Rev. Endocrinol.* **15**, 33–51 (2018).

[PubMed](#) [PubMed Central](#) [Article](#) [CAS](#) [Google Scholar](#)

2. 2.

Møller, T. C., Moreno-Delgado, D., Pin, J.-P. & Kniazeff, J. Class C G protein-coupled receptors: reviving old couples with new partners. *Biophys. Rep.* **3**, 57–63 (2017).

[PubMed](#) [PubMed Central](#) [Article](#) [CAS](#) [Google Scholar](#)

3. 3.

Conigrave, A. D., Quinn, S. J. & Brown, E. M. l-amino acid sensing by the extracellular Ca²⁺-sensing receptor. *Proc. Natl Acad. Sci. USA* **97**, 4814–4819 (2000).

[ADS](#) [CAS](#) [PubMed](#) [PubMed Central](#) [Article](#) [Google Scholar](#)

4. 4.

Riccardi, D. & Martin, D. The role of the calcium-sensing receptor in the pathophysiology of secondary hyperparathyroidism. *NDT Plus* **1** (Suppl 1), i7–i11 (2008).

[CAS](#) [PubMed](#) [PubMed Central](#) [Google Scholar](#)

5. 5.

Nemeth, E. F., Van Wagenen, B. C. & Balandrin, M. F. in *Progress in Medicinal Chemistry* Vol. 57 (eds Witty, D. R. & Cox, B.) 1–86 (Elsevier, 2018).

6. 6.

Geng, Y. et al. Structural mechanism of ligand activation in human calcium-sensing receptor. *eLife* **5**, e13662 (2016).

[PubMed](#) [PubMed Central](#) [Article](#) [CAS](#) [Google Scholar](#)

7. 7.

Zhang, C. et al. Structural basis for regulation of human calcium-sensing receptor by magnesium ions and an unexpected tryptophan

derivative co-agonist. *Sci. Adv.* **2**, e1600241 (2016).

[ADS](#) [PubMed](#) [PubMed Central](#) [Article](#) [CAS](#) [Google Scholar](#)

8. 8.

Koehl, A. et al. Structural insights into metabotropic glutamate receptor activation. *Nature* **566**, 79–84 (2019).

[ADS](#) [CAS](#) [PubMed](#) [PubMed Central](#) [Article](#) [Google Scholar](#)

9. 9.

Fantini, J. & Barrantes, F. J. How cholesterol interacts with membrane proteins: an exploration of cholesterol-binding sites including CRAC, CARC, and tilted domains. *Front. Physiol.* **4**, 31 (2013).

[CAS](#) [PubMed](#) [PubMed Central](#) [Google Scholar](#)

10. 10.

Isberg, V. et al. Generic GPCR residue numbers—aligning topology maps while minding the gaps. *Trends Pharmacol. Sci.* **36**, 22–31 (2015).

[CAS](#) [PubMed](#) [Article](#) [Google Scholar](#)

11. 11.

Kifor, O., Diaz, R., Butters, R., Kifor, I. & Brown, E. M. The calcium-sensing receptor is localized in caveolin-rich plasma membrane domains of bovine parathyroid cells. *J. Biol. Chem.* **273**, 21708–21713 (1998).

[CAS](#) [PubMed](#) [Article](#) [Google Scholar](#)

12. 12.

Timmers, H. J. L. M., Karperien, M., Hamdy, N. A., de Boer, H. & Hermus, A. R. M. M. Normalization of serum calcium by cinacalcet in a patient with hypercalcaemia due to a de novo inactivating mutation of the calcium-sensing receptor. *J. Intern. Med.* **260**, 177–182 (2006).

[CAS](#) [PubMed](#) [Article](#) [Google Scholar](#)

13. 13.

Kunishima, N. et al. Structural basis of glutamate recognition by a dimeric metabotropic glutamate receptor. *Nature* **407**, 971–977 (2000).

[ADS](#) [CAS](#) [PubMed](#) [Article](#) [Google Scholar](#)

14. 14.

Liu, H. et al. Illuminating the allosteric modulation of the calcium-sensing receptor. *Proc. Natl Acad. Sci. USA* **117**, 21711–21722 (2020).

[CAS](#) [PubMed](#) [PubMed Central](#) [Article](#) [Google Scholar](#)

15. 15.

Bushinsky, D. A. et al. One-year safety and efficacy of intravenous etelcalcetide in patients on hemodialysis with secondary hyperparathyroidism. *Nephrol. Dial. Transplant.* **35**, 1769–1778 (2020).

[CAS](#) [PubMed](#) [Article](#) [Google Scholar](#)

16. 16.

Alexander, S. T. et al. Critical cysteine residues in both the calcium-sensing receptor and the allosteric activator AMG 416 underlie the mechanism of action. *Mol. Pharmacol.* **88**, 853–865 (2015).

[CAS](#) [PubMed](#) [Article](#) [Google Scholar](#)

17. 17.

Hannan, F. M. et al. Identification of 70 calcium-sensing receptor mutations in hyper- and hypo-calcaemic patients: evidence for clustering of extracellular domain mutations at calcium-binding sites. *Hum. Mol. Genet.* **21**, 2768–2778 (2012).

[CAS](#) [PubMed](#) [Article](#) [Google Scholar](#)

18. 18.

Robertson, M. J., van Zundert, G. C. P., Borrelli, K. & Skiniotis, G. GemSpot: a pipeline for robust modeling of ligands into cryo-EM maps. *Structure* **28**, 707–716.e3 (2020).

[CAS](#) [PubMed](#) [PubMed Central](#) [Article](#) [Google Scholar](#)

19. 19.

Leach, K. et al. Towards a structural understanding of allosteric drugs at the human calcium-sensing receptor. *Cell Res.* **26**, 574–592 (2016).

[CAS](#) [PubMed](#) [PubMed Central](#) [Article](#) [Google Scholar](#)

20. 20.

Hlavackova, V. et al. Evidence for a single heptahelical domain being turned on upon activation of a dimeric GPCR. *EMBO J.* **24**, 499–509 (2005).

[CAS](#) [PubMed](#) [PubMed Central](#) [Article](#) [Google Scholar](#)

21. 21.

Jacobsen, S. E., Gether, U. & Bräuner-Osborne, H. Investigating the molecular mechanism of positive and negative allosteric modulators in the calcium-sensing receptor dimer. *Sci. Rep.* **7**, 46355 (2017).

[ADS](#) [CAS](#) [PubMed](#) [PubMed Central](#) [Article](#) [Google Scholar](#)

22. 22.

Seven, A. B. et al. G protein activation by a metabotropic glutamate receptor. *Nature* (in the press).

23. 23.

Huang, S. et al. Interdomain movements in metabotropic glutamate receptor activation. *Proc. Natl Acad. Sci. USA* **108**, 15480–15485 (2011).

[ADS](#) [CAS](#) [PubMed](#) [PubMed Central](#) [Article](#) [Google Scholar](#)

24. 24.

Ray, K., Fan, G.-F., Goldsmith, P. K. & Spiegel, A. M. The carboxyl terminus of the human calcium receptor. Requirements for cell-surface expression and signal transduction. *J. Biol. Chem.* **272**, 31355–31361 (1997).

[CAS](#) [PubMed](#) [Article](#) [Google Scholar](#)

25. 25.

Hu, J. et al. A region in the seven-transmembrane domain of the human Ca²⁺ receptor critical for response to Ca²⁺. *J. Biol. Chem.* **280**, 5113–5120 (2005).

[CAS](#) [PubMed](#) [Article](#) [Google Scholar](#)

26. 26.

Shiohara, M. et al. A novel gain-of-function mutation (F821L) in the transmembrane domain of calcium-sensing receptor is a cause of severe sporadic hypoparathyroidism. *Eur. J. Pediatr.* **163**, 94–98 (2004).

[PubMed](#) [Article](#) [Google Scholar](#)

27. 27.

Kobilka, B. K. G protein coupled receptor structure and activation. *Biochim. Biophys. Acta* **1768**, 794–807 (2007).

[CAS](#) [PubMed](#) [Article](#) [Google Scholar](#)

28. 28.

Wu, H. et al. Structure of a class C GPCR metabotropic glutamate receptor 1 bound to an allosteric modulator. *Science* **344**, 58–64 (2014).

[ADS](#) [CAS](#) [PubMed](#) [PubMed Central](#) [Article](#) [Google Scholar](#)

29. 29.

Doré, A. S. et al. Structure of class C GPCR metabotropic glutamate receptor 5 transmembrane domain. *Nature* **511**, 557–562 (2014).

[ADS](#) [PubMed](#) [Article](#) [CAS](#) [Google Scholar](#)

30. 30.

Punjani, A., Rubinstein, J. L., Fleet, D. J. & Brubaker, M. A. cryoSPARC: algorithms for rapid unsupervised cryo-EM structure determination. *Nat. Methods* **14**, 290–296 (2017).

[CAS](#) [Article](#) [Google Scholar](#)

31. 31.

Punjani, A., Zhang, H. & Fleet, D. J. Non-uniform refinement: adaptive regularization improves single-particle cryo-EM reconstruction. *Nat. Methods* **17**, 1214–1221 (2020).

[CAS](#) [PubMed](#) [PubMed Central](#) [Article](#) [Google Scholar](#)

32. 32.

Punjani, A. & Fleet, D. J. 3D variability analysis: resolving continuous flexibility and discrete heterogeneity from single particle cryo-EM. *J. Struct. Biol.* **213**, 107702 (2021).

[CAS](#) [PubMed](#) [Article](#) [Google Scholar](#)

33. 33.

Pettersen, E. F. et al. UCSF Chimera—a visualization system for exploratory research and analysis. *J. Comput. Chem.* **25**, 1605–1612 (2004).

[CAS](#) [Article](#) [Google Scholar](#)

34. 34.

Goudet, C. et al. Asymmetric functioning of dimeric metabotropic glutamate receptors disclosed by positive allosteric modulators. *J. Biol. Chem.* **280**, 24380–24385 (2005).

[CAS](#) [PubMed](#) [Article](#) [Google Scholar](#)

35. 35.

Waterhouse, A. et al. SWISS-MODEL: homology modelling of protein structures and complexes. *Nucleic Acids Res.* **46** (W1), W296–W303 (2018).

[CAS](#) [PubMed](#) [PubMed Central](#) [Article](#) [Google Scholar](#)

36. 36.

Adams, P. D. et al. PHENIX: a comprehensive Python-based system for macromolecular structure solution. *Acta Crystallogr. D* **66**, 213–221 (2010).

[CAS](#) [PubMed](#) [PubMed Central](#) [Article](#) [Google Scholar](#)

37. 37.

Emsley, P. & Cowtan, K. Coot: model-building tools for molecular graphics. *Acta Crystallogr. D* **60**, 2126–2132 (2004).

[PubMed](#) [Article](#) [CAS](#) [Google Scholar](#)

38. 38.

Chen, V. B. et al. MolProbity: all-atom structure validation for macromolecular crystallography. *Acta Crystallogr. D* **66**, 12–21 (2010).

[CAS](#) [PubMed](#) [Article](#) [Google Scholar](#)

39. 39.

Barad, B. A. et al. EMRinger: side chain-directed model and map validation for 3D cryo-electron microscopy. *Nat. Methods* **12**, 943–946 (2015).

[CAS](#) [PubMed](#) [PubMed Central](#) [Article](#) [Google Scholar](#)

40. 40.

Olsen, R. H. J. et al. TRUPATH, an open-source biosensor platform for interrogating the GPCR transducerome. *Nat. Chem. Biol.* **16**, 841–849 (2020).

[CAS](#) [PubMed](#) [PubMed Central](#) [Article](#) [Google Scholar](#)

41. 41.

Bond, S. R. & Naus, C. C. RF-Cloning.org: an online tool for the design of restriction-free cloning projects. *Nucleic Acids Res.* **40**, W209–W213 (2012).

[CAS](#) [PubMed](#) [PubMed Central](#) [Article](#) [Google Scholar](#)

42. 42.

Papasergi-Scott, M. M. et al. Structures of metabotropic GABA_B receptor. *Nature* **584**, 310–314 (2020).

[ADS](#) [CAS](#) [PubMed](#) [PubMed Central](#) [Article](#) [Google Scholar](#)

43. 43.

Isberg, V. et al. GPCRdb: an information system for G protein-coupled receptors. *Nucleic Acids Res.* **44** (D1), D356–D364 (2016).

[CAS](#) [PubMed](#) [Article](#) [Google Scholar](#)

44. 44.

Crooks, G. E., Hon, G., Chandonia, J. M. & Brenner, S. E. WebLogo: a sequence logo generator. *Genome Res.* **14**, 1188–1190 (2004).

[CAS](#) [PubMed](#) [PubMed Central](#) [Article](#) [Google Scholar](#)

[Download references](#)

Acknowledgements

We thank E. Montabana at the Stanford-SLAC cryo-EM facility for support with data collection and B. Kobilka for comments on the manuscript. This work was supported, in part, by R01 NS092695 (G.S. and J.M.M.) and a grant from the Mathers Foundation (G.S.); a Wellcome Trust Investigator Award (grant number 106995/Z/15/Z) (R.V.T); National Institute for Health Research (NIHR) Oxford Biomedical Research Centre Programme (R.V.T.); NIHR Senior Investigator Award (R.V.T.) (grant number NF-SI-0514–10091); T32-GM089626 (J.G.M.); and funding from the Faculty of Health and Medical Sciences (H.B.-O.).

Author information

Affiliations

1. Department of Molecular and Cellular Physiology, Stanford University School of Medicine, Stanford, CA, USA

Yang Gao, Michael J. Robertson, Alpay B. Seven, Chensong Zhang, Justin G. Meyerowitz, Ouliana Panova & Georgios Skiniotis

2. Department of Structural Biology, Stanford University School of Medicine, Stanford, CA, USA

Yang Gao, Michael J. Robertson, Alpay B. Seven, Chensong Zhang, Justin G. Meyerowitz, Ouliana Panova & Georgios Skiniotis

3. Department of Anesthesiology, Perioperative and Pain Medicine, Stanford University School of Medicine, Stanford, CA, USA

Justin G. Meyerowitz

4. Department of Drug Design and Pharmacology, Faculty of Health and Medical Sciences, University of Copenhagen, Copenhagen, Denmark

Sabrina N. Rahman, Hans Bräuner-Osborne & Jesper M. Mathiesen

5. Academic Endocrine Unit, Radcliffe Department of Medicine, University of Oxford, Oxford, UK

Fadil M. Hannan & Rajesh V. Thakker

6. Nuffield Department of Women's & Reproductive Health, University of Oxford, Oxford, UK

Fadil M. Hannan

Authors

1. Yang Gao

[View author publications](#)

You can also search for this author in [PubMed](#) [Google Scholar](#)

2. Michael J. Robertson

[View author publications](#)

You can also search for this author in [PubMed](#) [Google Scholar](#)

3. Sabrina N. Rahman

[View author publications](#)

You can also search for this author in [PubMed](#) [Google Scholar](#)

4. Alpay B. Seven

[View author publications](#)

You can also search for this author in [PubMed](#) [Google Scholar](#)

5. Chensong Zhang

[View author publications](#)

You can also search for this author in [PubMed](#) [Google Scholar](#)

6. Justin G. Meyerowitz

[View author publications](#)

You can also search for this author in [PubMed](#) [Google Scholar](#)

7. Ouliana Panova

[View author publications](#)

You can also search for this author in [PubMed](#) [Google Scholar](#)

8. Fadil M. Hannan

[View author publications](#)

You can also search for this author in [PubMed](#) [Google Scholar](#)

9. Rajesh V. Thakker

[View author publications](#)

You can also search for this author in [PubMed](#) [Google Scholar](#)

10. Hans Bräuner-Osborne

[View author publications](#)

You can also search for this author in [PubMed](#) [Google Scholar](#)

11. Jesper M. Mathiesen

[View author publications](#)

You can also search for this author in [PubMed](#) [Google Scholar](#)

12. Georgios Skiniotis

[View author publications](#)

You can also search for this author in [PubMed](#) [Google Scholar](#)

Contributions

Y.G. expressed and purified the proteins, prepared cryo-EM samples, collected and processed cryo-EM data, built and refined the structural models, designed the mutagenesis studies and generated the expression constructs. M.J.R. performed ligand docking and assisted in model refinement. S.N.R. performed IP₁ assays for profiling of allosteric modulators under the supervision of H.B.-O. A.B.S. assisted in data analysis. C.Z. assisted in cryo-EM data collection. J.G.M. performed the BRET assays and assisted in model refinement. O.P. assisted in cryo-EM data collection. F.M.H. and R.V.T. provided information on disease mutations and provided input in manuscript discussions. J.M.M. performed and analysed cellular signalling experiments. Y.G. and G.S. wrote the manuscript with input from J.G.M., R.V.T., F.M.H., H.B.-O, M.J.R. and J.M.M. G.S. supervised the project.

Corresponding authors

Correspondence to [Jesper M. Mathiesen](#) or [Georgios Skiniotis](#).

Ethics declarations

Competing interests

The authors declare no competing interests.

Additional information

Peer review information *Nature* thanks Alexandru Aricescu and the other, anonymous, reviewer(s) for their contribution to the peer review of this work. Peer reviewer reports are available.

Publisher's note Springer Nature remains neutral with regard to jurisdictional claims in published maps and institutional affiliations.

Extended data figures and tables

[Extended Data Fig. 1 Functional characterizations of human CaSR and structures of NAM-bound CaSR.](#)

a, size-exclusion chromatography profile of purified CaSR. **b**, BRET-based assay⁴⁰ monitoring G_q activation by CaSR upon Ca²⁺ addition. *n* = 3 independent experiments, data represent mean ± s.e.m. **c-f**, Functional responses of CaSR to Ca²⁺ alone or in combination with PAMs or NAM measured by IP₁ accumulation assays. *n* = 3 independent experiments, data represent mean ± s.e.m. **g**, Cryo-EM map and model of inactive state CaSR complexed with NAM. **h**, Cryo-EM map and model of the CaSR-NAM-Ca²⁺-Trp complex. **i**, Structure of the inactive-state CaSR ECD region showing an open-closed inactive VFT configuration.

[Extended Data Fig. 2 Cryo-EM data processing workflow.](#)

Representative cryo-EM micrographs of different CaSR complexes and flowcharts detailing data processing procedures.

[Extended Data Fig. 3 Cryo-EM maps and FSC curves of active-state CaSR complexes.](#)

a–d, Global and local refinement maps with corresponding FSC curves indicating nominal resolutions using the FSC = 0.143 criterion, model-vs-map FSC curves and local resolution maps of CaSR-etelecacetide-evocalcet (**a, b**) and CaSR-cinacalcet (**c, d**).

Extended Data Fig. 4 Cryo-EM maps and FSC curves of NAM-bound CaSR complexes.

a–d, Global and local refinement maps with corresponding FSC curves indicating nominal resolutions using the FSC = 0.143 criterion, model-vs-map FSC curves and local resolution maps of inactive-state CaSR (**a, b**) and CaSR-NAM-Ca²⁺-Trp (**c, d**).

Extended Data Fig. 5 Comparisons between CaSR cryo-EM structures and previous family C GPCR structures.

a, ECD from inactive-state CaSR cryo-EM structure with the loop tethering the opposing LB1 colored in red. **b**, ECD from inactive-state mGlu5 cryo-EM structure⁸ (PDB: 6N51). **c**, inactive-state CaSR ECD crystal structure⁶ (PDE: 5K5T). **d**, 7TMs from inactive-state CaSR cryo-EM structure (grey) superposed onto inactive CaSR ECD crystal structure based on CRD alignment. **e**, Comparison of inactive 7TMs orientations between CaSR and mGlu5. **f**, Active-state CaSR cryo-EM structure aligned with the active CaSR ECD crystal structure⁶ (grey, PDB: 5K5S) illustrating the difference in CRD orientations. **g**, Elongated densities observed at the TM6-TM6 interface in cryo-EM maps of active-state CaSR shown with TM6 residues forming the cholesterol-binding CARC motif. **h**, Sequence alignment logo showing the conservation of CARC motif residues among family C GPCRs (generated using alignment from GPCRdb⁴³ with WebLogo⁴⁴). **i**, Comparison of Ca²⁺ sites in active-state cryo-EM structures with Ca²⁺ sites in active CaSR ECD crystal structure (PDB: 5K5S)⁶. **j**, Alignment of the closed VFT protomer (dark blue) observed in our inactive-state CaSR structure with either the inactive open protomer (left, dark green) or the active closed protomer (right, light green). **k**, The tube shaped density observed in closed inactive CaSR VFT with L-Trp docked in. **l**, Crystal structure of open-closed mGlu1 VFTs¹³ (PDB: 1EWV).

Extended Data Fig. 6 PAM and NAM models and TM6-TM6 interfaces in cryo-EM densities.

a, Etelcalcetide model in cryo-EM density. **b**, Active-state CaSR TM6-TM6 interface model in cryo-EM density (shown here is CaSR-cinacalcet. The TM6-TM6 interface of CaSR-evocalcet-etelcalcetide is highly similar). **c**, Cinacalcet models in cryo-EM densities. **d**, Evocalcet models in cryo-EM densities. **e**, NAM model in cryo-EM density for the CaSR-NAM-Ca²⁺-Trp complex. **f**, CaSR-NAM-Ca²⁺-Trp complex TM6-TM6 interface model in cryo-EM density. **g**, Inactive-state NAM binding pocket. **h**, Inactive-state NAM model in cryo-EM density.

Extended Data Fig. 7 Binding modes of cinacalcet and evocalcet.

a, Interaction network in the CRD-ECL2-ECL3 region of cinacalcet-bound active-state CaSR. **b**, Chemical structures of evocalcet and cinacalcet. **c**, Structure of active-state CaSR 7TMs complexed with evocalcet. Similar to cinacalcet (Fig. 3a), evocalcet adopts an extended conformation in 7TM^A (green) and a bent conformation in 7TM^B (blue), making distinct interactions with the two protomers.

Extended Data Fig. 8 Cell surface expression levels and calcium response curves of various CaSR constructs.

a, Ca²⁺ response curves (left and middle panels) of the wild-type or Q681^{3,33}A mutant CaSR expressed at similar levels (plasma membrane expression levels shown on the right panel) in HEK293 cells in the absence or presence of the PAM cinacalcet or NAM NPS-2143 as monitored by IP₁ accumulation assays. Data represent mean ± s.e.m. from six independent experiments each performed in duplicate. **b**, Top three panels depict results from IP₁ accumulation assays monitoring the Ca²⁺ responses of the CaSR heterodimer without or with the PAM-binding deficient mutant E837A in both protomers. Middle and bottom left panels show results from cell surface ELISA assays verifying the different C1 and C2 construct

combinations yield similar expression levels of CaSR heterodimer at the plasma membrane. Bottom right panel shows the transfection with only one protomer containing either a C1 or C2 tail results in no IP₁ accumulation signals in response to stimulation with Ca²⁺. Functional IP₁ data represent mean ± s.e.m. from 5 independent experiments (top row) or 3 independent experiments (3rd row) each performed in duplicate, whereas cell surface ELISA data represent mean ± s.e.m. from 3 independent experiments performed in triplicate. **c**, Structural illustrations of how the introduced mutations would occlude extended or bent PAM conformations.

Extended Data Fig. 9 Ordered C terminus in CaSR and structural comparison between CaSR and mGlu2.

a, The ordered C terminus from the 7TM with a bent PAM (7TM^B) shown in cryo-EM densities with unsharpened maps. **b**, Asymmetric 7TMs in the active-state mGlu2 alone structure (accompanying manuscript). TM6 are shown as solid cartoon with representative residues shown as sticks to highlight the asymmetry. **c**, Superposition of the G protein-coupling 7TM (7TM^{GC}) from mGlu2-G_i complex structure (accompanying manuscript) onto the active-state CaSR 7TM with a straight PAM (7TM^A) showing that the G protein would fit well on the membrane plane and the tilt of CaSR 7TM^B leads to the sequestration of its C terminus in the membrane. The comparison between mGlu 7TM^{GC} and CaSR 7TM^A illustrates that the receptor likely would couple to G proteins through downward extensions of both ICL2 and C terminus.

Extended Data Fig. 10 Schematic of CaSR activation mechanism.

In the inactive state, CaSR is relatively flexible and the 7TMs are separated facing each other at the TM5-TM6 plane. The VFTs adopt inactive open-open/closed conformations. The open-closed conformation can be stabilized by aromatic amino acids (AAs) or their derivatives, thus priming the receptor for activation. NAM binds at both 7TMs with the same conformation and locks the TM6 toggle switch in an inactive conformation.

Under high Ca²⁺ and high Trp conditions, the ECD adopts a closed-closed active conformation, while the presence of the NAM prevents the 7TMs from adopting the active asymmetric configuration. Upon activation by high Ca²⁺ concentration, the VFTs adopt an active closed-closed conformation, which is stabilized by L-Trp bound at the cleft of each VFT and the ECD PAM etelcalcetide further stabilizes the interface between LB2 of the closed-closed VFTs. Closure of the VFTs leads to rearrangement of the CRDs, bringing the 7TMs together to form an asymmetric TM6-TM6 interface. The asymmetric configuration is stabilized by 7TM PAMs adopting distinct poses. The 7TM with a bent PAM is more tilted than the opposing 7TM with its C terminus sequestered in the membrane, and likely unable to couple to G protein.

Extended Data Table 1 Cryo-EM data collection, refinement and validation statistics.

[Full size table](#)

Supplementary information

[Reporting Summary](#)

[Peer Review File](#)

[Video 1](#)

: Inactive-state CaSR 3D variability analysis component 1. Particles of inactive-state CaSR were subjected to 3D variability analysis. This video illustrates the motions corresponding to the first principal component revealed by the analysis.

[Video 2](#)

: Inactive-state CaSR 3D variability analysis component 2. Particles of inactive-state CaSR were subjected to 3D variability analysis. This video illustrates the motions corresponding to the second principal component revealed by the analysis.

Video 3

: Inactive-state CaSR 3D variability analysis component 3. Particles of inactive-state CaSR were subjected to 3D variability analysis. This video illustrates the motions corresponding to the third principal component revealed by the analysis.

Video 4

: Active-state CaSR 3D variability analysis component 1. Particles of active-state CaSR complexed with etelcalcetide and evocalcet were subjected to 3D variability analysis. This video illustrates the motions corresponding to the first principal component revealed by the analysis.

Video 5

: Active-state CaSR 3D variability analysis component 2. Particles of active-state CaSR complexed with etelcalcetide and evocalcet were subjected to 3D variability analysis. This video illustrates the motions corresponding to the second principal component revealed by the analysis.

Video 6

: Active-state CaSR 3D variability analysis component 3. Particles of active-state CaSR complexed with etelcalcetide and evocalcet were subjected to 3D variability analysis. This video illustrates the motions corresponding to the third principal component revealed by the analysis.

Rights and permissions

[Reprints and Permissions](#)

About this article



Check for
updates

Cite this article

Gao, Y., Robertson, M.J., Rahman, S.N. *et al.* Asymmetric activation of the calcium-sensing receptor homodimer. *Nature* **595**, 455–459 (2021).
<https://doi.org/10.1038/s41586-021-03691-0>

Download citation

- Received: 23 December 2020
- Accepted: 03 June 2021
- Published: 30 June 2021
- Issue Date: 15 July 2021
- DOI: <https://doi.org/10.1038/s41586-021-03691-0>

Further reading

- [G-protein activation by a metabotropic glutamate receptor](#)
 - Alpay B. Seven
 - , Ximena Barros-Álvarez
 - , Marine de Lapeyrière
 - , Maka Å M. Papasergi-Scott
 - , Michael J. Robertson
 - , Chensong Zhang
 - , Robert M. Nwokonko
 - , Yang Gao
 - , Justin G. Meyerowitz
 - , Jean-Philippe Rocher
 - , Dominik Schelshorn

- , Brian K. Kobilka
- , Jesper M. Mathiesen
- & Georgios Skiniotis

Nature (2021)

Comments

By submitting a comment you agree to abide by our [Terms](#) and [Community Guidelines](#). If you find something abusive or that does not comply with our terms or guidelines please flag it as inappropriate.

[Access through your institution](#)

[Change institution](#)

[Buy or subscribe](#)

Advertisement

This article was downloaded by **calibre** from <https://www.nature.com/articles/s41586-021-03691-0>

| [Section menu](#) | [Main menu](#) |

Nature Outlook